



**Tailoring Ru(II) and Os(II) Luminophores to their application:  
from bioimaging and sensing to cytotoxic tools.**

**Karmel Sofia Gkika, B.Sc. (Hons)**

A thesis submitted for the award of Ph.D.

Supervisor: Prof. Tia E. Keyes


School of Chemical Sciences,

Dublin City University

September 2021

## Declaration

I hereby certify that this material, which I now submit for assessment on the programme of study leading to the award of Doctor of Philosophy (PhD) is entirely my own work, and that I have exercised reasonable care to ensure that the work is original, and does not to the best of my knowledge breach any law of copyright, and has not been taken from the work of others save and to the extent that such work has been cited and acknowledged within the text of my work.

Signed:  \_\_\_ ID No: 16213651 \_\_\_ Date: 01/09/21 \_\_\_

*My PhD thesis is dedicated to my parents,*

*Zacharias Gkikas and Mary Fox.*

*Η διδακτορική μου διατριβή είναι αφιερωμένη στους γονείς μου,*

*Ζαχαρίας Γκίκας και Μαίρη Φοξ.*

## Acknowledgements

Firstly, I would like to express my gratitude to my supervisor, Prof. Tia Keyes. Thank you for giving me the opportunity to complete my PhD studies as part of your research group and for offering a wealth of guidance, knowledge, and support.

I would like to extend my gratitude to those with whom I had the opportunity to collaborate with: Prof. A. Heise, Prof. J. Rusling, Assist. Prof. N. Walsh, Dr. A. Kaargard, Dr. Nipuni, S. Noorani, Dr. A. Byrne, Dr. C. S. Burke, and D. Cullinane.

I would like to thank Prof. Zoe Pikramenou and Assoc. Prof. Andrew Kellett for dedicating time to read my PhD thesis and for offering their valuable insight and comments at the viva examination.

The Irish Research Council (GOIPG/2016/702) and Science Foundation Ireland (19/FFP/6428, 14/IA/2488 and 18/TIDA/5862) are gratefully acknowledged for supporting the research work carried out.

I would like to thank all the technical staff in the School of Chemical Sciences: John, Vinny, Veronica, Damien, Ambrose, Mary R., Mary T., and Catherine. Each of you has *saved my day* many times throughout these years and I will forever be grateful for it. Sincere thanks also to the staff in the NRF for their training and support. Many thanks also to Gillian S. in NICB and Katarina M. in FPC. I wish to also thank Barry Byrne for his expertise on project management and biosafety and for his ongoing support.

Thank you to all past and present members of the Keyes's Research group for their support. Whether it was troubleshooting an experiment, a long conversation over coffee, or a simple good morning, each of you brought something positive in my everyday life at DCU.

Thank you to Aisling Byrne for introducing me to cell culture and imaging and for sharing your knowledge in the field.

Many thanks to Chris Burke! The first few months of my PhD would not have gone as smoothly as they did, had it not been for your support (*and patience*). Thank you for offering your advice on so many topics and for always sharing your knowledge on what happens *in the ruthenium case*.

Thank you Shane M. for all the coffees and for your help with cell culture lab management, especially during the pandemic!

Thank you to my wonderful friends for our heartfelt conversations, for making me laugh, for all our shared quotes and songs and for all our moments that filled me with happiness throughout these years. To my dearest Lingli thank you for everything you have taught me since the day we met and for encouraging and supporting me every step of the way.

“Θα ήθελα να ευχαριστήσω τον κ. Γιώργο και την κα. Βασιλική για όλη την αγάπη και την στήριξη που μου έχουν προσφέρει.

Ευχαριστώ στον Άρη μου, στον άνθρωπο μου. Το να είμαι δίπλα σου είναι απο μόνο του ευτυχία και έμπνευση. Σε ευχαριστώ για τα πάντα.



Ευχαριστώ σε όλους τους συγγενείς μου που βρίσκονται στην Ελλάδα, Ιρλανδία και στο εξωτερικό για την στήριξη και για όλες τις ευχές τους.

Ευχαριστώ τον αδερφό μου Δημήτρη Γκίκα για την στήριξη του όλα αυτά τα χρόνια.

Ευχαριστώ τον μπαμπά μου Ζαχαρία Γκίκα για όλη την αγάπη και την στήριξη που μου έχει δώσει για να κυνηγήσω τα όνειρά μου. Εσύ μου έμαθες να γράφω, να σκέφτομαι και να λύνω προβλήματα. Μα πάνω απ'όλα, εσύ μου έμαθες την σημασία του να δουλεύω για να δημιουργήσω.”

“ I would like to thank Mr. George and Ms. Vasiliki for all their love and support.

Thank you to my Ares, my person. To be next to you is in itself happiness and inspiration. Thank you for everything.

Thank you to all my family in Greece, Ireland and abroad for their support and for all their wishes.

Thank you to my brother, Dimitris Gkikas for all his support throughout the years.

Thank you to my dad, Zacharias Gkikas for all the love and support he has given in order for me to chase my dreams. You taught me how to write, think, and solve problems. Above all you taught me the meaning of working with the purpose to create.”

Thank you also to my dear Grandad for always supporting me throughout my studies and for always making me smile.

Thank you to my Rose for your huge amount of support and constant supply of hugs and motivation. You are more than my aunt; you are my everything person and I am forever grateful for you.

*My mum, you taught me strength, persistence and how to always believe in tomorrow.*

*You said I could do it and you were right,*

*I did it !*

## Research Outcomes

### Publications

- 
- 2021 **Gkika K. S.**, Kargaard A., Burke C. S., Dolan C., Heise A., Keyes T. E., *Ru(II)/BODIPY core co-encapsulated ratiometric nanotools for intracellular O<sub>2</sub> sensing in live cancer cells*, *Chem. Biol.*, 2021, published online.
- 2021 **Gkika K. S.**, Noorani S., Walsh N., Keyes T.E., *Os(II)-Bridged Polyarginine Conjugates: The Additive Effects of Peptides in Promoting or Preventing Permeation in Cells and Multicellular Tumor Spheroids*, *Inorg. Chem.*, 2021, **60**, 8123.
- 2020 Finn S., Byrne A., **Gkika K. S.** and Keyes T. E., *Photophysics and Cell Uptake of Self-Assembled Ru(II) Polypyridyl Vesicles*, *Front. Chem.*, 2020, **8**, 638
- 2020 Kankanamage RNT, Ghosh AB, Jiang D, et al. *Metabolites of Tobacco- and E-Cigarette-related Nitrosamines Can Drive Cu<sup>2+</sup>-mediated DNA Oxidation*, *Chem. Res. Toxicol.* 2020, 33, **8**, 2072–2086.
- 2020 Cullinane D., **Gkika K. S.**, Byrne A., Keyes T. E., *Photostable NIR emitting ruthenium(II) conjugates; uptake and biological activity in live cells*, *J. Inorg. Biochem.*, 2020, 111032.
- 2019 **Gkika K. S.**, Byrne A., Keyes T. E. *Mitochondrial targeted osmium polypyridyl probe shows concentration dependent uptake, localisation and mechanism of cell death*, *Dalton Trans.*, 2019, **48**, 17461. *Featured as the Front Cover of Dalton Transactions.*
- 

### Awards and Achievements

- 
- 2020 Highly commended for the “Irish Biological Inorganic Chemistry Society (IBICS) Postgraduate Gold Medal Award”.
- 2020 DCU Colin Barnes Award for Postgraduate Research Excellence.
- 2019 First author publication featured as the front cover of Dalton Transactions.
- 2019 First prize for poster presentation at DCU Chemistry Research Day.
- 2016 Irish Research Council Postgraduate Scholarship [GOIPG/2016/702].
-

## Conference Presentations

---

- 2021 **Inorganic Ireland** Symposium, **Oral presentation**, “*Osmium(II) Bridged Polyarginine Conjugates: from 2D cell imaging to in depth penetration of 3D multicellular tumor spheroids*”. (Zoom – NUI, Ireland)
- 2020 **IBICS-4**, Irish Biological Inorganic Chemistry Symposium, **Oral presentation**, “*Mitochondrial Targeted Osmium Polypyridyl Probe Shows Concentration Dependent Uptake, Localisation and Mechanism of Cell Death*”. (Zoom – RCSI, Ireland)
- 2020 Chemistry Research Day, **Oral presentation**, “*Ru(II)/BODIPY ratiometric oxygen-sensing nanotools*”. *Colin Barnes Award* (Zoom – DCU, Ireland)
- 2019 **23<sup>rd</sup> ISPPCC** International Symposium on the Photochemistry and Photophysics of Coordination Compounds, **Poster**, “*NIR Osmium(II) polypyridyl probe with a therapeutic twist: disrupting the mitochondrial membrane potential for targeted therapy.*” (CityU, Hong Kong)
- 2019 **Irish Universities** Chemistry Research Colloquium, **Poster**, “*NIR Osmium(II) polypyridyl probe with a therapeutic twist: disrupting the mitochondrial membrane potential for targeted therapy.*” Representing DCU School of Chemical Sciences. (TU Dublin, Ireland)
-

## Thesis Outline

### Chapter 1

Chapter 1 introduces the background to the thesis presented. Transition metal complexes with favourable photophysical properties and flexible design have shown great potential as multifunctional probes with applications in many fields extending from medicinal chemistry to bioimaging and biosensing. Conjugation of Ru(II)/ Os(II) luminophores to signal peptides has shown to successfully deliver the probes intracellularly and to specific organelles with complex membrane structures such as the nucleus and mitochondria. While conventional luminescence microscopy methods are used for cellular-imaging, luminescence biosensing, can range from simple fluorescence intensity-based measurements using a plate reader to fluorescence lifetime imaging microscopy (FLIM). Necessary to their application is achieving a balance between the desired photophysical properties and biocompatibility of the probes.

### Chapter 2

Chapter 2 presents a series of novel photostable Ru(biq)<sub>2</sub>(trzbenzCOOH)-conjugates (NLS,R8,MPP,PEG) studied in CHO and HeLa cell lines. The peptide-conjugates showed counterion-dependent permeability and high dark cytotoxicity, the origin of which is studied in detail using mitochondrial depolarization and polycaspase activity assays. This work demonstrates the importance of *striking a balance* between counterion selection, lipophilicity and targeting ability in order to promote uptake but reduce overall probe toxicity.

### Chapter 3

Chapter 3 describes an achiral Os(II) complex, [Os(tpybenzCOOH)<sub>2</sub>]<sup>2+</sup> conjugated to the mitochondrial targeting peptide, MPP, at two conjugation sites. The novel bis-MPP conjugate showed NIR emission coincident with the biological window and an interesting approach to theranostics was proposed whereby switch in cell death mechanism (dark toxicity) is reflected by specific probe delocalisation observed via confocal microscopy.

### Chapter 4

Chapter 4 extends the work from Chapter 3 by describing the preparation of polyarginine conjugates of the achiral Os(II) complex and their application as luminophore probes for imaging of 2D and 3D cell models. Comparative studies between [Os-(R<sub>4</sub>)<sub>2</sub>]<sup>10+</sup> and [Os-


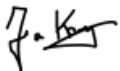
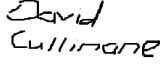
$(R_8)_2^{18+}$  showed that cell permeability can be promoted via non-contiguous sequences of arginine residues, but it is sequence dependent. The bis-R4 conjugate showed uptake in 2D cells and in multicellular spheroids, in-depth penetration was observed with no evidence of cytotoxicity rendering it suitable for 3D cell culture imaging.

## **Chapter 5**

Chapter 5 presents the preparation and characterization of novel self-referenced ratiometric Ru(II)/ BODIPY nanoparticles. Single excitation at 480 nm resulted in dual emission corresponding to the BODIPY and Ru(II) particle component. The poly-L-lysine coated particles were studied in two cancerous cell lines as oxygen sensors. The cells were exposed to hypoxic conditions and the response of the particles was monitored using a plate reader-based assay and xy-lambda ( $xy\lambda$ ) scanning microscopy.

## Author Contribution to Publications

Chapter	Title	Publication Status	Authors	Contribution by Candidate
2	Photostable NIR emitting ruthenium(II) conjugates; uptake and biological activity in live cells.	<i>J Inorg. Biochem.</i> , 2020, <b>207</b> , 111032.	Cullinane D., <b>Gkika K. S.</b> , Byrne A., Keyes T. E.	Co-author of manuscript with David Cullinane. Carried out MitoPT TMRE and Caspase FAM-FLICA assays, Rubiq-PEG cytotoxicity (Alamar Blue assay), Ru biq-NLS/FAM-FLICA imaging using confocal microscopy and IC <sub>50</sub> determination.
3	Mitochondrial targeted osmium polypyridyl probe shows concentration dependent uptake, localisation and mechanism of cell death.	<i>Dalton Trans.</i> , 2019, <b>48</b> , 17461	<b>Gkika K. S.</b> , Byrne A., Keyes T. E.	Manuscript primary author. Primary contributor to experimental design and execution.
4	Os(II)-Bridged Polyarginine Conjugates: The Additive Effects of Peptides in Promoting or Preventing Permeation in Cells and Multicellular Tumor Spheroids	<i>Inorg. Chem.</i> , 2021, <b>60</b> , 8123-8134.	<b>Gkika K. S.</b> , Noorani S., Walsh N., Keyes T. E.	Manuscript primary author. Primary contributor to experimental design and execution.
5	Ru(II)/BODIPY core co-encapsulated ratiometric nanotools for intracellular O <sub>2</sub> sensing in live cancer cells	<i>Chem.Biol.</i> , 2021; <i>Published online.</i>	<b>Gkika K. S.</b> , Kargaard A., Burke C., Dolan C., Heise A., Keyes T. E.	Manuscript primary author. Co-contributor to experimental design and execution. Carried out preparation of the Ru(II) parent complex, characterization of the NPs and biological studies.

Signed:			
	_____ Candidate	_____ Principal Investigator	_____ Co-author
	ID No: 16213651	Date: 01/09/21	Date: 01/09/21
	Date: 01/09/21	Date: 01/09/21	Date: 01/09/21

## Table of Contents

<b>Declaration</b> .....	<b>ii</b>
<b>Acknowledgements</b> .....	<b>iv</b>
<b>Research Outcomes</b> .....	<b>vi</b>
<b>Publications</b> .....	<b>vi</b>
<b>Awards and Achievements</b> .....	<b>vi</b>
<b>Conference Presentations</b> .....	<b>vii</b>
<b>Thesis Outline</b> .....	<b>viii</b>
<b>Author Contribution to Publications</b> .....	<b>x</b>
<b>Table of Contents</b> .....	<b>xi</b>
<b>Table of Figures</b> .....	<b>xvii</b>
<b>Table of Schemes</b> .....	<b>xxxiv</b>
<b>Table of Tables</b> .....	<b>xxxv</b>
<b>Abbreviations</b> .....	<b>xxxv</b>
<b>Units of measurement</b> .....	<b>xxxvii</b>
<b>Thesis Abstract</b> .....	<b>1</b>
<b>Chapter 1: Introduction</b> .....	<b>2</b>
1.1 Photophysical characteristics of a good luminophore for bioimaging .....	<b>2</b>
1.1.1 Principles of photophysics .....	<b>3</b>
1.1.2 Tuning of photophysical properties of metal complexes .....	<b>6</b>
1.2 Microscopy Techniques .....	<b>9</b>
1.2.1 Confocal Laser Scanning Microscopy (CLSM) .....	<b>9</b>
1.2.2 Fluorescence/Phosphorescence Lifetime Imaging (FLIM/PLIM).....	<b>11</b>
1.3 Cellular uptake and accumulation .....	<b>15</b>
1.3.1 Mechanisms of cellular and subcellular uptake .....	<b>15</b>
1.3.2 Strategies for uptake of metal complexes .....	<b>17</b>
1.4 Metal complexes as luminescent imaging/sensing probes and therapeutic agents ...	<b>27</b>

1.4.1	Mitochondrial targeted complexes.....	33
1.5	Oxygen sensing .....	40
1.5.1	The ratiometric approach: from molecular dyads to nano-sensors.....	42
1.5.2	Molecular oxygen sensing in 3D cell models .....	45
1.6	Conclusions .....	48
1.7	References .....	49
	<b>Chapter 2: Photostable NIR emitting ruthenium(II) conjugates; uptake and biological activity in live cells.....</b>	<b>66</b>
2.1	Abstract .....	67
2.2	Introduction .....	67
2.3	Experimental .....	70
2.3.1	Materials .....	70
2.3.2	Instrumentation .....	70
2.3.3	Synthesis .....	71
2.3.4	Photophysical Measurements.....	74
2.3.5	Cyclic voltammetry.....	74
2.3.6	Cell Culture.....	75
2.3.7	Cytotoxicity studies .....	75
2.3.8	Confocal microscopy: RuNLS.....	75
2.3.9	Caspase Activity .....	76
2.3.10	Mitochondrial Depolarization Assay .....	77
2.4	Results and discussion.....	77
2.4.1	Synthesis and characterisation .....	77
2.4.2	Photophysics and electrochemistry .....	78
2.4.3	Photostability .....	81
2.4.4	Counterion selection .....	81
2.4.5	Cell Imaging.....	82



2.4.6	Cytotoxicity studies .....	83
2.4.7	Cell death mechanism: caspase activation and loss of $\Delta\Psi_m$ .....	85
2.5	Conclusions .....	90
2.6	Supporting Material.....	90
2.7	References .....	90
<b>Chapter 3: Mitochondrial targeted osmium polypyridyl probe shows concentration dependent uptake, localisation and mechanism of cell death. ....</b>		<b>95</b>
3.1	Abstract .....	96
3.2	Introduction .....	96
3.3	Materials and Methods .....	98
3.3.1	Materials .....	98
3.3.2	Instrumentation .....	99
3.3.3	Preparation of 4-(4-carboxyphenyl)-2,2':6,2''-terpyridine, (tpybenzCOOH) ....	99
3.3.4	Preparation of $[\text{Os}(4-(4\text{-carboxyphenyl})-2,2':6,2\text{-terpyridine})_2][\text{PF}_6]_2$ , $[\text{Os}(\text{tpybenzCOOH})_2][\text{PF}_6]_2$ .....	100
3.3.5	Preparation of Os(II) bis-peptide conjugates .....	100
3.3.6	Photophysical Methods .....	101
3.3.7	Cyclic Voltammetry .....	101
3.3.8	Cell culture.....	102
3.3.9	Cytotoxicity.....	102
3.3.10	Confocal luminescent Imaging .....	102
3.3.11	Mitochondrial Depolarization Assay .....	102
3.3.12	Caspase Activity .....	103
3.4	Results and discussion.....	104
3.4.1	Synthesis .....	104
3.4.2	Photophysics and Electrochemistry .....	105
3.4.3	Cell Uptake studies .....	107
3.4.4	$\text{Os}^{\text{II}}$ MPP : Co- localization with MitoTracker Deep Red in live HeLa cells ..	109

3.4.5	Os <sup>II</sup> MPP cytotoxic effects: photo-induced or intracellular triggered process?	110
3.4.6	Mitochondrial depolarization assay (Mito PT TMRE) and Caspase Activity	112
3.4.7	Caspase Activation assay	114
3.5	Conclusions	115
3.6	Supporting Material	116
3.7	References	116

**Chapter 4: Os(II)-Bridged Polyarginine Conjugates: The Additive Effects of Peptides in Promoting or Preventing Permeation in Cells and Multicellular Tumor Spheroids. .... 120**

4.1	Abstract	121
4.2	Introduction	121
4.3	Experimental	125
4.3.1	Materials	125
4.3.2	Instrumentation	125
4.3.3	Synthesis	125
4.3.4	Photophysical Measurements	126
4.3.5	Monolayer cell and 3D spheroid cell cultures	127
4.3.6	Cytotoxicity studies	127
4.3.7	Confocal laser scanning microscopy (CLSM)	127
4.3.8	Phototoxicity	128
4.3.9	Spheroid Treatment with Os-compounds	128
4.3.10	Preparation of fixed spheroid sections	128
4.3.11	Confocal microscopy of HPAC spheroids	129
4.3.12	Evaluation of spheroid viability	129
4.3.13	Phosphorescence Lifetime Imaging Microscopy (PLIM)	129
4.4	Results and Discussion	129

4.4.1	Preparation and Characterization of the bis-tetra and bis- octa arginine Os(II) conjugates.....	129
4.4.2	Uptake studies of [Os-(R <sub>n</sub> ) <sub>2</sub> ] <sup>x+</sup> conjugates .....	131
4.4.3	Confocal imaging of HPAC spheroids .....	136
4.5	Conclusions .....	141
4.6	Supporting Material.....	141
4.7	References .....	142
	<b>Chapter 5: Ru(II)/BODIPY core co-encapsulated ratiometric nanotools for intracellular O<sub>2</sub> in live cancerous cells.....</b>	<b>146</b>
5.1	Abstract .....	147
5.2	Introduction .....	147
5.3	Experimental .....	151
5.3.1	Materials .....	151
5.3.2	Synthesis .....	151
5.3.3	Instrumentation .....	153
5.3.4	Oxygen Calibration Studies .....	154
5.3.5	Plate reader-based ratiometric O <sub>2</sub> response assay.....	154
5.3.6	Cell Culture.....	154
5.3.7	RuBDP NP uptake .....	155
5.3.8	Cytotoxicity assay.....	155
5.3.9	Co-localisation studies .....	155
5.4	Results and discussion.....	156
5.4.1	Synthesis .....	156
5.4.2	Photophysical Characterisation of RuBDP nanoparticles.....	158
5.4.3	Cell Studies .....	161
5.4.4	Uptake studies in live HeLa, CHO and A549 cell line .....	161
5.4.5	Cytotoxicity.....	164
5.4.6	Uptake mechanism and co-localization studies .....	166

5.4.7	Ratiometric response in induced hypoxic conditions .....	167
5.5	Conclusions .....	169
5.6	Supporting Material.....	170
5.7	References .....	170
	<b>Chapter 6: Conclusions and Future Perspectives.....</b>	<b>177</b>
<b>Appendices A-D</b>		
	<b>Appendix A.....</b>	<b>A1</b>
S2.1	Materials and Instrumentation. ....	A1
S2.2	Synthesis and structural characterisation. ....	A2
S2.2.1	Characterisation data. ....	A2
S2.2.2	HPLC Chromatograms of parent complex and conjugates .....	A15
S2.3	Photophysical Data .....	A17
S2.4	Cellular Studies .....	A18
S2.5	Mass Spectrometry of peptide sequences .....	A19
S2.6	FAM-VAD-FLICA caspase activity assay .....	A21
	<b>Appendix B.....</b>	<b>B1</b>
S3.1	<sup>1</sup> H NMR spectra of tpybenzCOOH and Os(II) complexes .....	B1
S3.2	Mass Spectrometry Analysis.....	B5
S3.3	HPLC Analysis of parent and conjugate Os(II) complex .....	B9
S3.4	Spectroscopic Measurements of Os(II) parent complex and Os(II) conjugate .....	B11
S3.5	Emission Decays of Os(II) parent and Os <sup>II</sup> MPP complex – Time- correlated single photon counting (TCSPC) measurements using NanoHarp 2.1, FluoTime100 (PicoQuant) and mono-exponentially fitted using PicoQuant Fluofit software. ....	B13
S3.6	Cytotoxicity Studies and determination of IC <sub>50</sub> of Os <sup>II</sup> MPP.....	B16
S3.7	Confocal Imaging.....	B17
S3.8	Polycaspase FAM-FLICA and MitoPT TMRE Assay .....	B20
	<b>Appendix C.....</b>	<b>C1</b>
S4.1	NMR Analysis .....	C1

S4.2 Mass Spectrometry.....	C4
S4. 3 RP-HPLC Analysis .....	C5
S4.4 Photophysical studies.....	C6
S4.5 Cell studies.....	C10
S4.5.1 Confocal images 2D cell monolayers.....	C10
S4.5.2 Cytotoxicity assay .....	C14
S4.5.3 Luminescence Lifetime Imaging.....	C15
S4.5.4 3D Multicellular pancreatic spheroids .....	C17
<b>Appendix D.....</b>	<b>D1</b>
S5.1 Synthesis and characterization .....	D1
S.5.1.1 Synthesis of ruthenium intermediate compounds and NPs .....	D1
S.5.1.1.2 NMR and Mass Spectrometry Analysis .....	D2
S.5.1.2 RuBDP NPs: SEM and DLS Characterization.....	D9
S.5.1.3 Photophysical Characterisation of RuBDP components and nanoparticles.....	D10
S5.2 Cell Studies .....	D15
S5.2.1 Uptake studies .....	D15
S5.2.2 Oxygen mapping .....	D24
S5.2.2 Plate reader-based ratiometric O <sub>2</sub> response assay .....	D25
S5.3 References.....	D26

## Table of Figures

<b>Figure 1.1</b> Jablonski Diagram collectively illustrating the photophysical phenomena upon photon absorption (adapted from reference). <sup>8</sup> .....	4
<b>Figure 1.2</b> Molecular orbital diagram for ML <sub>6</sub> complexes in O <sub>h</sub> symmetry (σ-bonding). The frontier orbitals (d-metal and π-ligand orbitals) are highlighted. Possible electronic transitions include: (1) ligand centred (LC) , (2) meta- to-ligand charge transfer (MLCT), (3) ligand-to-metal charge transfer and (4) metal centred (MC).....	7

<b>Figure 1.3</b> Schematic representation of the potential energy surface diagrams of $[\text{Ru}(\text{bpy})_3]^{2+}$ and $[\text{Os}(\text{bpy})_3]^{2+}$ describing key photophysical processes and illustrating greater separation of $^3\text{MC}$ from $^3\text{MLCT}$ in the case of Os(II) complexes preventing thermally activated crossing between the states as opposed to $[\text{Ru}(\text{bpy})_3]^{2+}$ . .....	8
<b>Figure 1.4</b> Diagram of a confocal microscope optical set up.....	10
<b>Figure 1.5</b> Time-correlated single photon counting principle. The arrival of single photons following excitation are detected with respect to the laser pulse and the histogram of the detection times (i.e., the waveform of the optical pulse) is constructed. Adapted from <sup>37</sup> .....	12
<b>Figure 1.6</b> FLIM images of <b>RuBODIPY</b> nanoparticles in live CHO cells where the lifetime mapping of (A) encapsulated phen-Ar-BODIPY-Br <sub>2</sub> and (B) surface-bound $[\text{Ru}(\text{bpy})_2(\text{phen-Ar-COOH})]^{2+}$ are shown. <sup>45</sup> .....	13
<b>Figure 1.7</b> Autofluorescence-free imaging of skin tissue samples. (a) Intensity image of unlabelled samples at i) 0-50 ns and ii) > 50 ns and (b) time-gated images of tissue labelled with <b>PtL<sup>1</sup>Cl</b> where i) intensity image acquired at higher spatial resolution and ii) the corresponding lifetime distribution. <sup>46</sup> .....	14
<b>Figure 1.8</b> Schematic illustration of the potential mechanisms by which molecules can enter cells (adapted from reference). <sup>55</sup> Passive and facilitated diffusion are energy-dependent processes whereas active transport and endocytosis are energy-independent. Here, receptor-mediated endocytosis is shown as an example of an endocytic pathway. ....	16
<b>Figure 1.9</b> Cellular staining of A549 cells following uptake of the positively charged and lipophilic $[\text{Ru}(\text{dip})_3]^{2+}$ complex (left) or the anionic $[\text{Ru}((\text{SO}_3)_2\text{-dip})_3]^{4-}$ (right). Incorporation of six sulfonic acids ( $\text{SO}_3^-$ ) into the dip ligands altered the subcellular localization properties of the complex rendering it mitochondrial excluding. Here, Ru(II) emission is shown in red and Mitotracker Green FM (in green) and Hoechst (in blue) are used as co-staining dyes to visualize the mitochondria and nucleus (adapted from reference) <sup>30</sup> .....	20
<b>Figure 1.10</b> Key ligands used as building blocks for the design of metal complexes. ....	22
<b>Figure 1.11</b> Confocal luminescence imaging of live mammalian cells incubated with octaarginine conjugates of Ir(III), Ru(II) and Os(II). A) Ir-R8 in CHO cells at 70 $\mu\text{M}$ / 15 min incubation , B) Ru-R8 in HeLa cells at 70 $\mu\text{M}$ / 4 h incubation and C) Os-R8 in CHO cells at 70 $\mu\text{M}$ / 2 h incubation in the absence of light at 37 °C. <sup>16,130,131</sup> .....	24
<b>Figure 1.12</b> Chemical structures of NLS-driven nuclear targeting Ru(II) complexes and representative images of their corresponding application in mammalian cells. A) $[\text{Ru}(\text{bpy})_2(\text{pic-NLS})]^{6+}$ and $[\text{Ru}(\text{dpp})_2(\text{pic-NLS})]^{6+}$ showed nuclei and nucleolus staining respectively. <sup>29</sup> B) Confocal (i) and STED (ii) images of $[\text{Ru}(\text{dppz})(\text{bpy})(\text{bpy-Ar-NLS})]^{6+}$	

nuclear and chromosomal DNA staining.<sup>130</sup> C) Following DNA binding of **Ru-TAP-NLS** in live HeLa cells, continuous photoirradiation of selected cells resulted in cellular damage as indicated by DRAQ 7 nuclear staining in blue.<sup>148</sup> .....26

**Figure 1.13** Distribution of **Ru(dppz)-RrRK** in HeLa cells. Confocal imaging showed cytoplasmic and nuclear staining of cells treated with 100  $\mu$ M for 2 h. Scale bar = 10  $\mu$ M. <sup>154</sup> .....28

**Figure 1.14** Confocal images of iridium complexes **[Ir(N<sup>^</sup>C)<sub>2</sub>(phenSe)]<sup>+</sup> (**8-11**) illustrating green, yellow, orange and red phosphorescence respectively. <sup>181,185</sup> .....30**

**Figure 1.15** Chemical structure of **OsIr** dinuclear complex and confocal images of uptake in MCF-7 cells. Following 1 h incubation at 37 °C, cytoplasmic staining is evident by the dual emission corresponding to the iridium (green) and osmium (red) channel. Nucleus staining was observed at 2 h incubation. The luminescence intensity profile at cytoplasmic and nucleolus regions revealed extensive accumulation **OsIr** in cells. <sup>202</sup> .....31

**Figure 1.16** Phosphorescence lifetime imaging of (A) **[Os(bpy)<sub>2</sub>(pic-R8)]<sup>10+</sup>** (70  $\mu$ M / 24 h) and (B) **[Ru(bpy)<sub>2</sub>(pic-R8)]<sup>10+</sup>** (350  $\mu$ M/ 15 min) in live SP2 cells. The false colour images and intensity mapping highlight the differences in emission lifetime of the luminophore pending on its localization in the cell. The emission lifetime of the osmium(II) conjugate was 18.8  $\pm$  0.6 ns at the cell membrane and 14.5  $\pm$  0.5 ns in the cytoplasm. <sup>131</sup> .....32

**Figure 1.17** Chemical structures of **[Os(pytz)<sub>3</sub>]<sup>2+</sup>** luminophore and confocal images showing the distribution of the complex (yellow) in EJ bladder carcinoma cells. **[Os(pytz)<sub>3</sub>]<sup>2+</sup>** (yellow) was found localize in endosomes and lysosomes. Scale bar = 20  $\mu$ m. <sup>206</sup> .....33

**Figure 1.18** Luminescence lifetime imaging of **[(Ru(bpy)<sub>2</sub>)<sub>2</sub>(phen-MPP-phen)]<sup>7+</sup>** in live HeLa cells, in response to Antimycin A treatment. PLIM was carried out following (A) incubation with Ru(II) conjugate at 70  $\mu$ M for 2 h in the absence of light, and treatment with Antimycin A (200  $\mu$ g/ mL) for (B) 10 min and (C) 100 min. <sup>152</sup> .....35

**Figure 1.19** Precision targeted **[Ru(dppz)(bpy)(bpy-Ar-MPP)]<sup>5+</sup>** (10  $\mu$ M / 2 h) light-switching probe in mitochondria of live HeLa cells. (A) Confocal image with inset showing a close up of the mitochondria co-stained with MitoTracker Deep Red (red) and (B) Luminescence lifetime distribution of the conjugate.<sup>222</sup> .....36

**Figure 1.20** Confocal images of **[Os(btzpy)<sub>2</sub>]<sup>2+</sup>** (green) localizing at the mitochondria of osteosarcoma cells as confirmed by co-staining with Mitoview (red). Scale bar = 20  $\mu$ m. <sup>203</sup>37

**Figure 1.21** Mitochondrial-localized Ir(III) complex undergoes hypoxia-induced reduction triggering ROS formation under TPE. (A) Two-photon excitation confocal images of A549 cells treated with **Ir4** (5  $\mu$ M) under varying oxygen concentrations (from hypoxic to normoxic

conditions). (B) Hypoxic A549 cells were pre-treated with **Ir4/ Ir4-red** and a ROS indicator dye (DCFH-DA). Confocal images were collected from 0 to 100 s following two-photon ( $\lambda_{\text{ex}} = 730 \text{ nm}$ ) irradiation and photo-induced ROS formation was evident by the DCFH-DA staining shown in green. Scale bar = 20  $\mu\text{m}$ .<sup>237</sup> .....38

**Figure 1.22** Chemical structure and cellular studies of mitochondrial-targeted **DFX-Re3** complex. Co-staining studies with MitoTracker Deep Red (150 nm) showed that DFX-Re3 (5  $\mu\text{M}$  / 2 h) localized at the mitochondria of MDA-MB-231 cells. The accumulation of iron in cellular compartments was measured using ICP-MS. The content of Fe in mitochondria increases producing reactive oxygen species. Generation of mitochondrial ROS following treatment of cells with DFX-Re3 (5  $\mu\text{M}$  / 4 h) was confirmed by the intense fluorescence of a ROS indicator dye, DCF (2',7'-dichlorofluorescein) localized at the mitochondria.<sup>239</sup> .....39

**Figure 1.23** Ratiometric FRET molecular probe, **C343-Pro4-BTP**, consisting of coumarin 343 as an oxygen-insensitive fluorophore, a linker and an iridium O<sub>2</sub> indicator phosphor.<sup>254</sup> .....43

**Figure 1.24** A) Dual emitting ruthenium(II)/BODIPY molecular dyad. Following uptake of the dyad in CHO cells, confocal imaging shows emission only from the ruthenium moiety as the BODIPY emission is extinguished in aqueous environment. B) The core-shell RuBODIPY nanoparticles showed ratiometric O<sub>2</sub> responsivity in aqueous media and in cells.<sup>271,272</sup> .....44

**Figure 1.25** A) Phosphorescence images comparing **NanO2** and **Pt-Glc** neurosphere staining.. B) PLIM oxygen mapping of Pt-Glc (2.5  $\mu\text{M}$  / 16 h) in pheochromocytoma (PC12) multicellular spheroid aggregates at resting conditions and upon addition of FCCP (4  $\mu\text{M}$ ).<sup>297</sup> .....46

**Figure 1.26** PLIM O<sub>2</sub> mapping studies of (btp)<sub>2</sub>Ir(acac-DM); **Ir-1** in HT-29 cell spheroids and hepatic lobules. A) Variation in PLIM of **Ir-1** – stained HT-29 spheroids upon metabolic stimulation with FCCP (1  $\mu\text{M}$ ). B) PLIM images of hepatic lobules stained with **Ir-1** and following NH<sub>4</sub>Cl administration. The graph illustrates the variation of average **Ir-1** lifetime over time of ROIs in the peripheral and periportal regions.<sup>303</sup> .....47

**Figure 2.1** Absorbance and emission profile of parent complex, [Ru(biq)<sub>2</sub>(benztrzCOOH)]<sup>1+</sup>, at 20  $\mu\text{M}$  concentration (1 % v/v DMSO) in water and acetonitrile. Excitation at absorbance  $\lambda_{\text{max}}$  and slit widths 20 nm for emission measurement. .... 79

**Figure 2.2** Cyclic Voltammetry (cycled 4 times) of 1 mM Ru(biq)<sub>2</sub>(trzbenzCOOH).PF<sub>6</sub> in MeCN with 0.1 M NBu<sub>4</sub>PF<sub>6</sub>. Potentials are reported versus the Ag/Ag<sup>+</sup> reference electrode. Scan rate: 0.05 V/s. ....81

**Figure 2.3** Confocal Images of live CHO cells treated with RuNLS at 15  $\mu\text{M}$ / 1 h in the absence of light and spiked with FAM-FLICA probe demonstrating caspase activity of cells triggered



by RuNLS. (A) Cells were irradiated at 568 nm and emission was collected between 680 nm and 800 nm. (B) FAM-FLICA channel showing active caspases excited at 490 nm. (C) Overlay of (B) with brightfield image. (Scale bar = 20  $\mu\text{m}$ ) .....83

**Figure 2.4** Viability of CHO (A) and HeLa (B) cells after 24 h exposure to Rubiq bioconjugates. Live cells were treated with the conjugates followed by addition of Resazurin for 6 h. Absorbance was read at 570 nm with background at 600 nm subtracted (n=3). .....84

**Figure 2.5** The percentage of cells showing caspase activity indicative of apoptosis obtained by FAM-FLICA Assay (n=3). .....86

**Figure 2.6** Confocal Imaging of CHO cells treated with RuNLS at 15  $\mu\text{M}$  and incubated for 1 hour in the absence of light followed by addition of the FAM-FLICA dye. (A) Caspase activity (green) was detected using a band pass filter (excitation 490, emission 520-535 nm). (B) Nuclear staining with DRAQ7 (3  $\mu\text{M}$ ) revealed damaged/ compromised cells. DRAQ7 was excited at 33 nm and emission was collected between 650- 850 nm. (C) The overlay with the brightfield image showed viable cells with no caspase activity. ....87

**Figure 2.7** Relative Fluorescence Units (RFU) obtained by MitoPT Assay (n=3); HeLa and CHO cells were exposed to DMSO (10 % v/v) (negative control 2) and CCCP depolarizing agent (positive control). Experimental populations were exposed to the Rubiq conjugates under the conditions previously described. All samples were incubated with MitoPT TMRE for 40 minutes at 37°C and washed. Aliquots were added in a black 96-well plate in triplicate and analyzed by Tecan fluorescence plate reader set at 540 nm excitation and 574 nm emission. Healthy cells exhibited a high level of orange fluorescence whereas metabolically stressed cells (positive control) exhibited a reduced fluorescence signal indicating MMP depolarization. Illustrated is the relative TMRE fluorescence signal as a percentage representative of the loss of mitochondrial membrane potential with respect to the non-exposed (negative control) cell populations.....88

**Figure 3.1** Absorbance and emission spectra of Os<sup>II</sup>MPP. Spectra were recorded at 25  $\mu\text{M}$  (PBS Buffer pH 7.4) under aerated and deaerated conditions with excitation and emission slit widths of 10nm and emission excitation wavelength of 490 nm..... 105

**Figure 3.2** Cyclic Voltammogram (n=3) of 1 mM [Os(tpybenzCOOH)<sub>2</sub>]<sup>2+</sup>. Sample in deaerated CH<sub>3</sub>CN containing 0.1 M nBu<sub>4</sub>NPF<sub>6</sub>. Scan rate 50 mV s<sup>-1</sup>. ..... 107

**Figure 3.3** Confocal luminescence images of Os<sup>II</sup> MPP in live HeLa cells where the conjugate and overlay channel are shown. Cells were incubated in the absence of light with 30  $\mu\text{M}$  for: 60 min, 120 min and 4 h. The bis-MPP complex was excited using 490 nm white light laser and the emission was collected between 590 and 800nm..... 108

**Figure 3.4** Confocal imaging: (A) Os<sup>II</sup> MPP at increased concentration (50 $\mu$ M) in HeLa cells following 1 hr incubation in the absence of light; z-scan reveals nucleoli staining (B) co-staining with DRAQ7 and (C) overlay. image..... 109

**Figure 3.5** Co-localization of Os<sup>II</sup> MPP with MitoTracker Deep Red where: (A) Confocal imaging of Os<sup>II</sup> MPP (red), MitoTracker (purple) and merged image (B) Fluorescence intensity profiles obtained from the line profile across the cell (Image J). The cells were also co-incubated with DRAQ7 and absence of nuclear staining confirms cells are live..... 110

**Figure 3.6:** Phototoxicity of Os<sup>II</sup> MPP (30  $\mu$ M) in HeLa cells using excitation with 490nm and scanning using increased laser power. (A, D) Normal imaging conditions (10 % laser power) before scanning, (B, E) after 10 minutes scanning at 30 % laser power and (C, F) additional 20 minutes scanning at 50 % laser power; Observed in blue is the emission of MitoTracker Deep Red due to co-excitation of MitoTracker Deep Red at 633 nm. .... 111

**Figure 3.7** Relative Fluorescence Units obtained by MitoPT Assay (n=3) expressed as a percentage of the negative control. HeLa and MCF 7 cells were exposed to DMSO (100  $\mu$ M/ 1 h) (negative control 2) and CCCP depolarizing agent (positive control). Experimental populations were exposed to Os<sup>II</sup> MPP under the conditions previously described. All samples were incubated with MitoPT TMRE for 30 minutes at 37°C and washed. Aliquots were added in a black 96-well plate in triplicate and analysed by Tecan fluorescence plate reader set at 540 nm excitation and 574 nm emission. Healthy cells exhibited a high level of orange fluorescence whereas metabolically stressed cells (positive control and Os<sup>II</sup> MPP treated) exhibited a reduced fluorescence signal indicating MMP depolarization. Illustrated is the percentage cell viability decline based on loss of mitochondrial membrane potential relative to the non-exposed (negative control) cell populations..... 112

**Figure 3.8** The percentage of cells showing caspase activity indicative of apoptosis obtained by FLICA Assay (n=3). Both cell lines were exposed to DMSO as a second negative control (S.I) and Staurosporine as the positive control. Experimental populations were exposed to Os<sup>II</sup> MPP at 30  $\mu$ M/ 2 h and 100  $\mu$ M/ 1 h. All samples were incubated with 30X FLICA reagent for 45 minutes at 37°C followed by two washing steps and re-suspension of spun down pellets. Aliquots were analyzed in a black 96-well plate by Tecan fluorescence plate reader set at 488 nm excitation and 520 nm emission. Healthy cells exhibited minimal green fluorescence whereas apoptotic cells due to caspase activity exhibited a green fluorescence signal..... 115

**Figure 4.1** A) General chemical structure of Os(II)-terpyridine based polyarginine conjugates following amide coupling of R<sub>n</sub> (n= 4, 8) to [Os(tpybenzCOOH)<sub>2</sub>]<sup>2+</sup> parent complex. B) Absorbance and normalised emission spectra of [Os-(R<sub>4</sub>)<sub>2</sub>]<sup>10+</sup> (30  $\mu$ M/ PBS buffer pH 7.4)

under aerated and deaerated conditions with  $\lambda_{exc}$  490 nm and excitation and emission slit widths of 10 nm. .... 130

**Figure 4.2** Uptake and colocalization studies of  $[\text{Os}-(\text{R}_4)_2]^{10+}$  in live A549 cells where the osmium channel is shown in green. Cells were incubated in the absence of light with 30  $\mu\text{M}$   $[\text{Os}-(\text{R}_4)_2]^{10+}$  for A) 24 h and for B-C) 48 h. Co-localization studies at 48 h with LysoTracker Green (50 nM) confirmed lysosomal confinement evident by the overlap of the D) osmium channel with E) LysoTracker Green (orange) in the F) overlay image (Pearson's coefficient = 0.69). A 490 nm white light laser was used to excite the conjugate and emission was collected between 650 and 800 nm. LysoTracker Green was excited at 504 nm and emission was collected at 511 nm. .... 133

**Figure 4.3** Confocal luminescence images of  $[\text{Os}-(\text{R}_4)_2]^{10+}$  in CHO cells. Live cells were incubated with 30  $\mu\text{M}$   $[\text{Os}-(\text{R}_4)_2]^{10+}$  for 24 h in the absence of light and co-stained with DRAQ7. (A-B) The distribution of the conjugate (in green) is shown in a group of cells co-stained with DRAQ7 (in blue). (C-D) Closeup image of a single A549 cell shows nucleoli staining. The 633 nm laser was used to excite DRAQ7 and emission was collected between 635–750 nm. .... 135

**Figure 4.4** Luminescence lifetime imaging  $[\text{Os}-(\text{R}_4)_2]^{10+}$  at 30  $\mu\text{M}$  in live A549 cells. A) Confocal image of a single cell following conjugate uptake at 24 h and B) lifetime distribution in the expanded cytoplasmic region of the cell. C) PLIM acquired following uptake at 48 h. The PLIM images were acquired using the 405 nm excitation laser line. The PLIM images of the entire cell of B and C and corresponding emission decays are shown in the Supplementary Information (Fig. S 18-19). .... 136

**Figure 4.5** 3D reconstruction depth coding images of whole live HPAC spheroids treated with  $[\text{Os}-(\text{R}_4)_2]^{10+}$  at (A) 30  $\mu\text{M}$  / 24 h and (B) 100  $\mu\text{M}$  / 24 h. Confocal images were acquired at different planes in the z direction throughout the spheroids (from the bottom to above each spheroid). A 490 nm white light laser was used to excite the conjugate and emission was collected between 650 and 800 nm. Scale bar reads 100  $\mu\text{m}$ . .... 137

**Figure 4.6** Z-stack images a single live HPAC spheroid pre-treated with  $[\text{Os}-(\text{R}_4)_2]^{10+}$  (100  $\mu\text{M}$ / 48 h) and co-stained with DAPI (10  $\mu\text{M}$ ). Each image corresponds to cross-section from the bottom to the upper part along the z-axis. Representative cross-sections are shown using brightfield contrast as the background. Scale bar reads 100  $\mu\text{m}$ . A 490 nm white light laser was used to excite the conjugate and emission was collected between 650 and 800 nm. The 405 nm excitation laser was used to excite DAPI and emission was collected between 423 and 580 nm. .... 138

**Figure 4.7** Confocal images (2D-projection) of HPAC spheroid regions treated with Os-(R<sub>4</sub>)<sub>2</sub> at (A) 30 μM/ 24 h , (B) 100 μM / 24 h and (C) 100 μM / 48 h at 37 °C. The spheroids were co-stained with DAPI (10 μM) and (D-F) Overlay images with DAPI channel. A 490 nm white light laser was used to excite the conjugate and emission was collected between 650 and 800 nm.. The 405 nm excitation laser was used to excite DAPI and emission was collected between 423 and 580 nm. (40X) ..... 139

**Figure 4.8** Confocal images of a single live HPAC spheroid treated with [Os-(R<sub>4</sub>)<sub>2</sub>]<sup>10+</sup> (100 μM/ 48 h). A 490 nm white light laser was used for excitation and emission was collected between (A) 650 – 800 nm; Os(II) channel and (B) 500 – 570 nm; autofluorescence window. (C) Os(II)/autofluorescence channel overlay..... 140

**Figure 5.1** (A) RuBDP response to change in oxygen concentration measured in μmol /L .Emission spectra of RuBDP NPs in PBS (pH 7.4) when excited at 480nm; both excitation and emission slit widths set at 10 nm. (B) Stern-Volmer Plot: the luminescence originating from the ruthenium component decreases with increase in oxygen concentration whilst the BODIPY reference probe is moderately affected (n = 3). ..... 159

**Figure 5.2** Confocal luminescence images of RuBDP NP uptake at 4.5 μg mL<sup>-1</sup> in live HeLa cells. Cells were incubated in the absence of light for 4 h. (A) The RuBDP NPs were excited using 480 nm white light laser and the emission for the Ru(II) component was collected between 569 nm and 850 nm. (B) Cells were co-stained with nuclear staining probe, DAPI. (C) Overlay of Ru(II) channel with DAPI. (D) Overlay with brightfield. .... 162

**Figure 5.3** Widefield fluorescence images of HeLa cells pre-treated with RuBDP NPs (4.5 μg mL<sup>-1</sup>) and monitored over time. Emission collected from the Ru(II) channel (A) following uptake of the particles and (B) at 4 h of incubation after NP uptake. The Ru(II) component of the NPs was excited at 470 nm using the GFP excitation filter. .... 163

**Figure 5.4** Cell Viability of HeLa, MCF 7 and CHO cells after 24 h exposure to RuBDP NPs over a range of concentrations. Live cells were treated with the nanoparticles followed by addition of Resazurin for 6 h. Absorbance readings at 570 nm with a background at 600 nm were performed. Data were expressed as averaged percentages and compared to non-treated cells. P ≤ 0.05; \*\*\*P ≤ 0.01, \*\*\*\* P ≤ 0.0001..... 165

**Figure 5.5** Co-localization of RuBDP NPs with late endosomal staining probe in live HeLa cells where: confocal imaging of (A) RuBDP NPs at 4.5 μg mL<sup>-1</sup>/ 4 h (green), (B) Rab7a-GFP (yellow), (C) overlay of RuBDP/Rab7a-GFP channels with the brightfield background. (D) The fluorescence intensity profile of RuBDP NPs and Rab7a-GFP obtained from the line profile across the cell is also shown (ImageJ). ..... 167

**Figure 5.6** Confocal imaging of A549 cells treated with RuBDP NPs at  $4.5 \mu\text{g mL}^{-1}$  for 4 h at  $37^\circ\text{C}$ . (A, C) Ru(II) channel (569 – 850 nm) and (B, D) BODIPY channel (505 – 550 nm) under normoxic and hypoxic conditions. (E) Confocal lambda ( $\lambda$ ) scan: emission spectra collected between 495 nm and 795 nm following single excitation at 480 nm at normoxic and hypoxic conditions where both the BODIPY and Ru(II) component emission maximum is observed ( $n=3$ ). ..... 168

**Figure S2. 1**  $^1\text{H}$  NMR spectrum (600 MHz) of **(1)** in DMSO- $d_6$ . ..... A2

**Figure S2. 2**  $^{13}\text{C}$  NMR spectrum (600 MHz) of **(1)** in DMSO- $d_6$ . ..... A3

**Figure S2. 3**  $^1\text{H}$  NMR spectrum (600 MHz) of **(2)** in DMSO- $d_6$ . ..... A3

**Figure S2. 4**  $^{13}\text{C}$  NMR spectrum (600 MHz) of **(2)** in DMSO- $d_6$ . ..... A4

**Figure S2. 5** HR-MS (ESI-QTOF): Single Mass Analysis of **(2)** indicating  $[\text{M} + \text{H}]^+$ . ..... A4

**Figure S2. 6**  $^1\text{H}$  NMR spectrum (600 MHz) of **(3)** in MeCN- $d_3$ . ..... A5

**Figure S2. 7**  $^{13}\text{C}$  NMR spectrum (600 MHz) of **(3)** in MeCN- $d_3$ . ..... A5

**Figure S2. 8**  $^1\text{H}$ - $^1\text{H}$  COSY NMR spectrum of **(3)** in MeCN- $d_3$ . (Aromatic region highlighted) ..... A6

**Figure S2. 9** HR-MS (MALDI-QTOF): Single Mass Analysis of **(3)** indicating  $[\text{M} - \text{H}]^+$ . A7

**Figure S2. 10**  $^1\text{H}$  NMR spectrum of **(4)** (600 MHz, MeOD + 1 drop of  $\text{D}_2\text{O}$ ) ..... A7

**Figure S2. 11**  $^1\text{H}$ - $^{13}\text{C}$  2D HSQC NMR spectrum of **(4)** (600 MHz, MeOD + 1 drop of  $\text{D}_2\text{O}$ ) ..... A8

**Figure S2. 12**  $^1\text{H}$ - $^{13}\text{C}$  DEPT135 2D HSQC NMR spectrum of **(4)** (600 MHz, MeOD + 1 drop of  $\text{D}_2\text{O}$ ) ..... A9

**Figure S2. 13** MALDI QTOF of **(4)**  $Z=7$ ,  $\text{C}_{104}\text{H}_{147}\text{N}_{42}\text{O}_{10}\text{Ru}$  Calc. 320.8761 Found 320.8758  $[\text{M} - 2\text{H}^+]$ . ..... A9

**Figure S2. 14** MALDI QTOF of **(4)**  $Z=6$ ,  $\text{C}_{104}\text{H}_{146}\text{N}_{42}\text{O}_{10}\text{Ru}$  Calc. 374.1875 Found 374.1876  $[\text{M} - 3\text{H}^+]$ . ..... A10

**Figure S2. 15** MALDI QTOF of **(4)**  $Z=5$ ,  $\text{C}_{104}\text{H}_{145}\text{N}_{42}\text{O}_{10}\text{Ru}$  Calc. 448.8234 Found 448.8232  $[\text{M} - 4\text{H}^+]$ . ..... A10

**Figure S2. 16**  $^1\text{H}$  NMR spectrum of **(5)** (600 MHz, MeOD + 1 drop of  $\text{D}_2\text{O}$ ) ..... A11

**Figure S2. 17** MALDI QTOF of **(5)**  $Z=5$ ,  $\text{C}_{118}\text{H}_{135}\text{N}_{26}\text{O}_{11}\text{Ru}$  Calc. 438.7969 Found 438.7983  $[\text{M} + 1\text{H}^+]$ . ..... A11

**Figure S2. 18** MALDI QTOF of **(5)**  $Z=4$ ,  $\text{C}_{118}\text{H}_{134}\text{N}_{26}\text{O}_{11}\text{Ru}$  Calc. 548.2442 Found 548.2465  $[\text{M}^+]$  ..... A12

<b>Figure S2. 19</b> MALDI QTOF of <b>(5)</b> Z=3, C <sub>118</sub> H <sub>134</sub> N <sub>26</sub> O <sub>11</sub> Ru Calc. 730.6563 Found 730.6578 [M -H <sup>+</sup> ]	A12
<b>Figure S2. 20</b> <sup>1</sup> H NMR spectrum of <b>(6)</b> (600 MHz, MeOD + 1 drop of D <sub>2</sub> O)	A13
<b>Figure S2. 21</b> MALDI QTOF of <b>(6)</b> Z=5 C <sub>111</sub> H <sub>146</sub> ClN <sub>30</sub> O <sub>13</sub> RuS Calc. 455.2027 Found 455.2125 [M-(H <sub>3</sub> O <sup>+</sup> )]	A13
<b>Figure S2. 22</b> <sup>1</sup> H NMR spectrum (600 MHz) of <b>(7)</b> in Acetone-d <sub>6</sub> .	A14
<b>Figure S2. 23</b> <sup>13</sup> C NMR spectrum (600 MHz) of <b>(7)</b> in Acetone-d <sub>6</sub> .	A14
<b>Figure S2. 24</b> HR-MS (MALDI-QTOF): Single Mass Analysis of <b>(7)</b> indicating [M] <sup>+</sup> ....	A15
<b>Figure S2. 25</b> Chromatogram of the parent complex Ru(biq) <sub>2</sub> (trzbenzCOOH).Cl - (Reverse Phase - C18, MeCN/Water 0.1 % TFA gradient, 554 nm).	A16
<b>Figure S2. 26</b> Chromatogram of [Ru(biq) <sub>2</sub> (trzbenz-CONH-R8)] <sup>9+</sup> <b>(5)</b> - (100 % pure relative to parent) -(Reverse Phase-C18, MeCN/Water 0.1 % TFA gradient, 554 nm)	A16
<b>Figure S2. 27</b> Chromatogram of Ru(biq) <sub>2</sub> (trzbenz-CONH-PEG <sub>12</sub> ).Cl - (100 % pure relative to parent) - (Reverse Phase-C18, MeCN/Water 0.1 % TFA gradient, 554 nm).....	A16
<b>Figure S2. 28</b> Chromatogram of [Ru(biq) <sub>2</sub> (trzbenz-CONH-MPP)] <sup>4+</sup> <b>(6)</b> - (98.5 % pure relative to parent) - (Reverse Phase-C18, MeCN/Water 0.1 % TFA gradient, 554 nm)	A16
<b>Figure S2. 29</b> Chromatogram of [Ru(biq) <sub>2</sub> (trzbenz-CONH-NLS)] <sup>5+</sup> <b>(7)</b> - (100 % pure relative to parent) - (Reverse Phase-C18, MeCN/Water 0.1 % TFA gradient, 554 nm)	A17
<b>Figure S2. 30</b> Photostability study of parent complex Ru(biq) <sub>2</sub> (trzbenzCOOH).Cl in H <sub>2</sub> O (1 % v/v DMSO), absorbance spectra measured at defined time intervals during continuous photo-irradiation with Xenon ARC Lamp 150W for 2 h at room temperature.	A17
<b>Figure S2. 31</b> UV-vis absorption spectrum of parent complex in acetonitrile at neutral pH and at acidic pH (1 % v/v perchloric acid). Picture (right) showing effect of pH on color of compound in acetonitrile solution.	A18
<b>Figure S2. 32</b> Confocal images of HeLa cells treated with RuNLS (A,B) and RuR8 (C,D) (100 μM) for 3 h. Cells were washed twice with PBS prior to imaging. (Rubiq emission shown in green (A,C) has been increased for printing purposes). Transmission fluorescence (B,D) showing the cell debris after 3 h incubation.	A18
<b>Figure S2. 33</b> Mass spectrometry spectrum of R8 peptide sequence NH <sub>2</sub> -Ahx-R-R-R-R-R-R-R-R-CONH <sub>2</sub> (Provided by Celtek Peptides).	A19
<b>Figure S2. 34</b> Mass spectrometry spectrum of MPP peptide sequence NH <sub>2</sub> -Ahx-F-r-F-K-F-r-F-K(Ac)-CONH <sub>2</sub> (Provided by Celtek Peptides)	A20
<b>Figure S2. 35</b> Mass spectrometry spectrum of NLS peptide sequence NH <sub>2</sub> -Ahx-V-Q-R-K-R-Q-K-L-M-P-CONH <sub>2</sub> (Provided by Celtek Peptides)	A21

<b>Figure S2. 36</b> Chemical structure of FAM-VAD-FMK polycaspase indicator dye. ....	A21
<b>Figure S3. 1</b> <sup>1</sup> H-NMR spectra of tpybenzCOOH in DMSO-d <sub>6</sub> (top) and TFA-d, (bottom) 600 MHz. ....	B1
<b>Figure S3. 2</b> <sup>1</sup> H NMR of purified [Os(tpybenzCOOH) <sub>2</sub> ] <sup>2+</sup> in DMSO-d <sub>6</sub> , 400 MHz. ....	B2
<b>Figure S3. 3</b> COSY spectrum of [Os(tpybenzCOOH) <sub>2</sub> ] <sup>2+</sup> in MeCN-d <sub>3</sub> , 600 MHz. ....	B3
<b>Figure S3. 4</b> <sup>1</sup> H NMR spectrum of Os <sup>II</sup> MPP in MeOH-d <sub>4</sub> , 400 MHz with key regions in the aromatic and aliphatic region highlighted. ....	B4
<b>Figure S3. 5</b> HRMS (TOF ES+) of [Os(tpybenzCOOH) <sub>2</sub> ] <sup>2+</sup> .....	B5
<b>Figure S3. 6</b> HPLC chromatogram (above) and Mass Spectrum (below) of Os <sup>II</sup> MPP complex following LC-MS analysis (Q-Exactive). Conditions; gradient extended from 10- 90 % (Formic Acid 0.1 %, 80 % MeCN). ....	B6
<b>Figure S3. 7</b> LC-MS analysis of Os <sup>II</sup> MPP Zoomed m/z 456-470 (RT 21-23 min). ....	B6
<b>Figure S3. 8</b> LC-MS analysis of Os <sup>II</sup> MPP Zoomed m/z 747-754 (RT 21-23 min) .....	B7
<b>Figure S3. 9</b> LC-MS analysis of Os <sup>II</sup> MPP Zoomed m/z 458-468 (RT 23-25 min). ....	B7
<b>Figure S3. 10</b> LC-MS analysis of Os <sup>II</sup> MPP Zoomed m/z 560-566 (RT 23-25 min).....	B8
<b>Figure S3. 11</b> Top: HPLC Chromatogram of Os <sup>II</sup> parent complex and Os <sup>II</sup> MPP conjugate obtained RP-C18 HPLC with MeCN mobile phase. Bottom three traces show traces using gradient mobile phase detected at 280 nm. (Gradient MeCN/ H <sub>2</sub> O 0.1 % TFA gradient, 1ml min <sup>-1</sup> ). Elution of Os <sup>II</sup> MPP conjugate at 8.3 min (Channel 1: 280 nm and Channel 2: 490nm). Diode array detection was used and the HPLC UV-vis spectrum of each peak was obtained during Os <sup>II</sup> MPP analysis and is shown below. ....	B9
<b>Figure S3. 12</b> HPLC UV-vis spectra obtained for peaks observed during Os <sup>II</sup> MPP HPLC analysis illustrating the absence of a component with absorbance only in the UV-vis region as the MLCT band at a longer wavelength confirms Osmium-coordinated complex for each peak. The distribution of peaks in the conjugate product is suspected to originate from different ionization states of the conjugate. ....	B10
<b>Figure S3. 13</b> Absorbance spectrum of parent complex [Os(tpybenzCOOH) <sub>2</sub> ] <sup>2+</sup> <b>1</b> in acetonitrile solution (25 μM). ....	B11
<b>Figure S3. 14</b> Emission spectra of parent complex [Os(tpybenzCOOH) <sub>2</sub> ] <sup>2+</sup> in acetonitrile (50 μM) under aerated and deaerated conditions (slit widths 10 nm / 10 nm). Solution was deaerated using nitrogen gas and oxygen concentration was measured using PreSence O <sub>2</sub> sensor. ....	B11

<b>Figure S3. 15</b> Absorbance spectra of parent complex $[\text{Os}(\text{tpybenzCOOH})_2]^{2+}$ ( $50 \mu\text{M}$ / PBS pH 7.4) following continuous photo-irradiation with ARC Lamp 150 W for 3 h at Room Temperature.....	B12
<b>Figure S3. 16</b> Emission Decays of parent complex $[\text{Os}(\text{tpybenzCOOH})_2]^{2+}$ in aerated and deaerated acetonitrile ( $50 \mu\text{M}$ ); Residual plots for the exponential fitting of both curves are shown below each plot. ....	B13
<b>Figure S3. 17</b> Emission Decays of parent complex $[\text{Os}(\text{tpybenzCOOH})_2]^{2+}$ in aerated and deaerated PBS pH 7.4 ( $50 \mu\text{M}$ ); The residual plots for the exponential fitting of both curves are shown below. ....	B14
<b>Figure S3. 18</b> Emission decay of conjugate $\text{Os}^{\text{II}}$ MPP under aerated and deaerated conditions ( $25 \mu\text{M}$ / PBS pH 7.4); Residual Plots of the exponential fitting for both curves are shown below. ....	B15
<b>Figure S3. 19</b> Cell Viability of HeLa and MCF 7 cells after 24 hr exposure to $\text{Os}^{\text{II}}$ MPP probe. Live cells were treated with the probe followed by addition of Resazurin for 6 h. Absorbance was read at 570 nm with background at 600 nm subtracted (n=3). ....	B16
<b>Figure S3. 20</b> Determination of EC50. HeLa cells were incubated in the presence of $\text{Os}^{\text{II}}$ MPP ( $0.1 \mu\text{M}$ to $150 \mu\text{M}$ ) for 24 h. Cell proliferation was assayed with Resazurin (n=3). The $\text{IC}_{50}$ value, the minimal amount of $\text{Os}^{\text{II}}$ MPP required to inhibit 50 % viability of HeLa cells was found to be $30.61 \mu\text{M}$ . ....	B17
<b>Figure S3. 21</b> Confocal Imaging studies of $[\text{Os}(\text{tpybenzCOOH})_2]^{2+}$ . Cells were treated with $[\text{Os}(\text{tpybenzCOOH})_2]^{2+}$ at $30 \mu\text{M}$ for 2 h. (A) Osmium Channel: uptake of the parent complex was not evident; (B) Background channels showing HeLa cells. Cells were excited with 490 nm WLL and emission was collected between 650nm and 850 nm. ....	B17
<b>Figure S3. 22</b> Confocal microscopy of HeLa cells incubated with $\text{Os}^{\text{II}}$ MPP at $30 \mu\text{M}$ for (A) 4 h, (B) 6 h and (C) 24 h in cell media at $37 \text{ }^\circ\text{C}$ in the absence of light. (a-c) Overlay images with the background channel. $\text{Os}^{\text{II}}$ MPP was excited using a 490 nm white light laser and emission was collected between 650nm and 850 nm. ....	B18
<b>Figure S3. 23</b> Confocal imaging of $\text{Os}^{\text{II}}$ MPP in HeLa and MCF 7 cells at increased concentrations; Uptake of $\text{Os}^{\text{II}}$ MPP probe is evident but changes are observed in the morphological features of cells indicative of cell death. ....	B19
<b>Figure S3. 24</b> Co-staining with DRAQ7 following $\text{Os}^{\text{II}}$ MPP $30\mu\text{M}/2\text{h}$ ; (A) Absence of nuclear staining confirms cells are viable; observed in blue is the emission of MitoTracker Deep Red due to co-excitation of MitoTracker Deep Red at 633 nm. (B) Overlay of all channels.....	B19



**Figure S3. 25** Control studies for the FLICA assay (n=3) in HeLa and MCF 7 cell line. Cells were cultivated at  $3 \times 10^5$  cells/well and were exposed to negative control 1 (non-treated) (B) negative control 2 DMSO (10 % v/v) (C) positive control (staurosporine 1  $\mu$ M/ 3 h). Cells were spiked with 30X FAM-FLICA reagent (v/v ratio of 1:30) and incubated for 45 minutes at 37 °C. Samples were analyzed in triplicate (3  $\times$ 100  $\mu$ l) in a black bottomed 96-well plate using Tecan Plate fluorescence plate reader set at 488 nm excitation and 520 nm emission. .... B20

**Figure S4. 1**  $^1\text{H}$  NMR analysis of  $[\text{Os}-(\text{R}_4)_2]^{10+}$  conjugate (MeOH- $d_4$ /D $_2$ O, 600 MHz) ..... C1

**Figure S4. 2** COSY analysis of  $[\text{Os}-(\text{R}_4)_2]^{10+}$  conjugate (MeOH- $d_4$ /D $_2$ O, 600 MHz) ..... C2

**Figure S4. 3**  $^1\text{H}$  NMR analysis of  $[\text{Os}-(\text{R}_8)_2]^{18+}$  conjugate (MeOH- $d_4$ /D $_2$ O, 600 MHz) ..... C3

**Figure S4. 4** LC-MS/MS (Q- Exactive) of bis-octaarginine Os(II) conjugate (RT 27.9-29.4 min), zoomed  $m/z$ ,  $z=2$ , A) 490 - 540 B) 1070 – 1190. .... C4

**Figure S4. 5** LC-MS/MS (Q-Exactive) of bis-tetraarginine Os(II) conjugate (RT 27.6 – 29 min), zoomed  $m/z$ ,  $z=2$ , A) 490 – 540 and B) 1020-1150. .... C4

**Figure S4. 6** RP-HPLC analysis of polyarginine Os(II) conjugates relative to  $[\text{Os}(\text{tpybenzCOOH})_2]^{2+}$  parent complex (C18, MeCN/H $_2$ O (0.1 % TFA) gradient, PDA 490 nm) ..... C5

**Figure S4. 7** Absorbance and emission spectra of  $[\text{Os}-(\text{R}_8)_2]^{18+}$  (Normalised to  $\lambda_{\text{max}}$ ). Spectra were recorded at 50  $\mu$ M (PBS buffer pH 7.4/ 0.1 % DMSO) under aerated and deaerated conditions with excitation and emission slit widths of 10 nm and  $\lambda_{\text{exc}}$  490 nm. .... C6

**Figure S4. 8** Emission Decays of bis-octaarginine Os(II) conjugate,  $[\text{Os}-(\text{R}_8)_2]^{18+}$  (50  $\mu$ M) in A) aerated and B) deaerated PBS (pH 7.4). Residual plots for the exponential fitting of both curves are shown below each plot. .... C7

**Figure S4. 9** Emission Decays of bis-tetraarginine Os(II) conjugate,  $[\text{Os}-(\text{R}_4)_2]^{10+}$  (30  $\mu$ M) in A) aerated and B) deaerated PBS (pH 7.4). Residual plots for the exponential fitting of both curves are shown below each plot. .... C8

**Figure S4. 10** Emission decay of bis-tetraarginine Os(II) conjugate,  $[\text{Os}-(\text{R}_4)_2]^{10+}$  (30  $\mu$ M) in PBS at pH 7.4 and pH 4.1 (using perchloric acid, 1 % v/v). The residual plot corresponds to the exponential fitting of the decay at pH 4.1, but the decays and fits are indistinguishable. C9

**Figure S4. 11** Confocal images of (A,C) A549 and (B,D) CHO cells treated with parent compound  $[\text{Os}(\text{tpybenzCOOH})_2]^{2+}$  at 100  $\mu$ M/ 24 h. Shown are the Os(II) channel and overlay with brightfield. The complex was excited using a 490 nm white light laser and the emission was collected between 650 and 800 nm..... C10

**Figure S4. 12** Confocal images of (A-B) A549 and (C-D) CHO cells treated with  $[\text{Os}-(\text{R}8)_2]^{18+}$  at 30  $\mu\text{M}$ / 24 h (left) and 100  $\mu\text{M}$ / 24 h (right) and co-stained with DRAQ7. Shown are the overlay images of  $[\text{Os}-(\text{R}8)_2]^{18+}$  and DRAQ7 channel with brightfield. The 633 nm laser was used to excite DRAQ7 and emission was collected between 635–750 nm. .... C11

**Figure S4. 13** Confocal fluorescence images of A549 cells treated with (A)  $[\text{Os}-(\text{R}_4)_2]^{10+}$  (30  $\mu\text{M}$ / 24 h) and co-stained with (B) MitoTracker Deep Red (100 nM). (C) Overlay of the two channels. The conjugate was excited using a 490 nm white light laser and the emission range was set to between 650 and 800 nm. MitoTracked Deep Red was excited at 644 nm and emission was collected between 655–720 nm ..... C12

**Figure S4. 14** Representative confocal images of A549 cells treated with 100  $\mu\text{M}$  of  $[\text{Os}-(\text{R}_4)_2]^{10+}$  and co-stained with DRAQ7 (3  $\mu\text{M}$ ). (A) Os(II) channel following 24 h incubation, (B) overlay with DRAQ7 channel and brightfield, (C) Os(II) channel following 48 h incubation, (D) overlay with DRAQ7 channel and brightfield, (E) overlay with DRAQ7 channel and brightfield of a wide region of cells. The 633 nm laser was used to excite DRAQ7 and emission was collected between 635–750 nm. .... C12

**Figure S4. 15** Confocal images of 4°C uptake studies of  $[\text{Os}-(\text{R}_4)_2]^{10+}$  at 30  $\mu\text{M}$ / 24 h where (A-B) A549 and (C-D) CHO cell line. No uptake was observed as shown by the  $[\text{Os}-(\text{R}_4)_2]^{10+}$  channel (A, C) and overlay with brightfield images. The conjugate was excited using a 490 nm white light laser and the emission range was set to between 650 and 800 nm. .... C13

**Figure S4. 16** Representative confocal images of A549 cells treated with 30  $\mu\text{M}$  of  $[\text{Os}-(\text{R}_4)_2]^{10+}$  for 48 h and co-stained with DRAQ7 (blue). (A) Os(II) channel, (B) Os(II)/DRAQ7 overlay and (C) overlay of channels with brightfield. .... C13

**Figure S4. 17** Confocal images of A549 cells treated with  $[\text{Os}-(\text{R}_4)_2]^{10+}$  (30  $\mu\text{M}$ / 24 h) and co-stained with DRAQ7. Shown are the overlay images of the (A) Os(II) channel with DRAQ7 and (B) Os(II)/DRAQ7 with brightfield following continuous irradiation (0.84  $\mu\text{W}/\text{cm}^2$ ) for 3 h. No photo-induced toxicity was evident as absence of nuclear staining by DRAQ7 (blue) confirmed cell viability. .... C14

**Figure S4. 18** Cell Viability assay performed for A549 and CHO cells treated with  $[\text{Os}-(\text{R}_4)_2]^{10+}$  probe at a range of concentrations for 24 h. (n=3) ..... C14

**Figure S4. 19** Representative luminescent lifetime imaging microscopy and fits for  $[\text{Os}-(\text{R}_4)_2]^{10+}$  (30  $\mu\text{M}$ / 24 h) in a live A549 cell. The decay was fitted to a tri-exponential model with lifetimes of 92.2 ns (67 %), 15.8 ns (25 %) and 2.02 ns (8 %) ( $\chi^2 = 1.0336$ ). The PLIM image was acquired by exciting at 405 nm and emission collected between 650 and 800nm.15

**Figure S4. 20** Representative luminescent lifetime imaging microscopy of  $[\text{Os}-(\text{R}_4)_2]^{10+}$  (30  $\mu\text{M}$ / 48 h) in a live A549 cell. The decay was fitted to a tri-exponential model with lifetimes of 37.0 ns (54 %), 9.3 ns (32 %) and 1.88 ns (14 %). ( $\chi^2 = 0.9955$ ). The PLIM image was acquired by exciting at 405 nm and emission collected between 650 and 800nm. .... C16

**Figure S4. 21** Confocal images of representative live HPAC spheroid control samples. (A) Os(II) channel of non-treated control spheroid sample, (B) overlay of channel with brightfield, (C) Os(II)/Brightfield overlay of spheroid incubated with parent complex  $[\text{Os}(\text{tpybenzCOOH})_2]^{2+}$  at 100  $\mu\text{M}$ / 48 h (D) Os(II)/Brightfield overlay of spheroid incubated with bis-octaarginine  $[\text{Os}-(\text{R}_8)_2]^{18+}$  at 100  $\mu\text{M}$ / 48 h. A 490 nm white light laser was used for excitation and emission for Os(II) was set to 650 – 800 nm. .... C17

**Figure S4. 22** Z-stack images of a single live HPAC spheroid pre-treated with  $[\text{Os}-(\text{R}_4)_2]^{10+}$  for at 100  $\mu\text{M}$ / 24 h. Each image corresponds to cross-section from the bottom (upper left image) to the upper part (lower right image) along the z-axis. Scale bar reads 200  $\mu\text{m}$ . Os(II) was excited at 490 nm and emission was collected between 650 and 850 nm. Representative slices are shown using contrast BF as the background. (10X) .... C18

**Figure S4. 23** Z-stack images of a single live HPAC spheroid pre-treated with  $\text{Os}-(\text{R}_4)_2$  (100  $\mu\text{M}$ / 24 h) and co-stained with DAPI. Each image corresponds to cross-section from the bottom (upper left image) to the upper part (lower right image) along the z-axis. Os(II) was excited at 490 nm and emission was collected between 650 and 850 nm. DAPI was excited at 405 nm and emission was collected between 423 nm and 580 nm. Representative images are shown using contrast brightfield as the background. Scale bar reads 100  $\mu\text{m}$ . (10X) .... C19

**Figure S4. 24** HPAC spheroid viability was measured after 24 and 48 h. of incubation with  $[\text{Os}-(\text{R}_4)_2]^{10+}$  at 100  $\mu\text{M}$ . (n=2) .... C20

**Figure S4. 25** Fixed slices of control HPAC spheroids treated only with DAPI dye. (A) Os(II) channel, (B) DAPI emission was collected between 423 nm and 580 nm. (C) Overlay with brightfield..... C20

**Figure S4. 26** Fixed cryosections of HPAC spheroids pre-treated with  $[\text{Os}-(\text{R}_4)_2]^{10+}$  at 100  $\mu\text{M}$  / 24 h and co-stained with DAPI post-fixation. (A-B) Os(II) emission channel from two representative cryosections, (C) co-staining with DAPI and (D) Os(II)/DAPI overlay with brightfield. A 490 nm white light laser was used to excite the conjugate and emission was collected between 650 and 800 nm.. The 405 nm excitation laser was used to excite DAPI and emission was collected between 423 and 580 nm. .... C21

**Figure S4. 27** A) Confocal and B) Luminescence lifetime imaging of  $[\text{Os}-(\text{R}_4)_2]^{10+}$  in fixed HPAC spheroid slice. The PLIM decay was fitted to a bi-exponential model with lifetimes of

16.4 ns, and 3.2 ns ( $\chi^2 = 1.0453$ ). The PLIM image was acquired by exciting at 405 nm and emission collected between 650 and 800nm..... C22

<b>Figure S5. 1</b> $^1\text{H}$ NMR of $[\text{Ru}(\text{dpp})(\text{DMSO})_2\text{Cl}_2]$ ( <b>1</b> ) in $\text{CDCl}_3$ with aromatic region of interest inset, 600 MHz.....	D2
<b>Figure S5. 2</b> COSY spectrum of <b>1</b> in $\text{CDCl}_3$ , 600 MHz. ....	D3
<b>Figure S5. 3</b> $^1\text{H}$ NMR of $[\text{Ru}(\text{dpp})(\text{phen-NH}_2)(\text{ox})]$ ( <b>2</b> ) in $\text{DMSO-d}_6$ , 600 MHz. ....	D3
<b>Figure S5. 4</b> COSY spectrum of <b>2</b> in $\text{DMSO-d}_6$ , 600 MHz. ....	D4
<b>Figure S5. 5</b> $^1\text{H}$ NMR of $[\text{Ru}(\text{dpp})(\text{phen-NH}_2)(\text{bpybenzCOOEt})]^{2+}$ ( <b>3</b> ) in $\text{MeCN-d}_3$ , 400 MHz. ....	D5
<b>Figure S5. 6</b> Full range COSY spectrum (top) and expanded aromatic region of compound <b>3</b> in $\text{MeCN-d}_3$ , 400 MHz.....	D6
<b>Figure S5. 7</b> $^1\text{H}$ NMR of 2, 6 diethyl- 1, 3, 5, 7- tetramethyl- 8-(2-fluorophenyl)-6 methoxy- 1, 5- naphthyridine-4,4'- difluoroboradiazaindacene ( <b>BODIPY</b> ) in $\text{CDCl}_3$ , 400 MHz.....	D7
<b>Figure S5. 8</b> HR-MS of <b>3</b> in ESI (+) mode: (a) full range, (b) expansion of the isotope model and (c) expansion of the isotope pattern obtained from the mass spectrum. ....	D8
<b>Figure S5. 9</b> (A) SEM image (9.00 kV x 37.0k) (B) DLS intensity particle size distribution; Zeta potential was measured to be $25 \pm 1.37$ mV and conductivity of 16.8 (n=3).....	D9
<b>Figure S5. 10</b> Emission spectra of a new and seven- month suspension of RuBDP NPs in PBS following excitation at 480 nm; excitation and emission slit widths set at 10 nm. ....	D10
<b>Figure S5. 11</b> Absorbance and emission spectra of $[\text{Ru}(\text{dpp})(\text{phen-NH}_2)(\text{bpy-benz-COOEt})]^{2+}$ in $\text{MeCN}$ at $15 \mu\text{M}$ . Emission spectra were recorded under aerated and deaerated conditions following excitation at 460 nm; excitation and emission slit widths set at 5 nm. ....	D10
<b>Figure S5. 12</b> Emission spectra of (A) core-shell RuBODIPY particle- (previously reported) <sup>3</sup> and (B) core co-encapsulated RuBDP NPs - supernatant collected following swelling with THF. ....	D11
<b>Figure S5. 13</b> Emission Decays of parent complex $[\text{Ru}(\text{dpp})(\text{phen-NH}_2)(\text{bpyArCOOEt})]^{2+}$ in aerated and deaerated acetonitrile ( $15 \mu\text{M}$ ); Residual plots for the exponential fitting of both curves are shown below each plot. ....	D12
<b>Figure S5. 14</b> Emission Decays of the BODIPY reference core component under (A) aerated and (B) deaerated conditions of RuBDP NPs in PBS (pH 7.4); Residual plots for the exponential fitting of both curves are shown below each plot. ....	D13

**Figure S5. 15** Emission Decays of the Ru(II) O<sub>2</sub> sensor core component under (A) aerated and (B) deaerated conditions of RuBDP NPs in PBS (pH 7.4); Residual plots for the exponential fitting of both curves are shown below each plot. ....D14

**Figure S5. 16** HeLa cells were treated with RuBDP NPs (4.5 μg mL<sup>-1</sup>), incubated for 4 h at 37 °C and excited using 480 nm white light laser. (A) Emission collected within 569 – 850 nm corresponding to the [Ru(dpp)(phen-NH<sub>2</sub>)(bpybenzCOOEt)]<sup>2+</sup> component and (B) Emission collected within 505 – 550 nm corresponding to the BODIPY dye. ....D15

**Figure S5. 17** Confocal luminescence images of RuBDP NPs in live HeLa cells where the Ru(II) emission channel and overlay are shown. Cells were incubated in the absence of light with 4.5 μg mL<sup>-1</sup> nanoparticles over 24 h. RuBDP NPs were excited using 480 nm white light laser and the emission was collected between 569 nm and 800 nm for the Ru(II) channel. D16

**Figure S5. 18** Uptake of RuBDP NPs in live CHO cells at variant concentrations and incubation periods. (A) Absence of NP internalization at 4.5 μg mL<sup>-1</sup>/ 4 h incubation, (B) co-staining with DAPI probe (3 μM), (C) Formation of NP aggregates at 12 μg mL<sup>-1</sup>/ 24 h and (D) Cell debris and co-staining with DRAQ7 (3 μM) revealed compromised cells. The 633 nm laser was used to excite DRAQ7 and emission was collected between 635 – 900 nm. ....D17

**Figure S5. 19** Confocal luminescence imaging of RuBDP NPs in live A549 cells showing efficient uptake of particles under the same conditions of 4.5 μg mL<sup>-1</sup> / 4 h in the absence of light at 37 °C time (63X oil immersion objective lens). (A) RuBDP NPs were excited using the 480 nm white light laser and the emission was collected between 569 nm and 800 nm for the Ru(II) channel. (B) Overlay with brightfield and (C) Overlay close-up image showing punctuate staining. ....D17

**Figure S5. 20** HeLa cells were treated with RuBDP NPs (4.5 μg mL<sup>-1</sup>) and incubated for 4 h at 4°C time (63X oil immersion objective lens). Confocal imaging of RuBDP NPs (A) Throughout the cells (C) At the cell surface (B-D) Overlay images with brightfield. NPs were excited using the 480 nm white light laser and emission was collected between 569 - 800 nm. ....D18

**Figure S5. 21** HeLa cells were treated with RuBDP NPs (4.5 μg mL<sup>-1</sup>) and incubated for 4 h at 4°C time (63X oil immersion objective lens). Confocal imaging of RuBDP NPs (A) Throughout the cells (C) At the cell surface (B-D) Overlay images with brightfield. NPs were excited using the 480 nm white light laser and emission was collected between 569 - 800 nm. ....D19

**Figure S5. 22** Co-localization study of RuBDP NPs with Late endosomal staining probe in live A549 cells. (A) Confocal image of Ru(II)- particle component (green) (B) Rab7a-GFP (yellow)

and (C) The fluorescence intensity profile of RuBDP NPs and Rab7a-GFP showing strong co-localization between the particles and the late-endosome staining dye. (ImageJ).....D20

**Figure S5. 23** Z-stack derived 3D Confocal Images of co-localization of RuBDP NPs with lysosomal staining probe in live HeLa cells where: (A) RuBDP NPs (green), (B) LysoTracker Deep Red (red;  $\lambda_{exc}$  647 nm,  $\lambda_{em}$  range: 650 – 800 nm)., (C) Merged image, (D) The fluorescence intensity profiles obtained revealing partial co-localization of RuBDP NPs with LysoTracker Deep Red (ImageJ). .....D21

**Figure S5. 24** Co-localization of RuBDP NPs with MitoTracker Deep Red in live HeLa cells. (A-B) RuBDP (green) and MitoTracker Deep Red (red) merged images. (C) The fluorescence intensity profile of RuBDP NPs and MitoTracker Deep red obtained from the line profile across the cell (ImageJ) showed poor co-localization between the particles and the mitochondria-staining dye. MitoTracker Deep Red was excited using the 644 nm white light laser and emission was collected between 650 and 800 nm. ....D22

**Figure S5. 25** Phototoxicity of RuBDP NPs in HeLa cells using excitation with 480 nm over time ( $63 \times$  oil immersion objective lens). (A) Confocal imaging of NPs at  $4.5 \mu\text{g mL}^{-1}$  at the 4 h timepoint, (C) overlay and absence of DRAQ7 confirm cell viability, (B) RuBDP NPs following 2 h of continuous irradiation, (D) overlay with DRAQ7 (blue) internalization confirms damaged cells. ....D23

**Figure S5. 26** Confocal imaging of HeLa cells treated with RuBDP NPs at  $4.5 \mu\text{g mL}^{-1}$  for 4 h at  $37^\circ\text{C}$ . Emission was collected corresponding to (A, C) Ru(II)  $\text{O}_2$  sensitive component and (B, D) BODIPY reference probe under normoxic and hypoxic conditions. ....D24

**Figure S5. 27** Emission spectra of RuBDP NPs in PBS (pH 7.4) recorded at different concentrations of oxygen on the ClarioStar Plus plate reader. The excitation wavelength was set to 480 nm with a detection range between 505 and 840 nm. Inset: Calibration ratiometric plot of the BODIPY and Ruthenium emission intensities, at 516 nm and 632 nm respectively, as a function of oxygen concentration ( $R^2$  0.99757). ....D25

**Figure S5. 28** RuBDP NPs ( $4.5 \mu\text{g mL}^{-1}$ ) internalized in A549 cells were excited at 480nm and emission spectra between 505 and 840 nm were collected upon treatment with sodium sulfite ( $5 \text{ mg mL}^{-1}$ ). The Stern-Volmer equation obtained from the calibration plot above was used to determine the  $[\text{O}_2]$  in cells following treatment with sodium sulfite using the ratiometric signal of  $I_{\text{Ru(II) } 632 \text{ nm}}/ I_{\text{BDP } 516 \text{ nm}}$ . ....D26

## Table of Schemes

<b>Scheme 2.1</b> Synthetic route to Ru(II) bioconjugates (i) EtOH/H <sub>2</sub> O (2:1), reflux, 3 h (ii) m-dPEG <sub>12</sub> , HATU, DIPEA, DCM, rt 24 h (iii) NH <sub>2</sub> -Ahx-peptide (ahx – aminohexyl linker), PyBOP, DIPEA, DMF, rt 24 h.....	78
<b>Scheme 3.1</b> Synthetic scheme for the preparation of Os <sup>II</sup> MPP conjugate complex.....	104
<b>Scheme 5.1</b> Route to synthesis of Ru(II) tris- heteroleptic polypyridyl complex ( <b>4</b> ; O <sub>2</sub> sensor) and preparation of self-referenced nanoparticles. ....	157

## Table of Tables

<b>Table 1.1</b> Lipophilicity and cytotoxicity of metal complexes upon synthetic modifications .	21
<b>Table 2.1</b> Summary of photophysical data of parent complex and conjugates.....	80
<b>Table 3.1</b> Summary of photophysical properties of Os(II)- complexes in MeCN and PBS under aerated and deaerated conditions. ....	106
<b>Table 5.1</b> Photophysical data of particle dye constituents and RuBDP NPs. <sup>[a]</sup> .....	160
<b>Table S3. 1</b> MitoPT and FLICA Assay: Cell Population Experimental Conditions.....	B20

## Abbreviations

3D	Three-dimensional
A172	Human glioblastoma cell line
A549	Human lung carcinoma cell line
AIF	Apoptosis-inducing factor
Arg	Arginine
ATP	Adenosine triphosphate
CCCP	Carbonyl cyanide m-chlorophenyl hydrazone
CHO	Chinese hamster ovary cell line
CLSM	Confocal Laser Scanning Microscopy
CPP	Cell penetrating peptide
DAPI	4',6-Diamidino-2-Phenylindole
DLS	Dynamic Light Scattering
DMSO	Dimethyl Sulfoxide
DNA	Deoxyribonucleic acid
dpp or dip	4,7-diphenyl-1,10-phenanthroline

Dppz	dipyrido[3,2-a:2',3'-c]phenazine
F	Phenylalanine
FAD	flavin adenine dinucleotide
FCCP	Carbonyl cyanide-p-trifluoromethoxyphenylhydrazone
FLIM	Fluorescence Lifetime Imaging
FRET	Föster resonance energy transfer
GFP	Green Fluorescent Protein
GSH	glutathione
HPAC	Human pancreatic cancer cell line
HSA	Human Serum Albumin
HSPG	Heparan Sulfate Proteoglycans
IC <sub>50</sub>	Concentration of a drug/substance required for 50 % inhibition in vitro
icO <sub>2</sub>	Intracellular oxygen
IP	imidazo[4,5-f][1,10]-phenanthroline
IRF	Instrument Response Function
K	Lysine
L	Leucine
LD	Lipid Droplet
LE	Late Endosomes
M	Methionine
MALDI-QTOF	Matrix Assisted Laser Desorption/Ionization Quadrupole Time-Of-Flight
MLCT	Metal-to-Ligand Charge Transfer
MMP	Mitochondrial Membrane Potential
MPP	Mitochondria penetrating peptide (FrFKFrFK)
mtDNA	mitochondrial DNA
NAD	Nicotinamide adenine dinucleotide
NPs	Nanoparticles
Ox	Oxalate
P	Proline
PBS	Phosphate Buffered Saline
PCP	Pentachlorophenol



PCT	Photochemotherapy
PDT	Photodynamic Therapy
PEG	Poly(ethyleneglycol)
phen	Phenanthroline
PLIM	Phosphorescence Lifetime Imaging Microscopy
PLIM	Phosphorescence Lifetime Imaging Microscopy
PMT	Photomultiplier Tube
PyBOP	Benzotriazol-1-yl-oxytripyrrolidinophosphonium hexafluorophosphate
Q	Glutamine
R	Arginine
RNS	Reactive Nitrogen Species
ROS	Reactive Oxygen Species
RPMI	Gibco Roswell Park Memorial Institute Medium
RT	Room temperature
SEM	Scanning Electron Microscopy
SIM	Structured Illumination Microscopy
SR-SIM	Super-Resolution Structured Illumination Microscopy
STED	Stimulated Emission Depletion <i>Microscopy</i>
TAP	1,4,5,8-tetraazaphenanthrene
TCSPC	Time Correlated Single Photon Counting
TMRE	Trimethylrhodamine, ethyl ester
TPE	Two-Photon Excitation
tpybenzCOOH	4'- (4-Carboxyphenyl)-2,2' :6', 2''- terpyridine
TREM	Time-Resolved Emission Imaging Microscopy
WLL	White Light Laser

## Units of measurement

$\mu\text{s}$	Microsecond
$\mu\text{W}/\text{cm}^2$	Microwatts per square centimetre
$\text{cm}^{-1}$	Reciprocal wavelength
equiv.	Equivalent

g	gram
h or hr	Hour or hours
Hz	Hertz
K	Kelvin
L	Litre
M	Molarity
min	Minute
mol	Mole
nm	Nanometre
ns	Nanosecond
°C	Degrees Celsius
v/v	Volume per volume

## **Karmel Sofia Gkika**

Tailoring Ru(II) and Os(II) Luminophores to their application: from bioimaging and sensing to cytotoxic tools.

### **Thesis Abstract**

Luminescent complexes of ruthenium and osmium possess many attractive properties for their application as cellular imaging/sensing probes. In the case of Ru(II) polypyridyl complexes, such properties include large Stokes shift, long emission lifetimes, good photostability and versatile synthetic chemistry. Conjugation to cell penetrating and signal peptides has proven to be a useful strategy in overcoming potential solubility issues, promoting cellular uptake, and driving subcellular targeting. Presented in this thesis, are experimental findings on Ru(II) conjugates (peptide and non-peptide) which highlight the importance of balancing cell membrane permeability, lipophilicity, and cytotoxicity.

Osmium(II) polypyridyl complexes share many of the photophysical advantages of the second row metal luminophores. Although their emission quantum yield and lifetimes tend to be lower, they exhibit emission maxima in the deep red to near-IR spectral region and robust thermal- and photo- stability which is particularly important in the context of cell imaging. A key aim of this thesis was to extend the application of luminescent Os(II) peptide conjugates as imaging probes particularly toward tissue imaging and sensing using confocal microscopy and luminescence lifetime imaging. The experimental work presented here demonstrates the first investigation of an Os(II) probe for luminescence imaging of multicellular tumor spheroids which mimic the tumor tissue microenvironment.

Luminescent Ru(II) complexes have long been studied as oxygen sensors and certain research areas such as oxygen mapping by lifetime-based imaging, are well developed. Efficient and reliable oxygen probes which can quantify intracellular O<sub>2</sub> using a luminescence ratiometric signal are particularly useful, as they can be applied to conventional methods without the need for specialised equipment. Using a core-shell approach, a novel oxygen responsive Ru(II) was co-encapsulated with a reference BODIPY dye into the core of polystyrene particles coated with poly-L-lysine. The particles were examined for their performance as O<sub>2</sub> sensors in live mammalian cells.

## Chapter 1: Introduction

### 1.1 Photophysical characteristics of a good luminophore for bioimaging

Luminescence imaging including particularly confocal fluorescence and FLIM methods, are widely used techniques in biochemistry and molecular biology as they offer high contrast, sensitivity, good resolution, and flexibility in choice of luminophore probe. The rapid advancement in luminescence microscopy methods have increased the demand for novel imaging probes with properties such as photostability and sensitive environmental responsiveness.

The ideal photophysical characteristics of a luminescent imaging probe may vary depending on the precise application of the probe and the imaging technique used. Indeed, a vast range of probes have been developed for fluorescence/luminescence imaging including fluorescent proteins, organic fluorophores, nanoparticles, quantum dots and metal complexes.

Organic fluorophores such as rhodamine, AlexaFluor and Atto dyes have been used extensively as contrast agents in fluorescence imaging as they exhibit high molecular brightness and diverse synthetic versatility which are favourable characteristics of a cellular imaging probe. However, intrinsic drawbacks of organic fluorophores include undesired inner filter effects at high optical densities, self-quenching and poor photostability. The likelihood of dye self-quenching is decreased in compounds possessing a large Stokes shift (*large gap between the excitation and emission maxima*).

Ideally, a dye for cellular or tissue luminescence imaging should emit in the near-infrared (NIR) spectral region as it aids the avoidance of autofluorescence. Autofluorescence at short excitation wavelengths occurs from naturally fluorescent molecules within the cell and tissue environment or medium and usually decays on the nanosecond timescale. Nicotinamide adenine dinucleotide (NAD) and flavin adenine dinucleotide (FAD) are examples of intrinsic biological fluorophores for which several studies on their fluorescent properties have been carried out.<sup>1-6</sup>

In the context of luminescence imaging but also therapy, a probe absorbing in the low energy visible or NIR region is desired as this allows for deeper light tissue penetration and avoids biological damage from continuous photo-irradiation into spectral regions where there is absorbance by tissue.

The long-lived luminescence of metal complexes allows for discrimination from short-lived autofluorescence. Additionally, the long-lived excited state is susceptible to quenching thus expanding their application from bioimaging to biosensing. Organic dyes on the contrary have short-lived luminescence, typically  $< 10$  ns, rendering them relatively unsuitable for monitoring long lived molecular processes such as oxygen diffusion since deactivation to the ground state occurs on a much faster time scale than the molecular process itself. Transition metal complexes have also shown good photostability, particularly in the case of osmium(II) polypyridyl luminophores, avoiding photodecomposition and photobleaching effects. To date, the coordination compounds of the (*second and third row*)  $d^6$ - metals Ru(II), Os(II) or Ir(III) are amongst the most widely studied transition metal imaging probes.

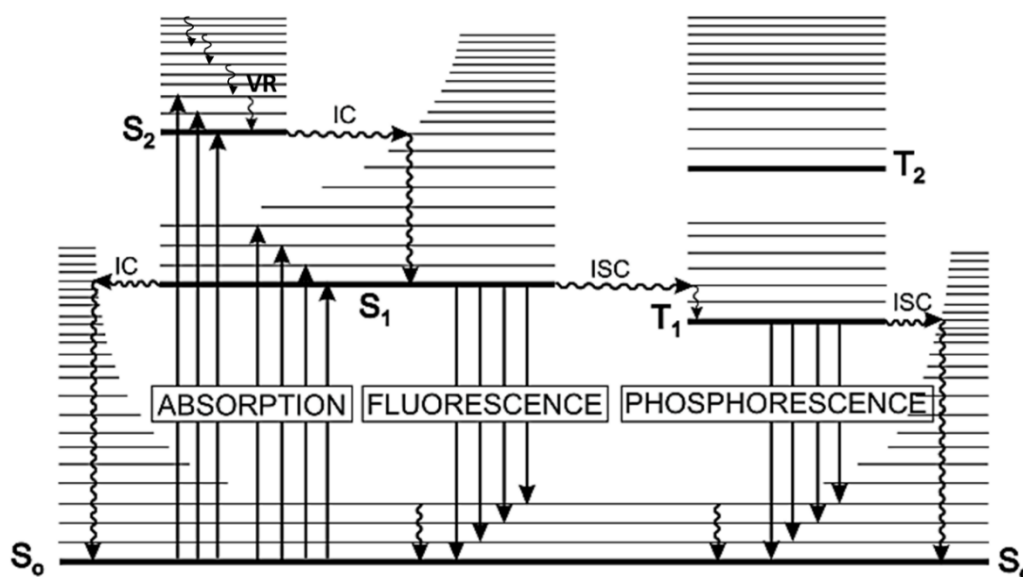
Aside from their favourable photophysical properties, which are synthetically tunable, metal complexes can also show aqueous solubility, cell permeability and uptake and can be driven to subcellular structures as discussed in later sections.

The focus of this thesis will be to examine how transition metal luminophores of Ru(II) and Os(II) can be tailored to their application, ranging from bioimaging/biosensing to therapy.

### 1.1.1 Principles of photophysics

The photophysical processes that occur upon electronic excitation of a molecule are mapped out by the Jablonski diagram, first proposed in 1933.<sup>7</sup> Figure 1.1 schematically illustrates the ground ( $S_0$ ), singlet ( $S_1$ ) and triplet ( $T_1$ ) state and their corresponding energy. Upon photon excitation, following promotion to the excited state ( $S_n$ ), deactivation occurs through internal conversion (IC), an isoenergetic crossover, to a vibrational level of equal energy of a  $S_{n-1}$  state followed by vibrational relaxation (VR) to the lowest vibrational level of the same state from where the molecule can return to its ground electronic state ( $S_0$ ) via radiative (luminescence) and non-radiative (IC/VR) pathways. Vibrational relaxation (VR) describes the relaxation from a vibrational state of an excited state ( $S_n$ ) to a vibrational state of lower energy within the  $S_n$  prior to relaxation between the excited states. Luminescence is the general term used to describe radiative decay pathways which includes fluorescence and phosphorescence. Fluorescence is red-shifted relative to the absorption band and phosphorescence is always observed at longer wavelengths than fluorescence in condensed media. Fluorescence describes the photon emission typically from the lowest singlet excited vibrational level to  $S_0$  and occurs in the time range of  $10^{-11} - 10^{-8}$  s. This process is said to be allowed as the excited and ground

electron have the same spin multiplicity. In contrast, phosphorescence, the process of emission from the triplet excited state to the ground state, is said to be forbidden due to parallel spins



**Figure 1.1** Jablonski Diagram collectively illustrating the photophysical phenomena upon photon absorption (adapted from reference).<sup>8</sup>

and occurs from  $10^{-6}$  s to the order of a few seconds. Phosphorescence involves intersystem crossing (ISC), an isoenergetic spin forbidden process which yields a change in multiplicity. This spin-forbidden emission is particularly observed for complexes of heavier atoms, i.e., *transition metals of the 2<sup>nd</sup> and 3<sup>rd</sup> transition series and lanthanides*, as spin-orbit coupling blurs the distinction between spin states. More specifically, the spin-orbit perturbative term in the Hamiltonian operator that describes the interaction of a molecule with the external electromagnetic field, allows for spin forbidden transitions. This perturbation scales with the fourth power of the atomic number of the atoms involved, meaning that it becomes more important for molecules consisting of heavy atoms.

There are a number of quantitative characteristics that define the photophysical performance of a probe including extinction coefficient, and quantum yield and emission lifetime which are determined by the rate constants characteristic of a luminescence decay.<sup>7</sup> The luminescence lifetime,  $\tau$ , can be defined as the average time a species occupies the excited state prior to deactivation and return to the ground state. More specifically, it is the time taken for the luminescence intensity to decay to  $1/e^{\text{th}}$  of its initial intensity or for the number of excited molecules to decay to  $1/e^{\text{th}}$  of the original population.

Equation 1.1 and 1.2 mathematically describe the luminescence lifetime of a molecule:

$$\tau = \frac{1}{k_r + k_{nr}} \quad [1.1]$$

Where  $k_{nr}$ : rate of non- radiative decay(s) ( $k_{IC}$ ,  $k_{ISC}$ ),  $k_r$  emissive rate often also labelled as  $\Gamma$ .

$$N(t) = N_0 e^{-t/\tau} \quad [1.2]$$

Where  $N(t)$ : population and time  $t$  and  $N_0$  original population.

Quantum yield,  $\phi$ , is mathematically expressed as the ratio of the non-radiative decay constant relative to the sum of rate decay constants (equation 1.3). In simple terms, it describes the number of photons emitted relative to the number of photons absorbed. This relationship depends largely on the molecular structure and photophysical processes that are favored upon photon excitation and is also directly related to the luminescence lifetime:

$$\phi = \frac{k_{nr}}{k_r + k_{nr}} = \tau * k_{nr} \quad [1.3]$$

Another important photophysical characteristic of a probe is molecular brightness which is defined as the product of molar extinction coefficient ( $\epsilon$ ) and quantum yield ( $\phi$ ). Molecular brightness is particularly important in the context of imaging as it can determine the sensitivity and signal-to-noise ratio for luminescence detection.

A variety of molecular interactions such as excited-state reactions, photoinduced electron transfer, energy transfer and collisional quenching can result in luminescence quenching.

The process of resonance energy transfer occurs when the excitation energy of one fluorophore (donor) is transferred to a second fluorophore (acceptor) resulting typically in the generation of an excited acceptor state. The two mechanisms of energy transfer are Dexter energy transfer and Förster energy transfer. Photoinduced electron transfer (PET) occurs when an electron from the excited donor state is transferred to a ground state molecule (acceptor). Inner filter effects can also result in luminescence quenching however this is the result of attenuation of the excitation and/or the emission energy and does not involve changes in the excited state lifetime of the fluorophore. Static quenching may also occur where the fluorophore and quencher interact in the ground state.

Collisional quenching occurs when the excited-state fluorophore is deactivated to the ground state upon contact with a molecule, *known as a quencher*, in solution. In collisional quenching, following diffusive encounter with the quencher, luminescence intensity and lifetime are both quantitatively reduced according to the Stern-Volmer equation:

$$\frac{I}{I_0} = \frac{\tau}{\tau_0} = K_{SV}[Q] + I = k_q\tau_0 \quad [1.4]$$

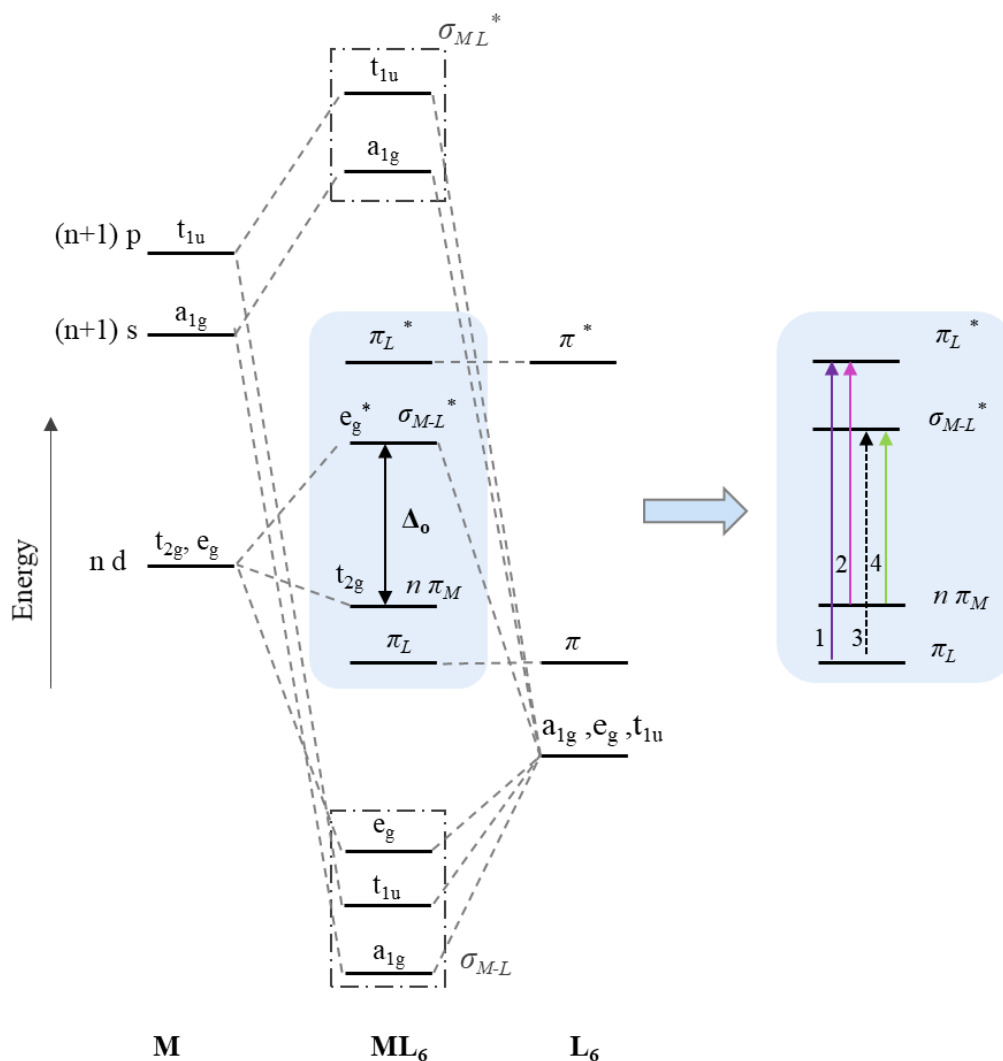
Where  $I_0$  and  $\tau_0$  are the luminescence intensity and lifetime respectively in the absence of quencher,  $K_{SV}$  is the Stern-Volmer quenching constant,  $[Q]$  is the quencher concentration and  $k_q$  is the rate of quenching constant.

### 1.1.2 Tuning of photophysical properties of metal complexes

The photophysics and photochemistry of the metal complex  $[\text{Ru}(\text{bpy})_3]^{2+}$  has thoroughly been studied and it is often used as an example to describe the photophysical activity of Ru(II) complexes.<sup>9-12</sup> The ultraviolet spectrum of  $[\text{Ru}(\text{bpy})_3]^{2+}$  is dominated by intense  $\pi - \pi^*$  ligand bands and the broad MLCT transition in the visible region. Spin forbidden transitions become more allowed with increase in the atomic number due to spin orbit coupling and so  $^3\text{MLCT}$  absorption transitions are observed for Ru(II) and Os(II) complexes. Upon photon absorption, the singlet  $^1\text{MLCT}$  excited state is populated and undergoes rapid intersystem crossing ( $k_{\text{ISC}}$ ) populating a triplet MLCT ( $^3\text{MLCT}$ ) excited state. In the case of  $[\text{Ru}(\text{bpy})_3]^{2+}$ , deactivation from the lowest excited MLCT state to the ground state ( $^1\text{A}_{1g}$  in  $\text{O}_h$  symmetry) is observed via emission or non-radiative decay via thermally activated ( $E_a$ ) population of the  $^3\text{MC}$  state ( $^3\text{T}_{1g}$  in  $\text{O}_h$  symmetry) which can lead to ligand dissociation. The  $^3\text{MC}$  surface intersects the GS at the minimum energy crossing point (MECP) as shown in figure 1.3. Enhanced ligand dissociation via  $^3\text{MC}$  population is observed for sterically strained complexes such as Ru(II) 2,2'-biquinoline (biq) complexes for example.<sup>13</sup> Distortion into the octahedral geometry by incorporating biq ligands, lowers the energy of the dissociative  $^3\text{MC}$  allowing its thermal population following photoexcitation to the  $^3\text{MLCT}$ , causing ligand dissociation.

Emission of Ru(II) complexes occurs in the range of 580 to 650 nm with  $\lambda_{\text{exc}} \approx 400 - 500$  nm. Luminescence lifetimes are typically on the order of hundreds of nanoseconds with quantum yields of 1 – 5 % (e.g.,  $[\text{Ru}(\text{bpy})_3]^{2+}$ ;  $\phi = 0.04$  in water (aerated)[57]).



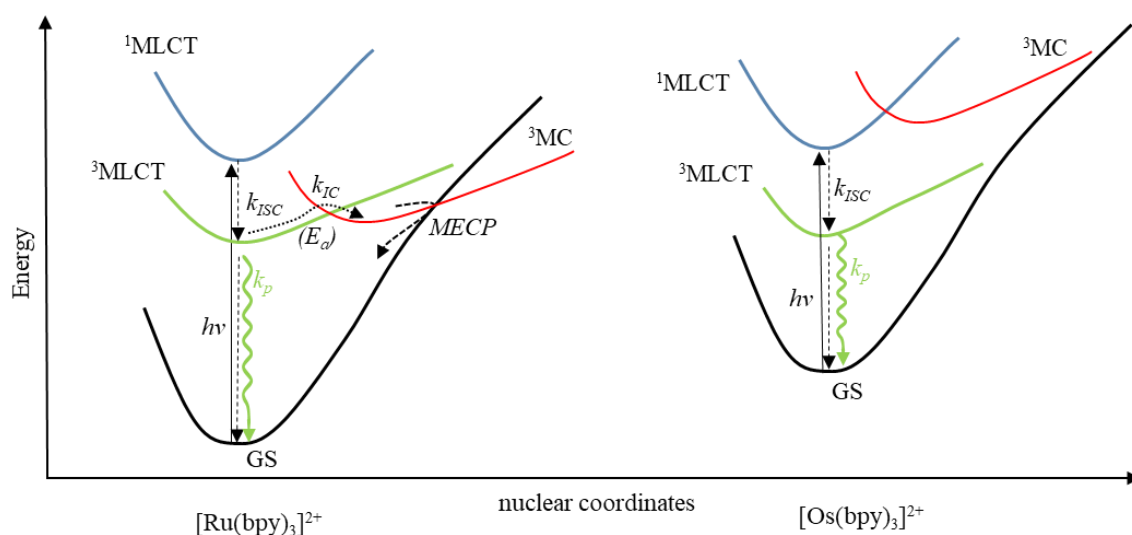


**Figure 1.2** Molecular orbital diagram for  $ML_6$  complexes in  $O_h$  symmetry ( $\sigma$ -bonding). The frontier orbitals (d-metal and  $\pi$ -ligand orbitals) are highlighted. Possible electronic transitions include: (1) ligand centred (LC), (2) metal- to-ligand charge transfer (MLCT), (3) ligand-to-metal charge transfer and (4) metal centred (MC).

It is important to note that a key advantage of Ir(III) complexes over Ru(II) polypyridyl complexes is the facile modification of their photophysical properties (e.g., *emission maximum*, *molecular brightness*) through ligand modification. Their excited states contain contributions from both  $^3LC$  and  $^3MLCT$  and permit greater photophysical tuning leading to complexes with a diverse range of emission properties across the visible to NIR spectrum. Nonetheless, modification of the  $\sigma$ -donor or  $\pi$ -acceptor properties of Ru and Os complexes can be used to tune these complexes, though less dramatically than for Ir(III). For example, coordination of strong  $\pi$ -acceptor ligands such as 2,2'-biquinoline (biq), decreases ligand field strength and stabilises  $d\pi$  orbitals leading to red-shifts in absorption and emission of Ru(II) complexes.<sup>14</sup>

Co-coordination of a strong  $\sigma$ -donor ligand such as pyridyl-1,2,4-triazolate (trz) is a means to promote photostability, by raising the energy of the  $^3\text{MC}$  preventing thus thermal population of this state and potential photodecomposition.<sup>14,15</sup> Although Ru(II) complexes are typically weaker emitters than Ir(III) complexes, they tend to exhibit lower cytotoxicity upon uptake in cells.<sup>16,17</sup>

Shifting the emission towards the NIR can also be achieved by synthetically modifying the metal centre of the complex. Os(II) polypyridyl complexes exhibit emission typically centred toward the NIR (>730 nm), which is advantageous in the context of bioimaging including cellular and tissue imaging.<sup>18–22</sup> Os(II) complexes share many of the same photophysical properties with their ruthenium analogues, with some key differences. As depicted in the energy level diagram (Fig. 1.3), the higher energy metal centred state ( $^3\text{MC}$ ) due to the increased crystal field splitting and higher lying antibonding  $e_g^*$  levels, is thermally inaccessible from the emitting  $^3\text{MLCT}$  state in the case of Os complexes.



**Figure 1.3** Schematic representation of the potential energy surface diagrams of  $[\text{Ru}(\text{bpy})_3]^{2+}$  and  $[\text{Os}(\text{bpy})_3]^{2+}$  describing key photophysical processes and illustrating greater separation of  $^3\text{MC}$  from  $^3\text{MLCT}$  in the case of Os(II) complexes preventing thermally activated crossing between the states as opposed to  $[\text{Ru}(\text{bpy})_3]^{2+}$ .

Hence Os(II) complexes are extremely photostable and their photophysics tend to show weak temperature dependence in contrast to their ruthenium analogues.<sup>23</sup> However, in comparison to  $[\text{Ru}(\text{bpy})_3]^{2+}$ , the  $^3\text{MLCT}$  excited state lifetime of Os(II) is much shorter and quantum yields are lower. The energy gap law applies to ruthenium and osmium complexes and predicts that the non-radiative rate decay increases as the energy gap between the excited and ground state

decreases.<sup>24</sup> Therefore, the low energy MLCT in the case of Os complexes leads to efficient non-radiative decay.

Complexes of the  $[M(\text{bpy})_3]^{2+}$  type exist as a mixture of optical and geometric isomers including two enantiomeric forms if one of the bi-pyridine ligands carries a substituent. Therefore, choosing a terpy ligand over bpy for example, allows for synthesis of achiral metal complexes avoiding stereoisomerism issues. The bis-terpy Ru(II) complex,  $[\text{Ru}(\text{tpy})_2]^{2+}$ , is short-lived and exhibits a significantly weak emission at room temperature owing to the easily quenched  $^3\text{MLCT}$ .

In contrast,  $[\text{Os}(\text{tpy})_2]^{2+}$  exhibits an intense long lived luminescence at room temperature due to the greater  $^3\text{MC}/^3\text{MLCT}$  energy gap.<sup>23</sup> Substitution of position 4' of the terpyridine ligands in  $[\text{Ru}(\text{tpy})_2]^{2+}$  with donor/acceptor moieties results in enhanced excited state properties.<sup>25</sup> Alternative bis-tridentate complexes include  $[\text{Ru}(\text{bqp})_2]^{2+}$  (where bqp = 2,6-bis(8'-quinolinyl)pyridine) which exhibit red-shifted and long-lived luminescence at room temperature ( $\tau \approx 3 \mu\text{s}$ ).<sup>26</sup>

In addition to photophysical tuning, coordination of specific ligands allows for the design and preparation of complexes with a responsive luminescence. For example, complexes of dipyrido[3,2-a:2',3'-c]phenazine (dppz) and derivatives exhibit no luminescence in aqueous solution but emission is switched on in hydrophobic environments such as upon DNA binding, leading to the design and development of a range of DNA "light-switch" dppz-complexes.<sup>27,28</sup> Separate to environmental sensing, sensing bio-relevant species such as oxygen can be achieved via coordination of the lipophilic diphenyl phenanthroline (dpp) ligand, for example, which also allows for cellular uptake and targeting of lipid rich regions.<sup>29-31</sup> Examples of metal complexes for intra-organelle and oxygen sensing are detailed in *section 1.4*.

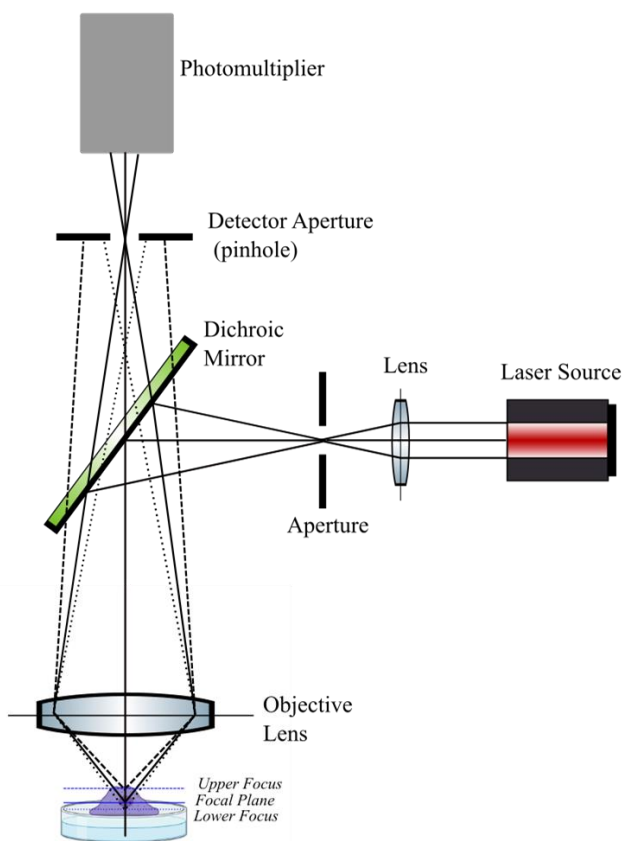
## 1.2 Microscopy Techniques

### 1.2.1 Confocal Laser Scanning Microscopy (CLSM)

In conventional wide-field microscopy, a high intensity arc or filament lamp is used to illuminate a sample. In this case, the entire sample is exposed to the light source leading to issues such as photo-bleaching. Confocal microscopy uses a laser excitation source, focused onto a small volume of the sample, and a detection pinhole which ensures that fluorescence from out-of-focus planes (i.e., *below or above the focal point of the sample volume*) is eliminated and only fluorescence from the focal plane focuses on the detector providing thus

images with improved resolution, and greater detail.<sup>32,33</sup> Luminescence from all focal planes of the sample reaches the detection pinhole which blocks out-of-focus light from reaching the detector, a photomultiplier tube (PMT). The dichroic mirror reflects light below a certain wavelength and the emission filter ensures that only specific fluorescence is transmitted to the detector. At any time, only a single spot is detected and in order to create a 2D image, this spot is moved in x- and y- direction over the sample (*scanning*) using rotating scan mirrors.<sup>32,34,35</sup>

The principle of a confocal microscope is illustrated in Figure 1.4. The laser light at a specific wavelength, is directed through an aperture and is focused on a specific point of the sample. A key advantage of CLSM is that 3D structural information of a sample can be obtained by scanning in the xy and z direction thus acquiring images of different focal planes in the z direction. Photobleaching remains a disadvantage in confocal microscopy particularly when



**Figure 1.4** Diagram of a confocal microscope optical set up.

using organic fluorophores.<sup>36</sup> Additionally, it is important to note that a sufficient probe quantum yield is required as use of a pinhole in confocal microscopy, means the amount of light reaching the detector is reduced compared to widefield methods. As aforementioned, metal luminophores exhibit characteristics such as good photostability, large Stokes shift and

long-lived excited states, which overcome common challenges in confocal microscopy such as autofluorescence, self-quenching and photo-bleaching.

### **1.2.2 Fluorescence/Phosphorescence Lifetime Imaging (FLIM/PLIM)**

Fluorescence lifetime imaging microscopy (FLIM) is a quantitative imaging technique that can be used for real-time mapping of the cellular and tissue microenvironment including cell functions and metabolic changes where the lifetime of a fluorophore is influenced by its local environment. In FLIM, in contrast to intensity-based imaging, the image is independent of luminophore concentration reflecting only the emission lifetime distribution of the probe. This is particularly helpful in the context of cellular studies where probe uptake in cells is often unpredictable.

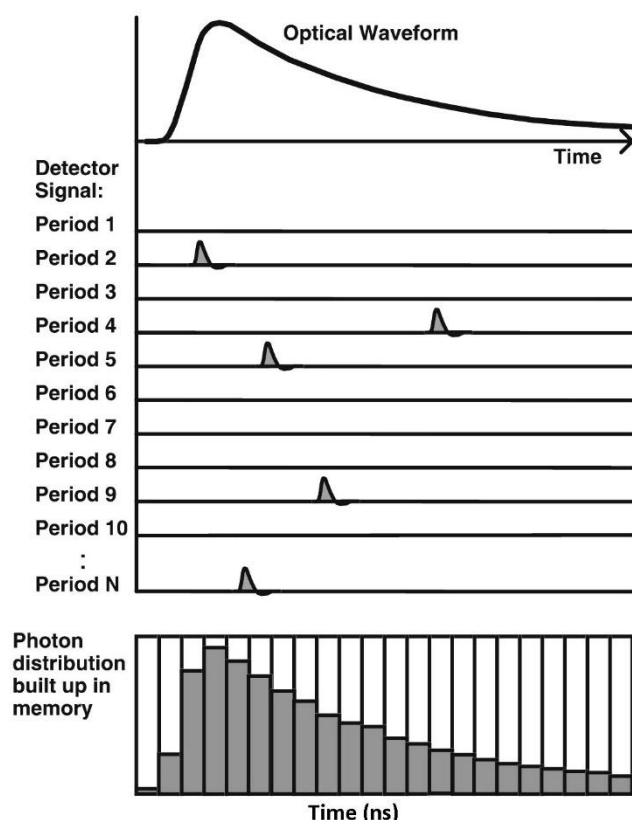
FLIM techniques are classified into time-domain (TD) and frequency-domain (FD) techniques. In FD-FLIM techniques the excitation light intensity is modulated or pulsed at a certain frequency and the fluorescence lifetime is derived from the modulation in intensity and the phase-shift of the fluorescence with respect to the excitation.<sup>37</sup> In TD-FLIM techniques the fluorescence decay can be measured using a multidimensional time-correlated single photon counting (TCSPC) system, which is an extension of the classic TCSPC technique.

In the classic TCSPC method, short pulses of light excite the sample and single photon events are collected over many cycles. The relative times between the laser excitation and corresponding fluorescence photon arrival are recorded in a histogram.<sup>38,39</sup> Following many thousands of pulse cycles, the histogram of arrival times of photons to the detector builds up a lifetime decay as shown in Figure 1.5. TCSPC relies on the presumption that for low power, high repetition rate (pulses per s) signals, the detection of more than one photon per laser pulse period in a single detector is improbable. The detection rate in fact is typically 1 photon per 100 excitation pulses.<sup>40</sup>

Similarly, in TCSPC FLIM used for imaging, the sample is scanned by a focused laser beam, single photons are detected and the arrival times ( $t$ ) of the photons with respect to the pulsed excitation are recorded. A three-dimensional data array is built based on the photon distribution over  $x$ -,  $y$ -, and  $t$ -. This array represents the pixels of a 2D scan, the FLIM image, where each pixel contains a fluorescence decay. The data obtained is analysed using a suitable exponential decay model. In the case of a single contributing fluorophore, a mono-exponential model is

used. Bi-exponential or multi-exponential emission decays can occur in the case of multiple fluorophores and also in cases where the fluorophore is imaged from a heterogeneous environment where the fluorophore lifetime is environmentally sensitive.

TCSPC FLIM delivers optimum photon efficiency<sup>41-43</sup>, can resolve complex decay profiles and is also compatible with confocal laser scanning and widefield microscopes.<sup>44</sup>

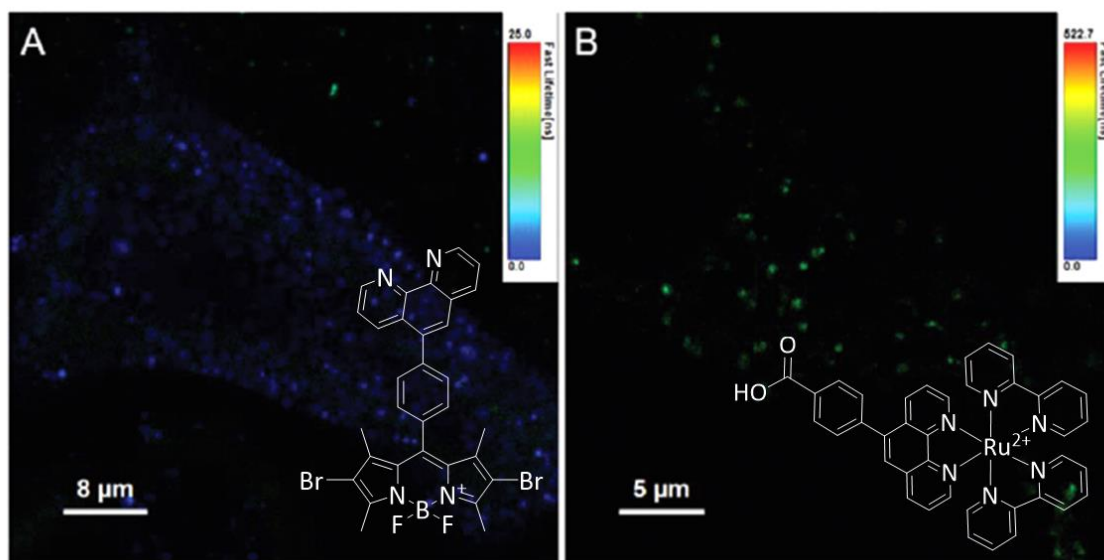


**Figure 1.5** Time-correlated single photon counting principle. The arrival of single photons following excitation are detected with respect to the laser pulse and the histogram of the detection times (i.e., the waveform of the optical pulse) is constructed. Adapted from <sup>37</sup>.

In the context of applying metal complex luminophores in lifetime imaging, the technique is referred to as *phosphorescence* lifetime imaging (PLIM) as emission is formally a phosphorescence.

As mentioned previously, the long-lived phosphorescence of metal complexes allows for discrimination from short-lived excited states that may have been co-excited, and several approaches can be used to achieve this.

The nanoparticle system **RuBODIPY** consisting of a short-lived BODIPY and a longer-lived ruthenium(II) component, was taken up by live CHO cells and luminescence lifetime imaging was carried out. The emission decays from the acquired lifetime images were fit to a bi-exponential model and each component was distinguished and mapped separately as shown in Figure 1.6.<sup>45</sup>



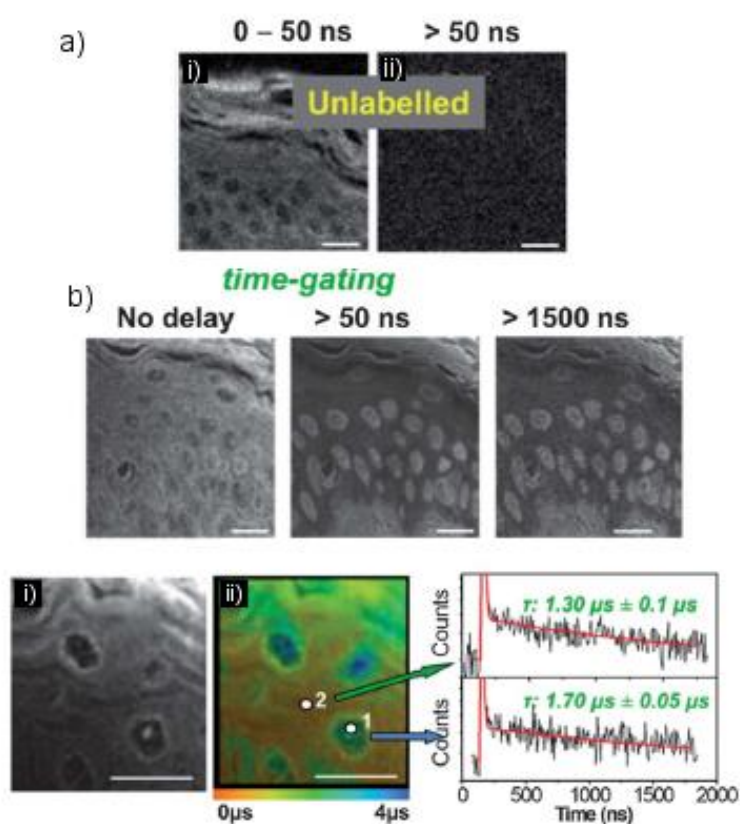
**Figure 1.6** FLIM images of **RuBODIPY** nanoparticles in live CHO cells where the lifetime mapping of (A) encapsulated phen-Ar-BODIPY-Br<sub>2</sub> and (B) surface-bound [Ru(bpy)<sub>2</sub>(phen-Ar-COOH)]<sup>2+</sup> are shown.<sup>45</sup>

Discrimination between short-lived and longer-lived components can also be achieved by using time-gated imaging where a time-gated delay is introduced after the laser excitation, and detection is switched on after the delay (time-gated detection window). This is particularly useful for improving contrast and removing autofluorescence background contributions from short-lived endogenous fluorescent biomolecules in the complex environment of cells and tissues. In time-resolved emission imaging microscopy (TREM), the autofluorescence occurring at early times can be gated out and emission lifetime of the long-lived probe can be obtained.

Figure 1.7 shows an example of two-photon time-gated imaging of tissue samples using a cyclometallated platinum(II) complex.<sup>46</sup> The **PtL<sup>1</sup>Cl** labelled tissue shows strong autofluorescence in the absence of a time delay, similar to the unlabelled sample (Fig. 1.7a,b). In contrast, after a time delay of >50 ns, intact cellular structures are observed from the Pt(II)-emission, free from background emission. Lifetime mapping also revealed variations in the

emission lifetime of the complex depending on its localization. The lifetime of the complex was approximately 1.7  $\mu\text{s}$  when localized in the nucleus and approximately 1.3  $\mu\text{s}$  when localized in the cytoplasm and extracellular regions.

Time-gated detection can also be exploited in dyad or dinuclear systems. For example in the case of a heterometallic complex, the lifetimes of the  $\text{Eu}^{\text{III}}$  and  $\text{Ir}^{\text{III}}$  differed by three orders of magnitude allowing for time-gated detection of each component.<sup>47</sup> Two-photon PLIM time-gated images showed that the Ir-based emission is no longer visible after a delay of 50  $\mu\text{s}$  allowing for detection of the Eu-based luminescence at longer timescales.



**Figure 1.7** Autofluorescence-free imaging of skin tissue samples. (a) Intensity image of unlabelled samples at i) 0-50 ns and ii) > 50 ns and (b) time-gated images of tissue labelled with  $\text{PtL}^1\text{Cl}$  where i) intensity image acquired at higher spatial resolution and ii) the corresponding lifetime distribution.<sup>46</sup>

While luminescence lifetime imaging is used to eliminate autofluorescence or to distinguish between lifetimes of different fluorophores, the real beauty of the technique lays in distinguishing lifetime changes relevant to a single fluorophore occupying different states of interaction within its environment.



For example, luminophore lifetime can be influenced by pH, ions, oxygen and molecular binding and following the first reported application of FLIM in cells in 1992<sup>48</sup>, there have been increasing reports of cellular and tissue fluorescence lifetime imaging monitoring changes in pH<sup>49</sup>, concentration of ions such as calcium ( $\text{Ca}^{2+}$ )<sup>50</sup>, oxygen levels<sup>51,52</sup> and cellular viscosity<sup>53,54</sup>. Application of metal complex luminophores in luminescence lifetime imaging are discussed throughout this thesis.

### **1.3 Cellular uptake and accumulation**

#### **1.3.1 Mechanisms of cellular and subcellular uptake**

In order for a luminophore to enter the cytosol of the cell, it must transport from the surrounding medium across the lipid bilayer of the cell membrane. Transport into the cell can be accomplished via a number of mechanisms which can either be energy-dependent or independent as shown in Figure 1.8.<sup>55</sup>

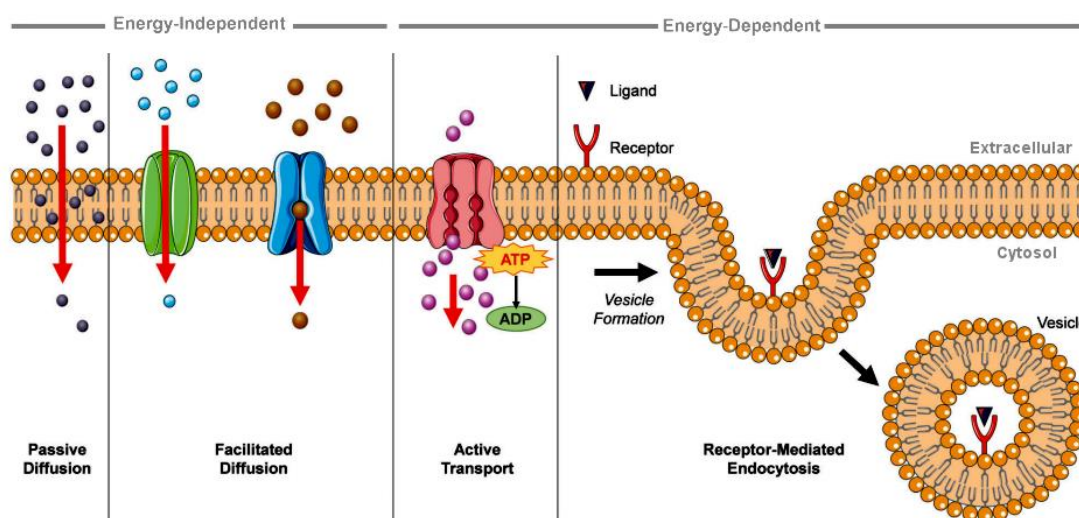
Passive diffusion is an energy-independent mechanism by which the molecule diffuses through the membrane bilayer and into the cell. This mode of uptake is not cell type specific and thus molecules internalized by passive diffusion find application across different cells.

Most mammalian cells have a negative transmembrane potential (typically *ca.* -60 to -70 mV) as defined by the difference in electric charges across the cell membrane with respect to the exterior environment.<sup>56</sup> Therefore, uptake of positively charged complexes can be driven by the membrane potential. However, complex lipophilicity still plays a critical role in overcoming the hydrophobicity of the bilayer core as discussed in *subsection 1.3.2.1*.

During facilitated diffusion, *which is also energy-independent*, uptake is mediated through transport proteins. These proteins can act as (i) carrier proteins by binding to specific molecules or (ii) channel proteins by forming pores in the membrane through which molecules of specific size and charge can pass.<sup>55,56</sup>

Active transport involves transporting molecules against their concentration gradient which requires energy. Transmembrane proteins (ATPases) hydrolyze ATP while molecules are simultaneously transported rendering the process energy-dependent.<sup>56</sup> Endocytosis is also an energy-dependent process and is typically used by cells to transport macromolecules and nanoparticles.

In endocytosis, the cell membrane engulfs the entrant species forming a membrane-bound vesicle around it that is then transported into the cell. A number of endocytic pathways exist including phagocytosis, pinocytosis, and receptor mediated endocytosis.<sup>57</sup> Receptor mediated endocytosis involves the recognition of molecules by specific receptors located on the surface of the cell membrane.



**Figure 1.8** Schematic illustration of the potential mechanisms by which molecules can enter cells (adapted from reference).<sup>55</sup> Passive and facilitated diffusion are energy-dependent processes whereas active transport and endocytosis are energy-independent. Here, receptor-mediated endocytosis is shown as an example of an endocytic pathway.

This mechanism of uptake has been exploited for the design and preparation of macromolecules but also nanoparticles which specifically target diseased cells that overexpress key receptors such as folate, transferrin and somatostatin at the membrane surface.<sup>58–61</sup> For example, enhanced uptake of a somatostatin-targeting Ru(II) conjugate was observed in A549 cells overexpressing somatostatin receptors.<sup>61</sup> The conjugate showed excellent photosensitized toxicity with an  $IC_{50}$  of  $300 \mu\text{M}$  in the absence of light *versus* an  $IC_{50}$  of  $13 \mu\text{M}$  upon irradiation.

Experimental methods to determine whether the mechanism of uptake requires energy or not include low temperature uptake studies where at  $4^\circ\text{C}$ , the cellular metabolic pathways are switched off and active endocytosis is inhibited.<sup>62</sup> Endocytic and metabolic inhibitors such as oligomycin and 2-Deoxy-D-glucose respectively may also be used alone or combined with  $4^\circ\text{C}$  studies to block specific uptake pathways.<sup>63</sup>

Following cellular uptake, subcellular targeting of organelles, such as the mitochondria, is typically of interest in the context of bioimaging/sensing and therapy.

The mitochondria comprise of two membranes, the *outer* and *inner* mitochondrial membrane. The latter is far less permeable allowing only very small molecules to cross into the *matrix* where mitochondrial DNA (mtDNA) and other biomolecules are contained. The inner mitochondrial membrane folds into ridges known as *cristae* which house the protein components for the electron transport chain (ETC) involved in ATP generation.<sup>64</sup> ATP production is driven by membrane-based proton pumps which generate an electrochemical gradient. This transmembrane electrochemical gradient is known as mitochondrial membrane potential (MMP),  $\Delta\Psi_m$ , and is typically between -80 and -180 mV for healthy cells. Depolarization of the inner membrane may result in loss of the MMP and release of pro-apoptotic proteins such as cytochrome c into the cytosol.<sup>65</sup> The double membrane and membrane potential of mitochondria introduce additional challenges to complex uptake.

The cell nucleus shares a similar structural complexity to the mitochondria. The nuclear envelope is a double membrane sheet comprising of the *inner* and *outer* nuclear membrane which are merged at several sites generating nuclear pores.<sup>66</sup> Uptake of ions, and small molecules is mediated through the nuclear pores containing a channel (~ 30 nm in diameter) via passive diffusion. On the contrary, uptake of larger molecules is mediated through transport receptors.<sup>67</sup> Alternative approaches to overcome nuclear and mitochondrial uptake challenges, include the use of signal peptides discussed in *section 1.3.2.2*.

Lysosomes and lipid droplets (LDs) are single-membrane (phospholipid monolayer) organelles. Differential organelle localisation can be achieved by simple tuning of the ligand substituents as reported in the case of rhenium tetrazolato complexes<sup>68</sup> or by conjugation to a lipid chain that can facilitate entry to LDs.<sup>69</sup>

### **1.3.2 Strategies for uptake of metal complexes**

Cell membrane permeability is a key barrier to the widespread application of metal complexes in cellular and tissue imaging. One approach to overcome this challenge, is the use of organic solvents such as dimethyl sulfoxide (DMSO) or detergents such as Triton-X to permeabilize the cell membrane of mammalian cells. Permeabilizing agents act by disrupting the integrity of the membrane lipid bilayer thus promoting entry of the compound into the cell.<sup>70</sup> This technique is widely used for organic fluorophores<sup>71-73</sup> and metal complexes<sup>74-77</sup> but it is not always explicitly explained.

For example, Zhang *et. al.* reported a lipophilic red-emitting iridium complex which was dissolved in a 10% DMSO solution prior to injection into mice for hypoxic tumor imaging.<sup>78</sup> The use of such high concentration of organic solvent was not addressed and neither were the potential effects on cell viability or tissue health. Williams *et.al.* reported the first application of MLCT-fluorescent rhenium complexes for cellular imaging.<sup>79</sup> The study comprised of a series of lipophilic and hydrophilic complexes showing moderate membrane permeabilities based on their interactions with liposomes. Interestingly, for cellular studies, the complexes were pre-dissolved in 100% DMSO and then introduced to cells at a final concentration of 5% DMSO. The authors do not discuss membrane permeabilization and although they report toxicity and cell lysis at high concentrations of the complex, they do not correlate these findings with the high % DMSO used. Permeabilization techniques can cause irreversible damage to the cell membrane and are particularly not suitable for tissue or in-vivo applications.

It is typical to use a small percentage (< 1 % v/v) of organic solvent to pre-dissolve the complex in order to solubilise it in aqueous solution for cellular administration.<sup>29,80,81</sup> However, in some cases where a solvent is used, it is difficult to differentiate the influence of compound properties from the influence of the solvent on the cellular uptake. Huang *et al.* have reported the cellular uptake of cationic iridium(III) pyridine complexes using a 2% DMSO solution.<sup>82,83</sup> The studies however do not detail whether this percentage of DMSO mediates internalization or whether the complexes are inherently cell permeable due to their charge or lipophilicity.

Transition metal complexes can be synthetically tuned, by altering the metal centre and/or the coordinated ligands, in order to achieve a balance between lipophilicity and charge which in turn can promote cellular uptake. Uptake may also be influenced by complex solubility and size. Improving the aqueous solubility of a complex can eliminate the need for a solvent or at least reduce the percentage of solvent required. It is important to note that these properties may also affect intracellular accumulation and potential cytotoxicity. Other approaches including the use of nanocarriers<sup>84-87</sup>, liposomes<sup>88</sup>, dendrimers<sup>89</sup>, glycoconjugates<sup>90,91</sup>, lipophilic moieties such as triphenylphosphonium (TPP)<sup>92</sup> and cell penetrating peptides (CPPs)<sup>93,94,81</sup> have also been shown to increase solubility and improve membrane permeability thus facilitating reliable uptake of complexes within cells for a range of applications.

### 1.3.2.1 Striking a balance: lipophilicity, charge, size and counterion

Efficient molecular cellular penetration and uptake is strongly influenced by the lipophilicity, charge and size of the complex.<sup>95–97</sup> The negatively charged cell membrane favours the uptake of cationic species and lipophilic cations tend to more efficiently permeate the lipid membrane. Early studies by Puckett and Barton on a series of dipyrrophenazine (dppz) complexes of ruthenium showed that increasing ligand lipophilicity promotes efficient uptake in mammalian cells. The lipophilic diphenyl-phenanthroline Ru(II) complex,  $[\text{Ru}(\text{dip})_2\text{dppz}]^{2+}$  (where dip = 4,7-diphenyl-1,10-phenanthroline) was readily transported into HeLa cells in comparison to the bis-bipyridine complex,  $[\text{Ru}(\text{bpy})_2\text{dppz}]^{2+}$ .<sup>62,98</sup> The uptake of  $[\text{Ru}(\text{dip})_2\text{dppz}]^{2+}$  in cells was not inhibited upon treatment with metabolic inhibitors, indicating that an energy-independent mechanism of uptake was in place. Similar to other lipophilic cations such as rhodamine 123,<sup>99,100</sup> uptake of the complex was influenced by changes to the cell membrane potential and thus a passive diffusion mode of entry was proposed. It should be noted that the Ru complex was introduced to cells from a concentrated DMSO stock and as aforementioned, determining the precise influence of compound lipophilicity *versus* solvent impact on uptake can be challenging.

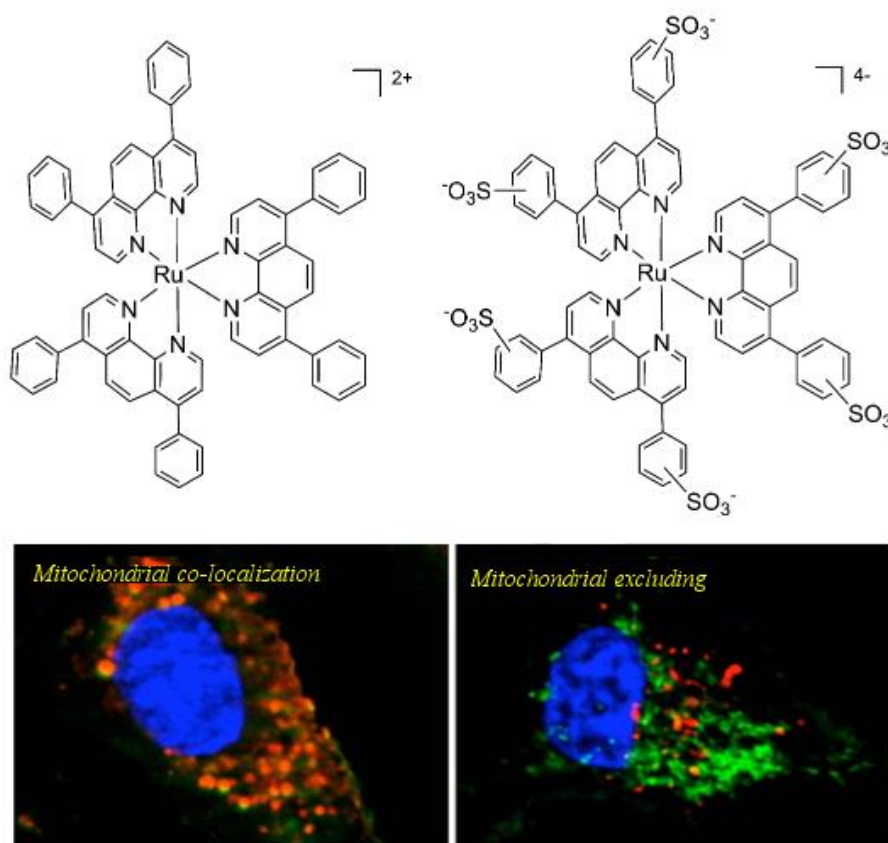
Gunnlaugsson and co-workers reported the incorporation of two TAP ligands (TAP= 1,4,5,8-tetraazaphenanthrene) yielding the water soluble  $[\text{Ru}(\text{TAP})_2(\text{dppz})]^{2+}$  complex which showed cytoplasmic staining in HeLa cells.<sup>101</sup> While the nature of the ancillary ligands is important, chemical modifications to the dppz ligand itself can also influence the lipophilicity and consequently cellular uptake and localization of the complex.<sup>102–104</sup> Increase in lipophilicity but also in dark cytotoxicity was observed for Ru(II) bis-phen and bis-TAP complexes coordinated to a hydrophobic alkylamide phen ligand.<sup>105</sup>

Coordination to cyclometalated ligands has been shown to enhance lipophilicity and improve cellular uptake for iridium and ruthenium complexes.<sup>106,107</sup> For example, exchanging the **bpy** ligand in  $[\text{Ru}(\text{bpy})_2(\text{dppz})]^{2+}$  for the cyclometalating 2-phenylpyridine (**phpy**) ligand, yielded a lipophilic and cell permeable Ru(II) complex.<sup>108</sup> However, such enhanced lipophilicity due to cyclometallation can promote toxicity<sup>109,110</sup> and importantly, cyclometallation can lead to excited state deactivation in the case of Ru(II) complexes.<sup>111</sup>

The intracellular environment consists of numerous and complex membranous structures and organelles, such as the previously described mitochondria and nucleus, which have unique membrane barriers. The importance of lipophilicity-charge balance in cellular uptake and

accumulation, was highlighted in a study by Glazer and co-workers on the uptake of two Ru(II) complexes differing in their charge but coordinated to the highly lipophilic *dip* ligand.<sup>30</sup> The complexes were successfully internalized by A549 cells where, the lipophilic  $[\text{Ru}(\text{dip})_3]^{2+}$  (log  $P = +1.8$ ) accumulated at the mitochondria and lysosomes while the anionic and less lipophilic  $[\text{Ru}((\text{SO}_3)_2\text{-dip})_3]^{4-}$  (log  $P = -2.2$ ) localized in the cytosol and was mitochondrial excluding (Figure 1.9). Studies on the uptake mechanism of these complexes would have contributed towards understanding the effect of charge/log  $P$  balance on interactions with the cell membrane. Both complexes showed photo-induced toxicity but interestingly the mitochondrial accumulating complex also showed dark toxicity with an  $\text{IC}_{50}$  between 0.62 and 3.75  $\mu\text{M}$ .

Several studies have been reported on uptake of iridium(III) complexes by tuning the charge/lipophilicity balance.<sup>83,112–114</sup> Also, it is important to consider the molecular size of a



**Figure 1.9** Cellular staining of A549 cells following uptake of the positively charged and lipophilic  $[\text{Ru}(\text{dip})_3]^{2+}$  complex (left) or the anionic  $[\text{Ru}((\text{SO}_3)_2\text{-dip})_3]^{4-}$  (right). Incorporation of six sulfonic acids ( $\text{SO}_3^-$ ) into the *dip* ligands altered the subcellular localization properties of the complex rendering it mitochondrial excluding. Here, Ru(II) emission is shown in red and Mitotracker Green FM (in green) and Hoechst (in blue) are used as co-staining dyes to visualize the mitochondria and nucleus (adapted from reference)<sup>30</sup>.

complex or its capability for aggregation as this may hinder efficient cellular uptake as reported by Lo *et.al.*<sup>115</sup> Examples of metal complexes and their corresponding estimated  $\log P$  and  $IC_{50}$  values are listed in Table 1.1 in order to highlight how synthetic modifications of the metal centre or coordinated ligands can alter these properties. Figure 1.10 illustrates the chemical structures of such coordinated ligands.

Another strategy to promote cell uptake is the incorporation of poly(ethyleneglycol) (PEG) groups into the complex structure. This approach also improves aqueous solubility. Lo and co-workers have reported efficient cell membrane permeation of Ir(III)-PEG conjugates and interestingly, the PEG-conjugates showed reduced cytotoxicity in comparison to the PEG-free counterparts.<sup>116,117</sup> The long PEG chains likely protect the Ir(III) complexes from nonspecific intracellular interactions with proteins, DNA, and organelles.

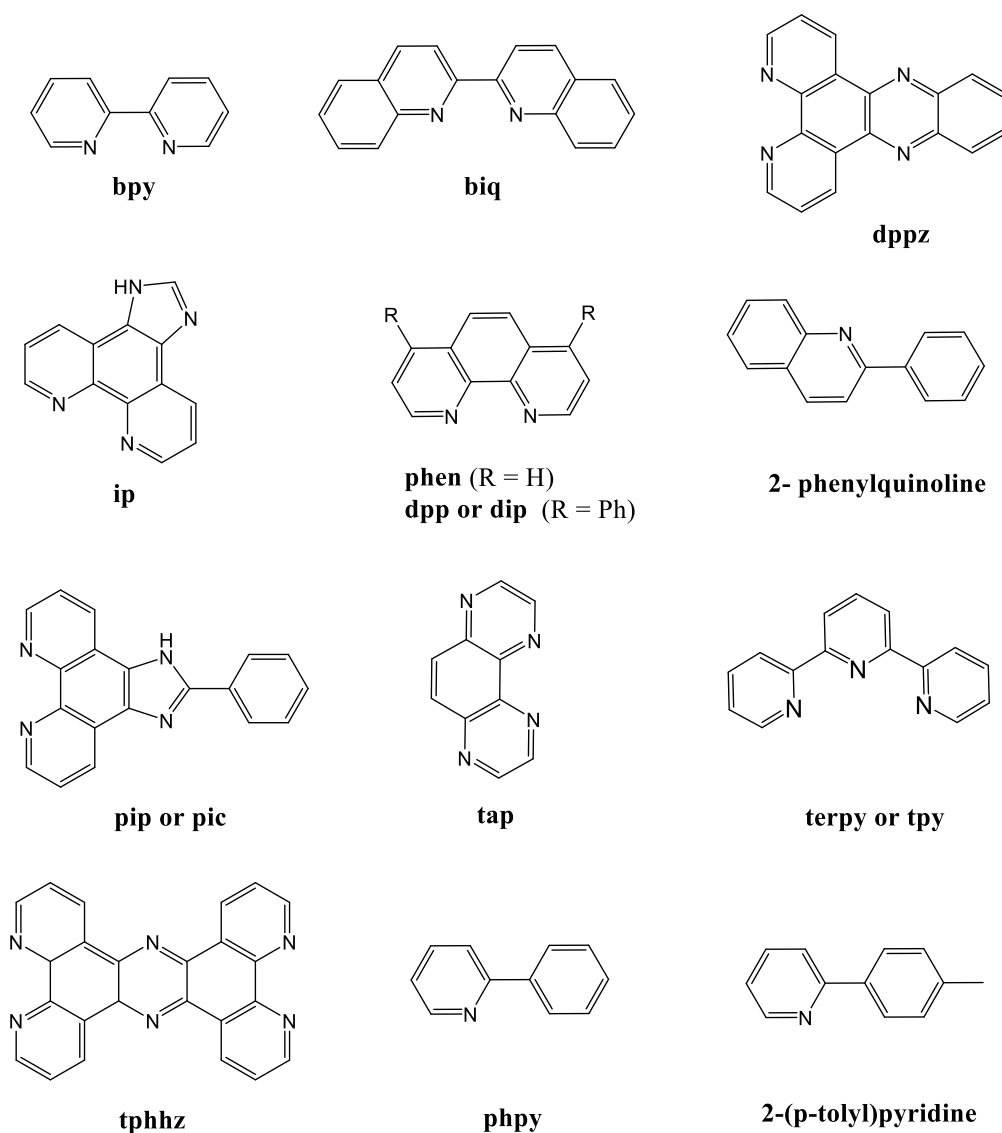
**Table 1.1** Lipophilicity and cytotoxicity of metal complexes upon synthetic modifications

Compound	$\log P_{o/w}$ [a]	$IC_{50}$ ( $\mu M$ ) [Cell Line]	Reference
Propidium iodide	-5.10	-	119
Hoechst 33342	-4.10 to +4.70	-	119
[Ru(phen) <sub>3</sub> ] <sup>2+</sup>	-0.33	268.0 [MCF-7] <sup>[b]</sup>	120
[Ru(bpy) <sub>3</sub> ] <sup>2+</sup>	-0.41	341.5 [MCF-7] <sup>[b]</sup>	120
[Ru(pic) <sub>3</sub> ] <sup>2+</sup>	+2.67	66.0 [MCF-7] <sup>[b]</sup>	120
[Ru(bpy) <sub>2</sub> (dppz)] <sup>2+</sup>	-2.50	159.9 [HeLa]	108
[Ru(dip) <sub>2</sub> (dppz)] <sup>2+</sup>	+1.30	-	62
[Ru(dip) <sub>2</sub> (dppz-NH <sub>2</sub> )] <sup>2+</sup>	-0.27	>100 [HeLa] <sup>[b]</sup>	104
[Ru(dip) <sub>2</sub> (dppz-CH <sub>2</sub> OH)] <sup>2+</sup>	-0.62	Cell impermeable [HeLa]	104
[Ru(bpy)(phpy)(dppz)] <sup>1+</sup>	+1.00	0.6 [HeLa]	108
phpy = 2-phenylpyridine			
[Os(phen) <sub>2</sub> (phpy)] <sup>+</sup>	+2.43	0.4 [A172] <sup>[b]</sup>	121
[Ir(phen)(C <sup>N</sup> ) <sub>2</sub> ] <sup>+</sup>	+0.63	1.68 [HeLa] <sup>[c]</sup>	122
<i>where N<sup>C</sup> = 2-(p-tolyl)pyridine</i>			

<sup>[a]</sup>Lipophilicity,  $\log P_{o/w}$ , was estimated by the partition coefficient of each compound in octanol/water. Propidium iodide and Hoechst are both commercially available organic nucleic acid dyes where the first is permeant only to damaged/dead cells and the latter is cell permeable.  $IC_{50}$  values for the metal complexes were determined based on incubation periods of 24 h unless stated otherwise where <sup>[b]</sup> 48 h, <sup>[c]</sup> 72 h.

Another approach to enhance solubility and promote cellular uptake includes simply selecting an appropriate soluble counterion. Zhu *et al.* reported the use of pentachlorophenol (PCP) for the efficient transport of an otherwise cell impermeable complex.<sup>118</sup> This strategy allowed for high contrast imaging of chromosomal DNA by selectively targeting each enantiomer of  $[\text{Ru}(\text{bpy})_2(\text{dppz})]^{2+}$  to the nucleus without structural modification of the intercalating probe.

Here, the bis-bipyridine,  $[\text{Ru}(\text{bpy})_2(\text{dppz})]^{2+}$  complex was shown to passively diffuse across the membrane of several mammalian cell lines via an ion pairing mechanism. It was proposed that a neutral lipophilic adduct, *ion pair*, was formed between the hydrophilic cationic Ru complex and the anionic pentachlorophenolate which permits penetration through the cell membrane. This was confirmed for an analogous Ru complex using single-crystal X-ray diffraction which showed the formation of the ion pair  $[\text{Ru}(\text{phen})_3]^{2+}[\text{PCP}]_2$ .



**Figure 1.10** Key ligands used as building blocks for the design of metal complexes.



### 1.3.2.2 Bioconjugation to cell penetrating and signal peptides

The ability of cationic peptide sequences to cross the cell membrane and facilitate uptake of small molecules was first demonstrated in 1965 by Ryser and Hancock with the cationic amino acid-mediated enhanced uptake of albumin followed by studies on conjugation of poly-L-lysine to albumin and horseradish peroxidase.<sup>123,124</sup>

The most studied cell penetrating peptide is likely the arginine rich HIV-Tat transduction protein (RKKRRQRRR) from immunodeficiency virus.<sup>125,126</sup> Homopolymers of arginine (polyarginines) have shown superior cellular uptake compared to other cationic analogues such as ornithine and histidine.<sup>127</sup> With studies showing no strict requirement for side chain length or backbone chirality (*D-Arg* vs *L-Arg*), it was concluded that the guanidinium head groups of arginine units are structural features crucial for cellular uptake. Barton *et al.* first reported peptide-facilitated cellular uptake of rhodium complexes.<sup>128</sup> Cargo transduction occurs for arginine sequences of Arg<sub>n</sub> or R<sub>n</sub>, where n = 6 – 11 residues with octaarginine (Arg<sub>8</sub>) and nonaarginine (Arg<sub>9</sub>) being most efficiently transported. Keyes's group reported the efficient transport of an otherwise cell-impermeable Ru(II) polypyridyl complex, [Ru(bpy)<sub>2</sub>(pic)]<sup>2+</sup> via conjugation to octaarginine.<sup>74</sup> The general conjugation strategy in the group involves incorporation of a carboxylic acid group in the metal complex which can be exploited for amide coupling with an amine-terminated peptide sequence in the presence of a suitable coupling reagent such as PyBOP (benzotriazol-1-yloxy-tripyrrolidinophosphonium hexafluorophosphate).<sup>1</sup> The conjugate was found to passively transport into myeloma cells within 12 min. Additionally, studies showed that Arg<sub>5</sub> or lower conjugates are not effective in promoting metal complex permeation. Wender *et al.* reported similar decrease in uptake efficiency of shorter polyarginines.<sup>129</sup>

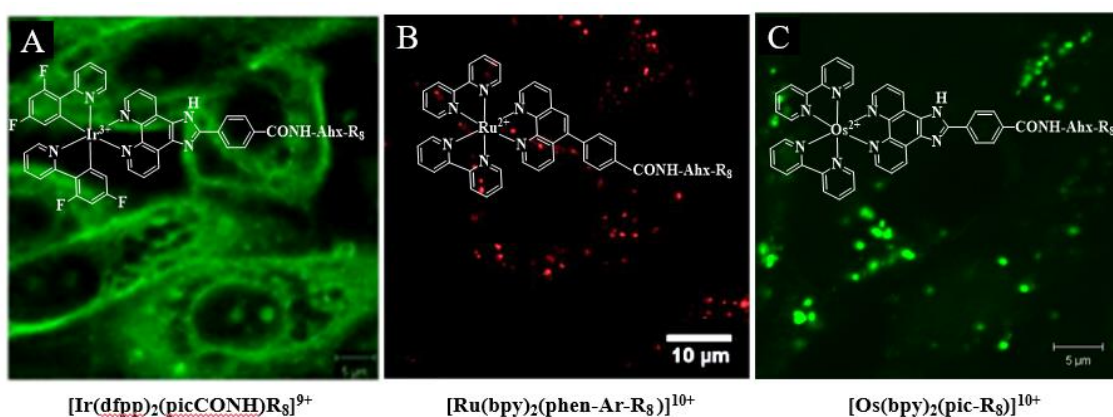
Octaarginine-driven cellular uptake has been reported for a range of complexes differing in their metal centre and coordinated ligands. Figure 1.11 illustrates the dye distribution of key examples of octaarginine conjugates of Ir(III), Ru(II) and Os(II). Conjugation to Arg<sub>8</sub> rendered all three complexes membrane permeable in aqueous solution without the requirement for permeabilization. A pH and oxygen sensitive iridium(III) complex was prepared by coordinating two cyclometalated ligands (2-(2,4-difluorophenyl)pyridine; dfpp) to an Ir(III)

---

<sup>1</sup>There are numerous coupling reactions suitable for peptide conjugations which involve crosslinkers, cleavable systems or “click” chemistry for example but a detailed review is beyond the scope of this thesis and so the reader is directed to the following book: *Bioconjugate Techniques*, Elsevier, 2013.

centre along with the pic(COOH) ligand, 2-(4-carboxyphenyl)imidazo[4,5-f][1,10]phenanthroline, carrying a terminal carboxyl moiety permitting amide coupling to an octaarginine sequence in order to improve aqueous solubility.<sup>16</sup>

Uptake of the  $[\text{Ir}(\text{dfpp})_2(\text{picCONH-R}_8)]^{9+}$  conjugate by SP2 and CHO cells was observed within 15 minutes of incubation. Cytotoxicity studies showed that both the Ir(III) parent complex and conjugate were cytotoxic towards these cell lines but interestingly, the conjugate showed increased toxicity with an  $\text{IC}_{50}$  of 35  $\mu\text{M}$  (SP2 cell line) and 54.1  $\mu\text{M}$  (CHO cell line).



**Figure 1.11** Confocal luminescence imaging of live mammalian cells incubated with octaarginine conjugates of Ir(III), Ru(II) and Os(II). A) Ir-R8 in CHO cells at 70  $\mu\text{M}$  / 15 min incubation, B) Ru-R8 in HeLa cells at 70  $\mu\text{M}$  / 4 h incubation and C) Os-R8 in CHO cells at 70  $\mu\text{M}$  / 2 h incubation in the absence of light at 37  $^{\circ}\text{C}$ .<sup>16,130,131</sup>

The cytotoxic character of iridium complexes has been reported in a number of studies<sup>80,109,132</sup> and it is likely that increased cytotoxicity is the result of rapid uptake and wide distribution of the conjugate within cells. In fact, it has been noted that cell viability may be affected by the precision of conjugate localization. For example, when conjugated to octaarginine, the  $[\text{Ru}(\text{bpy})_2(\text{phen-Ar-COOH})]^{2+}$  complex distributed throughout the cytoplasm and exhibited increased toxicity towards HeLa cells with an  $\text{IC}_{50} < 50 \mu\text{M}$ , whereas when conjugated to precision peptide signals which drive and restrict confinement of the complex to specific organelles (e.g., *endoplasmic reticulum*), reduced toxicity was observed ( $\text{IC}_{50} > 200 \mu\text{M}$ ).<sup>130</sup> Low cytotoxicity towards CHO cells was reported for an osmium(II) octaarginine conjugate,  $[\text{Os}(\text{bpy})_2(\text{pic-R}_8)]^{10+}$ .<sup>131</sup> The conjugate showed rapid internalization into the cytoplasm of CHO cells, similar to its ruthenium analogue, followed by partial mitochondrial and lysosomal localization.

There have been multiple pathways and mechanisms proposed by which polyarginines permeate the cell membrane. Although there are a number of studies that report that polyarginines can promote permeation through a passive mechanism<sup>133</sup> or through local changes at the membrane<sup>134</sup>, the key pathway in live cells appears to be ATP activated endocytosis<sup>135</sup>. Polyarginine interactions with cell surface lipids and formation of neutral complexes that transport across the bilayer have also been reported as well as surface attachment through interactions with heparan sulfate proteoglycans (HSPG).<sup>136–140</sup>

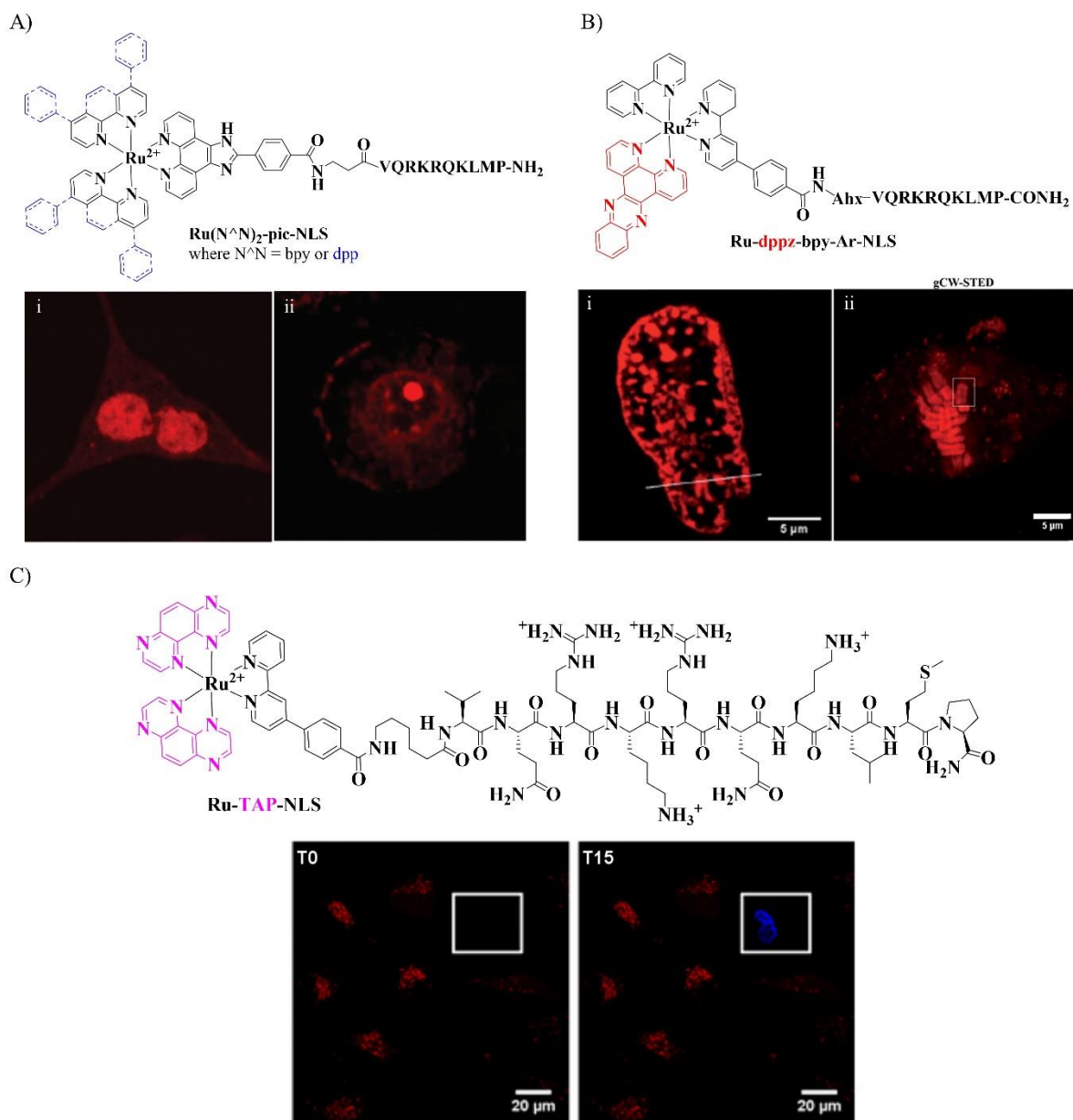
*Penetratin*, a cationic peptide sequence (RQIKIWFQNRRMKWKK) corresponding to the R-helix of the Antennapedia homeodomain, is capable of crossing lipid bilayers thus acting as a cell penetrating peptide.<sup>141</sup> Studies have shown that the uptake mechanism involves direct interaction of the peptide with membrane lipids and does not involve vesicle disruption or pore formation.<sup>142,143</sup> Peptide conjugation of *Penetratin* to [Ru(bpy)<sub>2</sub>-phen-Ar-COOH]<sup>9+</sup> allowed for delivery of the complex to the endoplasmic reticulum in live HeLa cells.<sup>130</sup>

Although cell penetrating peptides such as polyarginines can facilitate efficient cell permeability, specific organelle targeting of imaging probes or therapeutic agents can be achieved using signal peptides. Signal peptides can be naturally derived or designed sequences which are recognized by proteins in organelle membranes.

Nuclear localising signal (NLS) peptides are typically derived from transcription factors and can cross the cellular membrane and enter the nuclear envelope. To date, NLS sequences which have been derived from transcription factors include NFκB, TCF1-α, TFIIE-β, Oct-6 and SV40.<sup>144–146</sup> Studies by Ragin *et al.*, demonstrated that the NLS peptide, VQRKRQKLMP, derived from NFκB, was most effective in promoting nuclear penetration.<sup>145</sup> Based on this finding, Keyes's and co-workers exploited NFκB transcription factor bioconjugation for the efficient and selective nuclear uptake of Ru(II) complexes.<sup>29</sup> The lipophilic character of the metal complex remains important in the distribution of the complex as demonstrated in this study. In the case of the more hydrophilic [Ru(bpy)<sub>2</sub>(pip-NLS)]<sup>6+</sup>, nuclear staining was observed whereas the dpp-based complex, [Ru(dpp)<sub>2</sub>(pic-NLS)]<sup>6+</sup> showed accumulation to the nucleolus. High-resolution imaging of chromosomal DNA was achieved using a Ru-dppz NLS conjugate, [Ru(dppz)(bpy)(bpy-Ar-NLS)]<sup>6+</sup>.<sup>130,147</sup>

With aim to extend the application of Ru-NLS conjugates toward theranostics, a Ru(II)-bis-TAP (TAP = 1,4,5,8 – tetraazaphenanthrene) complex capable of photoactivated toxicity upon

DNA binding was presented.<sup>148</sup> **Ru-TAP-NLS** was targeted specifically to the nuclei of live HeLa and CHO cells and in the absence of light and under imaging conditions the cells remain



**Figure 1.12** Chemical structures of NLS-driven nuclear targeting Ru(II) complexes and representative images of their corresponding application in mammalian cells. A) **[Ru(bpy)<sub>2</sub>(pic-NLS)]<sup>6+</sup>** and **[Ru(dpp)<sub>2</sub>(pic-NLS)]<sup>6+</sup>** showed nuclei and nucleolus staining respectively.<sup>29</sup> B) Confocal (i) and STED (ii) images of **[Ru(dppz)(bpy)(bpy-Ar-NLS)]<sup>6+</sup>** nuclear and chromosomal DNA staining.<sup>130</sup> C) Following DNA binding of **Ru-TAP-NLS** in live HeLa cells, continuous photoirradiation of selected cells resulted in cellular damage as indicated by DRAQ 7 nuclear staining in blue.<sup>148</sup>

viable. Following nuclear uptake and DNA binding, evident by the extinguishing emission of the complex, increased photoirradiation of selected cells induced cellular destruction attributed to DNA oxidation by photoinduced electron transfer between guanine and the Ru(II) complex.

In a recent study by Pope *et. al.*, an alternative nuclear localisation sequence, *PAAKRVKLD*, was conjugated to a cyclometallated iridium(III) complex.<sup>149</sup> The c-Myc NLS is derived from the human c-Myc protein and is essential for nuclear localisation of the protein.<sup>150</sup> Confocal imaging and co-staining studies with Hoechst 33342 revealed that in contrast to the non-peptide Ir(III) complex, which showed cytoplasmic staining, the conjugate, Ir-CMYC, showed nuclear localisation facilitated by the NLS sequence. However, it is important to note that Ir-CMYC did not show preferential nuclear localisation as cytoplasmic staining was also observed. Interestingly, no cytotoxicity was observed for the NLS-conjugate for concentrations up to 100  $\mu$ M, in contrast to the non-peptide analogue which was cytotoxic ( $IC_{50} \geq 20 \mu$ M).<sup>149</sup>

Similar to nuclear penetration, mitochondrial penetration is also challenging owing to the inner mitochondrial membrane, a barrier limiting diffusive transport.

Mitochondria-penetrating peptides (MPPs) have been employed for the specific targeting of mitochondria with aim to study the complex processes associated with these organelles. Kelley et al carried out a detailed iterative study on synthetic peptide sequences relating to signal sequences effective in promoting mitochondrial targeting of fluorescent probes/drug analogues. Amongst the most effective of sequences was an 8-amino acid sequence, *FrFKFrFK*, containing *D*-arginine and hydrophobic residues.<sup>151</sup> Keyes's group then exploited conjugation to FrFKFrFK and the acetyl-blocked sequence, FrFKFrFK(Ac), to effectively and selectively drive mono- and di-nuclear Ru(II) complexes to the mitochondria.<sup>152,147</sup> The application of mitochondria-targeted probes in live mammalian cells for bioimaging/sensing and therapy are discussed in *section 1.4.1*.

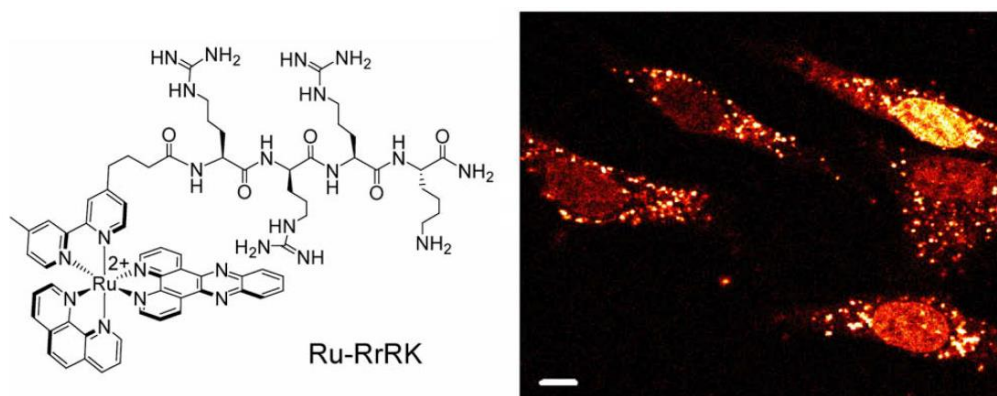
It is important to highlight that these studies collectively have shown that conjugation to signal peptides can drive *different* metal complexes specifically to the same organelle.

#### **1.4 Metal complexes as luminescent imaging/sensing probes and therapeutic agents**

As mentioned in *section 1.3*, a number of strategies have been reported to achieve reliable cellular uptake and specific organelle targeting of metal complexes. Bioconjugation to cell

penetrating peptides is a strategy that has proven to provide efficient cellular uptake and precise targeting of metal complexes in cells without the use of permeabilization agents.

Early examples of peptide driven metal complexes in confocal imaging include studies carried out by Barton and co-workers. Studies on rhodium(III) 5,6-chrysenequinone diimine (chrysi) and ruthenium(II) dipyrido-phenazine (dppz) complexes found that conjugation to octaarginine enhances cellular uptake and interestingly attachment of a fluorescein moiety, in the case of the Ru(II)-dppz complex, leads to nuclear localization.<sup>128,153</sup> In order to reduce nonspecific DNA binding owing to the highly charged R8, a shorter peptide sequence, **RrRK** (where r= D-arginine), was conjugated to a **Ru(dppz)** complex achieving cellular uptake and nuclear accumulation above a threshold concentration of 100  $\mu\text{M}$  in complete media (**Figure 1.13**).<sup>154</sup>



**Figure 1.13** Distribution of **Ru(dppz)-RrRK** in HeLa cells. Confocal imaging showed cytoplasmic and nuclear staining of cells treated with 100  $\mu\text{M}$  for 2 h. Scale bar = 10  $\mu\text{M}$ .<sup>154</sup>

A study by Keyes's group illustrated the multimodal imaging potential of peptide-linked Ru(II) complexes by studying the cellular uptake of  $[\text{Ru}(\text{dppz})_2\text{PIC}]^{2+}$  parent complex and octaarginine conjugate.<sup>81</sup> Using CLSM, emission was observed for cells treated with either parent or conjugate. However, complementary resonance Raman intensity mapping revealed that only the conjugate transferred across the cell membrane while the parent complex accumulated in the outer membrane of cells.

Complexes of ruthenium have been explored in detail for their interaction with nucleic acid materials<sup>155–158</sup>, mitochondria<sup>159,160</sup> and application in photodynamic therapy (PDT)<sup>161–166</sup> and photochemotherapy (PCT)<sup>167–169</sup>. By eliminating the reduction step of Ru<sup>III</sup> complexes, Ru<sup>II</sup> compounds can be activated via ligand exchange and/or photoirradiation. Complexes of other redox active metals such as Cu, Fe and Rh can promote oxidative DNA damage. Metallo-based

artificial metallo nucleases (AMNs), such as  $[\text{Cu}(\text{1, 10-phenanthroline})_2]^{2+}$ , have also been studied for their potential in DNA binding and oxidation.<sup>170-174</sup>

The overall potential of transition metal complexes for photodynamic therapy has been particularly highlighted by a recent breakthrough with the first Ru(II)- polypyridyl photosensitizer (**TLD1433**) for PDT to reach human clinical trials, developed by McFarland *et al.*<sup>161</sup> Photoirradiation of the imidazo-phenanthroline Ru(II),  $\text{rac-}[\text{Ru}(\text{dmb})_2(\text{IP-3T})]\text{Cl}_2$  (where IP = imidazo[4,5-f][1,10]-phenanthroline, 3T = chromophore and dmb = 4,4'-dimethyl-2,2'-bipyridine) results in  $^1\text{O}_2$  sensitization and electron transfer owing to its long-lived  $^3\text{IL}$  and  $^3\text{MLCT}$  excited state and has been shown to promote single and double strand DNA cleavage with enhanced activity in the presence of glutathione (GSH).<sup>175</sup>

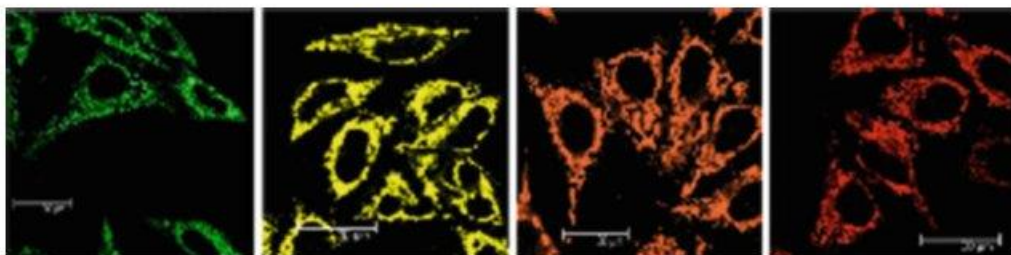
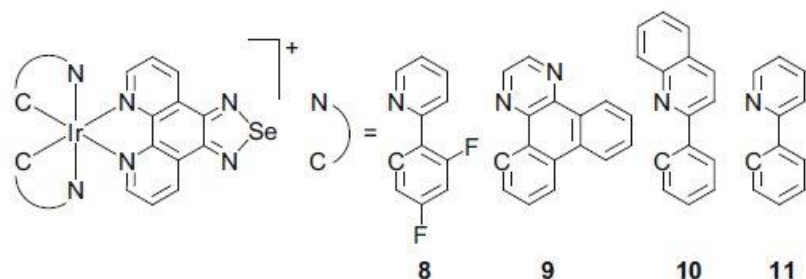
While the primary focus of this thesis is ruthenium(II) and osmium(II) polypyridyl complexes, it is important to note that iridium(III)<sup>16,116,176-179</sup> and rhenium(I)<sup>180</sup> complexes have been widely explored as luminophores in live cell imaging. Due to the lipophilic character of iridium(III) complexes, intracellular localization tends to be non-specific by showing nuclear-excluding cytoplasmic accumulation and staining of hydrophobic organelles such as the endoplasmic reticulum, Golgi apparatus or mitochondria.<sup>83,114</sup>

Specific mitochondrial accumulation in HeLa cells was achieved for a series of iridium(III) complexes,  $[\text{Ir}(\text{N}^{\wedge}\text{C})_2(\text{phenSe})]^+$  by incorporating carbonyl *m*-chlorophenylhydrazone, an oxidation phosphorylation uncoupler (Figure 1.14).<sup>181</sup> The complexes showed intense phosphorescence, good photostability and exhibited resistance to the loss in mitochondrial membrane potential. The application of luminescent iridium nanoparticles in bioimaging has also been reported<sup>182,183</sup> and has been extended towards multiphoton lifetime imaging<sup>184</sup>.

Briefly, following the breakthrough with cisplatin for cancer treatment in 1978<sup>190,191</sup> and the approval of carboplatin and oxaliplatin in 1992 and 2002 respectively, compounds of similar structure with other metals were investigated. Some of the Ru<sup>III</sup> clinically developed complexes include: KP1019<sup>192</sup>, NKP1339 (IT- 139)<sup>193,194</sup> and NAMI-A<sup>195,196</sup>. Although initially a very promising anticancer agent and first Ru-based compound to enter clinical trials, NAMI-A proved to not be effective as a solo drug or as a combined drug.<sup>195</sup>

Initial efforts involving the preparation of Os analogues of the Ru-based antiproliferative compounds showed mainly modest cytotoxic activity<sup>186,187</sup> and relative inertness towards ligand substitution resulting in poor hydrolysis or inactive hydroxido species under physiological conditions.<sup>197</sup>





**Figure 1.14** Confocal images of iridium complexes  $[\text{Ir}(\text{N}^{\text{C}})_2(\text{phenSe})]^+$  (**8-11**) illustrating green, yellow, orange and red phosphorescence respectively. <sup>181,185</sup>

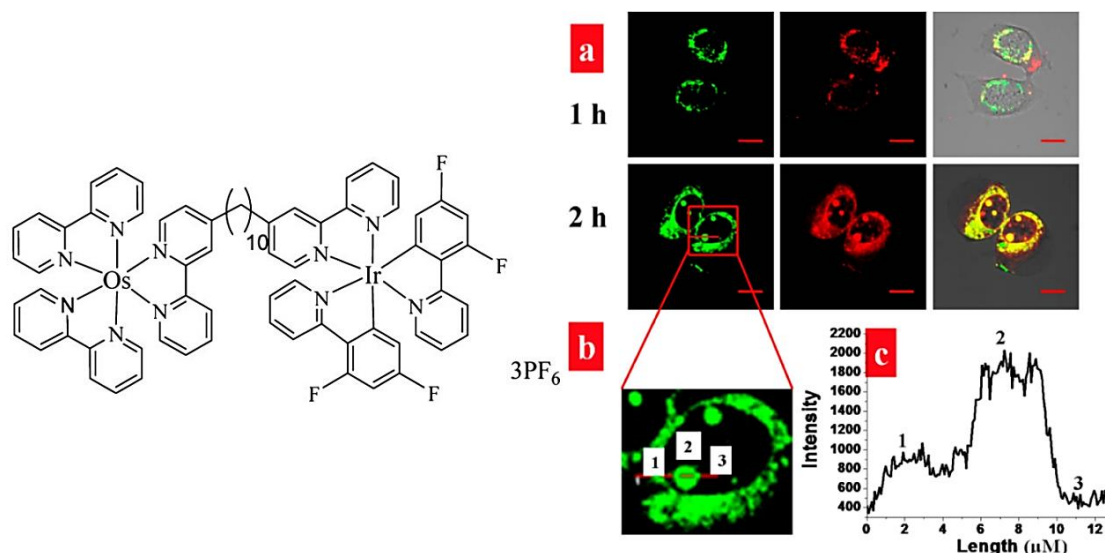
Osmium complexes share many of the photophysical advantages of their ruthenium(II) analogues but initial studies focused on their application as antiproliferative compounds in cancer therapy <sup>186-189</sup>.

Dyson and Sandler *et al* have worked extensively on the design and development of Ru(II) and Os(II)  $\eta^6$ -arene half-sandwich “piano-stool” complexes for medicinal applications. <sup>198,199</sup> For example, Sadler *et al.* reported a series of iodido Os<sup>II</sup> p-cymene arene complexes<sup>200</sup>, which exhibited dark toxicity against breast cancer cells through a route which does not involve DNA binding; in contrast to other Os<sup>II</sup> and Ru<sup>II</sup> arene compounds. <sup>188,189,201</sup>

A heterodinuclear complex, **OsIr**, containing iridium was the first to incorporate osmium(II) in a luminescent cell imaging probe.<sup>202</sup> The lipophilicity of the iridium(I) moiety facilitated transport of the dual-emissive probe ( $\lambda_{\text{em}}$  534 and 721 nm) across the cell membrane of MCF 7 cells where cytoplasmic and nucleolus staining was observed. Solution titrations with bovine serum albumin (BSA) and RNA revealed a ratiometric emission response between the Os and Ir moieties (Figure 1.15).

Considering these interactions, it would have been interesting to report on cell viability and potential antiproliferative effects of OsIr in order to explore the full capability of the complex.

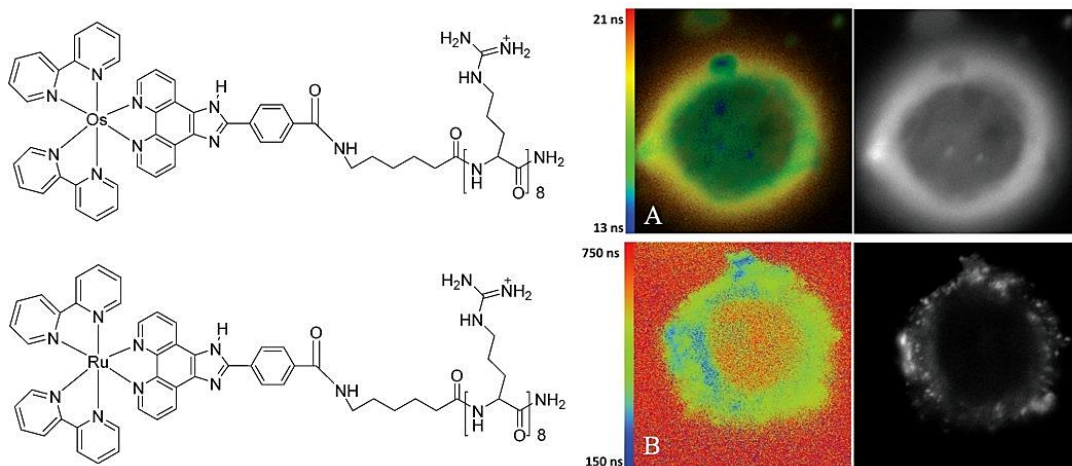




**Figure 1.15** Chemical structure of **OsIr** dinuclear complex and confocal images of uptake in MCF-7 cells. Following 1 h incubation at 37 °C, cytoplasmic staining is evident by the dual emission corresponding to the iridium (green) and osmium (red) channel. Nucleus staining was observed at 2 h incubation. The luminescence intensity profile at cytoplasmic and nucleolus regions revealed extensive accumulation **OsIr** in cells. <sup>202</sup>

Keyes's group reported the first application of an osmium(II) polypyridyl complex in live cell imaging by strategically conjugating an octaarginine sequence to an otherwise cell impermeable osmium(II) complex.<sup>131</sup> The octaarginine conjugate,  $[\text{Os}(\text{bpy})_2(\text{pic-R8})]^{10+}$  exhibited NIR emission ( $\lambda_{\text{max}}$  726 nm), robust photostability and a short luminescence lifetime of 33 ns, independent of variations in oxygen and temperature conditions. The osmium conjugate showed similar low cytotoxicity to its ruthenium(II) analogue enabling studies in live cells using confocal and luminescence.

PLIM studies showed that the emission lifetime of  $[\text{Ru}(\text{bpy})_2(\text{pic-R8})]^{10+}$  decreased from approximately 540 ns in the cytoplasm to 453 ns in the cell membrane of SP2 cells, attributed to higher solubility of oxygen in the cell membrane. Although the emission lifetime of  $[\text{Os}(\text{bpy})_2(\text{pic-R8})]^{10+}$  was not sensitive to oxygen, changes were observed in response to the cellular environment (Figure 1.16) and cell membrane composition of two mammalian cell lines.<sup>74,131</sup>

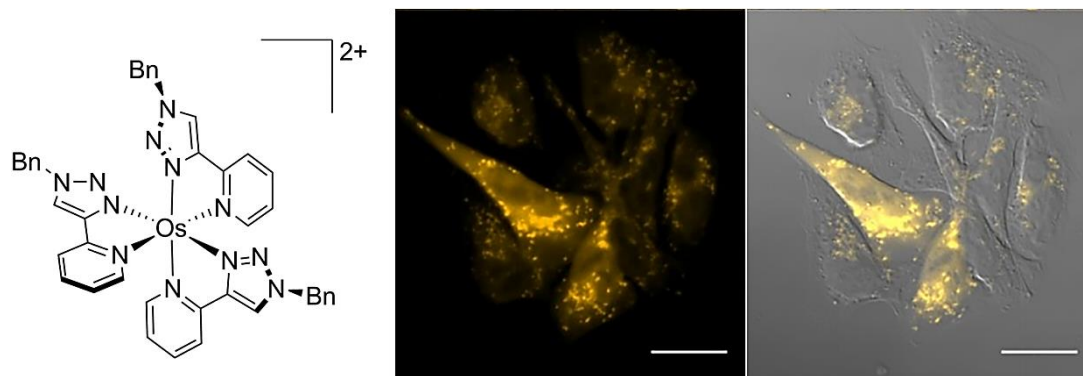


**Figure 1.16** Phosphorescence lifetime imaging of (A)  $[\text{Os}(\text{bpy})_2(\text{pic-R8})]^{10+}$  ( $70 \mu\text{M}$  / 24 h) and (B)  $[\text{Ru}(\text{bpy})_2(\text{pic-R8})]^{10+}$  ( $350 \mu\text{M}$ / 15 min) in live SP2 cells. The false colour images and intensity mapping highlight the differences in emission lifetime of the luminophore pending on its localization in the cell. The emission lifetime of the osmium(II) conjugate was  $18.8 \pm 0.6 \text{ ns}$  at the cell membrane and  $14.5 \pm 0.5 \text{ ns}$  in the cytoplasm. <sup>131</sup>

The application of osmium complexes in bioimaging but also theranostics has since received considerable attention.<sup>203–205</sup> Zhang and co-workers carried out comparative studies on the photophysics and cellular imaging of a red emitting Ru(II) complex and a NIR emitting Os(II) complex.<sup>204</sup> The two complexes, differing only in the metal centre, showed unique localization in live A549 cells. Lysosomal accumulation was observed for the osmium complex whereas the ruthenium complex showed mitochondrial staining. Interestingly, the Os(II) complex showed increased phototoxicity at 633 nm. Targeting cellular organelles or biomolecules and selectively triggering cell death while monitoring the process are key objectives of theranostics. This offers the advantage of determining dose requirements for probe uptake and accumulation without inducing toxicity unless it is photo-triggered.

Elliott and co-workers presented a triazole-based Os(II) complex,  $[\text{Os}(\text{pytz})_3]^{2+}$  (pytz = 1-benzyl-4-(pyrid-2-yl)-1,2,3-triazole), which showed endosomal and lysosomal uptake in EJ bladder and HeLa cancer cells.<sup>206</sup> The complex showed low dark and light toxicity rendering it suitable for luminescence imaging (Figure 1.17). However, it is important to note that the emission range (565- 615 nm) of the complex did not coincide ideally with the biological window. Interestingly, derivatives of the same triazole-Os(II) complex have recently found application as photoinduced antimicrobial agents.<sup>207</sup>

Complexes of Rh(III)<sup>128</sup> and Zn(II)<sup>208,209</sup> have also been applied in bioimaging, but to a lesser extent. Pt(II)/Pt(IV) compounds have historically found application mainly in therapy as anticancer agents<sup>210,211</sup> but recently have been studied in the context of imaging<sup>46,212,213</sup>. Due to their attractive photophysical properties including good photostability, transition metal complexes have also recently been applied to super-resolution imaging techniques including Stimulated Emission Depletion (STED) Microscopy and Structured illumination microscopy (SIM).<sup>130,214,215</sup>



**Figure 1.17** Chemical structures of [Os(pytz)<sub>3</sub>]<sup>2+</sup> luminophore and confocal images showing the distribution of the complex (yellow) in EJ bladder carcinoma cells. [Os(pytz)<sub>3</sub>]<sup>2+</sup> (yellow) was found localize in endosomes and lysosomes. Scale bar = 20  $\mu\text{m}$ .<sup>206</sup>

Overall, the application of metal complexes has extended from luminescent bioimaging to intracellular sensing but also therapy bridging the fields of bioimaging with medicinal chemistry.

#### 1.4.1 Mitochondrial targeted complexes

The intracellular environment consists of organelles, biomolecules and analytes with significant interest which are attractive for targeting. In parallel, the same targets of interest can pave the way for the design and development of novel therapeutic metallo-based agents. This section presents key examples of mitochondrial-targeting metal complexes with application in biosensing and therapy.

Mitochondria are key organelles involved in the energy metabolism and ATP production of eukaryotic cells. Critically involved in apoptosis initiation, oxidative metabolism, and reactive oxygen species (ROS) production, the role of mitochondria extends far beyond that of being “the power-house” of the cell. Mitochondrial dysfunctions are associated with several conditions and diseases including inflammatory diseases such as cancer.<sup>216</sup> Cancer cells exhibit

changes in energy metabolism and ROS production, increased transmembrane potential and upregulation of pro-apoptotic proteins.<sup>217,218</sup> Therefore, in depth understanding of the complexity of mitochondrial functions, dysfunctions, and physiological changes is of great biomedical importance.

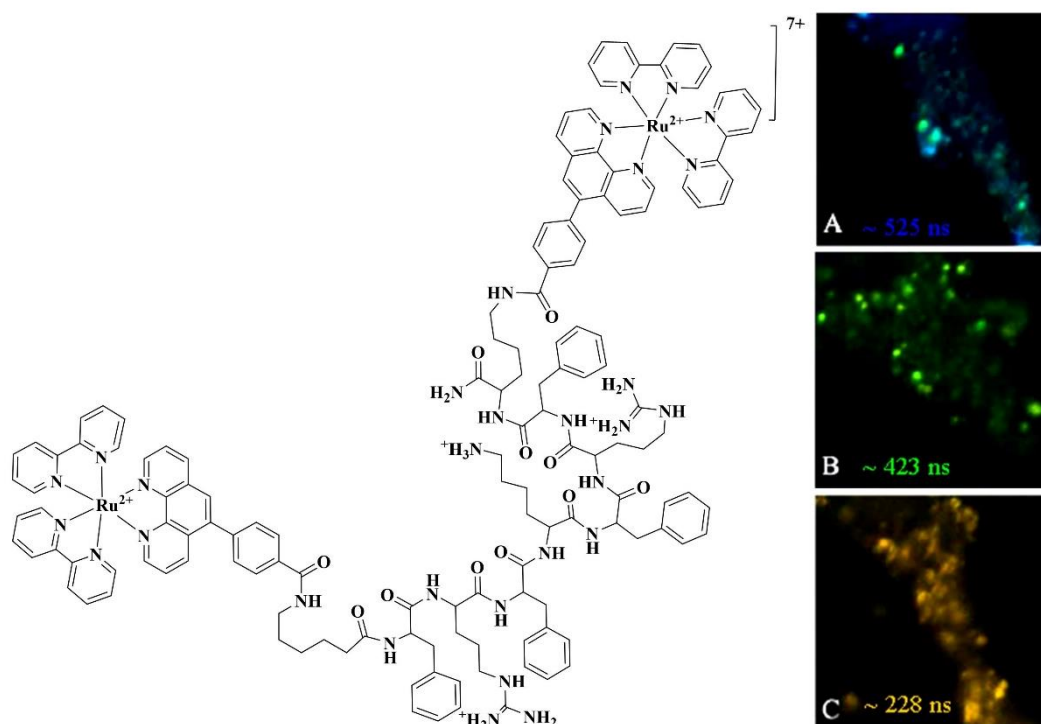
Targeting luminescent metal complexes to the mitochondria has received considerable attention from the perspective of imaging and sensing for monitoring mitochondrial health in understanding biochemical processes. Mitochondrial assessment by means of luminescence imaging can be useful also from the perspective of drug discovery for targeted therapy and of studying the overall activity of mitochondrial effectors.<sup>219</sup>

A mitochondrial localizing Ru(II) MPP conjugate, reported by Keyes's group, showed dynamic response to changes in local oxygen concentrations and to elevated levels of reactive oxygen species, using luminescence intensity and lifetime imaging.<sup>152</sup> The dinuclear ruthenium(II) probe was bridged across a mitochondrial penetrating peptide yielding **[(Ru(bpy)<sub>2</sub>)<sub>2</sub>(phen-MPP-phen)]<sup>7+</sup>**. Following exposure of HeLa cells to Antimycin A, a mitochondrial uncoupler agent, PLIM studies showed that the emission lifetime of **[(Ru(bpy)<sub>2</sub>phen-Ar)<sub>2</sub>-MPP]<sup>7+</sup>** in live HeLa cells quenched from approximately 525 ns to 228 ns, as shown in Figure 1.18. Monitoring changes in oxygen/ROS levels at the mitochondria is valuable to understanding disease state and disease progression. In addition to ROS, reactive nitrogen species (RNS) also play a crucial role in biological systems. For example, peroxynitrite (ONOO<sup>-</sup>), is the product of a reaction between nitric oxide (NO) free radicals and superoxide and at abnormal levels can induce oxidative changes in intracellular molecules including DNA and proteins.<sup>220</sup> A mitochondrial-localised ruthenium(II) complex-cyanine (Ru-Cy5) scaffold was used for sensing and imaging of ONOO<sup>-</sup> in live HeLa cells.<sup>221</sup> The energy transfer - based probe was prepared by incorporating a Ru(II) complex as the energy donor and Cy5 as the energy acceptor. Following cellular uptake and mitochondrial localization, the emission of Cy5 was decreased, in the presence of ONOO<sup>-</sup>, as a result of oxidative cleavage of the polymethine bridge which interrupts the energy transfer between Ru(II) and Cy5. The Ru-Cy5 system showed low cytotoxicity, efficient mitochondrial accumulation, and good selectivity for ONOO<sup>-</sup> (*over other reactive species*).

In a recent publication, precision targeting of mitochondrial DNA in live HeLa cells was achieved using an MPP driven light-switching Ru<sup>II</sup>- dppz complex.<sup>222</sup> Titration studies with

ctDNA showed that the DNA binding ability, mediated by dppz intercalation, of the parent complex, is retained for the Ru<sup>II</sup>-dppz MPP conjugate.

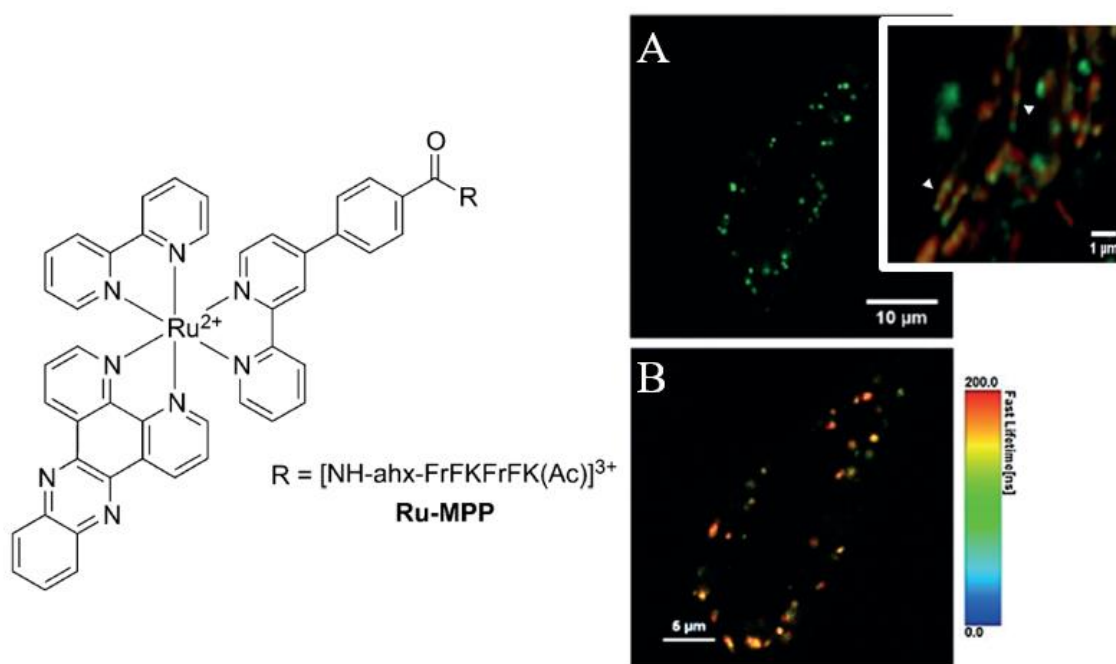
Additionally, an increased binding constant was reported, which was attributed to electrostatic interactions between the polycationic sequence of MPP and the anionic DNA backbone. Confocal laser scanning microscopy showed rapid cellular uptake of **[Ru(dppz)(bpy)(bpy-Ar-MPP)]<sup>5+</sup>** in live HeLa cells and localization to mitochondrial sub-structures was confirmed using luminescence lifetime imaging (Figure 1.19).



**Figure 1.18** Luminescence lifetime imaging of **[(Ru(bpy)<sub>2</sub>(phen-MPP-phen))<sup>7+</sup>** in live HeLa cells, in response to Antimycin A treatment. PLIM was carried out following (A) incubation with Ru(II) conjugate at 70  $\mu$ M for 2 h in the absence of light, and treatment with Antimycin A (200  $\mu$ g/ mL) for (B) 10 min and (C) 100 min. <sup>152</sup>

Importantly, although the conjugate showed low cytotoxicity in the dark and under imaging conditions, facilitating thus mtDNA visualization, photo-induced toxicity was observed under continuous and intense irradiation, facilitating thus controllable initiation of cell death. A previously reported ruthenium-containing human serum albumin (HAS) nanotransporter which targeted the mitochondria, exhibited enhanced <sup>1</sup>O<sub>2</sub> quantum yields and also demonstrated efficient photo-induced cytotoxicity, mediated by local ROS production. <sup>223</sup>

Luminescent transition metal complexes accumulating in the mitochondria have recently been combined with super-resolution microscopy techniques for the visualization of the dynamics of these organelles in living cells. For example mitochondrial images of sub-diffraction resolutions were presented using 3D-STED for a highly photostable dinuclear Ru(II) complex<sup>214</sup> and an iridium(III) complex was applied using SIM to image mitochondria ( $\approx 80$  nm resolution) and monitor mitochondria-lysosome contact and fusion events.<sup>224</sup>



**Figure 1.19** Precision targeted  $[\text{Ru}(\text{dppz})(\text{bpy})(\text{bpy-Ar-MPP})]^{5+}$  ( $10 \mu\text{M} / 2 \text{ h}$ ) light-switching probe in mitochondria of live HeLa cells. (A) Confocal image with inset showing a close up of the mitochondria co-stained with MitoTracker Deep Red (red) and (B) Luminescence lifetime distribution of the conjugate.<sup>222</sup>

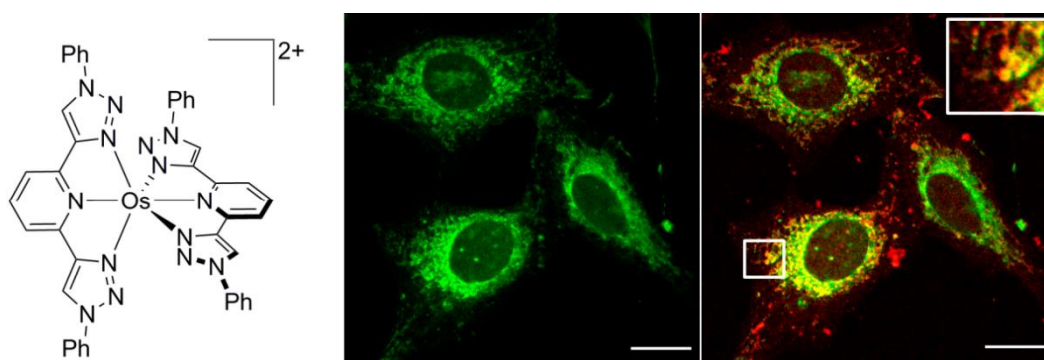
A recently reported dinuclear  $\text{Ru}^{\text{II}}/\text{Re}^{\text{I}}$  complex was found to initially localize in the mitochondria and lysosomes of live MCF-7 cells before rapidly migrating to the nucleus.<sup>225</sup> The photostability and low phototoxicity of the complex permitted visualization of this organelle migration at super resolutions using STED microscopy. The oxygen sensitive PEGylated Ir(III) complex was also used for SIM and two-photon microscopy.<sup>226</sup>

As mentioned iridium(III) complexes often tend to localize in the mitochondria due to their cationic charge and lipophilic character. Photostable cationic complexes of iridium(III) found application in the context of bioimaging/sensing by tracking mitochondrial dynamics and morphological changes during apoptosis.<sup>227</sup>



Intracellular targeting to the mitochondria has been exploited in the context of therapy to promote PDT-induced cell death. A series of Ru(II) mitochondria-accumulating complexes (RuL1-RuL4) exhibiting high  $^1\text{O}_2$  quantum yields and high two-photon absorption (TPA) cross sections, were shown to trigger cell death upon two-photon activation. In comparison to one-photon PDT, 2P-PDT resulted in superior inhibition towards 3D multicellular spheroids with an  $\text{IC}_{50}$  of  $1.9 \mu\text{M}$ .<sup>228</sup> Ruthenium-glucose conjugates have also been reported for mitochondria-targeted 2P-photodynamic therapy.<sup>229</sup> Two-photon excitation allows for in depth penetration of such cellular models resulting in generation of singlet oxygen at a deeper level in the multilayer of cells. This is crucial for efficient PDT anticancer agents.

Elliot and co-workers presented a mitochondrial accumulating osmium(II) complex,  $[\text{Os}(\text{btzpy})_2]^{2+}$  (btzpy = 2,6-bis(1-phenyl-1,2,3-triazol-4-yl)pyridine) (Figure 1.20) which also showed significant potential as a photosensitizer.<sup>203</sup> The compound exhibited high quantum yield ( $\phi_{\text{em}} = 9.3\%$ ) susceptible to oxygen quenching with a good quantum yield for singlet oxygen sensitization ( $\phi(^1\text{O}_2) = 57\%$ ).



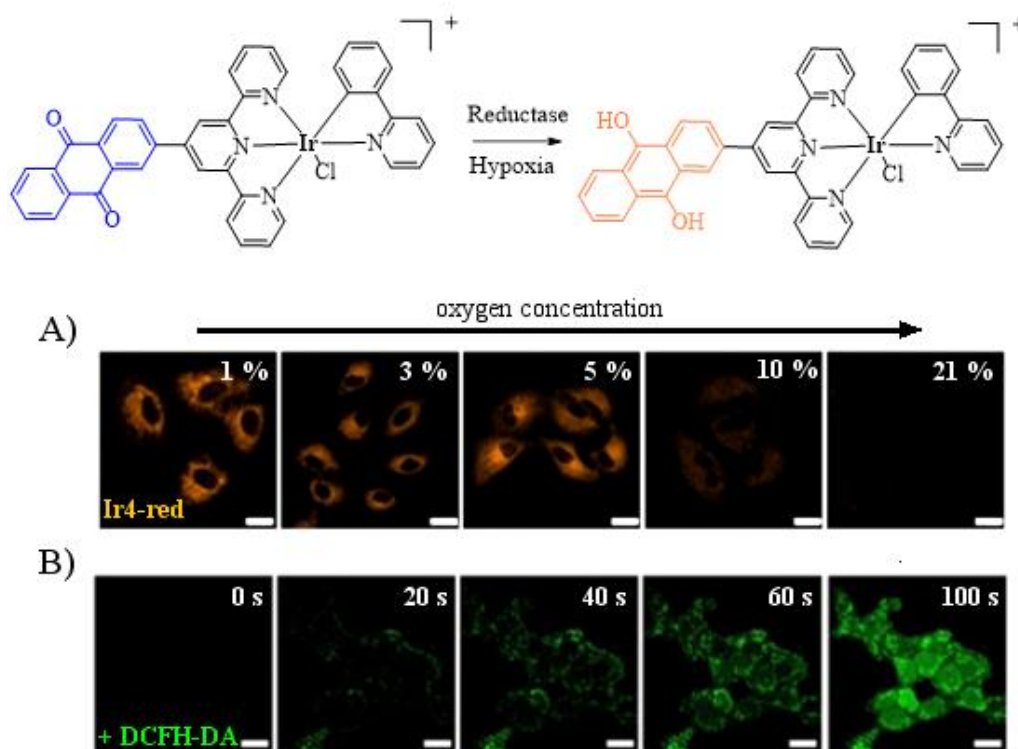
**Figure 1.20** Confocal images of  $[\text{Os}(\text{btzpy})_2]^{2+}$  (green) localizing at the mitochondria of osteosarcoma cells as confirmed by co-staining with Mitoview (red). Scale bar =  $20 \mu\text{m}$ .<sup>203</sup>

Generation of  $^1\text{O}_2$  at the mitochondria or the nucleus is more damaging to cells than if generated in cytoplasmic media or endosomes thus rendering the complex an attractive candidate for photodynamic therapy (PDT). The complex showed low dark toxicity with  $\text{IC}_{50} > 100 \mu\text{M}$ . In the case of osmium-based photosensitizers, a major advantage includes enabling activation with tissue-penetrating NIR light. This was demonstrated by a series of panchromatic Os(II)-biq complexes applied towards *in vitro* and *in vivo* studies.<sup>230</sup>

Phosphorescent cyclometalated Ir(III) polypyridine complexes showing mitochondrial accumulation and exhibiting high photo-induced cytotoxicity under one-photon<sup>117,231</sup> and two photon excitation<sup>232</sup> have been reported. The principle of photodynamic therapy relies on the

sufficient dosage of three crucial elements: light, the photosensitizer (PS), and oxygen. Although there are examples of complexes which exhibit strong photo-induced cytotoxicity even at hypoxic conditions,<sup>233–236</sup> the poor-oxygenated tumor environment often limits their *in vivo* application.

A recent study described the application of an Ir(III) anthraquinone complex as a mitochondrial-localized and *oxygen-independent* photosensitizer.<sup>237</sup> Here, the Ir(III) complex, **Ir4**, exhibits hypoxia-induced reduction and switch-on emission (Fig. 1.21A), and upon two-photon excitation (TPE), the reduced form of the complex, **Ir4-red**, triggers formation of carbon-radicals (Fig. 1.21B), leading to loss of mitochondrial membrane potential and cell death (photocytotoxicity index (PI) = 27.7).<sup>237</sup> *In vivo* studies also highlighted the promising two-photon PDT efficacy of **Ir4**.

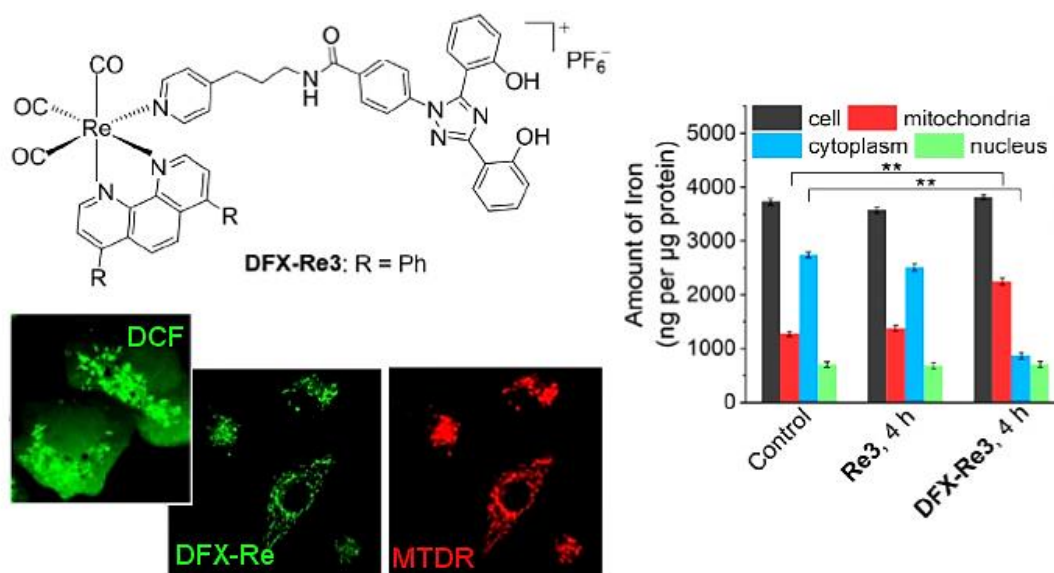


**Figure 1.21** Mitochondrial-localized Ir(III) complex undergoes hypoxia-induced reduction triggering ROS formation under TPE. (A) Two-photon excitation confocal images of A549 cells treated with **Ir4** (5  $\mu\text{M}$ ) under varying oxygen concentrations (from hypoxic to normoxic conditions). (B) Hypoxic A549 cells were pre-treated with **Ir4**/ **Ir4-red** and a ROS indicator dye (DCFH-DA). Confocal images were collected from 0 to 100 s following two-photon ( $\lambda_{\text{ex}} = 730 \text{ nm}$ ) irradiation and photo-induced ROS formation was evident by the DCFH-DA staining shown in green. Scale bar = 20  $\mu\text{m}$ .<sup>237</sup>



An alternative approach to designing metal complexes as therapeutic agents was presented by Mao and co-workers.<sup>238</sup> In this recent study, a mitochondria-targeted rhenium(I) complex containing an iron chelating agent was examined for its ability to attenuate both mitochondrial metabolism and iron homeostasis (Fig. 1.22). The Re(I) complex, **DFX-Re3** (where DFX = deferasirox chelator), accumulated iron to the mitochondria which caused production of reactive oxygen species thus affecting the methylation levels of DNA, RNA, and histone.

Modifying methylation levels of DNA, RNA and histone (epigenetic modifications) can affect chromatin state and gene transcription which can influence gene expression and induce immunogenic apoptosis as part of a unique therapeutic strategy.<sup>239</sup> DFX-Re showed potent anticancer activity in vivo, triggered by Re(I), and low systematic toxicity.



**Figure 1.22** Chemical structure and cellular studies of mitochondrial-targeted **DFX-Re3** complex. Co-staining studies with MitoTracker Deep Red (150 nm) showed that DFX-Re3 (5 µM / 2 h) localized at the mitochondria of MDA-MB-231 cells. The accumulation of iron in cellular compartments was measured using ICP-MS. The content of Fe in mitochondria increases producing reactive oxygen species. Generation of mitochondrial ROS following treatment of cells with DFX-Re3 (5 µM / 4 h) was confirmed by the intense fluorescence of a ROS indicator dye, DCF (2',7'-dichlorofluorescein) localized at the mitochondria.<sup>239</sup>

In the context of therapy, as Meier-Menches *et al.* mention in their detailed review on structure-activity relationships for anticancer compounds<sup>197</sup>, great challenges lay in realizing that DNA may not be the main target of metal complex therapeutic agents and their mechanisms of action

may not be comparable to cisplatin as they are unique compounds with distinct chemical properties leading to diverse modes of action.

In summary, the mitochondria-targeted complexes described in this section generally combined a high degree of lipophilicity with a cationic charge and potentially additional hydrophobic residues. The cationic charge provides an electrostatic driving force for transport across both the cellular and outer mitochondrial membrane and the residues/high lipophilicity allow partitioning through the hydrophobic inner mitochondrial membrane. Complexes exhibiting high molecular brightness, red to NIR emission, good photostability and low to moderate cytotoxicity have found application as imaging probes for confocal, PLIM or super-resolution studies whereas complexes triggering ROS production or exhibiting high quantum yields for singlet oxygen generation have been explored as photosensitizers.

## 1.5 Oxygen sensing

A key characteristic of ruthenium(II) and iridium(III) complexes is their long-lived luminescent triplet excited state which: 1) can be used in time-gated imaging to eliminate background scattering effects or autofluorescence and 2) is susceptible to oxygen quenching. Molecular oxygen ( $O_2$ ) is a well-known quencher, and the luminescence intensity and lifetime are both quantitatively reduced in the presence of  $O_2$  according to the Stern-Volmer equation described in *section 1.1.1*. Therefore, one can reliably monitor the luminescence lifetime or intensity changes in response to fluctuations in the oxygen environment.

The energies of the excited states of oxygen are lower than the energies of the excited states of most metal complexes which makes quenching via energy transfer favourable. Energy transfer from the luminophore in its triplet excited state to ground state oxygen ( $^3O_2$ ) is followed by non-radiative deactivation of the complex, to the ground state and formation of singlet oxygen ( $^1O_2$ ) as a byproduct.  $O_2$  sensing luminophores have a characteristic lifetime- and intensity-based response to oxygen concentration and calibration experiments are typically carried out to establish the instrumental response to the luminophore signal is measured over a range of oxygen concentrations.

For this reason, *quenched-phosphorescence* based  $O_2$  sensors have been applied for intracellular oxygen ( $icO_2$ ) sensing and most common dyes include Platinum(II)- and Palladium(II)- porphyrins and complexes of Ru(II) and Ir(III).

There are several methods for monitoring and measuring dissolved oxygen in biological systems some of which include Clark-type O<sub>2</sub> electrodes<sup>240</sup>, electron paramagnetic resonance (EPR) probes<sup>241</sup> and microelectrodes or needle probes<sup>242–246</sup>. However, overall, there is a demand for less invasive techniques for O<sub>2</sub> sensing. For example, although traditionally the Clark electrode has been utilized for monitoring oxygen,<sup>247</sup> the electrode itself consumes oxygen during the O<sub>2</sub> measurements and also introduces a source of contamination in cellular studies.

There are a number of examples of emissive probes which have been applied for oxygen sensing using lifetime- or intensity-based methods. As mentioned, a key advantage of lifetime-sensing is that lifetime is independent of probe concentration. Phosphorescence lifetime imaging/sensing however is rather a specialist technique and requires advanced equipment which is not always readily available in a biological laboratory. On the contrary, intensity-based sensing can be performed using conventional instrumentation such as a fluorescence microscope or plate reader. Additionally, issues concerning measurement artifacts and accuracy of the obtained intensity signal can be addressed by incorporating a reference signal which will be discussed in *section 1.5.1*. Choice of O<sub>2</sub> sensing method may also rely on the sample itself. For example, using a conventional plate reader, intensity-based measurements permit parallel analysis of monolayer cells exposed to various conditions in a single experiment while also carrying out several repetitions. For three-dimensional cell models or tissue samples, PLIM is typically the method of choice as it allows visualization of spatial O<sub>2</sub> distribution throughout the sample.

Complexes of ruthenium(II) have demonstrated in-cellulo oxygen response<sup>74,248</sup> and mitochondrial or nuclear targeted Ru(II) conjugates have enabled real-time monitoring of *local* oxygen fluctuations in live cells using emission intensity or lifetime imaging.<sup>152,249</sup> Although limited by their photostability iridium(III) complexes have shown promising in vitro and in vivo O<sub>2</sub> mapping with low cytotoxicity against 2D cell monolayers.<sup>250–255</sup> Notably, azo-based Ir(III) complexes applied for hypoxia imaging in 3D multicellular spheroids, exhibited an inhibition effect on the spheroids after one day of treatment.<sup>252</sup> Although this effect occurred outside the experimental imaging window, it remains an important factor to their application in solid tumor imaging.

Phosphorescent Pt(II)- and Pd(II)-porphyrins are also amongst popular O<sub>2</sub> sensors with lifetimes ranging from 40 – 100  $\mu$ s and 400 – 1000  $\mu$ s respectively.<sup>256</sup> Papkovsky and co-

workers have worked extensively on Pt(II)- and Pd(II)-porphyrin probes which show good photostability and quenching by oxygen.<sup>257–260</sup> Although promising as cellular O<sub>2</sub> sensors, these probes tend to aggregate and non-specifically bind to cellular components.

The solubility of such probes in water and targeting ability can be improved by conjugation to protein cargos, PEG chains or cell-penetrating peptides.<sup>259,261–263</sup> The emergence of nanotechnology has led to the development of several NP O<sub>2</sub> sensors which comprise of : 1) the O<sub>2</sub> probe alone 2) as part of a Förster resonance energy transfer (FRET) pair or 3) combined with a reference probe which does not require cross-communication.<sup>45,264–268</sup> Key advantages of a particle system include biocompatibility, flexibility in design, tunable targeting ability and relative ease of fabrication. Additionally, nanoparticles typically exhibit increased brightness due to being composed of more luminophores per particle. Some of the challenges however are often met at cellular applications and relate to difficulties in uptake, endosomal trapping, and cytotoxicity.

An important consideration for the application of metal complexes as O<sub>2</sub> sensors is the generation of singlet oxygen as a result of quenching by oxygen which can lead to oxidative damage of cellular components or even cell death particularly if <sup>1</sup>O<sub>2</sub> is generated at the nucleus or mitochondria.<sup>117,269,270</sup> While this phenomenon has found application in theranostics, it is not ideal in the context of O<sub>2</sub> sensing where low cytotoxicity is desired.

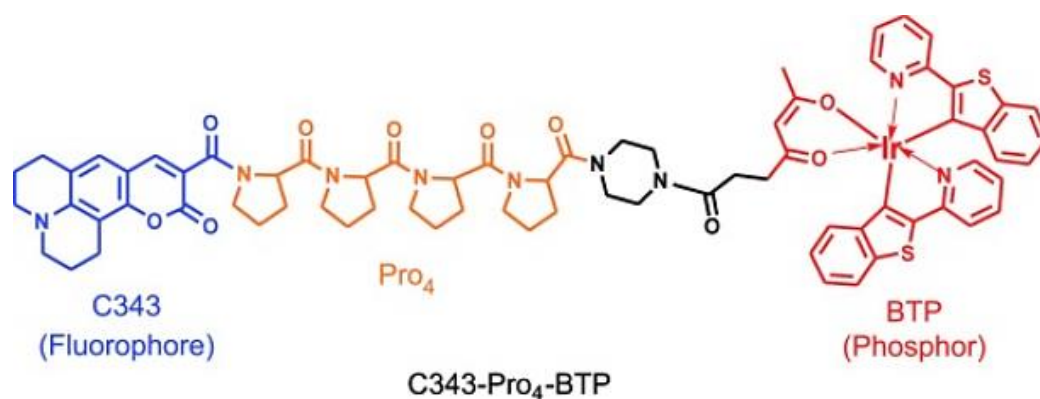
Overall practical considerations for an icO<sub>2</sub> sensor include oxygen responsivity, photostability, cell uptake efficacy, molecular brightness, biocompatibility, cytotoxicity, and subcellular targeting ability where desired.

### **1.5.1 The ratiometric approach: from molecular dyads to nano-sensors**

As mentioned, intensity-based sensing can be performed using conventional equipment, however an important limitation is that the intensity signal can be influenced by other factors beyond the target analyte. For example, physiochemical issues such as photodamage, probe leaching and interaction with other species within the cellular environment, can influence emission intensity. Additionally, intensity can be affected by the excitation source or detector drift and sensitivity. Importantly, in intracellular oxygen sensing, emission intensity can also be affected by inhomogeneous probe distribution within the cell.

A useful solution to this issue is *ratiometric sensing*. The ratiometric approach to reliable O<sub>2</sub> sensing, involves referencing the O<sub>2</sub>-probe emission signal against a stable emission from a

dye which does not respond to oxygen but is equally subject to fluctuations in other parameters which may influence intensity. Therefore, the ratiometric intensity signal (*or* lifetime) can be used for O<sub>2</sub> quantification. Figure 1.23 shows an example of an iridium- coumarin ratiometric probe, **C343-Pro<sub>4</sub>-BTP**.<sup>254</sup> Upon excitation at 405 nm, energy transfer from the coumarin moiety (C343) to the iridium (BTP) moiety occurs resulting in emission from both components at 480 nm and >610 nm respectively.



**Figure 1.23** Ratiometric FRET molecular probe, **C343-Pro<sub>4</sub>-BTP**, consisting of coumarin 343 as an oxygen-insensitive fluorophore, a linker and an iridium O<sub>2</sub> indicator phosphor.<sup>254</sup>

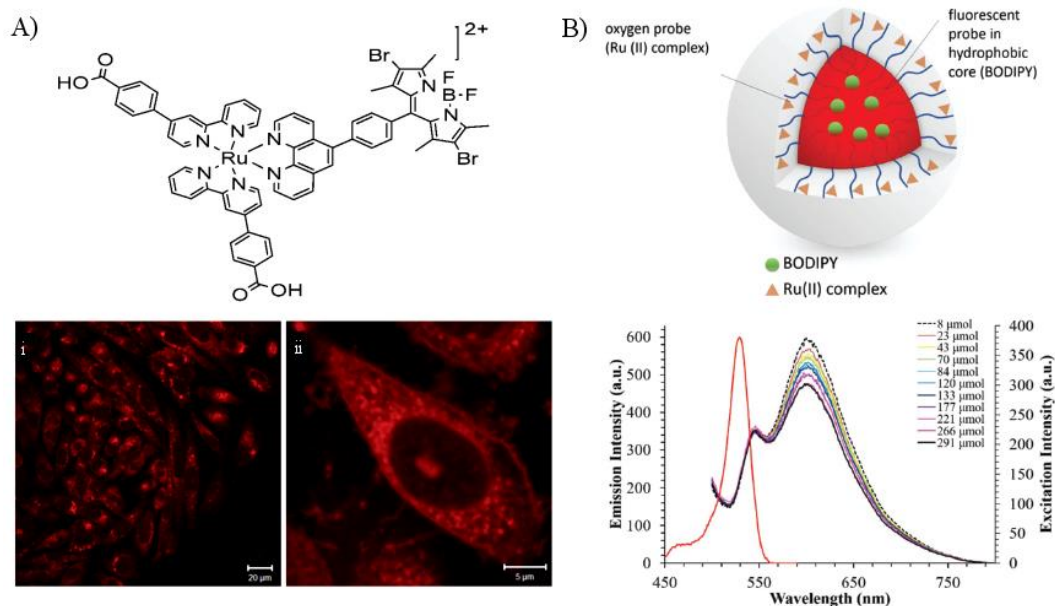
The phosphorescence emission signal of iridium is quenched by oxygen and the ratio of the emission from both moieties exhibits an O<sub>2</sub> dependent response both in solution and in live HeLa cells. For FRET pairs it is necessary to ensure that electron transfer and/or reverse energy transfer does not occur; this is often a synthetic and photophysical challenge.

In an alternative approach, Keyes's group reported a dual emitting molecular dyad which combined an oxygen responsive ruthenium probe and a BODIPY reference dye.<sup>271</sup> Here, mediated by the large Ru(II) Stokes shift, both indicator and reference dye can be excited at the same single wavelength and emit at different and distinguishable wavelengths without the need for cross-communication between the dyes. Although the dyad was used for quantitative ratiometric O<sub>2</sub> sensing in organic media, switch-off of the BODIPY emission in aqueous conditions, precluded its use for icO<sub>2</sub> ratiometric sensing in live cells. To expand the application of the ruthenium(II)-BODIPY dyad towards oxygen sensing in aqueous media and in mammalian cells, Keyes's group presented a ratiometric core-shell nanosensor, **RuBODIPY NP**, where the BODIPY reference probe was confined to a polystyrene core, offering protection and a stable reference signal, and the ruthenium probe was conjugated to the poly-lysine shell exterior, allowing direct exposure to the environment and O<sub>2</sub> accessibility.<sup>272</sup> Figure 1.24

illustrates the concept of moving from a molecular dyad toward a core-shell particle. Ratiometric sensing particles have been described in the literature for various systems<sup>273–275</sup> and optical PEBBLE (Probe Encapsulate By Biologically Localized Embedding) sensors<sup>276–278</sup> but very few reported nanosensors rely on co-excitation of the dyes rather than FRET.

In the RuBODIPY particle system the O<sub>2</sub> indicator and reference dye are spatially separated into their respective domains, *thus limiting any potential cross-communication*, and are simultaneously excited at a single wavelength. The nanoparticles showed good ratiometric response to oxygen in aqueous media with a rate of quenching of  $7.52 \times 10^8 \text{ M}^{-1} \text{ s}^{-1}$ . The emission intensity ratiometric data showed moderately good linearity ( $R^2 = 0.9525$ ) over a biologically relevant O<sub>2</sub> range. The particles were found to strongly bind to the membrane of cells but without pre-treatment with a cationic surfactant they were impermeable.

Following surfactant mediated uptake of RuBODIPY NPs in CHO cells, PLIM studies showed that the emission lifetime of the BODIPY dye, as expected, was unaffected by the surrounding intracellular environment in contrast to the ruthenium probe demonstrating the potential of the core-shell approach to designing new ratiometric nanotools.



**Figure 1.24** A) Dual emitting ruthenium(II)/BODIPY molecular dyad. Following uptake of the dyad in CHO cells, confocal imaging shows emission only from the ruthenium moiety as the BODIPY emission is extinguished in aqueous environment. B) The core-shell RuBODIPY nanoparticles showed ratiometric O<sub>2</sub> responsivity in aqueous media and in cells.<sup>271,272</sup>

### 1.5.2 Molecular oxygen sensing in 3D cell models

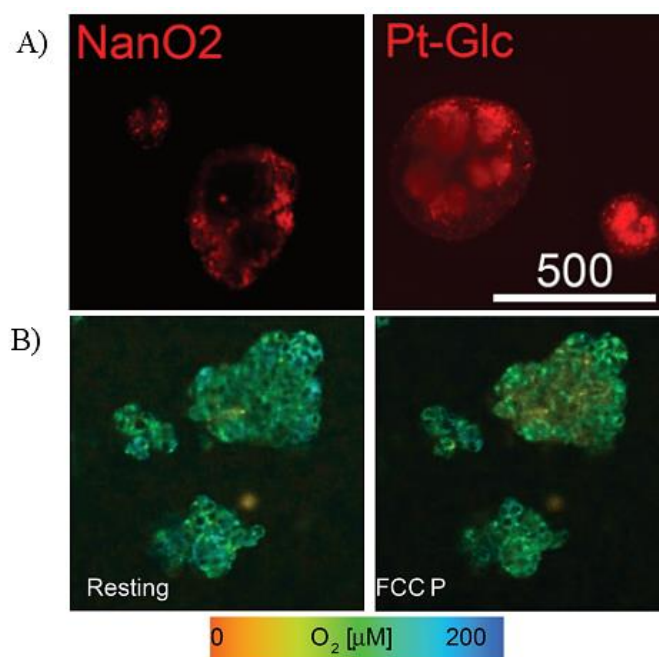
In cancer disease, the oxygen consumption is imbalanced between healthy and diseased cells leading to an overall reduction in oxygen concentration to below normal levels which is known as *hypoxia*. Hypoxia is a characteristic feature of the microenvironment of most solid tumours and so, monitoring, and quantifying tissue cell oxygenation is of great importance in understanding diseased states, variations in cell-tissue metabolism and drug treatment efficacy. The application of metal complexes for O<sub>2</sub> sensing has focused largely on conventional 2D monolayer cell cultures and while valuable information can be obtained from these studies, three-dimensional (3D) cell models such as cell aggregates, spheroids and organoids provide a more physiologically relevant tumor microenvironment.<sup>279–281</sup> Multicellular tumour spheroids (MCTS) are prepared by culturing cancer cells in a non-adherent environment, stimulating them to aggregate together and form tightly packed layers of cells.<sup>280,282–284</sup> The outermost layers of cells consume media nutrients by diffusion and discard waste whereas the cells towards the centre of the spheroid are nutrient deficient and accumulate waste products. Consequently, this leads to formation of spheroid regions with nutrient and metabolite deficiency, low pH and variation in O<sub>2</sub> concentration.<sup>285,286</sup> The size of 3D MCTS can be tailored and is typically in the range of 100 – 500 μm.<sup>287,288</sup> In the context of studying metallodrug efficacy, 3D models often show differences in drug response when compared to 2D monolayers.<sup>289–291</sup>

Confocal microscopy is capable of high resolution optical sectioning of 3D cultures and the recent emergence of advanced microscopy techniques such as multiphoton microscopy has opened a horizon of opportunities for use of 3D cell models in imaging/sensing and therapy. For example, as the optimal tissue penetration window is 700–900 nm, two-photon excitation can overcome the barrier of absorption in the UV/Vis of metal complexes. This has been exploited particularly in 2P-PDT using Ru(II) complexes as described in 1.4.<sup>161,228</sup>

Metal complexes fulfil many of the requirements necessary for bioimaging and sensing, not only of monolayer but also of 3D cell cultures. As aforementioned, metal complexes can offer photostability, synthetically tunable emission towards the NIR coinciding with the biological window and long-lived luminescence allowing for phosphorescence lifetime imaging/sensing and discrimination from short-lived autofluorescence. PLIM allows for spatial mapping of O<sub>2</sub> which is ideal for complex 3D tissue models.<sup>292</sup>

Although Pt(II)-porphyrin probes have been employed for PLIM-based spheroid O<sub>2</sub> sensing<sup>292,293</sup>, their uptake in cell monolayers and 3D cell models is often a hurdle. To overcome uptake issues, Dmitriev, Papkovsky and co-workers have developed cell-penetrating ratiometric nanoparticles, NanO<sub>2</sub> and MM2 for oxygenation mapping in neurospheres and tumour spheroids.<sup>273,294,295</sup> Both NanO<sub>2</sub> and MM2 nanoparticle materials are embedded with a photostable, O<sub>2</sub>-sensitive reporter dye Pt(II)-5,10,15,20-tetrakis-(2,3,4,5,6-pentafluorophenyl)-porphyrin (PtTFPP). The MM2 probes contain a second fluorophore, an O<sub>2</sub>-insensitive reference, poly(0,9)-dioctylfluorene (PFO), which acts as a 1P and 2P light harvesting antennae and FRET donor and allows for ratiometric and multiphoton imaging. Click-assembled Palladium(II)-porphyrin nanoconjugates have also been reported for NIR mapping of oxygen distribution in 3D microenvironments.<sup>295,296</sup>

In order to further improve uptake and particularly probe distribution in spheroids, Papkovsky and co-workers developed small molecule PtPFPP probes containing saccharide vectors.<sup>297</sup>



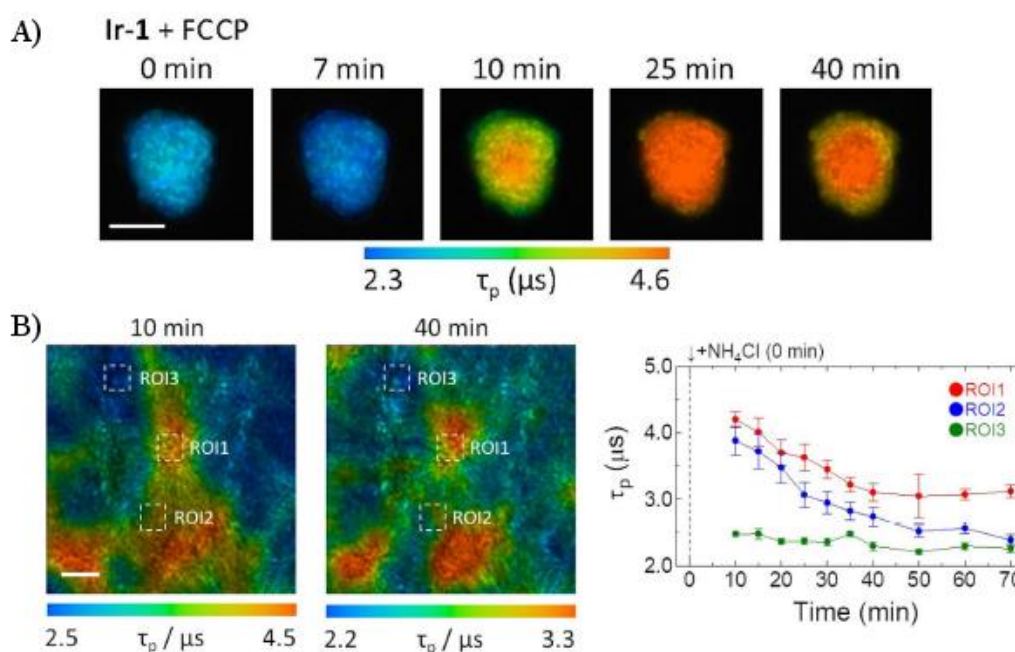
**Figure 1.25** A) Phosphorescence images comparing **NanO<sub>2</sub>** and **Pt-Glc** neurosphere staining. B) PLIM oxygen mapping of Pt-Glc (2.5 μM / 16 h) in pheochromocytoma (PC12) multicellular spheroid aggregates at resting conditions and upon addition of FCCP (4 μM).<sup>297</sup>

The hydrophilic glucose conjugate, **Pt-Glc** accumulated in neurospheres and showed in depth staining with a more uniform distribution than the particle-based **NanO<sub>2</sub>** sensor as shown in Fig.1.25A. Although the Pt-Glc probe was used for PLIM O<sub>2</sub> imaging for multicellular aggregates (Fig.1.25B), it is important to note that PtPFPP in this case lacks shielding and is



susceptible to influences from the intracellular environment. In addition, in comparison to NanO<sub>2</sub>, the saccharide conjugates exhibited decreased brightness in 2D cell studies.

The interaction of complexes of Ru(II), Os(II) and Ir(III) with 3D cell models is mainly reported in the context of therapy.<sup>228,236,290,298–300</sup> while very few reports focus on evaluating Ru(II)<sup>301,302</sup> and Ir(III)<sup>252,253,303</sup> complexes for their in-depth staining of spheroids for imaging. Recently, two iridium(III) complexes, (btp)<sub>2</sub>Ir(acac-DM) (**Ir-1**) and (btp-OH)<sub>3</sub>Ir (**Ir-2**) (btp = benzothienylpyridine, acac = acetylacetonate) were studied for *in vivo* PLIM O<sub>2</sub> mapping.<sup>303</sup> Both complexes were efficiently taken up by human colorectal adenocarcinoma (HT-29) cell monolayers and 3D spheroids. Phosphorescence lifetime imaging facilitated mapping of the oxygen distribution in HT-29 spheroids while also monitoring O<sub>2</sub> fluctuations upon metabolic stimulation with an uncoupling agent (Fig. 1.26A). Furthermore **Ir-1** allowed for PLIM visualization of the oxygen concentration gradient in hepatic tissue and lobules stimulated by ammonia (Fig. 1.26B).



**Figure 1.26** PLIM O<sub>2</sub> mapping studies of (btp)<sub>2</sub>Ir(acac-DM); **Ir-1** in HT-29 cell spheroids and hepatic lobules. A) Variation in PLIM of **Ir-1** – stained HT-29 spheroids upon metabolic stimulation with FCCP (1 μM). B) PLIM images of hepatic lobules stained with **Ir-1** and following NH<sub>4</sub>Cl administration. The graph illustrates the variation of average **Ir-1** lifetime over time of ROIs in the peripheral and periportal regions.<sup>303</sup>

Overall, a key challenge in the application of metal complexes in 3D cell culture imaging and also therapy, remains their capability to penetrate deeply and uniformly in 3D cell models and tissue.

## 1.6 Conclusions

Over the last decades, the application of metal complexes has rapidly extended across various fields including cellular imaging, intracellular sensing and theranostics. The beauty of metal complexes is that they can be tailored to their application by tuning their photophysical properties (e.g., *molecular brightness*, *emission maxima*), through modification of the metal centre and/or the coordinated ligands, and by conjugating appropriate cargos which facilitate cellular uptake and intracellular targeting. Furthermore, their design can also be tailored to meet the criteria of the technique used for their application whether that is phosphorescence lifetime imaging microscopy or luminescence intensity-based sensing using a plate reader.

Challenges are often met when targeting organelles with complex membrane structures such as the mitochondria. Keyes's group has focused extensively on the development of peptide conjugated metal complexes which show efficient cellular uptake and precise organelle targeting ability. The research described in this thesis focuses on red to near-infrared emitting complexes of ruthenium(II) and osmium(II) and the application of their respective cell penetrating conjugates in cells.

Chapter 2 describes the interaction of a series of photostable and NIR emitting Ru(II) biquinoline conjugates with live HeLa and CHO cells with respect to their permeability, targeting ability and cytotoxicity. Here, the importance of counterion selection in cellular uptake is highlighted. The peptide conjugates showed high cytotoxicity, the origin of which was investigated using caspase and mitochondrial depolarization assays. PEGylation of the complex increased hydrophilicity and reduced cytotoxicity significantly while retaining cell permeability.

An achiral Os(II) bis-terpyridine complex,  $[\text{Os}(\text{tpybenzCOOH})_2]^{2+}$  is the protagonist of Chapter 3 and 4 in this work. Chapter 3 describes the full synthetic, spectroscopic, and electrochemical characterization of the Os(II) parent complex. Owing to its favourable photophysical properties, including robust photostability and NIR-emission, the Os(II) complex was conjugated to two mitochondrial penetrating peptides (MMPs) and examined in 2D adherent cell monolayers using confocal microscopy.

Adherent cell monolayer studies can provide valuable information at the single cell level. However, in order to gain true insight into the complexity of tumor biology, one must look at a three-dimensional cell model, such as spheroids, which represents a more physiologically relevant tumor microenvironment. There are reports of Ru(II) and Os(II) complexes applied in 3D cell cultures, particularly in the context of therapy, but only limited studies focus on strategically driving *in-depth penetration* of the probes for luminescence imaging and sensing. Conjugation to octaarginine has been used to facilitate uptake of several metal complexes. In Chapter 4, the approach of conjugating polyarginine sequences of varying lengths to the achiral Os(II) complex for in-depth penetration of 3D spheroids was investigated. The conjugates were studied in 2D and 3D cell cultures using confocal and lifetime imaging.

This study highlights the potential of extending the application of analogous cell penetrating peptide-driven metal complexes from adherent cell monolayers toward 3D cell models and even tissue imaging/sensing or therapy.

Chapter 5 focuses on investigating the oxygen response of ratiometric nanoparticles in mammalian cells using two techniques, namely a conventional plate reader-based assay and confocal lambda ( $\lambda$ ) scanning microscopy. The poly-L-lysine decorated polystyrene particles consist of a novel oxygen sensitive ruthenium(II) complex,  $[\text{Ru}(\text{dpp})(\text{phen-NH}_2)(\text{bpybenzCOOEt})]^{2+}$ , and a reference BODIPY dye which are co-encapsulated in the particle core.

## 1.7 References

- 1 B. Chance, *Circ Res*, 1976, **38**, I31-38.
- 2 N. Nakashima, K. Yoshihara, F. Tanaka and K. Yagi, *J. Biol. Chem.*, 1980, **255**, 5261–5263.
- 3 B. Chance, B. Schoener, R. Oshino, F. Itshak and Y. Nakase, *J Biol Chem*, 1979, **254**, 4764–4771.
- 4 M. C. Skala, K. M. Riching, A. Gendron-Fitzpatrick, J. Eickhoff, K. W. Eliceiri, J. G. White and N. Ramanujam, *PNAS*, 2007, **104**, 19494–19499.
- 5 J. R. Lakowicz, H. Szmazinski, K. Nowaczyk and M. L. Johnson, *Proc. Natl. Acad. Sci.*, 1992, **89**, 1271–1275.
- 6 R. Drezek, C. Brookner, I. Pavlova, I. Boiko, A. Malpica, R. Lotan, M. Follen and R. Richards-Kortum, *Photochem Photobiol*, 2001, **73**, 636–641.
- 7 J. R. Lakowicz, *Principles of fluorescence spectroscopy*, Springer, New York, 3rd ed., 2006.

- 8 B. Valeur and I. John Wiley & Sons, *Molecular Fluorescence*, Wiley-VCH, Weinheim, 2002.
- 9 E. M. Kober and T. J. Meyer, *Inorg. Chem.*, 1982, **21**, 3967–3977.
- 10 F. Felix, J. Ferguson, H. U. Güdel and A. Ludi, *Chem. Phys. Lett.*, 1979, **62**, 153–157.
- 11 J. Ferguson, F. Herren, E. R. Krausz, M. Maeder and J. Vrbancich, *Coord. Chem. Rev.*, 1985, **64**, 21–39.
- 12 H. Yersin, E. Gallhuber and G. Hensler, *Chem. Phys. Lett.*, 1987, **134**, 497–501.
- 13 E. Wachter, D. K. Heidary, B. S. Howerton, S. Parkin and E. C. Glazer, *Chem. Commun.*, 2012, **48**, 9649.
- 14 T. E. Keyes, J. G. Vos, J. A. Kolnaar, J. G. Haasnoot, J. Reedijk and R. Hage, *Inorg. Chim. Acta*, 1996, **245**, 237–242.
- 15 M. Duati, S. Fanni and J. G. Vos, *Inorg. Chem. Commun.*, 2000, **3**, 68–70.
- 16 C. Dolan, R. D. Moriarty, E. Lestini, M. Devocelle, R. J. Forster and T. E. Keyes, *J. Inorg. Biochem.*, 2013, **119**, 65–74.
- 17 I. Gamba, I. Salvadó, R. F. Brissos, P. Gamez, J. Brea, M. I. Loza, M. E. Vázquez and M. V. López, *Chem. Commun.*, 2016, **52**, 1234–1237.
- 18 C. Moucheron, A. Kirsch-De Mesmaeker and J. M. Kelly, *J. Photochem. Photobiol. B.*, 1997, **40**, 91–106.
- 19 B. J. Pankuch, D. E. Lacky and G. A. Crosby, *J. Phys. Chem.*, 1980, **84**, 2061–2067.
- 20 G. A. Crosby and J. N. Demas, *J. Am. Chem. Soc.*, 1970, **92**, 7262–7270.
- 21 D. Braun, E. Gallhuber, G. Hensler and H. Yersin, *Mol. Phys.*, 1989, **67**, 417–430.
- 22 S. Decurtins, F. Felix, J. Ferguson, H. U. Guedel and A. Ludi, *J. Am. Chem. Soc.*, 1980, **102**, 4102–4106.
- 23 J. P. Sauvage, J. P. Collin, J. C. Chambron, S. Guillerez, C. Coudret, V. Balzani, F. Barigelletti, L. De Cola and L. Flamigni, *Chem. Rev.*, 1994, **94**, 993–1019.
- 24 S. D. Cummings and R. Eisenberg, *J. Am. Chem. Soc.*, 1996, **118**, 1949–1960.
- 25 K. Heinze, K. Hempel, S. Tschierlei, M. Schmitt, J. Popp and S. Rau, *Eur. J. Inorg. Chem.*, 2009, **2009**, 3119–3126.
- 26 M. Abrahamsson, M. Jäger, T. Österman, L. Eriksson, P. Persson, H.-C. Becker, O. Johansson and L. Hammarström, *J. Am. Chem. Soc.*, 2006, **128**, 12616–12617.
- 27 F. E. Poynton, J. P. Hall, P. M. Keane, C. Schwarz, I. V. Sazanovich, M. Towrie, T. Gunnlaugsson, C. J. Cardin, D. J. Cardin, S. J. Quinn, C. Long and J. M. Kelly, *Chem. Sci.*, 2016, **7**, 3075–3084.
- 28 G. Li, L. Sun, L. Ji and H. Chao, *Dalton Trans.*, 2016, **45**, 13261–13276.

- 29 L. Blackmore, R. Moriarty, C. Dolan, K. Adamson, R. J. Forster, M. Devocelle and T. E. Keyes, *Chem. Commun.*, 2013, **49**, 2658.
- 30 M. Dickerson, Y. Sun, B. Howerton and E. C. Glazer, *Inorg. Chem.*, 2014, **53**, 10370–10377.
- 31 K. Adamson, C. Dolan, N. Moran, R. J. Forster and T. E. Keyes, *Bioconjugate Chem.*, 2014, **25**, 928–944.
- 32 J. B. Pawley, Ed., *Handbook Of Biological Confocal Microscopy*, Springer US, Boston, MA, 2006.
- 33 C. Vonesch, F. Aguet, J.-L. Vonesch and M. Unser, *IEEE Signal Process. Mag.*, 2006, **23**, 20–31.
- 34 R. H. Webb, *Rep. Prog. Phys.*, 1996, **59**, 427–471.
- 35 H. Schneckenburger and V. Richter, *Applied Sciences*, 2021, **11**, 733.
- 36 A. Nwaneshiudu, C. Kuschal, F. H. Sakamoto, R. Rox Anderson, K. Schwarzenberger and R. C. Young, *J. Investig. Dermatol.*, 2012, **132**, 1–5.
- 37 B. R. Masters and P. T. C. So, Eds., *Handbook of biomedical nonlinear optical microscopy*, Oxford University Press, New York, 2008.
- 38 D. Phillips, R. C. Drake, D. V. O'Connor and R. L. Christensen, *Instrumentation Science & Technology*, 1985, **14**, 267–292.
- 39 W. Becker, *Journal of Microscopy*, 2012, **247**, 119–136.
- 40 J. R. Lakowicz, *Principles of fluorescence spectroscopy*, Springer, New York, 3rd ed., 2006.
- 41 M. Köllner and J. Wolfrum, *Chem. Phys. Lett.*, 1992, **200**, 199–204.
- 42 R. M. Ballew and J. N. Demas, *Anal. Chem.*, 1989, **61**, 30–33.
- 43 J. Philip and K. Carlsson, *J. Opt. Soc. Am. A*, 2003, **20**, 368.
- 44 W. Becker, *Advanced time-correlated single photon counting techniques*, Springer, Berlin; New York, 2005.
- 45 A. Byrne, J. Jacobs, C. S. Burke, A. Martin, A. Heise and T. E. Keyes, *Analyst*, 2017, **142**, 3400–3406.
- 46 E. Baggaley, S. W. Botchway, J. W. Haycock, H. Morris, I. V. Sazanovich, J. A. G. Williams and J. A. Weinstein, *Chem. Sci.*, 2014, **5**, 879–886.
- 47 E. Baggaley, D.-K. Cao, D. Sykes, S. W. Botchway, J. A. Weinstein and M. D. Ward, *Chem. Eur. J.*, 2014, **20**, 8898 – 8903.
- 48 J. R. Lakowicz, H. Szmajcinski, K. Nowaczyk, W. J. Lederer, M. S. Kirby and M. L. Johnson, *Cell Calcium*, 1994, **15**, 7–27.

- 49 D. Aigner, R. I. Dmitriev, S. M. Borisov, D. B. Papkovsky and I. Klimant, *J. Mater. Chem. B*, 2014, **2**, 6792–6801.
- 50 K. Zheng, T. P. Jensen and D. A. Rusakov, *Nat Protoc*, 2018, **13**, 581–597.
- 51 W. Zhong, P. Urayama and M.-A. Mycek, *J. Phys. D: Appl. Phys.*, 2003, **36**, 1689–1695.
- 52 J. Lecoq, A. Parpaleix, E. Roussakis, M. Ducros, Y. Goulam Houssen, S. A. Vinogradov and S. Charpak, *Nat Med*, 2011, **17**, 893–898.
- 53 J. A. Levitt, M. K. Kuimova, G. Yahiolu, P.-H. Chung, K. Suhling and D. Phillips, *J. Phys. Chem. C*, 2009, **113**, 11634–11642.
- 54 X. Peng, Z. Yang, J. Wang, J. Fan, Y. He, F. Song, B. Wang, S. Sun, J. Qu, J. Qi and M. Yan, *J. Am. Chem. Soc.*, 2011, **133**, 6626–6635.
- 55 F. E. Poynton, S. A. Bright, S. Blasco, D. C. Williams, J. M. Kelly and T. Gunnlaugsson, *Chem. Soc. Rev.*, 2017, **46**, 7706–7756.
- 56 Lodish, A. Berk, C. A. Kaiser, M. Krieger, A. Bretscher, H. Ploegh, A. Amon and K. C. Martin, *Molecular cell biology*, W.H. Freeman, Macmillan Learning, New York, Eighth edition, Global edition., 2016, pp 473-477, 497.
- 57 G. J. Doherty and H. T. McMahon, *Annu. Rev. Biochem.*, 2009, **78**, 857–902.
- 58 Y. Lu and P. S. Low, *Adv. Drug Delivery Rev.*, 2002, **54**, 675–693.
- 59 N. Viola-Villegas, A. E. Rabideau, J. Cesnavicious, J. Zubieta and R. P. Doyle, *ChemMedChem*, 2008, **3**, 1387–1394.
- 60 R. van der Meel, L. J. C. Vehmeijer, R. J. Kok, G. Storm and E. V. B. van Gaal, *Adv. Drug Delivery Rev.*, 2013, **65**, 1284–1298.
- 61 T. Wang, N. Zabarska, Y. Wu, M. Lamla, S. Fischer, K. Monczak, D. Y. W. Ng, S. Rau and T. Weil, *Chem. Commun.*, 2015, **51**, 12552–12555.
- 62 C. A. Puckett and J. K. Barton, *J. Am. Chem. Soc.*, 2007, **129**, 46–47.
- 63 J. Karges, J. Li, L. Zeng, H. Chao and G. Gasser, *ACS Appl. Mater. Interfaces*, 2020, **12**, 54433–54444.
- 64 J. R. Friedman and J. Nunnari, *Nature*, 2014, **505**, 335–343.
- 65 J. D. Ly, D. R. Grubb and A. Lawen, *Apoptosis*, 2003, **8**, 115–128.
- 66 R. Ungricht and U. Kutay, *Nat Rev Mol Cell Biol*, 2017, **18**, 229–245.
- 67 N. Freitas and C. Cunha, *CG*, 2009, **10**, 550–557.
- 68 C. A. Bader, R. D. Brooks, Y. S. Ng, A. Sorvina, M. V. Werrett, P. J. Wright, A. G. Anwer, D. A. Brooks, S. Stagni, S. Muzzioli, M. Silberstein, B. W. Skelton, E. M. Goldys, S. E. Plush, T. Shandala and M. Massi, *RSC Adv.*, 2014, **4**, 16345–16351.

- 69 D. O' Connor, A. Byrne, G. B. Berselli, C. Long and T. E. Keyes, *Analyst*, 2019, **144**, 1608–1621.
- 70 C. Oliver and M. C. Jamur, Eds., *Immunocytochemical Methods and Protocols*, Humana Press, Totowa, NJ, 2010, vol. 588.
- 71 S. Hennig, S. van de Linde, M. Lummer, M. Simonis, T. Huser and M. Sauer, *Nano Lett.*, 2015, **15**, 1374–1381.
- 72 M. Dekaliuk, K. Pyrshev and A. Demchenko, *J. Nanobiotechnology*, 2015, **13**, 86.
- 73 J. Rumin, H. Bonnefond, B. Saint-Jean, C. Rouxel, A. Sciandra, O. Bernard, J.-P. Cadoret and G. Bougaran, *Biotechnol Biofuels*, 2015, **8**, 42.
- 74 U. Neugebauer, Y. Pellegrin, M. Devocelle, R. J. Forster, W. Signac, N. Moran and T. E. Keyes, *Chem. Commun.*, 2008, 5307–5309.
- 75 C. Tan, S. Lai, S. Wu, S. Hu, L. Zhou, Y. Chen, M. Wang, Y. Zhu, W. Lian, W. Peng, L. Ji and A. Xu, *J. Med. Chem.*, 2010, **53**, 7613–7624.
- 76 Q. Zhao, C. Huang and F. Li, *Chem. Soc. Rev.*, 2011, **40**, 2508–2524.
- 77 E. Baggaley, M. R. Gill, N. H. Green, D. Turton, I. V. Sazanovich, S. W. Botchway, C. Smythe, J. W. Haycock, J. A. Weinstein and J. A. Thomas, *Angew. Chem., Int. Ed.*, 2014, **53**, 3367–3371.
- 78 F. R. Svensson, M. Matson, M. Li and P. Lincoln, *Biophys. Chem.*, 2010, **149**, 102–106.
- 79 A. J. Amoroso, M. P. Coogan, J. E. Dunne, V. Fernández-Moreira, J. B. Hess, A. J. Hayes, D. Lloyd, C. Millet, S. J. A. Pope and C. Williams, *Chem. Commun.*, 2007, 3066–3068.
- 80 L. Xiong, Q. Zhao, H. Chen, Y. Wu, Z. Dong, Z. Zhou and F. Li, *Inorg. Chem.*, 2010, **49**, 6402–6408.
- 81 L. Cosgrave, M. Devocelle, R. J. Forster and T. E. Keyes, *Chem. Commun.*, 2010, **46**, 103–105.
- 82 M. Yu, Q. Zhao, L. Shi, F. Li, Z. Zhou, H. Yang, T. Yi and C. Huang, *Chem Commun*, 2008, 2115–2117.
- 83 Q. Zhao, M. Yu, L. Shi, S. Liu, C. Li, M. Shi, Z. Zhou, C. Huang and F. Li, *Organometallics*, 2010, **29**, 1085–1091.
- 84 Y. Ellahioui, M. Patra, C. Mari, R. Kaabi, J. Karges, G. Gasser and S. Gómez-Ruiz, *Dalton Trans.*, 2019, **48**, 5940–5951.
- 85 A. B. Caballero, L. Cardo, S. Claire, J. S. Craig, N. J. Hodges, A. Vladyka, T. Albrecht, L. A. Rochford, Z. Pikramenou and M. J. Hannon, *Chem. Sci.*, 2019, **10**, 9244–9256.
- 86 J. Liang, Y. Zheng, X. Wu, C. Tan, L. Ji and Z. Mao, *Adv. Sci.*, 2020, **7**, 1901992.

- 87 A. N. Dosumu, S. Claire, L. S. Watson, P. M. Girio, S. A. M. Osborne, Z. Pikramenou and N. J. Hodges, *JACS Au*, 2021, **1**, 174–186.
- 88 J. Shen, H.-C. Kim, J. Wolfram, C. Mu, W. Zhang, H. Liu, Y. Xie, J. Mai, H. Zhang, Z. Li, M. Guevara, Z.-W. Mao and H. Shen, *Nano Lett.*, 2017, **17**, 2913–2920.
- 89 K. Y. Zhang, H.-W. Liu, T. T.-H. Fong, X.-G. Chen and K. K.-W. Lo, *Inorg. Chem.*, 2010, **49**, 5432–5443.
- 90 M. Gottschaldt, U. S. Schubert, S. Rau, S. Yano, J. G. Vos, T. Kroll, J. Clement and I. Hilger, *Chem. Eur. J. of Chem. Bio.*, 2010, **11**, 649–652.
- 91 M. Wenzel, A. de Almeida, E. Bigaeva, P. Kavanagh, M. Picquet, P. Le Gendre, E. Bodio and A. Casini, *Inorg. Chem.*, 2016, **55**, 2544–2557.
- 92 J. Zielonka, J. Joseph, A. Sikora, M. Hardy, O. Ouari, J. Vasquez-Vivar, G. Cheng, M. Lopez and B. Kalyanaraman, *Chem. Rev.*, 2017, **117**, 10043–10120.
- 93 K. Adamson, C. Dolan, N. Moran, R. J. Forster and T. E. Keyes, *Bioconjugate Chem.*, 2014, **25**, 928–944.
- 94 E. M. Hahn, N. Estrada-Ortiz, J. Han, V. F. C. Ferreira, T. G. Kapp, J. D. G. Correia, A. Casini and F. E. Kühn, *Eur. J. Inorg. Chem.*, 2017, **2017**, 1667–1672.
- 95 G. V. Kalayda, S. Fakhri, H. Bertram, T. Ludwig, H. Oberleithner, B. Krebs and J. Reedijk, *J. Inorg. Biochem.*, 2006, **100**, 1332–1338.
- 96 S. K. Jonas and P. A. Riley, *Cell Biochem. Funct.*, 1991, **9**, 245–253.
- 97 A. Ghezzi, M. Aceto, C. Cassino, E. Gabano and D. Osella, *J. Inorg. Biochem.*, 2004, **98**, 73–78.
- 98 C. A. Puckett and J. K. Barton, *Biochemistry*, 2008, **47**, 11711–11716.
- 99 S. Davis, M. J. Weiss, J. R. Wong, T. J. Lampidis and L. B. Chen, *J Biol Chem*, 1985, **260**, 13844–13850.
- 100 M. F. Ross, G. F. Kelso, F. H. Blaikie, A. M. James, H. M. Cochemé, A. Filipovska, T. Da Ros, T. R. Hurd, R. a. J. Smith and M. P. Murphy, *Biochemistry*, 2005, **70**, 222–230.
- 101 S. M. Cloonan, R. B. P. Elmes, M. Erby, S. A. Bright, F. E. Poynton, D. E. Nolan, S. J. Quinn, T. Gunnlaugsson and D. C. Williams, *J. Med. Chem.*, 2015, **58**, 4494–4505.
- 102 Y.-Y. Xie, G.-J. Lin, G.-B. Jiang, Z.-H. Liang, H.-L. Huang and Y.-J. Liu, *Transition Met Chem*, 2013, **38**, 563–571.
- 103 G.-B. Jiang, Y.-Y. Xie, G.-J. Lin, H.-L. Huang, Z.-H. Liang and Y.-J. Liu, *Journal of J. Photochem. Photobiol. B: Biology*, 2013, **129**, 48–56.
- 104 C. Mari, V. Pierroz, R. Rubbiani, M. Patra, J. Hess, B. Spingler, L. Oehninger, J. Schur, I. Ott, L. Salassa, S. Ferrari and G. Gasser, *Chem. Eur. J.*, 2014, **20**, 14421–14436.



- 105 S. Estalayo-Adrián, S. Blasco, S. A. Bright, G. J. McManus, G. Orellana, D. C. Williams, J. M. Kelly and T. Gunnlaugsson, *Chem. Commun.*, 2020, **56**, 9332–9335.
- 106 H. Huang, P. Zhang, H. Chen, L. Ji and H. Chao, *Chem. Eur. J.*, 2015, **21**, 715–725.
- 107 D.-L. Ma, H.-J. Zhong, W.-C. Fu, D. S.-H. Chan, H.-Y. Kwan, W.-F. Fong, L.-H. Chung, C.-Y. Wong and C.-H. Leung, *PLoS ONE*, 2013, **8**, e55751.
- 108 H. Huang, P. Zhang, B. Yu, Y. Chen, J. Wang, L. Ji and H. Chao, *J. Med. Chem.*, 2014, **57**, 8971–8983.
- 109 K. K.-W. Lo and K. Y. Zhang, *RSC Adv.*, 2012, **2**, 12069.
- 110 F.-X. Wang, M.-H. Chen, X.-Y. Hu, R.-R. Ye, C.-P. Tan, L.-N. Ji and Z.-W. Mao, *Sci Rep*, 2016, **6**, 38954.
- 111 C. Kreitner and K. Heinze, *Dalton Trans.*, 2016, **45**, 13631–13647.
- 112 P. Steunenberg, A. Ruggi, N. S. van den Berg, T. Buckle, J. Kuil, F. W. B. van Leeuwen and A. H. Velders, *Inorg. Chem.*, 2012, **51**, 2105–2114.
- 113 W. Jiang, Y. Gao, Y. Sun, F. Ding, Y. Xu, Z. Bian, F. Li, J. Bian and C. Huang, *Inorg. Chem.*, 2010, **49**, 3252–3260.
- 114 M. Yu, Q. Zhao, L. Shi, F. Li, Z. Zhou, H. Yang, T. Yi and C. Huang, *Chem. Commun.*, 2008, 2115–2117.
- 115 K. K.-W. Lo, P.-K. Lee and J. S.-Y. Lau, *Organometallics*, 2008, **27**, 2998–3006.
- 116 S. P.-Y. Li, H.-W. Liu, K. Y. Zhang and K. K.-W. Lo, *Chem. Eur. J.*, 2010, **16**, 8329–8339.
- 117 S. P.-Y. Li, C. T.-S. Lau, M.-W. Louie, Y.-W. Lam, S. H. Cheng and K. K.-W. Lo, *Biomaterials*, 2013, **34**, 7519–7532.
- 118 B.-Z. Zhu, X.-J. Chao, C.-H. Huang and Y. Li, *Chem. Sci.*, 2016, **7**, 4016–4023.
- 119 R. W. Horobin, J. C. Stockert and F. Rashid-Doubell, *Histochem Cell Biol*, 2006, **126**, 165–175.
- 120 Z. Luo, L. Yu, F. Yang, Z. Zhao, B. Yu, H. Lai, K.-H. Wong, S.-M. Ngai, W. Zheng and T. Chen, *Metallomics*, 2014, **6**, 1480–1490.
- 121 B. Boff, C. Gaiddon and M. Pfeffer, *Inorg. Chem.*, 2013, **52**, 2705–2715.
- 122 L. Lu, L.-J. Liu, W. Chao, H.-J. Zhong, M. Wang, X.-P. Chen, J.-J. Lu, R. Li, D.-L. Ma and C.-H. Leung, *Sci Rep*, 2015, **5**, 14544.
- 123 H. J.-P. Ryser and R. Hancock, *Science*, 1965, **150**, 501–503.
- 124 W. C. Shen and H. J. Ryser, *Proc. Natl. Acad. Sci.*, 1978, **75**, 1872–1876.
- 125 A. D. Frankel and C. O. Pabo, *Cell*, 1988, **55**, 1189–1193.
- 126 M. Green and P. M. Loewenstein, *Cell*, 1988, **55**, 1179–1188.

- 127 D. J. Mitchell, L. Steinman, D. T. Kim, C. G. Fathman and J. B. Rothbard, *J Pept. Res.*, 2000, **56**, 318–325.
- 128 J. Brunner and J. K. Barton, *Biochemistry*, 2006, **45**, 12295–12302.
- 129 P. A. Wender, D. J. Mitchell, K. Pattabiraman, E. T. Pelkey, L. Steinman and J. B. Rothbard, *Proc. Natl. Acad. Sci.*, 2000, **97**, 13003–13008.
- 130 A. Byrne, C. S. Burke and T. E. Keyes, *Chem. Sci.*, 2016, **7**, 6551–6562.
- 131 A. Byrne, C. Dolan, R. D. Moriarty, A. Martin, U. Neugebauer, R. J. Forster, A. Davies, Y. Volkov and T. E. Keyes, *Dalton Trans.*, 2015, **44**, 14323–14332.
- 132 M. Dobroschke, Y. Geldmacher, I. Ott, M. Harlos, L. Kater, L. Wagner, R. Gust, W. S. Sheldrick and A. Prokop, *ChemMedChem*, 2009, **4**, 177–187.
- 133 H. D. Herce, A. E. Garcia and M. C. Cardoso, *J. Am. Chem. Soc.*, 2014, **136**, 17459–17467.
- 134 C. Allolio, A. Magarkar, P. Jurkiewicz, K. Baxová, M. Javanainen, P. E. Mason, R. Šachl, M. Cebecauer, M. Hof, D. Horinek, V. Heinz, R. Rachel, C. M. Ziegler, A. Schröfel and P. Jungwirth, *Proc Natl Acad Sci USA*, 2018, **115**, 11923–11928.
- 135 J. S. Wadia, R. V. Stan and S. F. Dowdy, *Nat Med*, 2004, **10**, 310–315.
- 136 J. B. Rothbard, T. C. Jessop, R. S. Lewis, B. A. Murray and P. A. Wender, *J. Am. Chem. Soc.*, 2004, **126**, 9506–9507.
- 137 J. Rothbard, T. Jessop and P. Wender, *Adv. Drug Delivery Rev.*, 2005, **57**, 495–504.
- 138 S. M. Fuchs and R. T. Raines, *Protein Science*, 2009, **14**, 1538–1544.
- 139 N. Sakai and S. Matile, *J. Am. Chem. Soc.*, 2003, **125**, 14348–14356.
- 140 M. Nishihara, F. Perret, T. Takeuchi, S. Futaki, A. N. Lazar, A. W. Coleman, N. Sakai and S. Matile, *Org. Biomol. Chem.*, 2005, **3**, 1659.
- 141 D. Derossi, A. H. Joliot, G. Chassaing and A. Prochiantz, *J Biol Chem*, 1994, **269**, 10444–10450.
- 142 P. E. G. Thorén, D. Persson, M. Karlsson and B. Nordén, *FEBS Letters*, 2000, **482**, 265–268.
- 143 P. M. Fischer, N. Z. Zhelev, S. Wang, J. E. Melville, R. Fåhræus and D. P. Lane, *The J Pept. Res.*, 2000, **55**, 163–172.
- 144 L. J. Brandén, A. J. Mohamed and C. I. E. Smith, *Nat Biotechnol*, 1999, **17**, 784–787.
- 145 A. D. Ragin, R. A. Morgan and J. Chmielewski, *Chem. Biol.*, 2002, **9**, 943–948.
- 146 F. Noor, A. Wüstholtz, R. Kinscherf and N. Metzler-Nolte, *Angew. Chem., Int. Ed.*, 2005, **44**, 2429–2432.
- 147 C. S. Burke, A. Byrne and T. E. Keyes, *Angew. Chem. Int. Ed.*, 2018, **57**, 12420–12424.
- 148 C. S. Burke, A. Byrne and Tia. E. Keyes, *J. Am. Chem. Soc.*, 2018, **140**, 6945–6955.

- 149 A. H. Day, M. H. Übler, H. L. Best, E. Lloyd-Evans, R. J. Mart, I. A. Fallis, R. K. Allemann, E. A. H. Al-Wattar, N. I. Keymer, N. J. Buurma and S. J. A. Pope, *Chem. Sci.*, 2020, **11**, 1599–1606.
- 150 C. V. Dang and W. M. Lee, *Mol. Cell. Biol.*, 1988, **8**, 4048–4054.
- 151 K. L. Horton, K. M. Stewart, S. B. Fonseca, Q. Guo and S. O. Kelley, *Chem. Biol.*, 2008, **15**, 375–382.
- 152 A. Martin, A. Byrne, C. S. Burke, R. J. Forster and T. E. Keyes, *J. Am. Chem. Soc.*, 2014, **136**, 15300–15309.
- 153 C. A. Puckett and J. K. Barton, *J. Am. Chem. Soc.*, 2009, **131**, 8738–8739.
- 154 C. A. Puckett and J. K. Barton, *Bioorg. Med. Chem.*, 2010, **18**, 3564–3569.
- 155 M. R. Gill, J. Garcia-Lara, S. J. Foster, C. Smythe, G. Battaglia and J. A. Thomas, *Nature Chem*, 2009, **1**, 662–667.
- 156 V. Brabec and J. Kasparkova, *Coord. Chem. Rev.*, 2018, **376**, 75–94.
- 157 B. M. Zeglis, V. C. Pierre and J. K. Barton, *Chem. Commun.*, 2007, 4565.
- 158 H. K. Saeed, S. Sreedharan and J. A. Thomas, *Chem. Commun.*, 2020, **56**, 1464–1480.
- 159 M. J. Pisani, D. K. Weber, K. Heimann, J. G. Collins and F. R. Keene, *Metallomics*, 2010, **2**, 393.
- 160 L. Chen, G. Li, F. Peng, X. Jie, G. Dongye, K. Cai, R. Feng, B. Li, Q. Zeng, K. Lun, J. Chen and B. Xu, *Oncotarget*, 2016, **7**, 80716–80734.
- 161 M. Stephenson, C. Reichardt, M. Pinto, M. Wächtler, T. Sainuddin, G. Shi, H. Yin, S. Monro, E. Sampson, B. Dietzek and S. A. McFarland, *J. Phys. Chem. A*, 2014, **118**, 10507–10521.
- 162 S. Chakraborty, B. K. Agrawalla, A. Stumper, N. M. Vegi, S. Fischer, C. Reichardt, M. Kögler, B. Dietzek, M. Feuring-Buske, C. Buske, S. Rau and T. Weil, *J. Am. Chem. Soc.*, 2017, **139**, 2512–2519.
- 163 Y. Ellahioui, M. Patra, C. Mari, R. Kaabi, J. Karges, G. Gasser and S. Gómez-Ruiz, *Dalton Trans.*, 2019, **48**, 5940–5951.
- 164 F. Heinemann, J. Karges and G. Gasser, *Acc. Chem. Res.*, 2017, **50**, 2727–2736.
- 165 H.-G. Fu, Y. Chen, Q. Yu and Y. Liu, *Chem. Commun.*, 2019, **55**, 3148–3151.
- 166 F. Qu, R. W. Lamb, C. G. Cameron, S. Park, O. Oladipupo, J. L. Gray, Y. Xu, H. D. Cole, M. Bonizzoni, Y. Kim, S. A. McFarland, C. E. Webster and E. T. Papish, *Inorg. Chem.*, 2021, **60**, 2138–2148.
- 167 L. M. Loftus, J. K. White, B. A. Albani, L. Kohler, J. J. Kodanko, R. P. Thummel, K. R. Dunbar and C. Turro, *Chem. Eur. J.*, 2016, **22**, 3704–3708.

- 168 J. D. Knoll, B. A. Albani and C. Turro, *Acc. Chem. Res.*, 2015, **48**, 2280–2287.
- 169 M. Huisman, J. K. White, V. G. Lewalski, I. Podgorski, C. Turro and J. J. Kodanko, *Chem. Commun.*, 2016, **52**, 12590–12593.
- 170 T. Oyoshi and H. Sugiyama, *J. Am. Chem. Soc.*, 2000, **122**, 6313–6314.
- 171 A. Zaid, J.-S. Sun, C.-H. Nguyen, E. Bisagni, T. Garestier, D. S. Grierson and R. Zain, *ChemBioChem*, 2004, **5**, 1550–1557.
- 172 R. Galindo-Murillo, L. Ruíz-Azuara, R. Moreno-Esparza and F. Cortés-Guzmán, *Phys. Chem. Chem. Phys.*, 2012, **14**, 15539.
- 173 A. Prisecaru, V. McKee, O. Howe, G. Rochford, M. McCann, J. Colleran, M. Pour, N. Barron, N. Gathergood and A. Kellett, *J. Med. Chem.*, 2013, **56**, 8599–8615.
- 174 Z. Molphy, C. Slator, C. Chatgialloglu and A. Kellett, *Front. Chem.*, 2015, **3**:28
- 175 G. Shi, S. Monro, R. Hennigar, J. Colpitts, J. Fong, K. Kasimova, H. Yin, R. DeCoste, C. Spencer, L. Chamberlain, A. Mandel, L. Lilge and S. A. McFarland, *Coord. Chem. Rev.*, 2015, **282–283**, 127–138.
- 176 Q. Zhang, R. Cao, H. Fei and M. Zhou, *Dalton Trans.*, 2014, **43**, 16872–16879.
- 177 K. Qiu, H. Huang, B. Liu, Y. Liu, Z. Huang, Y. Chen, L. Ji and H. Chao, *ACS Appl. Mater. Interfaces*, 2016, **8**, 12702–12710.
- 178 A. Sorvina, C. A. Bader, J. R. T. Darby, M. C. Lock, J. Y. Soo, I. R. D. Johnson, C. Caporale, N. H. Voelcker, S. Stagni, M. Massi, J. L. Morrison, S. E. Plush and D. A. Brooks, *Sci Rep*, 2018, **8**, 8191.
- 179 F. Schibilla, A. Holthenrich, B. Song, A. L. Linard Matos, D. Grill, D. Rota Martir, V. Gerke, E. Zysman-Colman and B. J. Ravoo, *Chem. Sci.*, 2018, **9**, 7822–7828.
- 180 A. Palmioli, A. Aliprandi, D. Septiadi, M. Mauro, A. Bernardi, L. De Cola and M. Panigati, *Org. Biomol. Chem.*, 2017, **15**, 1686–1699.
- 181 Y. Chen, L. Qiao, L. Ji and H. Chao, *Biomaterials*, 2014, **35**, 2–13.
- 182 H. Wu, T. Yang, Q. Zhao, J. Zhou, C. Li and F. Li, *Dalton Trans.*, 2011, **40**, 1969.
- 183 T. Yang, Q. Liu, S. Pu, Z. Dong, C. Huang and F. Li, *Nano Res.*, 2012, **5**, 494–503.
- 184 S. M. King, S. Claire, R. I. Teixeira, A. N. Dosumu, A. J. Carrod, H. Dehghani, M. J. Hannon, A. D. Ward, R. Bicknell, S. W. Botchway, N. J. Hodges and Z. Pikramenou, *J. Am. Chem. Soc.*, 2018, **140**, 10242–10249.
- 185 K. K.-W. Lo, Ed., *Luminescent and Photoactive Transition Metal Complexes as Biomolecular Probes and Cellular Reagents*, Springer Berlin Heidelberg, Berlin, Heidelberg, 2015, vol. 165.

- 186 B. Cebrián-Losantos, A. A. Krokhin, I. N. Stepanenko, R. Eichinger, M. A. Jakupec, V. B. Arion and B. K. Keppler, *Inorg. Chem.*, 2007, **46**, 5023–5033.
- 187 G. E. Büchel, I. N. Stepanenko, M. Hejl, M. A. Jakupec, B. K. Keppler, P. Heffeter, W. Berger and V. B. Arion, *J. Inorg. Biochem.*, 2012, **113**, 47–54.
- 188 C. A. Wootton, C. Sanchez-Cano, H.-K. Liu, M. P. Barrow, P. J. Sadler and P. B. O'Connor, *Dalton Trans.*, 2015, **44**, 3624–3632.
- 189 A. F. A. Peacock, A. Habtemariam, S. A. Moggach, A. Prescimone, S. Parsons and P. J. Sadler, *Inorganic Chemistry*, 2007, **46**, 4049–4059.
- 190 A. Levina, A. Mitra and P. A. Lay, *Metallomics*, 2009, **1**, 458.
- 191 A. Bonetti, R. Leone, F. M. Muggia and S. B. Howell, Eds., *Platinum and Other Heavy Metal Compounds in Cancer Chemotherapy*, Humana Press, Totowa, NJ, 2009.
- 192 E. Alessio and L. Messori, in *Metallo-Drugs: Development and Action of Anticancer Agents*, eds. A. Sigel, H. Sigel, E. Freisinger and R. K. O. Sigel, De Gruyter, Berlin, Boston, 2018, pp. 141–170.
- 193 P.-S. Kuhn, V. Pichler, A. Roller, M. Hejl, M. A. Jakupec, W. Kandioller and B. K. Keppler, *Dalton Trans.*, 2015, **44**, 659–668.
- 194 R. Trondl, P. Heffeter, C. R. Kowol, M. A. Jakupec, W. Berger and B. K. Keppler, *Chem. Sci.*, 2014, **5**, 2925–2932.
- 195 S. Leijen, S. A. Burgers, P. Baas, D. Pluim, M. Tibben, E. van Werkhoven, E. Alessio, G. Sava, J. H. Beijnen and J. H. M. Schellens, *Investigational New Drugs*, 2015, **33**, 201–214.
- 196 D. Pluim, R. C. van Waardenburg, J. H. Beijnen and J. H. M. Schellens, *Cancer Chemother. Pharmacol.*, 2004, **54**, 71–78.
- 197 S. M. Meier-Menches, C. Gerner, W. Berger, C. G. Hartinger and B. K. Keppler, *Chem. Soc. Rev.*, 2018, **47**, 909–928.
- 198 A. F. A. Peacock, A. Habtemariam, R. Fernández, V. Walland, F. P. A. Fabbiani, S. Parsons, R. E. Aird, D. I. Jodrell and P. J. Sadler, *J. Am. Chem. Soc.*, 2006, **128**, 1739–1748.
- 199 A. Dorcier, W. H. Ang, S. Bolaño, L. Gonsalvi, L. Juillerat-Jeannerat, G. Laurency, M. Peruzzini, A. D. Phillips, F. Zanobini and P. J. Dyson, *Organometallics*, 2006, **25**, 4090–4096.
- 200 R. J. Needham, C. Sanchez-Cano, X. Zhang, I. Romero-Canelón, A. Habtemariam, M. S. Cooper, L. Meszaros, G. J. Clarkson, P. J. Blower and P. J. Sadler, *Angew. Chem., Int. Ed.*, 2017, **56**, 1017–1020.
- 201 A. Gatti, A. Habtemariam, I. Romero-Canelón, J.-I. Song, B. Heer, G. J. Clarkson, D. Rogolino, P. J. Sadler and M. Carcelli, *Organometallics*, 2018, **37**, 891–899.

- 202 J. Wang, S. Sun, D. Mu, J. Wang, W. Sun, X. Xiong, B. Qiao and X. Peng, *Organometallics*, 2014, **33**, 2681–2684.
- 203 S. Omar, P. Scattergood, L. McKenzie, H. Bryant, J. Weinstein and P. Elliott, *Molecules*, 2016, **21**, 1382.
- 204 Zhang, Y. Wang, K. Qiu, Z. Zhao, R. Hu, C. He, Q. Zhang and H. Chao, *Chem. Commun.*, 2017, **53**, 12341–12344.
- 205 C. Ge, H. Huang, Y. Wang, H. Zhao, P. Zhang and Q. Zhang, *ACS Appl. Bio Mater.*, 2018, **1**, 1587–1593.
- 206 S. A. E. Omar, P. A. Scattergood, L. K. McKenzie, C. Jones, N. J. Patmore, A. J. H. M. Meijer, J. A. Weinstein, C. R. Rice, H. E. Bryant and P. I. P. Elliott, *Inorg. Chem.*, 2018, **57**, 13201–13212.
- 207 K. L. Smitten, P. A. Scattergood, C. Kiker, J. A. Thomas and P. I. P. Elliott, *Chem. Sci.*, 2020, **11**, 8928–8935.
- 208 X. Tian, Q. Zhang, M. Zhang, K. Uvdal, Q. Wang, J. Chen, W. Du, B. Huang, J. Wu and Y. Tian, *Chem. Sci.*, 2017, **8**, 142–149.
- 209 Y. Shen, T. Shao, B. Fang, W. Du, M. Zhang, J. Liu, T. Liu, X. Tian, Q. Zhang, A. Wang, J. Yang, J. Wu and Y. Tian, *Chem. Commun.*, 2018, **54**, 11288–11291.
- 210 A. Bonetti, Ed., *Platinum and other heavy metal compounds in cancer chemotherapy: molecular mechanisms and clinical applications*, Humana Press, New York, 2009.
- 211 T. C. Johnstone, K. Suntharalingam and S. J. Lippard, *Chem. Rev.*, 2016, **116**, 3436–3486.
- 212 E. Baggaley, I. V. Sazanovich, J. A. G. Williams, J. W. Haycock, S. W. Botchway and J. A. Weinstein, *RSC Adv.*, 2014, **4**, 35003–35008.
- 213 J. Wu, Y. Li, C. Tan, X. Wang, Y. Zhang, J. Song, J. Qu and W.-Y. Wong, *Chem. Commun.*, 2018, **54**, 11144–11147.
- 214 S. Sreedharan, M. R. Gill, E. Garcia, H. K. Saeed, D. Robinson, A. Byrne, A. Cadby, T. E. Keyes, C. Smythe, P. Pellett, J. Bernardino de la Serna and J. A. Thomas, *J. Am. Chem. Soc.*, 2017, **139**, 15907–15913.
- 215 Y. Chen, T. W. Rees, L. Ji and H. Chao, *Curr. Opin. Chem. Biol.*, 2018, **43**, 51–57.
- 216 M. R. Duchon and G. Szabadkai, *Essays In Biochemistry*, 2010, **47**, 115–137.
- 217 D. C. Wallace, *Nat. Rev. Cancer*, 2012, **12**, 685–698.
- 218 S. Wen, D. Zhu and P. Huang, *Future Med. Chem.*, 2013, **5**, 53–67.
- 219 A. Wongrakpanich, S. M. Geary, M. A. Joiner, M. E. Anderson and A. K. Salem, *Nanomedicine*, 2014, **9**, 2531–2543.
- 220 N. Ashki, K. C. Hayes and F. Bao, *Neuroscience*, 2008, **156**, 107–117.

- 221 W. Zhang, Y. Liu, Q. Gao, C. Liu, B. Song, R. Zhang and J. Yuan, *Chem. Commun.*, 2018, **54**, 13698–13701.
- 222 C. S. Burke, A. Byrne and T. E. Keyes, *Angew. Chem., Int. Ed.*, 2018, **57**, 12420–12424.
- 223 S. Chakraborty, B. K. Agrawalla, A. Stumper, N. M. Vegi, S. Fischer, C. Reichardt, M. Kögler, B. Dietzek, M. Feuring-Buske, C. Buske, S. Rau and T. Weil, *J. Am. Chem. Soc.*, 2017, **139**, 2512–2519.
- 224 Q. Chen, C. Jin, X. Shao, R. Guan, Z. Tian, C. Wang, F. Liu, P. Ling, J.-L. Guan, L. Ji, F. Wang, H. Chao and J. Diao, *Small*, 2018, **14**, 1802166.
- 225 H. K. Saeed, S. Sreedharan, P. J. Jarman, S. A. Archer, S. D. Fairbanks, S. P. Foxon, A. J. Auty, D. Chekulaev, T. Keane, A. J. H. M. Meijer, J. A. Weinstein, C. G. W. Smythe, J. Bernardino de la Serna and J. A. Thomas, *J. Am. Chem. Soc.*, 2020, **142**, 1101–1111.
- 226 J. R. Shewring, A. J. Cankut, L. K. McKenzie, B. J. Crowston, S. W. Botchway, J. A. Weinstein, E. Edwards and M. D. Ward, *Inorg. Chem.*, 2017, **56**, 15259–15270.
- 227 C. Zhang, K. Qiu, C. Liu, H. Huang, T. W. Rees, L. Ji, Q. Zhang and H. Chao, *Dalton Trans.*, 2018, **47**, 12907–12913.
- 228 J. Liu, Y. Chen, G. Li, P. Zhang, C. Jin, L. Zeng, L. Ji and H. Chao, *Biomaterials*, 2015, **56**, 140–153.
- 229 J. Liu, X. Liao, K. Xiong, S. Kuang, C. Jin, L. Ji and H. Chao, *Chem. Commun.*, 2020, **56**, 5839–5842.
- 230 S. Lazic, P. Kaspler, G. Shi, S. Monro, T. Sainuddin, S. Forward, K. Kasimova, R. Hennigar, A. Mandel, S. McFarland and L. Lilje, *Photochem Photobiol*, 2017, **93**, 1248–1258.
- 231 Y. Li, C.-P. Tan, W. Zhang, L. He, L.-N. Ji and Z.-W. Mao, *Biomaterials*, 2015, **39**, 95–104.
- 232 L. K. McKenzie, I. V. Sazanovich, E. Baggaley, M. Bonneau, V. Guerschais, J. A. G. Williams, J. A. Weinstein and H. E. Bryant, *Chem. Eur. J.*, 2017, **23**, 234–238.
- 233 T. Xiong, M. Li, Y. Chen, J. Du, J. Fan and X. Peng, *Chem. Sci.*, 2021, **12**, 2515–2520.
- 234 V. Novohradsky, A. Rovira, C. Hally, A. Galindo, G. Vigueras, A. Gandioso, M. Svitelova, R. Bresolí-Obach, H. Kostrhunova, L. Markova, J. Kasparikova, S. Nonell, J. Ruiz, V. Brabec and V. Marchán, *Angew. Chem.*, 2019, **131**, 6377–6381.
- 235 Z. Lv, H. Wei, Q. Li, X. Su, S. Liu, K. Y. Zhang, W. Lv, Q. Zhao, X. Li and W. Huang, *Chem. Sci.*, 2018, **9**, 502–512.
- 236 R. Bevernaegie, B. Doix, E. Bastien, A. Diman, A. Decottignies, O. Feron and B. Elias, *J. Am. Chem. Soc.*, 2019, **141**, 18486–18491.

- 237 S. Kuang, L. Sun, X. Zhang, X. Liao, T. W. Rees, L. Zeng, Y. Chen, X. Zhang, L. Ji and H. Chao, *Angew. Chem. Int. Ed.*, 2020, **59**, 20697–20703.
- 238 Z. Pan, C. Tan, L. Rao, H. Zhang, Y. Zheng, L. Hao, L. Ji and Z. Mao, *Angew. Chem.*, 2020, **132**, 18914–18921.
- 239 H. P. Mohammad, O. Barbash and C. L. Creasy, *Nat Med*, 2019, **25**, 403–418.
- 240 J. B. Wittenberg, *Physiological Reviews*, 1970, **50**, 559–636.
- 241 A. A. Bobko, I. Dhimitruka, T. D. Eubank, C. B. Marsh, J. L. Zweier and V. V. Khrantsov, *Free Radic. Biol. Med.*, 2009, **47**, 654–658.
- 242 B. Wen, M. Urano, J. A. O’Donoghue and C. C. Ling, *Radiat Res*, 2006, **166**, 512–518.
- 243 J. Bussink, J. H. Kaanders, A. M. Strik, B. Vojnovic and A. J. van Der Kogel, *Radiat Res*, 2000, **154**, 547–555.
- 244 R. D. Braun, J. L. Lanzen, S. A. Snyder and M. W. Dewhirst, *Am J Physiol-Heart C*, 2001, **280**, H2533–H2544.
- 245 S. J. Cringle, P. K. Yu, E.-N. Su and D.-Y. Yu, *Invest. Ophthalmol. Vis. Sci.*, 2006, **47**, 4072.
- 246 P. Vaupel, K. Schlenger, C. Knoop and M. Höckel, *Cancer Res*, 1991, **51**, 3316–3322.
- 247 K. Mamchaoui and G. Saumon, *Am J Physiol-Lung*, 2000, **278**, L858–L863.
- 248 W. Zhong, P. Urayama and M.-A. Mycek, *J. Phys. D: Appl. Phys.*, 2003, **36**, 1689–1695.
- 249 D. Hara, Y. Umehara, A. Son, W. Asahi, S. Misu, R. Kurihara, T. Kondo and K. Tanabe, *ChemBioChem*, 2018, **19**, 956–962.
- 250 A. I. Solomatina, S.-H. Su, M. M. Lukina, V. V. Dudenkova, V. I. Shcheslavskiy, C.-H. Wu, P. S. Chelushkin, P.-T. Chou, I. O. Koshevoy and S. P. Tunik, *RSC Adv.*, 2018, **8**, 17224–17236.
- 251 S. Zhang, M. Hosaka, T. Yoshihara, K. Negishi, Y. Iida, S. Tobita and T. Takeuchi, *Cancer Res*, 2010, **70**, 4490–4498.
- 252 L. Sun, G. Li, X. Chen, Y. Chen, C. Jin, L. Ji and H. Chao, *Sci Rep*, 2015, **5**, 14837.
- 253 J. Li, H. Chen, L. Zeng, T. W. Rees, K. Xiong, Y. Chen, L. Ji and H. Chao, *Inorg. Chem. Front.*, 2019, **6**, 1003–1010.
- 254 T. Yoshihara, S. Murayama and S. Tobita, *Sensors*, 2015, **15**, 13503–13521.
- 255 K. Y. Zhang, T. Zhang, H. Wei, Q. Wu, S. Liu, Q. Zhao and W. Huang, *Chem. Sci.*, 2018, **9**, 7236–7240.
- 256 R. I. Dmitriev and D. B. Papkovsky, *Cell. Mol. Life Sci.*, 2012, **69**, 2025–2039.
- 257 D. B. Papkovsky, in *Methods in Enzymology*, Elsevier, 2004, vol. 381, pp. 715–735.
- 258 I. Dunphy, S. A. Vinogradov and D. F. Wilson, *Anal. Biochem.*, 2002, **310**, 191–198.



- 259 D. B. Papkovsky and T. C. O’Riordan, *J Fluoresc*, 2005, **15**, 569–584.
- 260 A. Fercher, G. V. Ponomarev, D. Yashunski and D. Papkovsky, *Anal Bioanal Chem*, 2010, **396**, 1793–1803.
- 261 A. Y. Lebedev, A. V. Cheprakov, S. Sakadžić, D. A. Boas, D. F. Wilson and S. A. Vinogradov, *ACS Appl. Mater. Interfaces*, 2009, **1**, 1292–1304.
- 262 R. I. Dmitriev, H. M. Ropiak, D. V. Yashunsky, G. V. Ponomarev, A. V. Zhdanov and D. B. Papkovsky, *FEBS Journal*, 2010, **277**, 4651–4661.
- 263 R. I. Dmitriev, H. M. Ropiak, G. V. Ponomarev, D. V. Yashunsky and D. B. Papkovsky, *Bioconjugate Chem.*, 2011, **22**, 2507–2518.
- 264 Y.-E. Koo Lee, R. Smith and R. Kopelman, *Annual Rev. Anal. Chem.*, 2009, **2**, 57–76.
- 265 Y.-E. Koo Lee, E. E. Ulbrich, G. Kim, H. Hah, C. Strollo, W. Fan, R. Gurjar, S. Koo and R. Kopelman, *Anal. Chem.*, 2010, **82**, 8446–8455.
- 266 M. P. Coogan, J. B. Court, V. L. Gray, A. J. Hayes, S. H. Lloyd, C. O. Millet, S. J. A. Pope and D. Lloyd, *Photochem. Photobiol. Sci.*, 2010, **9**, 103–109.
- 267 C. Wu, B. Bull, K. Christensen and J. McNeill, *Angew. Chem. Int. Ed.*, 2009, **48**, 2741–2745.
- 268 X. Wang, H. H. Gorris, J. A. Stolwijk, R. J. Meier, D. B. M. Groegel, J. Wegener and O. S. Wolfbeis, *Chem. Sci.*, 2011, **2**, 901.
- 269 A. Ruggi, F. W. B. van Leeuwen and A. H. Velders, *Coord. Chem. Rev.*, 2011, **255**, 2542–2554.
- 270 P. Ceroni, A. Y. Lebedev, E. Marchi, M. Yuan, T. V. Esipova, G. Bergamini, D. F. Wilson, T. M. Busch and S. A. Vinogradov, *Photochem. Photobiol. Sci.*, 2011, **10**, 1056.
- 271 A. Martin, A. Byrne, C. Dolan, R. J. Forster and T. E. Keyes, *Chem. Commun.*, 2015, **51**, 15839–15841.
- 272 A. Byrne, J. Jacobs, C. S. Burke, A. Martin, A. Heise and T. E. Keyes, *Analyst*, 2017, **142**, 3400–3406.
- 273 A. V. Kondrashina, R. I. Dmitriev, S. M. Borisov, I. Klimant, I. O’Brien, Y. M. Nolan, A. V. Zhdanov and D. B. Papkovsky, *Adv. Funct. Mater.*, 2012, **22**, 4931–4939.
- 274 R. I. Dmitriev, S. M. Borisov, H. Düssmann, S. Sun, B. J. Müller, J. Prehn, V. P. Baklaushev, I. Klimant and D. B. Papkovsky, *ACS Nano*, 2015, **9**, 5275–5288.
- 275 H. Shi, X. Ma, Q. Zhao, B. Liu, Q. Qu, Z. An, Y. Zhao and W. Huang, *Adv. Funct. Mater.*, 2014, **24**, 4823–4830.
- 276 Y.-E. L. Koo, Y. Cao, R. Kopelman, S. M. Koo, M. Brasuel and M. A. Philbert, *Anal. Chem.*, 2004, **76**, 2498–2505.

- 277 H. Xu, J. W. Aylott, R. Kopelman, T. J. Miller and M. A. Philbert, *Anal. Chem.*, 2001, **73**, 4124–4133.
- 278 Y.-E. Koo Lee, R. Smith and R. Kopelman, *Annual Rev. Anal. Chem.*, 2009, **2**, 57–76.
- 279 R. Sutherland, *Science*, 1988, **240**, 177–184.
- 280 R. M. Sutherland, *Cancer*, 1986, **58**, 1668–1680.
- 281 G. Mehta, A. Y. Hsiao, M. Ingram, G. D. Luker and S. Takayama, *J. Controlled Release*, 2012, **164**, 192–204.
- 282 R. Sutherland, *Science*, 1988, **240**, 177–184.
- 283 W. Metzger, D. Sossong, A. Bächle, N. Pütz, G. Wennemuth, T. Pohlemann and M. Oberringer, *Cytotherapy*, 2011, **13**, 1000–1012.
- 284 G. Mehta, A. Y. Hsiao, M. Ingram, G. D. Luker and S. Takayama, *J. Controlled Release*, 2012, **164**, 192–204.
- 285 W. Metzger, D. Sossong, A. Bächle, N. Pütz, G. Wennemuth, T. Pohlemann and M. Oberringer, *Cytotherapy*, 2011, **13**, 1000–1012.
- 286 L. C. Kimlin, G. Casagrande and V. M. Virador, *Mol. Carcinog.*, 2013, **52**, 167–182.
- 287 G. Mehta, A. Y. Hsiao, M. Ingram, G. D. Luker and S. Takayama, *J. Controlled Release*, 2012, **164**, 192–204.
- 288 W. MuellerKlieser, *Crit. Rev. Oncol. Hematol.*, 2000, **36**, 123–139.
- 289 J. Liu, Y. Chen, G. Li, P. Zhang, C. Jin, L. Zeng, L. Ji and H. Chao, *Biomaterials*, 2015, **56**, 140–153.
- 290 C. Sanchez-Cano, I. Romero-Canelón, K. Geraki and P. J. Sadler, *J. Inorg. Biochem.*, 2018, **185**, 26–29.
- 291 N. S. Bryce, J. Z. Zhang, R. M. Whan, N. Yamamoto and T. W. Hambley, *Chem. Commun.*, 2009, 2673.
- 292 H. Kurokawa, H. Ito, M. Inoue, K. Tabata, Y. Sato, K. Yamagata, S. Kizaka-Kondoh, T. Kadonosono, S. Yano, M. Inoue and T. Kamachi, *Sci Rep*, 2015, **5**, 10657.
- 293 A. Raza, H. E. Colley, E. Baggaley, I. V. Sazanovich, N. H. Green, J. A. Weinstein, S. W. Botchway, S. MacNeil and J. W. Haycock, *Sci Rep*, 2017, **7**, 10743.
- 294 A. Fercher, S. M. Borisov, A. V. Zhdanov, I. Klimant and D. B. Papkovsky, *ACS Nano*, 2011, **5**, 5499–5508.
- 295 R. I. Dmitriev, A. V. Zhdanov, Y. M. Nolan and D. B. Papkovsky, *Biomaterials*, 2013, **34**, 9307–9317.
- 296 A. J. Nichols, E. Roussakis, O. J. Klein and C. L. Evans, *Angew. Chem. Int. Ed.*, 2014, **53**, 3671–3674.

- 297 R. I. Dmitriev, A. V. Kondrashina, K. Koren, I. Klimant, A. V. Zhdanov, J. M. P. Pakan, K. W. McDermott and D. B. Papkovsky, *Biomater. Sci.*, 2014, **2**, 853–866.
- 297 S. P. Neves, N. C. de Carvalho, M. M. da Silva, A. C. B. C. Rodrigues, L. M. Bomfim, R. B. Dias, C. B. S. Sales, C. A. G. Rocha, M. B. P. Soares, A. A. Batista and D. P. Bezerra, *Front. Oncol.*, 2019, **9**, 562.
- 299 A. Raza, S. A. Archer, S. D. Fairbanks, K. L. Smitten, S. W. Botchway, J. A. Thomas, S. MacNeil and J. W. Haycock, *J. Am. Chem. Soc.*, 2020, **142**, 4639–4647.
- 300 J. Karges, S. Kuang, F. Maschietto, O. Blacque, I. Ciofini, H. Chao and G. Gasser, *Nat Commun*, 2020, **11**, 3262.
- 301 N. W. Choi, S. S. Verbridge, R. M. Williams, J. Chen, J.-Y. Kim, R. Schmehl, C. E. Farnum, W. R. Zipfel, C. Fischbach and A. D. Stroock, *Biomaterials*, 2012, **33**, 2710–2722.
- 302 D. Lambrechts, M. Roeffaers, G. Kerckhofs, S. J. Roberts, J. Hofkens, T. Van de Putte, H. Van Oosterwyck and J. Schrooten, *Biomaterials*, 2013, **34**, 922–929.
- 303 K. Mizukami, A. Katano, S. Shiozaki, T. Yoshihara, N. Goda and S. Tobita, *Sci Rep*, 2020, **10**, 21053.

## **Chapter 2: Photostable NIR emitting ruthenium(II) conjugates; uptake and biological activity in live cells.**

*Published in J Inorg. Biochem.*, 2020, **207**, 111032.

David Cullinane, Karmel S. Gkika, Aisling Byrne, Tia E. Keyes

### **Contributions:**

**David Cullinane:** Synthesis and structural and photophysical characterisation of ruthenium parent and conjugate compounds. Primary author and contributor to the experimental design, execution, analysis and manuscript preparation and revision.

**Karmel S. Gkika:** Contributor to the experimental preparation and execution of biological assays (MitoPT TMRE and Caspase FAM-FLICA), Rubiq-PEG cytotoxicity and Rubiq-NLS uptake and FAM-FLICA/DRAQ7 co-staining imaging using confocal microscopy. Contributor to the manuscript, discussion, and revision.

**Dr. Aisling Byrne:** Biological viability assay and cell uptake studies of the Rubiq-peptide conjugates. Manuscript discussion and revision.

**Prof. Tia E. Keyes:** Project conceptualization and management, discussion, and revision of the manuscript.

Supporting information associated with this chapter can be found in **Appendix A**.

## 2.1 Abstract

A photostable Ru(2,2-biquinoline)<sub>2</sub>(3-(2-pyridyl)-5-(4-carboxyphenyl)-1,2,4-triazolate) (Ru(biq)<sub>2</sub>(trzbenzCOOH)) complex that exhibits near-infrared (NIR) emission centred at 786 nm is reported. The parent complex was conjugated via amide coupling to a cell-penetrating peptide sequence octa-arginine (R8), and two signal peptide sequences; the nuclear localizing sequence (NLS) VQRKRQKLMP and the mitochondria penetrating peptide (MPP) FrFKFrFK(Ac) (r = D isomer of arginine, Ac = terminal lysine amine acetyl blocked). Notably, none of the peptide conjugates were cell-permeable as chloride salts but efficient and rapid membrane permeation was observed post ion exchange with perchlorate counterion. Also, surprisingly, all three peptide conjugates exhibited potent dark cytotoxicity in both CHO and HeLa cell lines. The peptide conjugates induce cell death through a caspase dependent apoptotic pathway. At the minimum concentration of dye (approx. 15 μM) required for cell imaging, only 20 % of the cells were viable after a 24 h incubation period. To overcome cytotoxicity, the parent complex was PEGylated; this dramatically decreased cytotoxicity, where 50 % of cells were viable even at 150 μM concentration after 24 h. Confocal luminescence microscopy indicated that all four bioconjugates, peptides in perchlorate form and polyethylene glycol (PEG) in chloride form, were rapidly internalized within the cell. However, interestingly the precise localisation by the signal peptides observed in related complexes was not observed here and the peptide conjugates were unsuitable as luminescent probes for cell microscopy due to their high cell toxicity. The poor targeting of signal peptides in this instance is attributed to the high lipophilicity of the metal centre.

## 2.2 Introduction

Over recent years, we and others have reported a number of ruthenium(II) polypyridyl luminophores suitable as probes for imaging and sensing within the cellular environment.<sup>1-6</sup> The focus on ruthenium(II) luminophores is driven by a range of attractive properties they possess for microscopy including their versatile synthetic chemistry, large Stokes shift, environmental sensitivity, and long emission lifetimes. However, compared to, for example, Ir(III) luminophores, Ru(II) polypyridyls are generally less optically tuneable, thus most reports focus on complexes that emit within the optical window between 600 to 700 nm.<sup>7,8</sup> Although such red emission is useful, and can for example, facilitate bioimaging with reduced autofluorescence background, ideally NIR probes with emission that coincides with the biological optical window (700-950 nm) offer the best advantage in terms of minimising the

effects of autofluorescence and light scattering.<sup>9,10</sup> In particular, NIR light is more penetrative through biological samples than visible light.<sup>11</sup> This becomes more important where probes are applied to luminescence imaging of tissues and spheroids (3D-clusters of cells). Os(II) polypyridyl luminophores are promising probes for NIR microscopy as they typically emit within the biological window, often within the range of 700 nm to 850 nm. Indeed, we have demonstrated Os(II) complexes with low cytotoxicity, suitable for imaging, promoted particularly by their robust photostability.<sup>12</sup> However, when targeted to mitochondria, perhaps due to their relatively low redox potentials and greater lipophilicity they can show greater toxicity than their Ru(II) analogues.<sup>13</sup>

To date, however, there have been no examples of NIR emitting Ru(II) complexes applied to cell imaging likely because there are two challenges associated with Ru(II) NIR emitters. The first is that the most common approach for extending Ru emission to the NIR is to apply strong  $\pi$ -acceptor ligands, such as such as 2,2'-bipyrazine or 2,2'-biquinoline (biq) to the ruthenium centre.<sup>14,15</sup> However, if strong  $\pi$ -acceptor ligands are coordinated alone or in combination with modest  $\sigma$ -donor ligands such as 2,2'-bipyridine, the resulting reduced splitting of the metal ligand field renders the dissociative triplet metal centred state ( $^3MC$ ) thermally accessible at room temperature. The effect is exacerbated under live-cell imaging conditions which are under elevated temperature conditions, typically 37 °C, and evident as ligand de-chelation or increased non-radiative decay/reduced emission quantum yield.<sup>16</sup> This can be exploited for therapeutic applications as demonstrated by Glazer *et al.*, Bonnet *et al.* and others who have used the photolability of Ru(II)-biquinoline complexes in light activated anticancer therapeutics.<sup>17,18</sup> However, for the purpose of cell imaging, photostability is essential. To offset photolability in Ru(II)-biquinoline complexes and engender photostability, co-coordination of a strong  $\sigma$ -donor ligand such as a pyridyl-1,2,4-triazolate can raise the energy of the  $^3MC$  in complexes with strong  $\pi$ -acceptor ligands preventing thermal population of this state under warmer biological conditions to yield photostable NIR emitting luminophores.<sup>14,19</sup>

The second issue in driving probes to the NIR spectral range is the energy gap law, that predicts that as the energy gap between the excited  $T_1$ , here the metal to ligand charge transfer ( $^3MLCT$ ), and ground  $S_0$  state decreases, the non-radiative decay rate increases<sup>20</sup>. The energy gap law has been shown to apply to ruthenium and osmium luminophores.<sup>21</sup> This is much more challenging to overcome, and frequently limits the quantum yields and lifetimes of NIR emitting metal complex luminophores to sub-100 ns. An exciting alternative approach to driving Ru(II) emission to NIR was recently described by Zaccheroni, Hanan and Campanga where strong

donor ligands were combined with terpyridine-like ligands that coordinated with large bite angles to yield Ru(II) complexes with emission extended to a remarkable 900 nm with room temperature lifetimes close to or above 100 ns.<sup>22</sup>

In addition to photostability, metal complexes applied to imaging or as phototherapeutics must be able to permeate the cell membrane of live cells and depending on application, may be required to target specific cell organelles i.e. mitochondria, nucleus or important cellular components such as DNA.<sup>13,23</sup> Generally, Ru(II) complexes are poorly membrane permeable, and so several strategies have been explored to achieve cell uptake. Simple but effective approaches have included the judicious selection of counterion which influences not only solubility but can promote cell uptake of the metal complex. For example, pentachlorophenol has been shown to facilitate membrane permeation of previously impermeable metal complexes through an ion pairing mechanism.<sup>24</sup> Barton *et al.* studied the effect of altering the lipophilicity of ancillary ligands, concluding that cellular uptake of metal complex cargo was higher with an increase in ligand lipophilicity.<sup>25</sup> Similarly, there are a number of examples of iridium complexes that target the mitochondria due to the fine tuning of the charge/lipophilicity balance of these complexes, avoiding the need for a mitochondrial targeting group like triphenylphosphine.<sup>26,27</sup> Selective targeting of cell organelles can be due to innate properties of the metal complex structure demonstrated by the [(phen)<sub>2</sub>Ru(tpphz)Ru(phen)<sub>2</sub>] (phen = 1,10-phenanthroline, tpphz = tetrapyrido[3,2-a:2',3'-c:3'',2''-h:2''',3'''-j]phenazine) complex that has been shown to selectively localise in the nucleus of live cells and intercalate with DNA.<sup>28</sup> Bioconjugation to the fluorophore has been employed widely in our research group to study relevant cellular structures. Cell penetrating peptides have been conjugated to facilitate cell uptake of metal complex cargo and signal peptide sequences have been shown to be highly effective in driving localisation to the mitochondria or nucleus while the addition of a cholesterol group to a fluorophore has been shown to target lipid droplets.<sup>29-31</sup>

Finally, cytotoxicity of an imaging probe is an important consideration. Metal complexes have been widely implicated as initiators of different apoptotic pathways.<sup>32-34</sup> Several cellular processes and changes occur during initiation of cell death including caspase activation,<sup>35,36</sup> loss of mitochondrial membrane potential<sup>37</sup> and production of reactive oxygen species and ATP depletion.<sup>38</sup> Although caspase-independent processes of cell death have been described,<sup>39,40</sup> caspase-dependent apoptosis is considered the major mechanism by which cells are eliminated in a tightly regulated and efficient manner.<sup>35</sup> Caspases are specific proteases divided into initiator and effector caspases involved in initiation and execution of the process of

programmed cell death.<sup>41</sup> Caspase-dependent apoptosis can be induced via the intrinsic or extrinsic apoptotic pathway. In short, the intrinsic pathway involves the release of cytochrome c into the cytosol from the mitochondria under cellular stress whereas the extrinsic pathway involves triggering of cell surface death receptors.<sup>42</sup> Cytochrome c released in the intrinsic pathway interacts with pro-caspase 9 (apoptosome) leading to activation of caspase-9.<sup>43</sup> Overall, both pathways involve caspase cascade activation which leads to degradation of intracellular components and cell death. It is important to note that active caspases are also involved in non-apoptotic cellular processes<sup>44</sup> and therefore it was also of interest to examine the mitochondrial environment since mitochondrial damage is key to activation of caspases in the intrinsic apoptotic pathway.

Herein, we report on a NIR emitting and photostable Ru(II) biquinoline complex and its three cargo carrying peptide conjugates. The peptides exploited have shown previously to be highly effective in driving related complexes to organelles.<sup>45,46</sup> We observe that the conjugates are cell permeable while the parent complex is not, and unlike previous reports, the conjugates are not directed to organelles and show high dark cytotoxicity. We examine the origin of this unexpected level of toxicity and applying PEG as a vector the complex remains cell permeable but is much less toxic and capable of acting as an imaging probe.

## **2.3 Experimental**

### **2.3.1 Materials**

Peptides (> 95 %) were procured from Celtek Peptides, TN, USA. Discrete methoxy-PEG<sub>12</sub>-amine, m-dPEG<sub>12</sub>, was purchased from Quanta Biodesign. All other materials were obtained from Sigma Aldrich and were used without further purification. 2-pyridinyl amidrazone<sup>47</sup>, 3-(2-pyridyl)-5-(5-methylphenyl)-1,2,4-triazole<sup>48</sup> and [Ru(biq)<sub>2</sub>Cl<sub>2</sub>]<sup>14</sup> were synthesised by reported literature procedures. Ru(II) complex synthesis took place under nitrogen and in the dark. Caution perchlorate salts of metal complexes can be explosive so therefore must be handled with care and synthesised in small quantities.

### **2.3.2 Instrumentation**

<sup>1</sup>H NMR spectra were recorded on either 400 MHz or 600 MHz Bruker spectrometer. The spectra were processed using Bruker Topspin NMR software and calibrated to published solvent peaks<sup>49</sup>. High Resolution Mass Spectrometry (HR-MS) was performed at the



Chemistry and Chemical Biology Laboratory, University College Dublin (parent complexes); or the Mass Spectrometry Unit, Trinity College Dublin or the Mass Spectrometry Facility, NUI Maynooth (peptide conjugates). Fluorescence lifetime measurements were carried out using a PicoQuant FluoTime 100 Compact FLS TCSPC system using a 450 nm pulsed laser source generated from a PicoQuant PDL800-B box.

### 2.3.3 Synthesis

#### 2.3.3.1 3-(2-pyridyl)-5-(4-carboxyphenyl)-1,2,4-triazole (*trzbenzCOOH*) (2)

3-(2-pyridyl)-5-(4-methylphenyl)-1,2,4-triazole (240 mg, 0.926 mmol), potassium permanganate (293 mg, 1.85 mmol) and sodium hydroxide (30 mg, 0.75mmol) were heated at reflux for 14 h in 10 ml of water. The reaction mixture was cooled to room temperature and then filtered. The filtered solid was washed with deionized water. Concentrated aqueous HCl was added dropwise to the filtrate under continuous stirring producing a voluminous white precipitate. The precipitate was filtered, and the solids washed with deionised water. The product was dried at 45 °C overnight. 200 mg of a white powder was obtained.

Yield 74 % <sup>1</sup>H NMR (600 MHz, DMSO-d<sub>6</sub>) (ppm) 15.01 (s, 1H), 13.08 (Br. S, 1H), 8.74 (d, 1H, J= 3.66 Hz), 8.24-8.14 (m, 3H), 8.10-7.99 (m, 3H), 7.54 (m, 1H) <sup>13</sup>C NMR (600 MHz, DMSO-d<sub>6</sub>) (ppm) 167.02, 166.68, 149.59, 146.29, 137.98, 134.49, 131.19, 129.93, 129.47, 125.95, 125.20, 121.52. HR-MS (ESI-QTOF) m/z: calculated for C<sub>14</sub>H<sub>11</sub>N<sub>4</sub>O<sub>2</sub> [M + H]<sup>+</sup> 267.0882 Found 267.0876

#### 2.3.3.2 Parent complex [Ru(*biq*)<sub>2</sub>(*trzbenzCOOH*)]<sup>1+</sup> (3)

[Ru(*biq*)<sub>2</sub>Cl<sub>2</sub>] (433 mg, 0.57 mmol) and 3-(2-pyridyl)-5-(4-carboxyphenyl)-1,2,4-triazole (199 mg, 0.68 mmol) were heated at reflux for 3 h in 30 ml of ethanol/water (2:1 v/v). The reaction mixture was reduced to approx. 15 ml *in vacuo*. Precipitation of the metal complex was achieved by adding the concentrated reaction mixture dropwise to a saturated aqueous NH<sub>4</sub>PF<sub>6</sub> solution. The resulting precipitate was filtered, and the solids were washed with deionised water. The crude reaction product was purified using column chromatography with silica gel and a mobile phase consisting of 90/10/1 MeCN: H<sub>2</sub>O: 20 % w/v KNO<sub>3</sub> (aq). The purple band was isolated. The volume of this fraction was reduced *in vacuo* and added dropwise to a saturated aqueous NH<sub>4</sub>PF<sub>6</sub> solution. The precipitate formed was filtered and the solids were washed with deionised water. The purple solid obtained was recrystallised from acidified

water/acetone mixture (5:1 v/v). The filtered solids were washed with copious amounts of deionised water and then diethyl ether. The filtered solids were dissolved in a minimum amount of acetonitrile. The resulting solution was added dropwise to a saturated solution of aqueous  $\text{NH}_4\text{PF}_6$ . The resulting purple precipitate was filtered. The filtered solids were washed with deionised water and then diethyl ether. The purple solid was dried under vacuum. 353 mg of a purple powder was obtained.

(3) Yield 48 %  $^1\text{H}$  NMR (600 MHz,  $\text{MeCN-d}_3$ ) (ppm) 14.07 (s, 1H), 9.83 (s, 1H), 9.07 (d, 1H,  $J = 8.94$  Hz), 9.01 (d, 1H,  $J = 8.94$  Hz), 8.97 (d, 1H,  $J = 8.94$  Hz), 8.88 (d, 1H,  $J = 8.94$  Hz), 8.84 (d, 1H,  $J = 8.94$  Hz), 8.80 (d, 1H,  $J = 9.66$  Hz), 8.53-8.49 (m, 2H), 8.17 (d, 1H,  $J = 4.14$  Hz), 8.13 (d, 2H,  $J = 8.94$  Hz), 8.07-8.04 (m, 3H), 7.88-7.82 (m, 4H), 7.76 (t, 1H,  $J = 7.68$  Hz, 1.5 Hz), 7.54-7.50 (m, 2H), 7.43-7.32 (m, 4H), 7.15 (d, 1H,  $J = 9.24$  Hz), 7.06-7.02 (m, 2H), 6.98-6.88 (m, 3H), 6.82 (t, 1H,  $J = 8.04$  Hz, 1.68 Hz)  $^{13}\text{C}$  NMR (600 MHz  $\text{MeCN-d}_3$ ) (ppm) 166.77, 163.90, 162.09, 161.96, 160.75, 152.92, 152.72, 152.46, 150.74, 150.69, 140.56, 140.11, 139.94, 139.84, 139.57, 133.30, 132.74, 131.71, 131.64, 131.36, 130.43, 130.28, 130.16, 130.07, 129.94, 129.89, 129.76, 129.66, 129.55, 129.45, 128.24, 127.67, 127.09, 126.99, 126.79, 126.26, 123.53, 123.06, 122.25, 122.19, 121.50. HR-MS (MALDI-QTOF)  $m/z$ : calculated for  $\text{C}_{50}\text{H}_{33}\text{N}_8\text{O}_2$   $[\text{M} - \text{PF}_6]^+$  879.1770 Found 879.1774

### 2.3.3.3 Synthesis of Ru(II) bioconjugates

#### 2.3.3.3.1 $[\text{Ru}(\text{biq})_2(\text{trzbenz-CONH-PEG}_{12})]^+$ (4)

$\text{Ru}(\text{biq})_2(\text{trzbenzCOOH})\cdot\text{PF}_6$  (42 mg, 0.0359 mmol),  $\text{N,N}$ -Diisopropylethylamine (DIPEA) (64  $\mu\text{L}$ , 0.46 mmol) and 1-[bis(dimethylamino)methylene]-1H-1,2,3-triazolo[4,5-b]pyridinium 3-oxid hexafluorophosphate (HATU) (20 mg, 0.0538 mmol) were dissolved in 3 ml of dichloromethane (DCM). 30 mg of  $m$ -dPEG<sub>12</sub>-NH<sub>2</sub> (0.0538 mmol) was dissolved in 2 ml of DCM and the resulting solution was added to the reaction vessel. The reaction mixture was stirred at room temperature for 24 h. The reaction mixture was then diluted with 20 ml of DCM and washed three times with 20 ml portions of deionised water. The organic phase was isolated and dried with magnesium sulphate. The magnesium sulphate was removed by filtering the solution. DCM was removed *in vacuo* and a purple tacky solid was obtained. Counterion metastasis from hexafluorophosphate salt to the chloride salt was achieved by dissolving complex in methanol and adding Amberlite 900 IRA chloride exchange resin. The suspension was stirred for 24 h and then filtered to remove exchange resin. Removal of solvent *in vacuo* provided the chloride salt of the bioconjugate.

Reverse phase HPLC (PDAD 550nm) Purity vs. parent 100 %  $^1\text{H}$  NMR (600 MHz, Acetone- $\text{d}_6$ ) (ppm) 9.30 (1H, d, 8.6 Hz), 9.21 (1H, d, J= 8.9 Hz), 9.11 (1H, d, J= 8.7 Hz), 9.03 (1H, d, J= 8.7 Hz), 8.98 (1H, d, J= 8.9 Hz), 8.94 (1H, d, J= 8.7 Hz), 8.60 (1H, d, J= 8.9 Hz), 8.51 (1H, d, J= 8.7 Hz), 8.22 (1H, d, J= 8.2 Hz), 8.09 (1H, d, J= 8.2 Hz), 8.01-7.99 (2H, m), 7.91-7.83 (5H, m), 7.75-7.69 (2H, m), 7.63 (1H, t, J= 7.4), 7.52 (1H, t, J= 7.4 Hz), 7.46 (1H, d, J= 8.9 Hz), 7.41-7.27 (6H, m), 7.07 (1H, t, J= 7.8 Hz), 7.01-6.98 (2H, m), 6.92 (1H, t, J= 7.7 Hz), 6.77 (1H, t, J= 7.8 Hz), 3.66-3.51 (45H, m), 3.44-3.43 (2H, m), 3.30 (1H, s), 3.25-3.24 (3H, m)  $^{13}\text{C}$  NMR (600 MHz Acetone- $\text{d}_6$ ) (ppm) 167.24, 164.98, 164.46, 162.67, 162.23, 160.95, 152.97, 152.89, 152.57, 151.31, 150.83, 150.68, 139.58, 139.06, 139.01, 136.70, 134.95, 132.85, 132.14, 131.22, 131.10, 130.41, 130.22, 130.15, 130.00, 129.87, 129.64, 129.40, 129.34, 129.28, 129.17, 129.03, 128.22, 128.08, 127.46, 127.33, 126.47, 126.11, 124.90, 122.87, 122.11, 121.98, 121.42, 120.11, 79.32, 72.70, 71.32, 71.24, 71.11, 71.07, 70.37, 58.86, 40.58. HR-MS (MALDI-QTOF) m/z:  $\text{C}_{75}\text{H}_{84}\text{N}_9\text{O}_{13}\text{Ru}$   $[\text{M-PF}_6]^+$  Calc. 1420.5258 Found 1420.5232

#### 2.3.3.3.2 General peptide conjugation procedure

$\text{Ru}(\text{biq})_2(\text{trzbenzCOOH})\cdot\text{PF}_6$  (1 equiv.), 20 mg of peptide (2 equiv.), N,N-diisopropylethylamine (DIPEA) (10 equiv.) and benzotriazole-1-yl-oxy-tris-pyrrolidino-phosphonium hexafluorophosphate (PyBOP) (4 equiv.) were dissolved in 700 $\mu\text{L}$  of dimethylformamide (DMF). The reaction mixture was stirred for 24 h at room temperature. The conjugate was then precipitated by adding saturated aqueous  $\text{NH}_4\text{PF}_6$  solution dropwise under continuous stirring until precipitation occurs. The precipitate was filtered, and the solids were washed with deionised water and then diethyl ether. The filtered solids were dissolved in a minimum amount of acetone and added dropwise to a saturated tetrabutylammonium chloride (TBAC) / acetone solution precipitating the chloride salt of the peptide conjugate. The precipitate formed was filtered and washed with copious amounts of acetone and then diethyl ether.

Counterion metathesis from chloride to perchlorate was achieved by dissolving the complex in a minimum amount of methanol and adding resulting the solution dropwise to a saturated aqueous solution of lithium perchlorate. The precipitate formed was filtered and washed with water and then diethyl ether. The perchlorate salt was isolated. Caution perchlorate salts can be explosive.

#### 2.3.3.3.3 $[Ru(biq)_2(trzbenz-CONH-R8)]^{9+}$ (5)

Reverse phase HPLC (PDAD 550nm) Purity vs. parent 100 %.  $^1H$  NMR (600 MHz, MeOD- $d_4$  + 1 drop of  $D_2O$ ) (ppm) 9.19 (d, 2H); 9.02-8.88 (m, 4H); 8.51 (t, 2H); 8.16 (d, 1H); 8.05 (d, 1H); 7.91-7.78 (m, 5H); 7.76-7.50 (m, 4H); 7.38-7.19 (m, 8H); 7.01-6.73 (m, 5H); 4.32 (m, 8H); 3.39 (m, 2H); 3.32 (m, 8H); 3.23 (m, 14H); 2.35 (m, 2H); 1.91-1.68 (m, 33H). HR-MS (MALDI-QTOF) m/z:  $C_{104}H_{147}N_{42}O_{10}Ru [M - 2H^+]^{7+}$  Calc. 320.8761 Found 320.8758

#### 2.3.3.3.4 $[Ru(biq)_2(trzbenz-CONH-MPP)]^{4+}$ (6)

Reverse phase HPLC (PDAD 550nm) Purity vs. parent 98.5 %.  $^1H$  NMR (600 MHz, MeOD- $d_4$  + 1 drop of  $D_2O$ ) (ppm) 9.21-9.03 (m, 2H); 9.01-8.73 (m, 5H); 8.54-8.30 (m, 2H); 8.14 (m, 1H); 8.05-7.87 (m, 4H); 7.87-7.67 (m, 5H); 7.65-7.52 (m, 3H); 7.47 (m, 1H); 7.38-7.04 (m, 23H); 7.03-6.76 (m, 5H); 6.67 (m, 1H); 4.57-3.86 (m, 7H); 3.45-3.33 (m, 2H); 3.24-3.08 (m, 5H); 3.07-2.70 (m, 7H); 2.32-2.13 (m, 2H); 1.96-1.79 (m, 3H); 1.79-0.55 (m, 21H). HR-MS (MALDI-QTOF) m/z:  $C_{118}H_{135}N_{26}O_{11}Ru [M + 1H^+]^{5+}$  Calc. 438.7969 Found 438.7983

#### 2.3.3.3.5 $[Ru(biq)_2(trzbenz-CONH-NLS)]^{5+}$ (7)

Reverse phase HPLC (PDAD 550nm) Purity vs. parent 100 %.  $^1H$  NMR (600 MHz, MeOD- $d_4$  + 1 drop of  $D_2O$ ) (ppm) 9.19-8.74 (m, 6H); 8.52-8.31 (m, 2H); 8.16-7.88 (m, 4H); 7.85-7.41 (m, 8H); 7.39-7.11 (m, 7H); 7.00-6.57 (m, 5H); 4.43-3.80 (m, 7H); 3.73-3.33 (m, 5H); 3.26-2.76 (m, 8H); 2.75-2.16 (m, 8H); 2.11-0.54 (m, 38H). HR-MS (MALDI-QTOF) m/z:  $C_{111}H_{146}ClN_{30}O_{13}RuS [M-(H_3O)]^{5+}$  Calc. 455.2027 Found 455.2125

### 2.3.4 Photophysical Measurements

UV-vis spectra were recorded on a Jasco spectrophotometer. Emission Spectra were recorded on a Varian Cary Eclipse fluorescence spectrophotometer with excitation and emission slit widths stated. Lifetime decay plots were analysed using PicoQuant NanoHarp software. The goodness of each fit to exponential decay kinetics was assessed using tailfit criteria (where  $0.9 > \chi^2 < 1.1$ ). All analyses were carried out using quartz cuvettes at room temperature and background correction was applied prior to measurement.

### 2.3.5 Cyclic voltammetry

Cyclic voltammetry was performed on a CHI 900 electrochemical analyzer. Anhydrous acetonitrile was used as solvent with tetrabutylammonium hexafluorophosphate ( $TBAPF_6$ ) (0.1 M) as the supporting electrolyte. Solutions were purged with  $N_2$  for 30 minutes prior to

experiment. A three electrode electrochemical cell comprising Ag/Ag<sup>+</sup> reference electrode, glassy carbon working electrode and Pt- wire counter electrode was used and solution contained 1mM of the metal complex.

### 2.3.6 Cell Culture

Two cell lines were studied; Chinese hamster ovarian (CHO-K1), an adherent mammalian cell line and HeLa cells, a cervical cancer cell line. The media used to culture the cells was Dulbecco's modified Eagle's medium (DMEM)/Hams F-12 for CHO cells and DMEM supplemented with 1 % L-glutamine, and MEM non-essential amino acids for HeLa cells. Both were supplemented with 10 % foetal bovine serum and 1 % penicillin–streptomycin and grown at 37 °C with 5 % CO<sub>2</sub>. Cells were harvested or split at 90 % confluency using 0.25 % trypsin for 5 minutes at 37 °C.

### 2.3.7 Cytotoxicity studies

Cells were seeded in 96-well plates (Sarstedt flat-bottom cell + culture plate) at  $1 \times 10^4$  for CHO and HeLa cells in 100  $\mu$ L media for 24 h at 37 °C with 5 % CO<sub>2</sub>. The Ru(II)-biquinoline conjugates; Ru(biq)<sub>2</sub>(trzbenzCONH-NLS) (RuNLS), Ru(biq)<sub>2</sub>(trzbenzCONH-MPP) (RuMPP), Ru(biq)<sub>2</sub>(trzbenzCONH-R8) (RuR8), Ru(biq)<sub>2</sub>(trzbenzCONH-PEG) (RuPEG), were added for 24 h at 37 °C with 5 % CO<sub>2</sub>. Final metal complex conjugate concentrations were 150, 100, 75, 50, 25, 10, 5 and 1  $\mu$ M.

The Alamar blue assay (Promocell GmbH) was used to measure cell viability by the addition of 10  $\mu$ L resazurin reagent and cells were incubated for 6 h at 37 °C in the dark. Absorbance was measured using a Tecan 96 well plate reader at 570 nm and 600 nm (corrected for background). Cell viability is presented as a percentage ( %) compared to control cells not exposed to Ru(II)-biquinoline (RubiQ) conjugates.

### 2.3.8 Confocal microscopy: RuNLS

*(counter-staining with Carboxyfluorescein Fluorochrome-Labeled Inhibitors of Caspases (FAM-FLICA) and Deep Red Anthraquinone 7 (DRAQ7))*

CHO cells were seeded at  $1.5 \times 10^5$  cells in 35 mm glass-bottom culture dishes (Ibidi, Germany) of 1.5 mL total volume and left for 24 h at 37 °C with 5 % CO<sub>2</sub>. RuNLS probe was added to the cells (15  $\mu$ M / phosphate buffered saline (PBS)) and incubated for 1 h at 37 °C.

The cells were counter-stained with FAM-FLICA (15  $\mu$ l of 30 X FLICA) polycaspase inhibitor and DRAQ7 (3  $\mu$ M) to assess cell death in CHO cells. Cells were washed with supplemented PBS (1.1 mM MgCl<sub>2</sub> and 0.9 mM CaCl<sub>2</sub>) and imaged directly using a Leica TSP DMI8 confocal microscope (100X oil immersion objective lens) with a heated stage. RuNLS was excited using a 568 nm white light laser and the emission range was set to 680-800 nm. FAM-FLICA probe was excited using the 490 nm white light laser and emission was collected between 520 and 535 nm. The 633 nm laser was used to excite DRAQ7 and emission was collected between 650-800 nm.

### 2.3.9 Caspase Activity

The Caspase Assay experiments were carried out on HeLa and CHO cells according to manufacturer's instructions (ImmunoChemistry Technologies). Cells were cultivated at  $3 \times 10^5$  cells/well and were spiked with 30X FAM-FLICA reagent (v/v ratio of 1:30) and incubated for 45 minutes at 37 °C. Control populations were prepared for each cell line: untreated population (negative control 1), DMSO (10 % v/v, negative control 2) and staurosporine 1 $\mu$ M/ 3 h (positive control). Experimental populations were exposed to Rubiq - conjugates at concentrations indicated by cytotoxicity studies. Samples were subsequently spiked with 30X FAM-VAD-FLICA<sup>1</sup> for 45 minutes at 37 °C. The loss of non-adherent cells during washing was accounted for by spinning down the overlay media and recombining the washed cell pellets with the overlay buffer prior to analysis. Samples were analysed in triplicate ( $3 \times 100 \mu$ l) in a black bottomed 96-well plate using Tecan Plate fluorescence plate reader set at 488 nm excitation and 520 nm emission. Polycaspase activity was monitored by the increase of relative fluorescence units (RFU) of the green fluorescent signal in the apoptotic cell populations. Unbound FLICA diffuses out of the cell and is removed during the wash steps. Data were quantified and expressed as the percentage of apoptotic cells based on the positive control cell populations.

---

<sup>1</sup>FAM-VAD-FLICA is a polycaspase indicator dye which consists of a short recognition peptide sequence (VAD) and a fluoromethyl ketone moiety that binds to all active caspases. There are commercially available dyes which can detect specific caspases such as caspase-1 for example by consisting of a different short amino acid sequence (YVAD). The structure of FAM-VAD-FLICA is shown in Appendix A.

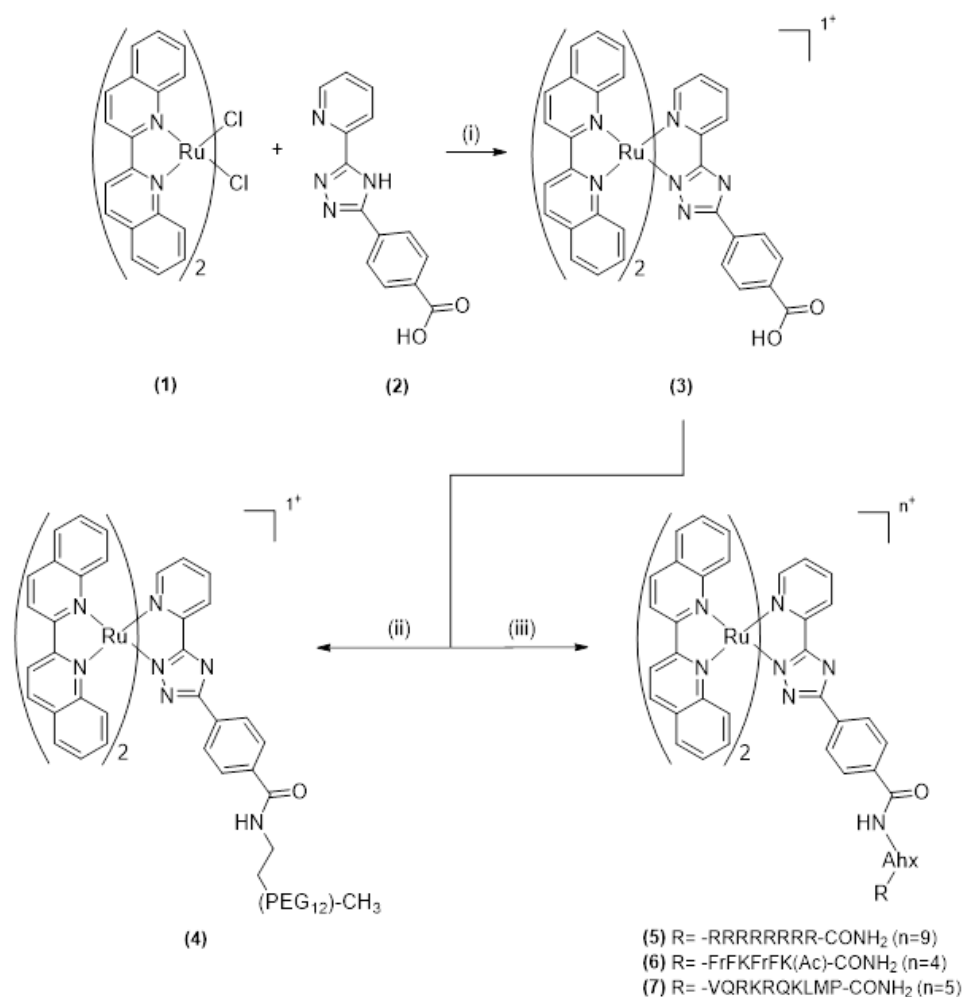
### 2.3.10 Mitochondrial Depolarization Assay

The Mitochondrial Membrane Potential (MitoPT) Assay was carried out on HeLa and CHO cells according to manufacturer's instructions. Cell populations were cultivated at  $5 \times 10^5$  cells/mL and MitoPT spiked suspensions of  $>3 \times 10^6$  cells/mL in 100  $\mu$ l/ well aliquots were prepared. The following control populations were prepared for each cell line: negative control 1 (untreated), negative control 2 DMSO (7.5 % v/v) and positive control Carbonyl cyanide m-chlorophenyl hydrazone (CCCP) (40  $\mu$ M / 1 h). Experimental populations were exposed to Rubiq-conjugates at the concentrations indicated by the FLICA assay. Samples were subsequently incubated with MitoPT Trimethylrhodamine ethyl ester (TMRE) dye for 40 minutes at 37 °C and washed. Aliquots were analysed in triplicate (3  $\times$  100  $\mu$ l) in a black bottomed 96-well plate using Tecan Plate fluorescence plate reader set at 540nm excitation and 574 nm emission. The amount of orange fluorescence from TMRE was measured as an indication of metabolically stressed cells and mitochondrial depolarization. Data were quantified and expressed as the percentage of TMRE fluorescence signal indicative of the loss of mitochondrial membrane potential relative to the control cell populations.

## 2.4 Results and discussion

### 2.4.1 Synthesis and characterisation

The synthetic route to preparation of the Ru(II) complex and conjugates is described in scheme 2.1. The triazole ligand **2** was synthesised with a sterically bulky group at the 5 position of the triazole core. The rationale behind this approach was to promote the selective metal coordination of the triazole via the N2 position over the N4.<sup>50</sup> This strategy typically results in >90 % of the N2 isomer forming with less than 5 % of the N4 isomer obtained. The removal of the N4 isomer is achieved through recrystallisation after column chromatography of the crude reaction product. The N4 isomer was not isolated in a pure form due to small amounts formed and difficulty in removing the residual N2 bound isomer. Conjugation of vectors to the parent complex **3** was achieved through amide coupling reaction between the carboxylic acid functionality of the metal complex and an amino group of the relevant vector. Structure and purity of the parent complex and conjugates confirmed by <sup>1</sup>H NMR, LC mass spectrometry and HPLC with a photodiode array detector (PDAD) (see SI for spectra and chromatograms). Minimum purity of the bioconjugates **4-7** was 98 % based on HPLC analysis.



**Scheme 2.1** Synthetic route to Ru(II) bioconjugates (i) EtOH/H<sub>2</sub>O (2:1), reflux, 3 h (ii) m-dPEG<sub>12</sub>, HATU, DIPEA, DCM, rt 24 h (iii) NH<sub>2</sub>-Ahx-peptide (ahx – aminohexyl linker), PyBOP, DIPEA, DMF, rt 24 h.

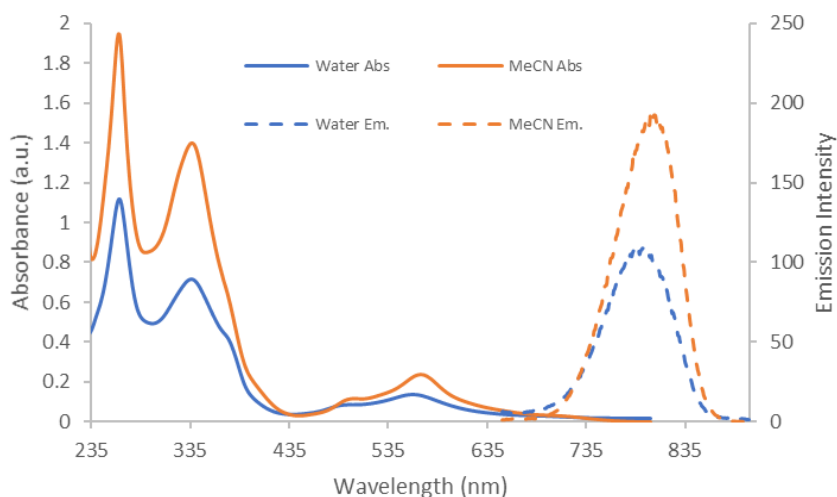
## 2.4.2 Photophysics and electrochemistry

The parent complex emits as expected, in the NIR spectral region in both water and acetonitrile. Spectra are shown in Fig. 2.1.<sup>2</sup> The photophysical data for all the compounds reported are summarized in Table 1. In neutral solution, including the biological media used here, the triazole is expected to be in the anionic triazolite form. Under these conditions, the parent complex exhibits a metal to ligand charge transfer (<sup>1</sup>MLCT) centred at 568 nm in both acetonitrile and water. The quantum yield of the parent complex in water is 0.0005 which is lower than the quantum yield of the conjugates which range from 0.0006 – 0.0007. A similar

<sup>2</sup>Contrast to classical light-switch complexes such as [Ru(bpy/phen)<sub>2</sub>dppz]<sup>2+</sup> which are non-emissive in aqueous environment but exhibit emission in organic media or when bound to DNA. This arises from two low lying <sup>3</sup>MLCT states localized on the dppz ligand and accessibility is strongly reliant on the polarity and hydrogen bonding capability of the solvent.



effect has been noted for Ru(II) polypyridyl peptide conjugates previously and is thought to originate from protection afforded to the complexes by the peptides/PEG chain against emission quenching by dissolved oxygen. In addition, the carboxylic acid functionality of the parent may be a factor compared to the amide of the conjugate.



**Figure 2.1** Absorbance and emission profile of parent complex,  $[\text{Ru}(\text{biq})_2(\text{benztrzCOOH})]^{1+}$ , at  $20 \mu\text{M}$  concentration (1 % v/v DMSO) in water and acetonitrile. Excitation at absorbance  $\lambda_{\text{max}}$  and slit widths 20 nm for emission measurement.

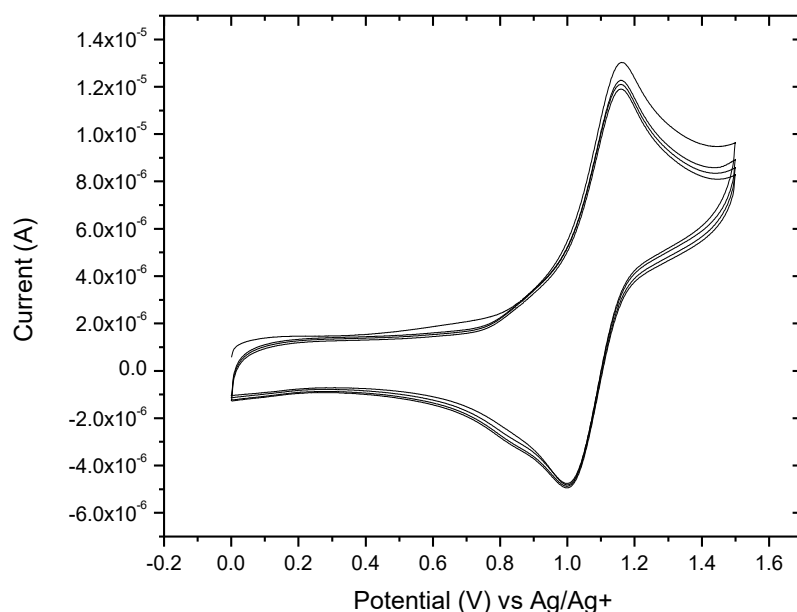
The emission lifetimes of the parent and the conjugates are similar in water. The differing photophysical properties of the anionic triazolates compared to the neutral triazole species was studied in acetonitrile because of more favourable solubility. A solution of the parent complex,  $[\text{Ru}(\text{biq})_2(\text{trzbenzCOOH})]^{1+}$ , in acetonitrile was acidified by adding perchloric acid (1 % v/v) to protonate the triazole. This resulted in a hypsochromic shift in the  $^1\text{MLCT}$  absorption band from 568 nm to 541 nm, and corresponding blue shift in the emission  $\lambda_{\text{max}}$  from 800 nm to 746 nm (ESI Fig. S2. 31). These changes were accompanied by a reduction in the emission lifetime of the complex from 266 ns to 134 ns. Such hypsochromic shifts and reduction in lifetime have been reported on protonation of Ru(II) triazolates complexes previously and are attributed to the reduced  $\sigma$ -donor capacity of the neutral ligand.<sup>50</sup> This leads to a reduction in ligand field splitting rendering the  $^3\text{MC}$  more thermally accessible and thus enhanced non-radiative decay of the excited state and increased photolability. Protonation of the triazole is expected to occur below pH 4<sup>13</sup> and so as described, the anionic form will persist under imaging conditions except potentially in acidic region such as the lysosomes.

The electrochemistry of the parent complex in acetonitrile is shown in Fig. 2.2. The complex exhibits a reversible anodic process at  $E^{\circ}_{1/2} = 1.159\text{V}$  assigned to the Ru(II)/Ru(III) couple and cathodic processes at  $-0.765\text{V}$ ,  $-0.986\text{V}$  and  $-1.151\text{V}$  which are attributed to ligand reductions. The oxidation potential is approximately  $100\text{mV}$  lower than comparable  $[\text{Ru}(\text{bpy})_3]^{2+}$  or related complexes attributed to the impact of the strong  $\sigma$ -donating capacity of the triazolate..

**Table 2.1** Summary of photophysical data of parent complex and conjugates.

Compound	Solvent	$\lambda$ absorbance ( $\epsilon$ ) nm ( $\times 10^4 \text{ M}^{-1} \text{ cm}^{-1}$ )	$\lambda_{\text{em}}$ nm	$\tau$ (ns)	$\Phi_{\text{lum}}$
$[\text{Ru}(\text{biq})_2(\text{trzbenzCOOH})]^{1+}$ (3)	MeCN	264 (8.15), 339 (4.84), 568 (0.90)	800	$266 \pm 4$	$0.0007 \pm 3.0 \times 10^{-6}$
	MeCN / 1 % v/v $\text{HClO}_4$	263, 319, 541	746	$134 \pm 6$	-
	$\text{H}_2\text{O}$	265 (4.98), 341 (3.46), 568 (0.72)	786	$159 \pm 4$	$0.0005 \pm 2.6 \times 10^{-6}$
$[\text{Ru}(\text{biq})_2(\text{trz-CONH-PEG}_{12})]^{1+}$ (4)	$\text{H}_2\text{O}$	264, 336, 560	789	$165 \pm 8$	$0.0007 \pm 4.6 \times 10^{-6}$
	$\text{H}_2\text{O}$	264, 336, 560	786	$152 \pm 2$	$0.0007 \pm 2.2 \times 10^{-6}$
$[\text{Ru}(\text{biq})_2(\text{trz-CONH-R8})]^{9+}$ (5)	$\text{H}_2\text{O}$	264, 336, 560	786	$146 \pm 2$	$0.0006 \pm 1.4 \times 10^{-6}$
$[\text{Ru}(\text{biq})_2(\text{trz-CONH-MPP})]^{4+}$ (6)	$\text{H}_2\text{O}$	264, 337, 563	793	$145 \pm 5$	$0.0006 \pm 2.2 \times 10^{-6}$
$[\text{Ru}(\text{biq})_2(\text{trz-CONH-NLS})]^{5+}$ (7)	$\text{H}_2\text{O}$	264, 337, 564	790	$145 \pm 5$	$0.0006 \pm 2.2 \times 10^{-6}$

All measurements performed at room temperature. Deionised water used. All solutions contained 1 % v/v DMSO. Lifetime data collected in triplicate and conformed to tail fit criteria of  $0.9 < \chi^2 < 1.10$ . Quantum yields measured in aerated solvents using  $[\text{Ru}(\text{bpy})_3]^{2+}$  as standard.<sup>51</sup>



**Figure 2.2** Cyclic Voltammetry (cycled 4 times) of 1 mM Ru(biq)<sub>2</sub>(trzbenzCOOH).PF<sub>6</sub> in MeCN with 0.1 M NBu<sub>4</sub>PF<sub>6</sub>. Potentials are reported versus the Ag/Ag<sup>+</sup> reference electrode. Scan rate: 0.05 V/s.

### 2.4.3 Photostability

Photostability of the parent complex was evaluated in deionised water by irradiating the complex in solution using a 150 mW Xenon Arc lamp ( $\lambda > 400$  nm cut off filter) and measuring the absorbance spectra at regular time intervals. After 2 h of continuous irradiation the complex showed photodegradation of less than 8 % in intensity of the <sup>1</sup>MLCT transition (ESI Fig. S2.30). This is consistent with photostability reported for related triazolate coordinated Ru(II)-biquinoline complexes confirming the balance of  $\sigma$ -donor and  $\pi$ -acceptor ligand properties promotes stabilization.<sup>14</sup>

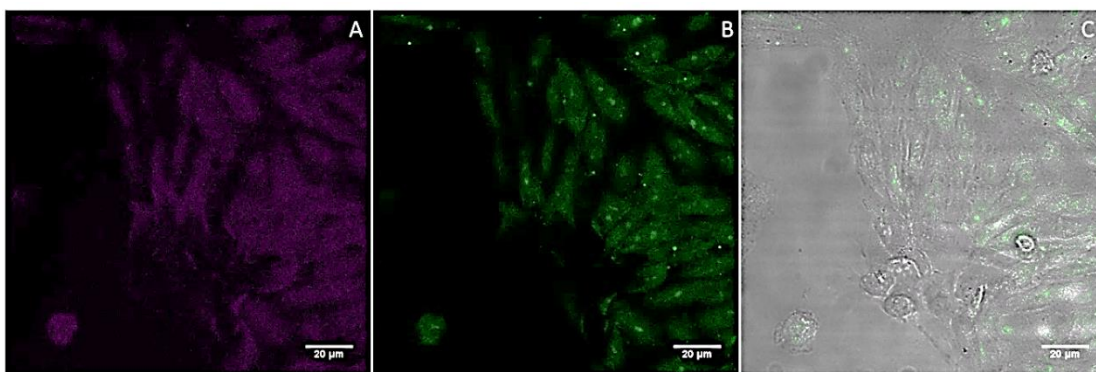
### 2.4.4 Counterion selection

The counterion can have profound impact both on solubility and also on the cell uptake of metal complexes.<sup>24,52</sup> Notably, we observed that none of the three peptide conjugates, RuR8, RuMPP and RuNLS, were taken up by live cells (CHO and HeLa cell lines) when the counterion for these complexes was the chloride anion. This observation contrasts with previously reported studies where such dependence was not observed. In contrast it was observed that exchanging the chloride counterion with perchlorate facilitated the uptake of the peptide conjugates. The origin of this difference is unclear, but we speculate that solubility of the conjugates with chloride counterion in the cell culture media may be lower.<sup>2,30</sup> Additionally,

we tentatively suggest that the perchlorate counterion is less prone to exchange with other anions present in the cell culture media for instance the phosphate anion. The RuPEG conjugate was studied in cells with the chloride counterion as this complex exhibited far superior aqueous solubility than the parent complex or the peptide conjugates. The selection of either a chloride or perchlorate counterion is not believed to have a substantial effect on the cytotoxicity profile of the relevant metal complex. This is based on previous peptide conjugated ruthenium complexes studied in live cells where whether in either the chloride/perchlorate salt both exhibited low levels of dark cytotoxicity.<sup>30,53</sup> Our previous results also indicate that cytotoxicity in the case of the biquinoline complex arises primarily from the metal complex.

#### **2.4.5 Cell Imaging**

The parent complex was poorly soluble in cell culture media and precipitation of the complex was visible which hindered the uptake of the complex. The conjugation of peptides/PEG to the parent complex increased aqueous solubility compared to the parent. The four Ru(II) bioconjugates exhibited relatively weak emission in cells compared to previously reported Ru(II) bioconjugates, which made luminescent microscopy imaging comparatively challenging.<sup>54</sup> No discernible localisation of the Ru(II) bioconjugates within the cell was observed from the luminescent imaging. This is a surprising result given the effectiveness of the MPP and NLS signal peptides in driving ruthenium polypyridyl complexes to mitochondria and nucleus.<sup>46,53</sup> The RuR8 and RuPEG complexes as expected, showed no organelle specific localisation in live cells. Co-localisation studies with relevant organelle stains to determine cellular localisation of the Rubiq conjugates was hindered by the weak emission from the Rubiq probes, but it is evident from Fig. 2.3A which is representative of the distribution of all the conjugates, that they distribute widely throughout the cytoplasm and do not appear to be nuclear excluding. CHO cells were treated with RuNLS at 15  $\mu$ M and incubated for 1 h in the absence of light at 37 °C. As shown in Fig. 2.3A, weak emission intensity from the RuNLS channel did not allow for determination of the precise localization of the probe. The cells were spiked with FAM-FLICA probe which showed even at this concentration apoptotic effects induced by the RuNLS probe. Active caspases indicative of apoptosis is shown in green in Fig. 2.3B.



**Figure 2.3** Confocal Images of live CHO cells treated with RuNLS at 15  $\mu\text{M}$ / 1 h in the absence of light and spiked with FAM-FLICA probe demonstrating caspase activity of cells triggered by RuNLS. (A) Cells were irradiated at 568 nm and emission was collected between 680 nm and 800 nm. (B) FAM-FLICA channel showing active caspases excited at 490 nm. (C) Overlay of (B) with brightfield image. (Scale bar = 20  $\mu\text{m}$ )

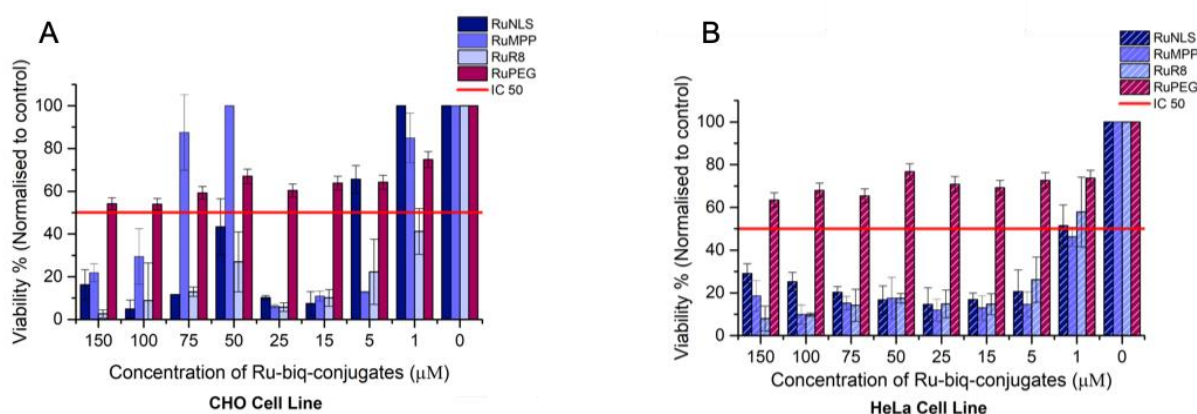
#### 2.4.6 Cytotoxicity studies

Given the notable differences both in uptake and distribution of these probes compared to other ruthenium polypyridyl complexes appended to the same peptide sequences we have reported on, we wanted to understand what effect the Rubiq conjugates have on live cells. Cytotoxicity studies were carried out using the Resazurin (Alamar Blue) assay to assess the viability of CHO and HeLa cells after 24 h exposure. A range of concentrations of each of the conjugates from 0 – 150  $\mu\text{M}$  were added to the cells and were incubated in the absence of light for 24 h. Fig. 2.4 shows the viability of the cells in response to the Rubiq conjugates as a function of concentration.

All three of the Rubiq peptide conjugates exhibit significant cytotoxicity in both cell lines at concentrations as low as 5  $\mu\text{M}$ . There are some interesting differences between cell lines in terms of dose dependence. For HeLa, cytotoxicity is dose dependent to approximately 50  $\mu\text{M}$  where it essentially stabilizes. In CHO cells, remarkably, the behaviour is more complex; the cytotoxicity is observed to be dose dependent in all peptide conjugates up to 25  $\mu\text{M}$ ; at 50  $\mu\text{M}$  the viability actually rises dramatically and then falls again in a dose dependent manner. This is especially dramatic in RuMPP, where at 25  $\mu\text{M}$  conjugate the viability has dropped to about 5 % but rises at 50  $\mu\text{M}$  to 80-90 % and remains similarly high at 75  $\mu\text{M}$  before falling at higher concentrations. A similar effect was noted recently in osmium(II) polypyridyl peptide conjugates where such a switch in viability at higher dye concentration was linked to a change in uptake mechanism where it was evident from imaging that localisation to the mitochondria

was reduced at higher concentrations. The same effect may be at play here however it is not clear from imaging because of the wide distribution of the dye and its weak emission if this is the case.<sup>13</sup> The effect being dependent on cell type suggests that biochemical differences in the cells are important. Interestingly as well, the octaarginine conjugate exhibits highest cytotoxicity to CHO cells, with an IC<sub>50</sub> of less than 1  $\mu$ M. IC<sub>50</sub> was similar for all three peptides in HeLa and confocal imaging showed that after only 3 h exposure HeLa cells treated with RuR8 appear to be in distress, and cell debris can be seen throughout the sample, indicating that cells have undergone apoptosis (ESI Fig S2. 32)

In attempt to reduce the cytotoxicity of the Rubiq complex, a PEGylated derivative of the parent complex was prepared. PEGylation was expected also to increase aqueous solubility and increase uptake. And, indeed as Fig. 2.4 shows, the RuPEG conjugate was significantly less toxic towards both HeLa and CHO cells in comparison to the peptide conjugates. Cell viability remained above 50 % over the range of RuPEG concentrations explored (1  $\mu$ M - 150  $\mu$ M). The PEGylation of metal complexes particularly iridium complexes as reported by Lo *et al.* has been shown previously to significantly reduce the cytotoxicity of the complex in live cells.<sup>55,56</sup> It has been hypothesised that the long uncharged PEG chain hinders the metal complex from interacting with intracellular biomolecules and/or organelles. Therefore, based on comparative toxicity data, it appears that the toxicity stems from the combination of the highly charged peptide attached to the relatively lipophilic Rubiq complex resulting in a toxic effect across both cell lines studied.



**Figure 2.4** Viability of CHO (A) and HeLa (B) cells after 24 h exposure to Rubiq bioconjugates. Live cells were treated with the conjugates followed by addition of Resazurin for 6 h. Absorbance was read at 570 nm with background at 600 nm subtracted (n=3).

Previously, where Ru(II)-biquinoline complexes has been studied in cell lines as potential PDT agents they are typically less toxic in the dark requiring light to instigate a toxic effect. For example, Gasser *et al.* reported IC<sub>50</sub> value of 47.3 μM for cancer cells exposed to [Ru(bpy)<sub>2</sub>(biq)]<sup>2+</sup> in the absence of light, which is considerably less toxic than the peptide conjugates reported here.<sup>57</sup> The low level of dark cytotoxicity of Ru(bpy)<sub>2</sub>(biq) compared to related compounds in this study, suggests that the peptides play a key role in toxic effect. This may be a direct effect or a consequence of greater absolute amount of complex internalized when the cell-penetrating sequence attached. Thus, it is notable, that despite similar uptake, the RuPEG complex shows relatively low cytotoxicity. Overall, our results suggest that the metal centre and the peptides exert a unique mode of action when combined to trigger cell death which may be related to the conjugated sequence and localization of the probes in the cellular environment. To investigate the origin of the cytotoxicity, the FAM-FLICA caspase assay (ImmunoChemistry Technologies, LLC) was used. This assay detects if cell death is occurring via apoptosis by fluorescently marking active caspase enzymes that are present during apoptosis, the results of which are discussed below.

#### **2.4.7 Cell death mechanism: caspase activation and loss of $\Delta\Psi_m$**

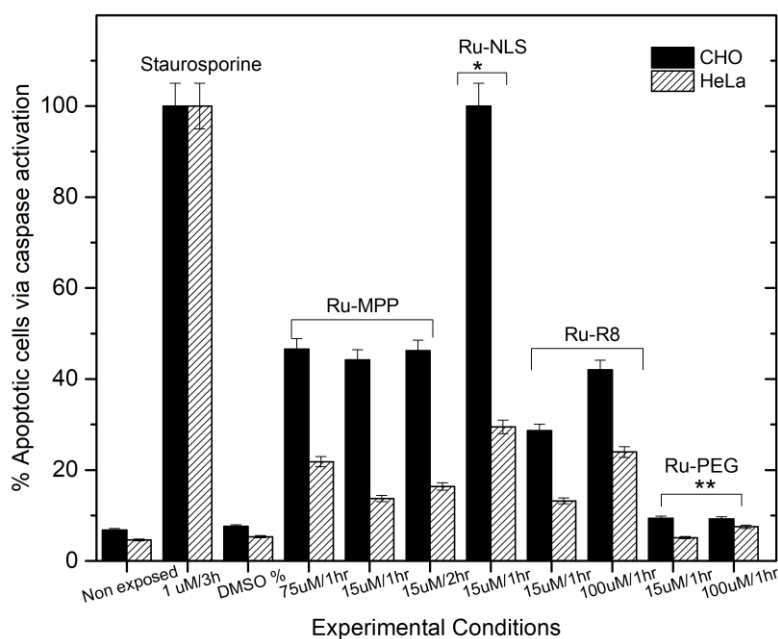
To gain greater insight into the mechanism behind the evident cytotoxicity of the Rubiq conjugates, polycaspase activity on probe exposure was examined using the FAM-FLICA assay. The FLICA reagent (FAM-VAD-FMK) consists of a recognition peptide sequence Valine- Arginine-Aspartate (VAD) and a fluoromethyl ketone (FMK) that covalently binds to active caspase to give a green fluorescence from the attached carboxyfluorescein (FAM) moiety.<sup>58</sup>

Here, CHO and HeLa cells were exposed to the conjugates over the range of concentrations indicated by the cytotoxicity studies. A positive control was prepared by treating both cell lines with staurosporine, a known caspase-inducing agent.<sup>42,59</sup> And, for a negative control both cell lines unexposed to any reagent and to DMSO 1 % v/v were examined. Results of the FLICA caspase activity assay for both cells lines are shown in Fig. 2.5.

RuMPP and RuR8 stimulated relatively moderate caspase activity with higher activity observed for the CHO cell line compared to HeLa. The difference can be attributed to the nature of the cell-lines wherein HeLa are a cancer line and CHO are not, as it is established that specific defects in apoptosis pathways allow mammalian cancer cells to escape programmed cell death leading to resistance to apoptosis.<sup>60,61</sup> RuR8 exhibited a concentration dependent

caspase activation. RuR8 at 15  $\mu\text{M}$  / 1 h triggered caspase activation in 26 % of CHO cells and only 15 % of HeLa cells. At an increased concentration of 100  $\mu\text{M}$  / 1 h, 40 % of CHO cells and 30 % of HeLa cells revealed caspase activity. Similar activity to RuR8 100  $\mu\text{M}$  / 1 h was observed for RuMPP at low and increased concentrations independent of incubation time. It may be related to the mitochondria-targeting peptide attached to the Rubiq-core.

Interestingly, the most marked increase in caspase activity was observed for CHO cells treated with RuNLS even at 15  $\mu\text{M}$  / 1 h, the caspase activity was equivalent to that stimulated by Staurosporine. The nuclear localizing signal (NLS) peptide sequence has been previously employed for targeting a Ru-tap complex to the nucleus of HeLa and CHO cells.<sup>45</sup> The Ru(II)-tap-NLS conjugate was found to be moderately toxic towards HeLa cells even at concentrations up to 200  $\mu\text{M}$ . In addition, the conjugate was found to distribute throughout the cytoplasm within 3 h of incubation at 100  $\mu\text{M}$  and nuclear localization was observed at the 5 h timeframe. In this case, Ru-biq-NLS induced apoptotic effects at the low concentration of 15  $\mu\text{M}$  within 1 h of incubation. CHO and HeLa cells exposed to RuPEG showed negligible caspase activity (comparable to the control populations) up to probe concentrations of 100  $\mu\text{M}$ .



**Figure 2.5** The percentage of cells showing caspase activity indicative of apoptosis obtained by FAM-FLICA Assay (n=3).

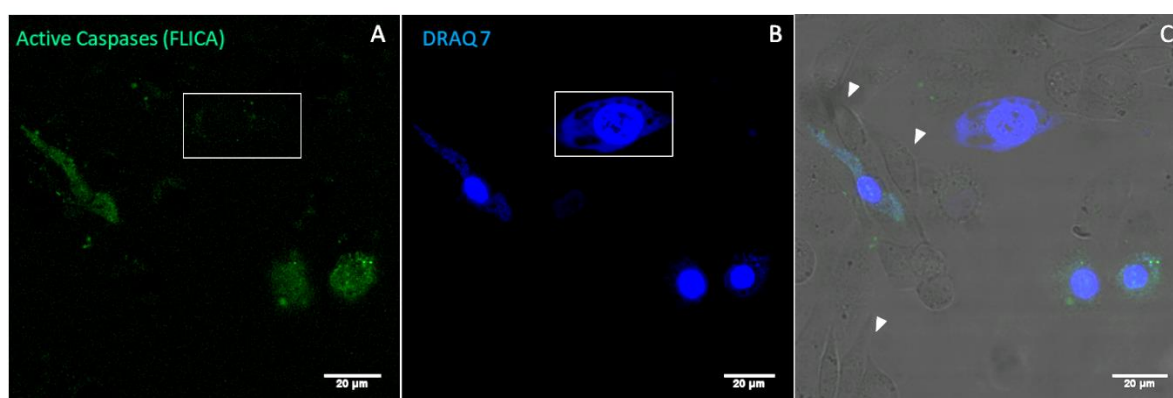
Experimental populations were exposed to RuMPP at 75  $\mu\text{M}$  / 1 h and 15  $\mu\text{M}$  / 1-2 h, RuNLS 15  $\mu\text{M}$  / 1 h, RuR8 and RuPEG at 15  $\mu\text{M}$  / 1 h and 100  $\mu\text{M}$  / 1 h. All samples were incubated with 30X FLICA reagent for 45 minutes at 37  $^{\circ}\text{C}$  followed by two washing steps and re-



suspension of spun down pellets. Aliquots were analyzed in a black 96-well plate using a Tecan fluorescence plate reader set at 488 nm excitation and 520 nm emission. Healthy cells exhibited minimal green fluorescence whereas apoptotic cells due to caspase activity exhibited an increased green fluorescence signal; expressed as a percentage relative to the positive control.

Fig 2.6. shows the effect of RuNLS on CHO cells which induces caspase activation leading to cell death. Fig. 2.6 (A) illustrates caspase activity and co-staining with DRAQ7 (B) reveals damaged cells. The white arrows in the overlay image (C) highlight healthy cells (absence of nuclear staining) and no active caspases (absence of FLICA probe).

The instigation of mitochondrial dysfunction due to the bioconjugates was investigated using a mitochondrial depolarization assay to determine what, if any, role this plays in the toxicity profile of the compounds. The mitochondrial depolarization assay applies a positively charged, cell-permeant rhodamine-based dye, TMRE, which localizes in active mitochondria.<sup>62</sup> The mitochondrial membrane potential (MMP) is monitored by the orange fluorescence signal of the dye as it is retained in healthy mitochondria. A decreased fluorescence signal is observed upon loss in MMP as TMRE is no longer retained by depolarized or inactive mitochondria.



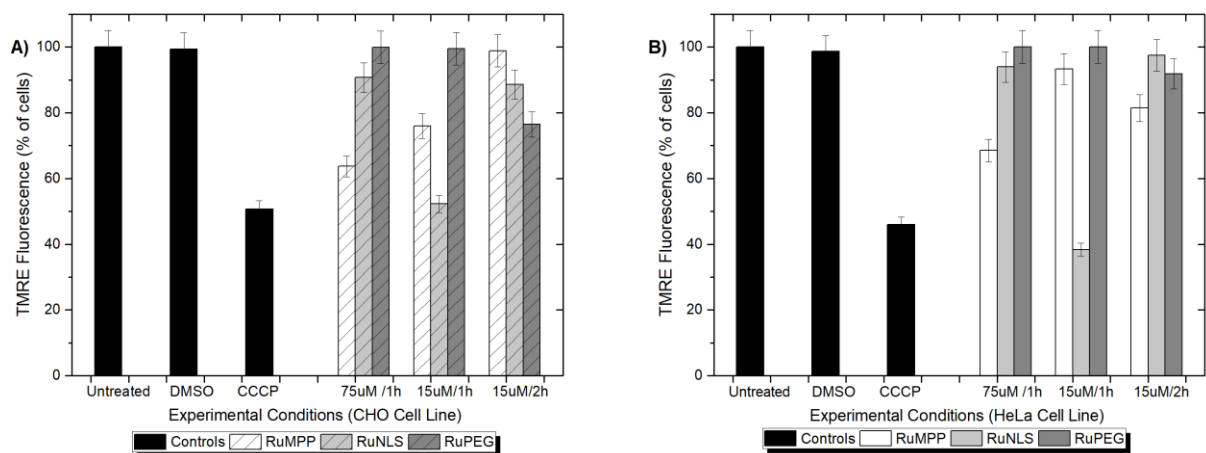
**Figure 2.6** Confocal Imaging of CHO cells treated with RuNLS at 15  $\mu\text{M}$  and incubated for 1 hour in the absence of light followed by addition of the FAM-FLICA dye. (A) Caspase activity (green) was detected using a band pass filter (excitation 490, emission 520-535 nm). (B) Nuclear staining with DRAQ7 (3  $\mu\text{M}$ ) revealed damaged/ compromised cells. DRAQ7 was excited at 33 nm and emission was collected between 650- 850 nm. (C) The overlay with the brightfield image showed viable cells with no caspase activity.

As described, RuPEG showed minimal caspase activity in CHO and HeLa cells while RuNLS induced extensive caspase activity particularly in CHO cells while moderate caspase activity was stimulated for both cell lines upon exposure to RuMPP and RuR8. Thus, using the MitoPT

TMRE assay, we examined the impact of the conjugates carrying a signal peptide sequence, RuMPP and RuNLS, and non-toxic RuPEG on the mitochondrial membrane potential.

CHO and HeLa cells were treated with different doses of Rubiq-conjugates for 1 h and 2 h followed by staining with TMRE. Untreated control populations showed a high percentage of TMRE stained cells whereas the positive control cells exposed to CCCP, a depolarizing agent acting by increasing mitochondrial proton permeability<sup>63</sup>, showed a reduced percentage of TMRE stained cells.

In both CHO and HeLa cells, RuMPP at increased concentrations (75  $\mu$ M / 1 h) caused a marked decrease in the TMRE signal indicative of mitochondrial depolarization (Fig. 2.7). RuNLS and RuPEG under these conditions did not disturb the mitochondrial membrane potential significantly as the TMRE signal remained above approximately 90 %. Interestingly, at a lower concentration (15  $\mu$ M / 1 h) a larger effect was observed for RuNLS on both cell lines compared to RuMPP and RuPEG.



**Figure 2.7** Relative Fluorescence Units (RFU) obtained by MitoPT Assay (n=3); HeLa and CHO cells were exposed to DMSO (10 % v/v) (negative control 2) and CCCP depolarizing agent (positive control). Experimental populations were exposed to the Rubiq conjugates under the conditions previously described. All samples were incubated with MitoPT TMRE for 40 minutes at 37°C and washed. Aliquots were added in a black 96-well plate in triplicate and analyzed by Tecan fluorescence plate reader set at 540 nm excitation and 574 nm emission. Healthy cells exhibited a high level of orange fluorescence whereas metabolically stressed cells (positive control) exhibited a reduced fluorescence signal indicating MMP depolarization. Illustrated is the relative TMRE fluorescence signal as a percentage representative of the loss of mitochondrial membrane potential with respect to the non-exposed (negative control) cell populations.

We might have expected RuMPP to cause a greater effect if the MPP targeting sequence were driving the complex to the mitochondria. Therefore; it is likely that RuNLS causes greater damage by targeting the nucleus and triggering signalling to the mitochondria. Mitonuclear communication involves the signalling from nucleus to mitochondria (and vice versa) upon cellular stress in order to maintain cellular function and homeostasis.<sup>64,65</sup>

It was observed for the cell populations exposed to RuNLS at 15  $\mu\text{M}$  for an additional hour of incubation, that the TMRE signal increased. Studies have shown that if caspase activity is blocked, mitochondria may re-generate their mitochondrial membrane potential despite cytochrome leakage.<sup>66</sup> It is important to note that mitochondrial depolarization may occur without progression to immediate cell death. In fact, a group of apoptosis regulator proteins (B-cell lymphoma 2 (Bcl-2) family), working at the mitochondrial level, may prevent mitochondrial degradation and thus prevent apoptosis.<sup>67</sup> Therefore the increased signal observed following an additional hour of incubation of RuNLS at 15  $\mu\text{M}$  may be indicative of repaired mitochondria. Conversely, RuMPP in HeLa cells revealed increased loss of TMRE signal at 15  $\mu\text{M}$  / 2 h suggesting that RuMPP may lead to an irreversible mitochondrial dysfunction. In summary, RuNLS causes significant mitochondrial depolarization initially but  $\Delta\Psi\text{m}$  seems to recover whereas RuMPP causes moderate but irreversible damage, such as mitochondrial outer membrane permeabilization, which may be related to the MPP-targeting ability of the probe and accumulation in the negatively charged mitochondria. It is worth noting that these Rubiq peptide driven complexes vary from the previously reported mitochondria- and nuclear- targeted complexes by our group. The newly synthesized RuMPP and RuNLS conjugates induce rapid mitochondrial depolarization within 1 to 2 h incubation whereas more hydrophilic derivatives, whose parents were water soluble as chloride or perchlorate salts could be employed for imaging and photoinduced targeted therapy in HeLa cells at 75  $\mu\text{M}$  / 2 h and 100  $\mu\text{M}$  / 3 h respectively without exhibiting substantial dark toxicity.<sup>45,46</sup>

In contrast, the RuPEG conjugate did not affect the mitochondria membrane potential at 75  $\mu\text{M}$  or 15  $\mu\text{M}$  following 1 h incubation and only a small degree of depolarization was observed following 15  $\mu\text{M}$  / 2 h incubation. It may be attributed to two characteristics of the conjugate: 1) the non-specific PEG pendant attached and 2) the low cationic charge which does not favour accumulation in the mitochondrial structures. Further, although permitting uptake, as previously discussed the PEG chain is believed to impede metal complex interaction with cell organelles which is supported by this work.

## 2.5 Conclusions

A novel and highly photostable Ru(II)-biquinoline complex **3** exhibiting emission in the NIR window centred at 786 nm has been developed. Complex **3** was membrane impermeable and insoluble in aqueous media. The parent complex **3** was successfully conjugated to three different cell penetrating peptide sequences and was also PEGylated. All four new conjugates **4-7** showed aqueous solubility. The counterion was found to dramatically influence uptake of the peptide conjugates none of the conjugates with chloride counterions were membrane permeable. Whereas the perchlorate analogues were readily permeable. The PEGylated conjugate showed good uptake as a chloride salt. All four conjugates distributed widely throughout the cell, the nuclear and mitochondrial signal peptide conjugates seemed to penetrate these organelles but were not specifically targeting. Despite the high thermal and photochemical stability, the peptide conjugates showed high cytotoxicity with IC<sub>50</sub> as low as 1 μM. Although dose dependent at lower concentrations, we observe that for CHO cells a rise in viability occurs at higher concentrations of the peptide conjugates. These effects are not observed in the PEGylated complex which shows only modest cytotoxicity across all concentrations explored. For the peptide conjugates caspase and mitochondrial depolarization assays indicate that the cytotoxicity is through initiation of apoptosis likely through mitochondrial depolarization.

The data presented demonstrate that in non-labile Ru(II) complexes the complex and peptide together drive cytotoxicity. We speculate that the poorer specific organelle targeting and higher toxicity of these conjugates compared to other related Ru(II) polypyridyl is due to the higher lipophilicity of the biquinoline complex. PEGylation of the complex increase's hydrophilicity and aqueous solubility and dramatically reduces cytotoxicity whilst retaining permeability.

## 2.6 Supporting Material

Supporting information associated with this chapter can be found in **Appendix A**.

## 2.7 References

- 1 M. R. Gill and J. A. Thomas, *Chem. Soc. Rev.*, 2012, **41**, 3179–3192.
- 2 A. Byrne, C. S. Burke and T. E. Keyes, *Chem. Sci.*, 2016, **7**, 6551–6562.

- 3 L. Xu, Y.-Y. Liu, L.-M. Chen, Y.-Y. Xie, J.-X. Liang and H. Chao, *J. Inorg. Biochem.*, 2016, **159**, 82–88.
- 4 C. A. Puckett and J. K. Barton, *J. Am. Chem. Soc.*, 2009, **131**, 8738–8739.
- 5 M. Gottschaldt, U. S. Schubert, S. Rau, S. Yano, J. G. Vos, T. Kroll, J. Clement and I. Hilger, *ChemBioChem*, 2010, **11**, 649–652.
- 6 S. Chakraborty, B. K. Agrawalla, A. Stumper, N. M. Vegi, S. Fischer, C. Reichardt, M. Kögler, B. Dietzek, M. Feuring-Buske, C. Buske, S. Rau and T. Weil, *J. Am. Chem. Soc.*, 2017, **139**, 2512–2519.
- 7 Ł. Skórka, M. Filapek, L. Zur, J. G. Małecki, W. Pisarski, M. Olejnik, W. Danikiewicz and S. Krompiec, *J. Phys. Chem. C*, 2016, **120**, 7284–7294.
- 8 L. Wang, H. Yin, P. Cui, M. Hetu, C. Wang, S. Monro, R. D. Schaller, C. G. Cameron, B. Liu, S. Kilina, S. A. McFarland and W. Sun, *Dalton Trans.*, 2017, **46**, 8091–8103.
- 9 E. Hemmer, A. Benayas, F. Légaré and F. Vetrone, *Nanoscale Horiz.*, 2016, **1**, 168–184.
- 10 V. Ntziachristos, J. Ripoll and R. Weissleder, *Opt. Lett.*, 2002, **27**, 333–335.
- 11 A. Martin, C. Long, R. J. Forster and T. E. Keyes, *Chem. Commun.*, 2012, **48**, 5617–5619.
- 12 A. Byrne, C. Dolan, R. D. Moriarty, A. Martin, U. Neugebauer, R. J. Forster, A. Davies, Y. Volkov and T. E. Keyes, *Dalton Trans.*, 2015, **44**, 14323–14332.
- 13 K. S. Gkika, A. Byrne and T. E. Keyes, *Dalton Trans.*, 2019, **48**, 17461–17471.
- 14 T. E. Keyes, J. G. Vos, J. A. Kolnaar, J. G. Haasnoot, J. Reedijk and R. Hage, *Inorg. Chim. Acta*, 1996, **245**, 237–242.
- 15 S. Kajouj, L. Marcélis, V. Lemaury, D. Beljonne and C. Moucheron, *Dalton Trans.*, 2017, **46**, 6623–6633.
- 16 C. Moucheron, A. Kirsch-De Mesmaeker and J. M. Kelly, *J. Photochem. Photobiol., B*, 1997, **40**, 91–106.
- 17 E. Wachter, D. K. Heidary, B. S. Howerton, S. Parkin and E. C. Glazer, *Chem. Commun.*, 2012, **48**, 9649–9651.
- 18 W. Sun, S. Li, B. Häupler, J. Liu, S. Jin, W. Steffen, U. S. Schubert, H.-J. Butt, X.-J. Liang and S. Wu, *Adv. Mater.*, 2017, **29**, 1603702.
- 19 M. Duati, S. Fanni and J. G. Vos, *Inorg. Chem. Commun.*, 2000, **3**, 68–70.
- 20 W. Siebrand, *J. Chem. Phys.*, 1967, **47**, 2411–2422.
- 21 S. D. Cummings and R. Eisenberg, *J. Am. Chem. Soc.*, 1996, **118**, 1949–1960.
- 22 A. K. Pal, S. Serroni, N. Zaccheroni, S. Campagna and G. S. Hanan, *Chem. Sci.*, 2014, **5**, 4800–4811.

- 23 U. Neugebauer, Y. Pellegrin, M. Devocelle, R. J. Forster, W. Signac, N. Moran and T. E. Keyes, *Chem. Commun.*, 2008, 5307–5309.
- 24 B.-Z. Zhu, X.-J. Chao, C.-H. Huang and Y. Li, *Chem. Sci.*, 2016, **7**, 4016–4023.
- 25 C. A. Puckett and J. K. Barton, *J. Am. Chem. Soc.*, 2007, **129**, 46–47.
- 26 Y. Chen, T. W. Rees, L. Ji and H. Chao, *Curr. Opin. Chem. Biol.*, 2018, **43**, 51–57.
- 27 K. K.-W. Lo and K. Y. Zhang, *RSC Adv.*, 2012, **2**, 12069–12083.
- 28 M. R. Gill, J. Garcia-Lara, S. J. Foster, C. Smythe, G. Battaglia and J. A. Thomas, *Nature Chem.*, 2009, **1**, 662–667.
- 29 L. Cosgrave, M. Devocelle, R. J. Forster and T. E. Keyes, *Chem. Commun.*, 2010, **46**, 103–105.
- 30 C. S. Burke, A. Byrne and T. E. Keyes, *Angew. Chem., Int. Ed.*, 2018, **57**, 12420–12424.
- 31 D. O. Connor, A. Byrne, G. B. Berselli, C. Long and T. E. Keyes, *Analyst*, 2019, **144**, 1608–1621.
- 32 V. Ramu, S. Aute, N. Taye, R. Guha, M. G. Walker, D. Mogare, A. Parulekar, J. A. Thomas, S. Chattopadhyay and A. Das, *Dalton Trans.*, 2017, **46**, 6634–6644.
- 33 M. Jakubaszek, B. Goud, S. Ferrari and G. Gasser, *Chem. Commun.*, 2018, **54**, 13040–13059.
- 34 V. Vidimar, X. Meng, M. Klajner, C. Licon, L. Fetzer, S. Harlepp, P. Hébraud, M. Sidhoum, C. Sirlin, J.-P. Loeffler, G. Mellitzer, G. Sava, M. Pfeffer and C. Gaiddon, *Biochem. Pharmacol.*, 2012, **84**, 1428–1436.
- 35 J.-B. Denault and G. S. Salvesen, *Chem. Rev.*, 2002, **102**, 4489–4500.
- 36 T. E. Allsopp, J. McLuckie, L. E. Kerr, M. Macleod, J. Sharkey and J. S. Kelly, *Cell Death Differ.*, 2000, **7**, 984–993.
- 37 L. D. Zorova, V. A. Popkov, E. Y. Plotnikov, D. N. Silachev, I. B. Pevzner, S. S. Jankauskas, V. A. Babenko, S. D. Zorov, A. V. Balakireva, M. Juhaszova, S. J. Sollott and D. B. Zorov, *Anal. Biochem.*, 2018, **552**, 50–59.
- 38 P. Golstein and G. Kroemer, *Trends Biochem. Sci.*, 2007, **32**, 37–43.
- 39 T. A. Chan, H. Hermeking, C. Lengauer, K. W. Kinzler and B. Vogelstein, *Nature*, 1999, **401**, 616–620.
- 40 W.-X. Zong, D. Ditsworth, D. E. Bauer, Z.-Q. Wang and C. B. Thompson, *Genes Dev.*, 2004, **18**, 1272–1282.
- 41 Y. Shi, *Molecular Cell*, 2002, **9**, 459–470.
- 42 A. Stepczynska, K. Lauber, I. H. Engels, O. Janssen, D. Kabelitz, S. Wesselborg and K. Schulze-Osthoff, *Oncogene*, 2001, **20**, 1193–1202.

- 43S. Desagher and J.-C. Martinou, *Trends Cell Biol.*, 2000, **10**, 369–377.
- 44S. W. G. Tait, G. Ichim and D. R. Green, *J. Cell Sci.*, 2014, **127**, 2135–2144.
- 45C. S. Burke, A. Byrne and Tia. E. Keyes, *J. Am. Chem. Soc.*, 2018, **140**, 6945–6955.
- 46A. Martin, A. Byrne, C. S. Burke, R. J. Forster and T. E. Keyes, *J. Am. Chem. Soc.*, 2014, **136**, 15300–15309.
- 47S. Tai, S. V. Marchi and J. D. Carrick, *Indian J. Heterocycl. Chem.*, 2016, **53**, 1138–1146.
- 48B. Szócs, É. Bokor, K. E. Szabó, A. Kiss-Szikszai, M. Tóth and L. Somsák, *RSC Adv.*, 2015, **5**, 43620–43629.
- 49H. E. Gottlieb, V. Kotlyar and A. Nudelman, *J. Org. Chem.*, 1997, **62**, 7512–7515.
- 50W. R. Browne, C. M. O'Connor, H. P. Hughes, R. Hage, O. Walter, M. Doering, J. F. Gallagher and J. G. Vos, *J. Chem. Soc., Dalton Trans.*, 2002, 4048–4054.
- 51K. Suzuki, A. Kobayashi, S. Kaneko, K. Takehira, T. Yoshihara, H. Ishida, Y. Shiina, S. Oishi and S. Tobita, *Phys. Chem. Chem. Phys.*, 2009, **11**, 9850–9860.
- 52J.-F. Lefebvre, D. Saadallah, P. Traber, S. Kupfer, S. Gräfe, B. Dietzek, I. Baussanne, J. D. Winter, P. Gerbaux, C. Moucheron, M. Chavarot-Kerlidou and M. Demeunynck, *Dalton Trans.*, 2016, **45**, 16298–16308.
- 53L. Blackmore, R. Moriarty, C. Dolan, K. Adamson, R. J. Forster, M. Devocelle and T. E. Keyes, *Chem. Commun.*, 2013, **49**, 2658–2660.
- 54R. Englman and J. Jortner, *Mol. Phys.*, 1970, **18**, 145–164.
- 55Li SP, Liu HW, Zhang KY, Lo KK. *Chemistry*, 2010, **16**, 8329-39.
- 56S. P.-Y. Li, C. T.-S. Lau, M.-W. Louie, Y.-W. Lam, S. H. Cheng and K. K.-W. Lo, *Biomaterials*, 2013, **34**, 7519–7532.
- 57C. Mari, V. Pierroz, S. Ferrari and G. Gasser, *Chem. Sci.*, 2015, **6**, 2660–2686.
- 58Z. Darzynkiewicz, P. Pozarowski, B. W. Lee and G. L. Johnson, in *DNA Damage Detection In Situ, Ex Vivo, and In Vivo: Methods and Protocols*, ed. V. V. Didenko, Humana Press, Totowa, NJ, 2011, pp. 103–114.
- 59G. Thuret, C. Chiquet, S. Herrag, J.-M. Dumollard, D. Boudard, J. Bednarz, L. Campos and P. Gain, *Br. J. Ophthalmol.*, 2003, **87**, 346–352.
- 60S. Fulda, *Int. J. Cancer*, 2009, **124**, 511–515.
- 61A. R. Safa, *Crit Rev Oncog.*, 2016, **21**, 203-219
- 62J. Jandova, J. Janda and J. E. Sligh, *Exp. Cell Res.*, 2013, **319**, 750–760.
- 63S. W. Perry, J. P. Norman, J. Barbieri, E. B. Brown and H. A. Gelbard, *BioTechniques*, 2011, **50**, 98–115.

- 64E. F. Fang, M. Scheibye-Knudsen, K. F. Chua, M. P. Mattson, D. L. Croteau and V. A. Bohr, *Nat. Rev. Mol. Cell Biol.*, 2016, **17**, 308–321.
- 65P. M. Quirós, A. Mottis and J. Auwerx, *Nat. Rev. Mol. Cell Biol.*, 2016, **17**, 213–226.
- 66N. J. Waterhouse, K. A. Sedelies, V. R. Sutton, M. J. Pinkoski, K. Y. Thia, R. Johnstone, P. I. Bird, D. R. Green and J. A. Trapani, *Cell Death Differ.*, 2006, **13**, 607–618.
- 67A. O. de Graaf, L. P. van den Heuvel, H. B. P. M. Dijkman, R. A. De Abreu, K. U. Birkenkamp, T. de Witte, B. A. van der Reijden, J. A. M. Smeitink and J. H. Jansen, *Exp. Cell Res.*, 2004, **299**, 533–540.



### **Chapter 3: Mitochondrial targeted osmium polypyridyl probe shows concentration dependent uptake, localisation and mechanism of cell death.**

Published in *Dalton Trans.*, 2019, **48**, 17461.

Karmel S. Gkika, Aisling Byrne and Tia E. Keyes.

#### **Contributions:**

**Karmel S. Gkika:** Synthesis, structural and photophysical characterisation of compounds along with cell imaging and toxicity studies. Primary author and contributor to the experimental design, execution, analysis of results and manuscript preparation and revision.

**Dr. Aisling Byrne:** Supervision of biological experiments and revision of the manuscript.

**Prof. Tia E. Keyes:** Project conceptualization and management, discussion, and revision of the manuscript.

Supporting information associated with this chapter can be found in **Appendix B**.

### 3.1 Abstract

A symmetric osmium(II) [bis-(4'-(4-carboxyphenyl)-2,2':6',2''-terpyridine)] was prepared and conjugated to two mitochondrial-targeting peptide sequences; FrFKFrFK (r = D-arginine). The parent and conjugate complexes showed strong near infra-red emission centred at  $\lambda_{\text{max}}$  745 nm that was modestly oxygen dependent in the case of the parent and oxygen independent in the case of the conjugate, attributed in the latter case, surprisingly, to a shorter emission lifetime of the conjugate compared to the parent. Confocal fluorescence imaging of sub-live HeLa and MCF 7 cells showed the parent complex was cell impermeable whereas the conjugate was rapidly internalised into the cell and distributed in a concentration dependent manner. At concentrations below approximately 30  $\mu\text{M}$ , the conjugate localised to the mitochondria of both cell types where it was observed to trigger apoptosis induced by the collapse of the mitochondrial membrane potential (MMP). At concentrations exceeding 30  $\mu\text{mol}$  the conjugate was similarly internalised rapidly but distributed throughout the cell, including to the nucleus and nucleolus. At these concentrations, it was observed to precipitate a caspase-dependent apoptotic pathway. The combination of concentration dependent organelle targeting, NIR emission coincident with the biological window, and distribution dependent cytotoxicity offers an interesting approach to theranostics with the possibility of eliciting site dependent therapeutic effect whilst monitoring the therapeutic effect with luminescence imaging.

### 3.2 Introduction

Mitochondria are the centres of cellular metabolism and like the nucleus are repositories for DNA in eukaryotic cells. Mitochondrial dysfunction, which often arises from mutation to mitochondrial DNA, is associated with numerous disease states including inflammatory diseases and cancer.<sup>1,2</sup> Consequently, molecular targeting to the mitochondrial has attracted significant attention, both in the fields of imaging/sensing and in the field of medicinal chemistry/therapeutics.<sup>3,4</sup> Cancer cells differ from normal cells in terms of their energy metabolism, ATP production, reactive oxygen species levels and present many dysfunctions. Therefore, targeted agents may be driven to interact with species that are upregulated in cancer cell mitochondria to achieve preferential targeting of cancer cells or accumulate within the organelle matrix environment depending on compound design and overall charge. A key role of mitochondria is ATP production driven by a membrane-based proton pump which generates an electrochemical gradient. This transmembrane electrical potential gradient, known as  $\Delta\Psi_{\text{m}}$ , is between -80 and -180 mV. Depolarization of the inner membrane of the mitochondrion

typically results in loss of  $\Delta\Psi_m$ , due to release of proteins triggering apoptosis. Small molecules such as silver(I) complexes, pancratistatin alkaloid or rhodamine 123 are known to penetrate the mitochondria where they induce apoptosis via depolarization of the mitochondrial membrane potential (MMP).<sup>5</sup> Metallo-anticancer therapeutic agents have attracted interest since the breakthrough with cisplatin and DNA interaction in 1978.<sup>6,7</sup> Although cisplatin is used in cancer treatment, it is inevitably limited by resistance phenomena and several side effects such as nephron- and neuro-toxicity owing to the mode of action of the drug.<sup>8</sup> Ruthenium(III) compounds of similar structure to cisplatin have been investigated for their anticancer activity including some that have been clinically developed: KP1019<sup>9</sup>, NKP1339 (IT- 139)<sup>10,11</sup> and NAMI-A<sup>12,13</sup>. Although more inert toward ligand substitution, osmium-based compounds have been shown to induce cell death via several pathways including inhibitory activity against kinases<sup>14,15</sup>, endoplasmic reticulum stress and DNA damage<sup>16-18</sup> and redox dependent activation in targeted mitochondria of ovarian cancer cells.<sup>19</sup> Work by Sadler, Dyson and Keppler and their respective groups have revealed the potent antiproliferative activity of organometallic osmium complexes.<sup>7,19,20</sup> More recently,<sup>21</sup> the capability of osmium polypyridyl complexes in imaging and in phototherapy has started to be explored.<sup>22-26</sup> These studies emphasize that along with Ru- complexes, osmium structures can also offer additional coordination chemistry and rich redox and photochemistry leading to alternative pathways for inducing antiproliferative effects.<sup>27,28</sup> We have focused on the development of peptide conjugated metal complexes capable of organelle selective targeting.<sup>29-31</sup> The importance of efficient localization for multimodal use of transition-metal complexes has been highlighted by MD Ward in a recent publication concerning mitochondria-targeted Ir(III) complexes.<sup>32</sup> Luminescent mitochondrial or nuclear- targeting metal complexes can act as real-time imaging/sensing probes and as therapeutic/theranostic agents.<sup>26,33,34</sup> Although emission quantum yields are frequently lower, osmium polypyridyl complexes share many photophysical advantages with their ruthenium(II) analogues with the additional benefits of NIR emission maxima in spectral region coincident with the biological optical window and they exhibit outstanding photostability. Consequently, they may be good alternatives to their ruthenium analogues as imaging probes because of their photostability.<sup>26</sup> To date there have been no examples of terpyridine-based ruthenium or osmium complexes applied in the context of cell imaging or therapy although such complexes have structural advantages compared to tris(bidentate) ligand bound complexes as they do not form stereoisomers. While stereoisomerism tends not to affect photophysical properties they can, in the biological context, affect recognition, which in turn can affect cytotoxicity as exemplified recently by Keene et

al.<sup>35</sup> Furthermore, terpy ligands offer stepwise coordination permitting spatial separation of functionality at the 4 positions. In contrast to other polypyridyl ligands, terpyridine-based osmium complexes tend to be more luminescent than their ruthenium analogues. For example, whereas prototype  $[\text{Ru}(\text{terpy})_2]^{2+}$  barely emits at room temperature  $[\text{Os}(\text{terpy})_2]^{2+}$  emits relatively strong.<sup>36</sup> This has been attributed to relatively weak ligand field strength of tpy, that facilitates population of  $^3\text{MC}$  states from the MLCT states at room temperature. This leads to rapid nonradiative decay and relatively poor photostability, which in the context of the cellular environment, will be exacerbated at temperatures typically used for cell culture. Hanan, Campagna and co-workers, have each reported clever strategies for improving the photophysical properties of Ru(II) terpy complexes through extension and rigidification of the terpy ligand.<sup>37-39</sup> Nonetheless, in contrast to biscoordinated ligand systems, osmium terpyridine complexes offer significant advantages over their ruthenium analogues in terms of quantum yield, photostability and emission wavelength.<sup>40</sup> We previously reported that in Ruthenium and Os(II) tris-ligand systems coordinated to polyarginines, Os(II) showed superior uptake/permeability, and notably lower cytotoxicity than their ruthenium analogues. We were interested to explore the performance of Os(II)terpy complexes in this regard to understand if they can be driven to organelles using peptides exploited in ruthenium complexes and also to exploit the symmetric nature of the terpy-like ligands to conjugate two peptides to a single complex.

Herein, we report on the preparation of a symmetric osmium(II)- terpyridine conjugated to two mitochondrial targeting peptides  $[\text{Os}(\text{tpybenz-Ahx-MPP})_2]^{8+}$ . We examined its photophysical behavior, uptake and toxicity in live cells and compared behavior to its parent. The conjugate shows precision targeting to the mitochondria was relatively cytotoxic. The effect of the Os<sup>II</sup> MPP probe on the mitochondrial membrane potential was studied in HeLa and MCF 7 cells and was found to be cytotoxic. Interestingly, however, the mechanism of cytotoxicity changed with concentration as distribution of the probe changed. This to our knowledge is the first metal complex bearing two mitochondrial penetrating peptides (MPP) to be studied in cells and first MPP-driven Os(II) complex.

### **3.3 Materials and Methods**

#### **3.3.1 Materials**

All chemicals and reagents, cell culture media and corresponding components were purchased from Sigma Aldrich (Ireland) and were used as received. The MPP peptide sequence was

purchased from Celtek Peptides, Franklin, USA. Co-localising dyes were purchased from Life Sciences and Resazurin agent from PromoKine.

### 3.3.2 Instrumentation

$^1\text{H}$  and  $^{13}\text{C}$  NMR spectra were recorded on a 400 MHz Bruker Spectrophotometer and processed and calibrated against solvent peaks using Bruker Topspin (v2.1) software. High Resolution LCMS with ESI was performed at the Mass Spectrometry Facility, NUI Maynooth. Thin layer chromatography (TLC) was performed on glass silica gel (Merck, 250  $\mu\text{m}$  thickness) or C18 plates (Sorbent Technologies, 250  $\mu\text{m}$  thickness). Analytical HPLC was performed on a Varian 940-LC with a Photometric Diode Array (PDA) detector for peak detection monitoring 280 nm and 490 nm channels. Gradient elution was applied, using 0.1 % v/v TFA in MeCN and deionised water using HICHRON C18 column (4.6  $\times$  250 mm). The mobile phase was of HPLC grade quality, filtered and purged with nitrogen prior to use. Prior to sample injection, samples were filtered (0.8  $\mu\text{m}$  pore size). Typical chromatographic run-times were 15-20 minutes at a flowrate of 1 ml/min.

Electronic absorption spectra were acquired on a Jasco V670 UV/vis NIR spectrophotometer using a quartz cuvette with a pathlength of 1 cm. Fluorescence spectra were collected on a Varian Cary Eclipse Fluorescence Spectrofluorometer with background correction. All photophysical measurements were performed at room temperature (293 K). Luminescent lifetime data were acquired up to 10,000 counts using a Time Correlated Single Photon Counting (TCSPC) system by PicoQuant with laser excitation source a 450 nm. Measurements were performed in triplicate and PicoQuant NanoHarp software was used for data analysis and fitting.

### 3.3.3 Preparation of 4-(4-carboxyphenyl)-2,2':6,2''-terpyridine, (tpybenzCOOH)

4-formylbenzoic acid (179 mg, 1.2 mmol) was dissolved in stirring  $\text{CH}_3\text{OH}$  (8 ml) followed by the addition of 2-Acetylpyridine (289 mg, 2.4 mmol). The mixture was allowed to stir for 5 minutes followed by the slow addition of 15 % potassium hydroxide (7.2 ml) and conc. ammonium hydroxide (0.8 ml) resulting in a bright green solution which turned yellow over time. The mixture was allowed to stand at room temperature for 3 days. The yellow/white emulsion that formed was filtered off and washed with cold chloroform (2  $\times$  2 ml) and cold methanol/water (1:1) to yield a white product which was suspended in methanol/water (80:20) and sonicated at 35  $^\circ\text{C}$  until a yellow solution was obtained. The solution was transferred to a large beaker and acidified to pH 2 by addition of 1M hydrochloric acid while stirring for 10

minutes. The resulting white precipitate was collected by vacuum filtration, rinsed with ice water and allowed to dry overnight yielding pure white solids of tpybenzCOOH (297mg, 73 %)

$^1\text{H}$  NMR (400MHz, TFA-d):  $\delta$  (ppm) 9.20 (dd, 2H,  $J= 5.2\text{Hz}$ ), 8.98 (d, 2H,  $J= 0.8\text{Hz}$ ), 8.90-8.85 (s, dd, 4H,  $J^*$ ), 8.42 (dd, 2H,  $J= 1.2\text{Hz}, 9.2\text{Hz}$ ), 8.28 (dd, 2H,  $J = 6.4\text{Hz}$ ), 8.04 (dd, 2H,  $J = 1.2, 9.6\text{Hz}$ ).  $^{13}\text{C}$  NMR (600MHz, TFA-d): 154.44, 148.33, 147.49, 146.65, 142.49, 140.64, 131.46, 130.63, 128.21, 127.36.

### 3.3.4 Preparation of $[\text{Os}(4-(4\text{-carboxyphenyl})-2,2:6,2\text{-terpyridine})_2][\text{PF}_6]_2$ , $[\text{Os}(\text{tpybenzCOOH})_2][\text{PF}_6]_2$

To a suspension of tpybenzCOOH (217 mg, 0.615 mmol) in deaerated hot ethylene glycol (20 ml) was added  $\text{OsCl}_3 \cdot 3\text{H}_2\text{O}$  (91.2 mg, 0.308 mmol), and the reaction was allowed to reflux for 4 days under  $\text{N}_2$ . Reaction progress was monitored using TLC (MeCN / $\text{H}_2\text{O}$ /20 %  $\text{KNO}_3$ ; 80:20:1). Following cooling at room temperature, a saturated aqueous solution of  $\text{NH}_4\text{PF}_6$  was added. The dark precipitate was filtered and washed with water and dried with diethyl ether. Column chromatography on silica using the aforementioned mobile phase gave a dark maroon solid (100 mg, 27.3 %)

$^1\text{H}$  NMR (400MHz, DMSO- $d_6$ ):  $\delta$  (ppm) 9.55 (4H, s), 9.10 (4H, d,  $J=7.2\text{Hz}$ ), 8.60 (4H,  $J=6.8\text{Hz}$ ), 8.31-8.36 (m, 4H), 7.96 (q, 4H, 7.6Hz), 7.46 (4H, d,  $J= 5.6\text{Hz}$ ), 7.23 (q, 4H, 6Hz). HR-MS(ESI-TOF) m/z: calculated for  $\text{C}_{44}\text{H}_{30}\text{N}_6\text{O}_4\text{Os}$  [ $\text{M}^{2+}$ ]: 449.0966; found: 449.0529.

### 3.3.5 Preparation of Os(II) bis-peptide conjugates

#### 3.3.5.1 $[\text{Os}(\text{tpybenz-Ahx-MPP})_2] \cdot 2(\text{Cl}^-)$ , $\text{Os}^{\text{II}}$ MPP

$[\text{Os}(\text{tpybenzCOOH})_2][\text{PF}_6]_2$  (4.46 mg, 1 equiv.) was weighed out directly into a glass vial followed by the addition of PyBOP (15.6mg, 8 equiv.), DIPEA(40 equiv.) and qualitative transfer of MPP peptide (20 mg, 4 equiv.) with DMF (700  $\mu\text{l}$ ). The mixture was allowed to stir at room temperature in dark overnight.

The reaction mixture was added dropwise to stirring saturated  $\text{NH}_4\text{PF}_6$  (aq) to obtain dark brown solids that were collected via vacuum filtration, washed with water and dried with diethyl ether. The solids were dissolved in minimal acetone and added to a tetrabutylammonium chloride/acetone solution in order to obtain the chloride salt of the conjugate. The solids were washed with plentiful acetone and dried with diethyl ether yielding

Os<sup>II</sup> MPP. Purity of the conjugate relative to the parent complex was confirmed by analytical Reverse Phase-HPLC and High-Resolution LCMS.

<sup>1</sup>H NMR (600MHz, MeOH-d<sub>4</sub>): δ (ppm) 9.35 (s, 4H), 8.89 (d, 4H), 8.40 (s, 8H), 8.21-7.88 (m, 7H), 7.46 (m, 4H), 7.22 (m, 40H), 4.58-3.31 (m, 31H), 3.23-2.81 (m, 20H), 2.34-2.12 (s, 47H), 2.08-1.06 (m, 64H). HR-MS (+)-MALDI *m/z*: calculated for C<sub>180</sub>H<sub>230</sub>N<sub>42</sub>O<sub>22</sub>Os indicative of [M-MPP<sup>5+</sup>+Cl<sup>-</sup>]: 739.7249, found: 739.4184.

### 3.3.6 Photophysical Methods

Stock solutions (1 mM) of the Os(II) parent and conjugate compound were prepared in MeCN or DMSO respectively and diluted in PBS for the preparation of working solutions. For oxygen measurements, the working solutions were purged with Nitrogen for 15minutes for de-aerated conditions and were allowed to re-aerate over time. The [O<sub>2</sub>]/ μmol L<sup>-1</sup> was measured using a PreSense Oxygen probe. The emission spectra and lifetimes were recorded at O<sub>2</sub> saturated and de-aerated conditions. Photostability studies were performed using a fan-cooled 150 W Orwell Xenon-Arc lamp on solutions of Os-complex in PBS pH 7.4. All photophysical studies were carried out at room temperature.

Luminescence quantum yield (φ) was determined using the relative method by comparing with the luminescence intensity of [Ru(bpy)<sub>3</sub>]<sup>2+</sup> as the standard sample using the following equation:

$$\phi_{\text{sample}} = \phi_{\text{standard}} \times \frac{A_{\text{sample}}}{A_{\text{standard}}} \times \frac{F_{\text{sample}}}{F_{\text{standard}}} \times \left( \frac{n_{\text{sample}}}{n_{\text{standard}}} \right)^2$$

Where A is the absorbance at the excitation wavelength, F is the area under the corrected emission spectrum and n is the refractive index of the solvent.

### 3.3.7 Cyclic Voltammetry

A CH 660 electrochemical analyzer was used to record cyclic voltammetry (CV). Stock solution of the complex was prepared as 1 mM/ 0.1 M TBAPF<sub>6</sub> (supporting electrolyte) in anhydrous acetonitrile. The electrochemical cell used an Ag/AgCl reference electrode, Pt- wire counter and glassy carbon working electrode. CV measurements were performed in triplicate using positive scan polarity and 5 mV s<sup>-1</sup> scan rate.

### **3.3.8 Cell culture**

Minimum Essential Medium Eagle (MEME); supplemented with 10 % foetal bovine serum and 1 % penicillin/ streptomycin and L-Glutamine (2 mM) was used as HeLa cell culture media. Dulbecco's Modified Eagle Medium (DMEM); supplemented with 10 % foetal bovine serum, 1 % penicillin/ streptomycin and L-Glutamine (2 mM) was used to culture the MCF 7 cell line. Cells were grown at 37 °C with 5 % CO<sub>2</sub> and harvested or split at 90 % confluency (using 1X Trypsin for 5 min at 37 °C).

### **3.3.9 Cytotoxicity**

HeLa cells were seeded in a 96- well plate in 100 µl media at 10<sup>4</sup> cells/ well for 24 h at 37 °C under 5 % CO<sub>2</sub>. Os<sup>II</sup> MPP was added in triplicate at the following final concentrations: 150, 100, 50, 25, 10, 1 and 0.1 µM. Control samples were prepared with 1 % and 0.5 % DMSO. Following 24 h incubation of the complex, 10 µl of Resazurin reagent was added to each well and incubated for 7 h in the dark at 37 °C. The Alamar Blue assay was used to estimate viable cells based on the absorbance measured at 570 nm with a background measured at 600 nm using a Tecan 96-well plate reader. The cytotoxicity study was carried out in triplicate.

### **3.3.10 Confocal luminescent Imaging**

HeLa cells were seeded at 1.5 × 10<sup>5</sup> cells in 35mm glass-bottom culture dishes (Ibidi, Germany) of 2mL total volume. Cells were allowed to grow for 48 h at 37 °C at 5 % CO<sub>2</sub>. The growth medium was removed, and specific concentration of the complex was added and allowed to incubate for 4 h at 37 °C at 5 % CO<sub>2</sub> in the dark. The dye/media solution was removed, and cells were washed with supplemented PBS (1.1 mM MgCl<sub>2</sub> and 0.9 mM CaCl<sub>2</sub>). For live cell imaging, cells were directly imaged using a Leica TSP DMI8 confocal microscope (100X oil immersion objective lens) with a heated stage at 37 °C. Os<sup>II</sup> MPP was excited using a 490 nm white light laser and the emission range was set to 650 and 800 nm. DRAQ7, a nuclear staining dye was added (3 µM) to distinguish intact live cells from permeabilized/ dead cells. The 633 nm laser was used to excite DRAQ7 and emission was collected between 635-800nm. MitoTracker Deep Red, a cell permeable probe used to selectively stain mitochondria, was excited at 644nm and emission was collected between 655-720 nm.

### **3.3.11 Mitochondrial Depolarization Assay**

The MitoPT TMRE Assays (ImmunoChemistry Technologies) were carried out on HeLa and MCF 7 cells. Cell populations were cultivated at 5 × 10<sup>5</sup> cells/ mL and MitoPT spiked



suspensions of  $>3 \times 10^6$  cells/ mL in 100  $\mu$ l/ well aliquots were prepared. The following control populations were prepared for each cell line: (A) negative control 1 (non-treated) (B) negative control 2 DMSO (100  $\mu$ M/ 1 h), (C) positive control CCCP<sup>1</sup> (20  $\mu$ M/ 1 h). Experimental populations were exposed to Os<sup>II</sup> MPP at concentrations and incubation periods indicated by confocal imaging. Samples were subsequently incubated with MitoPT TMRE dye for 30 minutes at 37 °C and washed. Aliquots were analyzed in triplicate (3  $\times$  100  $\mu$ l) in a black bottomed 96-well plate using Tecan Plate fluorescence plate reader set at 540nm excitation and 574 nm emission. The amount of orange fluorescence from TMRE was measured as an indication of metabolically stressed cells and mitochondrial depolarization. Data were quantified and expressed as the percentage cell viability decline based on loss of mitochondrial membrane potential relative to the control cell populations.

### 3.3.12 Caspase Activity

Polycaspase FAM-FLICA assays (ImmunoChemistry Technologies) were carried out on HeLa and MCF 7 cells. Cells were cultivated at  $3 \times 10^5$  cells/well. The following control populations were prepared for each cell line: negative control 1 (non-treated) (B) negative control 2 DMSO (100  $\mu$ M/ 1 h) (C) positive control (staurosporine 1  $\mu$ M/ 3 h). Experimental populations were exposed to Os<sup>II</sup> MPP at specific concentration and incubation times based on confocal imaging findings. Samples were subsequently spiked with 30X FAM-FLICA<sup>2</sup> for 45 minutes at 37 °C. The loss of non-adherent cells during washing was accounted for by spinning down the overlay media and recombining the washed cell pellets with the overlay buffer prior to analysis. Samples were analyzed in triplicate (3  $\times$  100  $\mu$ l) in a black bottomed 96-well plate using Tecan Plate fluorescence plate reader set at 488 nm excitation and 520 nm emission. Poly caspase activity was monitored by the increase of relative fluorescence units (RFU) of the green fluorescent signal in the apoptotic cell populations. Data were quantified and expressed as the percentage of apoptotic cells based on the positive control cell populations.

---

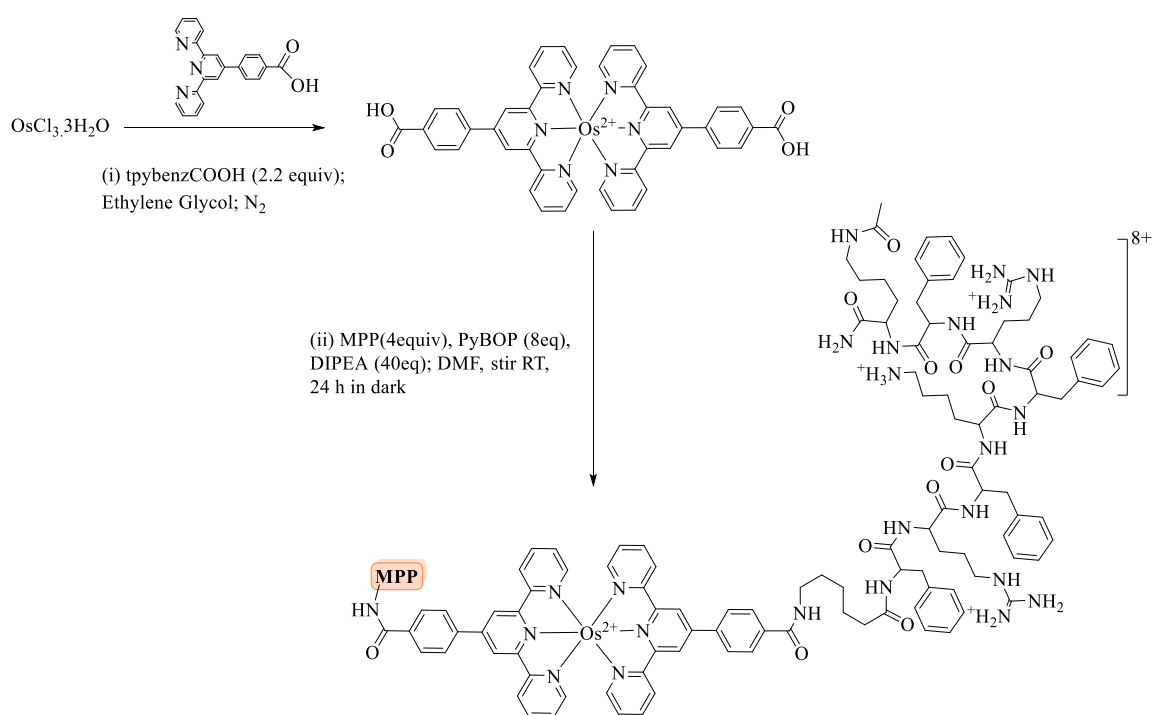
<sup>1</sup>CCCP is a lipid-soluble compound that enters intact mitochondria in its protonated form, releases a proton thus becoming anionic and crosses the mitochondrial membrane again leading to uncoupling of the proton gradient and overall disruption of ATP generation.

<sup>2</sup>FAM-VAD-FLICA is a polycaspase indicator dye which consists of a short recognition peptide sequence (VAD) and a fluoromethyl ketone moiety that binds to all active caspases. There are commercially available dyes which can detect specific caspases such as caspase-1 for example by consisting of a different short amino acid sequence (YVAD).

### 3.4 Results and discussion

#### 3.4.1 Synthesis

We exploited a tridentate, terpyridine-based ligand to facilitate the synthesis of an achiral Os(II) parent complex which, with carboxyl termini, allow for the bis-conjugation of the complex without the formation of multiple isomers. The synthetic route, and the molecular structures of the ligands and complex are summarized in Scheme 3.1. TpybenzCOOH was prepared according to modifications from previously reported syntheses.<sup>41,42</sup> And,  $[\text{Os}(\text{tpybenzCOOH})_2]^{2+}$  was synthesized by modifying a procedure reported for the synthesis of another tridentate Os(II)-complex.<sup>43</sup> Peptide conjugation to  $[\text{Os}(\text{tpybenzCOOH})_2]^{2+}$  was accomplished by amide coupling aided by PyBOP/DIPEA to yield bisconjugated  $[\text{Os}(\text{tpybenz-Ahx-MPP})_2]^{8+}$ .<sup>26,34</sup> The MPP sequence used is a 8-amino acid mitochondrial localization sequence FrFKFrFK (r= D-



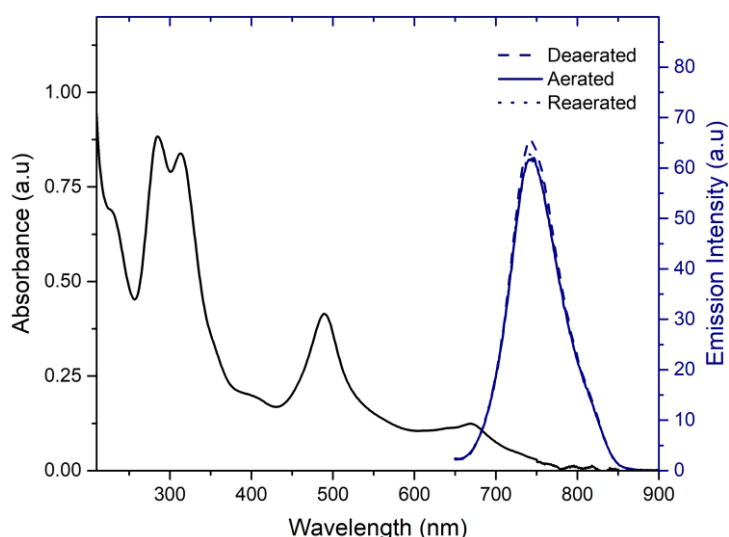
**Scheme 3.1** Synthetic scheme for the preparation of Os<sup>II</sup> MPP conjugate complex.

arginine) originally reported by Kelley et al<sup>44,45</sup> which we have found to be highly effective in driving metal complexes to the mammalian mitochondria.<sup>3</sup> The lysine (K) and arginine residues provide positive charge and phenylalanine (F) imparts lipophilicity. <sup>1</sup>H NMR spectroscopy, Mass spectrometry and HPLC analysis confirmed the structure and purity of the

parent complex and peptide conjugate. RP-HPLC in absence of gradient confirmed formation of the complex and conjugate with well resolved peaks with retention time of 2.33 min for the parent complex and 3.13 min for the conjugate with no evidence for free peptide or unreacted parent in the latter case (ESI). With gradient elution, using 0.1 % v/v TFA in MeCN and deionised water (Table 1) the retention time of the peptide conjugate was extended to 8.30 min but showed band broadening with peak splitting tentatively attributed to ion-pairing. The corresponding chromatograms and UV/vis spectra, collected using diode array detection, confirm the band only contains metal complex, with no evidence for free peptide or unreacted starting complex (shown in the ESI).

### 3.4.2 Photophysics and Electrochemistry

The absorbance and emission spectra of the peptide conjugate, Os<sup>II</sup>MPP, is shown in Fig. 3.1, analogous optical/photophysical behaviour was observed in the parent complex [Os(tpybenzCOOH)<sub>2</sub>]<sup>2+</sup> (ESI†). The Os(d<sub>π</sub>)- tpybenzCOOH (π\*) metal to ligand charge



**Figure 3.1** Absorbance and emission spectra of Os<sup>II</sup>MPP. Spectra were recorded at 25  $\mu$ M (PBS Buffer pH 7.4) under aerated and deaerated conditions with excitation and emission slit widths of 10nm and emission excitation wavelength of 490 nm.

transfer transitions are observed at  $\lambda_{\text{max}}$  490 nm (<sup>1</sup>MLCT) and 663 nm (<sup>3</sup>MLCT). Excitation at 490 nm into the singlet transition of the parent complex results in a relatively intense emission centered at 750 nm, and in aerated acetonitrile the quantum yield was determined as  $0.0115 \pm 0.0012$ . Under aerated conditions, the parent complex exhibits a lifetime of  $129.9 \pm 0.2$  ns in aqueous PBS (pH 7.4) which is increased to  $183.3 \pm 0.3$  ns on deaeration at room temperature. The photophysical data for the parent are consistent with those reported for a related phenyl

derivative  $[\text{Os}(\text{phtpy})_2]^{2+}$  albeit with red-shifted emission maxima and modification to lifetime attributed to the carboxylate substitution of the phenylterpyridine ligands here.<sup>43</sup> The peptide conjugate,  $\text{Os}^{\text{II}}$ MPP exhibits mono- exponential emission decay but, surprisingly, is somewhat shorter-lived than the parent complex with a lifetime of  $94.1 \pm 0.4$  ns in air saturated PBS that increases only to  $110 \pm 0.5$  ns upon deaeration and a quantum yield of  $0.0084 + 0.0005$ .

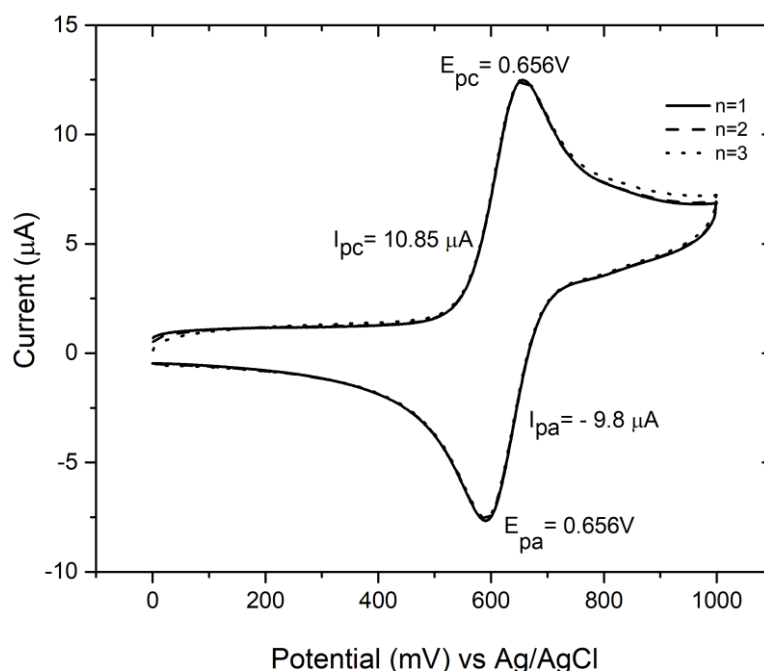
The emission spectra were also compared under air saturated and upon deaerated conditions under nitrogen. As shown, corresponding to the lifetime data, the emission intensity of the conjugate does not respond significantly to change in  $[\text{O}_2]$ . Table 3.1 summarizes the photophysical properties of the parent and conjugate complex. This behaviour contrasts with our previous reports on ruthenium polypyridyl peptide conjugates, including complexes bound to the same MPP sequence.<sup>3,34</sup> There, the lifetime of emission invariably increased in the peptide conjugate compared to the parent. The origin of the decrease with the osmium complex is unclear, as the thermodynamics of electron transfer seem to preclude quenching so the effect may be due to steric strain exerted on the terpy ligand in the conjugate, that increases non-radiative decay. Nonetheless, the effect is relatively weak, and the osmium peptide conjugate remains sufficiently luminescent for imaging, without the complication of being a significant generator of singlet oxygen. As photostability is an important issue in bioimaging, this was evaluated for  $[\text{Os}(\text{tpybenzCOOH})_2]^{2+}$  in PBS buffer by monitoring its absorbance spectrum during visible irradiation. Following 3 hours continuous irradiation by a 150 mW arc lamp (using a  $\lambda > 400$  nm cut off filter) less than 5 % photodegradation had occurred (ESI†). This

**Table 3.1** Summary of photophysical properties of Os(II)- complexes in MeCN and PBS under aerated and deaerated conditions.

Compound	Solvent	$\lambda_{\text{abs}} (\epsilon) / \text{nm} (\times 10^4 \text{ M}^{-1} \text{ cm}^{-1})$	$\lambda_{\text{em}} / \text{nm}$	$\tau / \text{ns} \pm \text{SD}$	
				Aerated	Deaerated
$[\text{Os}(\text{tpybenzCOOH})_2]^{2+}$	$\text{CH}_3\text{CN}$	<b>404</b> (0.83), <b>490</b> (2.54), <b>642</b> (0.51), <b>670</b> (0.61)	750	$120 \pm 0.2$	$194.6.1 \pm 0.7$
	PBS	<b>418</b> (1.90), <b>505</b> (2.67), <b>648</b> (1.32), <b>679</b> (1.54)	745	$129.9 \pm 0.2$	$183.3 \pm 0.3$
$[\text{Os}(\text{tpybenz-Ahx-MPP})_2]^{8+}$	PBS	<b>418</b> (0.26), <b>505</b> (0.47), <b>648</b> (0.14), <b>679</b> (0.15)	746	$94.1 \pm 0.4$	$110 \pm 0.5$

renders the  $^3\text{MC}$  state thermally inaccessible for Os(II) complexes in contrast to their Ru(II) analogues, particularly those of terpyridine complexes, that, as described tend to exhibit poor photophysical properties and photoinstability.

Electrochemistry of the parent complex is shown in Fig. 3.2. The complex shows well-behaved electrochemistry with a reversible anodic process attributed to the Os<sup>II</sup>/Os<sup>III</sup> oxidation at  $E_{1/2}$  656 mV versus Ag/AgCl in CH<sub>3</sub>CN/ nBu<sub>4</sub>NPF<sub>6</sub>. The observed photostability, large Stokes shift and modest O<sub>2</sub> quenching, marked these compounds as potentially attractive for cellular imaging applications. In particular, since in comparison to another reported Os(II) mono-conjugate, applied to cell imaging, the quantum yield of this conjugate is significantly higher ( $\phi = 0.0025 \pm 0.0008$ ).<sup>26</sup>

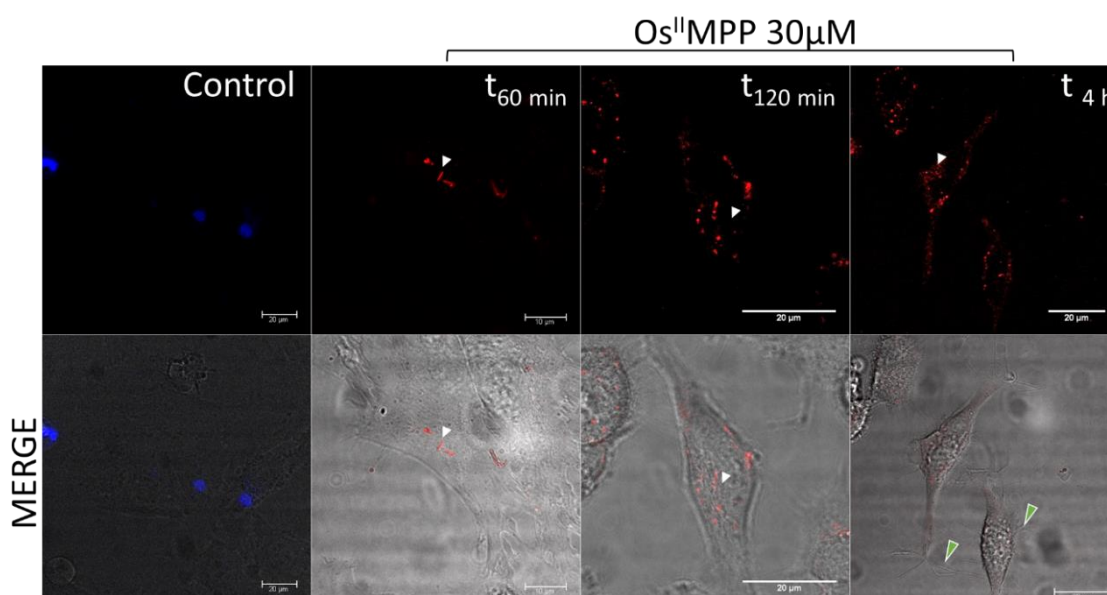


**Figure 3.2** Cyclic Voltammogram ( $n=3$ ) of 1 mM [Os(tpybenzCOOH)<sub>2</sub>]<sup>2+</sup>. Sample in deaerated CH<sub>3</sub>CN containing 0.1 M nBu<sub>4</sub>NPF<sub>6</sub>. Scan rate 50 mV s<sup>-1</sup>.

### 3.4.3 Cell Uptake studies

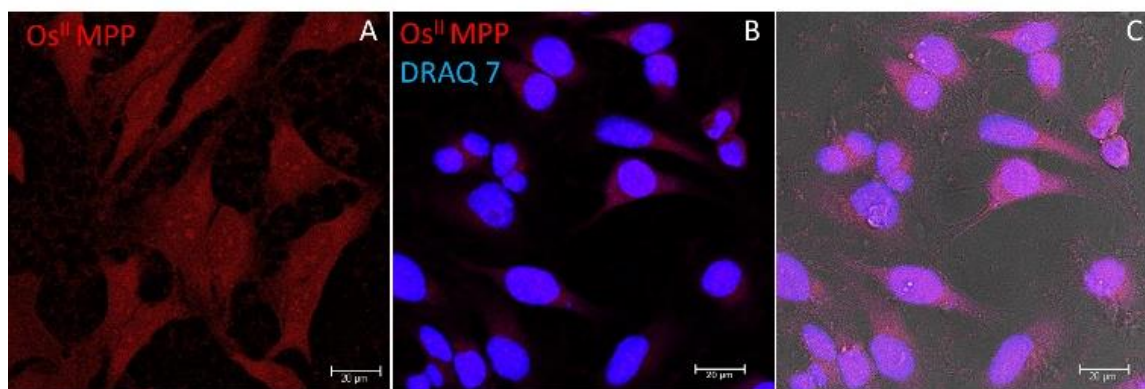
The uptake of [Os(tpybenzCOOH)<sub>2</sub>]<sup>2+</sup> and Os<sup>II</sup> MPP were evaluated in two cell lines: HeLa and MCF, as a function of conjugate concentration between the range 5 µM and 50 µM. While the parent complex does not permeate the cell membrane across this concentration range (see ESI†), the peptide conjugate is taken up by the cells at 30 µM within 1 to 2 hours incubation in the absence of light (Fig. 3.3). Within 2 hr incubation, highly localized emission was observed from small structures thought to be the mitochondria. The distribution of the dye remained unchanged over the next 1 to 2 hours but as shown in Fig. 3.3, by 4 hours, morphological

changes to the cells were evident including plasma membrane blebbing and retraction of pseudopods, indicating cell death by apoptosis. During this process, the probe started to leach from the mitochondria and at cell death (confirmed by DRAQ7 assay), the probe was evident in the cytoplasm attributed to loss of integrity of the mitochondrial membrane. At higher concentrations (Fig. 3.4, 50  $\mu\text{M}$ ) the uptake dynamics and distribution were significantly different. Uptake was far more rapid and complete in under 1 hour. Confocal Z- scan shows (Fig. 3.4A) that at higher concentrations  $\text{Os}^{\text{II}}$ MPP was no longer confined to the mitochondria but present throughout the cytoplasm where it had penetrated the nuclear envelope and localised in the nucleoli. DRAQ7 was applied to cells pre- incubated with the osmium conjugate to assess cell viability.



**Figure 3.3** Confocal luminescence images of  $\text{Os}^{\text{II}}$  MPP in live HeLa cells where the conjugate and overlay channel are shown. Cells were incubated in the absence of light with 30  $\mu\text{M}$  for: 60 min, 120 min and 4 h. The bis-MPP complex was excited using 490 nm white light laser and the emission was collected between 590 and 800nm.

DRAQ7 is a far-red fluorescent probe which only stains the nuclei of damaged or dead cells. As shown in Fig. 3.4B, nuclei staining in blue shows that DRAQ7 has entered the nuclei of essentially all cells indicating extensive cell death. Uptake of the dye and cell blebbing was observed when cells were incubated with complex above 40  $\mu\text{M}$ . This was surprising given the stability of the probe and lack of oxygen dependent emission. As they may offer therapeutic prospects we carried out more detailed investigation into the origin of the cytotoxicity.



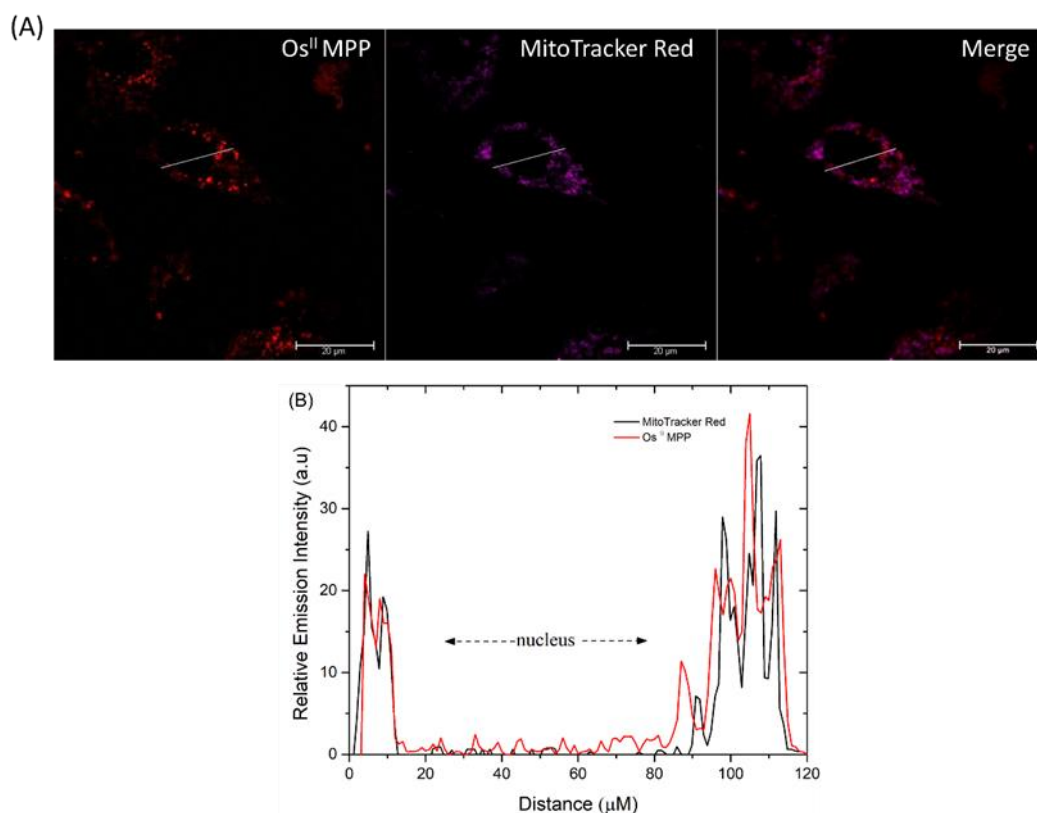
**Figure 3.4** Confocal imaging: (A) Os<sup>II</sup> MPP at increased concentration (50 μM) in HeLa cells following 1 hr incubation in the absence of light; z-scan reveals nucleoli staining (B) co- staining with DRAQ7 and (C) overlay. image.

### 3.4.4 Os<sup>II</sup> MPP : Co- localization with MitoTracker Deep Red in live HeLa cells

Co-localization with MitoTracker Deep Red confirmed the Os<sup>II</sup> MPP probe localized at the mitochondria at concentrations below 30 μM/ 2 h. Fig. 3.5 shows separate and super-imposed images of Os<sup>II</sup> MPP and MitoTracker Deep Red and the corresponding line profile scanning in the x-y direction (B). Absence of nuclear staining by DRAQ7 (ESI†) confirms viability of the cells. The line profile across the cell and the corresponding fluorescence intensity profile confirms co-localisation of the osmium conjugate and MitoTracker Deep Red in HeLa cells (Fig. 3.5B). In a previously reported [Os(bpy)<sub>2</sub>(pic-arg<sub>8</sub>)]<sup>10+</sup> conjugate, partial localization in both mitochondria and lysosomes in CHO cells was observed.<sup>26</sup> In addition, it was observed that the conjugate penetrated the nuclear envelope of SP2 myeloma and CHO cells via a photo- or thermally- activated process. In contrast, we observed strong confinement of the dye below 30 μM to the mitochondria and distribution does not change under irradiation.

Distribution is found to change over extended intervals where coincident with DRAQ7 permeation, the probe is found to leach into the cytoplasm and around the nuclear envelope, potentially the endoplasmic reticulum (ER). Whereas this is the first , mitochondrial directed osmium luminophore to be reported, Ruthenium-MPP conjugates previously reported have shown mitochondrial confinement following 2 h incubation.<sup>3,34</sup> The concentration dependent uptake observed here was not seen in comparable ruthenium complexes which exhibited only moderate toxicity in the dark following 24 h exposure over a range of concentrations. For

example, HeLa cells were tolerant to the MPP-bridged dinuclear Ru(II) at 75  $\mu\text{M}$  over periods of 4-6 h of imaging and in the case of the Ru-dppz, cell death was induced only under intense photoirradiation.



**Figure 3.5** Co-localization of  $\text{Os}^{\text{II}}$  MPP with MitoTracker Deep Red where: (A) Confocal imaging of  $\text{Os}^{\text{II}}$  MPP (red), MitoTracker (purple) and merged image (B) Fluorescence intensity profiles obtained from the line profile across the cell (Image J). The cells were also co-incubated with DRAQ7 and absence of nuclear staining confirms cells are live.

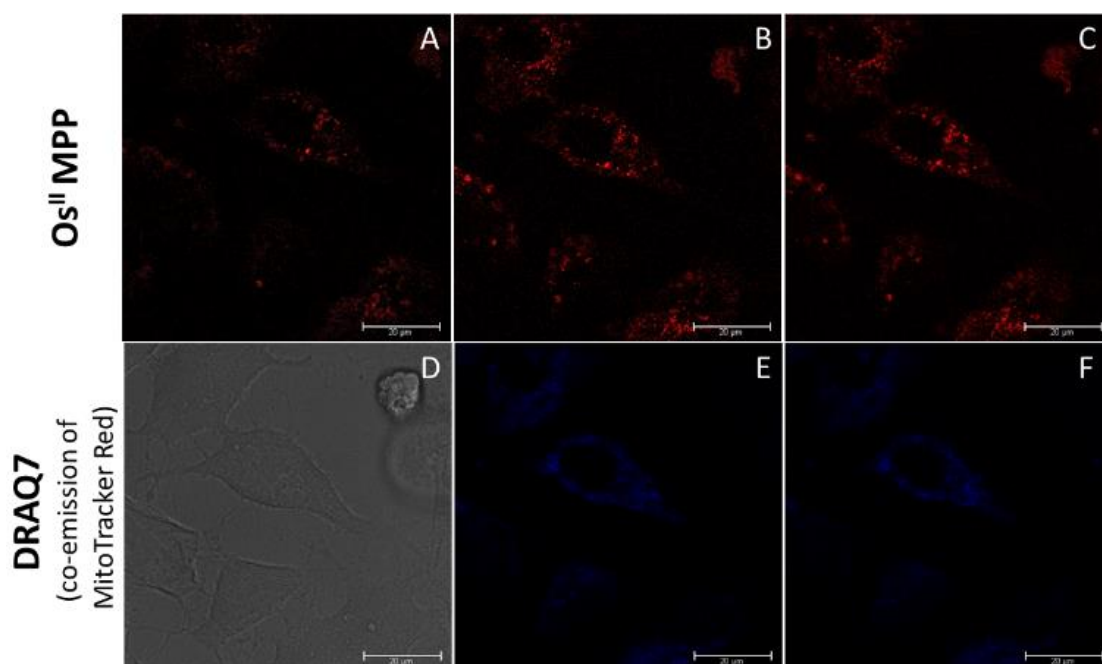
### 3.4.5 $\text{Os}^{\text{II}}$ MPP cytotoxic effects: photo-induced or intracellular triggered process?

#### 3.4.5.1 $\text{Os}^{\text{II}}$ MPP : Photo-toxicity studies in live HeLa cells

Given the phototoxicity of MPP-Ru complexes, phototoxicity was assessed in order to understand if the morphological changes observed during confocal imaging originated from photo-induced effects. In cells pre-incubated with 30  $\mu\text{M}$   $\text{Os}^{\text{II}}$  MPP, single cells were selected and irradiated over time with increasing laser power (from 0.2  $\mu\text{W}$  to 0.9  $\mu\text{W}$ ).

As shown in Fig. 3.6, no DRAQ7 was found to enter the nuclei of individual cells following continuous irradiation for 20 minutes at 490 nm. This confirmed that the cytotoxicity is not light induced. This is not surprising given the remarkable photostability of the complex and weak oxygen dependence.





**Figure 3.6:** Phototoxicity of Os<sup>II</sup> MPP (30  $\mu$ M) in HeLa cells using excitation with 490nm and scanning using increased laser power. (A, D) Normal imaging conditions (10 % laser power) before scanning, (B, E) after 10 minutes scanning at 30 % laser power and (C, F) additional 20 minutes scanning at 50 % laser power; Observed in blue is the emission of MitoTracker Deep Red due to co-excitation of MitoTracker Deep Red at 633 nm.

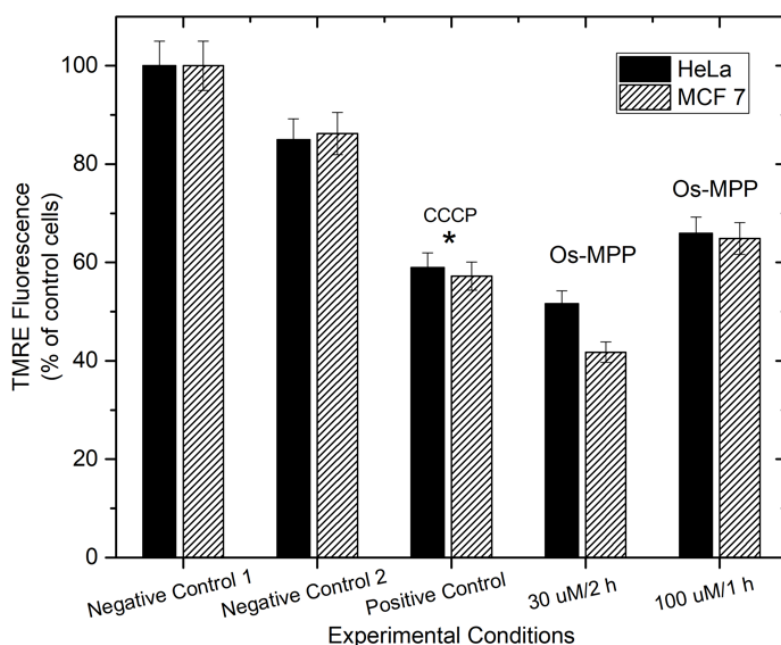
#### 3.4.5.2 Cytotoxicity

The viability of mammalian cells treated with Os<sup>II</sup> MPP was assessed by incubating HeLa and separately, MCF 7 cells, with the conjugate in the absence of light overnight at 37 °C. Cell death was investigated using the Alamar Blue viability assay. Reduction of resazurin dye to resorufin is used as a direct indicator of metabolically active cells. Both HeLa and MCF 7 cell lines presented poor tolerance to the Os<sup>II</sup> MPP at concentrations above 40  $\mu$ M (see ESI†). This coincides with the confocal imaging studies where 40 – 100  $\mu$ M of dye induced cell death within 60 min incubation. HeLa cells were shown to be more tolerant to Os<sup>II</sup> MPP at lower concentrations (5-30  $\mu$ M), with an IC<sub>50</sub> value of 30.61  $\mu$ M, in comparison to MCF 7 cells where viability of 35 % was observed upon incubation with the probe. These findings confirm that cell death is triggered by Os<sup>II</sup> MPP in a dose dependent manner that seems to follow the trend observed in the concentration dependent uptake. We evaluated the mitochondrial potential and

caspase activity to understand if the cytotoxicity observed originates at the mitochondria and if this switches at higher concentration.

### 3.4.6 Mitochondrial depolarization assay (Mito PT TMRE) and Caspase Activity

In healthy cells, an electrochemical potential is generated across the mitochondrial membrane due to the redox activity of the mitochondrial electron transport chain.<sup>46</sup> During apoptosis, the loss of mitochondrial membrane potential (MMP) coincides with the opening of the mitochondrial permeability transition pores, leading to the release of cytochrome c into the cytosol, which in turn triggers other downstream events in the apoptotic cascade. The mitochondrial membrane potential of cells can be assessed using the MitoPT TMRE assay. This assay uses a lipophilic and highly soluble rhodamine-based dye, TMRE, that penetrates live cells and accumulates within healthy mitochondria exhibiting fluorescence upon excitation. With loss of mitochondrial  $\Delta\Psi_m$ , TMRE is released into the cytosol resulting in a reduced fluorescence signal. Therefore, TMRE dye is used to detect apoptotic cell populations and to assess the mitochondrial membrane potential under varying conditions.<sup>47,48</sup> We performed MitoPT TMRE assays on HeLa and MCF 7 cells. Cell populations were prepared and then exposed to the assay conditions (ESI†).



**Figure 3.7** Relative Fluorescence Units obtained by MitoPT Assay (n=3) expressed as a percentage of the negative control. HeLa and MCF 7 cells were exposed to DMSO (100  $\mu$ M/ 1 h) (negative control 2) and CCCP depolarizing agent (positive control). Experimental populations were exposed to Os<sup>II</sup>MPP under the conditions previously described. All samples were incubated with MitoPT TMRE for 30

minutes at 37°C and washed. Aliquots were added in a black 96-well plate in triplicate and analysed by Tecan fluorescence plate reader set at 540 nm excitation and 574 nm emission. Healthy cells exhibited a high level of orange fluorescence whereas metabolically stressed cells (positive control and Os<sup>II</sup>MPP treated) exhibited a reduced fluorescence signal indicating MMP depolarization. Illustrated is the percentage cell viability decline based on loss of mitochondrial membrane potential relative to the non-exposed (negative control) cell populations.

Two negative controls were prepared: a non-exposed cell population and a cell population exposed to DMSO. A positive control was also prepared by exposing the cells to CCCP, an agent known to cause mitochondrial depolarization. Experimental cell populations were exposed to Os<sup>II</sup> MPP at a low concentration, 30  $\mu$ M/ 2 h at 37 °C, where confocal imaging confirmed mitochondrial targeting and at a higher concentration, 100  $\mu$ M/ 1 h at 37 °C, where imaging and cytotoxicity studies showed wide probe distribution and poor cell viability.

Following exposure to the experimental conditions, cell populations were spiked with MitoPT dye and incubated for 30 minutes at 37 °C. Fig. 3.7 summarizes the results of the assay. As expected, the percentage of viable cells decreased significantly upon exposure to the CCCP agent, validating the assay. Decreased cell viability was also observed for the population of cells exposed to Os<sup>II</sup> MPP 30  $\mu$ M/ 2 h indicating that cells were undergoing metabolic or apoptotic stress that can be attributed to collapse of the mitochondrial potential. Confocal imaging under these conditions had shown mitochondrial targeting and initiation of blebbing but that cells were still viable according to DRAQ7 co-staining. Over extended exposure collapse of the mitochondrial membrane potential gradually leads to irreversible mitochondrial damage triggering cell death and thus leakage of the Os<sup>II</sup> MPP probe from the cells. Interestingly, consistent with concentration dependent localization observed from confocal imaging, although some mitochondrial depolarization was also evident for cells exposed to Os<sup>II</sup> MPP at 100  $\mu$ M/ 1 h, the number of apoptotic cells due to collapsed  $\Delta\Psi_m$ , was significantly lower for Os<sup>II</sup> MPP 100  $\mu$ M/ 1 h than for 30  $\mu$ M/ 2 h. Therefore, we conclude that the altered localization of the probe at increased concentrations elicits the cytotoxic effect from a mechanism different to that observed at lower concentrations.

Mitochondrial apoptotic effectors released upon mitochondrial depolarization can be triggered outside the mitochondria by initiation of a cascade of caspase activation leading to apoptosis.<sup>5</sup> Given that the cytotoxicity is greater at higher Os<sup>II</sup> MPP concentrations but that mitochondrial depolarization, coincident with localization of Os<sup>II</sup> MPP to the mitochondria is more prevalent

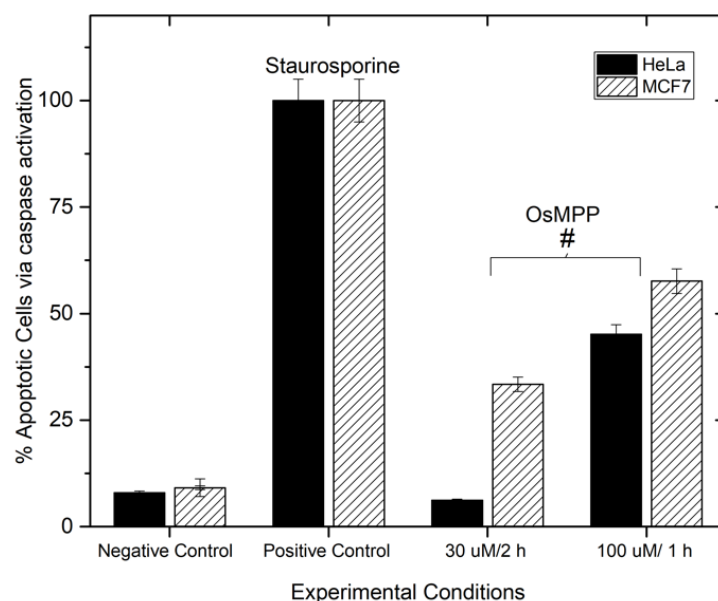
at lower concentrations we examined the caspase activity induction ability of Os<sup>II</sup>MPP in cells using the FLICA assay to evaluate caspase activity as a function of probe concentration.

### 3.4.7 Caspase Activation assay

In the caspase assay applied here, caspase activity is monitored via the green fluorescence signal from the FLICA probe, a carboxyfluorescein fluorophore with a fluoromethyl ketone unit that bonds covalently to an active caspase enzyme. Unbound FLICA diffuses out of the cell and is removed during the wash steps prior to analysis.

Experimental populations were prepared where staurosporine, known for caspase-3 activation,<sup>49</sup> was used to induce caspase activity (positive control) in both cell lines. Identical conditions of Os<sup>II</sup>MPP concentration and incubation times were used here as for the MitoPT Assay. As shown in Fig. 3.8, Os<sup>II</sup>MPP at 30  $\mu\text{M}$ / 2 h stimulated caspase activity in the MCF 7 cell line which corresponds with the confocal imaging which showed that imaging of mitochondrial targeting was possible for HeLa cells without cell damage whereas MCF 7 cells showed higher sensitivity to the Os<sup>II</sup>MPP complex. In addition, a higher apoptotic percentage was observed for the 100  $\mu\text{M}$ / 1 h probe incubation. Therefore, according to the MitoPT and FLICA assays findings, at Os<sup>II</sup>MPP concentrations exceeding 40  $\mu\text{M}$  there is a moderate release of apoptotic factors owing to collapse of  $\Delta\Psi_m$  but localization of the probe in other regions of the cell triggers activation of caspase enzymes leading to apoptosis. At lower concentrations (30  $\mu\text{M}$ / 2 h), when the complex localizes at the mitochondria, this stimulates the release of mitochondrial apoptotic effectors, owing to depolarization of MMP, and caspase activity is observed to a lesser extent.

It is plausible that this causes initiation of the mitochondrial (intrinsic) apoptotic pathway leading to cell death but allows for confocal imaging of the mitochondrial structures between 2 to 3 h incubation period. In contrast, increased concentrations of the conjugate lead to rapid uptake and wide distribution of the Os<sup>II</sup>MPP probe, in both HeLa and MCF 7 cells, which leads to mitonuclear communication and in turn, release of mitochondrial apoptotic effectors and caspase cascade activation.<sup>50,51</sup> Related Ru<sup>II</sup> polypyridyl complexes have been rerouted from nuclear DNA to mitochondrial targeting by controlling the delivery and uptake mechanism of the probes<sup>54</sup> thus highlighting the potential of these complexes in achieving change in activity based on cellular delivery and localisation.



**Figure 3.8** The percentage of cells showing caspase activity indicative of apoptosis obtained by FLICA Assay (n=3). Both cell lines were exposed to DMSO as a second negative control (S.I) and Staurosporine as the positive control. Experimental populations were exposed to Os<sup>II</sup>MPP at 30  $\mu$ M/ 2 h and 100  $\mu$ M/ 1 h. All samples were incubated with 30X FLICA reagent for 45 minutes at 37°C followed by two washing steps and re-suspension of spun down pellets. Aliquots were analyzed in a black 96-well plate by Tecan fluorescence plate reader set at 488 nm excitation and 520 nm emission. Healthy cells exhibited minimal green fluorescence whereas apoptotic cells due to caspase activity exhibited a green fluorescence signal.

### 3.5 Conclusions

A novel achiral Os(II) complex [Os(tpybenzCOOH)<sub>2</sub>]<sup>2+</sup> was synthesized and characterised. Bisconjugation of a mitochondrial penetrating peptide (MPP) to both conjugatable sites of the parent complex was achieved by amide coupling reaction. Both parent and conjugate exhibited relatively intense NIR-emission that coincides well with the biological window. Excellent photostability and good quantum yield rendered the probe attractive for cellular imaging application. However, rather unusually, the conjugate showed modest reduction of its emission lifetime and quantum yield compared to the parent.

Cell uptake studies were explored in live HeLa and MCF 7 cells. While the parent complex was cell impermeable, confocal imaging and co-localisation studies with MitoTracker Deep Red showed that the bis-MPP Os(II) system is membrane permeable and targets the mitochondria at concentrations below 50  $\mu$ M. With increased concentration, Os<sup>II</sup>MPP showed rapid uptake and wider distribution including penetration of the nuclear envelope and

localisation in the nucleoli structures. Extensive cell death was confirmed with DRAQ7 staining. Photocytotoxicity studies did not show any evidence for photo-induced cytotoxic effects. Loss in TMRE signal indicating mitochondrial depolarization was observed at Os<sup>II</sup> MPP 30  $\mu$ M/ 2 h where the probe localises solely at the mitochondria, caspase activity at these conditions was moderate with increased activity observed in MCF 7 over HeLa cells. At higher concentrations (100  $\mu$ M/ 1 h), the MitoPT and FLICA assays showed increased caspase activity and lower degree of mitochondrial depolarization indicating a switch in cell death mechanism with delocalisation of the probe.

### 3.6 Supporting Material

Supplementary data associated with this chapter can be found in **Appendix B**.

### 3.7 References

- 1 M. R. Duchen and G. Szabadkai, *Essays Biochem.*, 2010, **47**, 115–137.
- 2 D. C. Wallace, *Nat. Rev. Cancer*, 2012, **12**, 685–698.
- 3 A. Martin, A. Byrne, C. S. Burke, R. J. Forster and T. E. Keyes, *J. Am. Chem. Soc.*, 2014, **136**, 15300–15309.
- 4 C. Sanchez-Cano, I. Romero-Canelón, Y. Yang, I. J. Hands-Portman, S. Bohic, P. Cloetens and P. J. Sadler, *Chem. - Eur. J.*, 2017, **23**, 2512–2516.
- 5 S. Wen, D. Zhu and P. Huang, *Future Med. Chem.*, 2013, **5**, 53–67.
- 6 A. Levina, A. Mitra and P. A. Lay, *Metallomics*, 2009, **1**, 458.
- 7 A. Bonetti, R. Leone, F. M. Muggia and S. B. Howell, Eds., *Platinum and Other Heavy Metal Compounds in Cancer Chemotherapy*, Humana Press, Totowa, NJ, 2009.
- 8 S. M. Meier-Menches, C. Gerner, W. Berger, C. G. Hartinger and B. K. Keppler, *Chem. Soc. Rev.*, 2018, **47**, 909–928.
- 9 E. Alessio and L. Messori, in *Metallo-Drugs: Development and Action of Anticancer Agents*, eds. A. Sigel, H. Sigel, E. Freisinger and R. K. O. Sigel, De Gruyter, Berlin, Boston, 2018, pp. 141–170.
- 10 P.-S. Kuhn, V. Pichler, A. Roller, M. Hejl, M. A. Jakupec, W. Kandioller and B. K. Keppler, *Dalton Trans.*, 2015, **44**, 659–668.
- 11 R. Trondl, P. Heffeter, C. R. Kowol, M. A. Jakupec, W. Berger and B. K. Keppler, *Chem. Sci.*, 2014, **5**, 2925–2932.
- 12 S. Leijen, S. A. Burgers, P. Baas, D. Pluim, M. Tibben, E. van Werkhoven, E. Alessio, G. Sava, J. H. Beijnen and J. H. M. Schellens, *Investigational New Drugs*, 2015, **33**, 201–214.

- 13D. Pluim, R. C. . van Waardenburg, J. H. Beijnen and J. H. M. Schellens, *Cancer Chemother. Pharmacol.*, 2004, **54**, 71–78.
- 14E. Meggers, *Chem. Commun.*, 2009, 1001.
- 15J. Maksimoska, D. S. Williams, G. E. Atilla-Gokcumen, K. S. M. Smalley, P. J. Carroll, R. D. Webster, P. Filippakopoulos, S. Knapp, M. Herlyn and E. Meggers, *Chem. - Eur. J.*, 2008, **14**, 4816–4822.
- 16K. Suntharalingam, W. Lin, T. C. Johnstone, P. M. Bruno, Y.-R. Zheng, M. T. Hemann and S. J. Lippard, *J. Am. Chem. Soc.*, 2014, **136**, 14413–14416.
- 17G. Berger, K. Grauwet, H. Zhang, A. M. Hussey, M. O. Nowicki, D. I. Wang, E. A. Chiocca, S. E. Lawler and S. J. Lippard, *Cancer Letters*, 2018, **416**, 138–148.
- 18K. Suntharalingam, T. C. Johnstone, P. M. Bruno, W. Lin, M. T. Hemann and S. J. Lippard, *J. Am. Chem. Soc.*, 2013, **135**, 14060–14063.
- 19C. Sanchez-Cano, I. Romero-Canelón, Y. Yang, I. J. Hands-Portman, S. Bohic, P. Cloetens and P. J. Sadler, *Chem. - Eur. J.*, 2017, **23**, 2512–2516.
- 20C. G. Hartinger, N. Metzler-Nolte and P. J. Dyson, *Organometallics*, 2012, **31**, 5677–5685.
- 21C. A. Riedl, L. S. Flocke, M. Hejl, A. Roller, M. H. M. Klose, M. A. Jakupec, W. Kandioller and B. K. Keppler, *Inorg. Chem.*, 2017, **56**, 528–541.
- 22B. Boff, C. Gaiddon and M. Pfeffer, *Inorg. Chem.*, 2013, **52**, 2705–2715.
- 23S. Lazic, P. Kaspler, G. Shi, S. Monro, T. Sainuddin, S. Forward, K. Kasimova, R. Hennigar, A. Mandel, S. McFarland and L. Lilge, *J. Photochem. Photobiol.*, 2017, **93**, 1248–1258.
- 24S. A. E. Omar, P. A. Scattergood, L. K. McKenzie, C. Jones, N. J. Patmore, A. J. H. M. Meijer, J. A. Weinstein, C. R. Rice, H. E. Bryant and P. I. P. Elliott, *Inorg. Chem.*, 2018, **57**, 13201–13212.
- 25Y. Sun, L. E. Joyce, N. M. Dickson and C. Turro, *Chem. Commun.*, 2010, **46**, 6759.
- 26A. Byrne, C. Dolan, R. D. Moriarty, A. Martin, U. Neugebauer, R. J. Forster, A. Davies, Y. Volkov and T. E. Keyes, *Dalton Trans.*, 2015, **44**, 14323–14332.
- 27P. Zhang and H. Huang, *Dalton Trans.*, 2018, **47**, 14841–14854.
- 28E. C. Glazer, *J. Photochem. Photobiol.*, 2017, **93**, 1326–1328.
- 29L. Blackmore, R. Moriarty, C. Dolan, K. Adamson, R. J. Forster, M. Devocelle and T. E. Keyes, *Chem. Commun.*, 2013, **49**, 2658.
- 30A. Byrne, C. S. Burke and T. E. Keyes, *Chem. Sci.*, 2016, **7**, 6551–6562.
- 31U. Neugebauer, Y. Pellegrin, M. Devocelle, R. J. Forster, W. Signac, N. Moran and T. E. Keyes, *Chem. Commun.*, 2008, 5307.

- 32J. R. Shewring, A. J. Cankut, L. K. McKenzie, B. J. Crowston, S. W. Botchway, J. A. Weinstein, E. Edwards and M. D. Ward, *Inorg. Chem.*, 2017, **56**, 15259–15270.
- 33A. Jana, B. J. Crowston, J. R. Shewring, L. K. McKenzie, H. E. Bryant, S. W. Botchway, A. D. Ward, A. J. Amoroso, E. Baggaley and M. D. Ward, *Inorg. Chem.*, 2016, **55**, 5623–5633.
- 34C. S. Burke, A. Byrne and T. E. Keyes, *Angew. Chem., Int. Ed.*, 2018, **57**, 12420–12424.
- 35X. Li, A. K. Gorle, T. D. Ainsworth, K. Heimann, C. E. Woodward, J. Grant Collins and F. Richard Keene, *Dalton Trans.*, 2015, **44**, 3594–3603.
- 36J. P. Sauvage, J. P. Collin, J. C. Chambron, S. Guillerez, C. Coudret, V. Balzani, F. Barigelletti, L. De Cola and L. Flamigni, *Chem. Rev.*, 1994, **94**, 993–1019.
- 37Y.-Q. Fang, N. J. Taylor, G. S. Hanan, F. Loiseau, R. Passalacqua, S. Campagna, H. Nierengarten and A. V. Dorsselaer, *J. Am. Chem. Soc.*, 2002, **124**, 7912–7913.
- 38Y.-Q. Fang, N. J. Taylor, F. Laverdière, G. S. Hanan, F. Loiseau, F. Nastasi, S. Campagna, H. Nierengarten, E. Leize-Wagner and A. Van Dorsselaer, *Inorg. Chem.*, 2007, **46**, 2854–2863.
- 39E. A. Medlycott and G. S. Hanan, *Chem. Soc. Rev.*, 2005, **34**, 133.
- 40J. P. Collin, S. Guillerez, J. P. Sauvage, F. Barigelletti, L. De Cola, L. Flamigni and V. Balzani, *Inorg. Chem.*, 1992, **31**, 4112–4117.
- 41E. C. Constable, E. L. Dunphy, C. E. Housecroft, M. Neuburger, S. Schaffner, F. Schaper and S. R. Batten, *Dalton Trans.*, 2007, 4323.
- 42A. Stublla and P. G. Potvin, *Eur. J. Inorg. Chem.*, 2010, **2010**, 3040–3050.
- 43E. A. Alemán, C. D. Shreiner, C. S. Rajesh, T. Smith, S. A. Garrison and D. A. Modarelli, *Dalton Trans.*, 2009, 6562.
- 44K. L. Horton, K. M. Stewart, S. B. Fonseca, Q. Guo and S. O. Kelley, *Chem. Biol.*, 2008, **15**, 375–382.
- 45S. R. Jean, M. Ahmed, E. K. Lei, S. P. Wisnovsky and S. O. Kelley, *Acc. Chem. Res.*, 2016, **49**, 1893–1902.
- 46S. W. Perry, J. P. Norman, J. Barbieri, E. B. Brown and H. A. Gelbard, *BioTechniques*, 2011, **50**, 98–115.
- 47A. Wong and G. A. Cortopassi, *Biochem. Biophys. Res. Commun.*, 2002, **298**, 750–754.
- 48D. L. Farkas, M. D. Wei, P. Febroriello, J. H. Carson and L. M. Loew, *Biophys. J.*, 1989, **56**, 1053–1069.
- 49A. Stepczynska, K. Lauber, I. H. Engels, O. Janssen, D. Kabelitz, S. Wesselborg and K. Schulze-Osthoff, *Oncogene*, 2001, **20**, 1193–1202.



50E. F. Fang, M. Scheibye-Knudsen, K. F. Chua, M. P. Mattson, D. L. Croteau and V. A. Bohr, *Nat. Rev. Mol. Cell Biol.*, 2016, **17**, 308–321.

51P. M. Quirós, A. Mottis and J. Auwerx, *Nat. Rev. Mol. Cell Biol.*, 2016, **17**, 213–226.

52X. Tian, M. R. Gill, I. Cantón, J. A. Thomas and G. Battaglia, *ChemBioChem*, 2011, **12**, 548–551.

## **Chapter 4: Os(II)-Bridged Polyarginine Conjugates: The Additive Effects of Peptides in Promoting or Preventing Permeation in Cells and Multicellular Tumor Spheroids.**

Published in *Inorg. Chem.*, 2021, **60**, 8123.

Karmel S. Gkika, Sara Noorani, Naomi Walsh and Tia E. Keyes

### **Contributions:**

**Karmel S. Gkika:** Synthesis, structural and photophysical characterisation of compounds along with 2D and 3D confocal and phosphorescence lifetime imaging. Primary author and contributor to the experimental design, execution, analysis and manuscript preparation and revision.

**Sara Noorani:** Preparation of pancreatic tumor spheroids and Alamar Blue assay for treated spheroids. Discussion and revision of the manuscript.

**Assistant Prof. Naomi Walsh:** Management of the project, discussion, and revision of the manuscript.

**Prof. Tia E. Keyes:** Project conceptualization and management, discussion, and revision of the manuscript.

Supporting information associated with this chapter can be found in **Appendix C**.

## 4.1 Abstract

The preparation of two polyarginine conjugates of the complex Os(II) [bis-(4'-(4-carboxyphenyl)-2,2':6',2''-terpyridine)] [Os-(R<sub>n</sub>)<sub>2</sub>]<sup>x+</sup> (n = 4 and 8; x = 10 and 18) is reported, to explore whether the R8 peptide sequence that promotes cell uptake requires a contiguous amino acid sequence for membrane permeation or if this can be accomplished in a linearly bridged structure with the additive effect of shorter peptide sequences. The conjugates exhibit NIR emission centered at 754 nm and essentially oxygen-insensitive emission with a lifetime of 89 ns in phosphate-buffered saline. The uptake, distribution, and cytotoxicity of the parent complex and peptide derivatives were compared in 2D cell monolayers and a three-dimensional (3D) multicellular tumor spheroid (MCTS) model. Whereas, the bis-octaarginine sequences were impermeable to cells and spheroids, and the bis-tetraarginine conjugate showed excellent cellular uptake and accumulation in two 2D monolayer cell lines and remarkable in depth penetration of 3D MCTSs of pancreatic cancer cells. Overall, the data indicates that cell permeability can be promoted via non-contiguous sequences of arginine residues bridged across the metal centre.

## 4.2 Introduction

Metal complex luminophores, most widely, phosphors, have emerged in the past decade as feasible alternatives to organic fluorophores for intracellular imaging and sensing.<sup>1,2</sup> The attractive photophysical properties of such complexes have been widely reported, and for complexes of ruthenium for example, these include good photostability, long emission lifetimes and Stokes-shifted emission in the red spectral region.<sup>3-6</sup> While the emission maxima of complexes of Ir(III) and Ru(II) can be tuned toward the NIR, it can be synthetically challenging and such tuning may compromise photostability, exacerbated in the physiologic conditions of temperature and buffered media, as well as emission quantum yield.<sup>7-9</sup> Conversely, osmium(II) polypyridyl exhibit similar advantages to Ru(II) for imaging but with the addition benefits of outstanding photostability and deep-red to NIR emission in the 700 - 850 nm spectral region, making them attractive candidates, in particular for tissue imaging (although still prone to the impact of the energy gap law).

Although Os(II) polypyridyl complexes have to date, been much less explored for imaging applications than Ir or Ru, they are gaining increasing focus.<sup>10-15</sup>

Another advantage is that such complexes have long lifetimes in comparison to organic fluorophores. Os(II) complexes usually exhibit considerably shorter emission lifetimes than

Ru(II) analogues and thus show low oxygen sensitivity. With lower oxidation potentials than ruthenium analogues, osmium complexes may also show sensitivity to other redox species without interference from oxygen. Typically, molecular weight, charge, and lipophilicity mitigate against the membrane permeability of osmium(II) polypyridyl complexes, providing a barrier to in-cellulo applications but one rational approach to improve the efficacy of cellular uptake is to conjugate to short cationic peptides classified as cell-penetrating peptides (CPPs). The ability of cationic peptide sequences to cross the cell membrane and facilitate the uptake of small molecules was first demonstrated in 1965 by Ryser and Hancock with the cationic amino acid-mediated enhanced uptake of albumin, followed by studies on conjugation of poly-L-lysine to albumin and horseradish peroxidase.<sup>16,17</sup> The most studied CPP is likely the arginine-rich HIV-Tat transduction protein (RKKRRQRRR) from immunodeficiency virus that has been widely shown to efficiently cross lipid bilayers.<sup>18,19</sup> Indeed, homopolymers of arginine (polyarginines) have shown superior cellular uptake compared to other cationic analogues.<sup>20</sup> The details of the mechanism by which oligoarginines permeate the membrane remain under investigation. The key pathway in live cells appears to be ATP-activated endocytosis,<sup>21</sup> but there are also a number of studies that show that polyarginine can promote permeation through a passive mechanism,<sup>22</sup> and they have been shown in artificial membranes to induce leakiness and topological changes at the membrane.<sup>23</sup> Polyarginine interactions with cell surface lipids and formation of neutral complexes that transport across the bilayer have also been reported as well as surface attachment through interactions with heparan sulfate proteoglycans.<sup>24-28</sup> Cargo transduction seems to occur for 6-11 Arg residues, with octaarginine (Arg8 or R8) and nona-arginine (Arg9) being most efficiently transported.<sup>20</sup> We and others have reported that R5 or sequences of lower Arg residues are not CPPs,<sup>29</sup> whereas R8 is very effective at promoting metal complex permeation.<sup>30</sup>

Barton and Brunner first reported the cellular uptake of cargo-carrying peptide rhodium complexes.<sup>31</sup> Our group reported the efficient octaarginine-driven transport of an otherwise cell-impermeable Ru(II) polypyridyl compound,  $[\text{Ru}(\text{bpy})_2(\text{pic})]^{2+}$ , and its application in luminescence imaging.<sup>30</sup> Puckett and Barton also reported the uptake of ruthenium(II)-dppz (dipyrido[3,2-a:2',3'-c]phenazine) complexes conjugated to octaarginine.<sup>32</sup> Nona-arginine sequences containing phenylalanine residues have shown to enhance the cellular uptake of metallocene derivatives.<sup>33</sup> Shorter polymers of arginine, below Arg6, are less efficient in cellular uptake, whereas longer polymers have shown unpredictable uptake and can even exert toxic effects.<sup>20,30,34</sup> Sadler and co-workers reported improved uptake of a permeable Os(II)

arene complex upon conjugation to R5 and R8 with the latter showing increased accumulation and toxicity.<sup>35</sup> The monoarginine conjugate, however, showed a similar uptake to the unfunctionalized parent complex. Therefore, while there is a clear correlation between R-chain lengths and cellular uptake for metal complexes, the attachment of cationic amino acid residues below 5 or above 9 does not guarantee uptake in a predictable manner.

Our group exploited the use of non-specific and targeted CPPs to efficiently drive metal complexes across the cell membrane and target specific organelles.<sup>36-39,9,40</sup> For example, the light-switching Ru<sup>II</sup> complex with dppz conjugated to a nuclear localization signal sequence was highly effective in selectively driving the complex to the nucleus for imaging of chromosomal DNA using stimulated emission depletion (STED) microscopy,<sup>39</sup> whereas the Ru-dppz conjugate bearing a mitochondrial targeting peptide localized at the mitochondria, confirmed by Raman spectroscopy and luminescence lifetime imaging.<sup>41</sup> We recently demonstrated that polyarginines are equally effective in promoting the uptake of Os(II) polypyridyl complexes where R8 conjugated to [Os(bpy)<sub>2</sub>(pic)]<sup>2+</sup> (bpy = 2,2-bipyridyl, pic = 2(4-carboxylphenyl)imidazo[4,5f]-[1,10]phenanthroline) facilitated the uptake of the highly photostable and NIR emitting complex in mammalian cell lines.<sup>11</sup>

While 2D monolayer studies can provide valuable information at the single cell level for a given cell line, three-dimensional (3D) cell models such as cell aggregates and spheroid structures provide a more physiologically relevant tumor tissue microenvironment.<sup>42-44</sup> The multi-cellular layering of cells within spheroids leads to the formation of nutrient and oxygen gradients with hypoxic/necrotic regions toward the spheroid core and can better reflect permeation of a given species in vivo than in 2D cell culture where low cell density, lack of diffusion gradients, and cell-substrate interactions impact behavior.<sup>45-47</sup> 3D cell models are of growing importance in drug discovery and toxicity testing. Their application requires luminescent probes that can deeply permeate the tumor spheroid and also probes capable of sensing within this environment. It has been shown that for fluorophores used for contrast, permeation of 2D models does not guarantee permeation of 3D models and that significant differences in the extent of permeation and destination of fluorescent probes can occur.<sup>48</sup>

Conjugation to polyarginines has been used to facilitate the uptake of gadolinium(III)-based contrast agents for magnetic resonance imaging.<sup>49-51</sup> In addition, although polyarginines have been shown to be highly effective in promoting cellular uptake of transition metal luminophores, there have been no studies to date on whether this promotion extends to 3D cell

models. The importance of tumor penetration is also crucial in the context of therapy by metallodrugs and photodynamic therapy agents as drug response in 3D cell models may differ when compared to 2D monolayers.<sup>52-55</sup>

A number of non-peptidic approaches to promote metal complexes in spheroid models have been reported recently. In the context of therapy, a dinuclear photo-oxidizing Ru<sup>II</sup>(TAP)<sub>2</sub> (TAP = 1,4,5,8-tetraazaphenanthrene) complex was reported, showing in-depth photo-induced cell death of melanoma spheroids using two-photon excitation.<sup>56</sup> Pt(II)-porphyrin probes have been employed for 2D and cell spheroid imaging particularly in the context of phosphorescence-based oxygen sensing.<sup>57</sup> Haycock et al. reported the use of a small-molecule platinum(II) complex for oxygen mapping of melanoma spheroids using one-photon phosphorescence lifetime imaging microscopy (PLIM).<sup>58</sup> More recently, two Ir(III) complexes were studied for *in vivo* PLIM O<sub>2</sub> mapping.<sup>59</sup> Papkovsky, Dmitriev, and co-workers have reported metalloluminophores with long emissive states ranging from Pt(II)-porphyrin probes to click-assembled Pd(II)-porphyrin nanoconjugates for NIR mapping of oxygen distribution in 3D microenvironments.<sup>60,61</sup> Efficient cellular uptake of rather large porphyrins is often problematic in 2D monolayers and 3D models. While nanoparticles can provide a route for spontaneous or targeted cellular uptake, this strategy requires expertise in synthesis, and often cellular uptake is unpredictable. For example, despite the targeting capability of transferrin-conjugated gold nanoparticles, limited penetration was observed in multicellular spheroids.<sup>62</sup>

Herein, we investigate whether R8 is as effective in driving permeation of osmium NIR emitting luminophore in 3D tumor spheroids as it is in 2D cell monolayers. We recently reported the successful conjugation of two mitochondrial penetrating peptides (MPPs) to an achiral osmium(II) terpyridine complex.<sup>40</sup>

The conjugate showed relatively intense emission in the NIR and excellent photostability, making it suitable for tissue imaging. The advantage of this complex is that it does not form isomers and crucially it has conjugation points at the opposing apices of the complex, thus creating essentially a linear arrangement of the conjugation sites bridged by the metal. Here, the Os(II) parent complex [Os(tpybenzCOOH)<sub>2</sub>]<sup>2+</sup> was conjugated to two polyarginine chains of varying lengths (R4 and R8), and we explore whether the optimal R8 requires a contiguous peptide structure for uptake or whether it can be accomplished in a bridged structure with a shorter peptide sequence. We report on the cellular uptake and localization in a cancerous and non- cancerous cell line using confocal and lifetime imaging. For the first time, we investigate

the ability of the peptide conjugates to penetrate 3D cell models in pancreatic cancer multicellular tumor spheroids (MCTSs). To our knowledge, this is the first study of a polyarginine-driven osmium(II) conjugate used for 3D spheroid imaging.

### 4.3 Experimental

#### 4.3.1 Materials

All chemicals and reagents, cell culture media, and corresponding components were purchased from Sigma-Aldrich (Ireland) and were used as received without further purification. Fetal bovine serum (FBS), heat-inactivated, was purchased from Biosciences Limited. Polyarginine sequences R8 and R4 (> 95 %) were procured from Celtek Peptides, TN, USA. Resazurin reagent was purchased from PromoKine, and co-localizing dyes were purchased from Thermo Fisher Scientific.

#### 4.3.2 Instrumentation

$^1\text{H}$  and COSY NMR spectra were recorded at 600 MHz using a Bruker spectrometer, and a deuterated solvent was used for homonuclear lock. The spectra were processed and calibrated against solvent peaks using Bruker Topspin software (v3.6.2). High-resolution mass spectrometry (HR-MS) was performed at the mass spectrometry Facility, NUI Maynooth. Analytical HPLC was performed on a Varian 940-LC with a photometric diode array (PDA) detector with peak monitoring at 280 and 490 nm channels. Gradient elution was applied using a 0.1 % v/v TFA in the MeCN/water mixture. The mobile phase was of HPLC-grade quality and was filtered and purged with nitrogen prior to use. Prior to sample injection, the samples were filtered (0.8  $\mu\text{m}$  pore size). The typical chromatographic run time was 20 min at a flow rate of 1 mL  $\text{min}^{-1}$ .

#### 4.3.3 Synthesis

The  $[\text{Os}(\text{tpybenzCOOH})_2]^{2+}$  parent complex was prepared according to the synthetic procedure reported in the literature.<sup>40,63</sup> The general procedure for the preparation of Os(II) bioconjugates is described below. The purity and characterization data are included in the Supporting Information.

##### 4.3.3.1 Preparation of Os(II) bioconjugates, $[\text{Os}-(R_n)_2]^{x+}$ ( $n = 4, 8; x = 10, 18$ )

$[\text{Os}(\text{tpybenzCOOH})_2]^{2+}$  (1 equiv.), 20 mg of peptide (4 eq), DIPEA (20 equiv.) PyBOP (8 equiv.) were dissolved in 700  $\mu\text{L}$  of DMF. The reaction mixture was stirred for 24 h at room

temperature. The mixture was added dropwise to saturated  $\text{NH}_4\text{PF}_6$  (aq.) to obtain dark brown solids which were collected *via* vacuum filtration, washed with water and diethyl ether. The solids were dissolved in acetone and added dropwise to a TBAC/acetone solution to obtain the chloride salt of the peptide conjugate. The solids were washed copious amounts of acetone and diethyl ether yielding  $[\text{Os}-(\text{R}_n)_2]^{x+}$  ( $n= 4, 8; x = 10, 18$ ).

#### 4.3.3.1.1 $[\text{Os}-(\text{R}_8)_2]^{18+}$

$^1\text{H}$  NMR (600 MHz,  $\text{MeOH-d}_4/\text{D}_2\text{O}$ ):  $\delta$  (ppm) 9.31 (s, 4H), 8.86 (d, 4H), 8.44–8.35 (m, 8H), 7.85 (q, 4H), 7.39 (d, 4H), 7.19 (q, 4H), 5.22 (m, 9H), 4.44 (m, 18H), 3.88 (m, 3H), 3.42 (m, 9H), 3.22 (m, 9H), 3.10 (m, 3H), 2.96 (m, 2H), 2.82 (s, 1H), 2.18 (m, 2H), 1.99 (m, 7H), 1.70–1.09 (m, 76H), 0.96 (m, 2H), 0.82 (m, 9H). HR-MS(ESI-TOF)  $m/z$ : calculated for  $\text{C}_{152}\text{H}_{262}\text{N}_{74}\text{O}_{20}\text{Os}$   $[\text{M-bisR}8^{3+} - \text{Cl}^-]$  1188.7296, Found 1187.7218.

#### 4.3.3.1.2 $[\text{Os}-(\text{R}_4)_2]^{10+}$

$^1\text{H}$  NMR (600 MHz,  $\text{MeOH-d}_4/\text{D}_2\text{O}$ ):  $\delta$  (ppm) 9.34 (s, 4H), 8.88 (d, 4H), 8.45–8.38 (m, 8H), 7.90 (q, 4H), 7.45 (d, 4H), 7.23 (q, 4H), 5.22 (m, 1 H), 4.49 (m, 10H), 3.93 (m, 5H), 3.75–3.3.65 (m, 7H), 3.38 (m, 1H), 3.27–2.99 (m, 6H), 2.27 (m, 1H), 2.03 (m, 2H), 1.67– 1.05 (m, 36H), 0.91 (m, 1H), 0.85 (m, 6H). HR-MS(ESI-TOF)  $m/z$ : calculated for  $\text{C}_{105}\text{H}_{159}\text{N}_{43}\text{O}_{13}\text{Os}$   $[\text{M-bisR}4^{5+} + 8\text{H}^+ + \text{Cl}^-]$  493.0596, Found 493.1205.

### 4.3.4 Photophysical Measurements

All absorbance measurements were performed on a Jasco V670 Spectrophotometer (Jasco SpectraManager v2 software). Emission spectra were obtained using a Varian Cary Eclipse Fluorescence Spectrophotometer (Varian Cary Eclipse Software v1.1). The excitation and emission slit widths were set to 10nm unless stated otherwise. Lifetime measurements were performed on a PicoQuant FluoTime 100 FLS TCSPC system using a 450 nmpulsed laser (PicoQuant PDL800-B) and an external Thurlby Thandar Instruments TGP110 10 MHz pulse generator. Luminescence lifetime data were acquired up to 10,000 counts, and decay curves were analyzed using PicoQuant Fluofit software and tail-fit statistical modelling (tail-fit criteria;  $0.9 < \chi^2 < 1.1$ ). The samples were de-aerated by solution-purging with nitrogen for 20 min. All lifetime measurements were performed in triplicate at room temperature (293 K) and are reported as mean  $\pm$  SD. Luminescence quantum yield ( $\phi$ ) was determined using the relative method by comparing with the luminescence intensity of  $[\text{Ru}(\text{bpy})_3]^{2+}$  as the standard sample using the following equation:



$$\Phi_{\text{sample}} = \Phi_{\text{standard}} \times \frac{A_{\text{sample}}}{A_{\text{standard}}} \times \frac{F_{\text{sample}}}{F_{\text{standard}}} \times \left( \frac{n_{\text{sample}}}{n_{\text{standard}}} \right)^2$$

Where A is the absorbance at the excitation wavelength, F is the area under the corrected emission spectrum and n is the refractive index of the solvent.

#### 4.3.5 Monolayer cell and 3D spheroid cell cultures

Two cell lines were studied: an adherent mammalian cell line, Chinese hamster ovarian (CHO-K1), and a lung carcinoma cancer cell line (A549). Dulbecco's modified Eagle's medium (DMEM)/Hams F-12 was used for CHO cells and DMEM for A549 cells. Both media were supplemented with 10 % FBS and 1 % penicillin-streptomycin. The cells were grown at 37 °C with 5 % CO<sub>2</sub> and sub-cultured at 90 % confluency.

The human pancreatic cancer cell line (HPAC) was cultured in Gibco Roswell Park Memorial Institute medium supplemented with 5 % FBS at 37 °C with 5 % CO<sub>2</sub>. HPAC cells were seeded at  $2.5 \times 10^3$  cells/well of 96-well round-bottom plates pre-coated with poly-Hema (poly-2-hydroxyethyl methacrylate, Sigma). Cells were allowed to be compact and form 3D spheroid structures after 72 h.

#### 4.3.6 Cytotoxicity studies

The Alamar blue assay (Promocell GmbH) was used to assess the cell viability of A549 and CHO cells treated with the [Os-(R<sub>4</sub>)<sub>2</sub>]<sup>10+</sup> probe. The cells were seeded in 96-well plates (flat-bottomed culture treated) at 10<sup>4</sup> cells per well for 24 h at 37 °C with 5 % CO<sub>2</sub>. The probe was added at concentrations: 150, 100, 75, 50, 35, 25, 15, 10, 5 and 1 μM and incubated for 24 h prior to the addition of the Resazurin reagent (10 % v/v) for 7 h at 37 °C in the absence of light. Absorbance readings were carried out at 570 nm and 600 nm (corrected for background subtraction) using a CLARIOstar (plus) (v 5.70) plate reader. The viability assay was performed in triplicate for each cell line.

#### 4.3.7 Confocal laser scanning microscopy (CLSM)

Uptake studies were carried out for A549 and CHO cell lines. Cells were seeded at  $1.5 \times 10^5$  cells in 35 mm glass bottom culture dishes (Ibidi, Germany). Cells were allowed to grow for 24 h at 37 °C with 5 % CO<sub>2</sub>. The growth medium was removed, and specific concentration of [Os-(R<sub>n</sub>)<sub>2</sub>]<sup>x+</sup> (n= 4, 8; x= 10<sup>+</sup>, 18<sup>+</sup>) was added and allowed to incubate for 24 h and 48 h at 37 °C at 5 % CO<sub>2</sub> in the dark. The dye/media solution was removed, and cells were washed twice with supplemented PBS (1.1 mM MgCl<sub>2</sub> and 0.9 mM CaCl<sub>2</sub>). Cells were directly imaged using

a Leica TSP DMI8 confocal microscope (63X oil immersion objective lens unless stated otherwise) with a heated stage at 37 °C.

$[\text{Os}-(\text{R}_n)_2]^{x+}$  ( $n=4, 8$ ;  $x=10^+, 18^+$ ) was excited using a 490 nm white light laser and the emission range was set to between 650 and 800 nm. DRAQ7, a nuclear staining dye was added (3  $\mu\text{M}$ ) to distinguish intact live cells from permeabilized/dead cells. The 633 nm laser was used to excite DRAQ7 and emission was collected between 635–750 nm. For colocalization studies MitoTracker Deep Red (100 nM) and LysoTracker Green (50 nM) were used to selectively stain mitochondria and lysosomes respectively. MitoTracker Deep Red was excited at 644 nm and emission was collected between 655–720 nm and LysoTracker Green was excited at 504 nm and emission was collected at 511 nm.

#### **4.3.8 Phototoxicity**

DRAQ7 was added to live A549 cells treated with  $[\text{Os}-(\text{R}_4)_2]^{10+}$  (30  $\mu\text{M}$ / 24 h). A group of cells was selected for continuous irradiation using 490 nm excitation (0.84  $\mu\text{W}/\text{cm}^2$ ). Emission was collected between 650 and 800 nm for  $[\text{Os}-(\text{R}_4)_2]^{10+}$ . The 633 nm laser was used to excite DRAQ7 and emission was collected between 635–750 nm. This was repeated for an untreated control sample exposed to continuous irradiation and stained with DRAQ7.

#### **4.3.9 Spheroid Treatment with Os-compounds**

Spheroids were treated with  $[\text{Os}-(\text{R}_4)_2]^{10+}$  at 30  $\mu\text{M}$  for 24 h and 100  $\mu\text{M}$  for 24 h and 48 h. Control spheroids were treated with parent complex  $[\text{Os}(\text{tpybenzCOOH})_2]^{2+}$  and  $[\text{Os}-(\text{R}_8)_2]^{18+}$  at 100  $\mu\text{M}$  for 48 h. Non-treated spheroids were also prepared as a negative control. Spheroids were co-stained with DAPI at 10  $\mu\text{M}$  for 90 minutes. Each spheroid was collected individually and embedded in collagen in eight-well chamber slides, incubated for 90 minutes and observed under confocal microscopy.

#### **4.3.10 Preparation of fixed spheroid sections**

HPAC spheroids were treated with  $[\text{Os}-(\text{R}_4)_2]^{10+}$  at 100  $\mu\text{M}$  for 48 h. The spheroids were collected, washed with PBS, and fixed in 4 % NBF (neutral buffered formalin) for 30 minutes. The spheroids were then washed with PBS again and transferred into 10 %, 20 % and 30 % sucrose in PBS at 4°C overnight until spheroids sank to the bottom. Spheroids were placed in optimal cutting temperature (OCT) embedding matrix gel in a histology mold and placed at -80 °C overnight. Spheroids were cut into 5  $\mu\text{m}$  sections using a cryostat. Sections were co-stained with DAPI. The slides were observed under confocal microscopy.

#### **4.3.11 Confocal microscopy of HPAC spheroids**

For imaging, HPAC spheroids were plated in collagen treated 8-well chamber slides. HPAC spheroids were directly imaged from the 8-well chamber using a Leica TSP DMI8 confocal microscope (10X dry and 40X oil immersion objective). Z-scanning was used to acquire images across the z-axis of the spheroid sample. On average, 45 - 50 images were acquired at approximately 5  $\mu\text{m}$  apart. 3D Z-stack images were used for spheroid reconstructions and 2D projection images are also reported. The Os(II) parent and bioconjugates were excited using a 490 nm white light laser and the emission range was set to between 650 and 800 nm (a false red colour was used for the Os(II) channel). DAPI was excited at 405 nm and emission was collected between 423 nm and 580 nm.

#### **4.3.12 Evaluation of spheroid viability**

The 3D spheroid viability was evaluated using Alamar Blue. Briefly,  $2.5 \times 10^3$  cells were seeded in each well of a 96 well round bottom plate pre-coated with poly-Hema. The cells were allowed to grow and form spheroids for 72 h. Spheroids were then treated with  $[\text{Os}-(\text{R}_4)_2]^{10+}$  at 100  $\mu\text{M}$  for 24 h and 48 h. Alamar Blue reagent at a concentration of 10 % was added to each well and incubated for 5 h at 37  $^\circ\text{C}$ . Fluorescence was measured at 535/590 excitation/emission wavelengths on a plate reader (Biotek) using Gen4 software. Background fluorescence was calculated by using a blank consisting of medium only. Percentage viability was calculated relative to untreated controls.

#### **4.3.13 Phosphorescence Lifetime Imaging Microscopy (PLIM)**

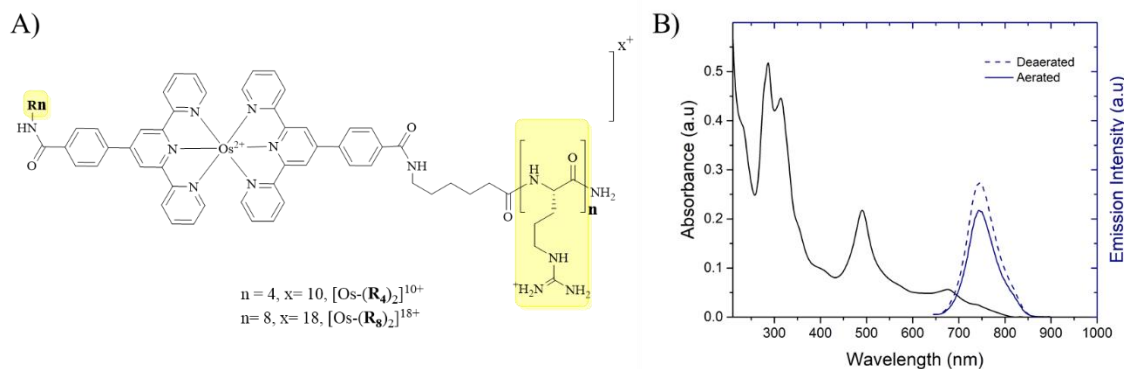
Live A549 cells or HPAC spheroids were prepared and treated with  $[\text{Os}-(\text{R}_4)_2]^{10+}$  as described previously. Luminescence lifetime imaging was carried out using a PicoQuant 100 system attached to Leica TSP inverted (DMI8) confocal microscope using a 63X or 40X oil immersion objective. Each sample was acquired for 120 s with a  $512 \times 512$  resolution using the 405 nm. Data was analysed using PicoQuant Symphotime software.

### **4.4 Results and Discussion**

#### **4.4.1 Preparation and Characterization of the bis-tetra and bis-octa arginine Os(II) conjugates.**

We reported recently on the preparation and photophysical characteristics of the achiral Os(II) parent complex,  $[\text{Os}(\text{tpybenzCOOH})_2]^{2+}$ , used in this study.<sup>40,64</sup> For an osmium polypyridyl

complex, it exhibits a comparatively high emission quantum yield and in particular, as described, has the advantage from the perspective of the current application of a linear structure with bilateral conjugation sites, offering the possibility to extend a linear peptide sequence bridged by the metal center. The tridentate ligand structure also avoids the complexity of the possibility of preparation of isomers.



**Figure 4.1** A) General chemical structure of Os(II)-terpyridine based polyarginine conjugates following amide coupling of  $R_n$  ( $n = 4, 8$ ) to  $[\text{Os}(\text{tpybenzCOOH})_2]^{2+}$  parent complex. B) Absorbance and normalised emission spectra of  $[\text{Os}-(R_4)_2]^{10+}$  ( $30 \mu\text{M}$ / PBS buffer pH 7.4) under aerated and deaerated conditions with  $\lambda_{\text{exc}}$  490 nm and excitation and emission slit widths of 10 nm.

Here, we explore the impact of polyarginine chains of different lengths to each carboxyl termini of the Os(II) complex, to understand in such an arrangement, if the octaarginine sequence we have observed to be so efficient in driving related metal complexes across the cell membrane and into the cytoplasm require that the arginine residues are contiguous and if longer arginine chains further improve the uptake. A comparative study on multivalent antimicrobial peptides reported enhanced antimicrobial activity for divalent metallocene conjugates.<sup>65</sup> The general chemical structure of the conjugates,  $[\text{Os}-(R_n)_2]^{x+}$  ( $n = 4, 8$ ;  $x = 10^+, 18^+$ ), is shown in Figure 4.1A. Each polyarginine chain was composed of four or eight D-Arg residues. Studies have shown that internalization is not stereospecific as both D- and L-Arg enter cells efficiently.<sup>20</sup>

Bis-octaarginine and bis-tetraarginine conjugation to the carboxyl termini of  $[\text{Os}(\text{tpybenzCOOH})_2]^{2+}$  was achieved via amide coupling using PyBOP/DIPEA following the procedures reported previously.<sup>40,41</sup> The structure and purity of the conjugates were confirmed by  $^1\text{H}$  and COSY NMR, reverse-phase HPLC (PDA 490 nm), and high-resolution LC mass spectrometry. Both polyarginine conjugates showed very similar photophysical properties in PBS (pH 7.4) to the parent complex and OsII MPP previously reported.<sup>40</sup> The absorbance and emission spectra of  $[\text{Os}-(R_4)_2]^{10+}$  ( $30 \mu\text{M}$ ) are shown in Figure 4.1B. The emission maximum

centered at 754 nm coincides well with the biological window and is usefully situated outside of the range of cellular autofluorescence.  $[\text{Os}-(\text{R}_4)_2]^{10+}$  and  $[\text{Os}-(\text{R}_8)_2]^{18+}$  in aerated PBS (pH 7.4) exhibited luminescence lifetimes of  $89.6 \pm 5.3$  ns and  $89.2 \pm 6.1$  ns respectively, which, as for their related MPP conjugates, were only modestly affected by deaeration ( $\tau_{\text{Os-R4}}$   $103 \pm 6.9$  ns and  $\tau_{\text{Os-R8}}$   $108.6 \pm 11.1$  ns).

#### 4.4.2 Uptake studies of $[\text{Os}-(\text{R}_n)_2]^{x+}$ conjugates

As reported previously, the parent complex without peptide is cell membrane impermeable. Uptake of the Os(II) bis-octaarginine conjugate was studied in live A549 lung carcinoma and a non-cancerous CHO cell line. Surprisingly, confocal laser scanning microscopy (CLSM) revealed that bis-conjugation to octaarginine did not facilitate transport of the complex.<sup>66</sup> The conjugate remained as impermeable to the cell membrane as the parent Os(II) complex at 30  $\mu\text{M}$  / 24 h and 100  $\mu\text{M}$  / 24 h (Figure S4. 11). As expected, in absence of any permeation, A549 and CHO cells remained healthy as confirmed by co-staining with DRAQ7, a dye which stains the nucleus of damaged/dead cells.

As previously mentioned, evidence suggests that cargo cellular uptake is enhanced with an increase in arginine chain length for polyarginine CPPs. However, whereas it has been widely observed that R8 or R9 provides optimal uptake, the inhibition of uptake with longer polyarginine chains has also been noted. For example, Sugiura et al. noted, consistent with our data, that fluorescently labeled R8 was efficiently drawn across live cell membranes, whereas R16 was not.<sup>67</sup> Studies have also shown that the cellular uptake ability of oligoarginine conjugates depends on the total number of Arg residues and not necessarily on the exact arginine sequence.<sup>68,69</sup> As the chain length increases, the uptake behavior becomes less predictable. For example, studies found that R15 conjugation showed superior uptake to R20-R30 and R75 proved to be toxic toward cells.<sup>20</sup> Long peptides of lysine have also shown cellular toxic effects.<sup>70</sup> The reason for reduced uptake by longer arginine chains is not entirely clear as the mechanism of arginine-mediated uptake is still debated. If translocation is the key mechanism, it may be that the longer chain lengths, associate too strongly with the membrane or do not cause the appropriate degree of curvature at the cell membrane or are an inappropriate length to span the membrane in endocytosis. It is notable that long-term incubation with the complex did not cause cytotoxicity, confirmed by the absence of DRAQ7 from the nucleus, indicating that membrane destabilization by these long R chains can be excluded.

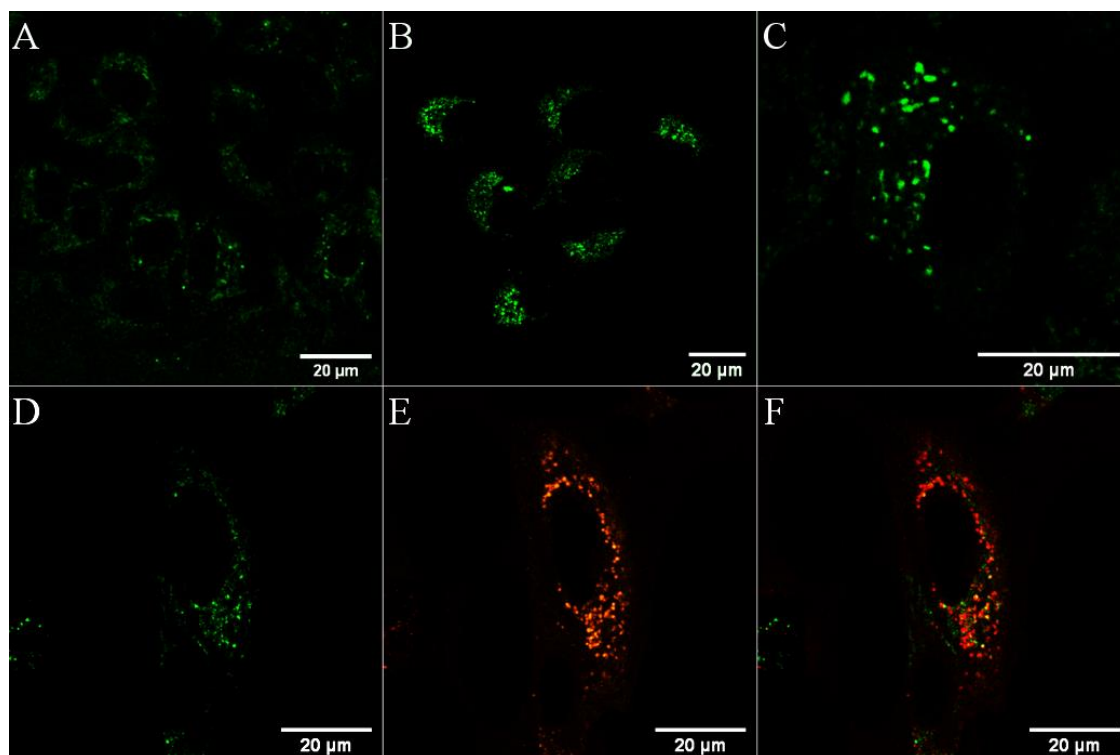
As reported previously, R8 promotes the uptake of Ru and Os(II) polypyridyl complexes across live cell membranes, so we then conjugated two R4 chains to each terminus of the complex.

In contrast to  $[\text{Os}-(\text{R}_8)_2]^{18+}$ ,  $[\text{Os}-(\text{R}_4)_2]^{10+}$  was rapidly and efficiently internalized into live A549 and CHO cells at 30  $\mu\text{M}$  following 24 h incubation in the dark. As shown in Figure 4.2, emission from the cytoplasm was evident at 24 h and by 48 h as punctuate staining. Previously reported ruthenium octaarginine conjugates have generally been found to be nuclear excluding with non-specific distribution throughout the cytoplasm.<sup>38,39</sup> Uptake of an osmium polypyridyl phenanthroline imidazole complex conjugated to R<sub>8</sub>,  $[\text{Os}(\text{bpy})_2(\text{pic-arg}_8)]^{10+}$  showed comparable uptake to its ruthenium analogue, although unlike the Ru analogue, nuclear penetration of the osmium complex was observed in CHO cells particularly under photoirradiation.<sup>11</sup> The increased lipophilic character of the osmium complex compared to its ruthenium analogue was suggested as a reason for its nuclear permeation.

Given the punctate distribution of the complex at later time points, to establish distribution of  $[\text{Os}-(\text{R}_4)_2]^{10+}$ , co-localization studies were carried out using Lysotracker Green for the lysosomes and MitoTracker Deep Red for the mitochondria. Staining with DRAQ7 was used to identify damaged cells. A Pearson's coefficient value of 0.56 revealed only moderate co-localization with MitoTracker Deep Red at 30  $\mu\text{M}$ /24 h, suggesting that at these conditions, the conjugate enters but is not exclusively localized at the mitochondria (Figure S4. 13).

As shown in Figure 4.2D-F, the punctate staining of  $[\text{Os}-(\text{R}_4)_2]^{10+}$  (green) at 30  $\mu\text{M}$ /48 h co-localized with Lysotracker Green (orange) confirming localization of the conjugate in lysosomal structures. Trafficking to the lysosomes of HIV-TAT and octaarginine following uptake has been reported previously and has been linked to an endocytic uptake mechanism.<sup>71</sup> A similar uptake and distribution in A549 cells were observed when incubated for 24 h at higher complex concentrations of 100  $\mu\text{M}$   $[\text{Os}-(\text{R}_4)_2]^{10+}$  (Figure S4. 14) Uptake of  $[\text{Os}-(\text{R}_4)_2]^{10+}$  was also studied in a non-cancerous CHO cell line. As shown in Figure 4.3A,B, CHO cells treated with  $[\text{Os}-(\text{R}_4)_2]^{10+}$  at 30  $\mu\text{M}$  and incubated for 24 h showed extensive cytoplasmic

and nucleoli staining. In this case, nuclear penetration did not concern a photo or thermally activated process as penetration was observed following incubation of  $[\text{Os}-(\text{R}_4)_2]^{10+}$  in the dark. The  $[\text{Os}-(\text{R}_4)_2]^{10+}$  conjugate exhibited temperature dependent uptake as cell permeation of



**Figure 4.2** Uptake and colocalization studies of  $[\text{Os}-(\text{R}_4)_2]^{10+}$  in live A549 cells where the osmium channel is shown in green. Cells were incubated in the absence of light with  $30 \mu\text{M}$   $[\text{Os}-(\text{R}_4)_2]^{10+}$  for A) 24 h and for B-C) 48 h. Co-localization studies at 48 h with LysoTracker Green (50 nM) confirmed lysosomal confinement evident by the overlap of the D) osmium channel with E) LysoTracker Green (orange) in the F) overlay image (Pearson's coefficient = 0.69). A 490 nm white light laser was used to excite the conjugate and emission was collected between 650 and 800 nm. LysoTracker Green was excited at 504 nm and emission was collected at 511 nm.

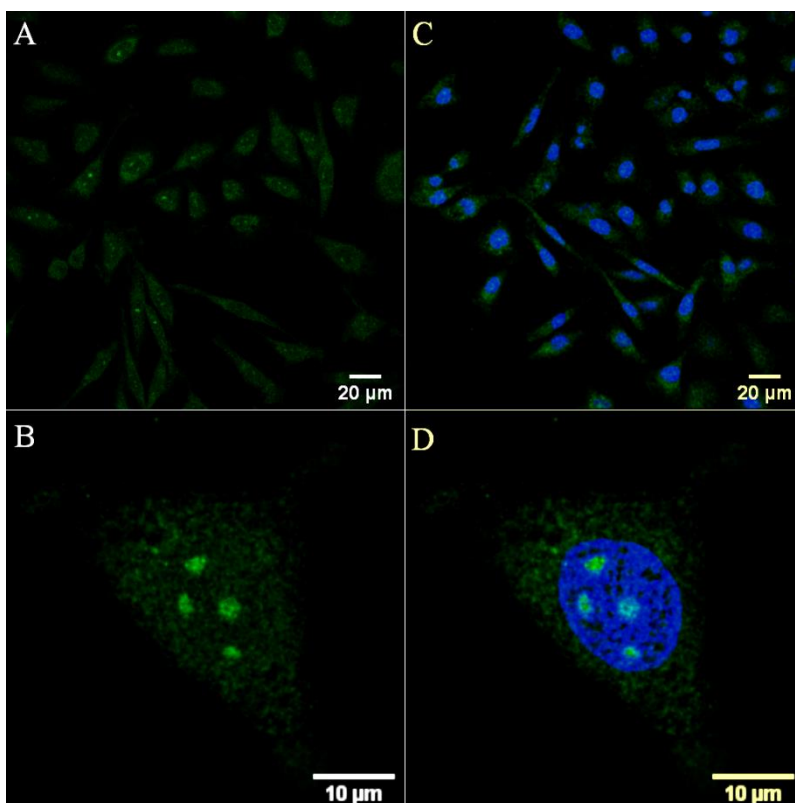
A549 and CHO cells was inhibited at  $4^\circ\text{C}$ , suggesting that an activated process, such as endocytosis, is involved for cellular entry (Figure S4. 15). Previously reported octaarginine conjugates of metal complex cargo have been shown to be internalized via an activated membrane transport process.<sup>11,72,73</sup>

Co-staining studies using DRAQ7 confirmed that the A549 cells remained viable after both 24 h and 48 h treatment with the conjugate at  $30 \mu\text{M}$  (Figure S4. 16). The absence of DRAQ7 from the cell nuclei of A549 cells treated with the conjugate at a higher concentration of  $100 \mu\text{M}/24$  h confirmed that no cell death was induced at this higher concentration (Figure S4.

14A,B). After extending the incubation time for 100  $\mu\text{M}$   $[\text{Os}-(\text{R}_4)_2]^{10+}$  to 48 h, some DRAQ7 staining was evident, indicating modest cytotoxic effects at extended incubations and higher probe concentration (Figure S4. 14C-E). In order to assess potential photo-induced toxic effects, a group of A549 cells, pretreated with  $[\text{Os}-(\text{R}_4)_2]^{10+}$  (30  $\mu\text{M}/24$  h) and stained with DRAQ7, was continuously irradiated using 490 nm excitation (at 0.84  $\mu\text{W}/\text{cm}^2$ , approximately 3 times higher than the imaging intensity). Under these conditions, no DRAQ7 was found to enter cell nuclei following 3 h of irradiation, confirming that the osmium conjugate is non-photocytotoxic under these conditions (Figure S4. 17). We attribute this to the insensitivity of the excited state of this species to molecular oxygen. It is not quenched by  $\text{O}_2$  and thus does not generate cytotoxic singlet oxygen under irradiation, and the low excited-state oxidation potential of the complex limits photoredox reactions with DNA or protein constituents. The extent of nucleoli staining of  $[\text{Os}-(\text{R}_4)_2]^{10+}$  and cellular damage in CHO cells, following 24 h of incubation at 30  $\mu\text{M}$ , was evident by the entry of DRAQ7 (blue) in several cell nuclei (Figure 4.3C,D). The viability of A549 and CHO cells treated with  $[\text{Os}-(\text{R}_4)_2]^{10+}$  was assessed by incubating the conjugate overnight at concentrations up to 150  $\mu\text{M}$  at 37  $^\circ\text{C}$  with 5 % v/v  $\text{CO}_2$  using the Alamar Blue assay (Figure S4. 18).

The reduction of the resazurin reagent to resorufin was used to directly measure cell viability. The conjugate was found to be remarkably non-toxic toward A549 cells with an  $\text{IC}_{50}$  exceeding 150  $\mu\text{M}$  and cell viability was above 71 % up to 100  $\mu\text{M}$ .  $[\text{Os}-(\text{R}_4)_2]^{10+}$  was found to be somewhat more toxic to CHO cells where viability decreased to <70 % above 35  $\mu\text{M}$  with an  $\text{IC}_{50} \approx 75.1 \pm 1.1$   $\mu\text{M}$ . It is likely that the cytotoxicity in CHO cells is the result of wider distribution of the conjugate in this cell line, which is evident by confocal imaging where cytoplasmic staining and nucleoli staining were observed. The previously reported  $[\text{Os}(\text{tpybenzCOOH})_2]^{2+}$  complex conjugated to two MPPs exhibited a concentration-dependent localization and cytotoxicity toward HeLa and MCF 7 cells with an  $\text{IC}_{50} \approx 30$   $\mu\text{M}$ .<sup>40</sup> However, here conjugation of the Os(II) complex to two tetraarginine chains leads to significantly decreased toxicity likely owing to the preferential cytoplasmic staining of the conjugate. Overall,  $[\text{Os}-(\text{R}_4)_2]^{10+}$  is not photocytotoxic, and the dark toxicity of the bis-tetraarginine Os(II) conjugate toward A549 and CHO cell lines is low and comparable to the reported ruthenium and osmium octaarginine compounds.<sup>11,37</sup>



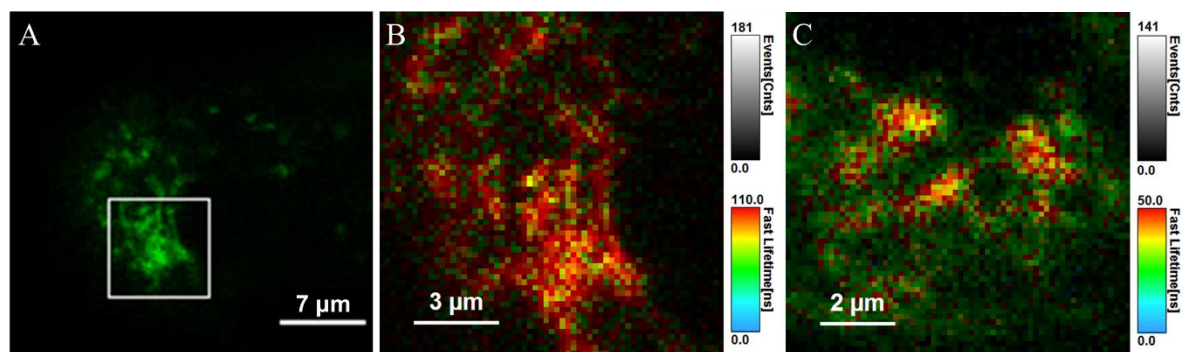


**Figure 4.3** Confocal luminescence images of  $[\text{Os}-(\text{R}_4)_2]^{10+}$  in CHO cells. Live cells were incubated with  $30 \mu\text{M}$   $[\text{Os}-(\text{R}_4)_2]^{10+}$  for 24 h in the absence of light and co-stained with DRAQ7. (A-B) The distribution of the conjugate (in green) is shown in a group of cells co-stained with DRAQ7 (in blue). (C-D) Closeup image of a single A549 cell shows nucleoli staining. The 633 nm laser was used to excite DRAQ7 and emission was collected between 635–750 nm.

In addition,  $[\text{Os}-(\text{R}_4)_2]^{10+}$  was less toxic than the octaarginine conjugate  $[\text{Ir}(\text{dfpp})_2(\text{picCHONH})(\text{Arg}_8)]^{9+}$  with  $\text{IC}_{50}$  values of 54.1 and  $35 \mu\text{M}$  against CHO and SP2 cells, respectively.<sup>73</sup> The relatively long emission lifetimes of the metal complexes render them potentially useful as probes for mapping of the environment of live cells using luminescence lifetime imaging. For example, Ir(III) and Ru(II) polypyridyl complexes have been employed as  $\text{O}_2$  sensors using PLIM studies.<sup>29,52,53</sup> PLIM was carried out here to investigate the emission lifetime of the conjugate in the environment of live cells.

Figure 4.4 shows the false-colour images of the lifetime distributions of the Os(II) probe in A549 cells at  $30 \mu\text{M}$  following uptake at 24 h and 48 h incubation. The emission lifetime of the conjugate was found to vary with localization, attributed to environmental effects. When taken up in the cytoplasm and partially confined in mitochondria at 24 h, the lifetimes fit to a tri-exponential decay with a very short component ( $\tau_3$ ) that was present under all circumstances of 2 ns and attributed to background scatter/reflectance. The dominant amplitude component (67 %) of the decay,  $\tau_1$ , was measured as  $92.2 \text{ ns} \pm 2.9 \text{ ns}$  with a second component of lifetime,

$\tau_2$ , recorded as  $15.8 \pm 1.5$  ns (25 %). Notably, when confined to the lysosomes and the surrounding cytoplasm at  $30 \mu\text{M}/48$  h, the  $[\text{Os}-(\text{R}_4)_2]^{10+}$  conjugate exhibited significantly reduced lifetimes of  $37 \pm 1.8$  ns (54 %) and  $9.3 \pm 0.6$  ns (32 %). Although  $\text{O}_2$ -insensitive, the conjugate is expected to respond to redox-active species in the sub-cellular environment, but response on the basis of the pH of the lysosome can be excluded as the emission lifetime of



**Figure 4.4** Luminescence lifetime imaging  $[\text{Os}-(\text{R}_4)_2]^{10+}$  at  $30 \mu\text{M}$  in live A549 cells. A) Confocal image of a single cell following conjugate uptake at 24 h and B) lifetime distribution in the expanded cytoplasmic region of the cell. C) PLIM acquired following uptake at 48 h. The PLIM images were acquired using the 405 nm excitation laser line. The PLIM images of the entire cell of B and C and corresponding emission decays are shown in the Supplementary Information (Fig. S 18-19).

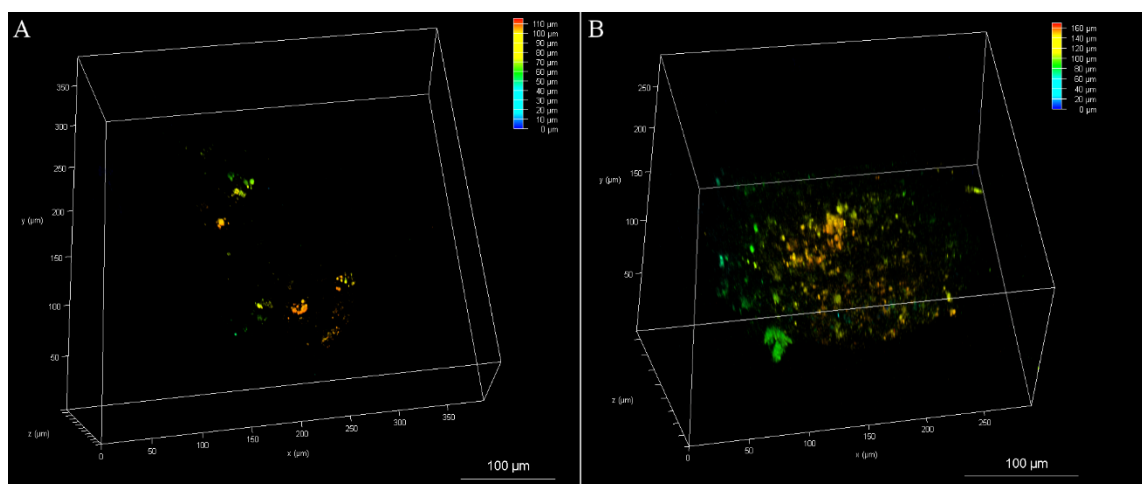
the parent complex in aqueous solution (pH 4.1) showed no response to acidic pH (Figure S4.10). The oxidation potential of osmium is typically 300 mV lower than comparable Ru analogues, and for the parent complex here, the oxidation potential is 656 mV versus  $\text{Ag}/\text{AgCl}$ .<sup>40</sup> The lysosome is an acidic organelle with a rich cocktail of redox-active species including metalloenzymes and thiols likely to quench and thus modulate the excited-state lifetime of this complex. The absence of  $\text{O}_2$  sensitivity but potential redox sensitivity to other species offers an advantage of Os polypyridyl complexes over ruthenium and iridium complexes in imaging, offering opportunities to monitor localization and metabolic changes in cells or tissues without interference from oxygen.

#### 4.4.3 Confocal imaging of HPAC spheroids

The excellent membrane permeability of the bis-tetraarginine Os(II) conjugate, its low photocytotoxicity, and NIR emission suggests its suitability as a probe for tissue imaging, and to date, there have been no applications of Os luminophores applied as 3D multicellular spheroids imaging probes. However, as noted, multicellular spheroids present a very different

microenvironment. Thus, we investigated their penetration into 3D MCTSs. 3D cell spheroids are prepared by culturing cancer cells in a non-adherent environment, which promotes the formation of aggregates of cell layers.<sup>42–45</sup>

We performed studies on MCTSs composed of HPACs grown in ultra-low attachment well plates for 3 days. The spheroids were incubated with the  $[\text{Os}-(\text{R}_4)]^{10+}$  conjugate at 30 and 100  $\mu\text{M}$  for 24 and 48 h each. For comparison, the ability of the Os(II) parent complex and the bis-octaarginine conjugate,  $[\text{Os}-(\text{R}_8)_2]^{18+}$ , to penetrate 3D spheroids was also assessed by incubating with the compounds at 100  $\mu\text{M}$  for 48 h. In the latter cases, no spheroid penetration or accumulation was observed for either parent or bis-octaarginine compound, consistent with studies on 2D cell monolayers (Figure S4. 21).

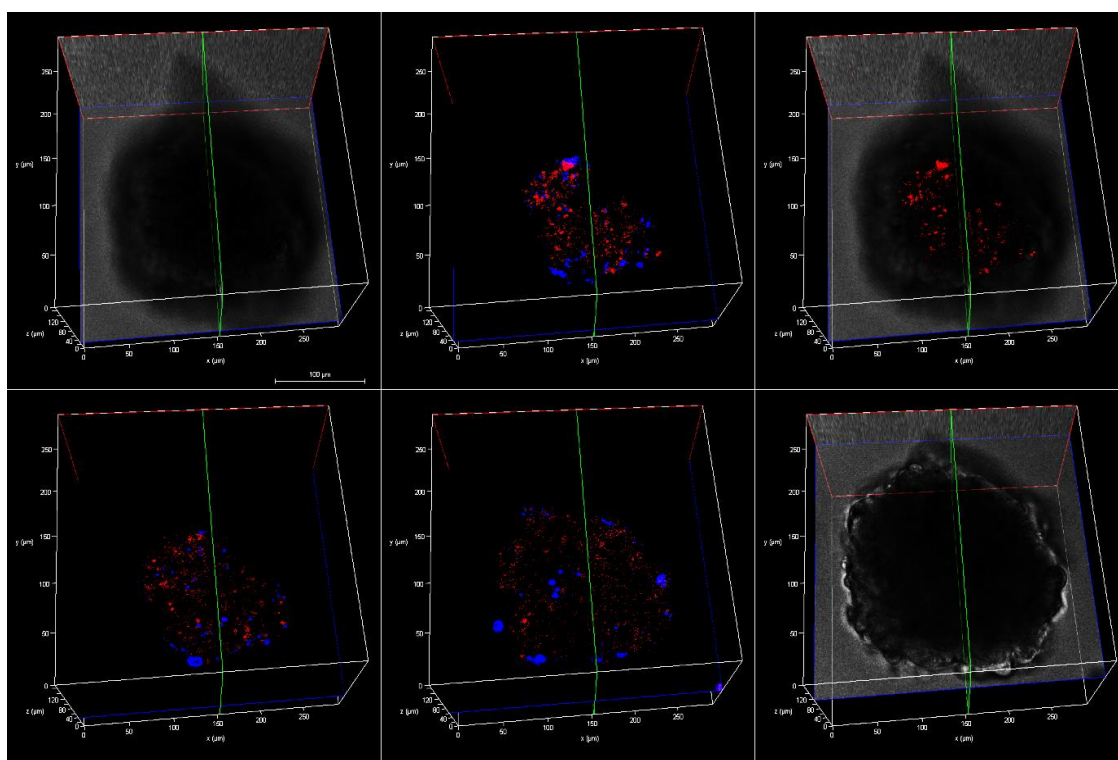


**Figure 4.5** 3D reconstruction depth coding images of whole live HPAC spheroids treated with  $[\text{Os}-(\text{R}_4)_2]^{10+}$  at (A) 30  $\mu\text{M}$  / 24 h and (B) 100  $\mu\text{M}$  / 24 h. Confocal images were acquired at different planes in the z direction throughout the spheroids (from the bottom to above each spheroid). A 490 nm white light laser was used to excite the conjugate and emission was collected between 650 and 800 nm. Scale bar reads 100  $\mu\text{m}$ .

Conversely, confocal luminescence microscopy studies revealed that the bis-tetraarginine conjugate readily permeates the HPAC spheroids. It is important to note that the probes are incubated with the live spheroid in aqueous buffer/media without application of a permeant such as detergent or solvent. As shown in the 3D reconstruction depth coding images, spheroid penetration was evident following incubation with  $[\text{Os}-(\text{R}_4)]^{10+}$  at 30  $\mu\text{M}$  / 24 h, although staining at the centre of the spheroid, at  $72 \pm 5 \mu\text{m}$ , was not observed at this concentration (Figure 4.5A). However, by increasing complex concentration to 100  $\mu\text{M}$  / 24 h

extensive probe penetration and distribution to the core of the spheroid was achieved (Figure 4.5B).

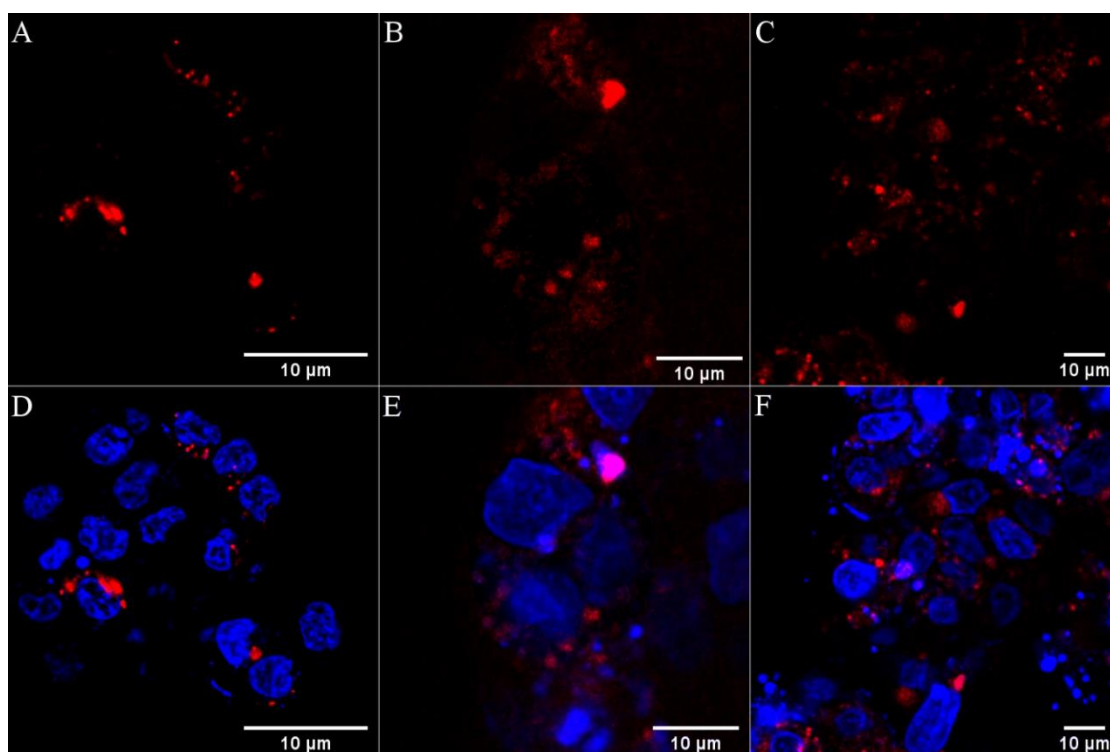
Hambley et. al. reported on the depth of penetration of a series of platinum complexes in cancer cell spheroids observing it was inversely proportional to the rate of cellular uptake.<sup>54</sup> It is likely that rapid accumulation of the probe at 30  $\mu\text{M}$  results in penetration and accumulation of complex at the first few cell layers, leaving insufficient concentration of probe to measurably diffuse to the center of the MCTS at lower concentrations. Full Z-stack images are shown in the Supporting Information (Figures S4. 22-S4. 23).



**Figure 4.6** Z-stack images a single live HPAC spheroid pre-treated with  $[\text{Os}-(\text{R}_4)_2]^{10+}$  (100  $\mu\text{M}$ / 48 h) and co-stained with DAPI (10  $\mu\text{M}$ ). Each image corresponds to cross-section from the bottom to the upper part along the z-axis. Representative cross-sections are shown using brightfield contrast as the background. Scale bar reads 100  $\mu\text{m}$ . A 490 nm white light laser was used to excite the conjugate and emission was collected between 650 and 800 nm. The 405 nm excitation laser was used to excite DAPI and emission was collected between 423 and 580 nm.

Figure 4.6 shows representative z-stack images of a single live HPAC spheroid treated with  $[\text{Os}-(\text{R}_4)_2]^{10+}$  at 100  $\mu\text{M}$  for 48 h. Emission from the conjugate (in red) is observed throughout cell layers and deep into the spheroid core. A nuclear localizing dye, DAPI (in blue), was used as a co-staining contrast dye.

Figure 4.7 shows the extent of probe distribution in spheroid regions following incubation with  $[\text{Os}-(\text{R}_4)_2]^{10+}$ , where uniform cytoplasmic staining, that is mainly nuclear excluding, is observed at  $100 \mu\text{M}/24 \text{ h}$  and  $48 \text{ h}$ . Furthermore, following treatment with the tetraarginine conjugate, the live spheroids were examined for morphological changes by comparing with non-treated (control) spheroids, and the viability assay showed no evidence of toxicity (Figure S4. 24).

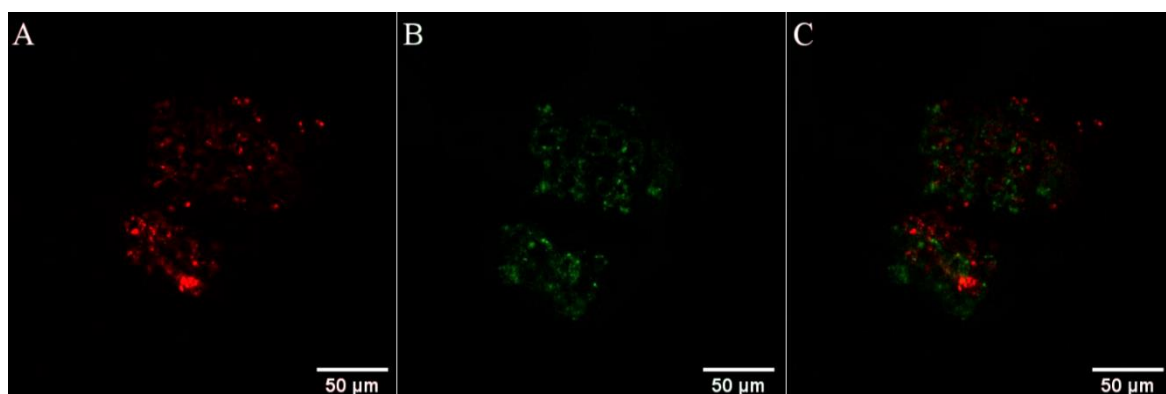


**Figure 4.7** Confocal images (2D-projection) of HPAC spheroid regions treated with  $\text{Os}-(\text{R}_4)_2$  at (A)  $30 \mu\text{M}/24 \text{ h}$ , (B)  $100 \mu\text{M}/24 \text{ h}$  and (C)  $100 \mu\text{M}/48 \text{ h}$  at  $37^\circ\text{C}$ . The spheroids were co-stained with DAPI ( $10 \mu\text{M}$ ) and (D-F) Overlay images with DAPI channel. A  $490 \text{ nm}$  white light laser was used to excite the conjugate and emission was collected between  $650$  and  $800 \text{ nm}$ . The  $405 \text{ nm}$  excitation laser was used to excite DAPI and emission was collected between  $423$  and  $580 \text{ nm}$ . (40X)

A key advantage of  $\text{Os}(\text{II})$  polypyridyl complexes is that they exhibit NIR emission well resolved from the autofluorescence window. Emission from cellular fluorophores, such as nicotinamide adenine dinucleotide ( $\text{NAD}^+/\text{NADH}$ ) and flavins, occurs mainly at shorter light wavelengths ( $350\text{-}550 \text{ nm}$ ); thus; in detecting fluorophores emitting below  $700 \text{ nm}$ , autofluorescence can be readily filtered out.<sup>4,74,75</sup>  $[\text{Os}-(\text{R}_4)_2]^{10+}$  exhibits an emission maximum centered at  $750 \text{ nm}$  and the emission collected here between  $650$  and  $800 \text{ nm}$  corresponding to the  $\text{Os}(\text{II})$  channel (Figure 4.8A) avoids any background signal from biological autofluorescence (Figure 4.8B). Furthermore, as shown in the above PLIM images, the



relatively long lifetimes of these probes also enable facile discrimination of contributions from autofluorescence in lifetime data.



**Figure 4.8** Confocal images of a single live HPAC spheroid treated with  $[\text{Os}-(\text{R}_4)_2]^{10+}$  ( $100 \mu\text{M}/48 \text{ h}$ ). A 490 nm white light laser was used for excitation and emission was collected between (A) 650 – 800 nm; Os(II) channel and (B) 500 – 570 nm; autofluorescence window. (C) Os(II)/autofluorescence channel overlay.

To further evaluate the distribution of the conjugate inside the spheroids, fixed cryosections of HPAC spheroids that were pre-treated with  $[\text{Os}-(\text{R}_4)_2]^{10+}$  ( $100 \mu\text{M}$ ) when live were prepared and imaged. The confocal fluorescence images confirm the wide distribution of the conjugate throughout the spheroid (Figures S4. 25-S4. 26). Punctuate staining and overlap with DAPI dye in the fixed samples suggest preferential accumulation of the conjugate at certain regions and some nuclear penetration and localization. The latter was not noted in the live pancreatic spheroid samples. However, it is important to note that the process of fixation has a profound impact on the cellular structures and can alter the distribution of probes within cells. Indeed, redistribution of nona-arginine- modified fluorescent dyes was noted after fixation where nucleolus migration was observed.<sup>76</sup>

Furthermore, as shown in the PLIM image of punctuate staining of  $[\text{Os}-(\text{R}_4)_2]^{10+}$  in fixed HPAC spheroids (Figure S4. 27), the lifetime distribution is very uniform. Here, the decay conforms to a bi-exponential fit where the osmium conjugate shows only a single-component decay with a lifetime of 16.4 ns, which is short-lived than in solution ( $\tau \approx 89.6 \pm 5.3 \text{ ns}$ ) but comparable to the lifetimes recorded in the 2D monolayer cell studies. However the lifetime of  $[\text{Os}-(\text{R}_4)_2]^{10+}$  and its uniformity are likely to reflect the sample fixation, which causes extensive cross-linking of protein structures into a gel state within the cell.<sup>77,78</sup>

## 4.5 Conclusions

Using an achiral Os(II) bisterpyridinyl-coordinated complex with linear bilateral conjugation sites, we demonstrate that assembly of polyarginine at opposing ends of the structure exhibits an additive effect in terms of cargo cellular permeation. Whereas the parent complex is completely impermeable to live 2D and 3D cells, the octaarginine conjugate prepared as two tetraarginine moieties conjugated to the termini of the Os centre shows excellent permeability and behaves in an analogous way to previously reported octaarginine derivatives of related complexes. In contrast, when two octaarginine peptides are appended to the termini, the conjugate is rendered completely impermeable to the 2D and 3D cell cultures.

The  $[\text{Os}-(\text{R}_4)_2]^{10+}$  conjugate exhibited exceptionally low cytotoxicity and photocytotoxicity and an emission maximum at 754 nm coinciding with the biological window. The  $[\text{Os}-(\text{R}_4)_2]^{10+}$  emission is essentially oxygen-insensitive but exhibits a relatively long-lived emission lifetime of approximately 89 ns in PBS that facilitates its use in phosphorescence lifetime imaging. Uptake was found to be efficient in all cell lines explored, but the distribution varied with cell type and where  $[\text{Os}-(\text{R}_4)_2]^{10+}$  accessed the lysosome its emission lifetime was significantly reduced likely attributed to emission quenching redox-active species in that organelle. We examined the application of conjugates in imaging a multilayer pancreatic cancer cell model; to our knowledge, this is the first example of an Os luminophore applied to imaging of 3D multicellular spheroids. While the parent complex and  $[\text{Os}-(\text{R}_8)_2]^{18+}$  conjugate were found to be impermeable, widespread and in-depth staining into the 3D MCTS was achieved with  $[\text{Os}-(\text{R}_4)_2]^{10+}$  without any impact on cellular function. The emission collected was well outside the autofluorescence window toward the NIR region of the spectrum suitable for tissue imaging. Our data demonstrate that the efficiency of octaarginine as a permeant does not require contiguous arrangement of the amino acids but shows that the sequence can be bridged at the luminophore termini. This approach may be more broadly applicable and could pave the way to novel compounds that combine shorter peptide sequences such as signal and CPP sequences and could also address issues in peptide synthesis concerning cumulative lower yields with longer peptides. This work also illustrates the value of non-cytotoxic osmium derivatives as probes for studying the MCTS environment.

## 4.6 Supporting Material

Supporting information associated with this chapter can be found in **Appendix C**.

## 4.7 References

- 1 C. Dolan, C. S. Burke, A. Byrne and T. E. Keyes, in *Inorganic and Organometallic Transition Metal Complexes with Biological Molecules and Living Cells*, Elsevier, 2017, pp. 55–89.
- 2 K. K.-W. Lo, *Acc. Chem. Res.*, 2015, **48**, 2985–2995.
- 3 J. Sowell, L. Streckowski and G. Patonay, *J. Biomed. Opt.*, 2002, **7**, 571.
- 4 E. Hemmer, A. Benayas, F. Légaré and F. Vetrone, *Nanoscale Horiz.*, 2016, **1**, 168–184.
- 5 K. Welsher, S. P. Sherlock and H. Dai, *Proc. Natl. Acad. Sci.*, 2011, **108**, 8943–8948.
- 6 J. Shum, P. K.-K. Leung and K. K.-W. Lo, *Inorg. Chem.*, 2019, **58**, 2231–2247.
- 7 M. Duati, S. Fanni and J. G. Vos, *Inorg. Chem. Commun.*, 2000, **3**, 68–70.
- 8 A. K. Pal, S. Serroni, N. Zaccheroni, S. Campagna and G. S. Hanan, *Chem. Sci.*, 2014, **5**, 4800–4811.
- 9 D. Cullinane, K. S. Gkika, A. Byrne and T. E. Keyes, *J. Inorg. Biochem.*, 2020, 111032.
- 10 R. E. Holmlin and J. K. Barton, *Inorg. Chem.*, 1995, **34**, 7–8.
- 11 A. Byrne, C. Dolan, R. D. Moriarty, A. Martin, U. Neugebauer, R. J. Forster, A. Davies, Y. Volkov and T. E. Keyes, *Dalton Trans.*, 2015, **44**, 14323–14332.
- 12 C. Ge, H. Huang, Y. Wang, H. Zhao, P. Zhang and Q. Zhang, *ACS Appl. Bio Mater.*, 2018, **1**, 1587–1593.
- 13 R. Huang, F.-P. Feng, C.-H. Huang, L. Mao, M. Tang, Z.-Y. Yan, B. Shao, L. Qin, T. Xu, Y.-H. Xue and B.-Z. Zhu, *ACS Appl. Mater. Interfaces*, 2020, **12**, 3465–3473.
- 14 K. R. A. Schneider, A. Chettri, H. D. Cole, K. Reglinski, J. Brückmann, J. A. Roque, A. Stumper, D. Nauroozi, S. Schmid, C. B. Lagerholm, S. Rau, P. Bäuerle, C. Eggeling, C. G. Cameron, S. A. McFarland and B. Dietzek, *Chem. Eur. J.*, 2020, **26**, 14844–14851.
- 15 K. L. Smitten, P. A. Scattergood, C. Kiker, J. A. Thomas and P. I. P. Elliott, *Chem. Sci.*, 2020, **11**, 8928–8935.
- 16 H. J.-P. Ryser and R. Hancock, *Science*, 1965, **150**, 501–503.
- 17 W. C. Shen and H. J. Ryser, *Proc. Natl. Acad. Sci.*, 1978, **75**, 1872–1876.
- 18 M. Green and P. M. Loewenstein, *Cell*, 1988, **55**, 1179–1188.
- 19 A. D. Frankel and C. O. Pabo, *Cell*, 1988, **55**, 1189–1193.
- 20 D. J. Mitchell, L. Steinman, D. T. Kim, C. G. Fathman and J. B. Rothbard, *J. Pept. Res.*, 2000, **56**, 318–325.
- 21 J. S. Wadia, R. V. Stan and S. F. Dowdy, *Nat Med*, 2004, **10**, 310–315.
- 22 H. D. Herce, A. E. Garcia and M. C. Cardoso, *J. Am. Chem. Soc.*, 2014, **136**, 17459–17467.



- 23C. Allolio, A. Magarkar, P. Jurkiewicz, K. Baxová, M. Javanainen, P. E. Mason, R. Šachl, M. Cebecauer, M. Hof, D. Horinek, V. Heinz, R. Rachel, C. M. Ziegler, A. Schröfel and P. Jungwirth, *Proc Natl Acad Sci USA*, 2018, **115**, 11923–11928.
- 24J. B. Rothbard, T. C. Jessop, R. S. Lewis, B. A. Murray and P. A. Wender, *J. Am. Chem. Soc.*, 2004, **126**, 9506–9507.
- 25J. Rothbard, T. Jessop and P. Wender, *Adv. Drug Delivery Rev.*, 2005, **57**, 495–504.
- 26S. M. Fuchs and R. T. Raines, *Protein Science*, 2009, **14**, 1538–1544.
- 27N. Sakai and S. Matile, *J. Am. Chem. Soc.*, 2003, **125**, 14348–14356.
- 28M. Nishihara, F. Perret, T. Takeuchi, S. Futaki, A. N. Lazar, A. W. Coleman, N. Sakai and S. Matile, *Org. Biomol. Chem.*, 2005, **3**, 1659.
- 29G. Tünnemann, G. Ter-Avetisyan, R. M. Martin, M. Stöckl, A. Herrmann and M. C. Cardoso, *J. Pept. Sci.*, 2008, **14**, 469–476.
- 30U. Neugebauer, Y. Pellegrin, M. Devocelle, R. J. Forster, W. Signac, N. Moran and T. E. Keyes, *Chem. Commun.*, 2008, 5307.
- 31J. Brunner and J. K. Barton, *Biochemistry*, 2006, **45**, 12295–12302.
- 32C. A. Puckett and J. K. Barton, *J. Am. Chem. Soc.*, 2009, **131**, 8738–8739.
- 33A. Gross, H. Alborzinia, S. Piantavigna, L. L. Martin, S. Wölfl and N. Metzler-Nolte, *Metallomics*, 2015, **7**, 371–384.
- 34A. Kloß, P. Henklein, D. Siele, M. Schmolke, S. Apcher, L. Kuehn, P. W. Sheppard and B. Dahlmann, *Eur. J. Pharm. Biopharm.*, 2009, **72**, 219–225.
- 35S. H. van Rijt, H. Kostrhunova, V. Brabec and P. J. Sadler, *Bioconjugate Chem.*, 2011, **22**, 218–226.
- 36L. Blackmore, R. Moriarty, C. Dolan, K. Adamson, R. J. Forster, M. Devocelle and T. E. Keyes, *Chem. Commun.*, 2013, **49**, 2658.
- 37L. Cosgrave, M. Devocelle, R. J. Forster and T. E. Keyes, *Chem. Commun.*, 2010, **46**, 103–105.
- 38A. Martin, A. Byrne, C. S. Burke, R. J. Forster and T. E. Keyes, *J. Am. Chem. Soc.*, 2014, **136**, 15300–15309.
- 39A. Byrne, C. S. Burke and T. E. Keyes, *Chem. Sci.*, 2016, **7**, 6551–6562.
- 40K. S. Gkika, A. Byrne and T. E. Keyes, *Dalton Trans.*, 2019, **48**, 17461–17471.
- 41C. S. Burke, A. Byrne and T. E. Keyes, *Angew. Chem. Int. Ed.*, 2018, **57**, 12420–12424.
- 42R. Sutherland, *Science*, 1988, **240**, 177–184.
- 43R. M. Sutherland, *Cancer*, 1986, **58**, 1668–1680.

- 44G. Mehta, A. Y. Hsiao, M. Ingram, G. D. Luker and S. Takayama, *J. Controlled Release*, 2012, **164**, 192–204.
- 45W. Metzger, D. Sossong, A. Bächle, N. Pütz, G. Wennemuth, T. Pohlemann and M. Oberringer, *Cytotherapy*, 2011, **13**, 1000–1012.
- 46L. C. Kimlin, G. Casagrande and V. M. Virador, *Mol. Carcinog.*, 2013, **52**, 167–182.
- 47E. Leary, C. Rhee, B. T. Wilks and J. R. Morgan, *SLAS Technol*, 2018, **23**, 231–242.
- 48S. Mohapatra, S. Nandi, R. Chowdhury, G. Das, S. Ghosh and K. Bhattacharyya, *Phys. Chem. Chem. Phys.*, 2016, **18**, 18381–18390.
- 49M. J. Allen and T. J. Meade, *J Biol Inorg Chem*, 2003, **8**, 746–750.
- 50M. J. Allen, K. W. MacRenaris, P. N. Venkatasubramanian and T. J. Meade, *Chem. Biol.*, 2004, **11**, 301–307.
- 51E. L. Que, E. J. New and C. J. Chang, *Chem. Sci.*, 2012, **3**, 1829.
- 52J. Liu, Y. Chen, G. Li, P. Zhang, C. Jin, L. Zeng, L. Ji and H. Chao, *Biomaterials*, 2015, **56**, 140–153.
- 53C. Sanchez-Cano, I. Romero-Canelón, K. Geraki and P. J. Sadler, *J. Inorg. Biochem.*, 2018, **185**, 26–29.
- 54N. S. Bryce, J. Z. Zhang, R. M. Whan, N. Yamamoto and T. W. Hambley, *Chem. Commun.*, 2009, 2673.
- 55K. Lin, Z.-Z. Zhao, H.-B. Bo, X.-J. Hao and J.-Q. Wang, *Front. Pharmacol.*, 2018, **9**, 1323.
- 56A. Raza, S. A. Archer, S. D. Fairbanks, K. L. Smitten, S. W. Botchway, J. A. Thomas, S. MacNeil and J. W. Haycock, *J Am Chem Soc*, 2020, **142**, 4639–4647.
- 57H. Kurokawa, H. Ito, M. Inoue, K. Tabata, Y. Sato, K. Yamagata, S. Kizaka-Kondoh, T. Kadonosono, S. Yano, M. Inoue and T. Kamachi, *Sci Rep*, 2015, **5**, 10657.
- 58A. Raza, H. E. Colley, E. Baggaley, I. V. Sazanovich, N. H. Green, J. A. Weinstein, S. W. Botchway, S. MacNeil and J. W. Haycock, *Sci Rep*, 2017, **7**, 10743.
- 59K. Mizukami, A. Katano, S. Shiozaki, T. Yoshihara, N. Goda and S. Tobita, *Sci Rep*, 2020, **10**, 21053.
- 60R. I. Dmitriev, A. V. Zhdanov, Y. M. Nolan and D. B. Papkovsky, *Biomaterials*, 2013, **34**, 9307–9317.
- 61A. J. Nichols, E. Roussakis, O. J. Klein and C. L. Evans, *Angew. Chem. Int. Ed.*, 2014, **53**, 3671–3674.
- 62T. Liu, I. Kempson, M. de Jonge, D. L. Howard and B. Thierry, *Nanoscale*, 2014, **6**, 9774–9782.

- 63E. A. Alemán, C. D. Shreiner, C. S. Rajesh, T. Smith, S. A. Garrison and D. A. Modarelli, *Dalton Trans.*, 2009, 6562.
- 64R. N. T. Kankanamage, A. B. Ghosh, D. Jiang, K. Gkika, T. Keyes, L. A. Achola, S. Suib and J. F. Rusling, *Chem. Res. Toxicol.*, 2020, **33**, 2072–2086.
- 65B. C. Hoffknecht, P. Prochnow, J. E. Bandow and N. Metzler-Nolte, *J. Inorg. Biochem.*, 2016, **160**, 246–249.
- 66Uptake studies were also carried out using live HeLa and MCF 7 cells where the Os(II) bis-octaarginine conjugate remained cell membrane impermeable, .
- 67S. Futaki, T. Suzuki, W. Ohashi, T. Yagami, S. Tanaka, K. Ueda and Y. Sugiura, *J. Biol. Chem.*, 2001, **276**, 5836–5840.
- 68S. Futaki, I. Nakase, T. Suzuki, Zhang and Y. Sugiura, *Biochemistry*, 2002, **41**, 7925–7930.
- 69R. I. Dmitriev, H. M. Ropiak, G. V. Ponomarev, D. V. Yashunsky and D. B. Papkovsky, *Bioconjugate Chem.*, 2011, **22**, 2507–2518.
- 70L. J. Arnold, A. Dagan, J. Gutheil and N. O. Kaplan, *Proc. Natl. Acad. Sci.*, 1979, **76**, 3246–3250.
- 71S. Al-Taei, N. A. Penning, J. C. Simpson, S. Futaki, T. Takeuchi, I. Nakase and A. T. Jones, *Bioconjugate Chem.*, 2006, **17**, 90–100.
- 72S. M. Fuchs and R. T. Raines, *Cellular and Molecular Life Sciences*, 2006, **63**, 1819–1822.
- 73C. Dolan, R. D. Moriarty, E. Lestini, M. Devocelle, R. J. Forster and T. E. Keyes, *J. Inorg. Biochem.*, 2013, **119**, 65–74.
- 74J. E. Aubin, *J Histochem Cytochem.*, 1979, **27**, 36–43.
- 75Y. Liu, P. Zhang, X. Fang, G. Wu, S. Chen, Z. Zhang, H. Chao, W. Tan and L. Xu, *Dalton Trans.*, 2017, **46**, 4777–4785.
- 76S. M. Fuchs and R. T. Raines, *Biochemistry*, 2004, **43**, 2438–2444.
- 77X. Wang, Y. Xie, M. Huang, L. Yao, Y. Wang, Y. Fei, J. Ma and L. Mi, *IEEE J. Select. Topics Quantum Electron.*, 2019, **25**, 1–6.
- 78Y. Li, L. M. Almassalha, J. E. Chandler, X. Zhou, Y. E. Stypula-Cyrus, K. A. Hujsak, E. W. Roth, R. Bleher, H. Subramanian, I. Szleifer, V. P. Dravid and V. Backman, *Exp. Cell Res.*, 2017, **358**, 253–259.

## Chapter 5: Ru(II)/BODIPY core co-encapsulated ratiometric nanotools for intracellular O<sub>2</sub> in live cancerous cells.

*Published in Chem. Biol, 2021.*

Karmel S. Gkika, Anna Kargaard, Christopher S. Burke,  
Ciaran Dolan, Andreas Heise and Tia E. Keyes.

### Contributions:

**Karmel S. Gkika:** Preparation of the tris-heteroleptic Ru(II) complex, the structural and photophysical characterisation of precursor compounds and nanoparticles and the cell studies. Primary author and co-contributor to the experimental design, execution, analysis and manuscript preparation and revision.

**Dr. A. Kargaard:** Contribution towards the experimental design and carried out stepwise fabrication of the nanoparticle materials. Discussion and revision of the manuscript.

**Dr. Christopher S. Burke:** Preparation of bpybenzCOOH ligand. Revision of the manuscript.

**Dr. Ciaran Dolan:** : Preparation of the BODIPY reference compound and revision of the manuscript.

**Prof. Andreas Heise:** Project management and discussion and revision of the manuscript.

**Prof. Tia E. Keyes:** Project conceptualization and management, discussion, and revision of the manuscript.

Supporting information associated with this chapter can be found in **Appendix D**.

## 5.1 Abstract

Oxygen is a crucial reagent in many biochemical processes within living cells and its concentration can be an effective marker in disease, particularly in cancer where tissue hypoxia has been shown to indicate tumour growth. Probes that can reflect oxygen concentration and distribution using ratiometric signal can be applied to a range of conventional methods without the need for specialised equipment are particularly useful. The preparation and in-cellulo study of luminescent ratiometric core-shell nanoparticles is presented. Here, a new lipophilic and oxygen responsive Ru(II) tris-heteroleptic polypyridyl complex is co-encapsulated with a reference BODIPY dye into the core of poly-L-lysine coated polystyrene particles. Co-core encapsulation ensures oxygen response but reduces impact of the environment on both probes. Single wavelength excitation of the particles, suspended in aqueous buffer, at 480 nm triggers well-resolved dual emission from both dyes with peak maxima at 515 nm and 618 nm. A robust ratiometric oxygen response is observed from water, with a linear dynamic range of 3.6 to 262  $\mu\text{M}$  which matches well to typical biological ranges. The uptake of RuBDP NPs was found to be cell line dependent but in cancerous cell lines the particles were strongly permeable with late endosomal and partial lysosomal co-staining observed within 3 to 4 hours eventually leading to extensive staining of the cytoplasm. Co-localisation of the ruthenium and BODIPY emission confirm that the particles remain intact in-cellulo with no indication of dye leaching. The ratiometric  $\text{O}_2$  sensing response of the particles in-cellulo was demonstrated using a plate-based assay and by confocal xy $\lambda$  scanning of cells exposed to hypoxic conditions.

## 5.2 Introduction

Molecular oxygen ( $\text{O}_2$ ) plays a central role in the biochemistry of mammalian cells including in oxidative phosphorylation, production of reactive oxygen species and hypoxia response.<sup>1-3</sup> Hypoxia, a reduction in tissue oxygen concentration below normal levels, is associated with a number of disease states including tissue injury and metastasis in cancer. It has also been identified as a marker of radiotherapeutic resistance in cancer disease.<sup>4</sup> Indeed, recently, the Nobel Prize in Physiology and Medicine was awarded for the discoveries made on the molecular response and adaptation of cells to oxygen availability.<sup>5</sup> Reliable and quantitative oxygen sensors with real-time responsivity that can be deployed within the cellular environment, are of significant biomedical value, including for prognosis and therapy.<sup>6-8</sup>

Although there are a number of examples of very effective oxygen sensing luminescent probes reported for in-cell sensing, they primarily focus on phosphorescence lifetime imaging which is a rather specialist technique.<sup>9-11</sup> Whereas for widest application, probes that are amenable to instrumentation such as fluorescence microscopy and plate reader assays that are widely available within biology laboratories are ideally required. Such applications require that sensing and mapping of intracellular O<sub>2</sub> be based on intensity rather than lifetime measurements.<sup>12,13</sup>

Luminescent metal complexes are attractive probes for sensing of O<sub>2</sub> in live cells due to the following characteristics: (1) facile photophysical tuning by metal center *i.e.* Ru(II) or Ir(III) or ligand substitution<sup>14-18</sup>, (2) red emission that coincides well with the photobiological optical window (650 – 950 nm) and avoids interfering autofluorescence from biological media, (3) good quantum yield, (4) long-lived, triplet-based excited states (*i.e.* hundreds ns to ~ 3 μs), that provides oxygen sensitivity and can be exploited in time-gating to eliminate background,<sup>19</sup> and (5) the ability to incorporate ligand functionalities for post modification such as the attachment of targeting vectors.<sup>20-25,26-30</sup> The latter has been instrumental in overcoming a key limitation in application of metal complex oxygen probes in cellular imaging. Metal complexes because of their mass, charge and relative hydrophilicity, are typically not cell membrane permeable, but coupling to cargo carrying moieties can promote permeation, enabling their application in monitoring of oxygen levels even at the level of specific cellular organelles as reported in the case of the nuclear-targeting Ru(II) bis-bpy (bpy = 2,2'-bipyridine) complex.<sup>31</sup>

A significant drawback of intensity-based measurement for sensing is that even for probes with excellent responsivity, selectivity and large linear range, the intensity of emission is influenced by many parameters beyond the target analyte. These include technical issues around stability of the excitation source, detector drift, stray light, and physiochemical issues such as, photodamage, leaching of probe or interaction with other species within the cellular environment, for example protein or membrane. Also, if the probe is inhomogeneously distributed within the sensing environment this will affect intensity which is a key issue in cells.

Ratiometric sensing where probe signal is referenced to a stable emission from a species that does not respond to environment, but will be equally subject to fluctuations in the light source intensity or detector sensitivity etc., is a useful solution to this issue.<sup>32,33</sup> Such ratiometric

response to O<sub>2</sub> have been demonstrated both in molecular probes<sup>34-39</sup> and in particle-based sensors.<sup>40-49</sup>

In practice, in ratiometric sensing it is important to ensure that both probe and reference signal can be generated with a single excitation source. One approach taken has been to excite the reference indirectly through energy transfer from the O<sub>2</sub> indicator which is directly excited. Usually achieved by a Förster Resonance Energy Transfer (FRET), the extent of energy transfer is itself influenced by quenching and so the ratiometric signal is modulated by molecular oxygen.<sup>50</sup> Such FRET based ratiometric probes can be challenging to build, as it can be difficult to ensure that competing photophysical or photochemical processes that can be influenced by the environment, such as photoinduced electron transfer quenching, do not occur.<sup>51</sup> Although this FRET based approach has primarily been demonstrated in molecular species, it has also been demonstrated in conjugated polymer nanoparticles.<sup>32,52</sup>

An alternative, and more direct approach, is to build structures in which both signal and reference luminophores are both excited at the same wavelength, but that emit at different and distinguishable wavelengths. This is a challenge for purely organic fluorophores but is feasible where probe or reference is Stokes shifted; thus, metal complex luminophores are attractive for use in such systems. We recently demonstrated this approach in a ruthenium-BODIPY probe-reference dyad used as a ratiometric probe for oxygen sensing in non-aqueous media. Negligible electronic cross-talk between the photoactive moieties is an essential criteria for this approach.<sup>53</sup>

While molecular species have been widely explored in ratiometric sensing, there are particular advantages to encapsulating sensing species in particles, particularly for sensing within heterogenous environments, such as in the living cell. In relation to gaseous species such as oxygen, particles can isolate the sensor and reference from any confounding environmental impact the cellular interior may have on the photophysics of the probe and reference. Particles also can be very stable, may promote uptake through endocytosis and can, depending on materials, show low cytotoxicity relative to molecular species.<sup>54</sup> Ratiometric particle-based approaches frequently involve incorporation of both the O<sub>2</sub>- sensitive component and reference probe in a single system for built-in correction of the O<sub>2</sub> response.<sup>55-62</sup> Examples include ratiometric dual-wavelength emission at 800 nm and 670 nm reported for single excitation of polystyrene nanoparticles doped with Pd meso-tetraphenylporphyrin and DY-635 reference dye resulted.<sup>58</sup> Kopelman and co-workers reported ratiometric nanosensors incorporating an

O<sub>2</sub>-insensitive reference dye such as Alexa 647 with the O<sub>2</sub>-sensitive and NIR emitting Pd-tetra- (4-carboxyphenyl) tetrabenzoporphyrin dendrimer.<sup>63</sup> Papkovsky *et al.* incorporated a phosphorescent O<sub>2</sub> sensor dye, PtTFPP, and poly(9,9-dioctylfluorene) (PFO) reference dye also acting as a FRET donor, in a single nanoparticle system for multimodal O<sub>2</sub> sensing.<sup>60</sup>

However, there are relatively few examples of ratiometric nanoparticle sensors that have been applied to produce quantitative intensity based ratiometric oxygen sensitivity in live cells and none to our knowledge that use direct co-excitation of the probe and reference rather than FRET.

We recently exploited the ratiometric particle-based approach using a core-shell particle design, where the Ru(II) component was conjugated to the poly-lysine shell as oxygen sensor and BODIPY reference was spatially isolated to the polystyrene particle core respectively.<sup>64</sup> These polymer-based particles showed excellent photostability and good ratiometric response to oxygen in aqueous media. However, without pre-treatment with a cationic surfactant, the particles were impermeable to the cell membrane. Furthermore, with the metal complex luminophore located at the exterior of the complex, it is difficult to distinguish environmental impact, on the complex photophysics e.g. from membrane, protein, from that of oxygen.

Conversely, nanoparticles, polymer-based carriers, and liposomes have been used to facilitate uptake and accumulation of ruthenium probes within cells particularly for photodynamic therapy applications.<sup>65–68</sup> Incorporation of ruthenium complexes into nanoparticles can also improve their photophysical properties, by increasing their luminescence quantum yield for example.<sup>69,70</sup>

Here, using a simplified approach, we describe fabrication of a core-shell ratiometric sensor in which both oxygen sensor and reference dye are encapsulated within the particle core, and demonstrate that by isolating the sensor complex to the particle core the poly-L-lysine shell promotes efficient live cell uptake of the nanoparticles. This approach eliminates the need for a membrane permeabilizing reagent and simultaneously permits protection of the probe as well as reference, resulting in a self-referenced oxygen responsive signal that can be observed within live cells.

We demonstrate for the first time, using confocal microscopy and lambda ( $\lambda$ ) scanning, emission spectra ratiometric oxygen response to normoxic and oxygen deprived (hypoxia) conditions in A549 lung carcinoma and HeLa cells. We also demonstrate that this probe is suitable for use in assays with a conventional plate reader.



## 5.3 Experimental

### 5.3.1 Materials

All chemicals and reagents, cell culture media and corresponding components were purchased from Sigma Aldrich (Ireland) and were used as received. Co-localising dyes were purchased from Bio-Sciences and Resazurin agent from PromoKine.

### 5.3.2 Synthesis

The BODIPY reference probe was synthesised as described previously.<sup>71</sup> Ru(II) parent complex was synthesized by modifying the reported synthetic route for preparation of (tris)heteroleptic Ru(II) compounds via an oxalate route.<sup>72</sup> *cis*- Ru(DMSO)<sub>4</sub>Cl<sub>2</sub><sup>72,73</sup> precursor (**1**) and ligands phen-NH<sub>2</sub><sup>74</sup>, bpybenzCOOEt<sup>53</sup> were synthesised according to literature procedures. The synthesis of the intermediate ruthenium compounds (**2**, **3**) is described in the supplementary information.

#### 5.3.2.1 Preparation of Ru(II) parent complex, [Ru(dpp)(phen-NH<sub>2</sub>)(bpybenzCOOEt)][PF<sub>6</sub>]<sub>2</sub> (**4**)

[Ru(dpp)(phen-NH<sub>2</sub>)(ox)] (22.1 mg, 0.031 mmol) was dissolved in acetonitrile (2 mL) prior to the addition of 1 M perchloric acid (2 mL). The mixture was heated to reflux overnight. The red-brown solution was cooled on an ice bath and added in 3 mL stirring water. The Ru-intermediate precipitate was collected and transferred to a hot mixture of bpybenzCOOEt (0.031 mmol) in ethylene glycol (3 mL). Following overnight reflux, the mixture was cooled to RT and was added to stirring aqueous ammonium hexafluorophosphate. The deep red solids were collected via vacuum filtration, washed with water and diethyl ether. Purification was carried out by performing column chromatography on silica gel using 80:20:1 (MeCN/H<sub>2</sub>O/ 20 % w/v KNO<sub>3</sub>). Re-precipitation of product fractions yielded a mixture of geometric isomers of the Ru(II) complex as vivid red solids. Yield isomer mixture: 27.6 mg (72 %). <sup>1</sup>H NMR (600 MHz, MeCN-d<sub>3</sub>) δ (ppm): 8.88-8.78 (dd, 2 H), 8.35- 8.30 (d, 1 H), 8.29-8.14 (m, 7 H), 8.13 – 8.07 (m, 1 H), 8.04- 7.94 (m, 3 H) 7.93-7.83 (m, 1 H), 7.81 – 7.69 (m, 3 H), 7.68 – 7.49 (m, 13 H), 7.48 – 7.31 (m, 2 H), 7.24 – 7.18 (d, 1 H) 5.58 (s, 1 H) 4.40 – 4.34 (q, 2H), 1.41 – 1.35 (t, 3H).

<sup>13</sup>C NMR (600 MHz, MeCN-d<sub>3</sub>) δ (ppm): 165.05, 151.69, 151.56, 147.69, 143.98, 135.13, 133.14, 129.59, 129.26, 129.21, 129.09, 128.54, 128.31, 127.15, 127.10, 126.97, 125.44,

125.16, 124.27, 123.46, 102.75. HR-MS (ESI-TOF) m/z: calculated for C<sub>55</sub>H<sub>41</sub>N<sub>7</sub>O<sub>2</sub>Ru [M-2PF<sub>6</sub>]<sup>+</sup>: 466.6177; found: 466.6657.

### 5.3.2.2 Preparation of poly(styrene) nano-structures and characterization

A triblock copolymer poly(styrene-*b*- $\epsilon$ -benzyloxycarbonyl-L-Lysine-*b*-Fmoc-L-lysine) PS<sub>38</sub>-PZLL<sub>64</sub>-PFL<sub>5</sub> was prepared as previously described.<sup>64</sup> For the first deprotection step of the Fmoc group, the triblock copolymer (0.8 g) was dissolved in 8 ml DMF. To this 2 ml of piperidine was added and the solution stirred for 2 h at room temperature. The resulting polymer was recovered *via* precipitation in diethyl ether. The copolymer was then re-dissolved in chloroform and precipitated in diethyl ether three times and isolated as a white powder (yield: 0.70 g).

To 80 mg of this copolymer the ruthenium complex **4** (10 mg, 0.0082 mmol) was added and the mixture exposed to a Z protecting group deprotection procedure by slowly adding a solution of HBr (33 wt. % in acetic acid) (0.3 mL) at 0 °C to a solution of the copolymer and ligand in trifluoroacetic acid (6 mL).<sup>1</sup> After 4 h, the diblock copolymer/ligand mixture was precipitated in diethyl ether. The precipitate was washed several times with diethyl ether and after drying, was dissolved in DDI water and dialyzed against DDI water using Spectra/Por dialysis membranes (MWCO, 3.5 kDa) for 72 h at room temperature. The product was lyophilized and isolated as an orange powder (yield: 57 mg).

The mini-emulsion polymerization of a 95/5 (v/v) solution of styrene/divinyl benzene (DVB) and BODIPY were carried out in a 10 mL two-neck reactor equipped with a reflux condenser, nitrogen inlet and magnetic stirrer. In a typical reaction, the diblock copolymer PS<sub>38</sub>-PLys<sub>68</sub>/Ru(II)(**4**)<sub>2</sub> mixture (40 mg) was added to the reactor under an inert atmosphere and dissolved in 4.5 mL degassed distilled water. A styrene/DVB monomer solution (0.40 g) was deoxygenated separately for 20 min by bubbling nitrogen through it. The BODIPY dye (0.15 mg) was dissolved in this solution and injected into the reactor. The reaction mixture was left under max stir (1400 rpm) for 5 min, while being kept on an ice bath. The reaction flask was transferred to a heated oil bath (70 °C) and a deoxygenated initiator solution (5 mg of potassium persulfate in 0.5 mL of water) was injected to start the polymerization. The reaction was left to

---

<sup>1</sup>The HBr/TFA step may be omitted for the encapsulation of lipophilic dyes but is necessary when aiming to isolate the carboxyl complex analogue to the particle exterior. See reference [64] for this particle preparation approach.

proceed for 4 hours after which the resulting latex was dialyzed against DDI for 48 hours using Spectra/Por dialysis membranes (MWCO, 3.5 kDa).

### 5.3.3 Instrumentation

<sup>1</sup>H NMR, <sup>13</sup>C NMR and COSY spectra were recorded on a 600 MHz Bruker Spectrophotometer (unless stated otherwise) and processed and calibrated against solvent peaks using Bruker Topspin (v2.1) software. High Resolution Mass Spectrometry (HR-MS) with Electrospray Ionization in positive mode on a Waters Micromass LCT system was carried out at the Mass Spectrometry Facility in University College Dublin. Thin layer chromatography (TLC) was performed on glass silica gel (Merck, 250 μm thickness) or C18 plates (Sorbent Technologies, 250 μm thickness).

Electronic absorption spectra were acquired on a Jasco V670 UV/vis NIR spectrophotometer using a quartz cuvette with a pathlength of 1 cm. Fluorescence spectra were collected on a Varian Cary Eclipse Fluorescence Spectrofluorometer with background correction. Luminescent lifetime data were acquired up to 10, 000 counts using a Time Correlated Single Photon Counting (TCSPC) system by PicoQuant with laser excitation source a 450 nm. PicoQuant NanoHarp and TimeHarp software were used for data analysis and fitting. The emission spectra and lifetimes were collected also under deaerated conditions. All photophysical measurements were performed at room temperature (293 K) and in triplicate (n=3). Luminescence quantum yield (φ) was determined using the relative method by comparing with the luminescence intensity of [Ru(bpy)<sub>3</sub>]<sup>2+</sup> as the standard sample using the following equation:

$$\phi_{\text{sample}} = \phi_{\text{standard}} \times \frac{A_{\text{sample}}}{A_{\text{standard}}} \times \frac{F_{\text{sample}}}{F_{\text{standard}}} \times \left( \frac{n_{\text{sample}}}{n_{\text{standard}}} \right)^2$$

Where A is the absorbance at the excitation wavelength, F is the area under the corrected emission spectrum and n is the refractive index of the solvent.

Delsa Nano C Submicron Particle Size and Zeta Potential Particle Analyzer with the standard size cell accessory were used for Dynamic Light Scattering (DLS) and zeta potential measurements. Scanning Electron Microscopy was carried out on the Hitachi S3400 Variable Pressure SEM.

RuBDP NPs were sonicated for 20 minutes at room temperature prior to characterization or cell culture studies.

### 5.3.4 Oxygen Calibration Studies

RuBDP NPs were dissolved in PBS (pH 7.4) at 0.01 % w/v. Following purging of the solution with nitrogen for 20 minutes at room temperature, the solution was allowed to re-aerate whilst recording emission spectra at various oxygen concentrations measured in  $\mu\text{mol/L}$  using a PreSense Oxygen Probe. The emission spectra were collected with an excitation and emission slit width of 10 nm. Oxygen calibration curves were constructed (n=3).

### 5.3.5 Plate reader-based ratiometric O<sub>2</sub> response assay

For the assessment of oxygen quenching in a plate reader-based assay, samples of RuBDP NPs ( $4.5 \mu\text{g mL}^{-1}$ ) were dispensed in 100  $\mu\text{l}$  aliquots into three wells of a 96-well plate and treated with sodium sulfite ( $\text{Na}_2\text{SO}_3$ ;  $5 \text{ mg mL}^{-1}$ ). The emission spectra of RuBDP NPs were recorded using a CLARIOstar (plus) (v 5.70) plate reader with excitation at 480 nm and emission range of 505 nm to 840 nm. The concentration of oxygen was monitored and measured in  $\mu\text{mol/L}$  using a PreSense Oxygen Probe and an Oxygen calibration curve was constructed.

A549 cells were seeded at  $10^4$  cells/ well in 100  $\mu\text{l}$  media for 24 h at 37 °C under 5 % v/v CO<sub>2</sub>. RuBDP NPs were added at uptake conditions,  $4.5 \mu\text{g mL}^{-1}$ / 4 h. The cells were then washed with PBS ( $\times 2$ ) prior to exposure to sodium sulfite ( $5 \text{ mg mL}^{-1}$ ). The intracellular NP ratiometric response to changing oxygen concentration following  $\text{Na}_2\text{SO}_3$  treatment, was monitored by recording the emission spectra using a CLARIOstar (plus) (v 5.70) plate reader with excitation at 480 nm and emission range of 505 nm to 840 nm.

### 5.3.6 Cell Culture

Minimum Essential Medium Eagle (MEME) supplemented with 10 % foetal bovine serum (FBS), 1 % penicillin/ streptomycin and L-Glutamine (2mM) was used as HeLa cell culture media. MEME supplemented with 10 % FBS, 2mM L-Glutamine and 1 % Non-essential amino acids was used to subculture MCF 7 cells. Ham's F12K supplemented with 10 % FBS and L-Glutamine (2mM) was used to subculture A549 cells. CHO Cell culture media was composed of F-12 Ham/ DMEM media (1:1) supplemented with 10 % FBS and 1 % penicillin/ streptomycin. Cells were grown at 37 °C with 5 % CO<sub>2</sub> and harvested or split at 90 % confluency using 1X Trypsin. PBS was supplemented with 1.1mM MgCl<sub>2</sub> and 0.9mM CaCl<sub>2</sub>.

### 5.3.7 RuBDP NP uptake

CHO, HeLa and A549 cells were seeded at  $1.5 \times 10^5$  cells in 35 mm glass-bottom culture dish (Ibidi, Germany) of 1.5 mL total volume and cultured for 2 days at 37 °C with 5 % CO<sub>2</sub>. The growth medium was removed and RuBDP NPs were added at 4.5 µg/ mL. Following 4 h incubation the cells were washed with supplemented PBS three times and imaged directly using a Leica TSP DMI8 confocal microscope (100 X oil immersion objective lens unless stated otherwise) with a heated stage at 37 °C and a O<sub>2</sub>, CO<sub>2</sub> chamber was used for the oxygen mapping studies. RuBDP NPs were excited using a 480 nm white light laser and the emission range was set to 505 to 550 nm for the BODIPY component and 569 to 850 nm for the Ru(II) component. DRAQ7 was added (3 µM) to distinguish live cells from damaged/ permeabilized cells. The 633 nm laser was used to excite DRAQ7 and emission was collected between 635 – 900 nm. The time-lapse series was carried out using a Nikon Ti2 fluorescence microscope (100 X oil immersion objective lens) with a heated stage at 37 °C and 5 % v/v CO<sub>2</sub>.

### 5.3.8 Cytotoxicity assay

HeLa, CHO, MCF 7 , A549 cells were seeded separately in a 96- well plate in 100 µl media at  $10^4$  cells/ well for 24 h at 37 °C under 5 % CO<sub>2</sub>. RuBDP NPs were added at concentrations between 0.9 and 100 µg mL<sup>-1</sup> in triplicate wells. Control samples were prepared with 1 % PBS. Following 24 h incubation of the nanoparticles, Resazurin reagent was added to each well (10 µl/ well) and incubated for 6 h in the dark at 37 °C. The Alamar blue assay was used to estimate viable cells based on the absorbance measured at 570nm with a background measurement at 600nm using a Tecan plate reader. The assay was performed at n=3. Comparisons between the data were made using two-way ANOVA Post hoc Tukey analysis at 95 % confidence level. Differences between tested groups were considered statistically significant if  $P \leq 0.05$ .

### 5.3.9 Co-localisation studies

Commercially available dyes DAPI, LysoTracker Deep Red (Invitrogen), Rab7a-GFP (CellLight BacMam 2.0, Invitrogen) and MitoTracker Deep Red were used in co-localisation studies for the determination of the localisation of RuBDP NPs following cell uptake. Nuclear staining DAPI dye was added at 3 µM and incubated for 20 min prior to imaging. DAPI was excited using the 405 nm laser and emission was collected between 425 – 580 nm. LysoTracker Deep Red, used for staining of lysosomes, was added at 50 nM and incubated for 75 min prior to imaging ( $\lambda_{exc}$  647 nm,  $\lambda_{em}$  range: 650 – 800 nm). Rab7a-GFP, used to stain late endosomes,

was added to the cell dish and incubated overnight at 37 °C prior to addition of RuBDP NPs. Rab7a-GFP was excited using a 488 nm white light laser and emission was collected between 490 nm – 540 nm. MitoTracker Deep Red (25 nM) was incubated for 40 min prior to imaging and was excited at 644 nm with emission collected between 650 – 800 nm. Following incubation, dye/growth medium was removed, and cells were washed with supplemented PBS prior to imaging. Fluorescence intensity profiles were obtained using ImageJ.

## 5.4 Results and discussion

### 5.4.1 Synthesis

The synthetic route to the metal complex, reference probe and the oxygen sensor core shell nanoparticles are summarized in Scheme 5.1. The oxygen insensitive BODIPY reference compound; 2, 6 diethyl- 1, 3, 5, 7- tetramethyl- 8- (2-fluorophenyl) – 6 methoxy- 1,5-naphthyridine- 4, 4'- difluoroboradiazaindacene was prepared as reported previously.<sup>71</sup>

In an effort to improve the photophysical response of the Ru(II) oxygen sensor, we prepared a novel tris-heteroleptic complex;  $[\text{Ru}(\text{dpp})(\text{phen-NH}_2)(\text{bpybenzCOOEt})]^{2+}$ . Ru(II) complexes comprising of 4,7-diphenyl-1,10- phenanthroline (dpp) ligands have been shown extensively, to promote sensitivity to O<sub>2</sub>.<sup>75-81</sup> The bpybenzCOOEt was selected as a counter-ligand along with diphenyl phenanthroline to increase lipophilicity to facilitate the PS core encapsulation.

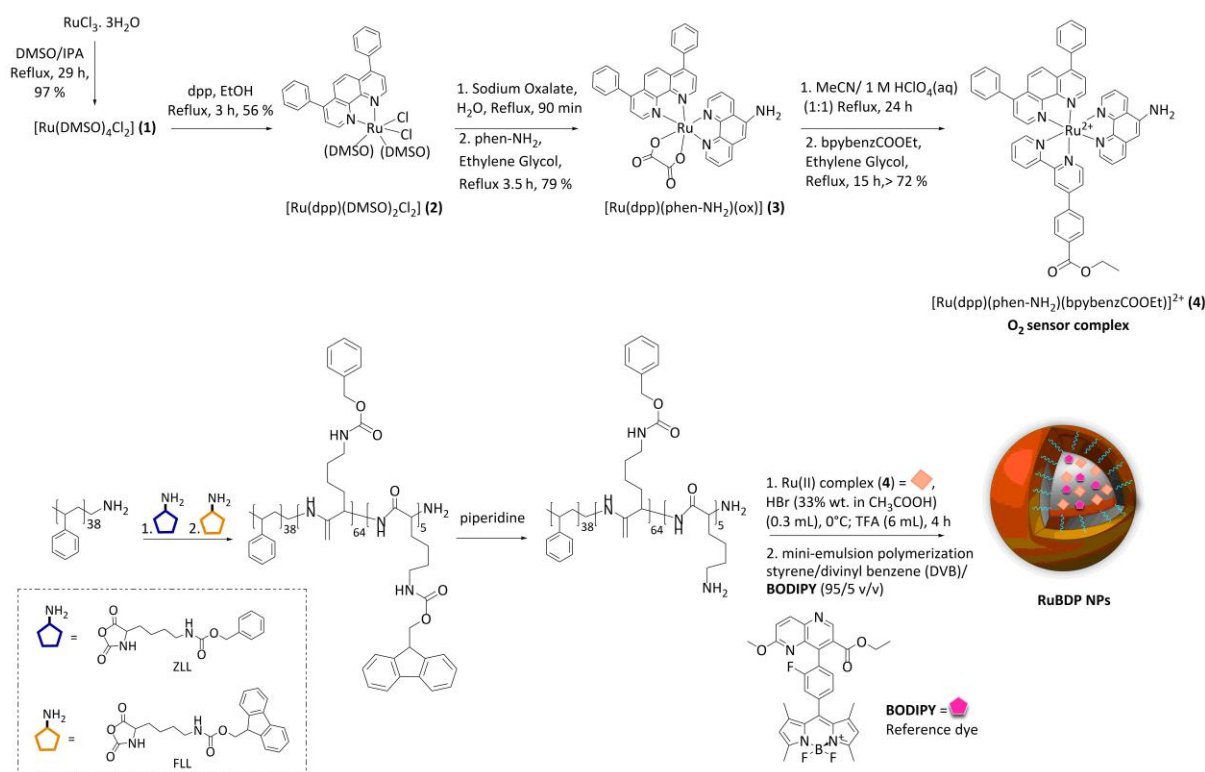
This tris-heteroleptic Ru(II) polypyridyl sensor was synthesised in high yield via an oxalate intermediate (**3**) to form the tris-heteroleptic Ru(II) complex (**4**), through a method adapted from one previously reported by us.<sup>72</sup>

<sup>1</sup>H NMR, <sup>13</sup>C NMR, COSY and Mass Spectrometry were used to confirm the structure and purity of the resulting complex. <sup>1</sup>H NMR showed the expected inequivalence of dpp and phen-NH<sub>2</sub>, arising from the *cis*- configuration of the bidentate complex, across the signals in the aromatic region of the <sup>1</sup>H NMR spectrum. The ester moiety of bpybenzCOOEt was confirmed present from the characteristic quartet and triplet signals in the aliphatic region of the <sup>1</sup>H NMR spectrum integrating to 2 H and 3 H at 4.36 ppm and 1.34 ppm respectively. Coupling interaction between these protons was confirmed by COSY analysis. HRMS confirmed a mass cluster with Ru isotope pattern that corresponded to  $[\text{M} - 2\text{PF}_6^-]^+$  (m/z calculated: 466.6177; found: 466.6657).

The Ru(II) polypyridyl complex was co-encapsulated with the O<sub>2</sub> insensitive BODIPY reference probe, into the nanoparticle core for self-referenced ratiometric luminescence response to oxygen. The rationale for this approach was that with co- encapsulation into a core-

shell structure, probe and reference are both protected from any environmental effects which may interfere with the ratiometric response signal. The shell offering spatial separation between probes and environment, and the high oxygen permeability of polystyrene along with the enhanced O<sub>2</sub> sensitivity of dpp-coordinated Ru(II) would permit a stable and selective O<sub>2</sub> access to the sensor. Importantly, the exterior of the particle is free for surface modifications such as coating with poly-L-lysine.

Adopting a modified synthesis, the particles were prepared by miniemulsion polymerisation of styrene/divinyl benzene (DVB) using an amphiphilic diblock copolymer poly(styrene-*b*-L-lysine) (PS<sub>38</sub>-PLL<sub>69</sub>) as a surfactant.<sup>64,82,83</sup> The lipophilicity of both BODIPY and Ru(II) complex allowed for their co-encapsulation into the non-polar cross-linked polystyrene core at the miniemulsion step, yielding RuBDP NPs. Physical anchoring of the amphiphilic surfactant rendered the NP surface hydrophilic.



**Scheme 5.1** Route to synthesis of Ru(II) tris- heteroleptic polypyridyl complex (**4**; O<sub>2</sub> sensor) and preparation of self-referenced nanoparticles.

Dynamic light scattering (DLS) was carried out to determine the size, zeta potential and conductivity of the RuBDP NPs in PBS (pH 7.4). The diameter of the particles was measured as 98.2 ± 1.09 nm and the average zeta potential measured was + 25 ± 1.37 mV. The positive charge on the particles can be attributed the polylysine polymer. The spherical shape and size

uniformity of the nanoparticles was confirmed by SEM imaging under 9.00 kV x 37.0k (Fig. S5. 9).

The magnitude of the zeta potential indicates that the particles form a stable dispersion in aqueous buffered solution and indeed it was confirmed that there was no decomposition or precipitate formation over seven months period of the particles in suspension. In addition, the absolute emission intensity and ratio of Ru(II) to BDP emission remained unchanged over this time window (Fig. S5. 10), indicating that there was no leaching of the probes from particle.

In a separate study, to confirm location of the probes within the particle, we soaked the particles in THF as a swelling agent and evaluated the fluorescence spectroscopy of the supernatant following centrifugation of the particles. (Fig. S5. 11). We compared then the supernatant from similarly treatment of our previously reported core-shell RuBODIPY particles, in which Ru is bound to particle surface and BODIPY to core.<sup>64</sup> From the latter we observed release of the ruthenium from the particle outer shell under these conditions, whereas with the co-core encapsulated particles we did not observe any release of ruthenium to the supernatant. This we conclude confirms Ru is confined to the PS core, where PS cross-linkage prevents leaching of the sensor from the core due to size exclusion. Whereas, in both cases, BODIPY, which is smaller, was observed to release on particle swelling.

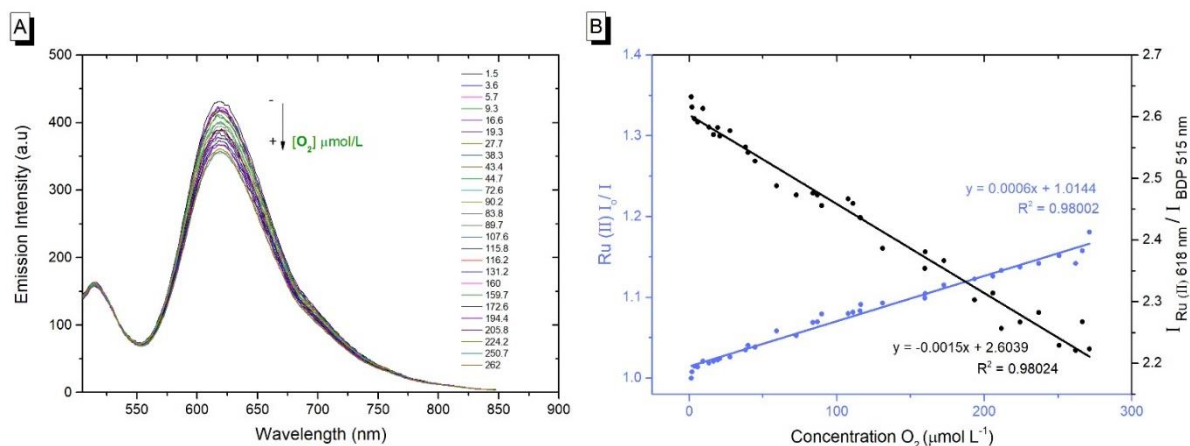
#### 5.4.2 Photophysical Characterisation of RuBDP nanoparticles

The photophysical properties of the parent ruthenium complex was first characterised in acetonitrile, Table 1.  $[\text{Ru}(\text{dpp})(\text{phen-NH}_2)(\text{bpybenzCOOEt})]^{2+}$ , exhibits a metal to ligand charge transfer (<sup>1</sup>MLCT) transition centred  $\lambda_{\text{max}}$  460 nm (Fig. S5. 12). And, when excited at  $\lambda_{\text{max}}$ , exhibits a broad intense emission with a maximum at 622 nm.  $[\text{Ru}(\text{dpp})(\text{phen-NH}_2)(\text{bpybenzCOOEt})]^{2+}$  emission shows strong oxygen sensitivity in acetonitrile. The quantum yield of **4** was measured in aerated and deaerated acetonitrile as  $0.0173 \pm 0.0003$  and  $0.0291 \pm 0.0003$  respectively, using  $[\text{Ru}(\text{bpy})_3]^{2+}$  as the reference standard.<sup>84</sup> The parent complex exhibits monoexponential luminescent decay in acetonitrile with a lifetime,  $\tau \approx 372$  ns under air saturated conditions (Fig. S5. 13). The BODIPY derivative was selected as reference in this study because control studies in solution confirmed lack of quenching or other interactions that might predict cross-talk in the particle. Indeed, as shown below, photophysical properties of the particle confirm probe and reference do not cross talk to any significant extent. Furthermore, both ruthenium and BODIPY derivatives can be simultaneously excited at 480



nm. Iteration of the ratios of probe and reference under this excitation wavelength were carried out in solution to ensure appropriate relative scale of signal and a ratio of 1:2 (BODIPY/Ru(II)) for particle preparation was used then in all particle preparation.

The photophysics of the RuBDP NPs were examined in aqueous PBS solution, pH 7.4, as this was the medium used for biological studies. The photophysical characteristics of the particles correlate well with the solution phase behaviour of the constituent luminophores. The RuBDP particles exhibited dual, well resolved emission signals with maxima of 618 nm and 515 nm attributed to the ruthenium probe and BODIPY reference. While the relative emission intensity of each (Ru and BODIPY) luminophore varies with excitation wavelength, the emission of both probe and reference was retained with no evidence for cross talk. 480 nm was used as excitation throughout subsequent measurements as this gave dual emission with appropriate relative intensity of probe and reference Fig. 5.1A.



**Figure 5.1** (A) RuBDP response to change in oxygen concentration measured in  $\mu\text{mol/L}$ . Emission spectra of RuBDP NPs in PBS (pH 7.4) when excited at 480nm; both excitation and emission slit widths set at 10 nm. (B) Stern-Volmer Plot: the luminescence originating from the ruthenium component decreases with increase in oxygen concentration whilst the BODIPY reference probe is moderately affected ( $n = 3$ ).

As shown in Figure 5.1B the emission intensity of the NP encapsulated Ru(II) varies linearly with  $[\text{O}_2]$  whereas, as expected, the emission intensity of the BODIPY reference probe remains, within experimental error, constant. Calibrating oxygen concentration in the contacting solution using a PreSense Oxygen Probe the emission intensity data was fit to the Stern-Volmer equation (Eqn. 1)<sup>26</sup> (Fig. 5.1B) where the ratiometric intensity data shows good linearity ( $R^2 = 0.9802$ ).

$$\frac{I}{I_0} = \frac{\tau_0}{\tau} = K_{SV}[\text{O}_2] + 1 \quad (1)$$

$$K_{SV} = k_q \tau_o \quad (2)$$

The Stern Volmer quenching constant ( $K_{SV}$ ), was obtained from the slope of the Stern Volmer fit (--) and  $k_q$ , the rate of quenching was found to be  $4.25 \times 10^8 \text{ M}^{-1} \text{ s}^{-1}$  in PBS (pH 7.4), according to Eqn. 2 (where  $\tau_o$  is the lifetime in the absence of oxygen). While the  $\text{O}_2$  permeability of polystyrene is high<sup>85</sup>, the  $k_q$  is lower than metal complex reported in solution, and this is likely attributed to some impedance of the diffusion of oxygen in the PS core or inaccessibility of some metal complex to  $\text{O}_2$  on encapsulation.

The linear dynamic range for ratiometric signal, from the RuBDP particles was measured as 3.6 and 262  $\mu\text{M}$   $\text{O}_2$ , which coincides well with the  $\text{O}_2$  range anticipated in-vitro studies (0 – 250  $\mu\text{M}$ )<sup>13</sup>, spanning oxygen concentrations ranges indicative of hypoxia. Although the magnitude of signal change in response to oxygen is not as large as reported for molecular systems such as porphyrin or iridium coordination compounds, such species typically show high singlet oxygen yields and/or cytotoxicity, compared to the nanoparticle encapsulated complexes reported here, that show limited toxicity even under extended photoirradiation, as discussed *vide infra*.<sup>86-90</sup>

**Table 5.1** Photophysical data of particle dye constituents and RuBDP NPs.<sup>[a]</sup>

Compound	Solvent	$\lambda_{\text{abs}}$ / nm	$\lambda_{\text{em}}$ / nm	$\tau_{\text{aerated}}^{\text{b}}$ / ns	$\tau_{\text{deaerated}}^{\text{b}}$ / ns	$\Phi_{\text{lum}}^{\text{c}}$
						aerated deaerated
<b>[Ru(dpp)(phen-NH<sub>2</sub>)(bpy-benz-COOEt)]<sup>2+</sup> (4)</b>	MeCN	460	626	$371.9 \pm 5.3$	$599.4 \pm 7.3$	$0.0173 \pm$
						$0.0003$
						$0.0291 \pm$
						$0.0004$
<b>BODIPY dye</b>	MeCN	498	512	$3.85 \pm 0.03$	-	-
<b>RuBDP NPs</b>	PBS (pH 7.4)	480	515	$3.87 \pm 0.01$	-	-
			618	$523.0 \pm 12.1$	$708.9 \pm 10.2$	

<sup>[a]</sup> All measurements were performed at room temperature. <sup>[b]</sup> Percentage relative amplitudes are given in parentheses. <sup>[c]</sup> [Ru(bpy)<sub>3</sub>]<sup>2+</sup> was used as a reference standard.

The emission decay of the RuBDP particles was collected under aerated and deaerated conditions. Emission decay from the particles was found to fit to a dual exponential kinetics. In air saturated PBS ( $[\text{O}_2]$  262  $\mu\text{mol/L}$ ) lifetimes of  $523.0 \pm 12.1$  ns and  $3.87 \pm 0.01$  ns were recorded corresponding to the amplitude averaged lifetime of Ru(II) and BODIPY component,

respectively. Upon deaeration ( $[O_2]$   $3.6 \mu\text{mol/L}$ ) the emission lifetime of the Ru(II) component of the decay increased to  $708.9 \pm 10.2$  ns while the BODIPY lifetime remained unchanged (Fig. S5. 14- S5. 15). The photophysical data for the Ru(II)-parent compound, BODIPY core and RuBDP NPs are summarized in Table 5.1.

### 5.4.3 Cell Studies

Having confirmed the RuBDP NP stability in PBS, ratiometric signal and oxygen responsiveness, we next investigated the permeability of the NPs to live cells.

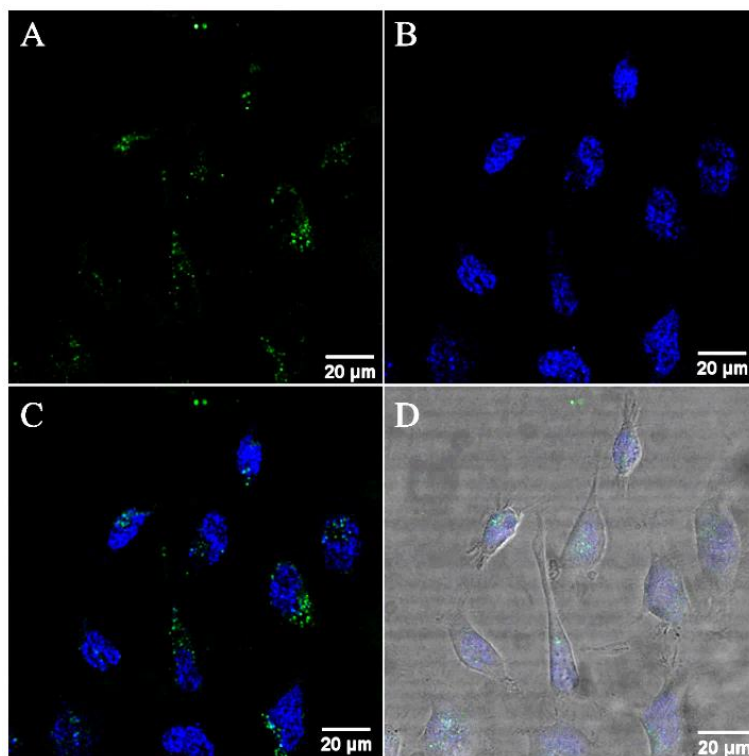
### 5.4.4 Uptake studies in live HeLa, CHO and A549 cell line

The cell uptake of RuBDP nanoparticles was assessed across several concentrations in live HeLa cells over time by incubating the nanoparticles in the absence of light at  $37^\circ\text{C}$  with 5 % v/v  $\text{CO}_2$ . Uptake of the nanoparticles at  $4.5 \mu\text{g mL}^{-1}$  into the cytoplasm is observed to have commenced after 3 h. By 4 h the particles are dispersed throughout the cytoplasm. Critically, in contrast to our previously reported nanoparticle system, uptake was spontaneous and did not require facilitation by solvent or surfactant.<sup>64</sup> The cationic poly-lysine shell of the particles likely promotes interaction with cell membrane. This is in contrast to the previously reported particles, where it would seem that when ruthenium complex was appended to the particle exterior this inhibited uptake.<sup>64</sup>

Consistent with solution studies, 480 nm was used as excitation wavelength in cell imaging to excite both probe and reference. Figure S5. 16 shows the images collected from two channels with range of 505 – 550 nm and 569 – 850 nm, coincident with the BODIPY reference and Ru(II) probe respectively. The spatial coincidence of the two signals confirms the particles are present and that dual emission is observed from each luminophore under this excitation wavelength. The spatial coincidence of each emission signal also confirms that the particle cores are intact.

Co-staining with nuclear staining probe, DAPI, revealed that the RuBDP NPs are excluded from the nucleus but accumulate in the nuclear peripheral environment (Fig. 5.2). Crossing of the nuclear membrane in live cells typically requires interaction with the nuclear pore complex via a small nuclear localization signal (NLS) or via significantly smaller particle size.<sup>91–93</sup>

While nuclear targeting is often desirable in drug delivery/therapeutic applications, nuclear exclusion is preferable for monitoring of oxygen levels in other cellular compartments involved in ATP production and cellular metabolism.<sup>94</sup>



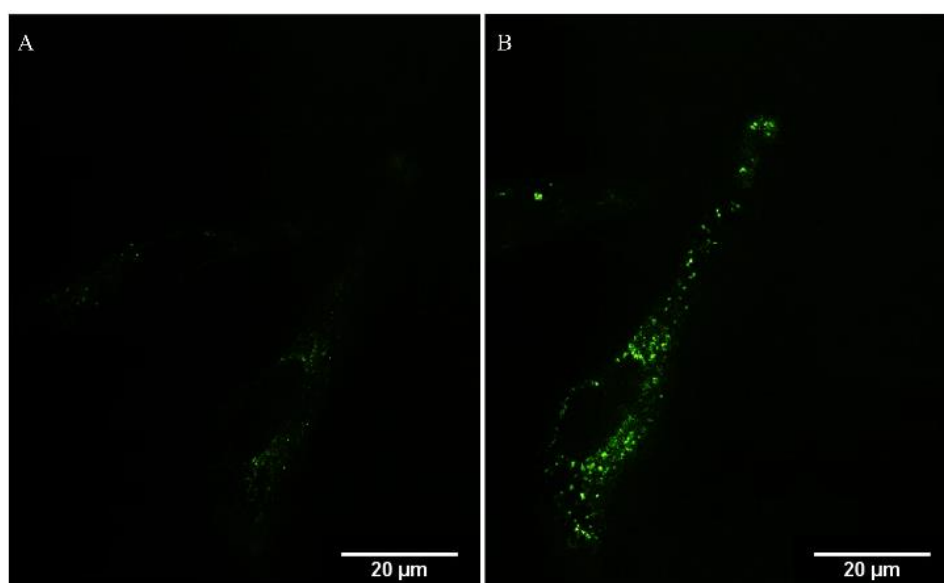
**Figure 5.2** Confocal luminescence images of RuBDP NP uptake at  $4.5 \mu\text{g mL}^{-1}$  in live HeLa cells. Cells were incubated in the absence of light for 4 h. (A) The RuBDP NPs were excited using 480 nm white light laser and the emission for the Ru(II) component was collected between 569 nm and 850 nm. (B) Cells were co-stained with nuclear staining probe, DAPI. (C) Overlay of Ru(II) channel with DAPI. (D) Overlay with brightfield.

Confocal imaging indicated that HeLa cells remain viable following post incubation with RuBDP NPs for 24 h at  $4.5 \mu\text{g mL}^{-1}$  with no evidence for cytotoxicity despite wide cytoplasmic distribution over extended windows (Fig. S5. 17). A time-lapse study was carried out to investigate the fate of RuBDP NPs in live HeLa cells following uptake. HeLa cells were treated with RuBDP NPs at the imaging conditions ( $4.5 \mu\text{g mL}^{-1}$  / 4 h) for uptake (Fig. 5.3A) and were monitored over time using a widefield fluorescence microscope.

Emission from the Ru(II) channel was acquired every 10 minutes overnight on a heated stage ( $37 \text{ }^\circ\text{C}$ ) under an atmosphere of 5 % v/v  $\text{CO}_2$ . As shown in Figure 5.3, emission intensity from the particles increased sharply following 4 h of incubation (Fig. 5.3B). This was also observed by confocal microscopy for HeLa cells pre-treated at the same conditions and imaged post 4 h

of initial incubation. The precise origin of this increase in emission intensity signal from the Ru(II)-component is unknown so far but we tentatively attribute it to endosomal escape of the particles from late stage endosome, where acidity of the environment may impact the Ru intensity.

Contributions from proteolysis of the shell over extended windows in the lysosome, are unlikely given the relatively low partitioning into the lysosome and also continuous co-localisation of the BODIPY and Ru emission signal over the extended range of time scales indicates that irrespective of origin, the particle core remains intact.



**Figure 5.3** Widefield fluorescence images of HeLa cells pre-treated with RuBDP NPs ( $4.5 \mu\text{g mL}^{-1}$ ) and monitored over time. Emission collected from the Ru(II) channel (A) following uptake of the particles and (B) at 4 h of incubation after NP uptake. The Ru(II) component of the NPs was excited at 470 nm using the GFP excitation filter.

Furthermore, comparison with behaviour of the related nanoparticle where Ru was immobilised at the protein surface, persistence of co-localisation indicated that the particle is not proteolyzed in-cellulo under imaging conditions. Future studies will focus on assessing promotion of particle-release from late endosomal structures into other cellular compartments and organelles such as the mitochondria in surface modified structures.<sup>95,96</sup>

RuBDP uptake in a non-cancerous cell line was also studied. Here, CHO cells were incubated with RuBDP NPs under the same conditions ( $4.5 \mu\text{g mL}^{-1}$  for 4 h), however interestingly, at this concentration, in contrast to HeLa and the other cancer cell lines studied *vide infra*, there was no evidence of nanoparticle uptake. Rather the particles adhered to the cell membrane

exterior (Fig. S5. 18). Incubation of CHO cells with increased concentration of  $12 \mu\text{g mL}^{-1}$  NPs for 24 h did lead to particle uptake and non-specific distribution within the cytoplasm (Fig. S5. 18C). However, in addition, at this concentration, cell debris was observed and by confocal imaging on DRAQ7 staining damaged CHO cells were evident.

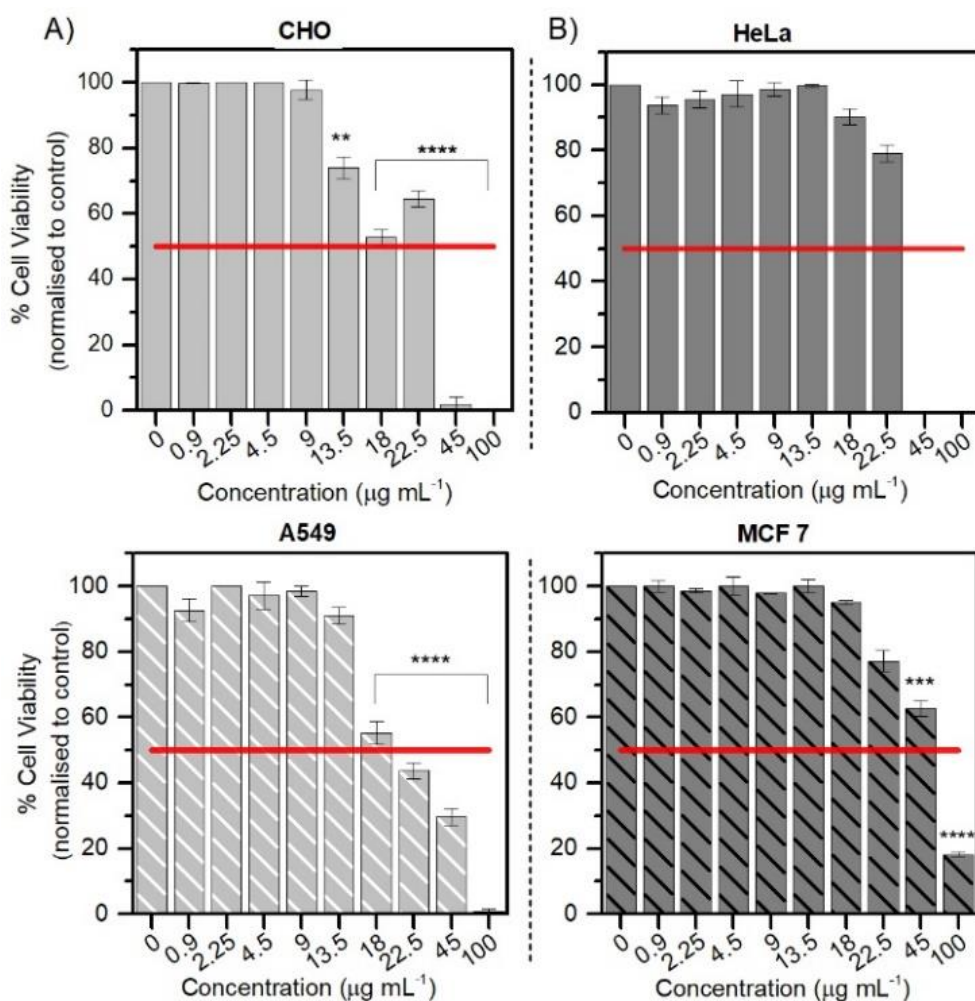
The contrasting uptake between CHO and HeLa is interesting and we speculate may be due to the differences widely noted between cancerous and non-cancer cell lines.<sup>97-100</sup> This includes differences in pathways for endocytosis<sup>101</sup> as well as the composition of the cell membrane which can differ significantly in terms of lipid composition, membrane fluidity and lipid rafts.<sup>102,103</sup> Cancer cells are characterized by a highly negative surface charge due to exposure of phosphatidylserine (PS) at the outer membrane.<sup>104,105</sup>

In order to investigate further, uptake studies were also carried out for a second cancerous cell line, the human lung carcinoma A549 cell line. A549 cells were treated with RuBDP NPs at  $4.5 \mu\text{g mL}^{-1}$  and incubated at  $37 \text{ }^\circ\text{C}$  and  $5 \%$   $\text{CO}_2$ . Similar to HeLa cells the RuBDP nanoparticles were internalized within 3-4 h of incubation and the same punctuate staining was observed throughout the cytoplasm (Fig. S5. 19).

#### **5.4.5 Cytotoxicity**

The Alamar Blue (Resazurin) Viability assay was used to evaluate the cytotoxicity of RuBDP NPs between  $0.9$  and  $100 \mu\text{g mL}^{-1}$  in HeLa, A549 and CHO cells over 24 h in the absence of light at  $37 \text{ }^\circ\text{C}$ . It was found that HeLa and A549 cell lines were remarkably tolerant to the particles up to  $9 \mu\text{g mL}^{-1}$  (Fig. 5.4) which is twice the working concentration of  $4.5 \mu\text{g mL}^{-1}$  used in our confocal imaging studies. Above  $9 \mu\text{g mL}^{-1}$  viability varied depending on the cell line. This may be attributed to the particle uptake mechanism and localization.

The results for the cancer lines, correspond well with the cell imaging where no cell death was observed at  $4.5 \mu\text{g mL}^{-1}$  and decrease in cell viability is observed for the CHO cell line above  $9 \mu\text{g mL}^{-1}$ . As mentioned previously, no particle uptake was observed for CHO cells at the working concentration and non-specific distribution within the cytoplasm could be observed post incubation at high particle concentration ( $12 \mu\text{g mL}^{-1}$ ). In addition, HeLa cells show good tolerance with  $73 \%$  of cells still viable up to  $22.5 \mu\text{g mL}^{-1}$ .



**Figure 5.4** Cell Viability of HeLa, MCF 7 and CHO cells after 24 h exposure to RuBDP NPs over a range of concentrations. Live cells were treated with the nanoparticles followed by addition of Resazurin for 6 h. Absorbance readings at 570 nm with a background at 600 nm were performed. Data were expressed as averaged percentages and compared to non-treated cells.  $P \leq 0.05$ ;  $***P \leq 0.01$ ,  $**** P \leq 0.0001$ .

RuBDP NPs were found to be more toxic towards A549 cells at these concentrations with an  $IC_{50}$  between 18 and 22.5 µg/ mL. Decrease in viability of A549 cells in comparison to HeLa cells may be attributed to an increased rate of nanoparticle uptake as suggested by confocal imaging. Similarly, Platinum(II)-porphyrin nanoparticles were shown to be non-toxic between 5 - 20 µg mL<sup>-1</sup> and concentrations above 40 µg mL<sup>-1</sup> resulted in cluster formation and cell morphological changes.<sup>106</sup> The viability of particle-treated MCF 7 cells, showed these cells had superior tolerance, with an  $IC_{50}$  above 45 µg mL<sup>-1</sup>, ten times the working NP concentration for confocal imaging in A549 and HeLa cells. Overall, from these results the uptake and toxicity of RuBDP NPs is both concentration and cell-line dependent.

#### 5.4.6 Uptake mechanism and co-localization studies

Particle uptake studies in HeLa and A549 cells were also carried out at 4°C. At low temperature, uptake was inhibited with accumulation of RuBDP NPs at the cell surface observed for both cell lines (Fig. S5. 20- S5. 21). And, notably, no particle permeation to the cell interior indicating that uptake occurs through an energy dependent mechanism, likely, endocytosis.

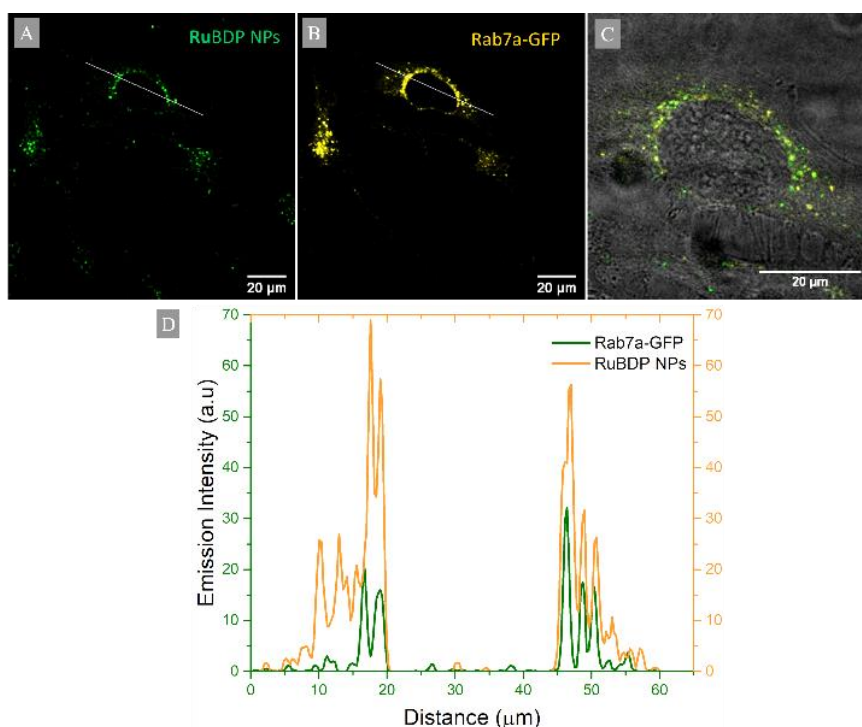
Nanomaterials are widely reported to be transported across the cell membrane of mammalian cells via endocytosis and specifically pinocytosis when the particle size, as is the case here is < 200 nm.<sup>107</sup> Internalization of nanoparticles via an endocytic pathway typically involves multivesicular bodies known as endosomes.<sup>108</sup> To evaluate particle localization was to endosomes, co-localization studies in HeLa and A549 cells were carried out using Late Endosome Rab7a-GFP. Emission Intensity Profiling showed strong co-localization of RuBDP NPs with Rab7a-GFP following uptake at 4.5 µg mL<sup>-1</sup> after 4 h of incubation (Fig. 5.5D). The Pearson's Coefficient, which quantifies the degree of co-localization between the NPs and Rab7a-GFP, was determined to be 0.88. This observation strongly supports the notion that uptake in these cancer lines is through endocytosis where following this mechanism of uptake the RuBDP NPs will be transported by endosomes which mature into late endosomes (LE).

Co-localization studies with LysoTracker Deep Red and MitoTracker Deep Red were carried out to determine the fate of the particles at 4.5 µg mL<sup>-1</sup> following 4 h incubation and transport in late endosomes. Late endosomes and therefore potentially, the NPs can undergo lysosomal fusion, exocytosis or can be released in the cytoplasm and/or then enter cellular compartments and organelles.<sup>109</sup> Co-staining studies with LysoTracker Deep Red revealed a Pearson's coefficient value of 0.32 and thus a low degree of co-localization suggesting only partial lysosomal distribution of RuBDP NPs in HeLa cells (Fig. S5. 23). Whereas, co-staining with MitoTracker Deep Red (Fig. S5. 24) showed that under these conditions, the RuBDP NPs do not localize to the mitochondria.

More homogeneous emission, without the punctuate staining characteristic of endosomal entrapment followed 24 h incubation, suggesting the particles are released to cytoplasm without targeting specific organelles, making them potentially useful oxygen probes. However, another consideration is that quenching of the triplet-excited state of Ru(II) complexes leads to singlet oxygen formation, that can lead to damage of cellular components.<sup>110-112</sup> Therefore, to assess photo-toxicity of RuBDP NPs following uptake in HeLa cells, a ROI of cells was selected for



continuous irradiation at 480 nm. Viability of cells was monitored by presence or absence of nuclear staining DRAQ7 dye. A control sample was also irradiated under the same conditions in the absence of RuBDP NPs and viability was monitored with DRAQ7. As shown in Fig. S5.25, toxicity was observed, but only after two hours of continuous irradiation which would be outside the time interval used in conventional imaging/sensing studies, where irradiation would rarely be continuous over such windows.



**Figure 5.5** Co-localization of RuBDP NPs with late endosomal staining probe in live HeLa cells where: confocal imaging of (A) RuBDP NPs at  $4.5 \mu\text{g mL}^{-1}$  / 4 h (green), (B) Rab7a-GFP (yellow), (C) overlay of RuBDP/Rab7a-GFP channels with the brightfield background. (D) The fluorescence intensity profile of RuBDP NPs and Rab7a-GFP obtained from the line profile across the cell is also shown (ImageJ).

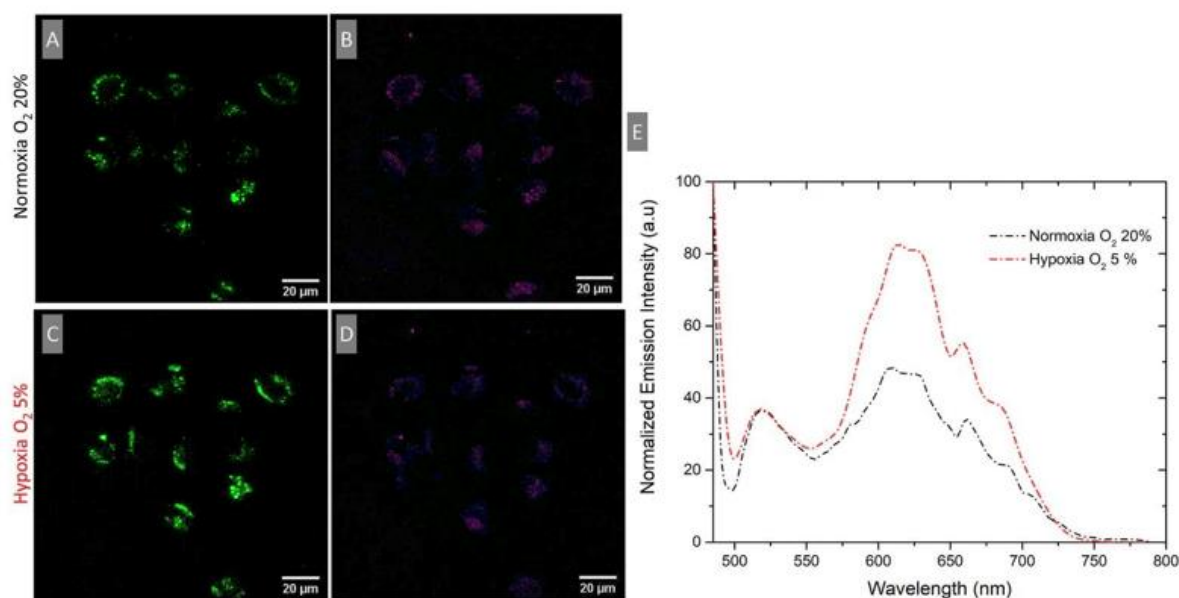
The absence of photo-toxic effects over shorter term may be attributed to the particle stability and enclosure within the LE. This is a key advantage to the RuBDP NPs for continuous real-time oxygen sensing in live cells.

#### 5.4.7 Ratiometric response in induced hypoxic conditions

To evaluate if a ratiometric signal that reflects  $\text{O}_2$  variation can be measured intracellularly, the emission spectrum of intracellular RuBDP NPs was collected using the  $\text{xyl}$  scanning mode of a confocal microscope. The spectra were collected under normoxic (20 %  $\text{O}_2$ ) and hypoxic conditions (5 %  $\text{O}_2$ ). A549 cells were treated with the particles under normoxic conditions, washed with PBS and immediately imaged (Fig. 5.6A,B). The emission spectrum was collected

at this point between 495 and 795 nm at 5 nm intervals using  $\lambda$ . The chamber conditions were adjusted from normoxic to hypoxic by gradually switching to 5 % v/v  $O_2$ . The images are normalised to BODIPY emission intensity, figure 5.6 E, which was observed not to change with oxygen concentration but there is a clear increase in luminescence intensity for the Ru(II) channel was observed during confocal imaging of the same region of cells (Fig. 5.6C) in moving from normoxic to hypoxic conditions. An analogous response was also observed in HeLa cells under the same experimental conditions (Fig. S5. 26). Emission spectra were acquired in this manner for three different cell regions and averaged in Figure 5.6E.

Figure 5.6E shows an approximate two-fold increase in the intensity of the Ru(II) component while the reference BODIPY probe intensity remains unchanged. Using the ratio of  $I_{Ru(II) 616} / I_{BDP 515}$  under hypoxic conditions, the intracellular  $[O_2]$  was estimated to be  $< 2.6 \mu\text{mol L}^{-1}$ .



**Figure 5.6** Confocal imaging of A549 cells treated with RuBDP NPs at  $4.5 \mu\text{g mL}^{-1}$  for 4 h at  $37^\circ\text{C}$ . (A, C) Ru(II) channel (569 – 850 nm) and (B, D) BODIPY channel (505 – 550 nm) under normoxic and hypoxic conditions. (E) Confocal lambda ( $\lambda$ ) scan: emission spectra collected between 495 nm and 795 nm following single excitation at 480 nm at normoxic and hypoxic conditions where both the BODIPY and Ru(II) component emission maximum is observed (n=3).

The particles show good uptake to the cytoplasm, low dark toxicity and phototoxicity and good self-referenced response to oxygen in solution and in cells. Finally, a key motivation in creating ratiometric oxygen sensing particles is that they are suitable for intensity based studies with conventional lab instruments rather than specialised techniques such as lifetime imaging. Therefore, the ratiometric oxygen response of the particles in cells at oxygen levels between

normoxic and hypoxic conditions was assessed using a plate reader-based assay. To establish instrument response (notably the detector sensitivity was greater towards the red region of the spectrum), a plate-based calibration plot was obtained by recording the particle spectra at various oxygen concentrations using a CLARIOStar (plus) reader and a PreSense Oxygen Probe. The emission intensity data was fit to the Stern-Volmer equation as shown in Fig. S5. 27.

A quantitative cell based study was then carried out where A549 cells were pre-treated with RuBDP NPs ( $4.5 \mu\text{g mL}^{-1}$ ) and using a plate reader, the emission spectra of the particles was collected prior to and sequentially in time, following exposure to oxygen scavenger, sodium sulfite<sup>113</sup> (Fig. S5. 28). The absolute emission intensity was naturally lower for the cell encapsulated nanoparticles but the RuBDP NPs showed a quantitative ratiometric response to gradually changing oxygen concentration on incubation of the cells with  $\text{Na}_2\text{SO}_3$  ( $5 \text{ mg mL}^{-1}$ ). The  $[\text{O}_2]$  could be readily quantified as 156.6, 98.9, 72.6 and  $32.8 \mu\text{mol/L}$  at several timepoints by the intracellular probe following treatment with  $\text{Na}_2\text{SO}_3$  using the ratiometric signal with the calibration plot.

## 5.5 Conclusions

The preparation of highly stable and lipophilic ratiometric nanoparticles is described. Here, the probe and reference, an  $\text{O}_2$  sensitive novel Ru(II) complex and BODIPY fluorophore are co-encapsulated in particle polystyrene (PS) core that is decorated with a poly-L-lysine exterior. This approach promotes cell permeability and isolates the core bound components from environmental effects except for oxygen which is PS permeable. Solution studies of the RuBDP NPs confirm sensitive ratiometric response to oxygen with dynamic range that is expected to be suitable for biological studies. The particles were studied in cells. Uptake of RuBDP NPs in cancer cell lines; HeLa and A549 cells was observed at  $4.5 \mu\text{g mL}^{-1}$  within 4 h of incubation at  $37^\circ\text{C}$  but was inhibited at  $4^\circ\text{C}$ . In contrast, the particles were impermeable to CHO cells under these conditions and cell viability studies showed a concentration and cell line dependent cytotoxicity. Dynamic widefield microscopy studies reveal that in cancer cell lines an emission enhancement from the Ru(II) component occurred within a further 4 hours following initial uptake, the origin of which is thought to reflect NP endosomal escape. Although RuBDP NPs can offer a ratiometric response to changes in late-endosomal oxygen levels, future studies will focus on exploiting modifications to the particle exterior to achieve efficient endosomal escape and targeting of specific cellular organelles. Overall, the data

indicates that these probes are suitable for non-invasive, dynamic, and quantitative measurement of oxygen in-cellulo using a plate reader assay or confocal microscopy ( $\text{xy}\lambda$ ) and thus may be a useful tool for monitoring oxygen for mechanistic insights in cancer biology and in diagnostics. Future studies will focus on promoting targeting to key organelles and enhancing the Oxygen response from the sensor.

## 5.6 Supporting Material

Supporting information associated with this chapter can be found in **Appendix D**.

## 5.7 References

- 1 G. L. Semenza, *Science*, 2007, **318**, 62–64.
- 2 T. C. O’Riordan, A. V. Zhdanov, G. V. Ponomarev and D. B. Papkovsky, *Anal. Chem.*, 2007, **79**, 9414–9419.
- 3 G. L. Semenza, *Biochem. J.*, 2007, **405**, 1–9.
- 4 A. L. Harris, *Nat Rev Cancer*, 2002, **2**, 38–47.
- 5 Press release: The Nobel Prize in Physiology or Medicine 2019. NobelPrize.org. Nobel Media AB 2020. Sun. 04 Jan 2020. <https://www.nobelprize.org/prizes/medicine/2019/press-release/>.
- 6 X. Wang and O. S. Wolfbeis, *Chem. Soc. Rev.*, 2014, **43**, 3666–3761.
- 7 X. Zheng, X. Wang, H. Mao, W. Wu, B. Liu and X. Jiang, *Nat Commun*, 2015, **6**, 5834.
- 8 M. Quaranta, S. M. Borisov and I. Klimant, *Bioanal Rev*, 2012, **4**, 115–157.
- 9 H. Kurokawa, H. Ito, M. Inoue, K. Tabata, Y. Sato, K. Yamagata, S. Kizaka-Kondoh, T. Kadonosono, S. Yano, M. Inoue and T. Kamachi, *Sci Rep*, 2015, **5**, 10657.
- 10 V. I. Shcheslavskiy, A. Neubauer, R. Bukowiecki, F. Dinter and W. Becker, *Appl. Phys. Lett.*, 2016, **108**, 091111.
- 11 S. M. Borisov, R. Pommer, J. Svec, S. Peters, V. Novakova and I. Klimant, *J. Mater. Chem. C*, 2018, **6**, 8999–9009.
- 12 D. B. Papkovsky, in *Methods in Enzymology*, Elsevier, 2004, vol. 381, pp. 715–735.
- 13 R. I. Dmitriev and D. B. Papkovsky, *Cell. Mol. Life Sci.*, 2012, **69**, 2025–2039.
- 14 A. Juris, S. Campagna, V. Balzani, G. Gremaud and A. Von Zelewsky, *Inorg. Chem.*, 1988, **27**, 3652–3655.

- 15V. Balzani, G. Bergamini, S. Campagna and F. Puntoriero, in *Photochemistry and Photophysics of Coordination Compounds I*, eds. V. Balzani and S. Campagna, Springer Berlin Heidelberg, Berlin, Heidelberg, 2007, vol. 280, pp. 1–36.
- 16A. Juris, V. Balzani, F. Barigelletti, S. Campagna, P. Belser and A. von Zelewsky, *Coord. Chem. Rev.*, 1988, **84**, 85–277.
- 17Y.-Q. Fang, N. J. Taylor, G. S. Hanan, F. Loiseau, R. Passalacqua, S. Campagna, H. Nierengarten and A. V. Dorsselaer, *J. Am. Chem. Soc.*, 2002, **124**, 7912–7913.
- 18S. M. Borisov, G. Nuss and I. Klimant, *Anal. Chem.*, 2008, **80**, 9435–9442.
- 19M. Abrahamsson, M. Jäger, T. Österman, L. Eriksson, P. Persson, H.-C. Becker, O. Johansson and L. Hammarström, *J. Am. Chem. Soc.*, 2006, **128**, 12616–12617.
- 20D. Hara, Y. Umehara, A. Son, W. Asahi, S. Misu, R. Kurihara, T. Kondo and K. Tanabe, *ChemBioChem*, 2018, **19**, 956–962.
- 21L. Cosgrave, M. Devocelle, R. J. Forster and T. E. Keyes, *Chem. Commun.*, 2010, **46**, 103–105.
- 22C. S. Burke, A. Byrne and T. E. Keyes, *Angew. Chem. Int. Ed.*, 2018, **57**, 12420–12424.
- 23A. Byrne, C. S. Burke and T. E. Keyes, *Chem. Sci.*, 2016, **7**, 6551–6562.
- 24L. Blackmore, R. Moriarty, C. Dolan, K. Adamson, R. J. Forster, M. Devocelle and T. E. Keyes, *Chem. Commun.*, 2013, **49**, 2658.
- 25R. I. Dmitriev, H. M. Ropiak, G. V. Ponomarev, D. V. Yashunsky and D. B. Papkovsky, *Bioconjugate Chem.*, 2011, **22**, 2507–2518.
- 26B. D. MacCraith, C. M. McDonagh, G. O’Keeffe, E. T. Keyes, J. G. Vos, B. O’Kelly and J. F. McGilp, *Analyst*, 1993, **118**, 385–388.
- 27S. Zhang, M. Hosaka, T. Yoshihara, K. Negishi, Y. Iida, S. Tobita and T. Takeuchi, *Cancer Res*, 2010, **70**, 4490–4498.
- 28A. Martin, A. Byrne, C. S. Burke, R. J. Forster and T. E. Keyes, *J. Am. Chem. Soc.*, 2014, **136**, 15300–15309.
- 29S. Tobita, T. Yoshihara, R. Mukai, Y. Shimoda, I. Takahashi and H. Akiyama, *Photochem. Photobiol. Sci.*, 2018, **17**, 846.
- 30D. Wencel, C. Dolan, M. Barczak, T. E. Keyes and C. McDonagh, *Nanotechnology*, 2013, **24**, 365705.
- 31D. Hara, Y. Umehara, A. Son, W. Asahi, S. Misu, R. Kurihara, T. Kondo and K. Tanabe, *ChemBioChem*, 2018, **19**, 956–962.
- 32R. I. Dmitriev, S. M. Borisov, H. Düsselmann, S. Sun, B. J. Müller, J. Prehn, V. P. Baklaushev, I. Klimant and D. B. Papkovsky, *ACS Nano*, 2015, **9**, 5275–5288.

- 33Z. Jiang, X. Yu, S. Zhai and Y. Hao, *Sensors*, 2017, **17**, 548.
- 34Y. Feng, J. Cheng, L. Zhou, X. Zhou and H. Xiang, *Analyst*, 2012, **137**, 4885.
- 35T. Yoshihara, Y. Yamaguchi, M. Hosaka, T. Takeuchi and S. Tobita, *Angew. Chem. Int. Ed.*, 2012, **51**, 4148–4151.
- 36D. Hara, H. Komatsu, A. Son, S. Nishimoto and K. Tanabe, *Bioconjugate Chem.*, 2015, **26**, 645–649.
- 37H. Bian, X. Song, N. Li, H. Man and Y. Xiao, *J. Mater. Chem. B*, 2018, **6**, 1699–1705.
- 38K. Y. Zhang, P. Gao, G. Sun, T. Zhang, X. Li, S. Liu, Q. Zhao, K. K.-W. Lo and W. Huang, *J. Am. Chem. Soc.*, 2018, **140**, 7827–7834.
- 39T. Yoshihara, S. Murayama and S. Tobita, *Sensors*, 2015, **15**, 13503–13521.
- 40Y.-E. L. Koo, Y. Cao, R. Kopelman, S. M. Koo, M. Brasuel and M. A. Philbert, *Anal. Chem.*, 2004, **76**, 2498–2505.
- 41X. Wang, H. H. Gorris, J. A. Stolwijk, R. J. Meier, D. B. M. Groegel, J. Wegener and O. S. Wolfbeis, *Chem. Sci.*, 2011, **2**, 901.
- 42A. V. Kondrashina, R. I. Dmitriev, S. M. Borisov, I. Klimant, I. O'Brien, Y. M. Nolan, A. V. Zhdanov and D. B. Papkovsky, *Adv. Funct. Mater.*, 2012, **22**, 4931–4939.
- 43R. I. Dmitriev, S. M. Borisov, H. Dössmann, S. Sun, B. J. Müller, J. Prehn, V. P. Baklaushev, I. Klimant and D. B. Papkovsky, *ACS Nano*, 2015, **9**, 5275–5288.
- 44Q. Zhao, X. Zhou, T. Cao, K. Y. Zhang, L. Yang, S. Liu, H. Liang, H. Yang, F. Li and W. Huang, *Chem. Sci.*, 2015, **6**, 1825–1831.
- 45Q. Zhao, T. Pan, G. Xiang, Z. Mei, J. Jiang, G. Li, X. Zou, M. Chen, D. Sun, S. Jiang and Y. Tian, *Sens. Actuators, B*, 2018, **273**, 242–252.
- 46L. Zang, H. Zhao, J. Hua, F. Qin, Y. Zheng, Z. Zhang and W. Cao, *Sens. Actuators, B*, 2016, **231**, 539–546.
- 47P. J. Cywinski, A. J. Moro, S. E. Stanca, C. Biskup and G. J. Mohr, *Sens. Actuators, B*, 2009, **135**, 472–477.
- 48X.-H. Wang, H.-S. Peng, H. Ding, F.-T. You, S.-H. Huang, F. Teng, B. Dong and H.-W. Song, *J. Mater. Chem.*, 2012, **22**, 16066.
- 49D. Lambrechts, M. Roeffaers, G. Kerckhofs, S. J. Roberts, J. Hofkens, T. Van de Putte, H. Van Oosterwyck and J. Schrooten, *Biomaterials*, 2013, **34**, 922–929.
- 50T. Mayr, S. M. Borisov, T. Abel, B. Enko, K. Waich, G. Mistlberger and I. Klimant, *Anal. Chem.*, 2009, **81**, 6541–6545.
- 51T. Yoshihara, Y. Yamaguchi, M. Hosaka, T. Takeuchi and S. Tobita, *Angew. Chem. Int. Ed.*, 2012, **51**, 4148–4151.

- 52H. Shi, X. Ma, Q. Zhao, B. Liu, Q. Qu, Z. An, Y. Zhao and W. Huang, *Adv. Funct. Mater.*, 2014, **24**, 4823–4830.
- 53A. Martin, A. Byrne, C. Dolan, R. J. Forster and T. E. Keyes, *Chem. Commun.*, 2015, **51**, 15839–15841.
- 54S. M. King, S. Claire, R. I. Teixeira, A. N. Dosumu, A. J. Carrod, H. Dehghani, M. J. Hannon, A. D. Ward, R. Bicknell, S. W. Botchway, N. J. Hodges and Z. Pikramenou, *J. Am. Chem. Soc.*, 2018, **140**, 10242–10249.
- 55Y. Cao, Y.-E. Lee Koo and R. Kopelman, *Analyst*, 2004, **129**, 745.
- 56C. Wu, B. Bull, K. Christensen and J. McNeill, *Angew. Chem. Int. Ed.*, 2009, **48**, 2741–2745.
- 57X. Wang, H. H. Gorris, J. A. Stolwijk, R. J. Meier, D. B. M. Groegel, J. Wegener and O. S. Wolfbeis, *Chem. Sci.*, 2011, **2**, 901.
- 58J. Napp, T. Behnke, L. Fischer, C. Würth, M. Wottawa, D. M. Katschinski, F. Alves, U. Resch-Genger and M. Schäferling, *Anal. Chem.*, 2011, **83**, 9039–9046.
- 59N. W. Choi, S. S. Verbridge, R. M. Williams, J. Chen, J.-Y. Kim, R. Schmehl, C. E. Farnum, W. R. Zipfel, C. Fischbach and A. D. Stroock, *Biomaterials*, 2012, **33**, 2710–2722.
- 60A. V. Kondrashina, R. I. Dmitriev, S. M. Borisov, I. Klimant, I. O'Brien, Y. M. Nolan, A. V. Zhdanov and D. B. Papkovsky, *Adv. Funct. Mater.*, 2012, **22**, 4931–4939.
- 61D. Lambrechts, M. Roeffaers, G. Kerckhofs, S. J. Roberts, J. Hofkens, T. Van de Putte, H. Van Oosterwyck and J. Schrooten, *Biomaterials*, 2013, **34**, 922–929.
- 62R. I. Dmitriev, S. M. Borisov, H. Dössmann, S. Sun, B. J. Müller, J. Prehn, V. P. Baklaushev, I. Klimant and D. B. Papkovsky, *ACS Nano*, 2015, **9**, 5275–5288.
- 63Y.-E. Koo Lee, E. E. Ulbrich, G. Kim, H. Hah, C. Strollo, W. Fan, R. Gurjar, S. Koo and R. Kopelman, *Anal. Chem.*, 2010, **82**, 8446–8455.
- 64A. Byrne, J. Jacobs, C. S. Burke, A. Martin, A. Heise and T. E. Keyes, *Analyst*, 2017, **142**, 3400–3406.
- 65G. Bœuf, G. V. Roullin, J. Moreau, L. Van Gulick, N. Zambrano Pineda, C. Terryn, D. Ploton, M. C. Andry, F. Chuburu, S. Dukic, M. Molinari and G. Lemercier, *ChemPlusChem*, 2014, **79**, 171–180.
- 66W. Sun, S. Li, B. Häupler, J. Liu, S. Jin, W. Steffen, U. S. Schubert, H.-J. Butt, X.-J. Liang and S. Wu, *Adv. Mater.*, 2017, **29**, 1603702.
- 67J. Shen, H.-C. Kim, J. Wolfram, C. Mu, W. Zhang, H. Liu, Y. Xie, J. Mai, H. Zhang, Z. Li, M. Guevara, Z.-W. Mao and H. Shen, *Nano Lett.*, 2017, **17**, 2913–2920.
- 68N. Soliman, G. Gasser and C. M. Thomas, *Adv. Mater.*, 2020, **32**, 2003294.

- 69 Y. Ellahioui, M. Patra, C. Mari, R. Kaabi, J. Karges, G. Gasser and S. Gómez-Ruiz, *Dalton Trans.*, 2019, **48**, 5940–5951.
- 70 N. Soliman, L. K. McKenzie, J. Karges, E. Bertrand, M. Tharaud, M. Jakubaszek, V. Guérineau, B. Goud, M. Hollenstein, G. Gasser and C. M. Thomas, *Chem. Sci.*, 2020, **11**, 2657–2663.
- 71 A. Martin, R. D. Moriarty, C. Long, R. J. Forster and T. E. Keyes, *Asian J. Org. Chem.*, 2013, **2**, 763–778.
- 72 C. S. Burke and T. E. Keyes, *RSC Advances*, 2016, **6**, 40869–40877.
- 73 I. P. Evans, A. Spencer and G. Wilkinson, *J. Chem. Soc., Dalton Trans.*, 1973, 204.
- 74 T. Gunnlaugsson, J. P. Leonard, K. Sénéchal and A. J. Harte, *J. Am. Chem. Soc.*, 2003, **125**, 12062–12063.
- 75 J. N. Demas, E. W. Harris and R. P. McBride, *J. Am. Chem. Soc.*, 1977, **99**, 3547–3551.
- 76 K. Adamson, C. Dolan, N. Moran, R. J. Forster and T. E. Keyes, *Bioconjugate Chem.*, 2014, **25**, 928–944.
- 77 G. A. Crosby and R. J. Watts, *J. Am. Chem. Soc.*, 1971, **93**, 3184–3188.
- 78 E. R. Carraway, J. N. Demas, B. A. DeGraff and J. R. Bacon, *Anal. Chem.*, 1991, **63**, 337–342.
- 79 S. Draxler, M. E. Lippitsch, I. Klimant, H. Kraus and O. S. Wolfbeis, *J. Phys. Chem.*, 1995, **99**, 3162–3167.
- 80 C. Zhou, L. Ma, J. Ping, L. Guo, J. Qin, M. Yuan, Z. Geng, F. You and H. Peng, *Anal Bioanal Chem*, 2020, **412**, 2579–2587.
- 81 R. M. Bukowski, R. Ciriminna, M. Pagliaro and F. V. Bright, *Anal. Chem.*, 2005, **77**, 2670–2672.
- 82 J. Jacobs, N. Gathergood and A. Heise, *Macromol. Rapid Commun.*, 2013, **34**, 1325–1329.
- 83 J. Jacobs, A. Byrne, N. Gathergood, T. E. Keyes, J. P. A. Heuts and A. Heise, *Macromolecules*, 2014, **47**, 7303–7310.
- 84 K. Suzuki, A. Kobayashi, S. Kaneko, K. Takehira, T. Yoshihara, H. Ishida, Y. Shiina, S. Oishi and S. Tobita, *Phys. Chem. Chem. Phys.*, 2009, **11**, 9850.
- 85 Y. Michiels, P. Puyvelde and B. Sels, *Applied Sciences*, 2017, **7**, 665.
- 86 C.-W. Lai, Y.-H. Wang, C.-H. Lai, M.-J. Yang, C.-Y. Chen, P.-T. Chou, C.-S. Chan, Y. Chi, Y.-C. Chen and J.-K. Hsiao, *Small*, 2008, **4**, 218–224.
- 87 S. P.-Y. Li, C. T.-S. Lau, M.-W. Louie, Y.-W. Lam, S. H. Cheng and K. K.-W. Lo, *Biomaterials*, 2013, **34**, 7519–7532.



- 88P. Ceroni, A. Y. Lebedev, E. Marchi, M. Yuan, T. V. Esipova, G. Bergamini, D. F. Wilson, T. M. Busch and S. A. Vinogradov, *Photochem. Photobiol. Sci.*, 2011, **10**, 1056.
- 89S. Hirohara, M. Obata, H. Alitomo, K. Sharyo, T. Ando, S. Yano and M. Tanihara, *Bioconjugate Chem.*, 2009, **20**, 944–952.
- 90A. Ruggi, F. W. B. van Leeuwen and A. H. Velders, *Coord. Chem. Rev.*, 2011, **255**, 2542–2554.
- 91A. G. Tkachenko, H. Xie, D. Coleman, W. Glomm, J. Ryan, M. F. Anderson, S. Franzen and D. L. Feldheim, *J. Am. Chem. Soc.*, 2003, **125**, 4700–4701.
- 92A. K. Oyelere, P. C. Chen, X. Huang, I. H. El-Sayed and M. A. El-Sayed, *Bioconjugate Chem.*, 2007, **18**, 1490–1497.
- 93B. Kang, M. A. Mackey and M. A. El-Sayed, *J. Am. Chem. Soc.*, 2010, **132**, 1517–1519.
- 94N. S. Chandel and P. T. Schumacker, *Journal of Applied Physiology*, 2000, **88**, 1880–1889.
- 95C. T. Taylor, *Biochem. J.*, 2008, **409**, 19–26.
- 96H. Bian, X. Song, N. Li, H. Man and Y. Xiao, *J. Mater. Chem. B*, 2018, **6**, 1699–1705.
- 97P. V. Escribá, *Trends Mol Med*, 2006, **12**, 34–43.
- 98P. V. Escribá, J. M. González-Ros, F. M. Goñi, P. K. J. Kinnunen, L. Vigh, L. Sánchez-Magraner, A. M. Fernández, X. Busquets, I. Horváth and G. Barceló-Coblijn, *J Cellular Mol Med*, 2008, **12**, 829–875.
- 99D. C. Wallace, *Nat Rev Cancer*, 2012, **12**, 685–698.
- 100 R. J. DeBerardinis and N. S. Chandel, *Sci. Adv.*, 2016, **2**, e1600200.
- 101 I. Mellman and Y. Yarden, *Cold Spring Harbor Perspectives in Biology*, 2013, **5**, a016949–a016949.
- 102 N. Bernardes and A. Fialho, *IJMS*, 2018, **19**, 3871.
- 103 M. Sok, M. Šentjurg, M. Schara, J. Stare and T. Rott, *Ann. Thorac. Surg.*, 2002, **73**, 1567–1571.
- 104 R. F. A. Zwaal, P. Comfurius and E. M. Bevers, *CMLS, Cell. Mol. Life Sci.*, 2005, **62**, 971–988.
- 105 S. Riedl, B. Rinner, M. Asslaber, H. Schaidler, S. Walzer, A. Novak, K. Lohner and D. Zweytick, *Biochim Biophys Acta Biomembr.*, 2011, **1808**, 2638–2645.
- 106 A. Fercher, S. M. Borisov, A. V. Zhdanov, I. Klimant and D. B. Papkovsky, *ACS Nano*, 2011, **5**, 5499–5508.
- 107 S. Behzadi, V. Serpooshan, W. Tao, M. A. Hamaly, M. Y. Alkawareek, E. C. Dreaden, D. Brown, A. M. Alkilany, O. C. Farokhzad and M. Mahmoudi, *Chem. Soc. Rev.*, 2017, **46**, 4218–4244.

- 108 J. Gruenberg and H. Stenmark, *Nat Rev Mol Cell Biol*, 2004, **5**, 317–323.
- 109 J. P. Luzio, P. R. Pryor and N. A. Bright, *Nat Rev Mol Cell Biol*, 2007, **8**, 622–632.
- 110 J. M. Kelly, A. B. Tossi, D. J. McConnell and C. OhUigin, *Nucl Acids Res*, 1985, **13**, 6017–6034.
- 111 M. B. Fleisher, K. C. Waterman, N. J. Turro and J. K. Barton, *Inorg. Chem.*, 1986, **25**, 3549–3551.
- 112 Y. Liu, R. Hammitt, D. A. Lutterman, L. E. Joyce, R. P. Thummel and C. Turro, *Inorg. Chem.*, 2009, **48**, 375–385.
- 113 R. D. Srivastava, A. F. Mcmillan and I. J. Harris, *Can. J. Chem. Eng.*, 1968, **46**, 181–184.

## Chapter 6: Conclusions and Future Perspectives

Over the past decade, there have been several studies focusing on the application of transition metal complexes. In the context of cellular imaging and sensing applications, some of the attractive properties of transition metal luminophores such as ruthenium(II) include synthetically tunable optical properties, typically long-luminescent lifetimes, photostability and large Stokes shifts. In the past, the application of transition metal luminophores in cells has been limited by their generally poor cell permeability and nonspecific or unpredictable cellular uptake. Several strategies have since been developed to improve their uptake and targeted delivery into cells (e.g., bioconjugation, nanocarriers, cell penetrating and signal peptides) which in turn has aided their cellular applications including imaging and theranostics.

In Chapter 2, a series of NIR emitting Ru(II)-biquinoline conjugates were studied in CHO and HeLa cell lines. All conjugates (peptide: NLS,MPP,R8 and PEGylated) showed aqueous solubility and cellular uptake. Interestingly, the counterion was found to influence uptake of the peptide conjugates where only the perchlorate analogues were membrane permeable. The peptide conjugates showed wide cellular distribution and high dark cytotoxicity which limited their application as imaging probes. Mitochondrial depolarization and caspase activity assays revealed that cell death was triggered through apoptosis initiation likely through depolarization of the mitochondrial membrane. The unexpected cytotoxicity was attributed to the wide cellular distribution of the conjugates combined with the increased lipophilicity of the Ru(II)-biquinoline complex as the more hydrophilic PEGylated conjugate was significantly less cytotoxic.

Chapter 3 presents the novel achiral Os(II) complex  $[\text{Os}(\text{tpybenzCOOH})_2]^{2+}$  and introduces the concept of bioconjugation of a cell penetrating peptide to each carboxyl terminus of the complex via amide coupling to promote cellular uptake. A mitochondrial penetrating peptide (MPP) was selected in order to drive the Os(II) complex to the mitochondria. Both parent and conjugate exhibited relatively intense NIR-emission and robust photostability suitable for cellular imaging. Uptake studies were carried out in HeLa and MCF 7 cells. While the parent complex was cell impermeable, confocal microscopy and co-localisation imaging studies with showed that the  $\text{Os}^{\text{II}}\text{MPP}$  was membrane permeable and targeted the mitochondria at concentrations below  $50 \mu\text{M}$ . At increased concentrations,  $\text{Os}^{\text{II}}\text{MPP}$  showed rapid uptake, wider distribution, penetration of the nuclear envelope and cell death. The localisation switch

of the conjugate, observed by confocal imaging, was also reflected by a change in the cell death mechanism as evident by the mitochondrial depolarization and caspase activity assay.

The attractive photophysical properties of the Os(II) complex (i.e., NIR emission, good quantum yield, photostability) described in Chapter 3 lead to the investigation of its application as an imaging and potentially sensing probe in 2D cell monolayers and 3D tumor spheroids. In Chapter 4, the Os(II) parent complex was conjugated to two polyarginine chains of varying lengths (R4 and R8) in order to examine whether the optimal octaarginine sequence requires a contiguous peptide structure for cellular uptake or whether it can be achieved through a bridged structure. Similar to 2D cell monolayer studies, when examined in 3D multicellular spheroids, the parent complex and bis-octaarginine conjugate were found to be impermeable. The bis-tetraarginine conjugate however showed 2D cell uptake. These results showed that the octaarginine sequence does not require a contiguous arrangement for cellular uptake and can be bridged across the complex. These findings may pave the way towards investigation of novel bridged peptide conjugates. Additionally, the tetraarginine probe showed widespread and in-depth staining into the 3D MCTS without any impact on spheroid viability. The emission collected from the probe was well outside the autofluorescence window toward the NIR region of the spectrum suitable for tissue imaging. Based on literature to date, this is the first example of an osmium(II) luminophore probe applied to imaging of 3D multicellular spheroids. The short emission lifetimes and absence of O<sub>2</sub> sensitivity but potential redox sensitivity to other biorelevant species offers an advantage to Os(II) complexes potentially expanding their application toward sensing and monitoring of metabolic changes in cells or tissues without the interference of oxygen. Overall, this work highlights the potential of non-cytotoxic NIR-emitting metal complex bioconjugates in cellular and tissue imaging and sensing.

In Chapter 5, the fabrication of ratiometric nanoparticles for intracellular O<sub>2</sub> sensing was presented. The core-shell approach of co-encapsulating Ru(II) O<sub>2</sub> sensor and BODIPY reference dye in the particle core and decorating the exterior with poly-L-lysine proved to be successful in achieving 1) isolation of the dyes from environment effects and 2) promotion of cellular uptake. The particles showed good response to changes in intracellular oxygen levels and were suitable both for confocal microscopy ( $xy\lambda$ ) and for a plate reader assay. It is advantageous for oxygen probes to permit O<sub>2</sub>-measurements using different techniques. When rapid and multiple measurements of monolayer cell samples are desired, a conventional plate reader may be used. Luminescence microscopy can then be used for O<sub>2</sub> mapping of three-dimensional cell models or tissue samples. Future studies will focus on achieving endosomal

escape and subcellular targeting potentially by exploiting the surface chemistry of the particle and amide coupling of the Ru(II) complex to a targeting vector.

As described in the introduction of this thesis, an area which has received attention is the application of transition metal luminophores in super-resolution imaging techniques which offer sub-diffraction resolved structural information. Such techniques include Stimulated Emission Depletion (STED) Microscopy, structured illumination microscopy (SIM) or super-resolution SIM (SR-SIM) and photoactivation localization microscopy (PALM). Complexes of zinc, osmium and even platinum are also receiving attention for their applications in bioimaging.

In the context of medicinal chemistry and theranostics, as mentioned, TLD1433 is the first Ru(II)- polypyridyl complex for photodynamic therapy to reach human clinical trials and it is expected that further efforts will follow in designing and developing analogous complexes with increased efficacy and specificity. Development of  $d^6$  metal-ion complexes with antibiotic activity is also another emerging research area. Finally, more recently, attention has also been devoted towards the application of metal complexes as potential antiviral agents against SARS-CoV-2. The synthetic versatility and rich redox chemistry of metal complexes combined with their unique physicochemical properties, may lead to the development of novel therapeutics.

## **Appendices A-D**

## Appendix A

Supplementary material associated with **Chapter 2** “*Photostable NIR emitting ruthenium(II) conjugates; uptake and biological activity in live cells*”.

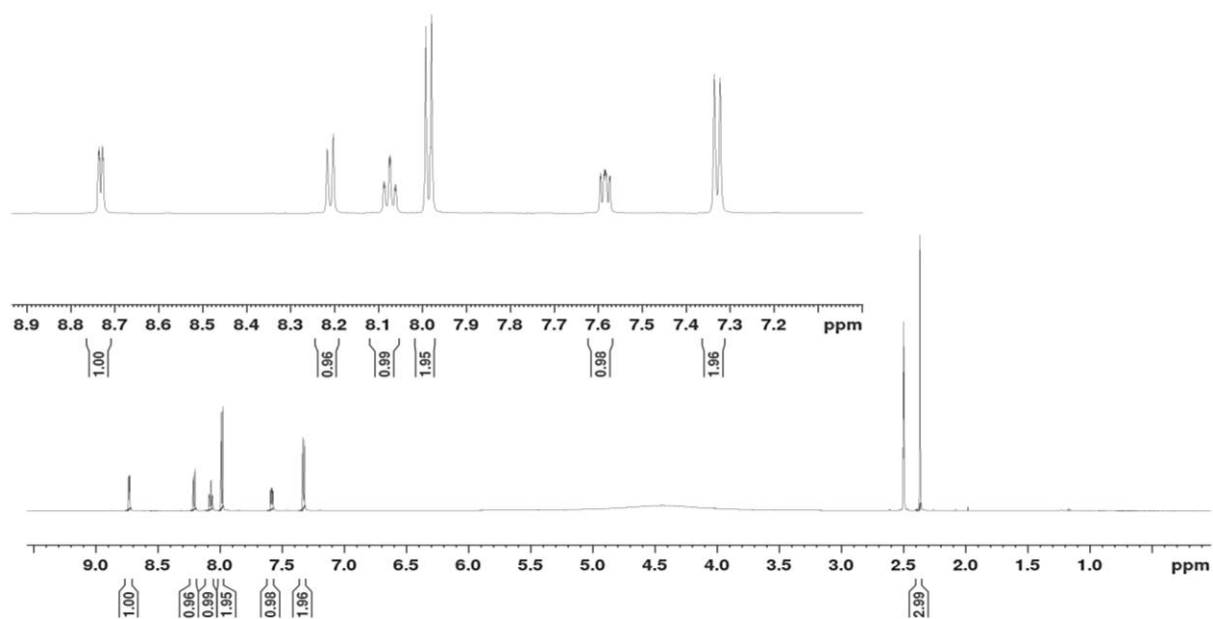
### S2.1 Materials and Instrumentation.

Peptides (> 95 %) were purchased from Celtek Peptides, TN, USA. Mass spectrometry data for peptides used in this work was provided by Celtek Peptide and included here. All other materials were obtained from Sigma Aldrich and were used without further purification. <sup>1</sup>H NMR and <sup>13</sup>C spectra were recorded at either 400/600 MHz as indicated using Bruker spectrometers and deuterated solvent for homo-nuclear lock. The spectra were processed using Bruker Topspin software and were calibrated against solvent peaks according to published values.<sup>1</sup> High Resolution Mass Spectrometry (HR-MS) was performed at the HR-MS facility, Trinity College Dublin, MS Spectrometry facility University College Dublin or the Mass Spectrometry Facility, NUI Maynooth (for peptide conjugates). The syntheses of the Ru(II) complexes described below were performed under nitrogen and in the absence of light. Analytical HPLC was performed on a Varian 940-LC Liquid Chromatograph using an Agilent Pursuit XRs 5 C18 column (5 μm, 4.6 × 250 mm). Samples were prepared in 99/1 Water/Acetonitrile containing 0.1 % TFA. Gradient elution at 1 mL/min flowrate was employed in the separation using a 0.1 % TFA in Water/Acetonitrile mixture starting at 99 %/1 % and changing linearly to 30 %/70 % over 15 minutes and then held at 30 %/70 % for 5 minutes. A Photodiode Array detector, PDAD was used for peak detection, this permitted complete UV-vis spectra )200 to 600 nm to recorded for each peak and elution was followed by monitoring at 554 nm. UV – Vis absorption spectra were recorded on Varian Cary 50 spectrometer. Emission Spectra were recorded on a Varian Cary Eclipse fluorescence spectrophotometer with excitation and emission slit widths stated. All analyses were carried out using quartz cuvettes and background scans applied. Fluorescence lifetime measurements were carried out using a PicoQuant FluoTime 100 Compact FLS TCSPC system using a 450 nm pulsed laser source.

## S2.2 Synthesis and structural characterisation.

### S2.2.1 Characterisation data.

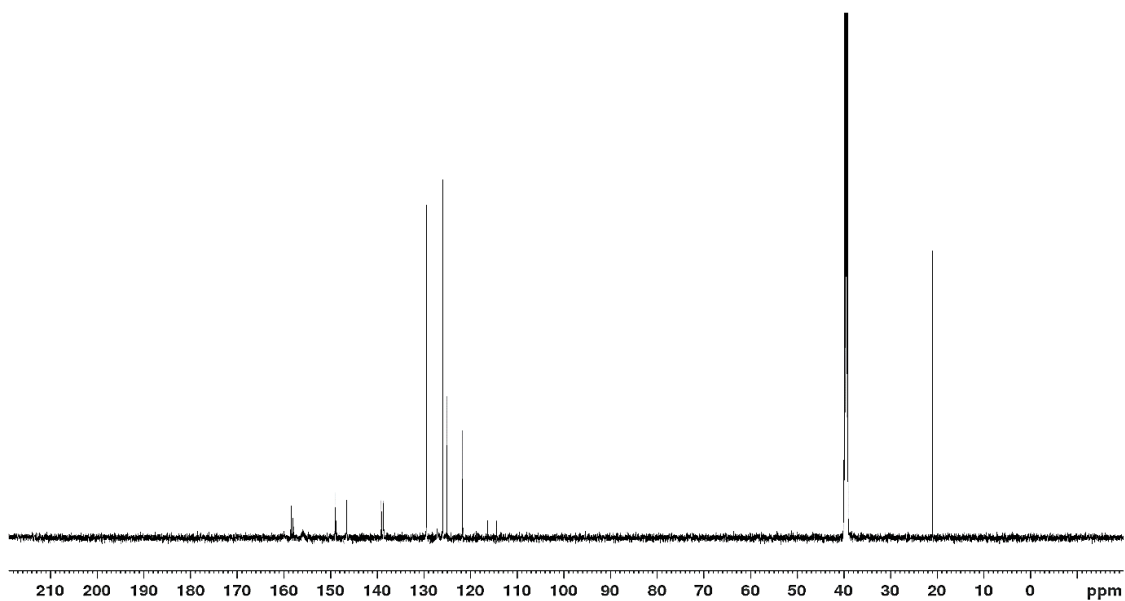
#### S2.2.1.1 3-(2-pyridyl)-5-(4-methylphenyl)-1,2,4-triazole (1)



**Figure S2. 1** <sup>1</sup>H NMR spectrum (600 MHz) of (**1**) in DMSO-d<sub>6</sub>.

(**1**) 8.73 (d, 1H, J= 4.62 Hz), 8.20 (d, 1H, J= 8.10 Hz), 8.07 (t, 1H, J= 7.56 Hz, 1.62 Hz), 7.98 (d, 2H, J= 8.28 Hz), 7.59-7.56 (m, 1H), 7.32 (d, 2H, J=7.98 Hz)

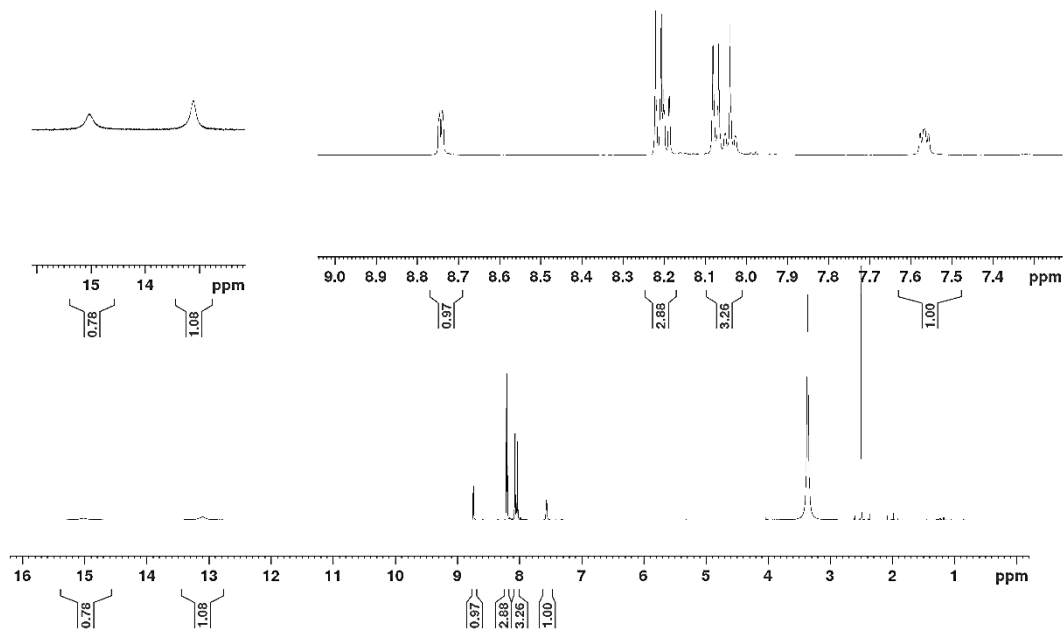




**Figure S2. 2**  $^{13}\text{C}$  NMR spectrum (600 MHz) of **(1)** in  $\text{DMSO-d}_6$ .

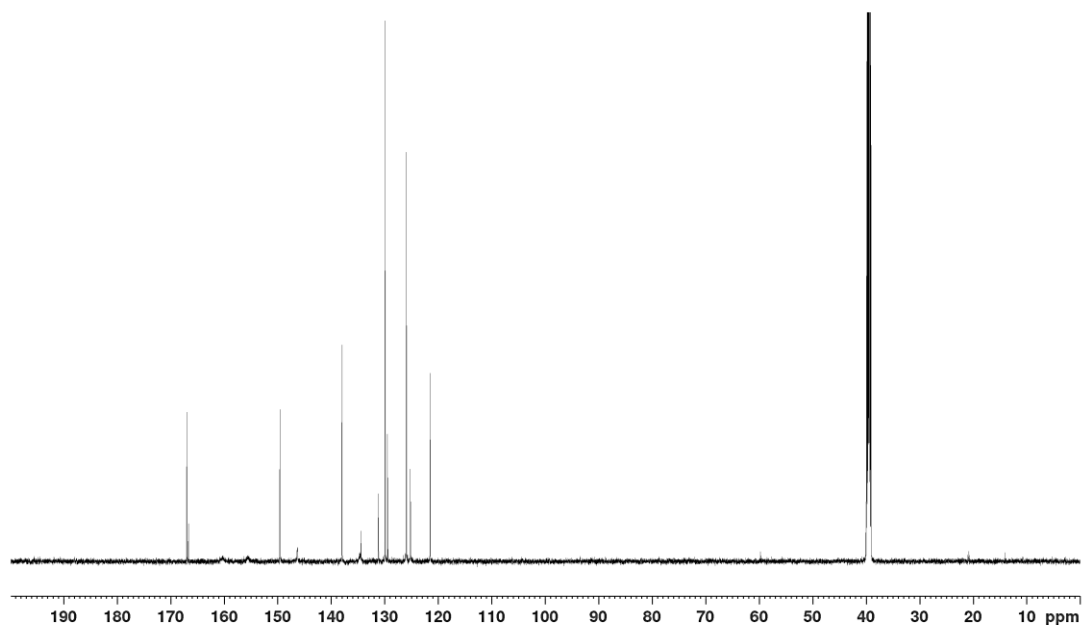
**(1)** 158.66, 149.14, 146.26, 139.05, 129.53, 126.07, 124.91, 121.74, 116.54, 114.24, 21.05

*S2.2.1.2 13-(2-pyridyl)-5-(4-carboxyphenyl)-1,2,4-triazole (2)*



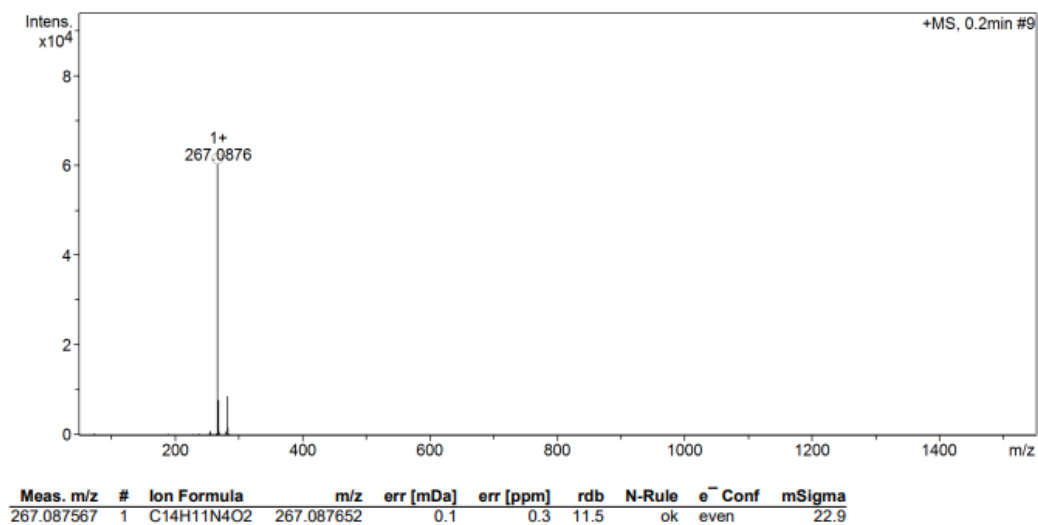
**Figure S2. 3**  $^1\text{H}$  NMR spectrum (600 MHz) of **(2)** in  $\text{DMSO-d}_6$ .

**(2)** 15.01 (s, 1H), 13.08 (Br. S, 1H), 8.74 (d, 1H,  $J = 3.66$  Hz), 8.24-8.14 (m, 3H), 8.10-7.99 (m, 3H), 7.54 (m, 1H).



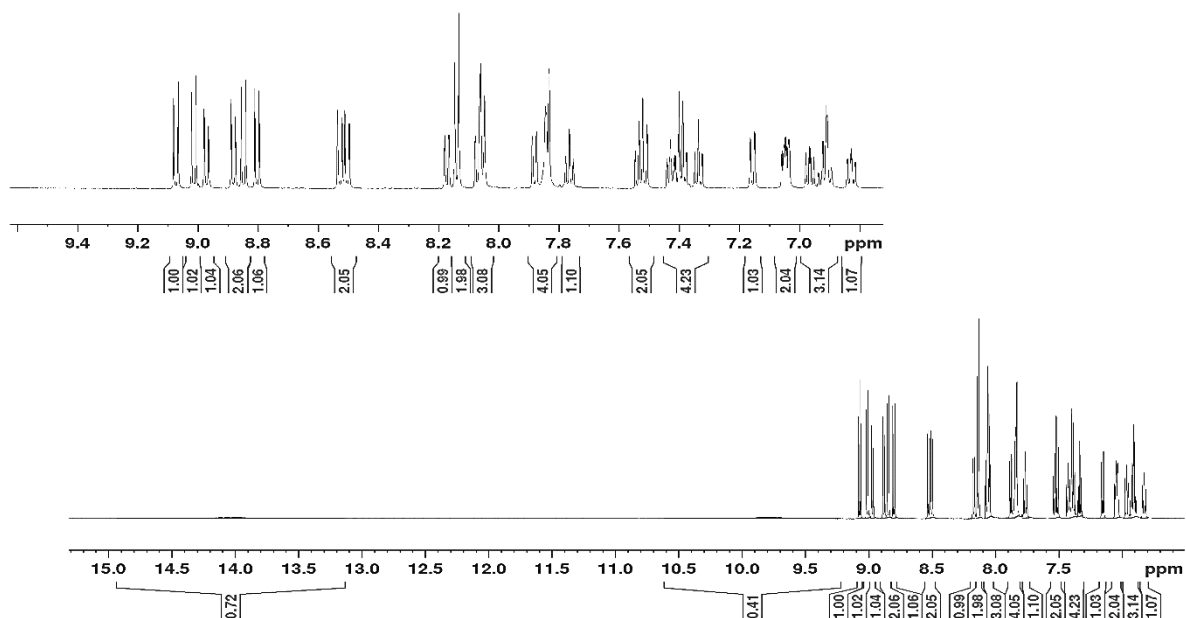
**Figure S2. 4**  $^{13}\text{C}$  NMR spectrum (600 MHz) of **(2)** in  $\text{DMSO-d}_6$ .

**(2)** 167.02, 166.68, 149.59, 146.29, 137.98, 134.49, 131.19, 129.93, 129.47, 125.95, 125.20, 121.52.



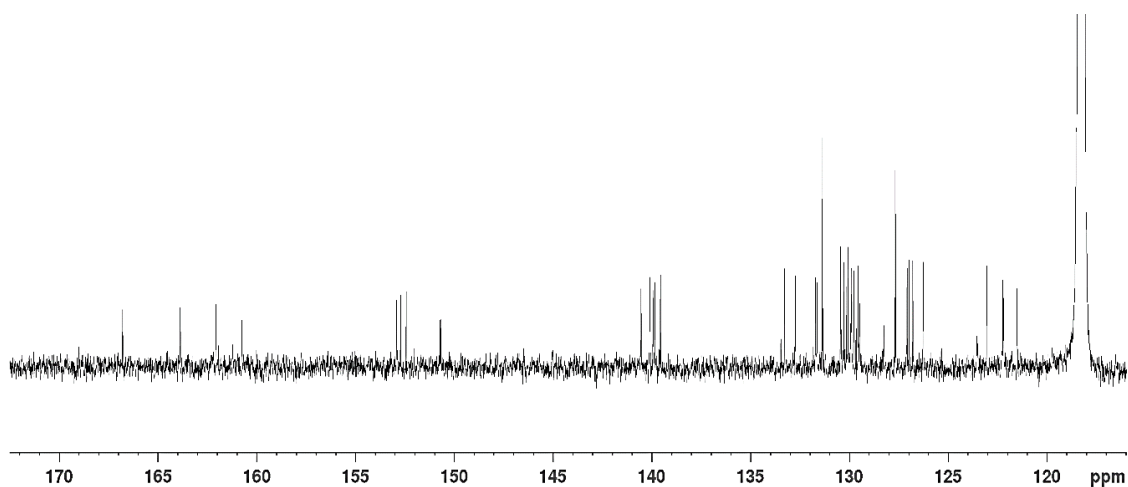
**Figure S2. 5** HR-MS (ESI-QTOF): Single Mass Analysis of **(2)** indicating  $[\text{M} + \text{H}]^+$ .

S2.2.1.3 *Ru(biq)2(3-(2-pyridyl)-5-(4-carboxyphenyl)-1,2,4-triazole) (3)*



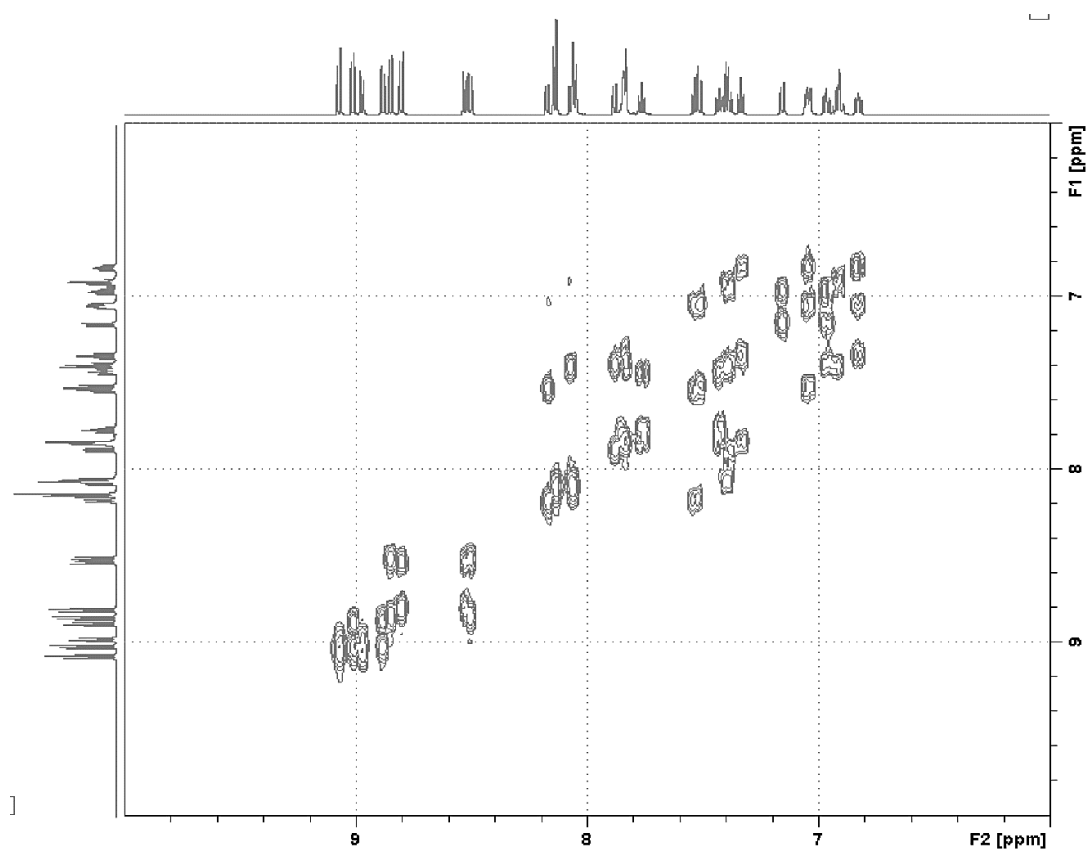
**Figure S2. 6** <sup>1</sup>H NMR spectrum (600 MHz) of **(3)** in MeCN-d<sub>3</sub>.

**(3)** 14.07 (s, 1H), 9.83 (s, 1H), 9.07 (d, 1H, J= 8.94 Hz), 9.01 (d, 1H, J= 8.94 Hz), 8.97 (d, 1H, J= 8.94 Hz), 8.88 (d, 1H, J= 8.94 Hz), 8.84 (d, 1H, J= 8.94 Hz), 8.80 (d, 1H, J= 9.66 Hz), 8.53-8.49 (m, 2H), 8.17 (d, 1H, J= 4.14 Hz), 8.13 (d, 2H, J= 8.94 Hz), 8.07-8.04 (m, 3H), 7.88-7.82 (m, 4H), 7.76 (t, 1H, J= 7.68 Hz, 1.5 Hz), 7.54-7.50 (m, 2H), 7.43-7.32 (m, 4H), 7.15 (d, 1H, J= 9.24 Hz), 7.06-7.02 (m, 2H), 6.98-6.88 (m, 3H), 6.82 (t, 1H, J= 8.04 Hz, 1.68 Hz).



**Figure S2. 7** <sup>13</sup>C NMR spectrum (600 MHz) of **(3)** in MeCN-d<sub>3</sub>.

(3) 166.77, 163.90, 162.09, 161.96, 160.75, 152.92, 152.72, 152.46, 150.74, 150.69, 140.56, 140.11, 139.94, 139.84, 139.57, 133.30, 132.74, 131.71, 131.64, 131.36, 130.43, 130.28, 130.16, 130.07, 129.94, 129.89, 129.76, 129.66, 129.55, 129.45, 128.24, 127.67, 127.09, 126.99, 126.79, 126.26, 123.53, 123.06, 122.25, 122.19, 121.50.



**Figure S2. 8**  $^1\text{H}$ - $^1\text{H}$  COSY NMR spectrum of (3) in MeCN- $\text{d}_3$ . (Aromatic region highlighted)

## Single Mass Analysis

Tolerance = 50.0 PPM / DBE: min = -1.5, max = 200.0

Element prediction: Off

Number of isotope peaks used for i-FIT = 5

Monoisotopic Mass, Odd and Even Electron Ions

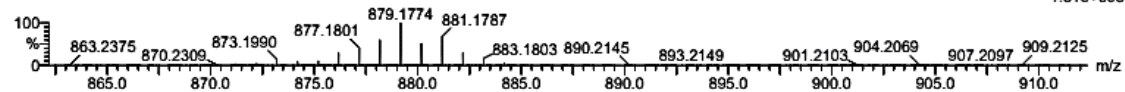
94 formula(e) evaluated with 1 results within limits (up to 10 best isotopic matches for each mass)

Elements Used:

C: 0-50 H: 0-34 N: 0-8 O: 0-2 Ru: 0-2

David Cullinane (TK), DJCTK001

Q-TOF20180618MF014 36 (0.666) AM (Cen,6, 80.00, Ht,10000.0,1570.68,0.70); Sm (SG, 2x3.00); Sb (15,10.00); Cm (13:83-78:81)

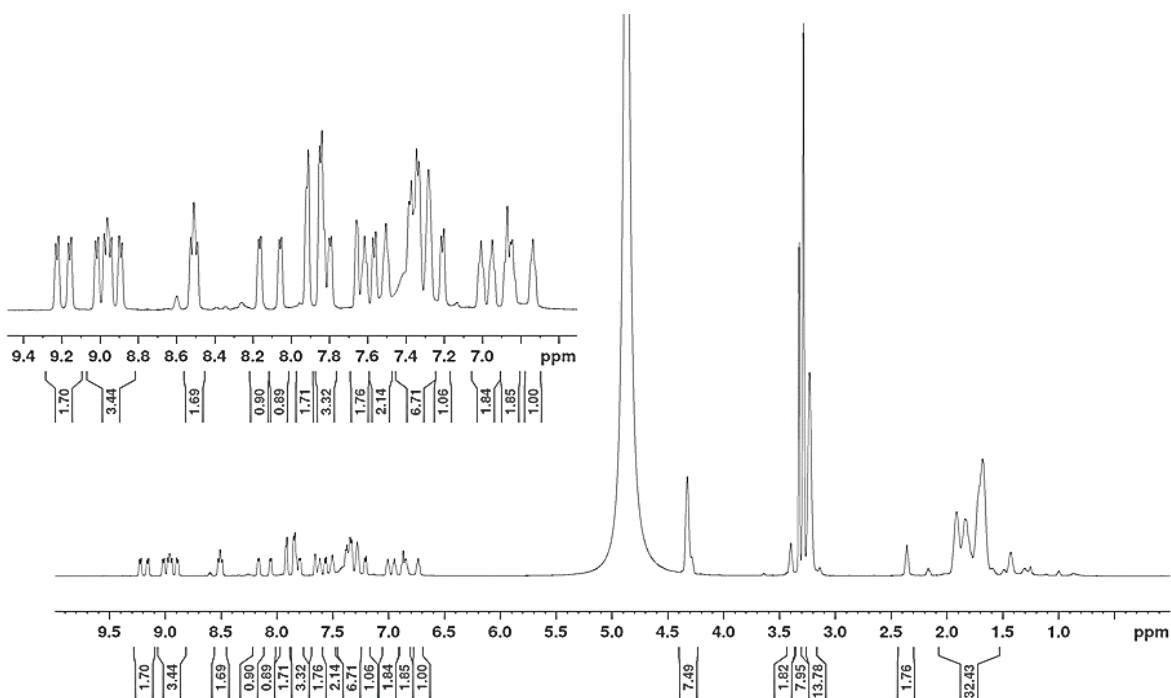
TOF MS LD+  
1.81e+003

Minimum: -1.5  
Maximum: 5.0 50.0 200.0

Mass	Calc. Mass	mDa	PPM	DBE	i-FIT	i-FIT (Norm)	Formula
879.1774	879.1770	0.4	0.5	38.5	134.7	0.0	C50 H33 N8 O2 Ru

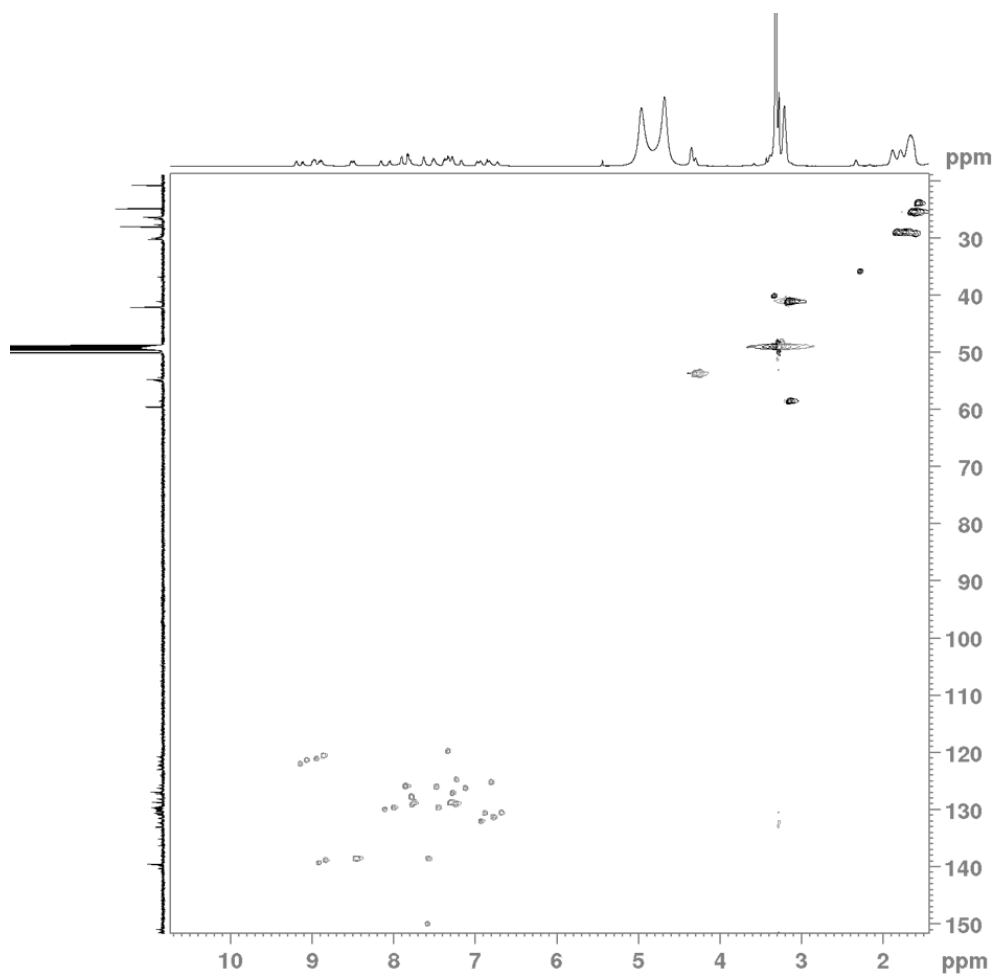
**Figure S2. 9** HR-MS (MALDI-QTOF): Single Mass Analysis of **(3)** indicating  $[M - H]^+$ .

S2.2.1.4 *Ru(biq)2(trzbenz-CONH-R8) (4)*

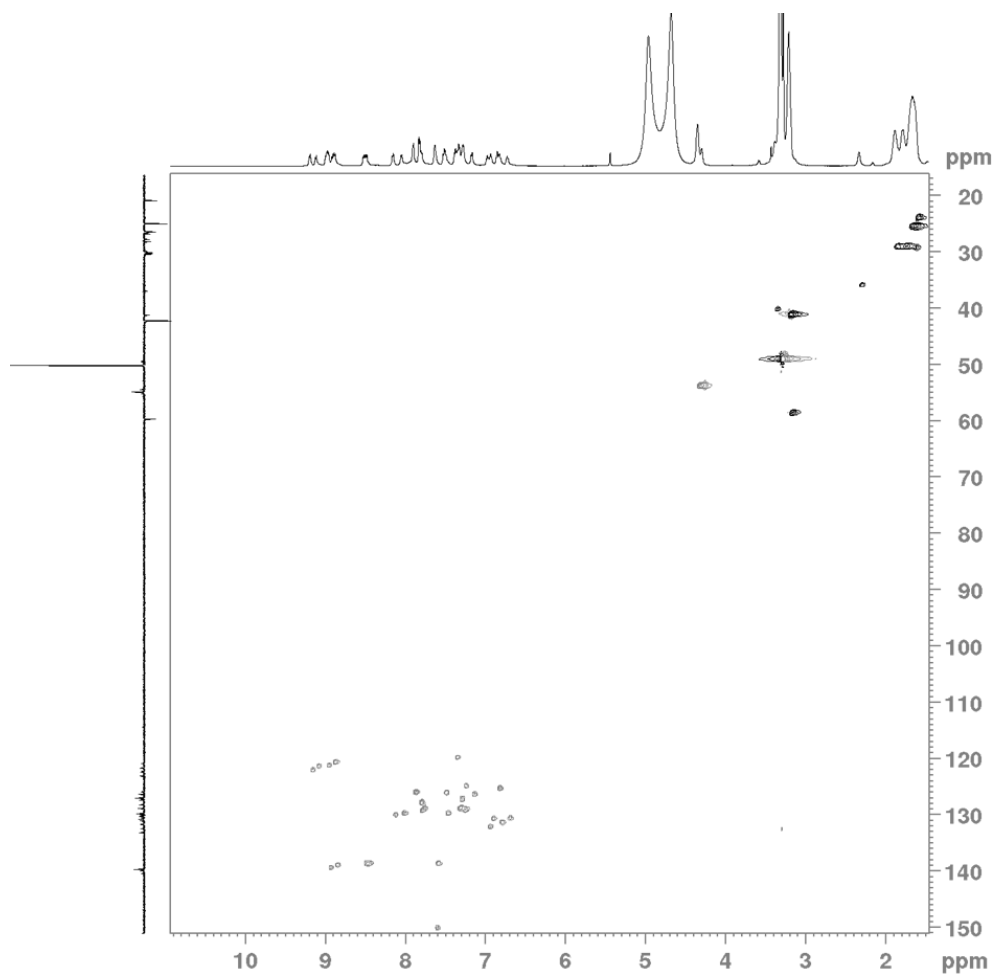


**Figure S2. 10**  $^1\text{H}$  NMR spectrum of **(4)** (600 MHz, MeOD + 1 drop of  $\text{D}_2\text{O}$ )

9.19 (d, 2H); 9.02-8.88 (m, 4H); 8.51 (t, 2H); 8.16 (d, 1H); 8.05 (d, 1H); 7.91-7.78 (m, 5H); 7.76-7.50 (m, 4H); 7.38-7.19 (m, 8H); 7.01-6.73 (m, 5H); 4.32 (m, 8H); 3.39 (m, 2H); 3.32 (m, 8H); 3.23 (m, 14H); 2.35 (m, 2H); 1.91-1.68 (m, 33H).

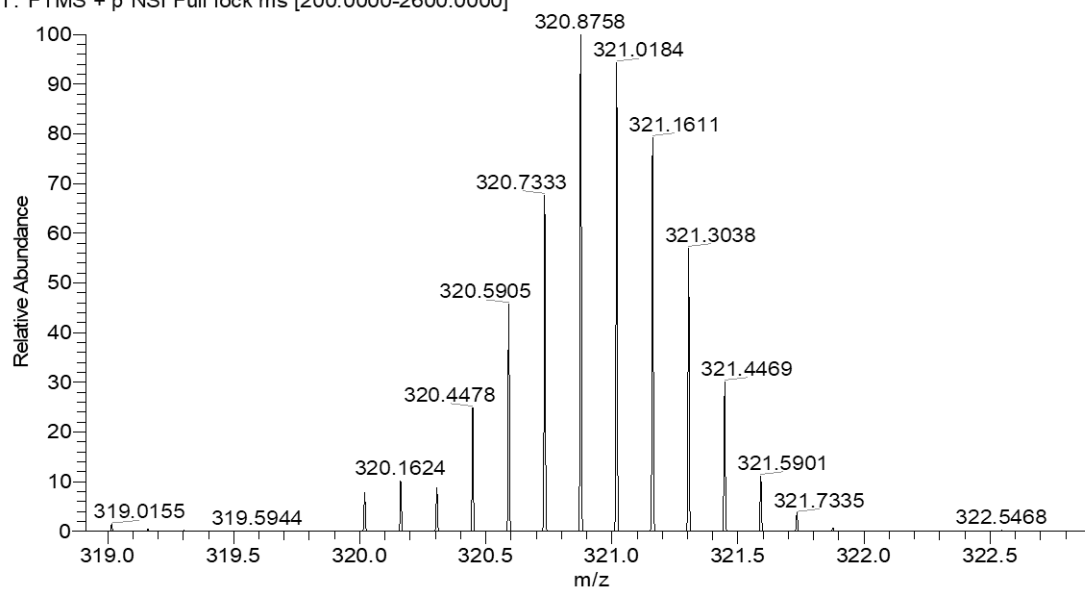


**Figure S2. 11**  $^1\text{H}$ - $^{13}\text{C}$  2D HSQC NMR spectrum of **(4)** (600 MHz, MeOD + 1 drop of  $\text{D}_2\text{O}$ )



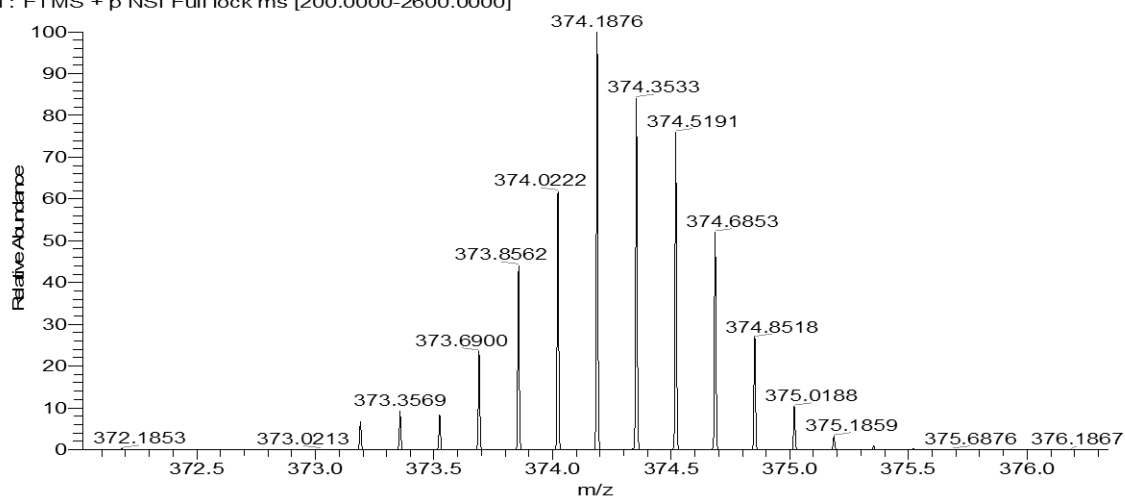
**Figure S2. 12**  $^1\text{H}$ - $^{13}\text{C}$ DEPT135 2D HSQC NMR spectrum of (**4**) (600 MHz, MeOD + 1 drop of  $\text{D}_2\text{O}$ )

DJCTK\_004\_5ul\_DCU\_290618 #10179-10513 RT: 22.40-23.09 AV: 84 NL: 4.61E8  
 T: FTMS + p NSI Full lock ms [200.0000-2600.0000]



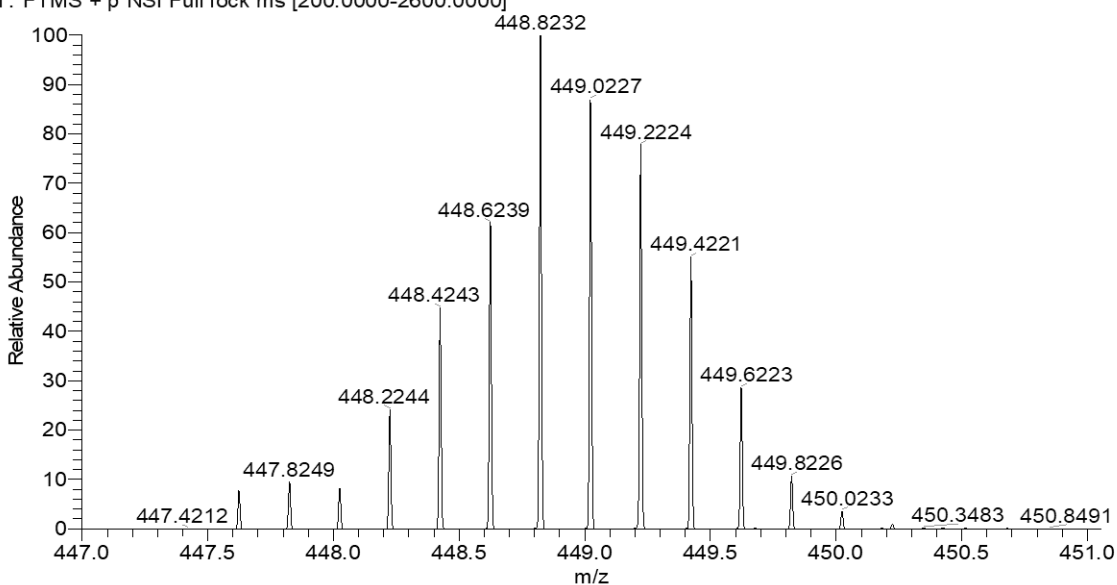
**Figure S2. 13** MALDI QTOF of (**4**)  $Z=7$ ,  $\text{C}_{104}\text{H}_{147}\text{N}_{42}\text{O}_{10}\text{Ru}$  Calc. 320.8761 Found 320.8758 [ $\text{M} - 2\text{H}^+$ ]

DJCTK\_004\_5ul\_DCU\_290618 #10179-10513 RT: 22.40-23.09 AV: 84 NL: 2.05E9  
T: FTMS + p NSI Full lock ms [200.0000-2600.0000]



**Figure S2. 14** MALDI QTOF of (4) Z= 6, C<sub>104</sub>H<sub>146</sub>N<sub>42</sub>O<sub>10</sub>Ru Calc. 374.1875 Found 374.1876 [M - 3H<sup>+</sup>]

DJCTK\_004\_5ul\_DCU\_290618 #10179-10513 RT: 22.40-23.09 AV: 84 NL: 1.10E9  
T: FTMS + p NSI Full lock ms [200.0000-2600.0000]

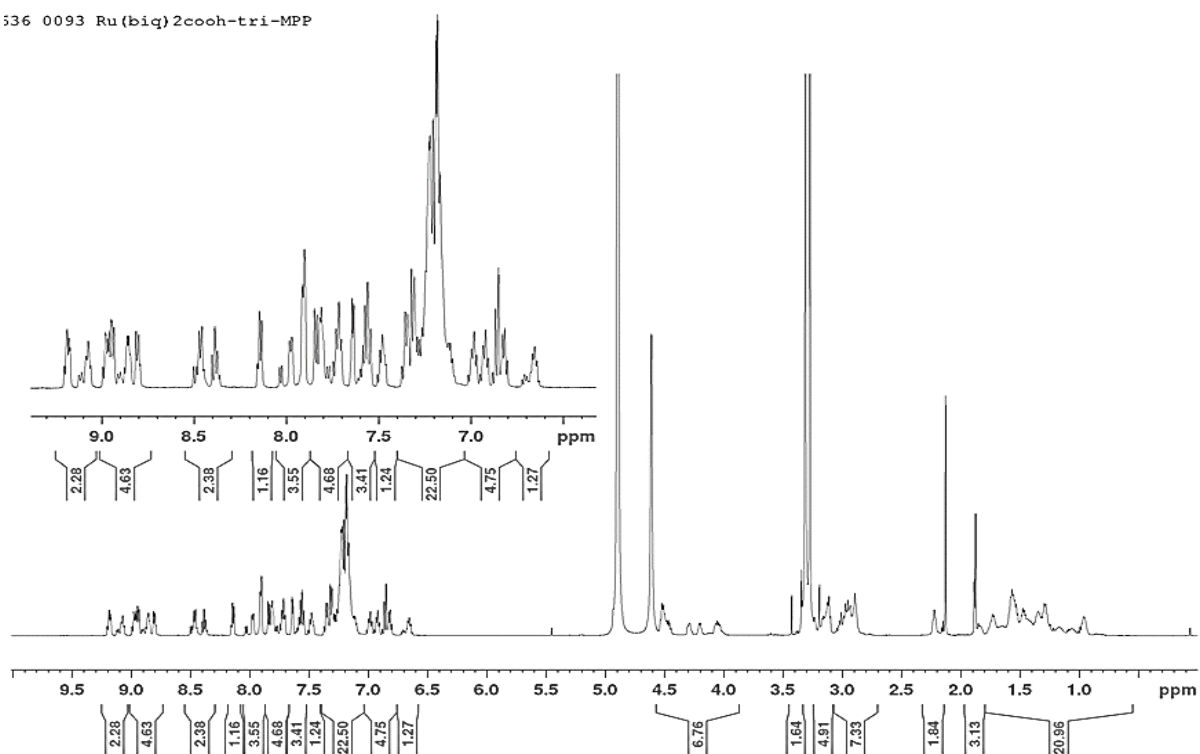


**Figure S2. 15** MALDI QTOF of (4) Z= 5, C<sub>104</sub>H<sub>145</sub>N<sub>42</sub>O<sub>10</sub>Ru Calc. 448.8234 Found 448.8232 [M - 4H<sup>+</sup>]



### S2.2.1.5 Ru(biq)<sub>2</sub>(trzbenz-CONH-MPP) (5)

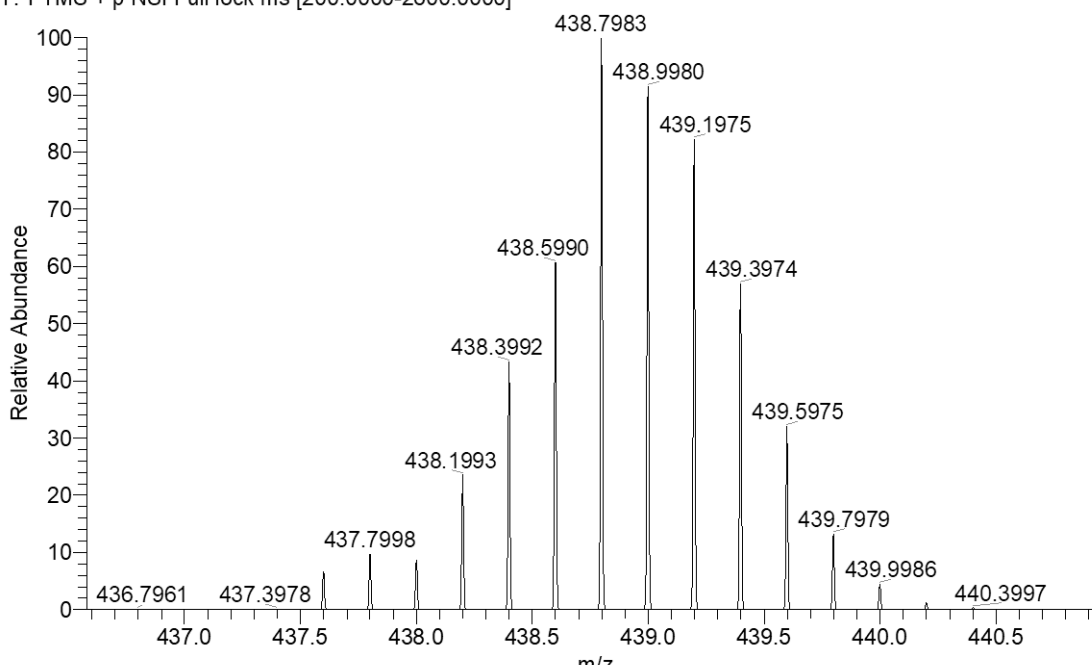
536 0093 Ru(biq)<sub>2</sub>cooh-tri-MPP



**Figure S2. 16** <sup>1</sup>H NMR spectrum of (5) (600 MHz, MeOD + 1 drop of D<sub>2</sub>O)

9.21-9.03 (m, 2H); 9.01-8.73 (m, 5H); 8.54-8.30 (m, 2H); 8.14 (m, 1H); 8.05-7.87 (m, 4H); 7.87-7.67 (m, 5H); 7.65-7.52 (m, 3H); 7.47 (m, 1H); 7.38-7.04 (m, 23H); 7.03-6.76 (m, 5H); 6.67 (m, 1H); 4.57-

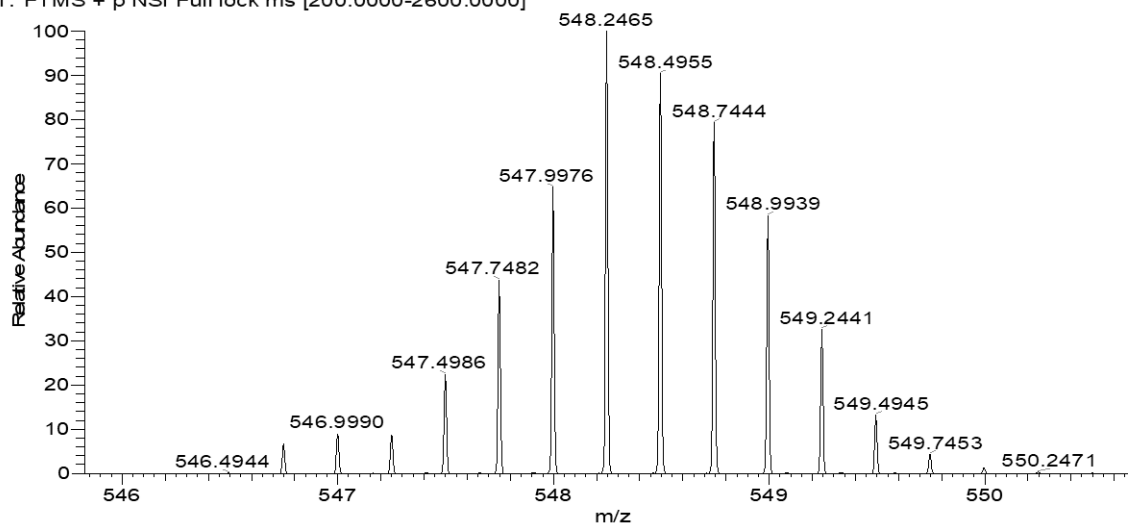
DJCTK\_006\_5ul\_DCUI\_290618 #13313-13649 RT: 29.34-30.06 AV: 85 NL: 2.07E8  
T: FTMS + p NSI Full lock ms [200.0000-2600.0000]



**Figure S2. 17** MALDI QTOF of (5) Z=5, C<sub>118</sub>H<sub>135</sub>N<sub>26</sub>O<sub>11</sub>Ru Calc. 438.7969 Found 438.7983 [M + 1H<sup>+</sup>]

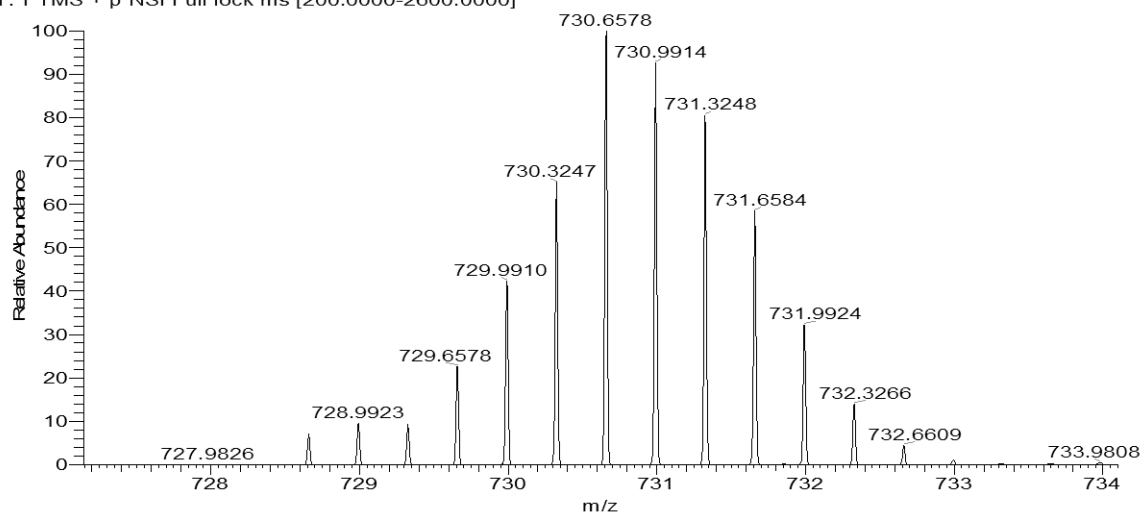
3.86 (m, 7H); 3.45-3.33 (m, 2H); 3.24-3.08 (m, 5H); 3.07-2.70 (m, 7H); 2.32-2.13 (m, 2H); 1.96-1.79 (m, 3H); 1.79-0.55 (m, 21H).

DJCTK\_006\_5ul\_DCU\_290618 #13313-13649 RT: 29.34-30.06 AV: 85 NL: 6.17E8  
T: FTMS + p NSI Full lock ms [200.0000-2600.0000]



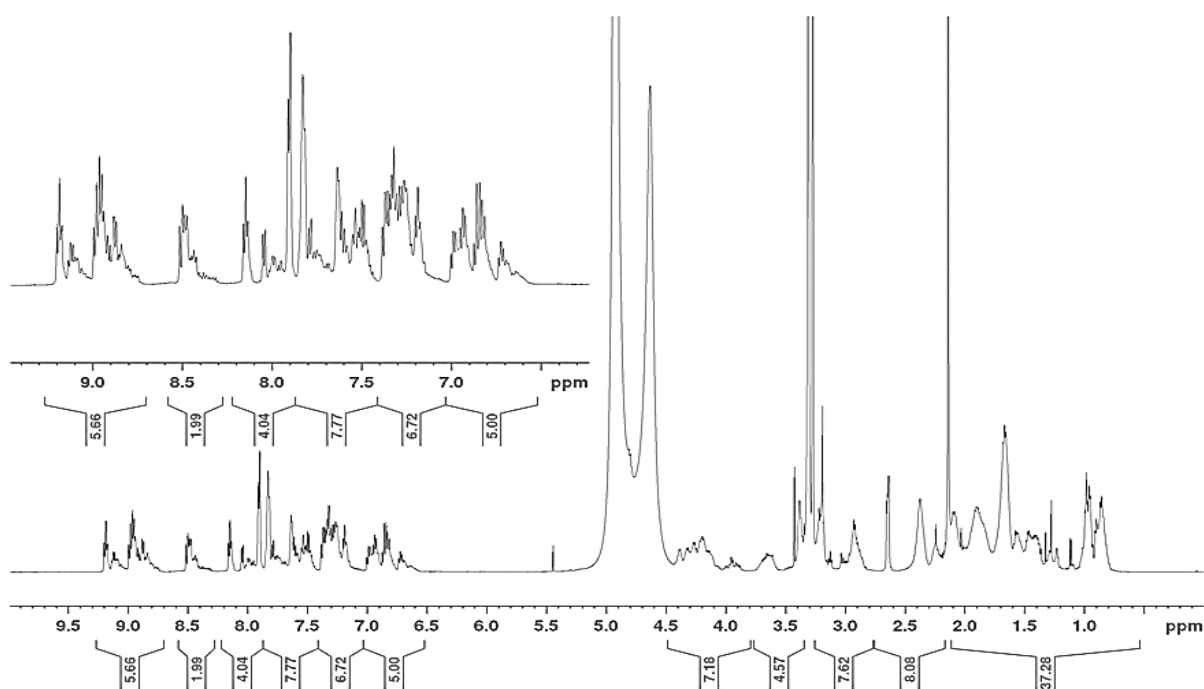
**Figure S2. 18** MALDI QTOF of (5) Z=4, C<sub>118</sub>H<sub>134</sub>N<sub>26</sub>O<sub>11</sub>Ru Calc. 548.2442 Found 548.2465 [M<sup>+</sup>]

DJCTK\_006\_5ul\_DCU\_290618 #13313-13649 RT: 29.34-30.06 AV: 85 NL: 1.00E8  
T: FTMS + p NSI Full lock ms [200.0000-2600.0000]



**Figure S2. 19** MALDI QTOF of (5) Z=3, C<sub>118</sub>H<sub>134</sub>N<sub>26</sub>O<sub>11</sub>Ru Calc. 730.6563 Found 730.6578 [M -H<sup>+</sup>]

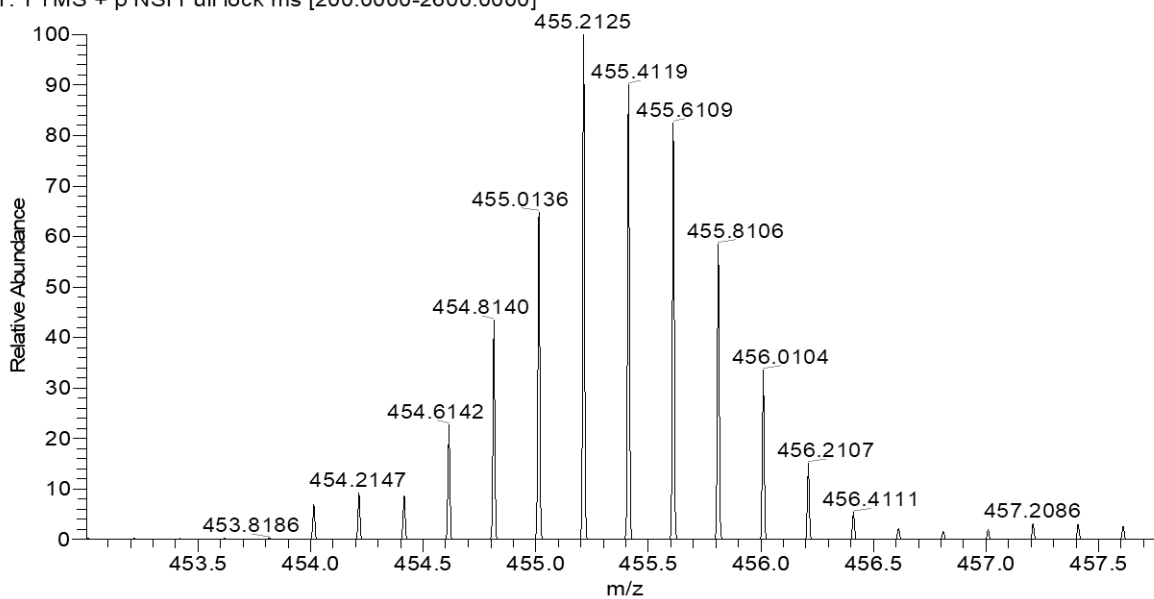
S2.2.1.6 Ru(biq)2(trzbenz-CONH-NLS) (6)



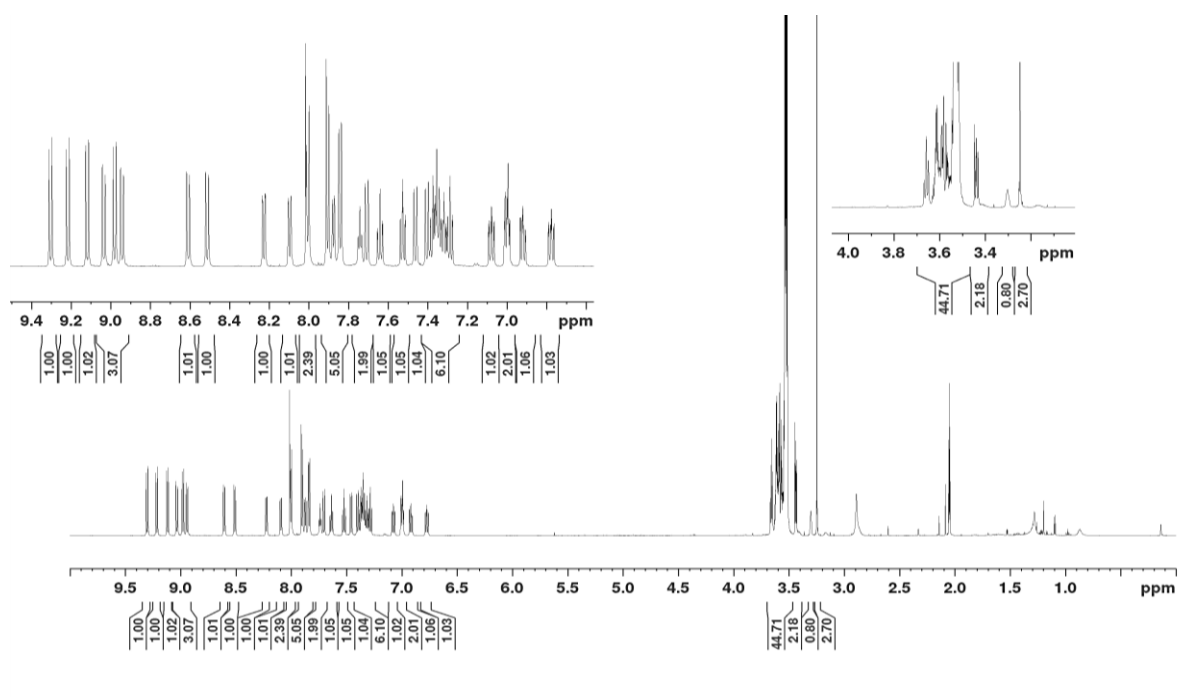
**Figure S2. 20** <sup>1</sup>H NMR spectrum of (6) (600 MHz, MeOD + 1 drop of D<sub>2</sub>O)

9.19-8.74 (m, 6H); 8.52-8.31 (m, 2H); 8.16-7.88 (m, 4H); 7.85-7.41 (m, 8H); 7.39-7.11 (m, 7H); 7.00-6.57 (m, 5H); 4.43-3.80 (m, 7H); 3.73-3.33 (m, 5H); 3.26-2.76 (m, 8H); 2.75-2.16 (m, 8H); 2.11-0.54 (m, 38H).

DJCTK\_005\_5uL\_DCUI\_290618 #11715-12816 RT: 25.79-28.11 AV: 275 NL: 4.18E8  
T: FTMS + p NSI Full lock ms [200.0000-2600.0000]

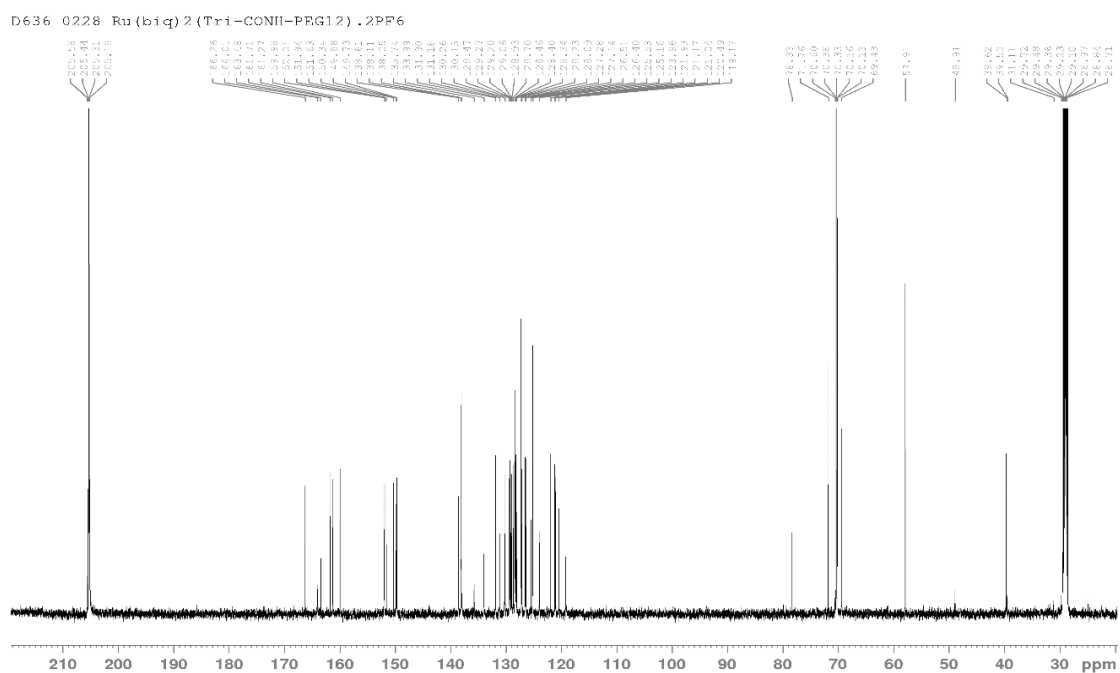


**Figure S2. 21** MALDI QTOF of (6) Z=5 C<sub>111</sub>H<sub>146</sub>ClN<sub>30</sub>O<sub>13</sub>RuS Calc. 455.2027 Found 455.2125 [M-(H<sub>3</sub>O<sup>+</sup>)]



**Figure S2. 22**  $^1\text{H}$  NMR spectrum (600 MHz) of (**7**) in Acetone- $\text{d}_6$ .

9.30 (1H, d, 8.6 Hz), 9.21 (1H, d,  $J = 8.9$  Hz), 9.11 (1H, d,  $J = 8.7$  Hz), 9.03 (1H, d,  $J = 8.7$  Hz), 8.98 (1H, d,  $J = 8.9$  Hz), 8.94 (1H, d,  $J = 8.7$  Hz), 8.60 (1H, d,  $J = 8.9$  Hz), 8.51 (1H, d,  $J = 8.7$  Hz), 8.22 (1H, d,  $J = 8.2$  Hz), 8.09 (1H, d,  $J = 8.2$  Hz), 8.01-7.99 (2H, m), 7.91-7.83 (5H, m), 7.75-7.69 (2H, m), 7.63 (1H, t,  $J = 7.4$ ), 7.52 (1H, t,  $J = 7.4$  Hz), 7.46 (1H, d,  $J = 8.9$  Hz), 7.41-7.27 (6H, m), 7.07 (1H, t,  $J = 7.8$  Hz),



**Figure S2. 23**  $^{13}\text{C}$  NMR spectrum (600 MHz) of (**7**) in Acetone- $\text{d}_6$ .

7.01-6.98 (2H, m), 6.92 (1H, t, J= 7.7 Hz), 6.77 (1H, t, J= 7.8 Hz), 3.66-3.51 (45H, m), 3.44-3.43 (2H, m), 3.30 (1H, s), 3.25-3.24 (3H, m).

167.24, 164.98, 164.46, 162.67, 162.23, 160.95, 152.97, 152.89, 152.57, 151.31, 150.83, 150.68, 139.58, 139.06, 139.01, 136.70, 134.95, 132.85, 132.14, 131.22, 131.10, 130.41, 130.22, 130.15, 130.00, 129.87, 129.64, 129.40, 129.34, 129.28, 129.17, 129.03, 128.22, 128.08, 127.46, 127.33, 126.47, 126.11, 124.90, 122.87, 122.11, 121.98, 121.42, 120.11, 79.32, 72.70, 71.32, 71.24, 71.11, 71.07, 70.37, 58.86, 40.58.

### Elemental Composition Report

Page 1

#### Single Mass Analysis

Tolerance = 50.0 PPM / DBE: min = -1.5, max = 400.0

Element prediction: Off

Number of isotope peaks used for i-FIT = 5

#### Monoisotopic Mass, Odd and Even Electron Ions

260 formula(e) evaluated with 1 results within limits (up to 10 closest results for each mass)

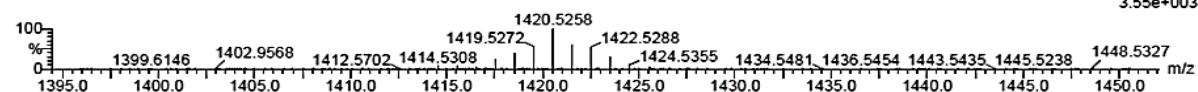
Elements Used:

C: 0-75 H: 0-84 N: 0-9 O: 0-13 Ru: 0-1

David Cullinane (TK), DJCTK015

Q-TOF20191205MF010 81 (1.501) AM (Cen,8, 80.00, Ht,10000.0,1570.68,0.70); Sm (SG, 2x3.00); Sb (15,10.00); Cm (28:135)

TOF MS LD+  
3.55e+003



Minimum: -1.5  
Maximum: 5.0 50.0 400.0

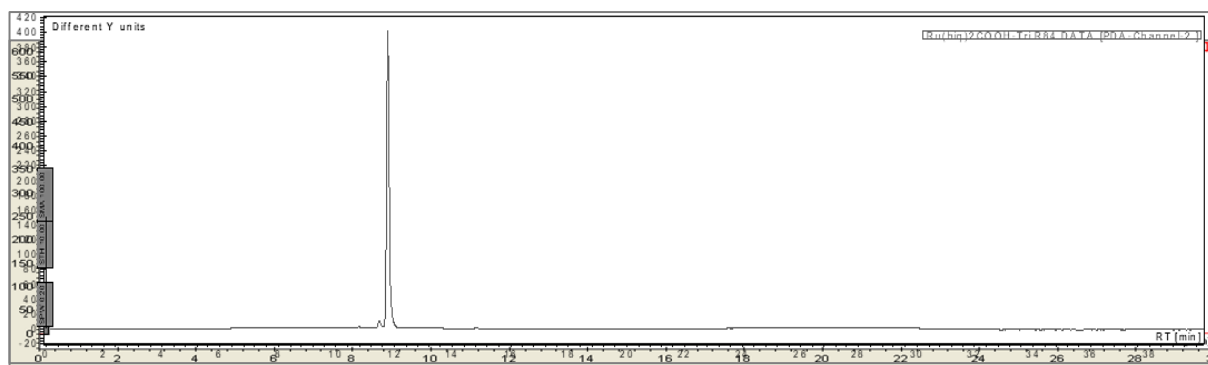
Mass	Calc. Mass	mDa	PPM	DBE	i-FIT	i-FIT (Norm)	Formula
1420.5258	1420.5232	2.6	1.8	38.5	120.6	0.0	C75 H84 N9 O13 Ru

**Figure S2. 24** HR-MS (MALDI-QTOF): Single Mass Analysis of (7) indicating [M]<sup>+</sup>.

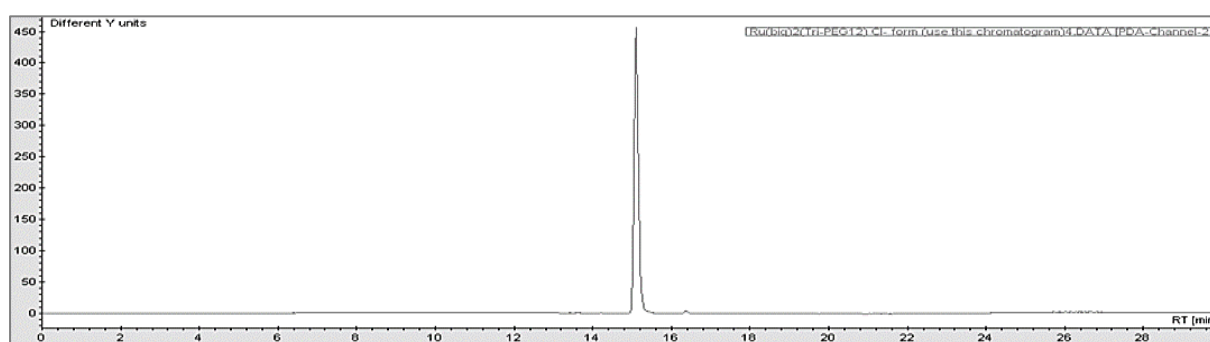
### S2.2.2 HPLC Chromatograms of parent complex and conjugates

-Indicates purity of the conjugate relative to the parent complex

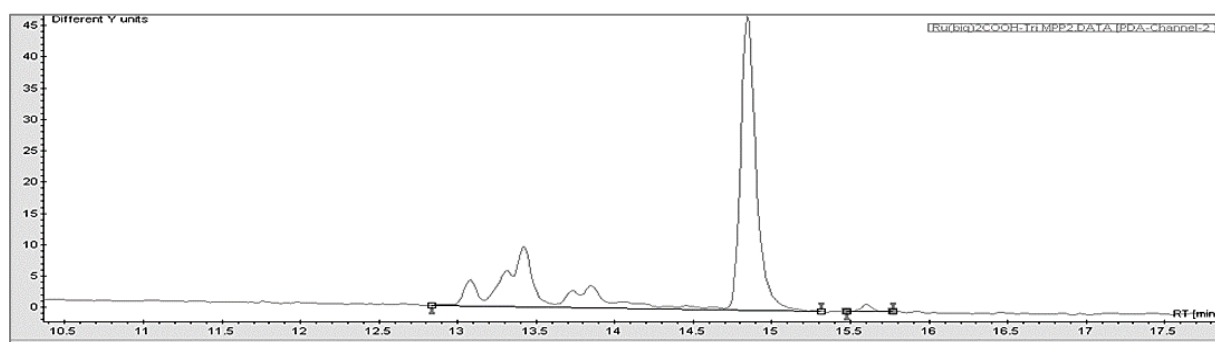
-(RP-C18, MeCN/Water 0.1 % TFA gradient, 554 nm)



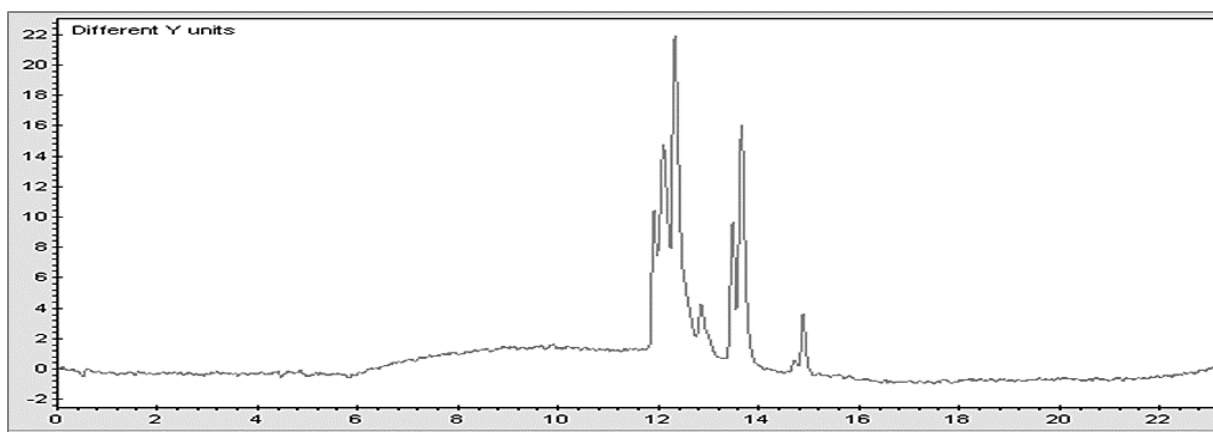
**Figure S2. 26** Chromatogram of  $[\text{Ru}(\text{biq})_2(\text{trzbenz-CONH-R8})]^{9+}$  (**5**)- (100 % pure relative to parent).  
 - (Reverse Phase-C18, MeCN/Water 0.1 % TFA gradient, 554 nm)



**Figure S2. 27** Chromatogram of  $\text{Ru}(\text{biq})_2(\text{trzbenz-CONH-PEG}_{12})\cdot\text{Cl}$  - (100 % pure relative to parent)  
 - (Reverse Phase-C18, MeCN/Water 0.1 % TFA gradient, 554 nm).

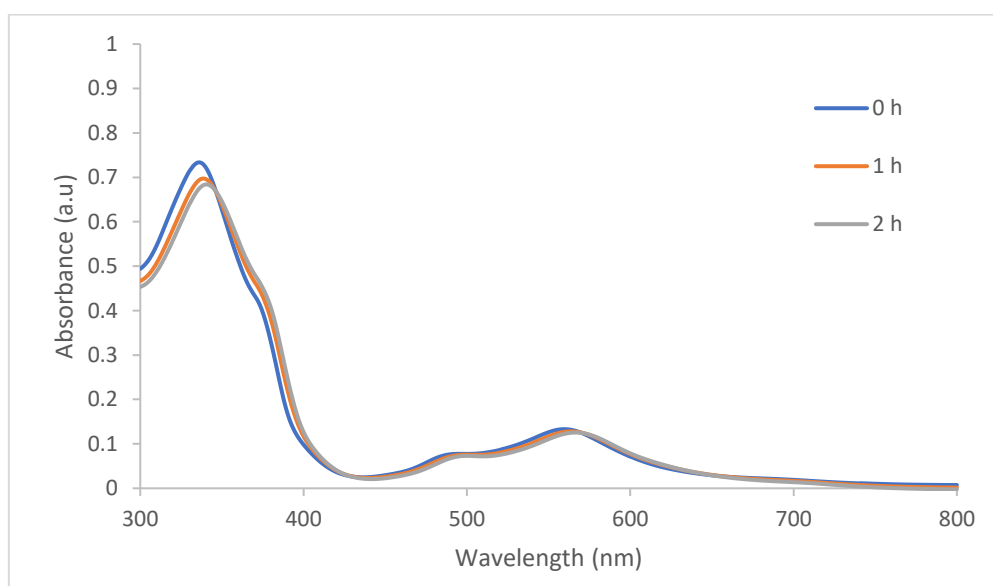


**Figure S2. 28** Chromatogram of  $[\text{Ru}(\text{biq})_2(\text{trzbenz-CONH-MPP})]^{4+}$  (**6**)- (98.5 % pure relative to parent)  
 - (Reverse Phase-C18, MeCN/Water 0.1 % TFA gradient, 554 nm)

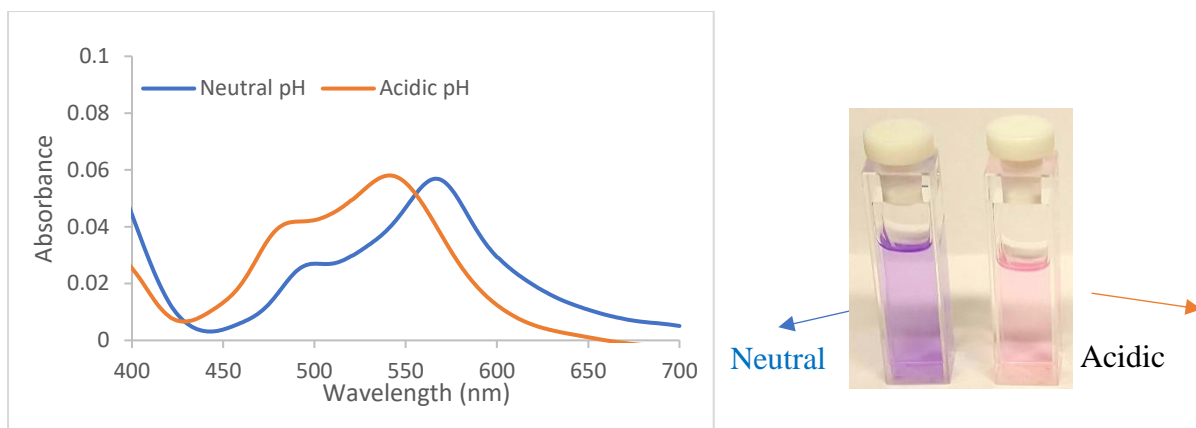


**Figure S2. 29** Chromatogram of  $[\text{Ru}(\text{biq})_2(\text{trzbenz-CONH-NLS})]^{5+}$  (7)- (100 % pure relative to parent) - (Reverse Phase-C18, MeCN/Water 0.1 % TFA gradient, 554 nm)

### S2.3 Photophysical Data

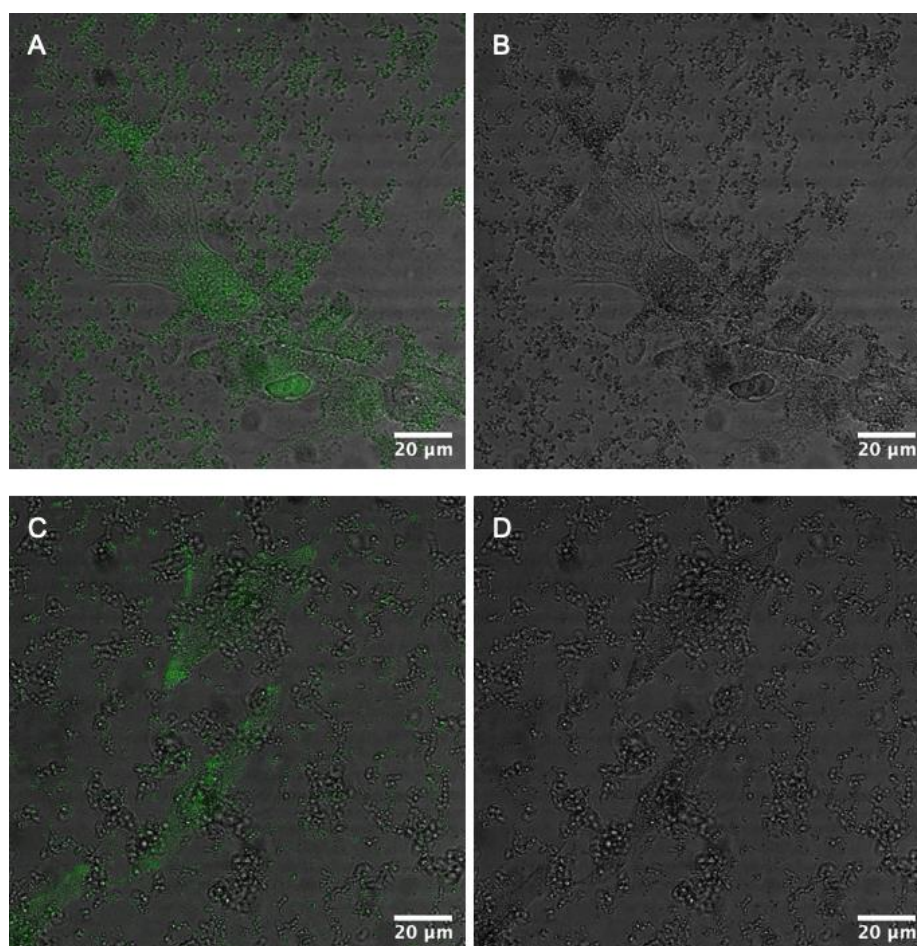


**Figure S2. 30** Photostability study of parent complex  $\text{Ru}(\text{biq})_2(\text{trzbenzCOOH}).\text{Cl}$  in  $\text{H}_2\text{O}$  (1 % v/v DMSO), absorbance spectra measured at defined time intervals during continuous photo-irradiation with Xenon ARC Lamp 150W for 2 h at room temperature.



**Figure S2. 31** UV-vis absorption spectrum of parent complex in acetonitrile at neutral pH and at acidic pH (1 % v/v perchloric acid). Picture (right) showing effect of pH on color of compound in acetonitrile solution.

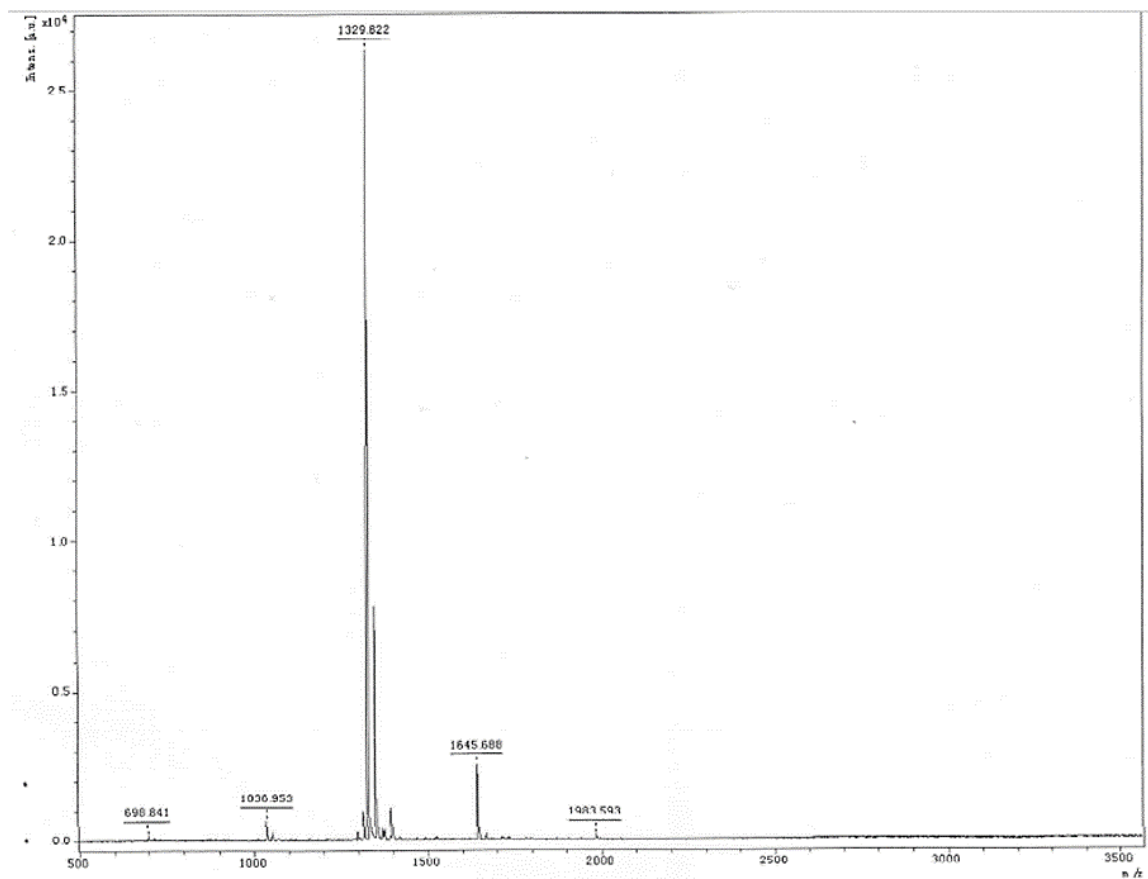
## S2.4 Cellular Studies



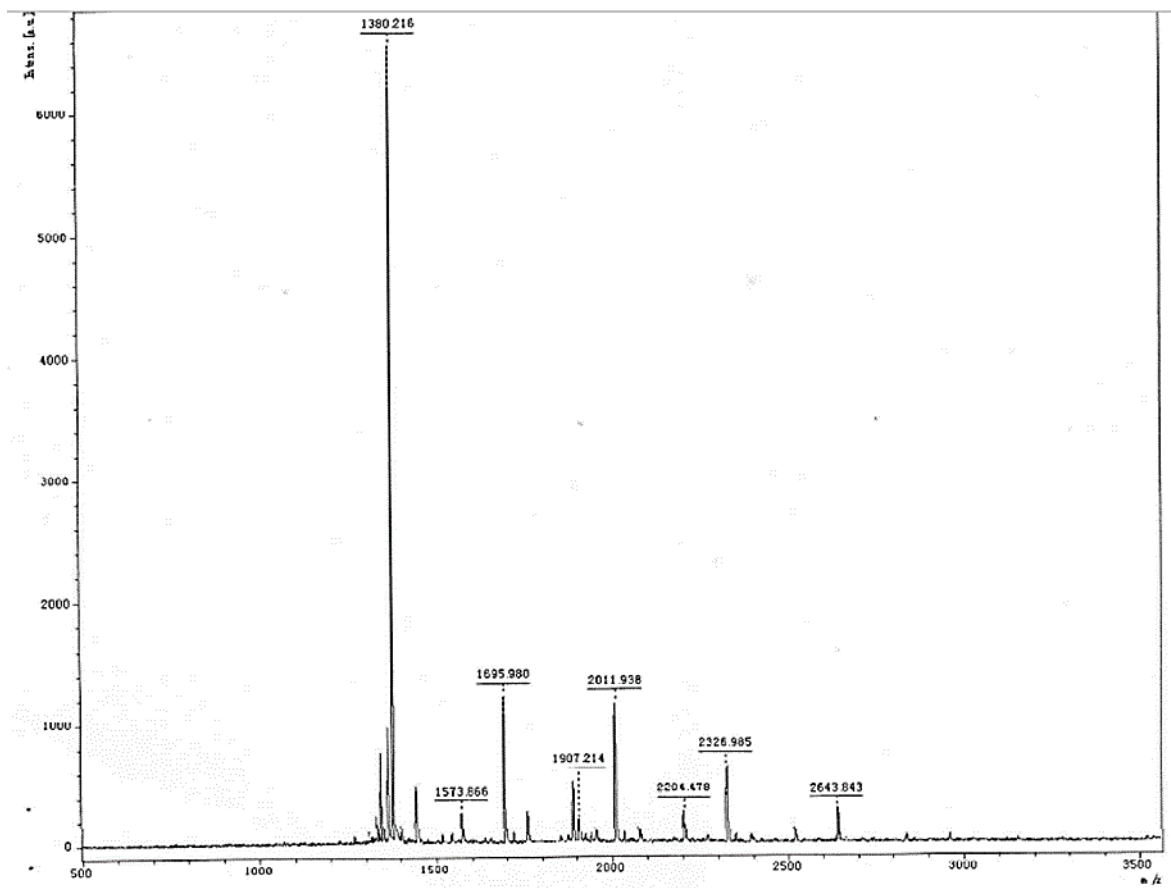
**Figure S2. 32** Confocal images of HeLa cells treated with RuNLS (A,B) and RuR8 (C,D) (100 μM) for 3 h. Cells were washed twice with PBS prior to imaging. (Rubiq emission shown in green (A,C) has been increased for printing purposes). Transmission fluorescence (B,D) showing the cell debris after 3 h incubation.



## S2.5 Mass Spectrometry of peptide sequences



**Figure S2. 33** Mass spectrometry spectrum of R8 peptide sequence NH<sub>2</sub>-Ahx-R-R-R-R-R-R-R-R-CONH<sub>2</sub> (Provided by Celtek Peptides).



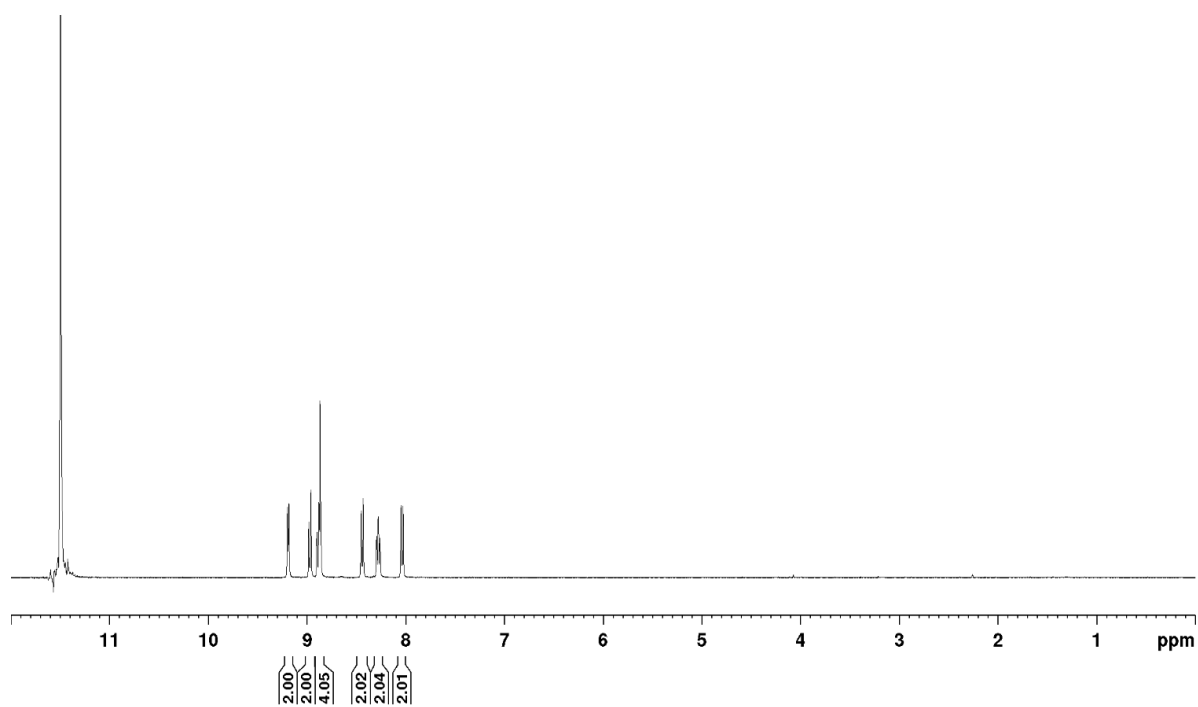
**Figure S2. 34** Mass spectrometry spectrum of MPP peptide sequence  $\text{NH}_2\text{-Ahx-F-r-F-K-F-r-F-K(Ac)-CONH}_2$  (Provided by Celtek Peptides)



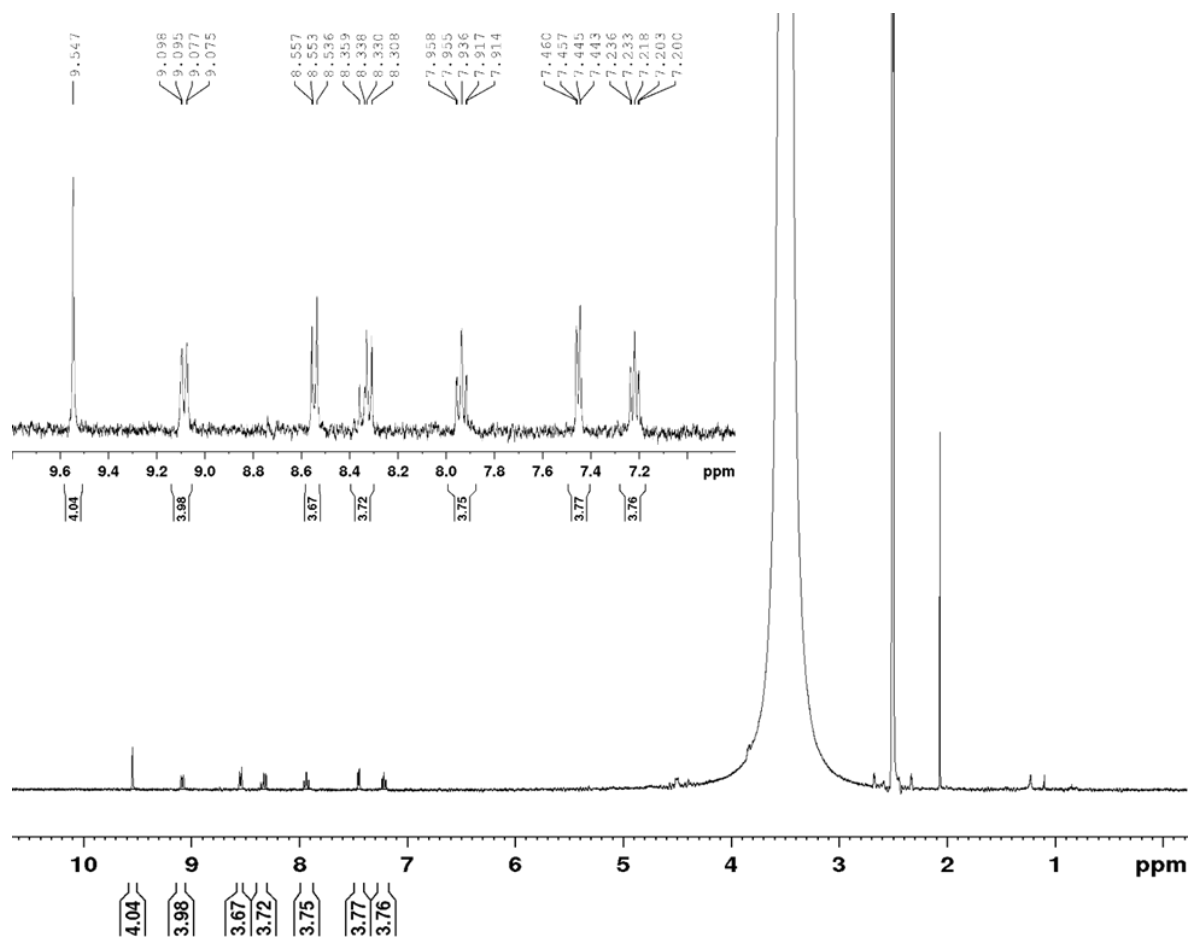
## Appendix B

Supplementary material associated with **Chapter 3** “*Mitochondrial targeted osmium polypyridyl probe shows concentration dependent uptake, localisation and mechanism of cell death*”.

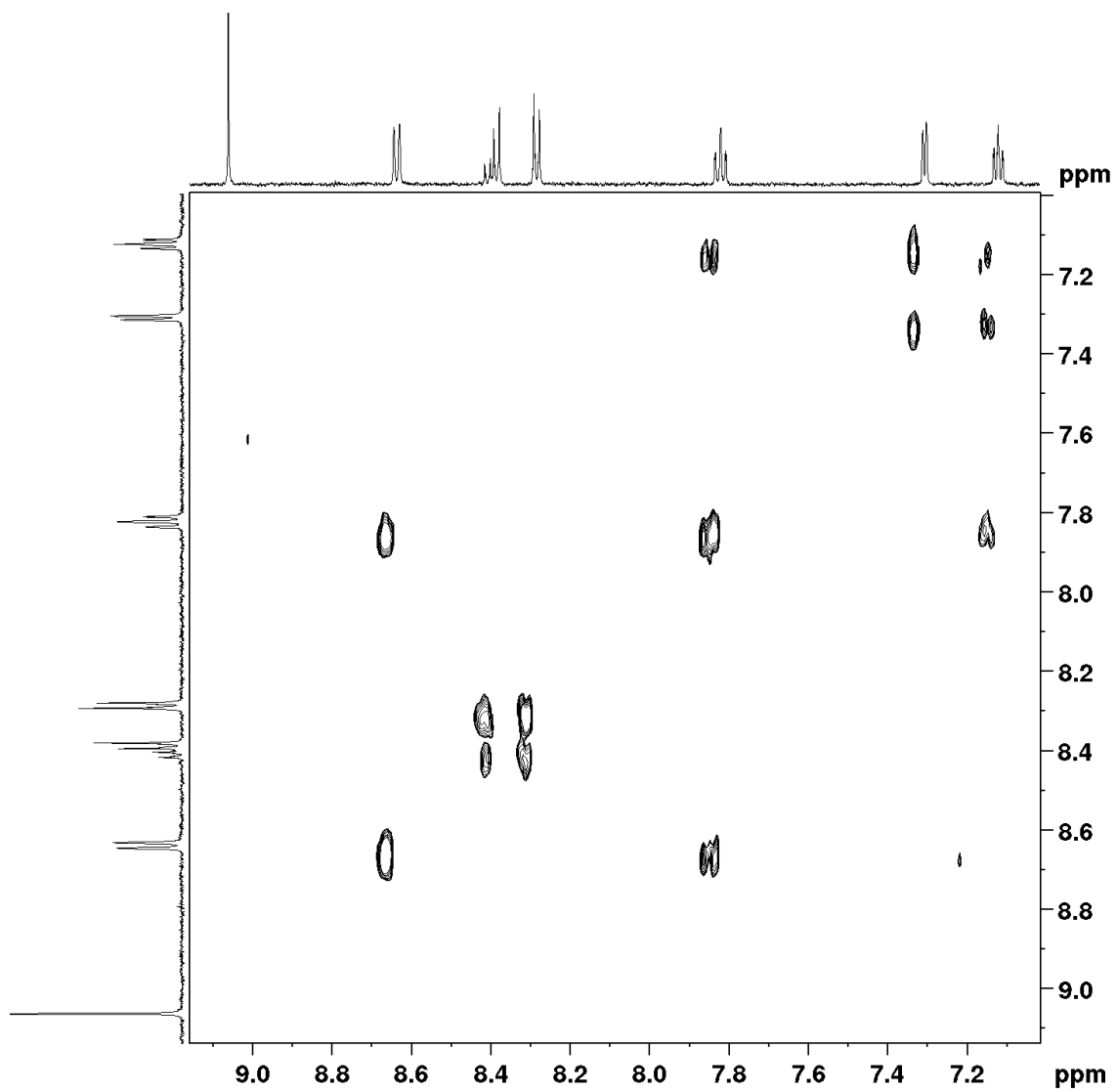
### S3.1 $^1\text{H}$ NMR spectra of tpybenzCOOH and Os(II) complexes



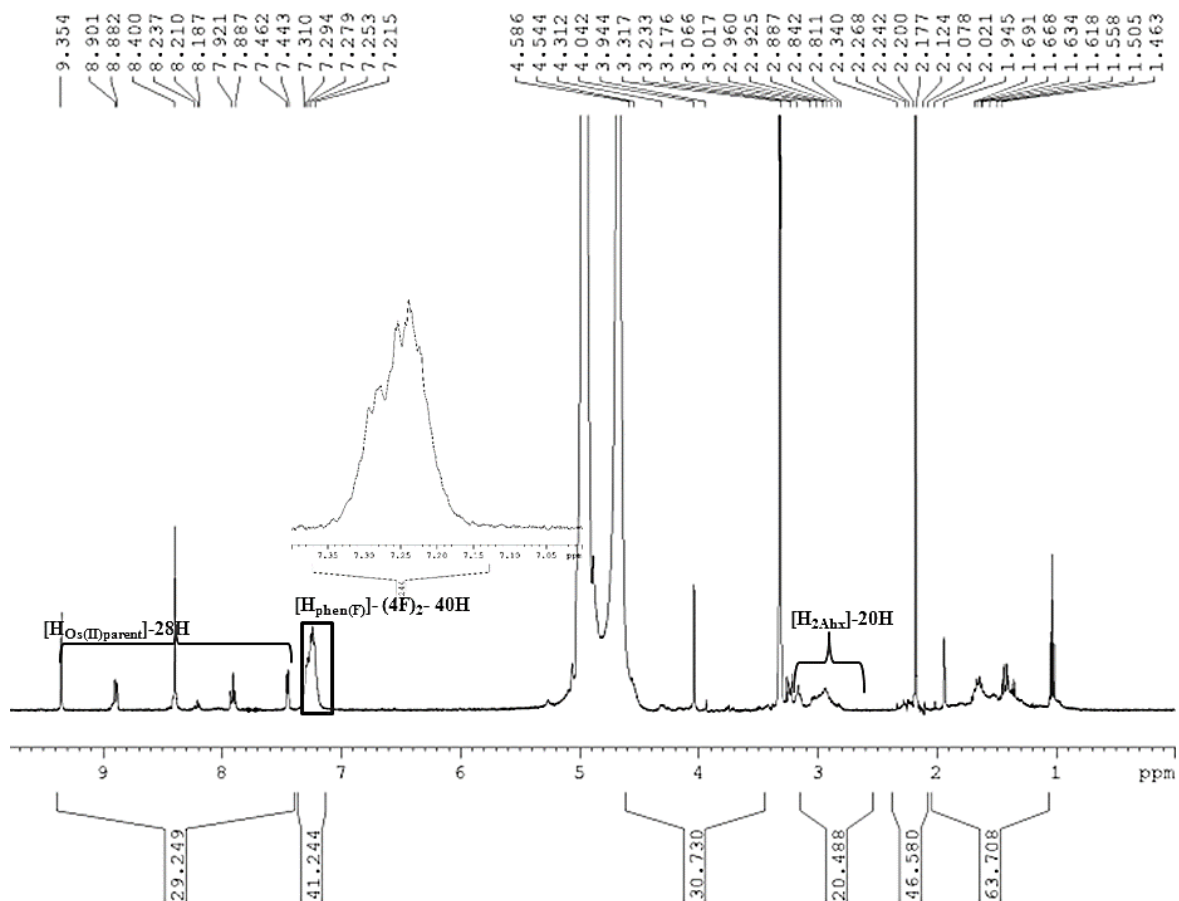
**Figure S3. 1**  $^1\text{H}$ -NMR spectra of tpybenzCOOH in DMSO- $d_6$  (top) and TFA- $d$ , (bottom) 600 MHz.



**Figure S3. 2**  $^1\text{H}$  NMR of purified  $[\text{Os}(\text{tpybenzCOOH})_2]^{2+}$  in  $\text{DMSO-d}_6$ , 400 MHz.

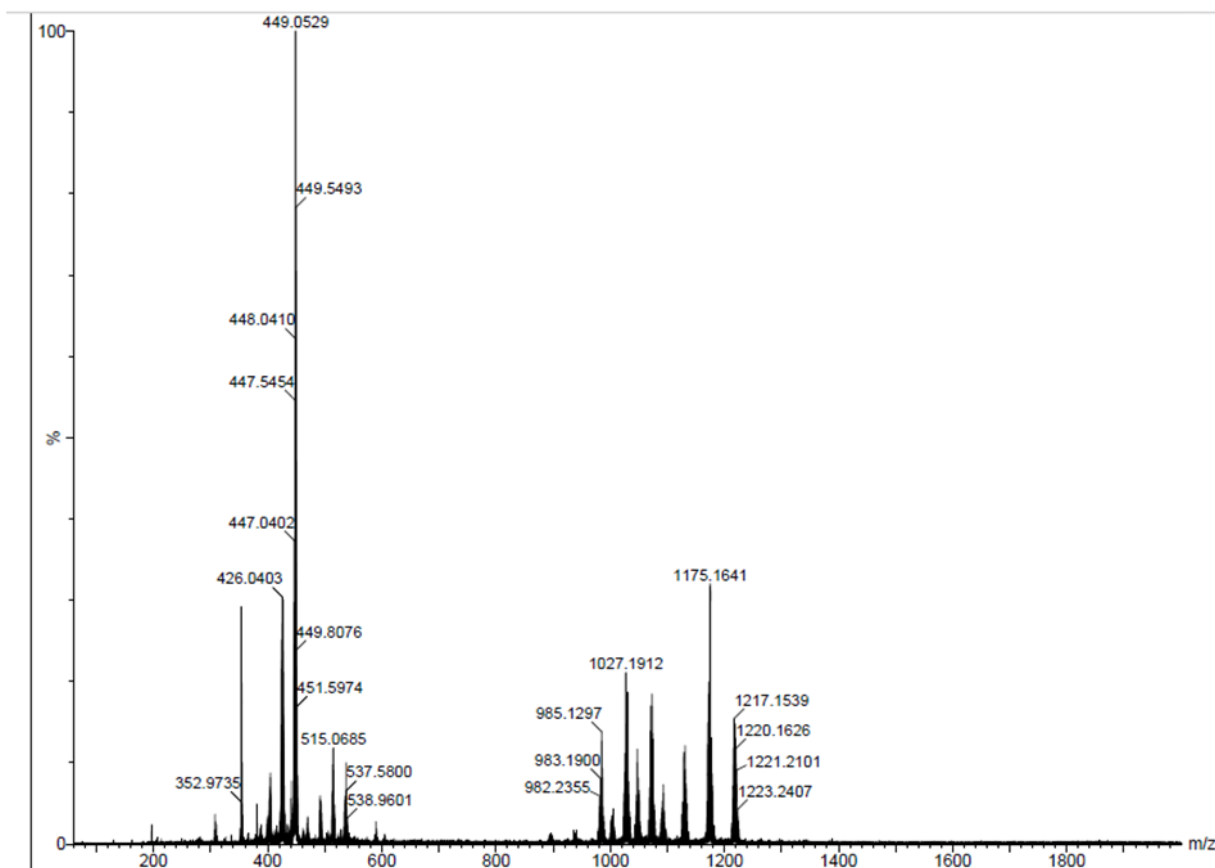


**Figure S3. 3** COSY spectrum of  $[\text{Os}(\text{tpybenzCOOH})_2]^{2+}$  in  $\text{MeCN-d}_3$ , 600 MHz.



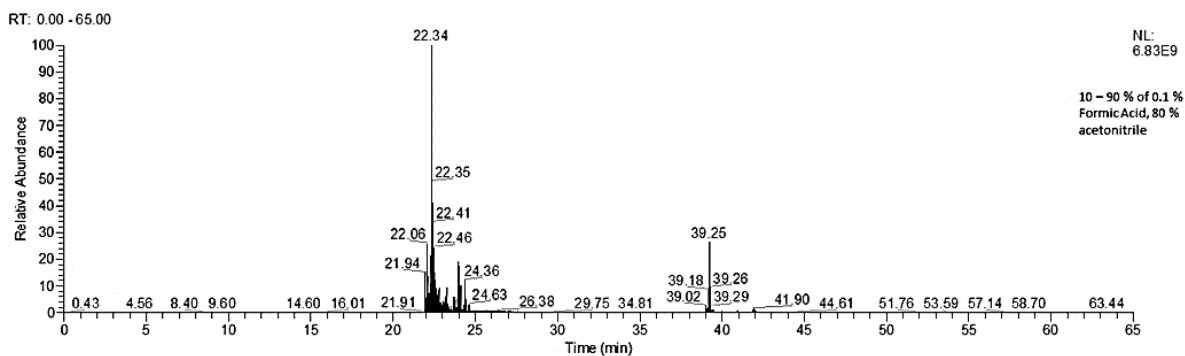
**Figure S3. 4**  $^1H$  NMR spectrum of  $Os^{II}MPP$  in  $MeOH-d_4$ , 400 MHz with key regions in the aromatic and aliphatic region highlighted.

### S3.2 Mass Spectrometry Analysis

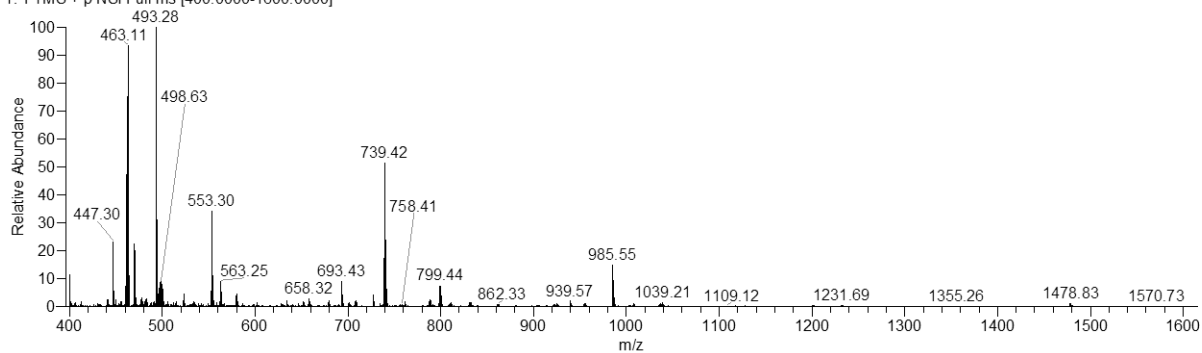


**Figure S3. 5** HRMS (TOF ES+) of  $[\text{Os}(\text{tpybenzCOOH})_2]^{2+}$

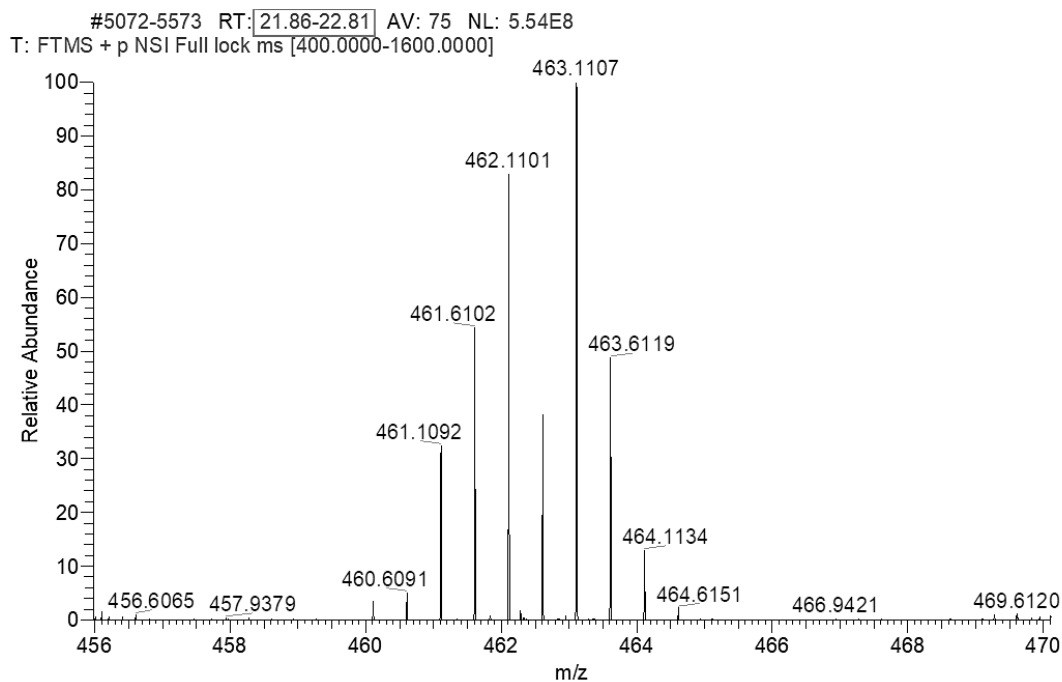




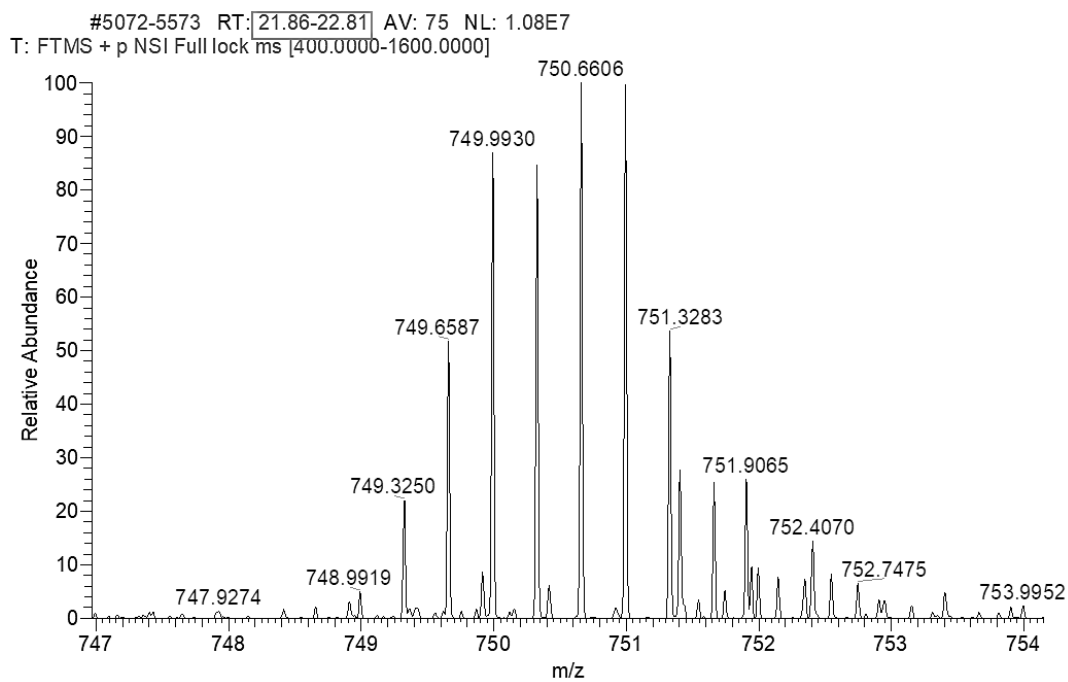
Blank 6 #5550-6384 RT: 22.75-24.81 AV: 215 NL: 8.44E7  
 T: FTMS + p NSI Full ms [400.0000-1600.0000]



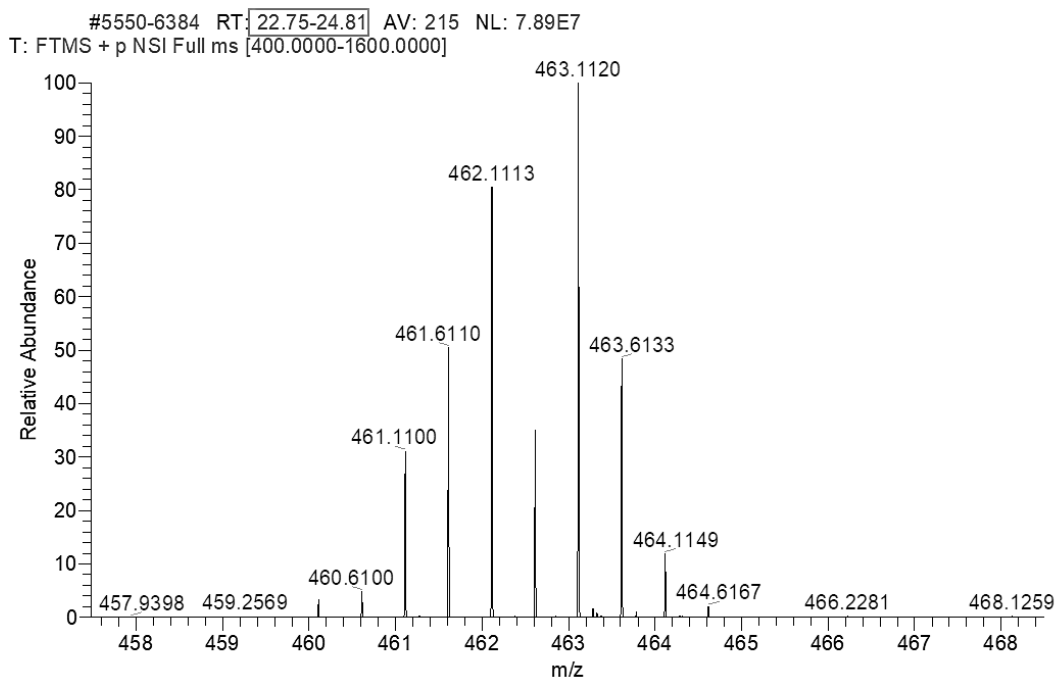
**Figure S3. 6** HPLC chromatogram (above) and Mass Spectrum (below) of Os<sup>II</sup> MPP complex following LC-MS analysis (Q-Exactive). Conditions; gradient extended from 10- 90 % (Formic Acid 0.1 %, 80 % MeCN).



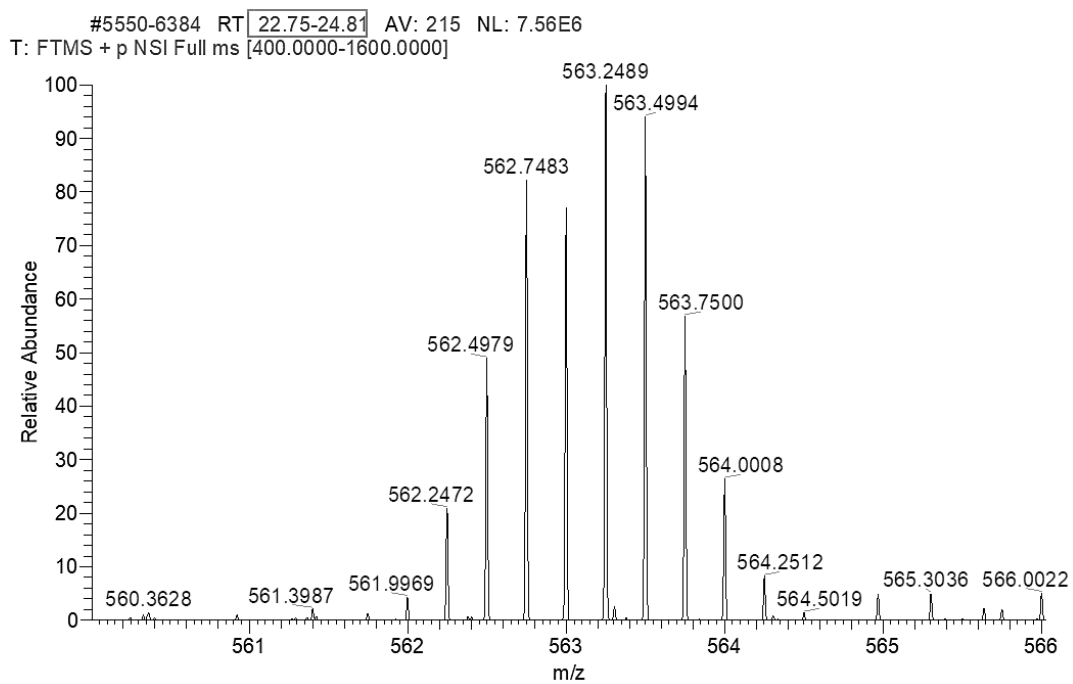
**Figure S3. 7** LC-MS analysis of Os<sup>II</sup>MPP Zoomed m/z 456-470 (RT 21-23 min).



**Figure S3. 8** LC-MS analysis of Os<sup>II</sup>MPP Zoomed m/z 747-754 (RT 21-23 min)

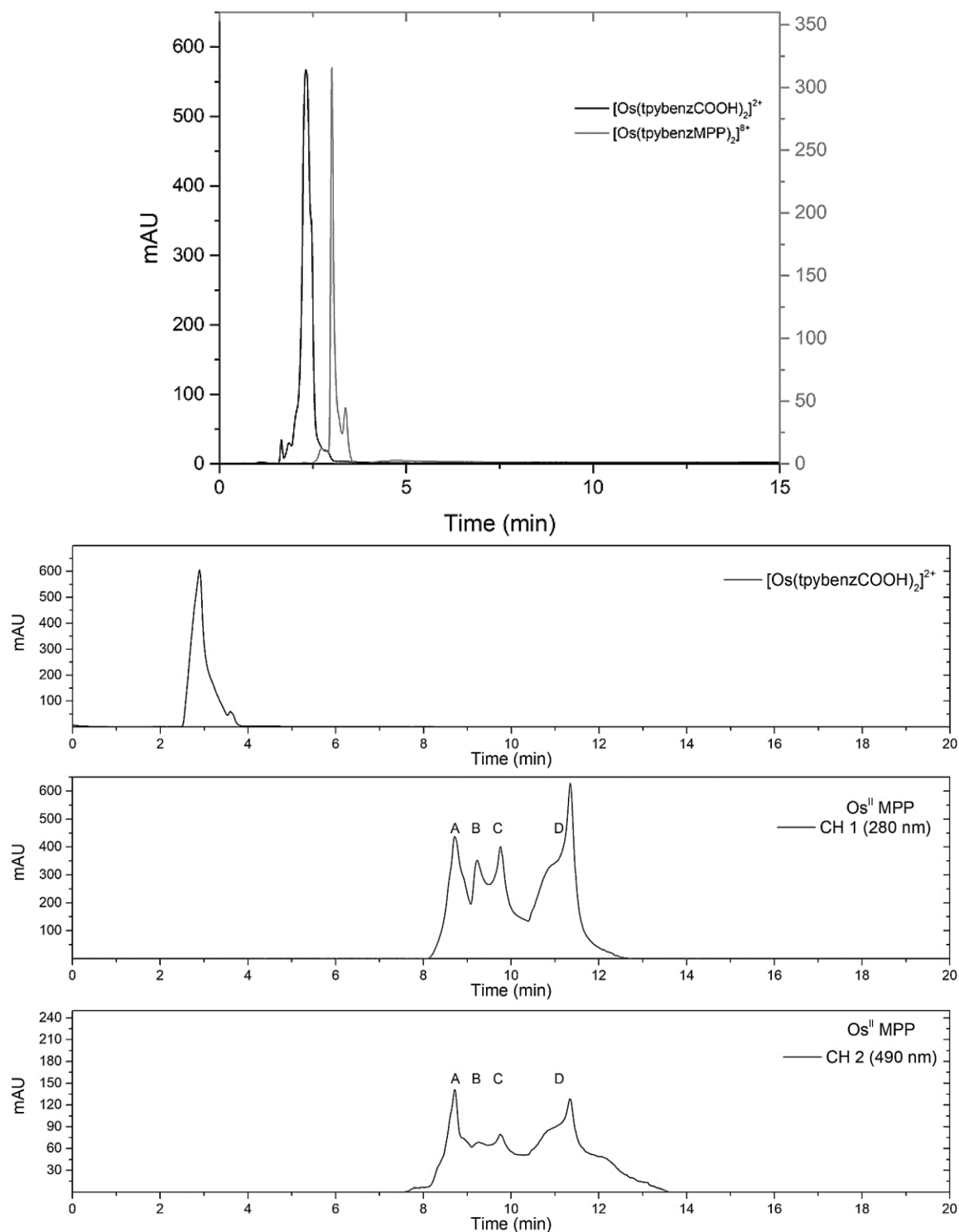


**Figure S3. 9** LC-MS analysis of Os<sup>II</sup>MPP Zoomed m/z 458-468 (RT 23-25 min).

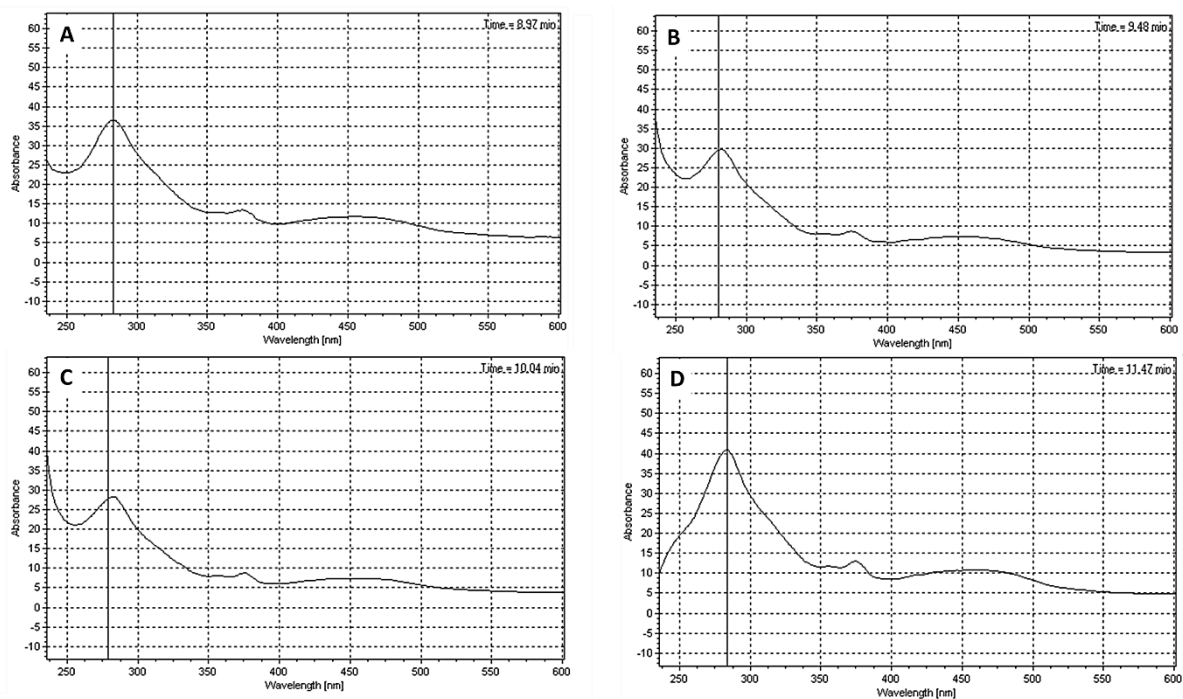


**Figure S3. 10** LC-MS analysis of Os<sup>II</sup>MPP Zoomed m/z 560-566 (RT 23-25 min).

### S3.3 HPLC Analysis of parent and conjugate Os(II) complex

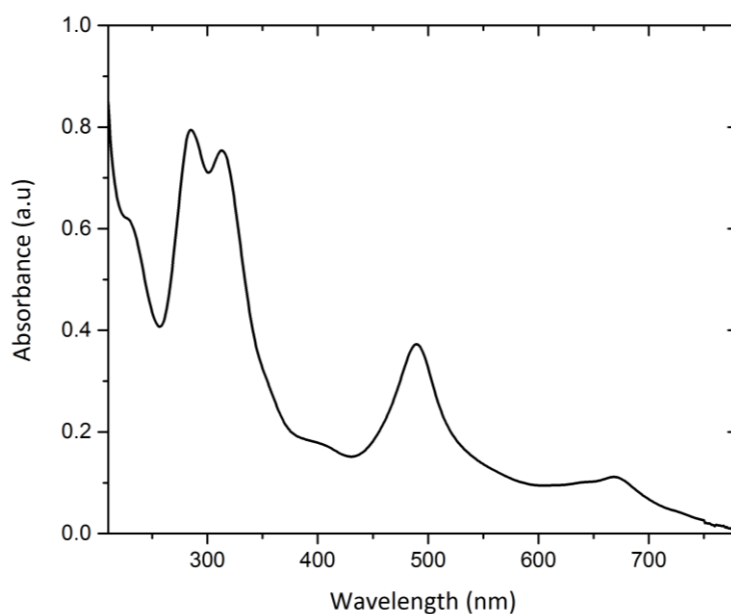


**Figure S3.11** Top: HPLC Chromatogram of  $\text{Os}^{\text{II}}$  parent complex and  $\text{Os}^{\text{II}}$ MPP conjugate obtained RP-C18 HPLC with MeCN mobile phase. Bottom three traces show traces using gradient mobile phase detected at 280 nm. (Gradient MeCN/  $\text{H}_2\text{O}$  0.1 % TFA gradient,  $1\text{ ml min}^{-1}$ ). Elution of  $\text{Os}^{\text{II}}$ MPP conjugate at 8.3 min (Channel 1: 280 nm and Channel 2: 490nm). Diode array detection was used and the HPLC UV-vis spectrum of each peak was obtained during  $\text{Os}^{\text{II}}$  MPP analysis and is shown below.

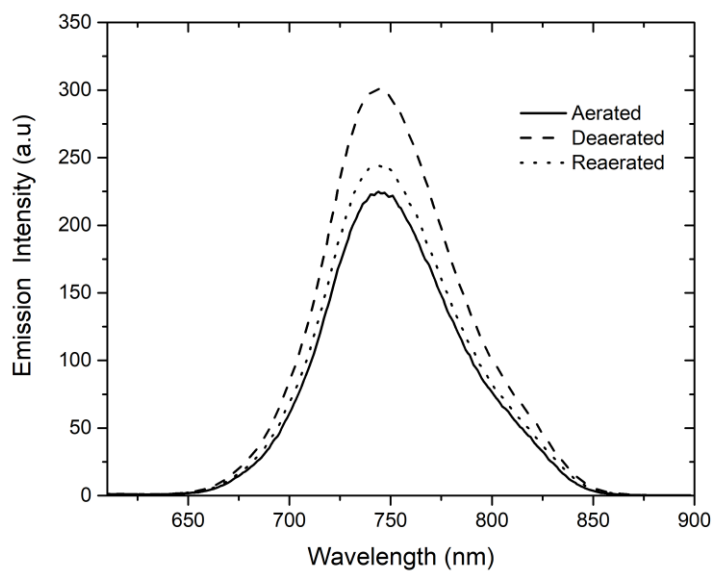


**Figure S3. 12** HPLC UV-vis spectra obtained for peaks observed during Os<sup>II</sup>MPP HPLC analysis illustrating the absence of a component with absorbance only in the UV-vis region as the MLCT band at a longer wavelength confirms Osmium-coordinated complex for each peak. The distribution of peaks in the conjugate product is suspected to originate from different ionization states of the conjugate

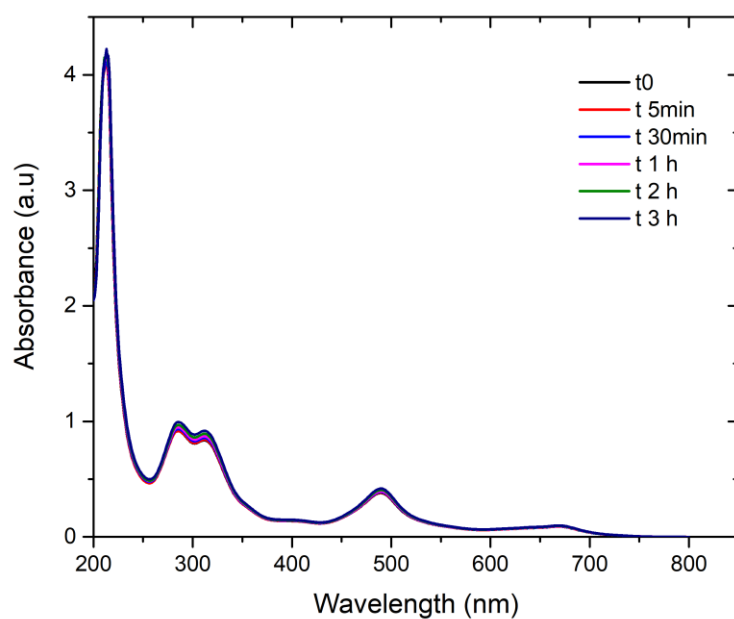
### S3.4 Spectroscopic Measurements of Os(II) parent complex and Os(II) conjugate



**Figure S3. 13** Absorbance spectrum of parent complex  $[\text{Os}(\text{tpybenzCOOH})_2]^{2+}$  **1** in acetonitrile solution ( $25 \mu\text{M}$ ).

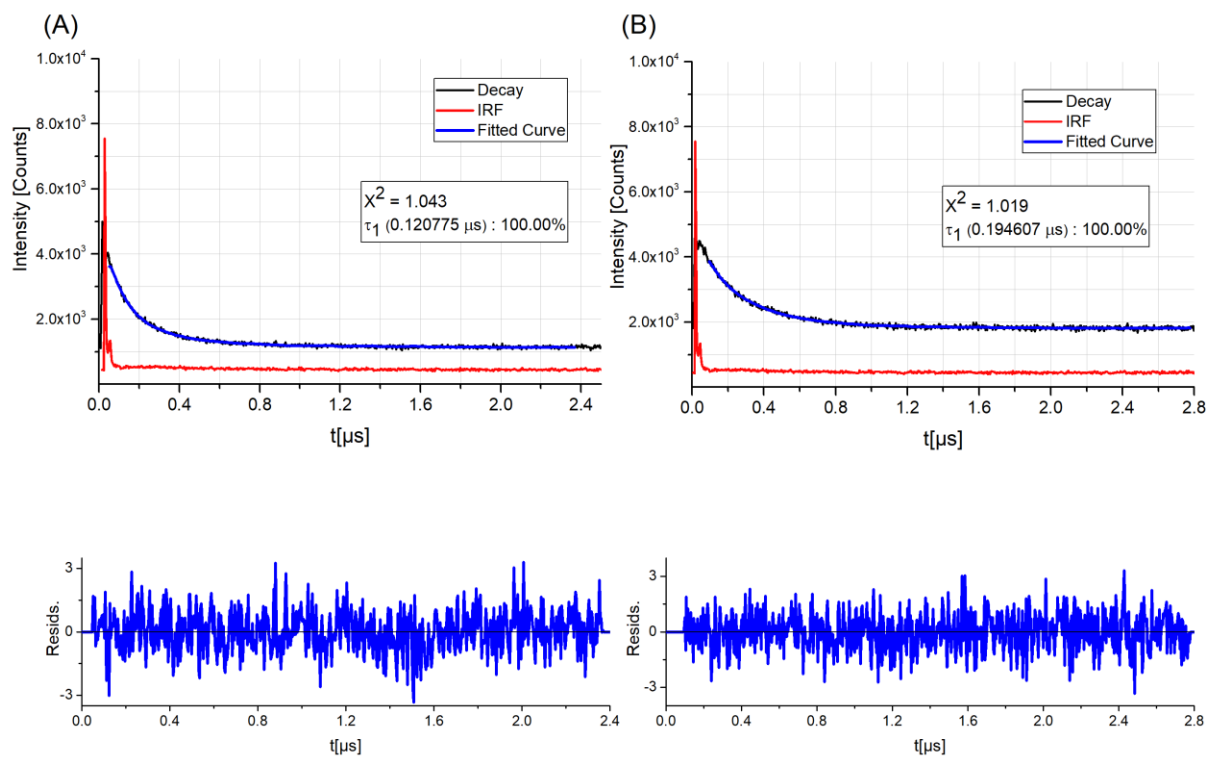


**Figure S3. 14** Emission spectra of parent complex  $[\text{Os}(\text{tpybenzCOOH})_2]^{2+}$  in acetonitrile ( $50 \mu\text{M}$ ) under aerated and deaerated conditions (slit widths  $10 \text{ nm} / 10 \text{ nm}$ ). Solution was deaerated using nitrogen gas and oxygen concentration was measured using PreSense  $\text{O}_2$  sensor.



**Figure S3. 15** Absorbance spectra of parent complex  $[\text{Os}(\text{tpybenzCOOH})_2]^{2+}$  ( $50 \mu\text{M}$ / PBS pH 7.4) following continuous photo-irradiation with ARC Lamp 150 W for 3 h at Room Temperature.

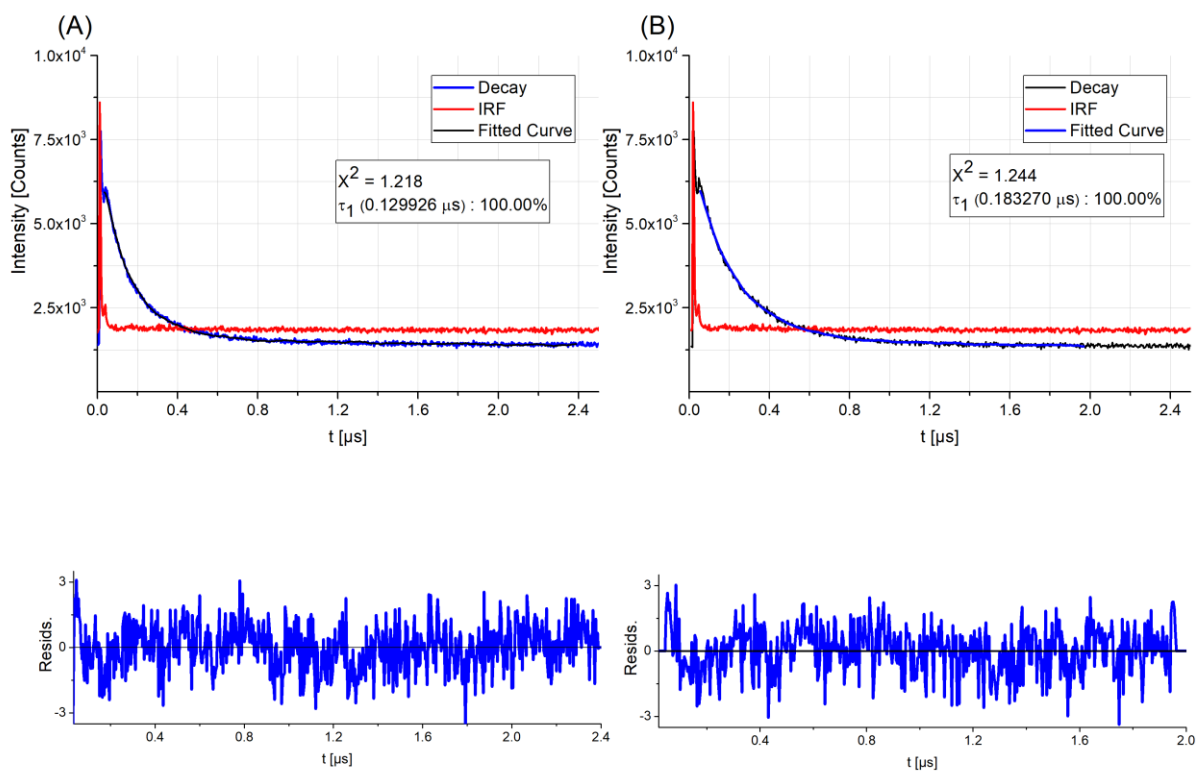
**S3.5 Emission Decays of Os(II) parent and Os<sup>II</sup> MPP complex – Time- correlated single photon counting (TCSPC) measurements using NanoHarp 2.1, FluoTime100 (PicoQuant) and mono-exponentially fitted using PicoQuant Fluofit software.**



$$\int_{-\infty}^t IRF(t') \sum_{i=1}^x A_i e^{-\frac{t-t'}{\tau_i}} dt'$$

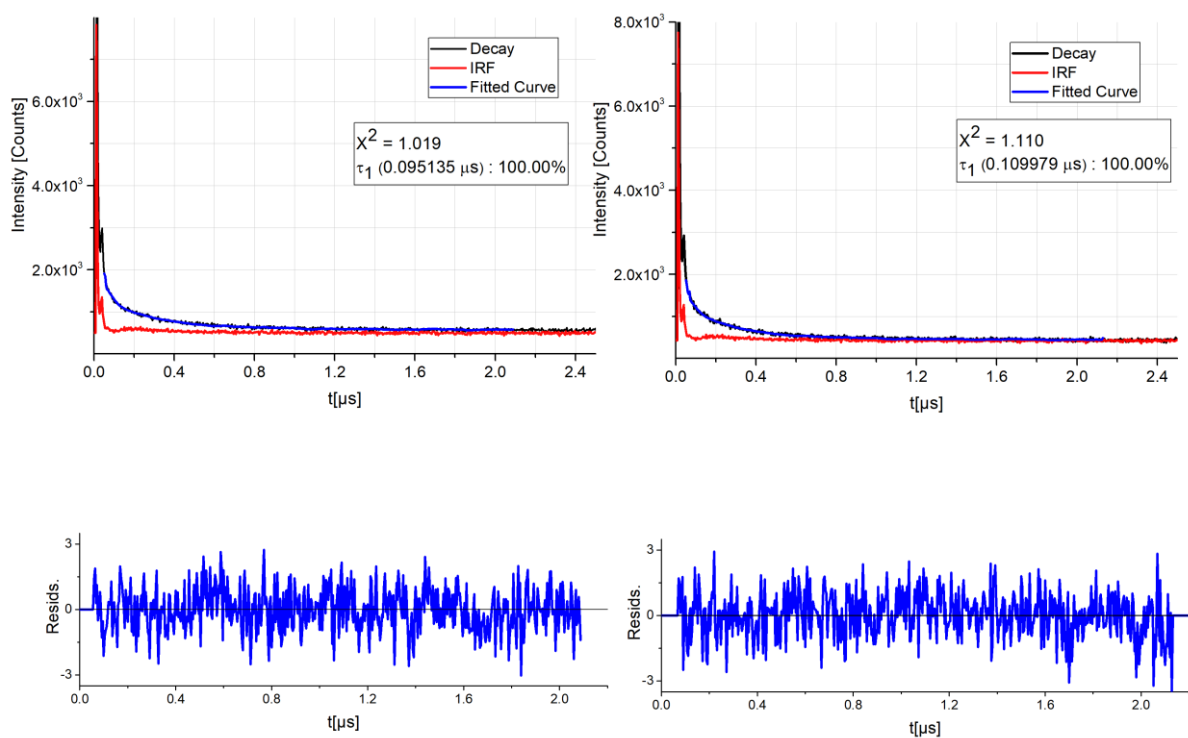
**Figure S3. 16** Emission Decays of parent complex  $[Os(tpybenzCOOH)_2]^{2+}$  in aerated and deaerated acetonitrile ( $50 \mu M$ ); Residual plots for the exponential fitting of both curves are shown below each plot.





$$\int_{-\infty}^t IRF(t') \sum_{i=1}^x A_i e^{-\frac{t-t'}{\tau_i}} dt'$$

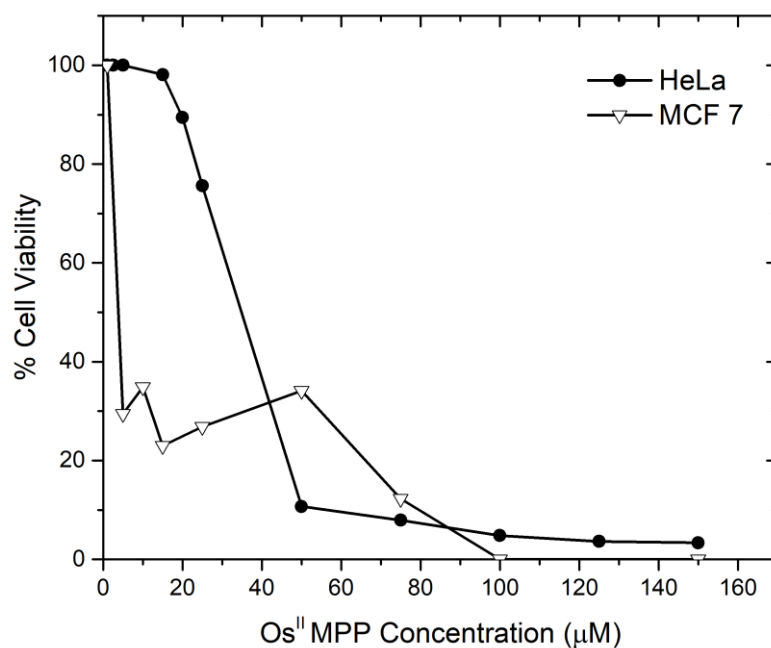
**Figure S3. 17** Emission Decays of parent complex  $[\text{Os}(\text{tpybenzCOOH})_2]^{2+}$  in aerated and deaerated PBS pH 7.4 ( $50 \mu\text{M}$ ); The residual plots for the exponential fitting of both curves are shown below.



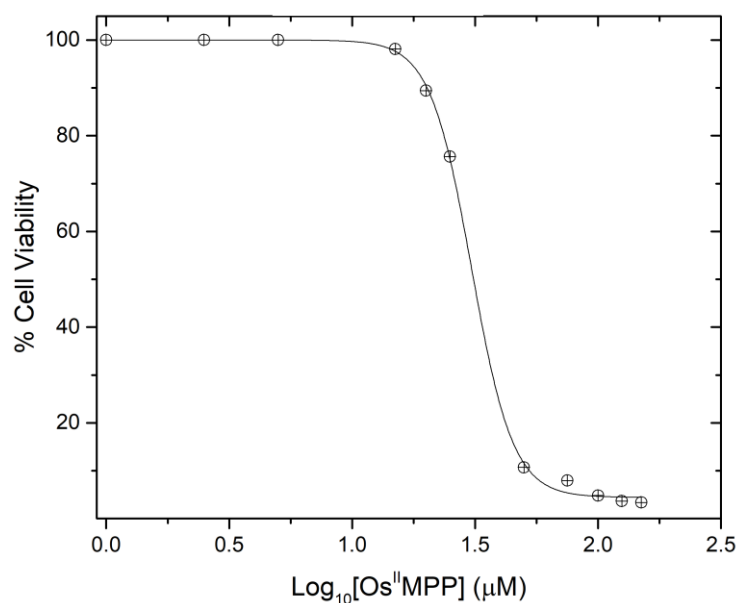
$$\int_{-\infty}^t IRF(t') \sum_{i=1}^x A_i e^{-\frac{t-t'}{\tau_i}} dt'$$

**Figure S3. 18** Emission decay of conjugate Os<sup>II</sup> MPP under aerated and deaerated conditions (25 μM/ PBS pH 7.4); Residual Plots of the exponential fitting for both curves are shown below.

### S3.6 Cytotoxicity Studies and determination of IC<sub>50</sub> of Os<sup>II</sup> MPP

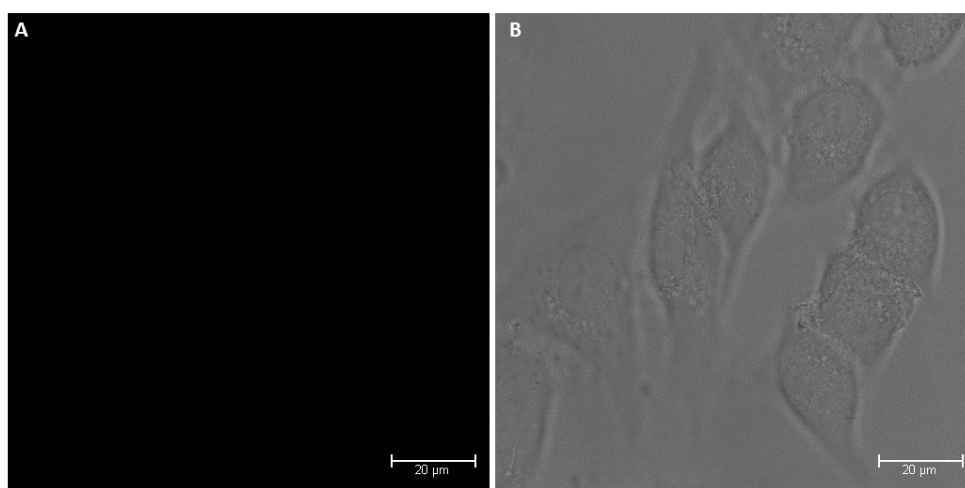


**Figure S3. 19** Cell Viability of HeLa and MCF 7 cells after 24 hr exposure to Os<sup>II</sup> MPP probe. Live cells were treated with the probe followed by addition of Resazurin for 6 h. Absorbance was read at 570 nm with background at 600 nm subtracted (n=3).

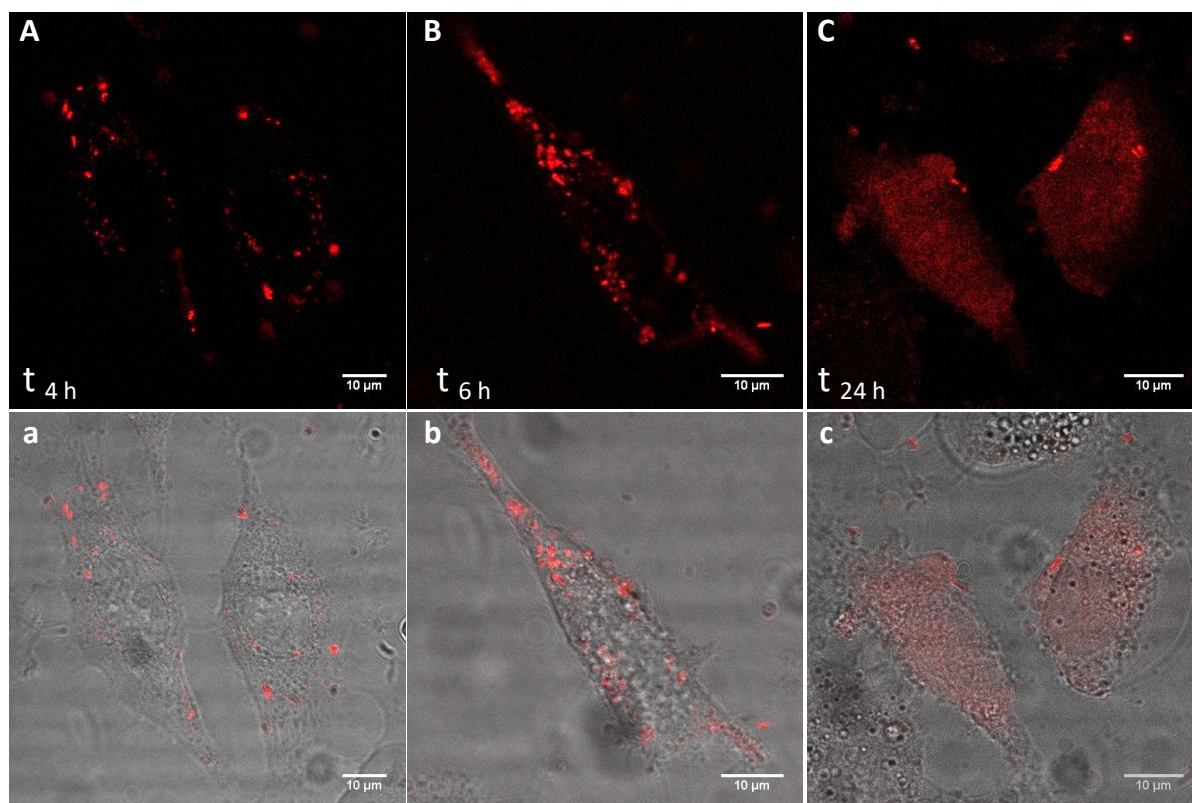


**Figure S3. 20** Determination of EC<sub>50</sub>. HeLa cells were incubated in the presence of Os<sup>II</sup> MPP (0.1 μM to 150 μM) for 24 h. Cell proliferation was assayed with Resazurin (n=3). The IC<sub>50</sub> value, the minimal amount of Os<sup>II</sup> MPP required to inhibit 50 % viability of HeLa cells was found to be 30.61 μM.

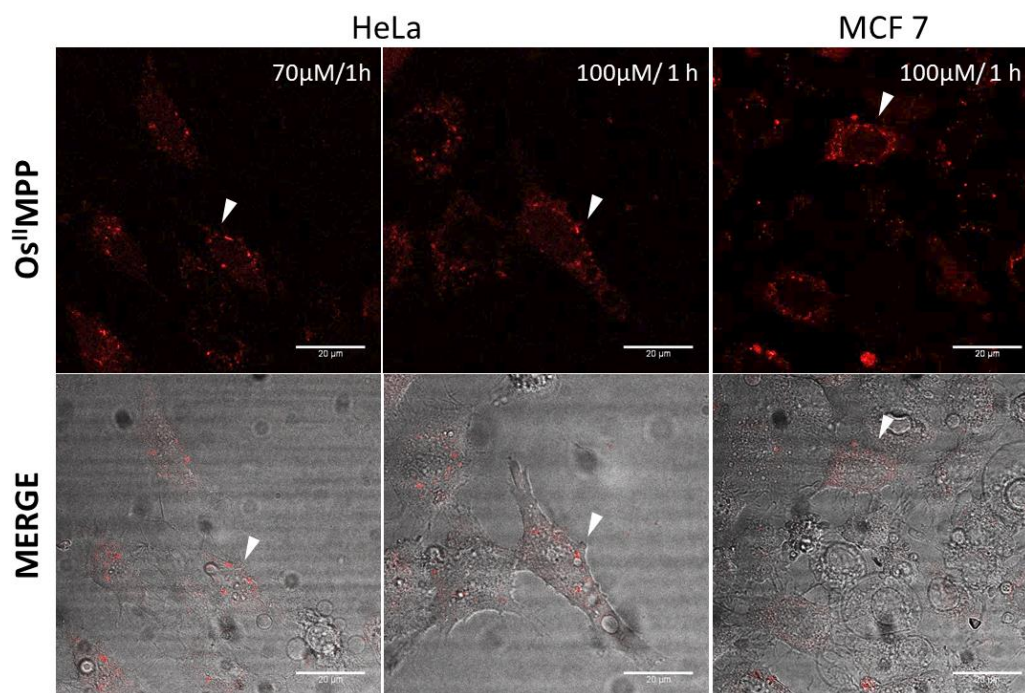
### S3.7 Confocal Imaging



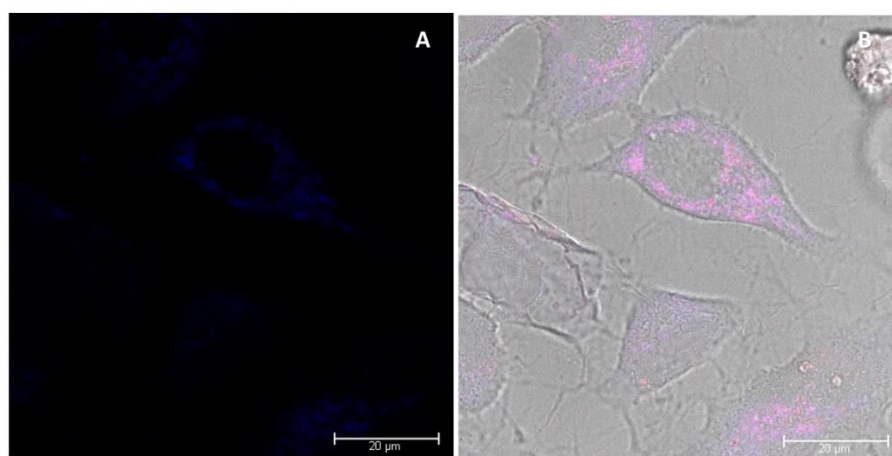
**Figure S3. 21** Confocal Imaging studies of [Os(tpybenzCOOH)<sub>2</sub>]<sup>2+</sup>. Cells were treated with [Os(tpybenzCOOH)<sub>2</sub>]<sup>2+</sup> at 30 μM for 2 h. (A) Osmium Channel: uptake of the parent complex was not evident; (B) Background channels showing HeLa cells. Cells were excited with 490 nm WLL and emission was collected between 650nm and 850 nm.



**Figure S3. 22** Confocal microscopy of HeLa cells incubated with Os<sup>II</sup> MPP at 30  $\mu$ M for (A) 4 h, (B) 6 h and (C) 24 h in cell media at 37 °C in the absence of light. (a-c) Overlay images with the background channel. Os<sup>II</sup>MPP was excited using a 490 nm white light laser and emission was collected between 650nm and 850 nm.



**Figure S3. 23** Confocal imaging of Os<sup>II</sup> MPP in HeLa and MCF 7 cells at increased concentrations; Uptake of Os<sup>II</sup> MPP probe is evident but changes are observed in the morphological features of cells indicative of cell death.

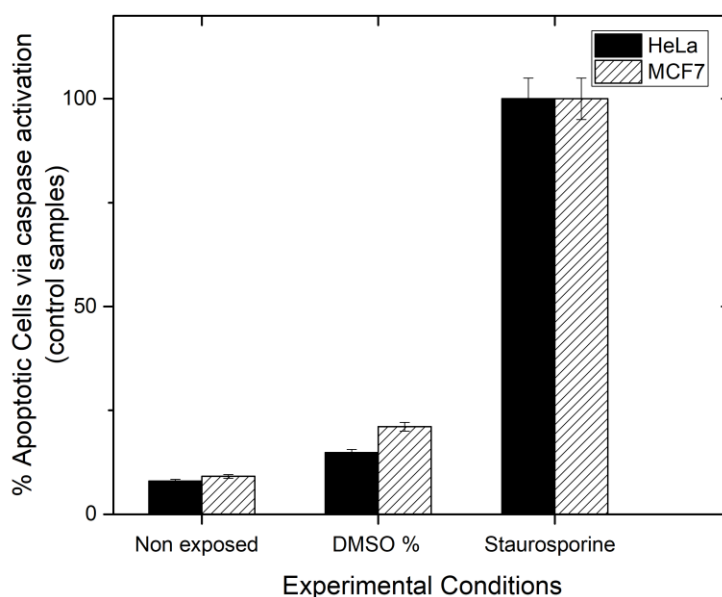


**Figure S3. 24** Co-staining with DRAQ7 following Os<sup>II</sup> MPP 30 μM/2h; (A) Absence of nuclear staining confirms cells are viable; observed in blue is the emission of MitoTracker Deep Red due to co-excitation of MitoTracker Deep Red at 633 nm. (B) Overlay of all channels.

### S3.8 Polycaspase FAM-FLICA and MitoPT TMRE Assay

**Table S3. 1** MitoPT and FLICA Assay: Cell Population Experimental Conditions

Assay	Negative Populations	Control	Positive Population	Control	Experimental Populations
Mito PT	(1) Non-exposed population	exposed	CCCP (20 $\mu$ M/ 2 h)		Os <sup>II</sup> MPP 30 $\mu$ M/ 2 h
	(2) DMSO (100 $\mu$ M/ 1 h)				Os <sup>II</sup> MPP 100 $\mu$ M/ 1 h
FLICA	(1) Non-exposed population	exposed	Staurosporine (1 $\mu$ M/ 3 h)		Os <sup>II</sup> MPP 30 $\mu$ M/ 2 h
	(2) DMSO (100 $\mu$ M/ 1 h)				Os <sup>II</sup> MPP 100 $\mu$ M/ 1 h

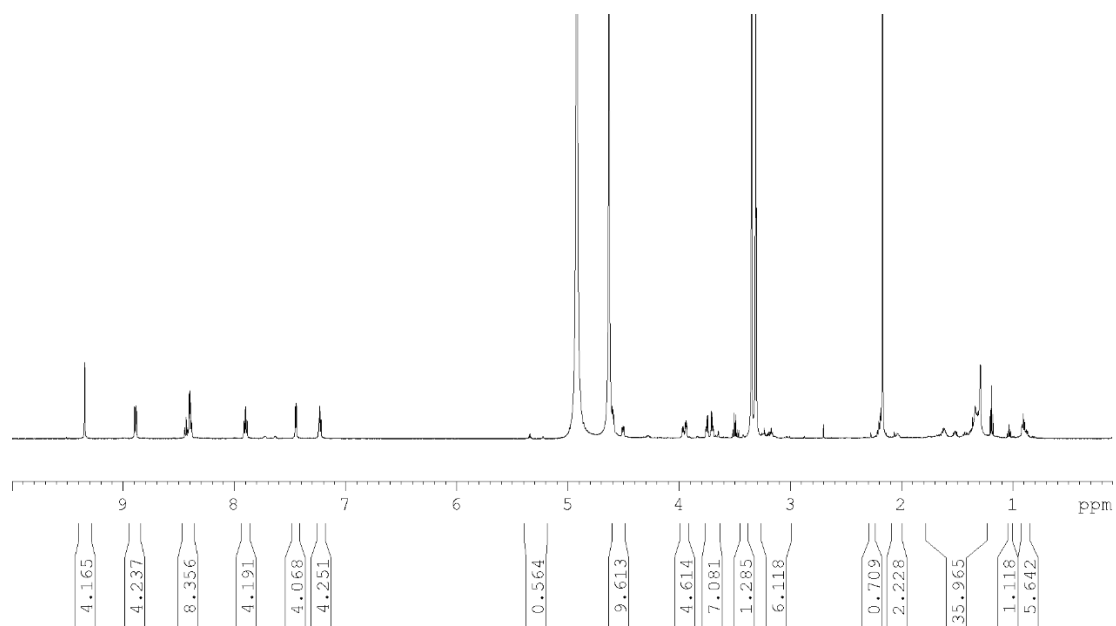


**Figure S3. 25** Control studies for the FLICA assay (n=3) in HeLa and MCF 7 cell line. Cells were cultivated at  $3 \times 10^5$  cells/well and were exposed to negative control 1 (non-treated) (B) negative control 2 DMSO (10 % v/v) (C) positive control (staurosporine 1  $\mu$ M/ 3 h). Cells were spiked with 30X FAM-FLICA reagent (v/v ratio of 1:30) and incubated for 45 minutes at 37 °C. Samples were analyzed in triplicate ( $3 \times 100 \mu$ l) in a black bottomed 96-well plate using Tecan Plate fluorescence plate reader set at 488 nm excitation and 520 nm emission.

## Appendix C

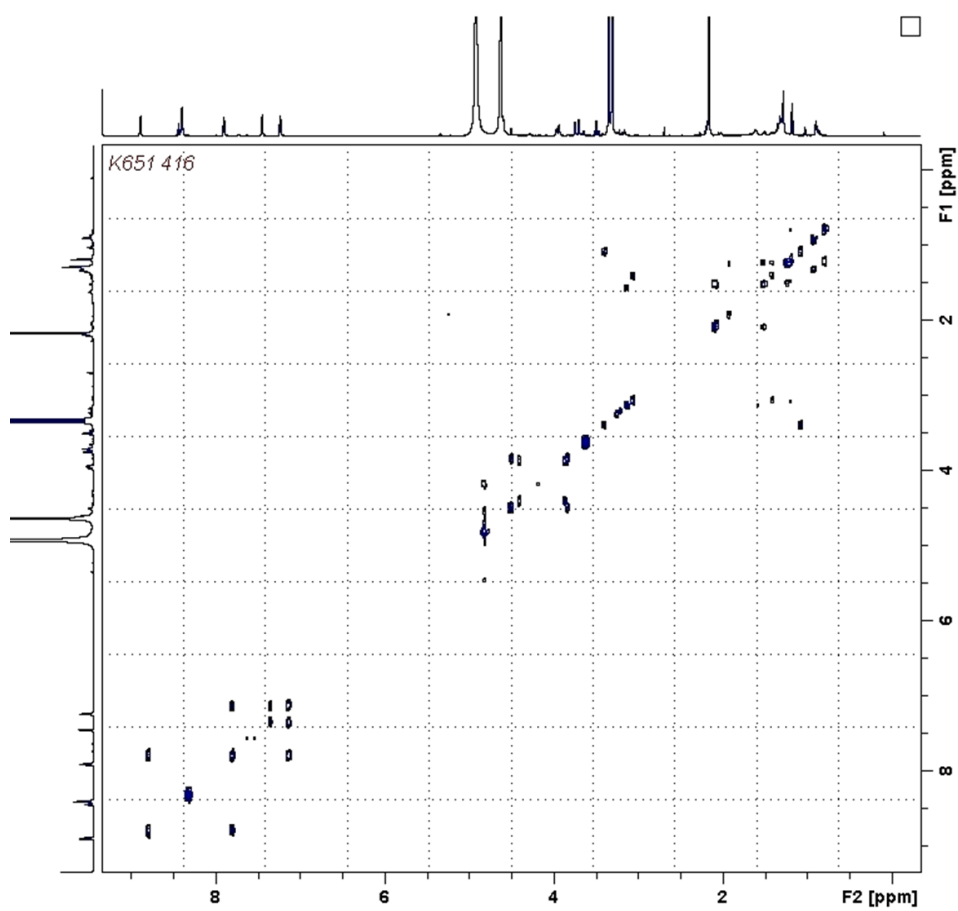
Supplementary material associated with **Chapter 4** “*Os(II) Bridged Polyarginine Conjugates; The Additive effects of Peptides in Promoting or Preventing Permeation in Cells and Multicellular Tumor Spheroids*”.

### S4.1 NMR Analysis

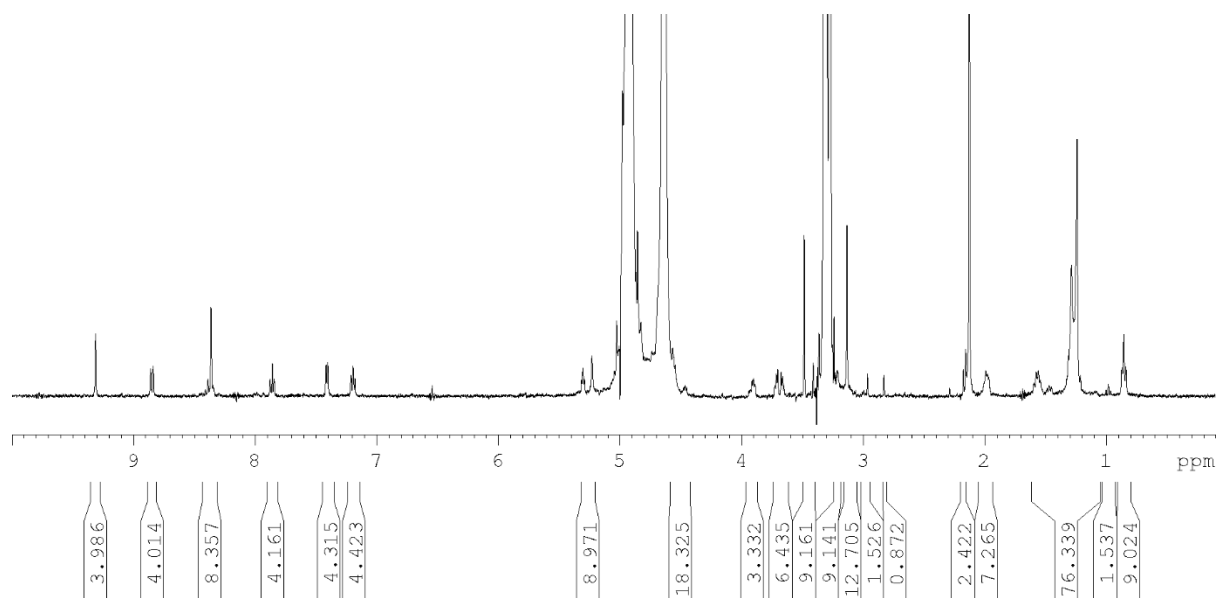


**Figure S4. 1** <sup>1</sup>H NMR analysis of [Os-(R<sub>4</sub>)<sub>2</sub>]<sup>10+</sup> conjugate (MeOH-d<sub>4</sub>/D<sub>2</sub>O, 600 MHz)





**Figure S4. 2** COSY analysis of  $[\text{Os}-(\text{R}_4)_2]^{10+}$  conjugate (MeOH- $d_4$ / $\text{D}_2\text{O}$ , 600 MHz)



**Figure S4. 3**  $^1\text{H}$  NMR analysis of  $[\text{Os}-(\text{R}_8)_2]^{18+}$  conjugate (MeOH- $\text{d}_4/\text{D}_2\text{O}$ , 600 MHz)

## S4.2 Mass Spectrometry

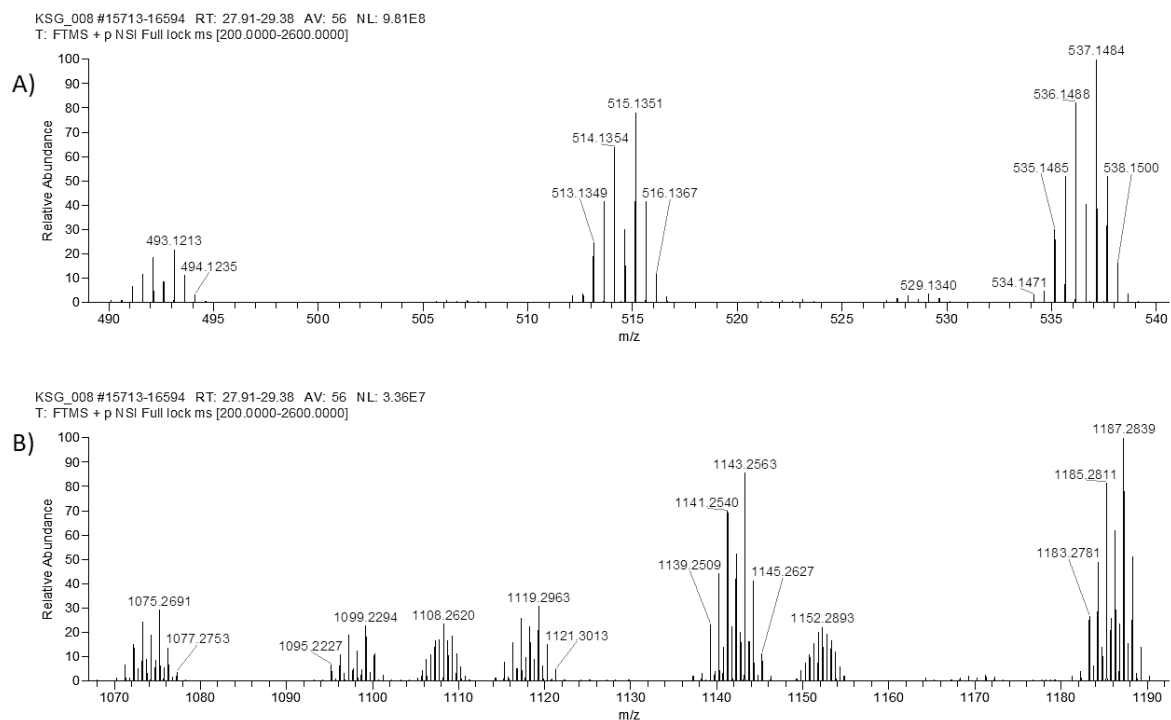


Figure S4. 4 LC-MS/MS (Q- Exactive) of bis-octaarginine Os(II) conjugate (RT 27.9-29.4 min), zoomed  $m/z$ ,  $z=2$ , A) 490 - 540 B) 1070 - 1190.

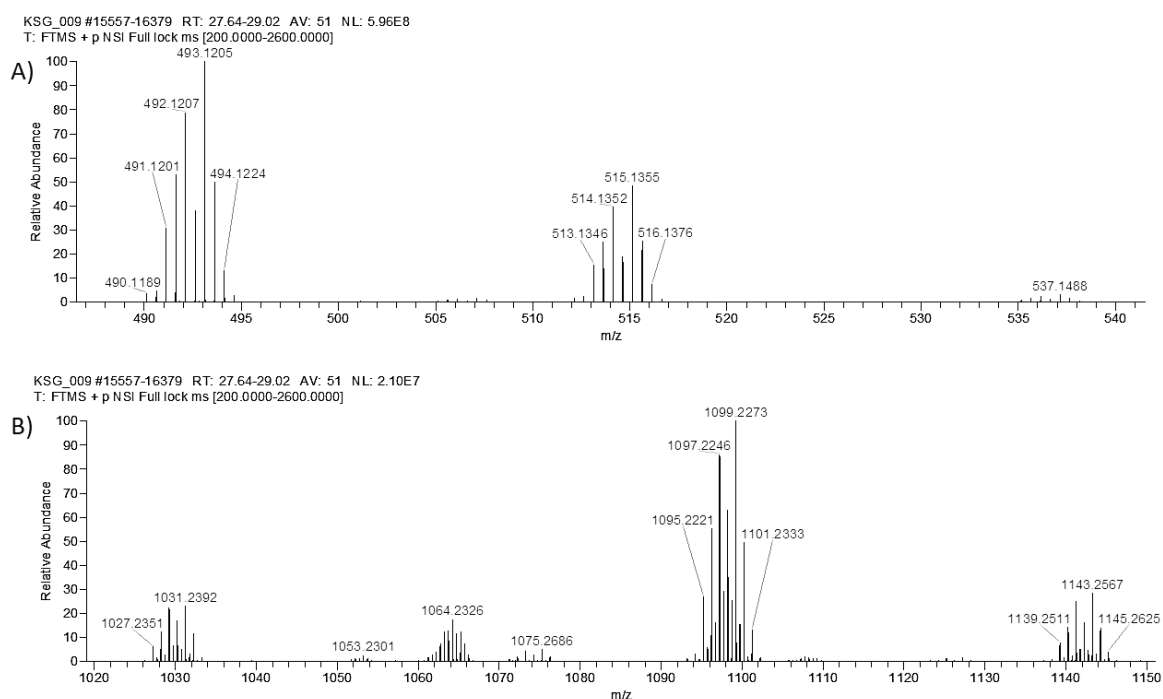
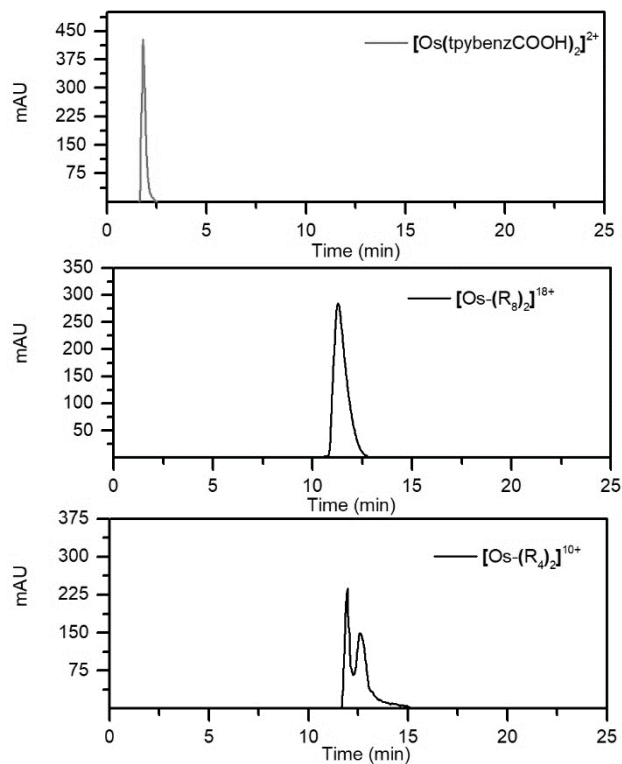


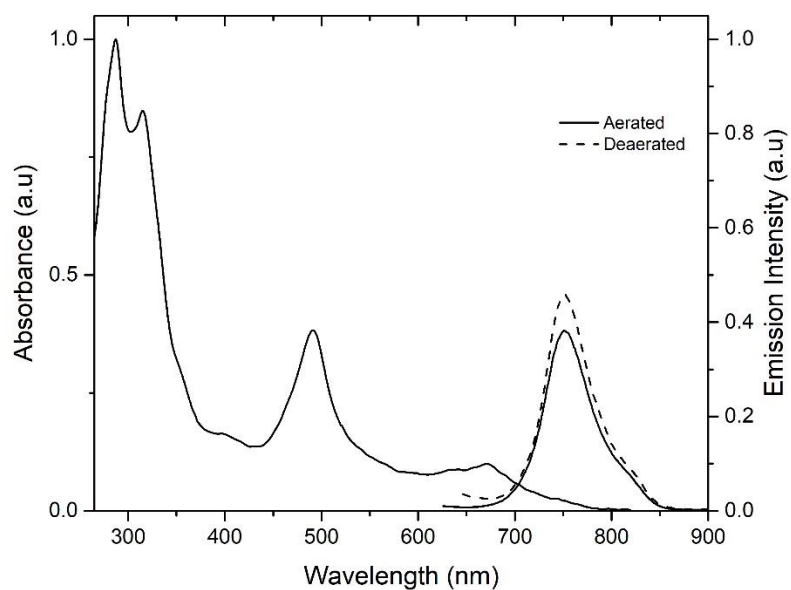
Figure S4. 5 LC-MS/MS (Q-Exactive) of bis-tetraarginine Os(II) conjugate (RT 27.6 - 29 min), zoomed  $m/z$ ,  $z=2$ , A) 490 - 540 and B) 1020-1150.

### S4. 3 RP-HPLC Analysis

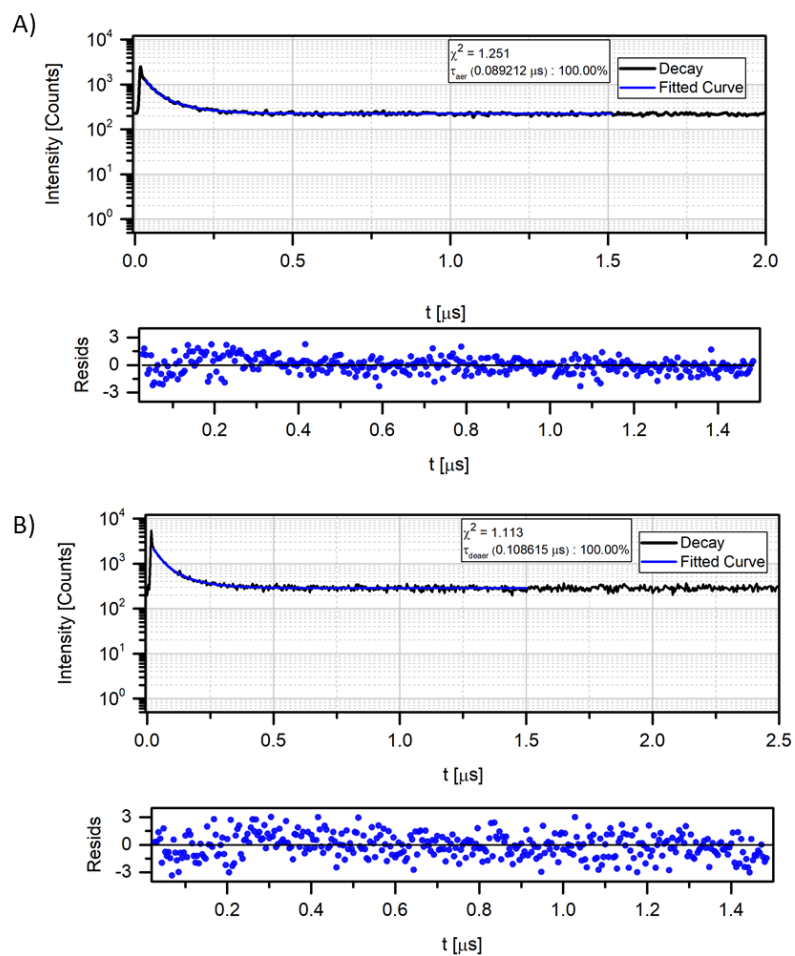


**Figure S4. 6** RP-HPLC analysis of polyarginine Os(II) conjugates relative to  $[\text{Os}(\text{tpybenzCOOH})_2]^{2+}$  parent complex (C18, MeCN/H<sub>2</sub>O (0.1 % TFA) gradient, PDA 490 nm)

#### S4.4 Photophysical studies

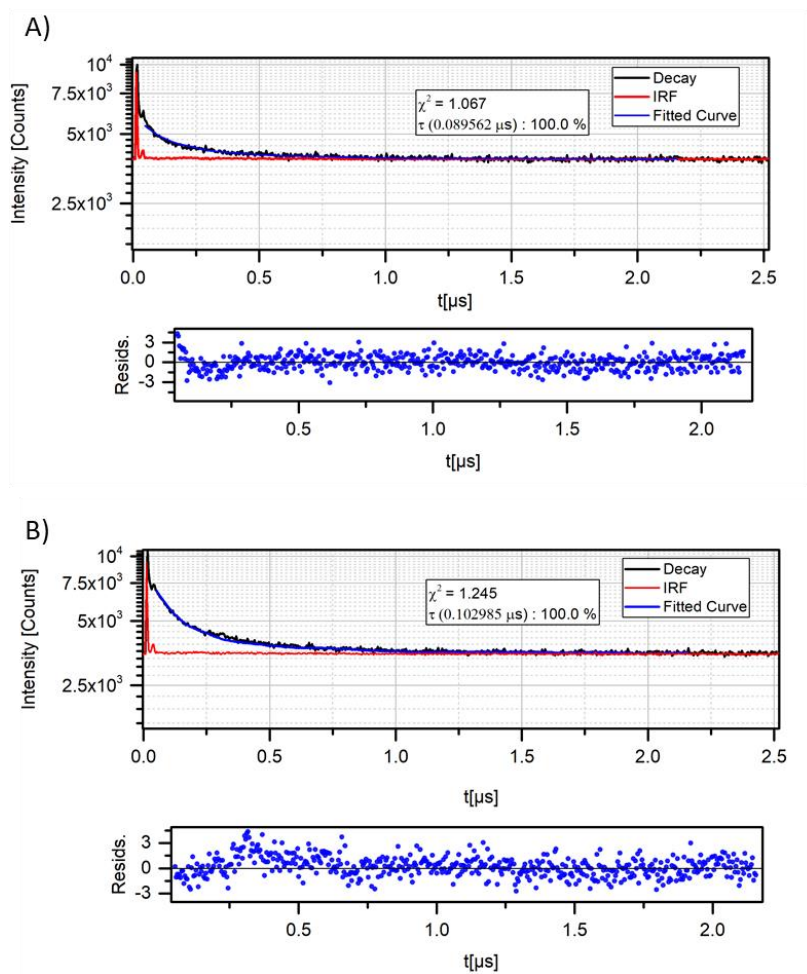


**Figure S4. 7** Absorbance and emission spectra of  $[\text{Os}-(\text{R}_8)_2]^{18+}$  (Normalised to  $\lambda_{\text{max}}$ ). Spectra were recorded at  $50 \mu\text{M}$  (PBS buffer pH 7.4/ 0.1 % DMSO) under aerated and deaerated conditions with excitation and emission slit widths of 10 nm and  $\lambda_{\text{exc}}$  490 nm.



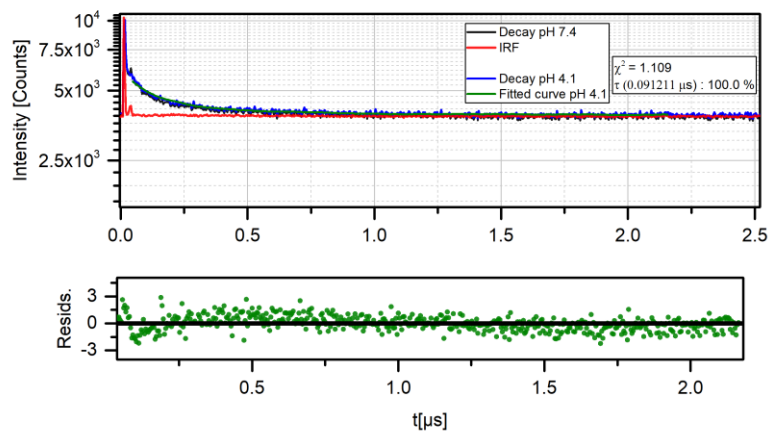
$$\int_{-\infty}^t IRF(t') \sum_{i=1}^x A_i e^{-\frac{t-t'}{\tau_i}} dt'$$

**Figure S4. 8** Emission Decays of bis-octaarginine Os(II) conjugate,  $[\text{Os}-(\text{R}_8)_2]^{18+}$  ( $50 \mu\text{M}$ ) in A) aerated and B) deaerated PBS (pH 7.4). Residual plots for the exponential fitting of both curves are shown below each plot.



$$\int_{-\infty}^t IRF(t') \sum_{i=1}^x A_i e^{-\frac{t-t'}{\tau_i}} dt'$$

**Figure S4.9** Emission Decays of bis-tetraarginine Os(II) conjugate, [Os-(R<sub>4</sub>)<sub>2</sub>]<sup>10+</sup> (30 μM) in A) aerated and B) deaerated PBS (pH 7.4). Residual plots for the exponential fitting of both curves are shown below each plot.

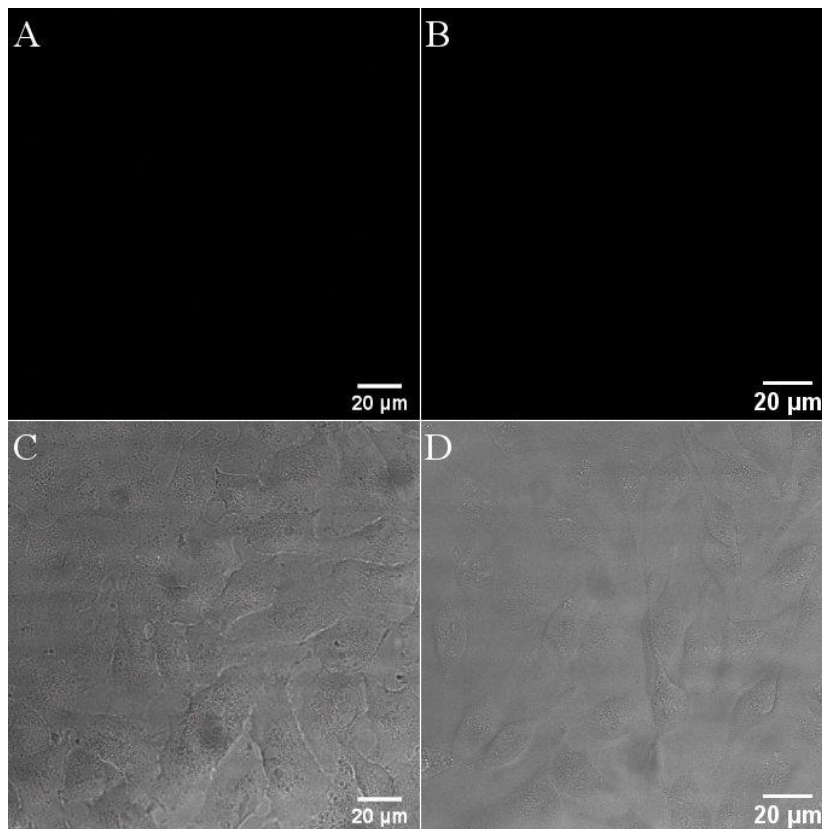


**Figure S4. 10** Emission decay of bis-tetraarginine Os(II) conjugate,  $[\text{Os}-(\text{R}_4)_2]^{10+}$  ( $30 \mu\text{M}$ ) in PBS at pH 7.4 and pH 4.1 (using perchloric acid, 1 % v/v). The residual plot corresponds to the exponential fitting of the decay at pH 4.1, but the decays and fits are indistinguishable.

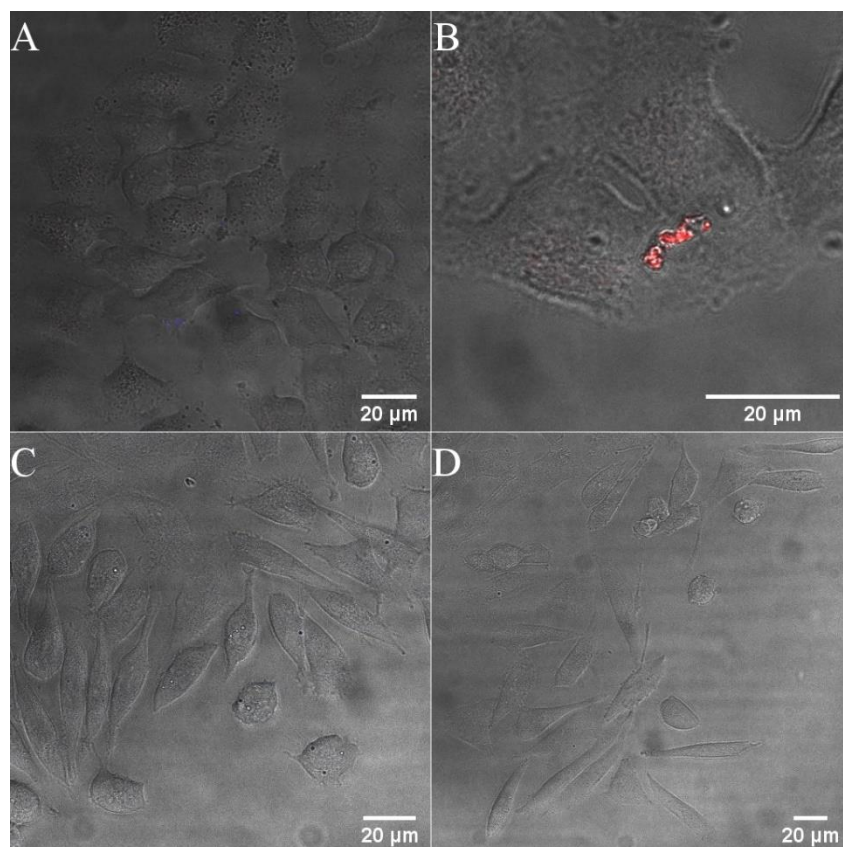


## S4.5 Cell studies

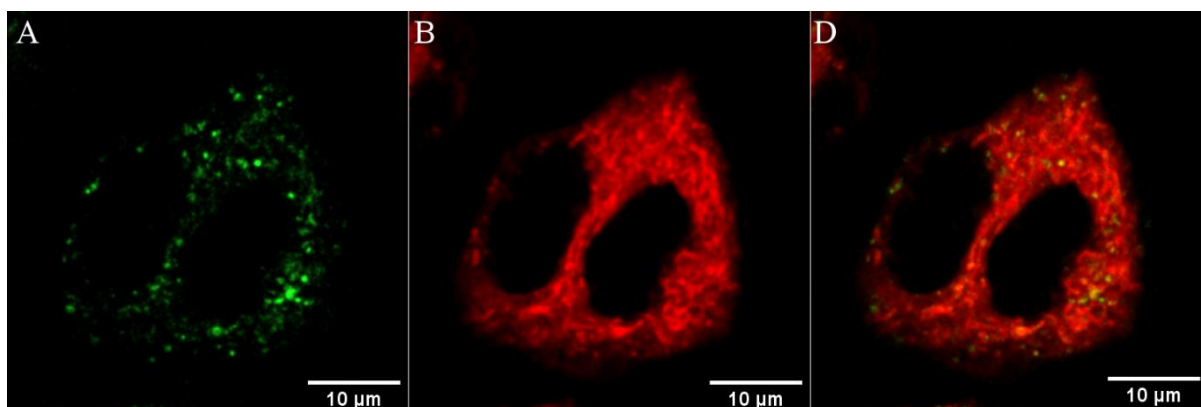
### S4.5.1 Confocal images 2D cell monolayers



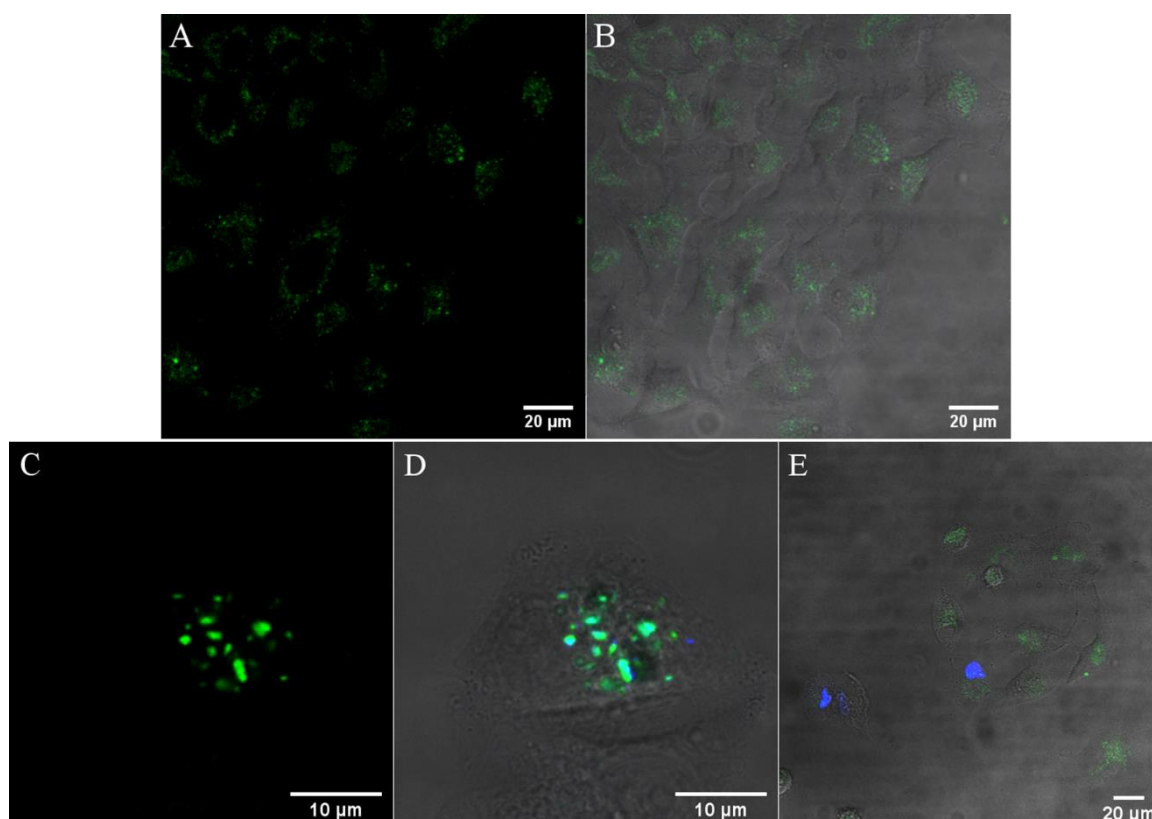
**Figure S4. 11** Confocal images of (A,C) A549 and (B,D) CHO cells treated with parent compound  $[\text{Os}(\text{tpybenzCOOH})_2]^{2+}$  at  $100 \mu\text{M}/ 24 \text{ h}$ . Shown are the Os(II) channel and overlay with brightfield. The complex was excited using a 490 nm white light laser and the emission was collected between 650 and 800 nm.



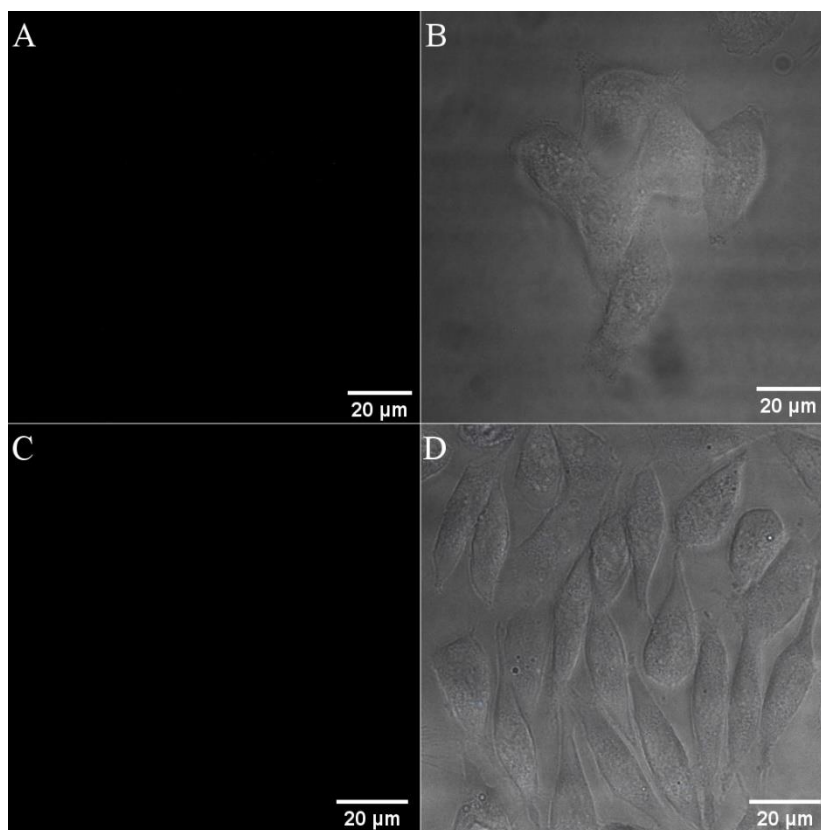
**Figure S4. 12** Confocal images of (A-B) A549 and (C-D) CHO cells treated with [Os-(R8)<sub>2</sub>]<sup>18+</sup> at 30 μM/ 24 h (left) and 100 μM/ 24 h (right) and co-stained with DRAQ7. Shown are the overlay images of [Os-(R8)<sub>2</sub>]<sup>18+</sup> and DRAQ7 channel with brightfield. The 633 nm laser was used to excite DRAQ7 and emission was collected between 635–750 nm.



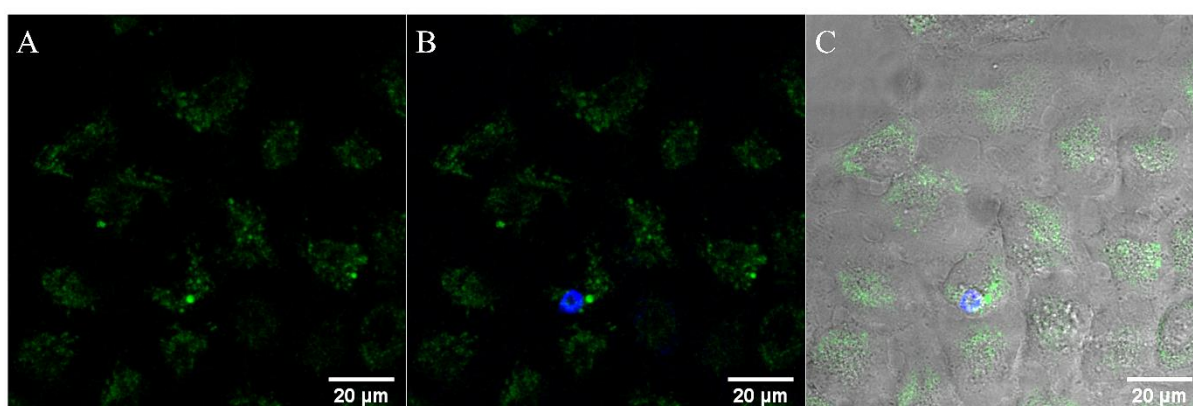
**Figure S4. 13** Confocal fluorescence images of A549 cells treated with (A)  $[\text{Os}-(\text{R}_4)_2]^{10+}$  (30  $\mu\text{M}$ / 24 h) and co-stained with (B) MitoTracker Deep Red (100 nM). (C) Overlay of the two channels. The conjugate was excited using a 490 nm white light laser and the emission range was set to between 650 and 800 nm. MitoTracked Deep Red was excited at 644 nm and emission was collected between 655–720 nm



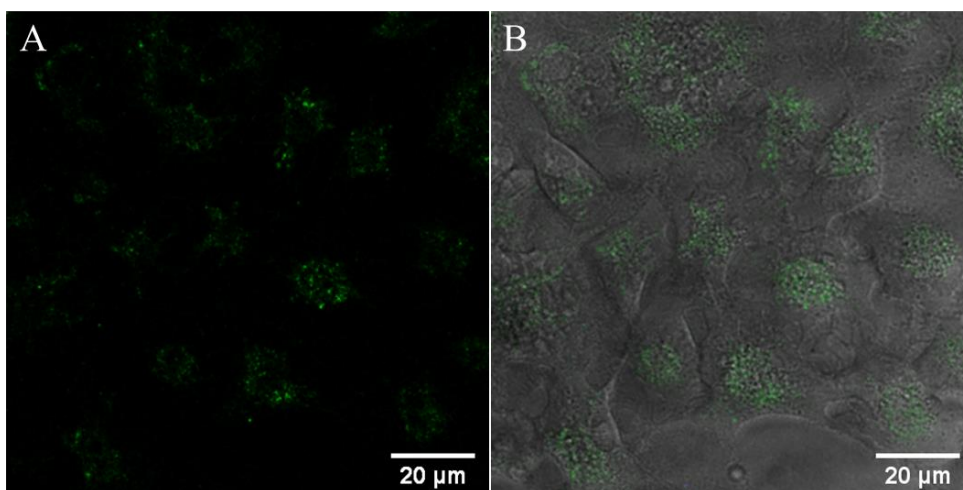
**Figure S4. 14** Representative confocal images of A549 cells treated with 100  $\mu\text{M}$  of  $[\text{Os}-(\text{R}_4)_2]^{10+}$  and co-stained with DRAQ7 (3  $\mu\text{M}$ ). (A) Os(II) channel following 24 h incubation, (B) overlay with DRAQ7 channel and brightfield, (C) Os(II) channel following 48 h incubation, (D) overlay with DRAQ7 channel and brightfield, (E) overlay with DRAQ7 channel and brightfield of a wide region of cells. The 633 nm laser was used to excite DRAQ7 and emission was collected between 635–750 nm.



**Figure S4. 15** Confocal images of 4°C uptake studies of  $[\text{Os}-(\text{R}_4)_2]^{10+}$  at 30  $\mu\text{M}$ / 24 h where (A-B) A549 and (C-D) CHO cell line. No uptake was observed as shown by the  $[\text{Os}-(\text{R}_4)_2]^{10+}$  channel (A, C) and overlay with brightfield images. The conjugate was excited using a 490 nm white light laser and the emission range was set to between 650 and 800 nm.

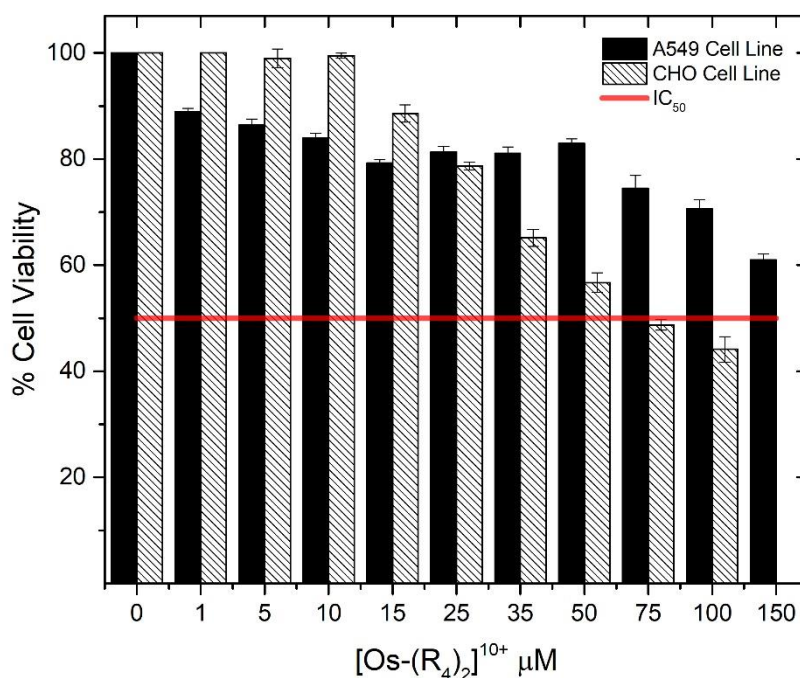


**Figure S4. 16** Representative confocal images of A549 cells treated with 30  $\mu\text{M}$  of  $[\text{Os}-(\text{R}_4)_2]^{10+}$  for 48 h and co-stained with DRAQ7 (blue). (A) Os(II) channel, (B) Os(II)/DRAQ7 overlay and (C) overlay of channels with brightfield.



**Figure S4. 17** Confocal images of A549 cells treated with  $[\text{Os}-(\text{R}_4)_2]^{10+}$  ( $30 \mu\text{M}/24 \text{ h}$ ) and co-stained with DRAQ7. Shown are the overlay images of the (A) Os(II) channel with DRAQ7 and (B) Os(II)/DRAQ7 with brightfield following continuous irradiation ( $0.84 \mu\text{W}/\text{cm}^2$ ) for 3 h. No photo-induced toxicity was evident as absence of nuclear staining by DRAQ7 (blue) confirmed cell viability.

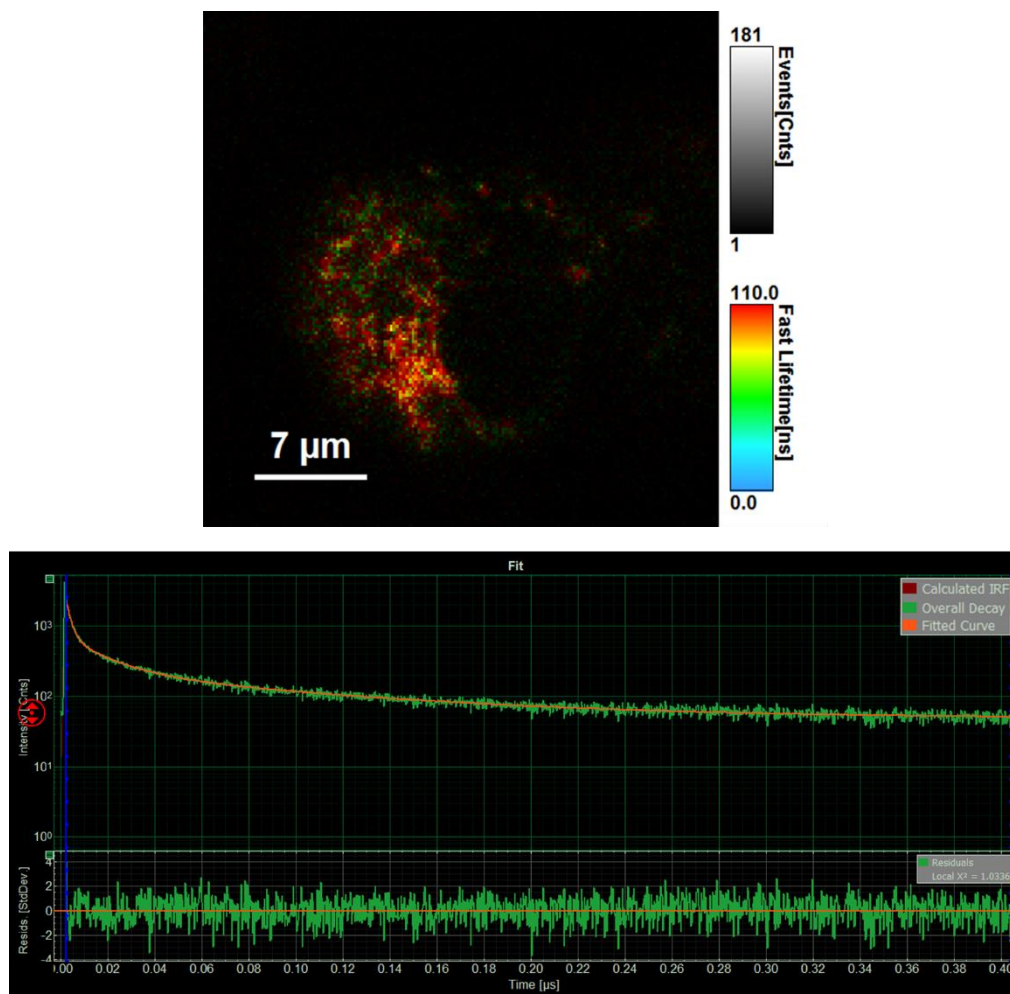
#### S4.5.2 Cytotoxicity assay



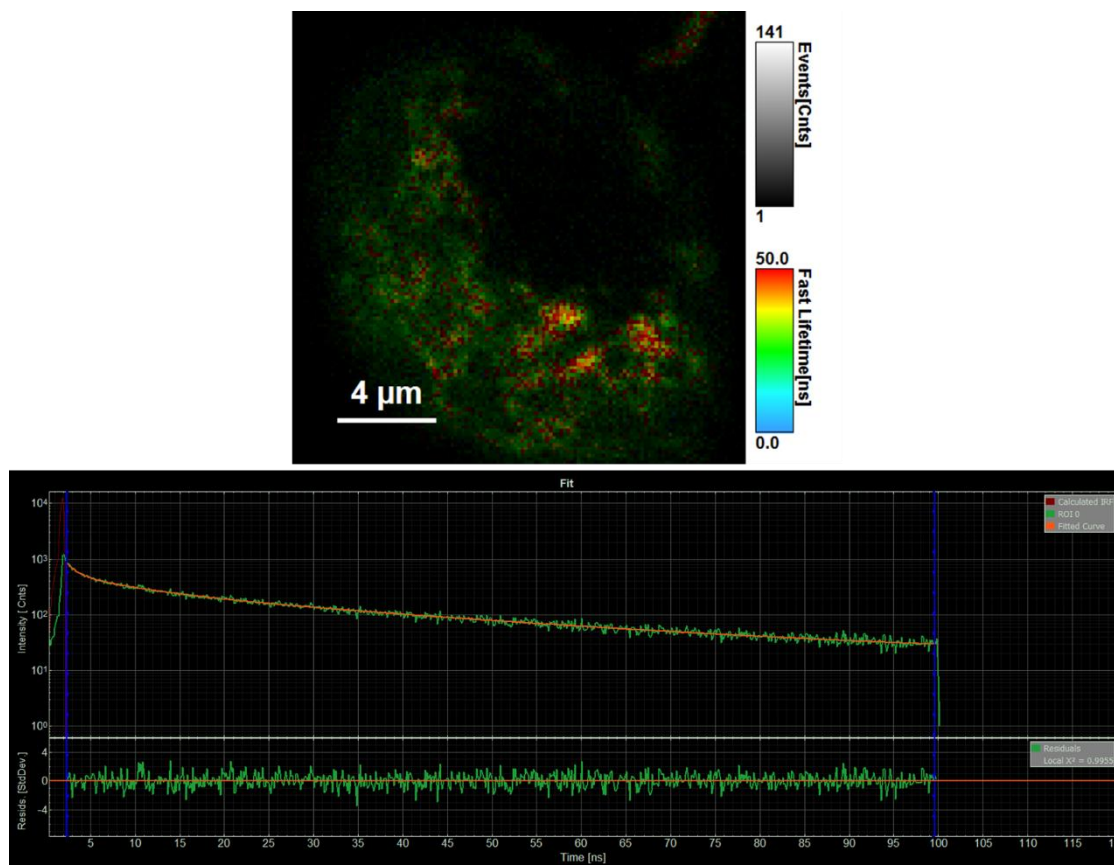
**Figure S4. 18** Cell Viability assay performed for A549 and CHO cells treated with  $[\text{Os}-(\text{R}_4)_2]^{10+}$  probe at a range of concentrations for 24 h. (n=3)



### S4.5.3 Luminescence Lifetime Imaging

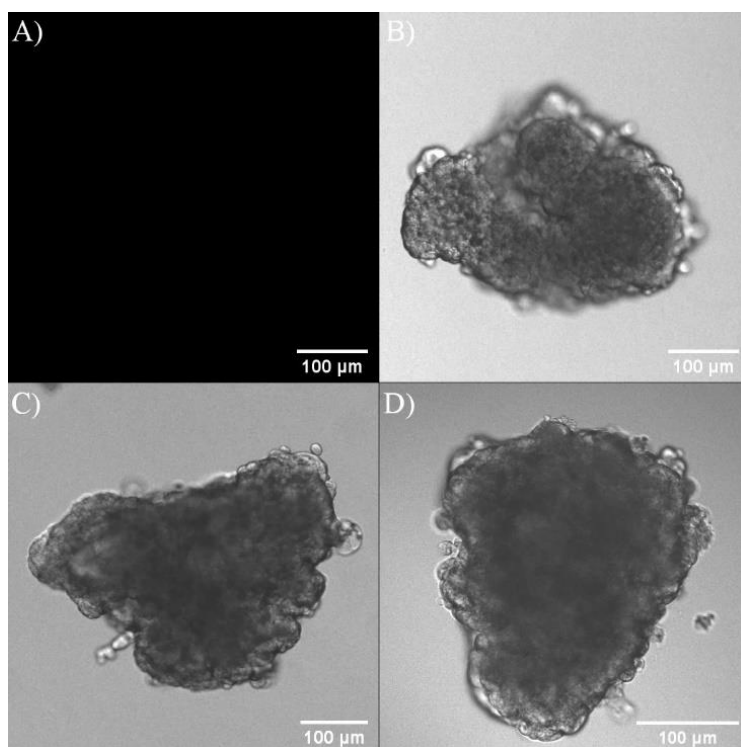


**Figure S4.19** Representative luminescent lifetime imaging microscopy and fits for  $[\text{Os}-(\text{R}_4)_2]^{10+}$  ( $30 \mu\text{M}/24 \text{ h}$ ) in a live A549 cell. The decay was fitted to a tri-exponential model with lifetimes of 92.2 ns (67 %), 15.8 ns (25 %) and 2.02 ns (8 %) ( $\chi^2 = 1.0336$ ). The PLIM image was acquired by exciting at 405 nm and emission collected between 650 and 800nm.



**Figure S4. 20** Representative luminescent lifetime imaging microscopy of  $[\text{Os}-(\text{R}_4)_2]^{10+}$  ( $30 \mu\text{M}/48 \text{ h}$ ) in a live A549 cell. The decay was fitted to a tri-exponential model with lifetimes of 37.0 ns (54 %), 9.3 ns (32 %) and 1.88 ns (14 %). ( $\chi^2 = 0.9955$ ). The PLIM image was acquired by exciting at 405 nm and emission collected between 650 and 800nm.

#### S4.5.4 3D Multicellular pancreatic spheroids

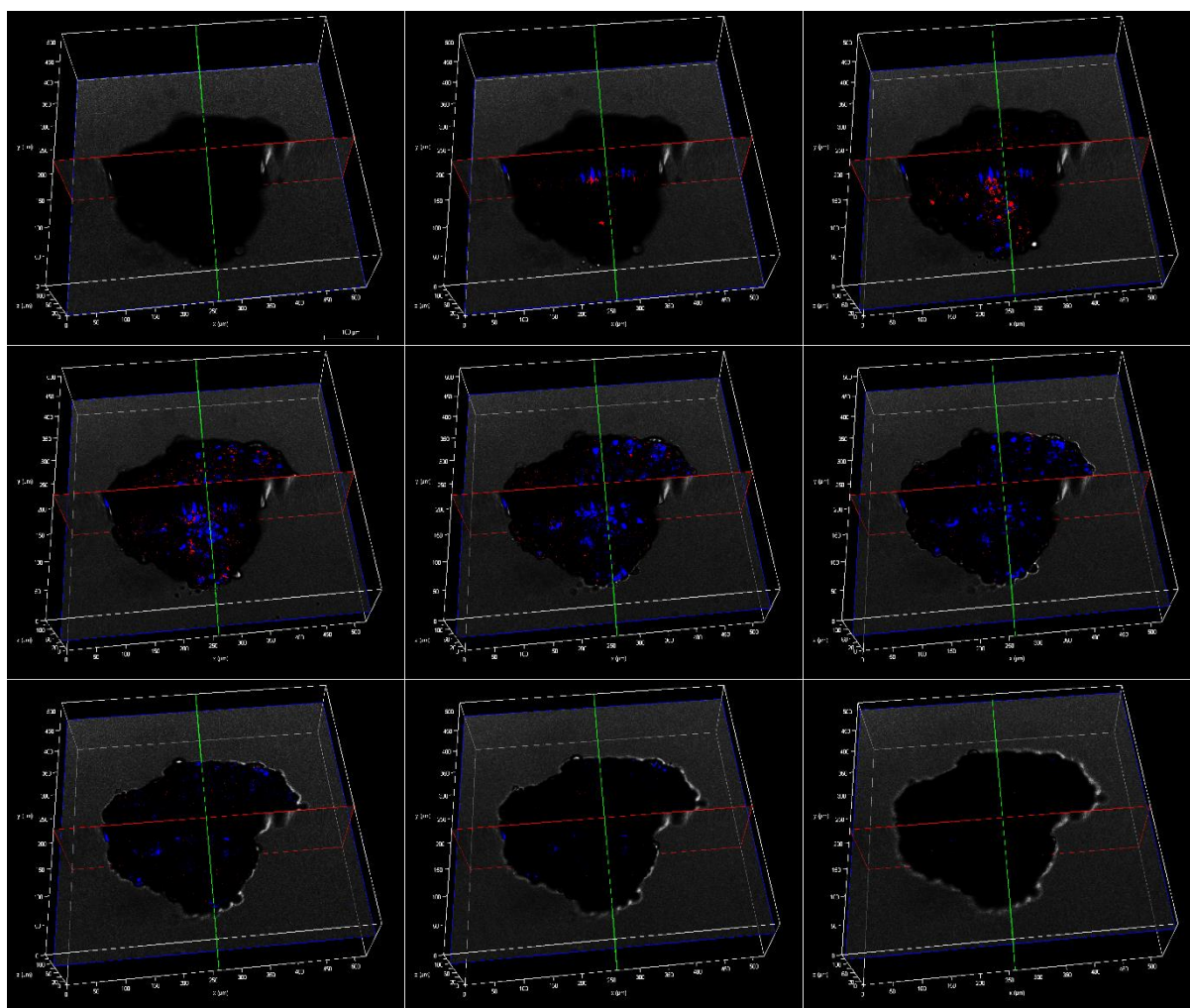


**Figure S4. 21** Confocal images of representative live HPAC spheroid control samples. (A) Os(II) channel of non-treated control spheroid sample, (B) overlay of channel with brightfield, (C) Os(II)/Brightfield overlay of spheroid incubated with parent complex  $[\text{Os}(\text{tpybenzCOOH})_2]^{2+}$  at  $100 \mu\text{M}/ 48 \text{ h}$  (D) Os(II)/Brightfield overlay of spheroid incubated with bis-octaarginine  $[\text{Os}-(\text{R}_8)_2]^{18+}$  at  $100 \mu\text{M}/ 48 \text{ h}$ . A 490 nm white light laser was used for excitation and emission for Os(II) was set to 650 – 800 nm.

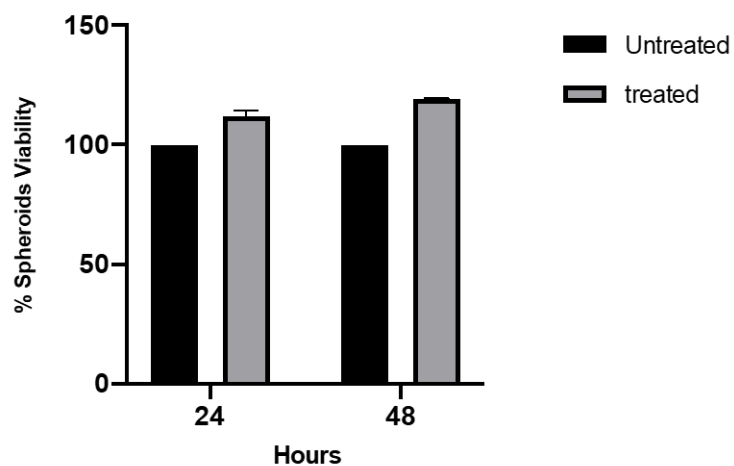




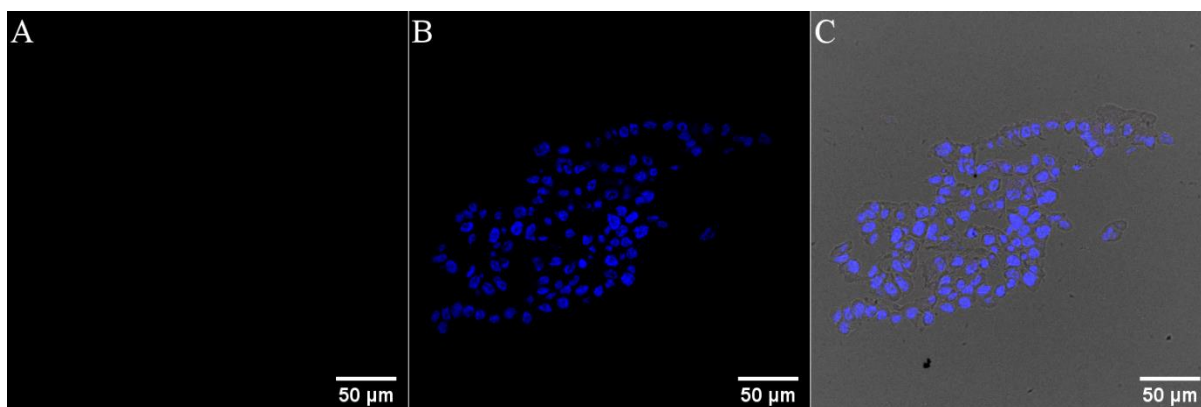
**Figure S4.22** Z-stack images of a single live HPAC spheroid pre-treated with  $[\text{Os}-(\text{R}_4)_2]^{10+}$  for at  $100 \mu\text{M}/24 \text{ h}$ . Each image corresponds to cross-section from the bottom (upper left image) to the upper part (lower right image) along the z-axis. Scale bar reads  $200 \mu\text{m}$ . Os(II) was excited at  $490 \text{ nm}$  and emission was collected between  $650$  and  $850 \text{ nm}$ . Representative slices are shown using contrast BF as the background. (10X)



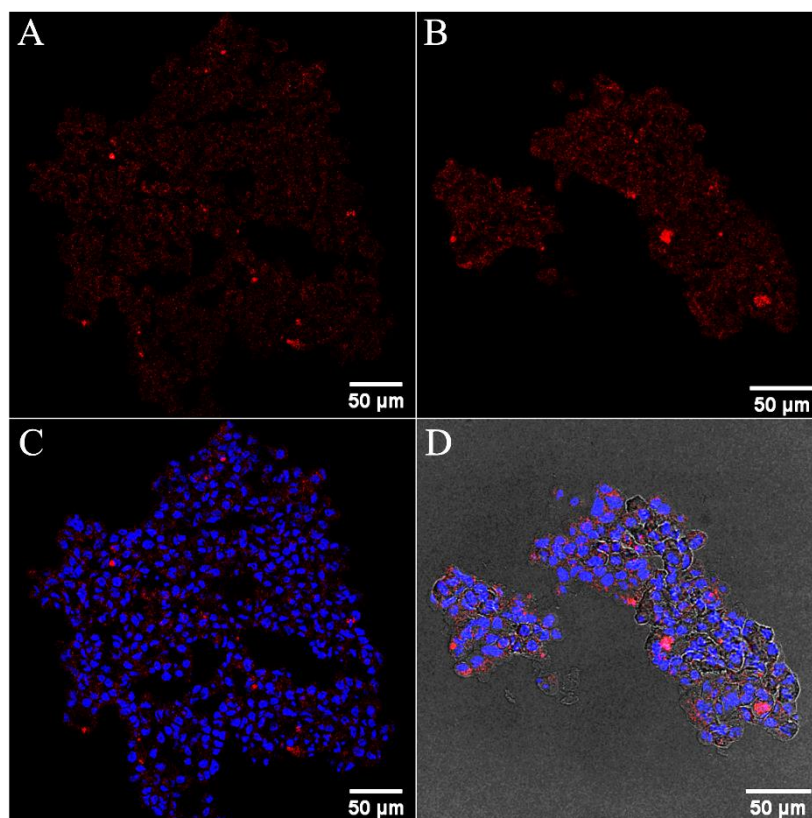
**Figure S4. 23** Z-stack images of a single live HPAC spheroid pre-treated with  $\text{Os}-(\text{R}_4)_2$  ( $100 \mu\text{M}/24 \text{ h}$ ) and co-stained with DAPI. Each image corresponds to cross-section from the bottom (upper left image) to the upper part (lower right image) along the z-axis.  $\text{Os}(\text{II})$  was excited at  $490 \text{ nm}$  and emission was collected between  $650$  and  $850 \text{ nm}$ . DAPI was excited at  $405 \text{ nm}$  and emission was collected between  $423 \text{ nm}$  and  $580 \text{ nm}$ . Representative images are shown using contrast brightfield as the background. Scale bar reads  $100 \mu\text{m}$ . (10X)



**Figure S4. 24** HPAC spheroid viability was measured after 24 and 48 h. of incubation with  $[\text{Os}-(\text{R}_4)_2]^{10+}$  at 100  $\mu\text{M}$ . (n=2)

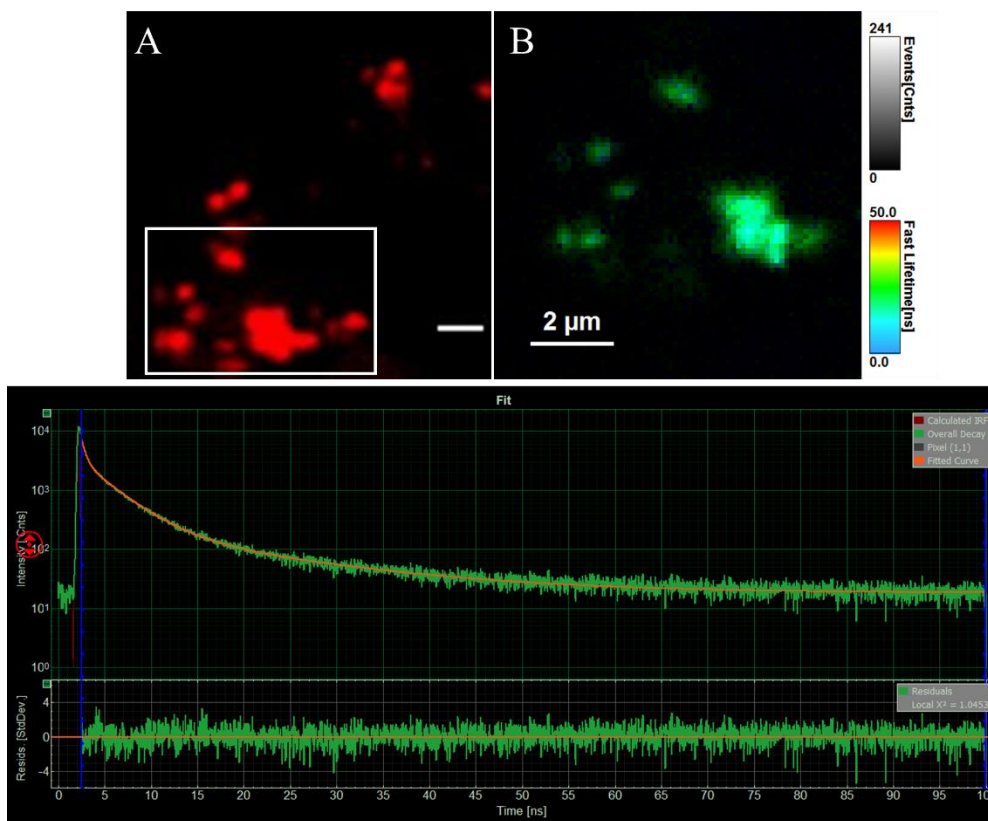


**Figure S4. 25** Fixed slices of control HPAC spheroids treated only with DAPI dye. (A) Os(II) channel, (B) DAPI emission was collected between 423 nm and 580 nm. (C) Overlay with brightfield.



**Figure S4. 26** Fixed cryosections of HPAC spheroids pre-treated with  $[\text{Os}-(\text{R}_4)_2]^{10+}$  at  $100 \mu\text{M} / 24 \text{ h}$  and co-stained with DAPI post-fixation. (A-B) Os(II) emission channel from two representative cryosections, (C) co-staining with DAPI and (D) Os(II)/DAPI overlay with brightfield. A 490 nm white light laser was used to excite the conjugate and emission was collected between 650 and 800 nm.. The 405 nm excitation laser was used to excite DAPI and emission was collected between 423 and 580 nm.





**Figure S4. 271** A) Confocal and B) Luminescence lifetime imaging of  $[\text{Os}-(\text{R}_4)_2]^{10+}$  in fixed HPAC spheroid slice. The PLIM decay was fitted to a bi-exponential model with lifetimes of 16.4 ns, and 3.2 ns ( $\chi^2 = 1.0453$ ). The PLIM image was acquired by exciting at 405 nm and emission collected between 650 and 800nm.

## Appendix D

Supplementary material associated with **Chapter 5** “*Ru(II)/BODIPY core co-encapsulated self-referenced nanotools for intracellular O<sub>2</sub> in live cancerous cells*”.

### S5.1 Synthesis and characterization

#### S.5.1.1 Synthesis of ruthenium intermediate compounds and NPs

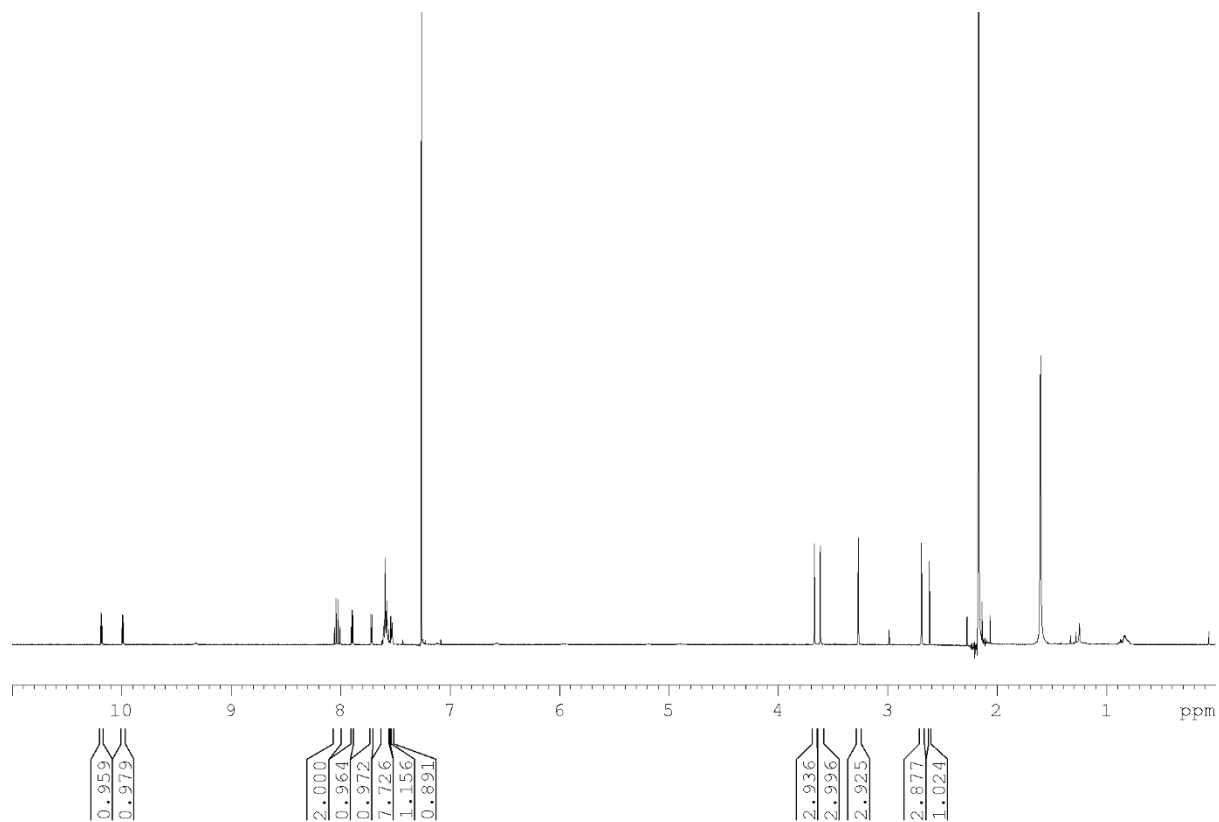
##### *Preparation of [Ru(dpp)(DMSO)<sub>2</sub>Cl<sub>2</sub>] (2)*

cis, fac-[Ru(DMSO)<sub>4</sub>Cl<sub>2</sub>] (408.7 mg, 0.844 mmol) and dpp (0.844 mmol) were heated at reflux in ethanol (30 mL) for 3 h where the solution progressed from a yellow/brown to an orange/brown solution. The mixture was cooled to RT and was then concentrated in vacuo, filtered and washed with minimal cold ethanol. The light-orange solids were washed with diethyl ether and dried under vacuum. Yield: 296.2 mg (56 %). <sup>1</sup>H NMR (600 MHz, CDCl<sub>3</sub>) δ (ppm): 10.16 (d, 1H); 9.96 (d, 1H); 8.01 (q, 2H); 7.88 (d, 1H); 7.72 (d, 1H); 7.62 – 7.56 (m, 8H), 7.53 (d, 1H), 7.52 (d, 1H), 3.67 (s, 3H); 3.61 (s, 3H); 3.26 (s, 3H); 2.69 (s, 3H).

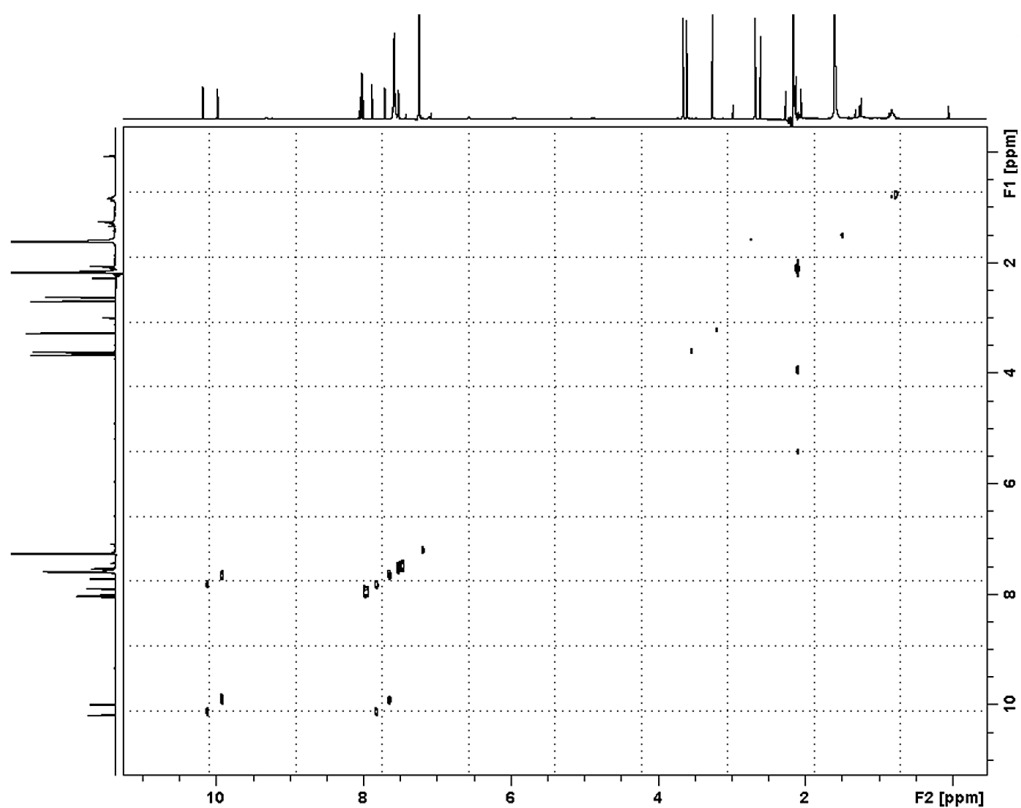
##### *Preparation of [Ru(dpp)(phen-NH<sub>2</sub>)(ox)] (3)*

[Ru(dpp)(phen)(DMSO)<sub>2</sub>Cl<sub>2</sub>] (680 mg, 1.096 mmol) and sodium oxalate (1.6 mmol) were heated at reflux in water (10 mL) for 90 min (orange solution). The reaction was cooled to RT. A hot solution of phen-NH<sub>2</sub> (1.096 mmol) in Ethylene Glycol (5 mL) was added to the reaction and was refluxed for 3 ½ h. The dark brown/purple mixture was cooled to RT and was added dropwise to stirring water (20 mL). After 30 min the dark purple precipitate formed was filtered through a 0.45 μm membrane and was washed with water (15 mL) and minimal acetone and dried overnight under vacuum. Yield isomer mixture: 620.3 mg (79 %). <sup>1</sup>H NMR (600 MHz, DMSO-d<sub>6</sub>) δ (ppm): 9.81 (dd, 2H); 9.69 (d, 1H); 9.38 (d, 1H), 8.64 (dd, 1H), 8.63-8.62 (2H), 8.51 (d, 1 H), 8.43-8.36 (m, 2H), 8.24 (d, 2H); 8.09 (dd, 1 H); 8.14-8.11 (dd, 2H); 8.07-8.04 (dd, 1H); 7.93-8.01 (6H), 7.81 (d, 1H), 7.65 (q, 1H); 7.42 (2 s, 1H); 7.13 (2 s, 2H).

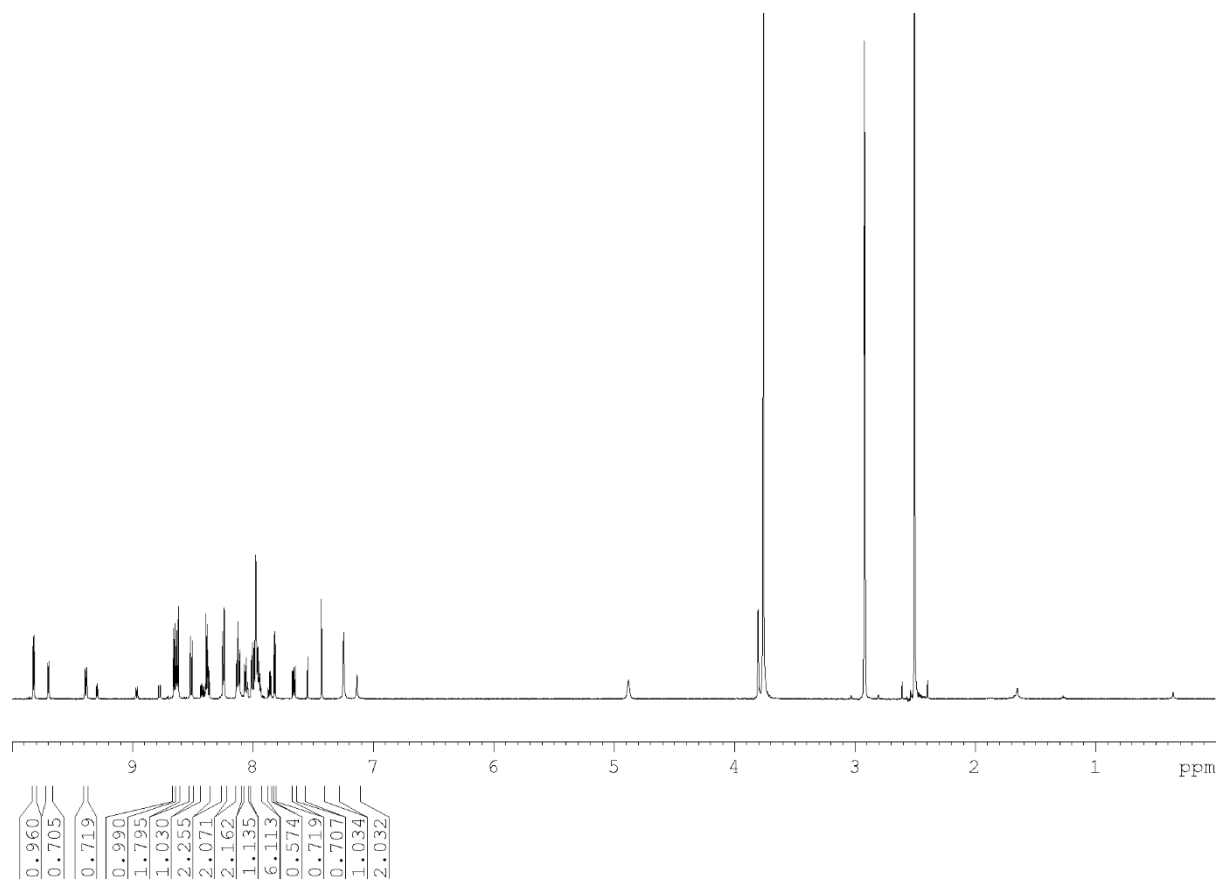
### S.5.1.1.2 NMR and Mass Spectrometry Analysis



**Figure S5. 1**  $^1\text{H}$  NMR of  $[\text{Ru}(\text{dpp})(\text{DMSO})_2\text{Cl}_2]$  (1) in  $\text{CDCl}_3$  with aromatic region of interest inset, 600 MHz.



**Figure S5. 2** COSY spectrum of **1** in  $\text{CDCl}_3$ , 600 MHz.



**Figure S5. 3**  $^1\text{H}$  NMR of  $[\text{Ru}(\text{dpp})(\text{phen-NH}_2)(\text{ox})]$  (**2**) in  $\text{DMSO-d}_6$ , 600 MHz.



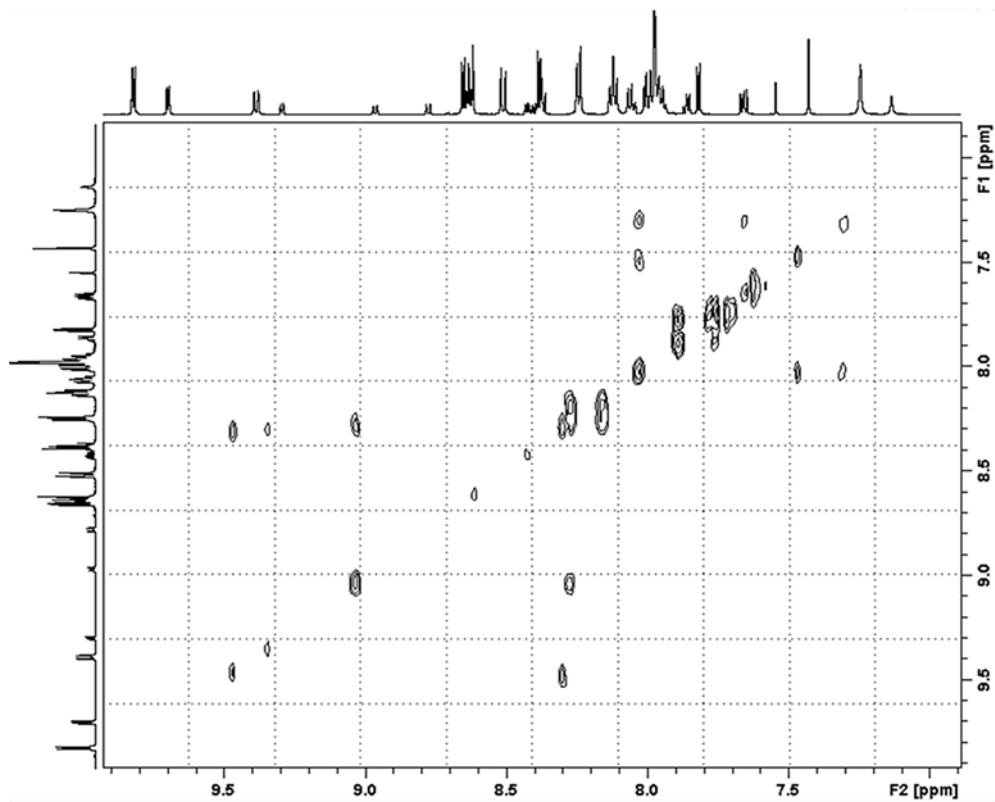
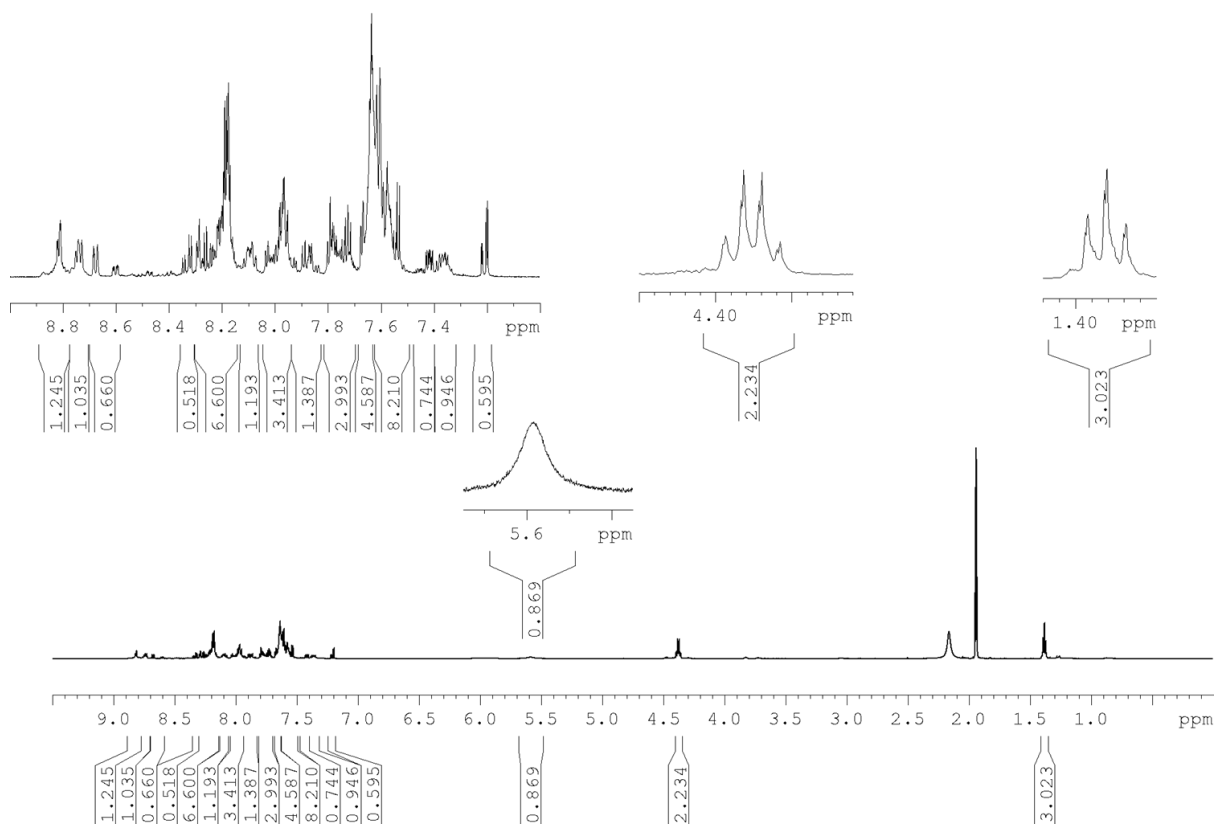
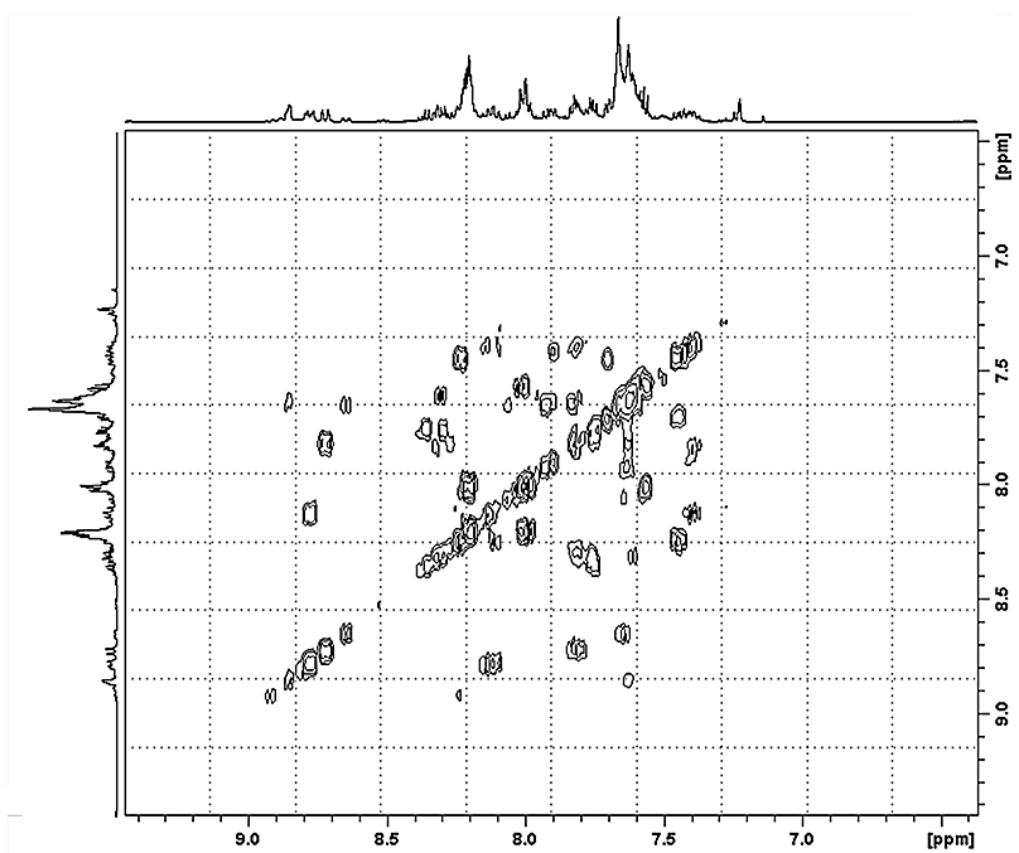
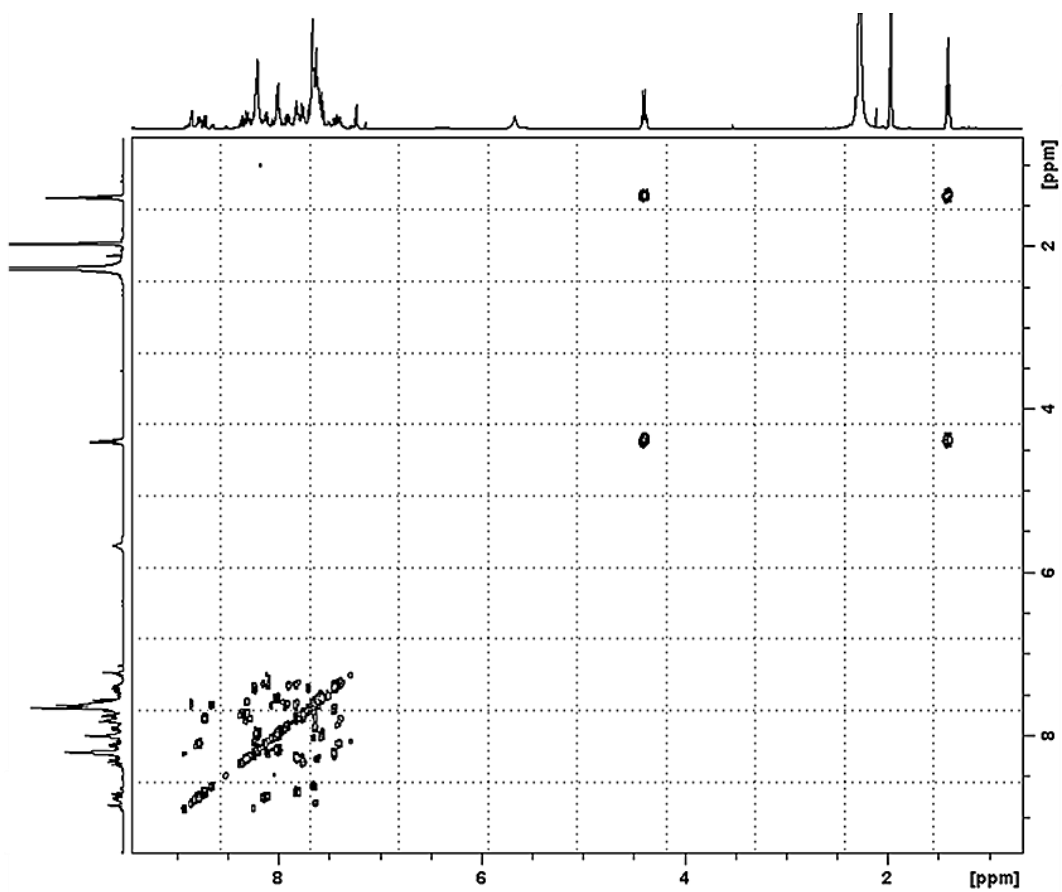


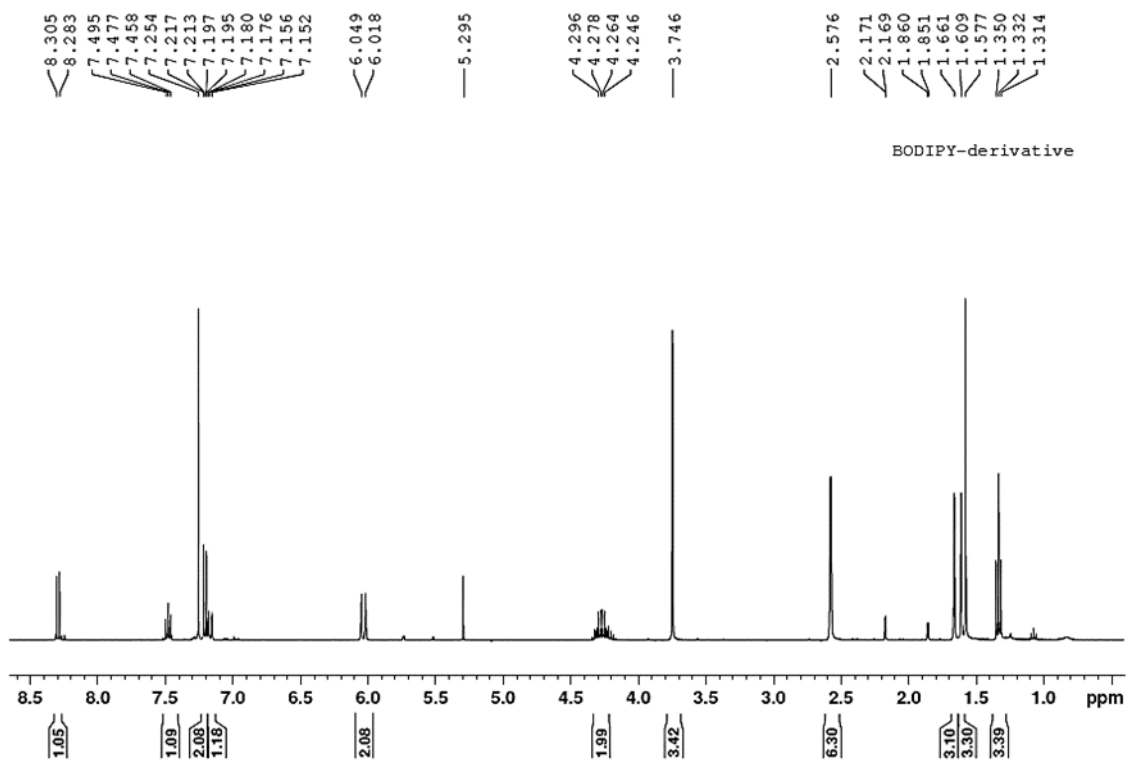
Figure S5. 4 COSY spectrum of **2** in DMSO-d<sub>6</sub>, 600 MHz



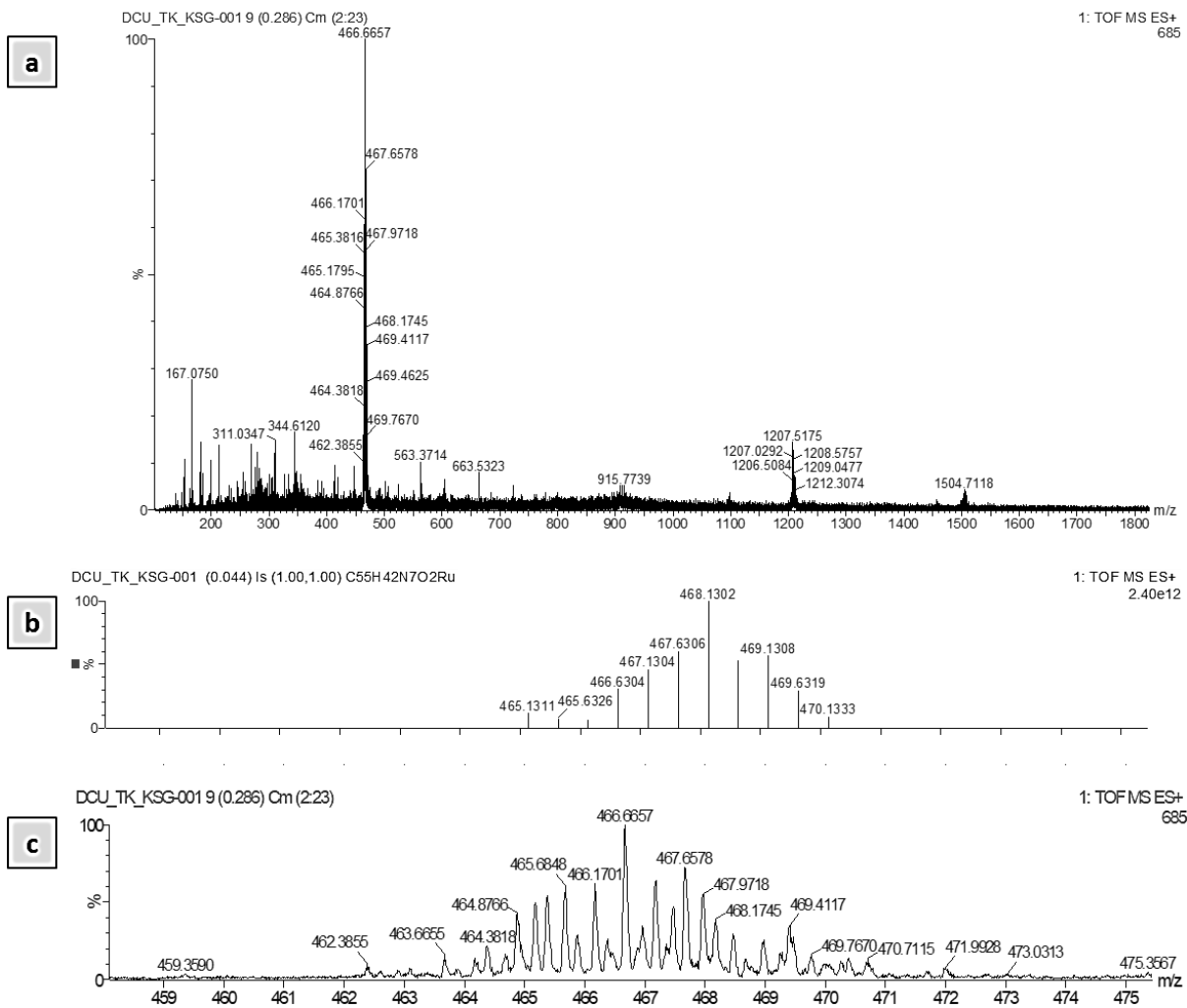
**Figure S5. 5**  $^1\text{H}$  NMR of  $[\text{Ru}(\text{dpp})(\text{phen-NH}_2)(\text{bpybenzCOEt})]^{2+}$  (**3**) in  $\text{MeCN-d}_3$ , 400 MHz.



**Figure S5. 6** Full range COSY spectrum (top) and expanded aromatic region of compound **3** in MeCN- $d_3$ , 400 MHz

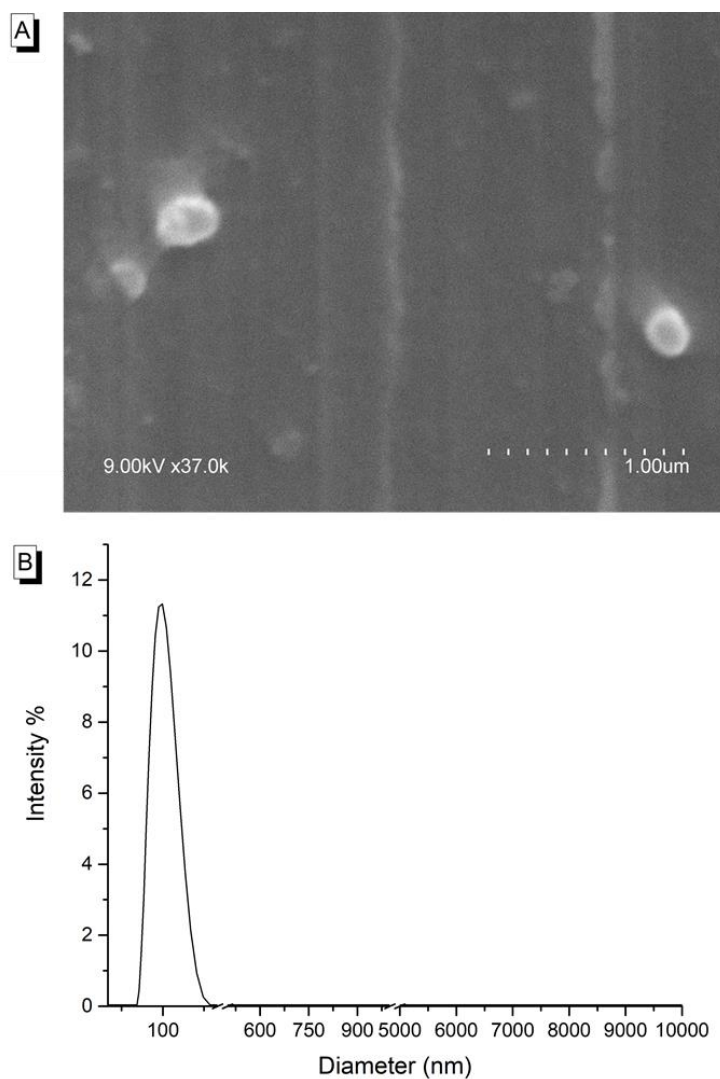


**Figure S5.**  $^7\text{H}$  NMR of 2, 6 diethyl- 1, 3, 5, 7- tetramethyl- 8-(2-fluorophenyl)-6 methoxy- 1, 5- naphthyridine-4,4'- difluoroboradiazaindacene (**BODIPY**) in  $\text{CDCl}_3$ , 400 MHz



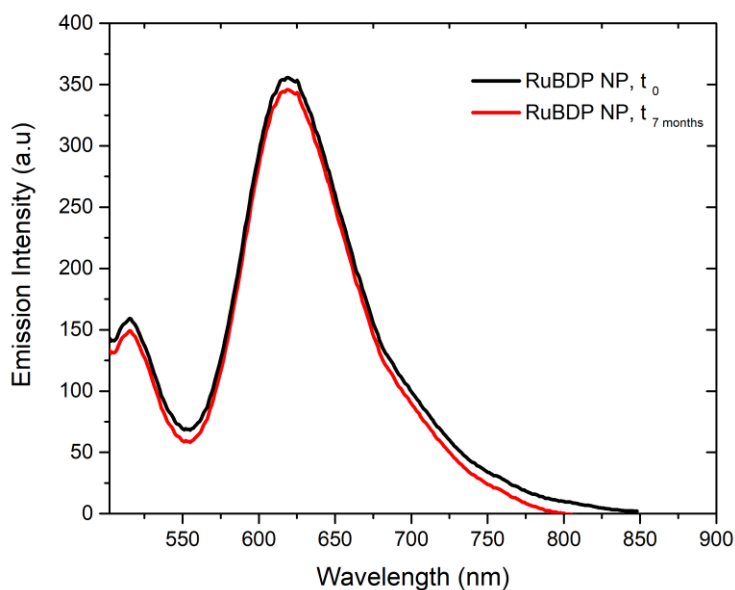
**Figure S5. 8** HR-MS of **3** in ESI (+) mode: (a) full range, (b) expansion of the isotope model and (c) expansion of the isotope pattern obtained from the mass spectrum.

### S.5.1.2 RuBDP NPs: SEM and DLS Characterization

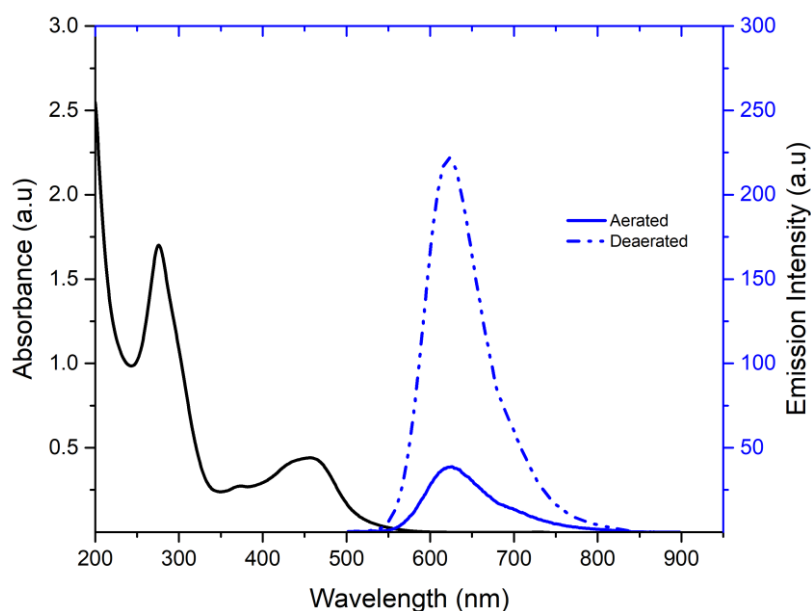


**Figure S5. 9** (A) SEM image (9.00 kV x 37.0k) (B) DLS intensity particle size distribution; Zeta potential was measured to be  $25 \pm 1.37$  mV and conductivity of 16.8 (n=3).

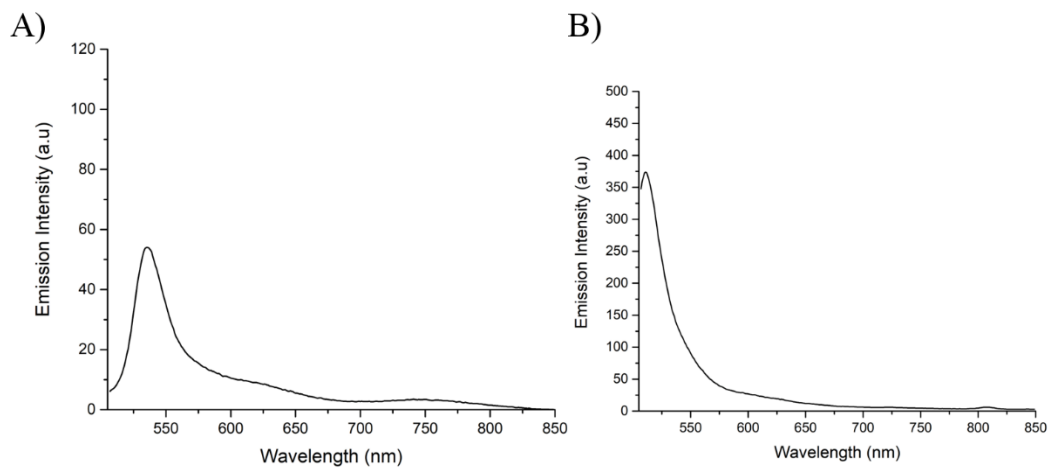
### S.5.1.3 Photophysical Characterisation of RuBDP components and nanoparticles



**Figure S5. 10** Emission spectra of a new and seven-month suspension of RuBDP NPs in PBS following excitation at 480 nm; excitation and emission slit widths set at 10 nm.

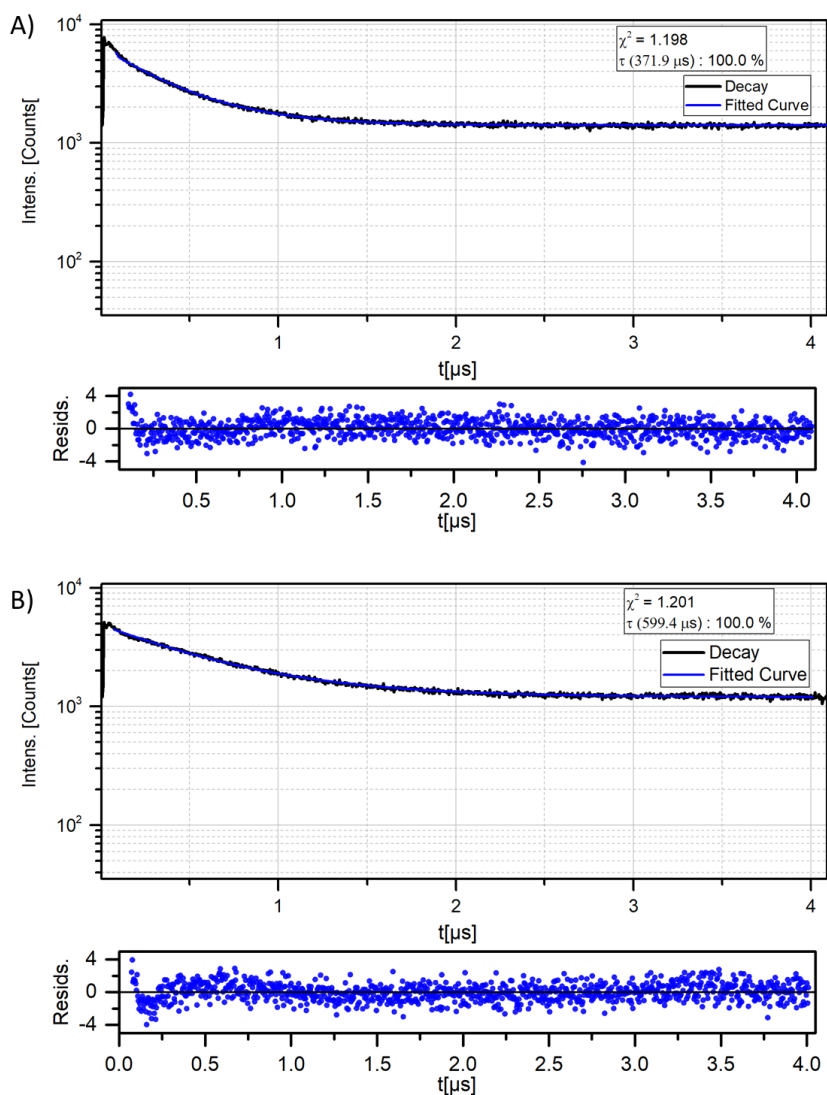


**Figure S5. 11** Absorbance and emission spectra of  $[\text{Ru}(\text{dpp})(\text{phen-NH}_2)(\text{bpy-benz-COOEt})]^{2+}$  in MeCN at  $15 \mu\text{M}$ . Emission spectra were recorded under aerated and deaerated conditions following excitation at 460 nm; excitation and emission slit widths set at 5 nm.



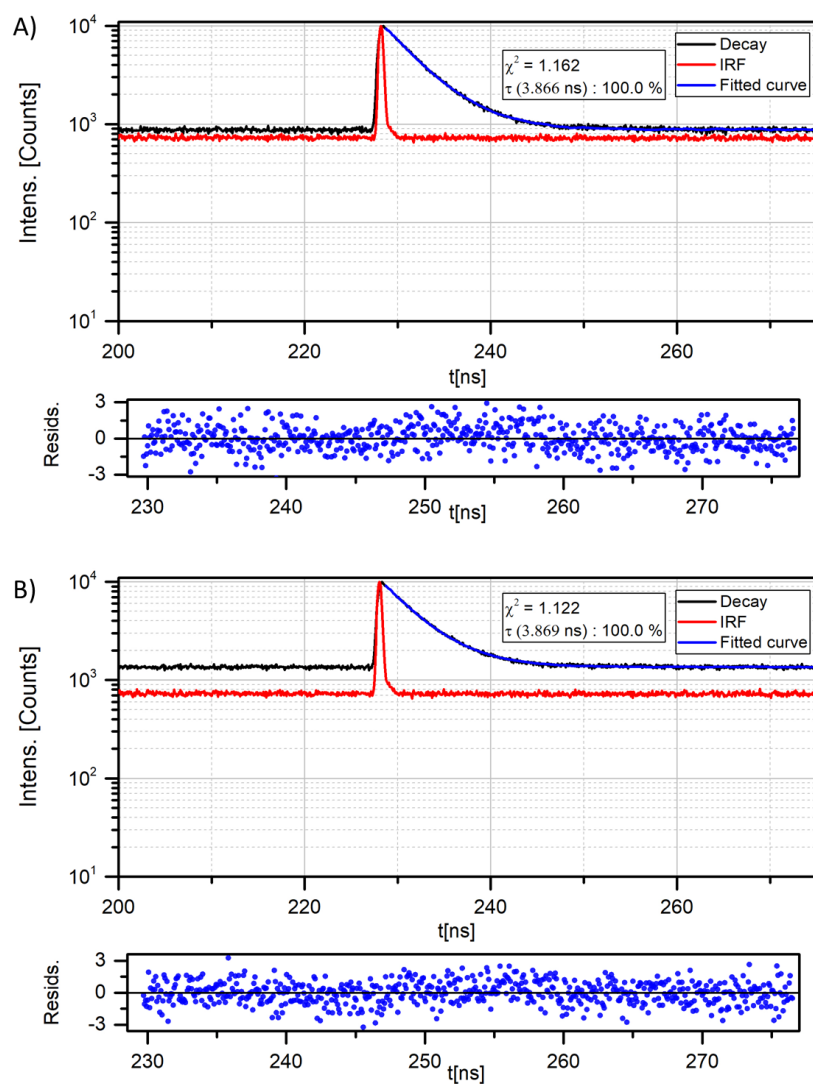
**Figure S5. 12** Emission spectra of (A) core-shell RuBODIPY particle- (previously reported)<sup>3</sup> and (B) core co-encapsulated RuBDP NPs - supernatant collected following swelling with THF.





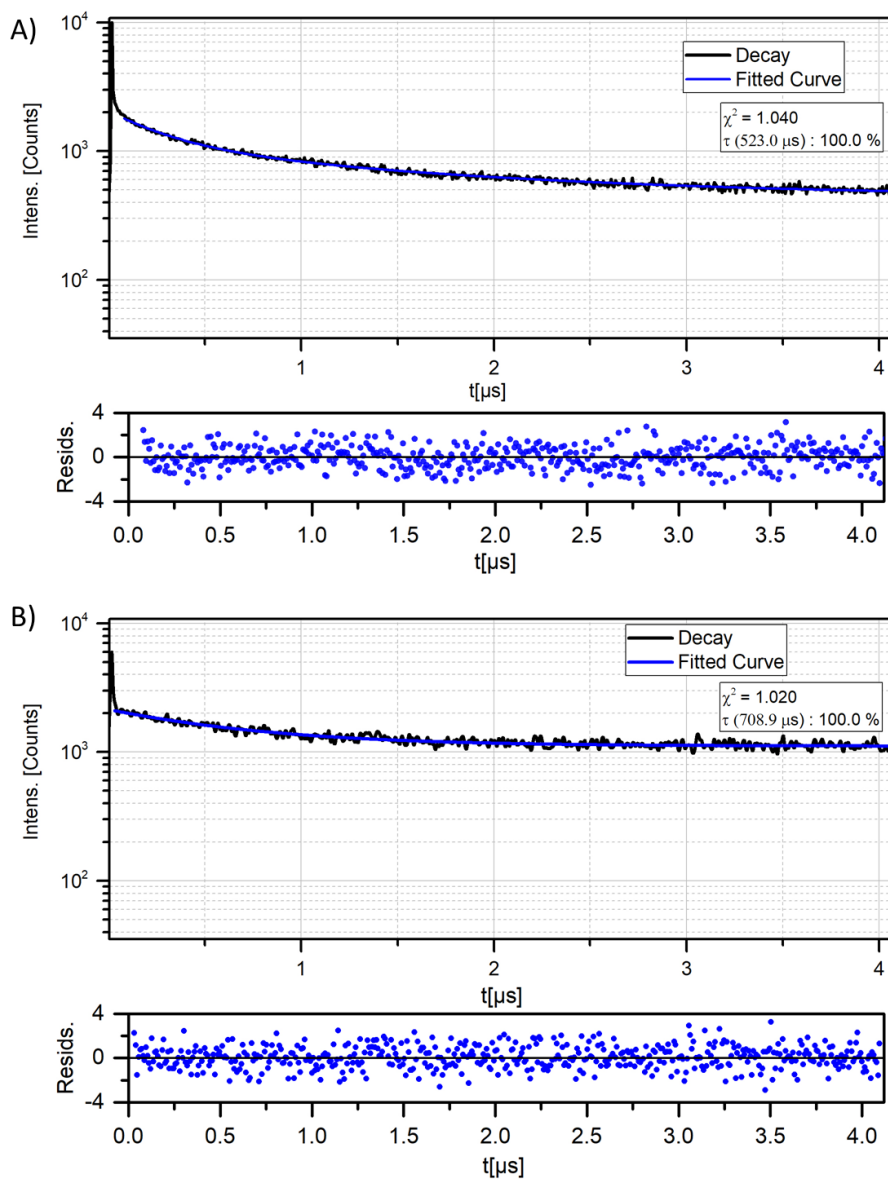
$$\int_{-\infty}^t IRF(t') \sum_{i=1}^x A_i e^{-\frac{t-t'}{\tau_i}} dt'$$

**Figure S5. 13** Emission Decays of parent complex  $[\text{Ru}(\text{dpp})(\text{phen-NH}_2)(\text{bpyArCOOEt})]^{2+}$  in aerated and deaerated acetonitrile (15  $\mu\text{M}$ ); Residual plots for the exponential fitting of both curves are shown below each plot.



$$\int_{-\infty}^t IRF(t') \sum_{i=1}^x A_i e^{-\frac{t-t'}{\tau_i}} dt'$$

**Figure S5. 14** Emission Decays of the BODIPY reference core component under (A) aerated and (B) deaerated conditions of RuBDP NPs in PBS (pH 7.4); Residual plots for the exponential fitting of both curves are shown below each plot.

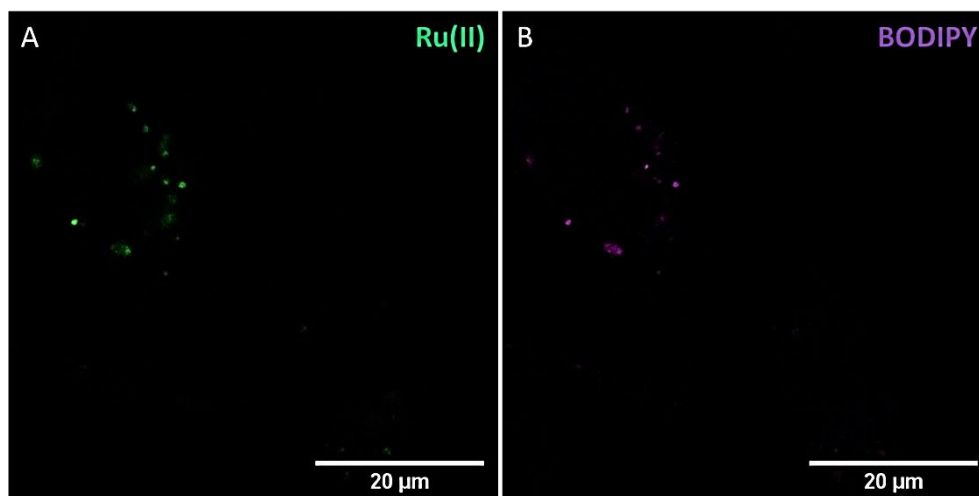


$$\int_{-\infty}^t IRF(t') \sum_{i=1}^x A_i e^{-\frac{t-t'}{\tau_i}} dt'$$

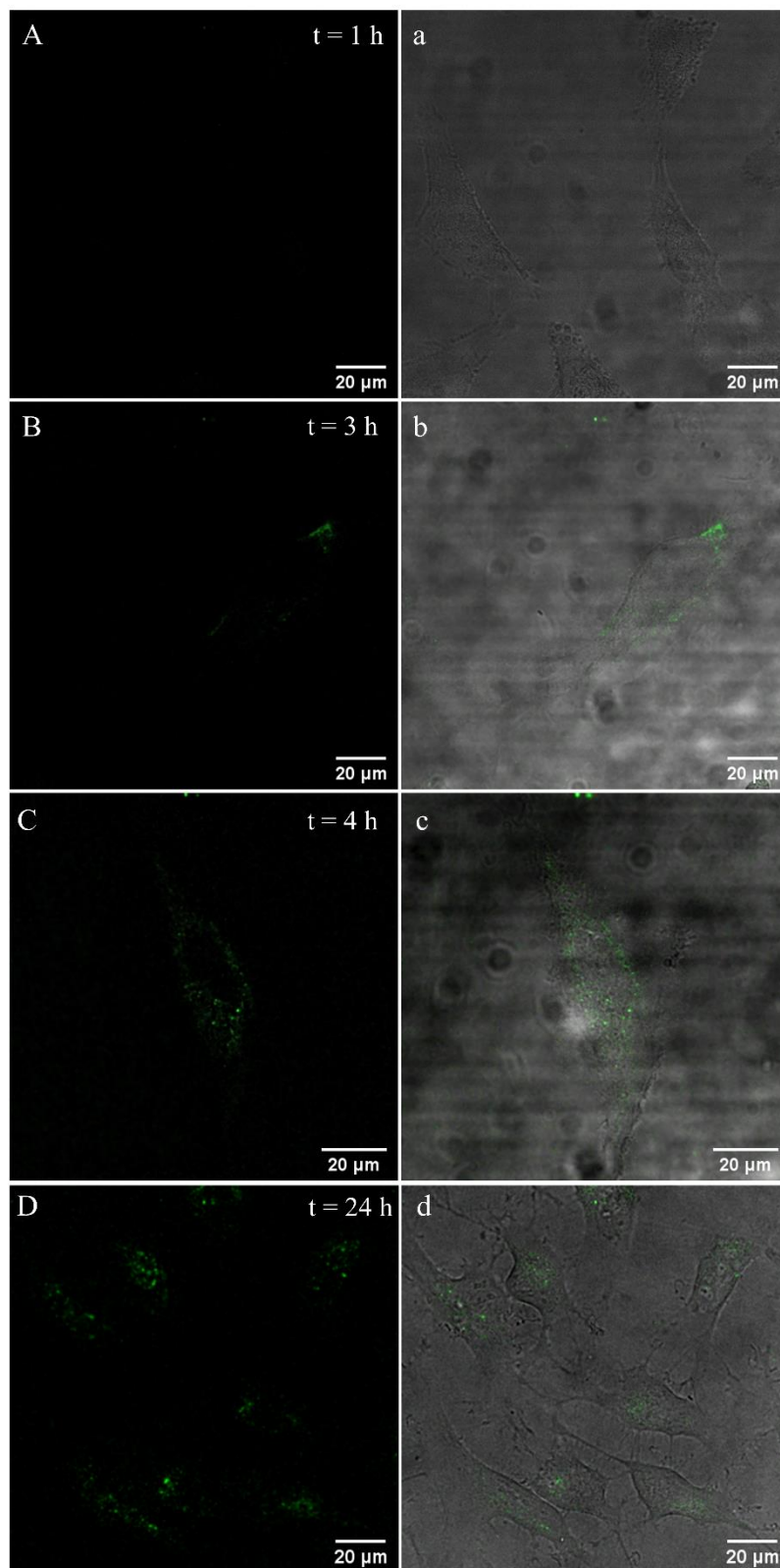
**Figure S5. 15** Emission Decays of the Ru(II) O<sub>2</sub> sensor core component under (A) aerated and (B) deaerated conditions of RuBDP NPs in PBS (pH 7.4); Residual plots for the exponential fitting of both curves are shown below each plot.

## S5.2 Cell Studies

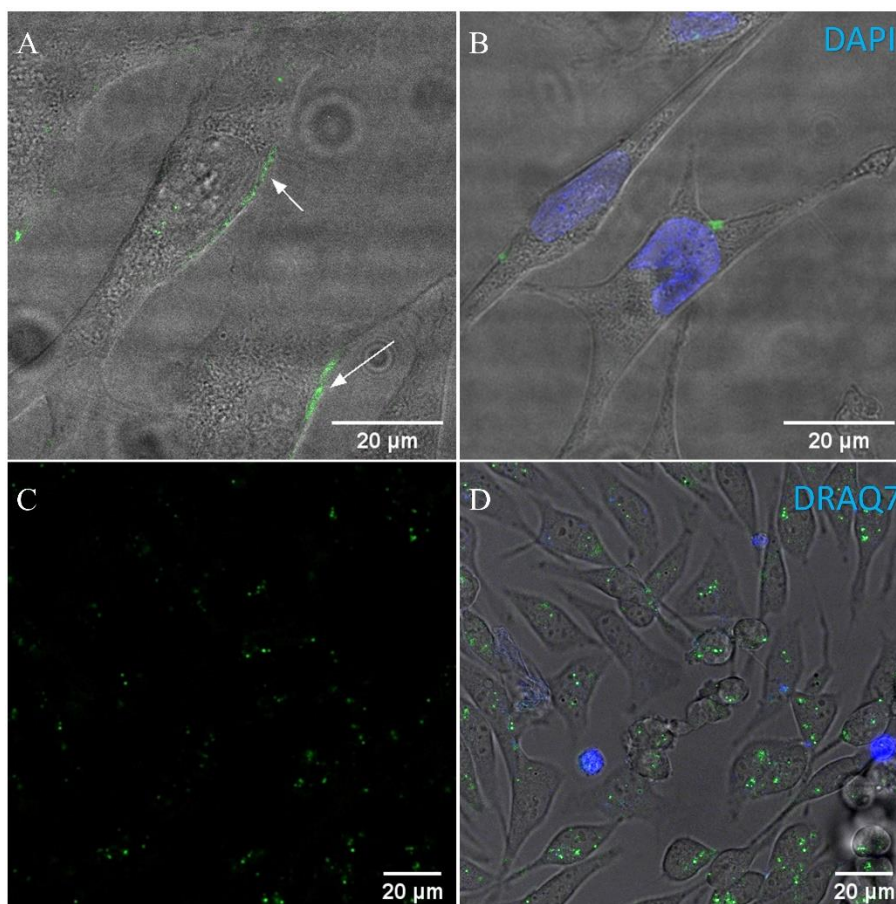
### S5.2.1 Uptake studies



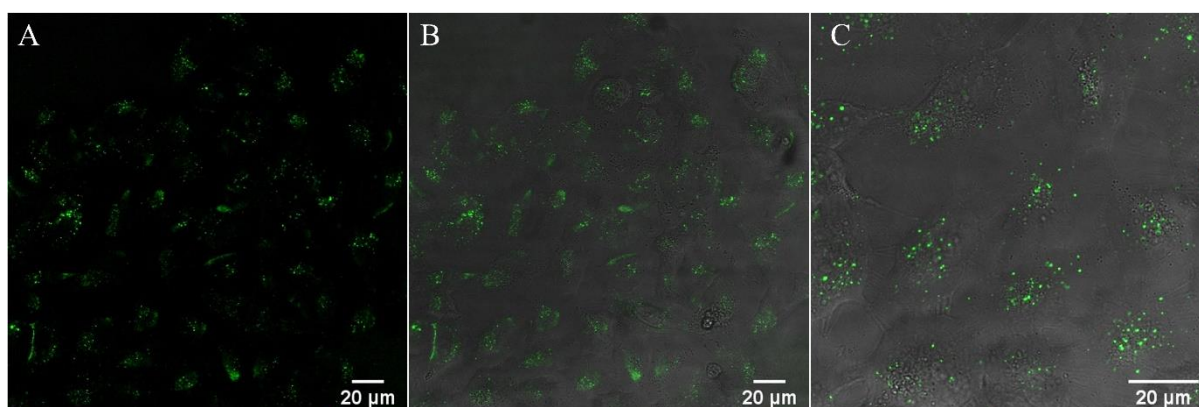
**Figure S5. 16** HeLa cells were treated with RuBDP NPs ( $4.5 \mu\text{g mL}^{-1}$ ), incubated for 4 h at  $37 \text{ }^\circ\text{C}$  and excited using 480 nm white light laser. (A) Emission collected within 569 – 850 nm corresponding to the  $[\text{Ru}(\text{dpp})(\text{phen-NH}_2)(\text{bpybenzCOOEt})]^{2+}$  component and (B) Emission collected within 505 – 550 nm corresponding to the BODIPY dye.



**Figure S5. 17** Confocal luminescence images of RuBDP NPs in live HeLa cells where the Ru(II) emission channel and overlay are shown. Cells were incubated in the absence of light with  $4.5 \mu\text{g mL}^{-1}$  nanoparticles over 24 h. RuBDP NPs were excited using 480 nm white light laser and the emission was collected between 569 nm and 800 nm for the Ru(II) channel.



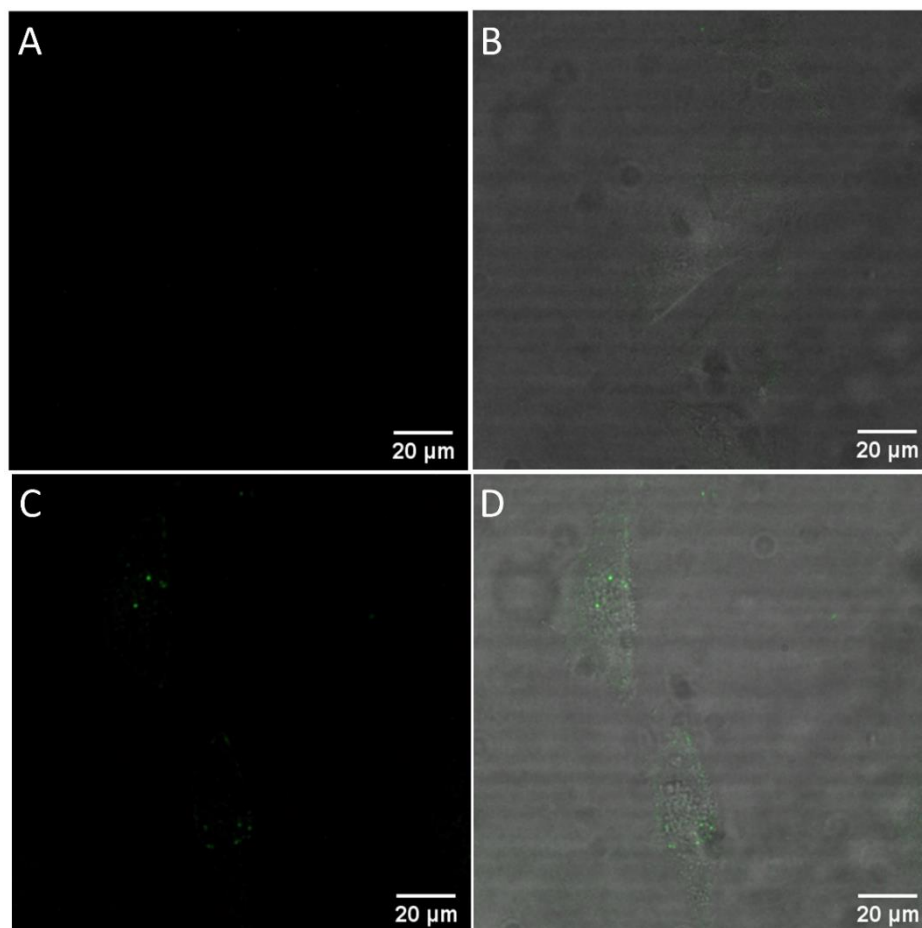
**Figure S5. 18** Uptake of RuBDP NPs in live CHO cells at variant concentrations and incubation periods. (A) Absence of NP internalization at  $4.5 \mu\text{g mL}^{-1}$  / 4 h incubation, (B) co-staining with DAPI probe ( $3 \mu\text{M}$ ), (C) Formation of NP aggregates at  $12 \mu\text{g mL}^{-1}$  / 24 h and (D) Cell debris and co-staining with DRAQ7 ( $3 \mu\text{M}$ ) revealed compromised cells. The 633 nm laser was used to excite DRAQ7 and emission was collected between 635 – 900 nm.



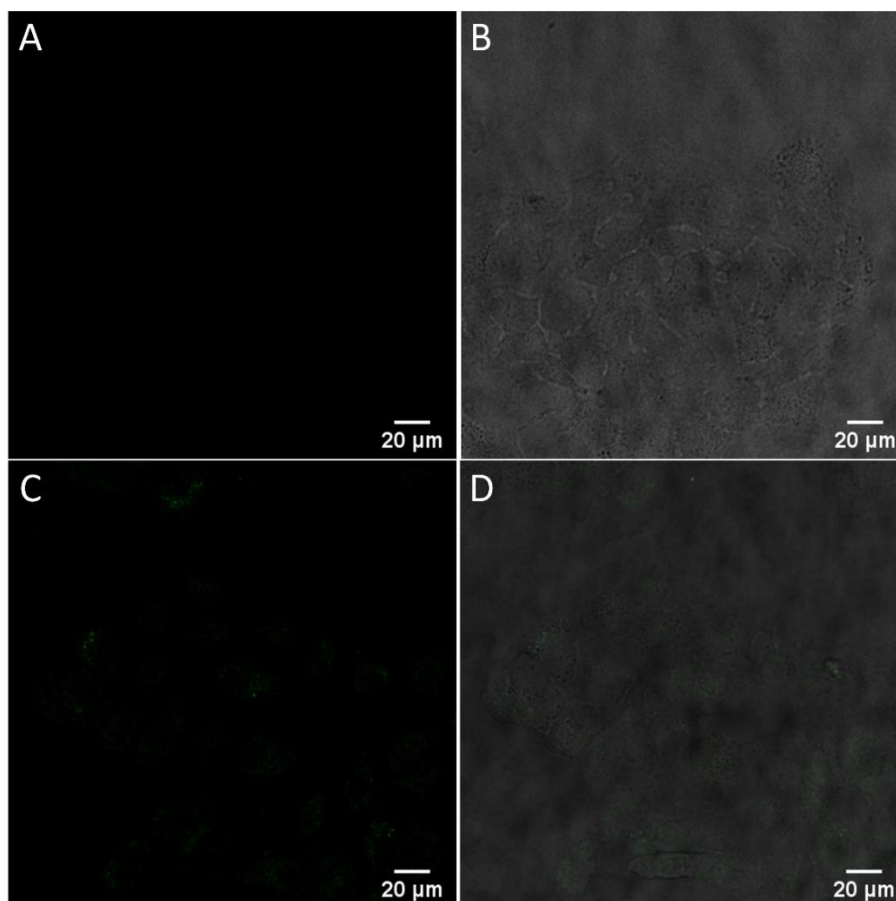
**Figure S5. 19** Confocal luminescence imaging of RuBDP NPs in live A549 cells showing efficient uptake of particles under the same conditions of  $4.5 \mu\text{g mL}^{-1}$  / 4 h in the absence of light at  $37 \text{ }^\circ\text{C}$  time (63X oil immersion objective lens). (A) RuBDP NPs were excited using the 480 nm white light laser



and the emission was collected between 569 nm and 800 nm for the Ru(II) channel. (B) Overlay with brightfield and (C) Overlay close-up image showing punctuate staining.

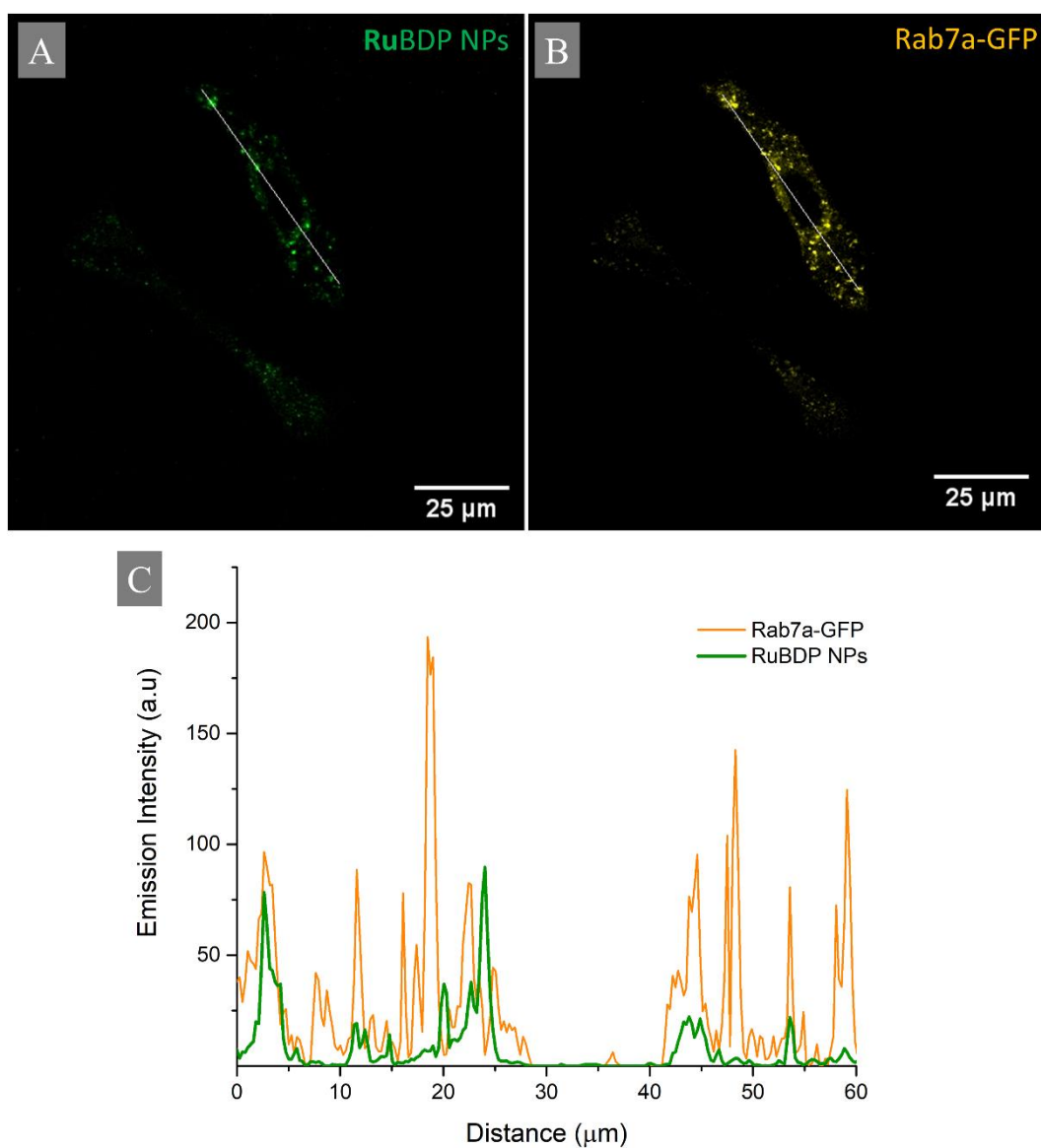


**Figure S5.** 20 HeLa cells were treated with RuBDP NPs ( $4.5 \mu\text{g mL}^{-1}$ ) and incubated for 4 h at  $4^\circ\text{C}$  time (63X oil immersion objective lens). Confocal imaging of RuBDP NPs (A) Throughout the cells (C) At the cell surface (B-D) Overlay images with brightfield. NPs were excited using the 480 nm white light laser and emission was collected between 569 - 800 nm.

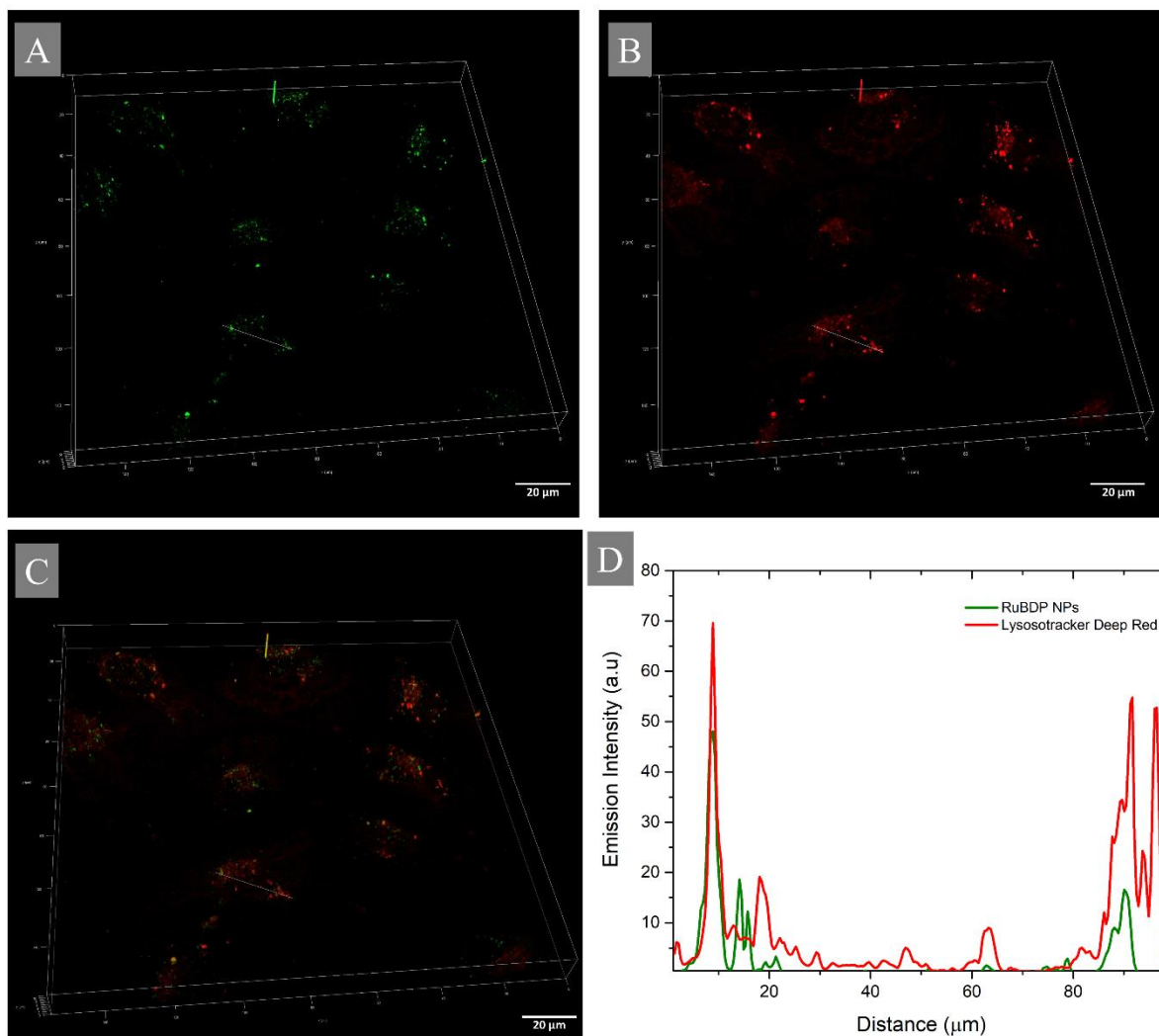


**Figure S5. 21** HeLa cells were treated with RuBDP NPs ( $4.5 \mu\text{g mL}^{-1}$ ) and incubated for 4 h at  $4^\circ\text{C}$  time (63X oil immersion objective lens). Confocal imaging of RuBDP NPs (A) Throughout the cells (C) At the cell surface (B-D) Overlay images with brightfield. NPs were excited using the 480 nm white light laser and emission was collected between 569 - 800 nm.

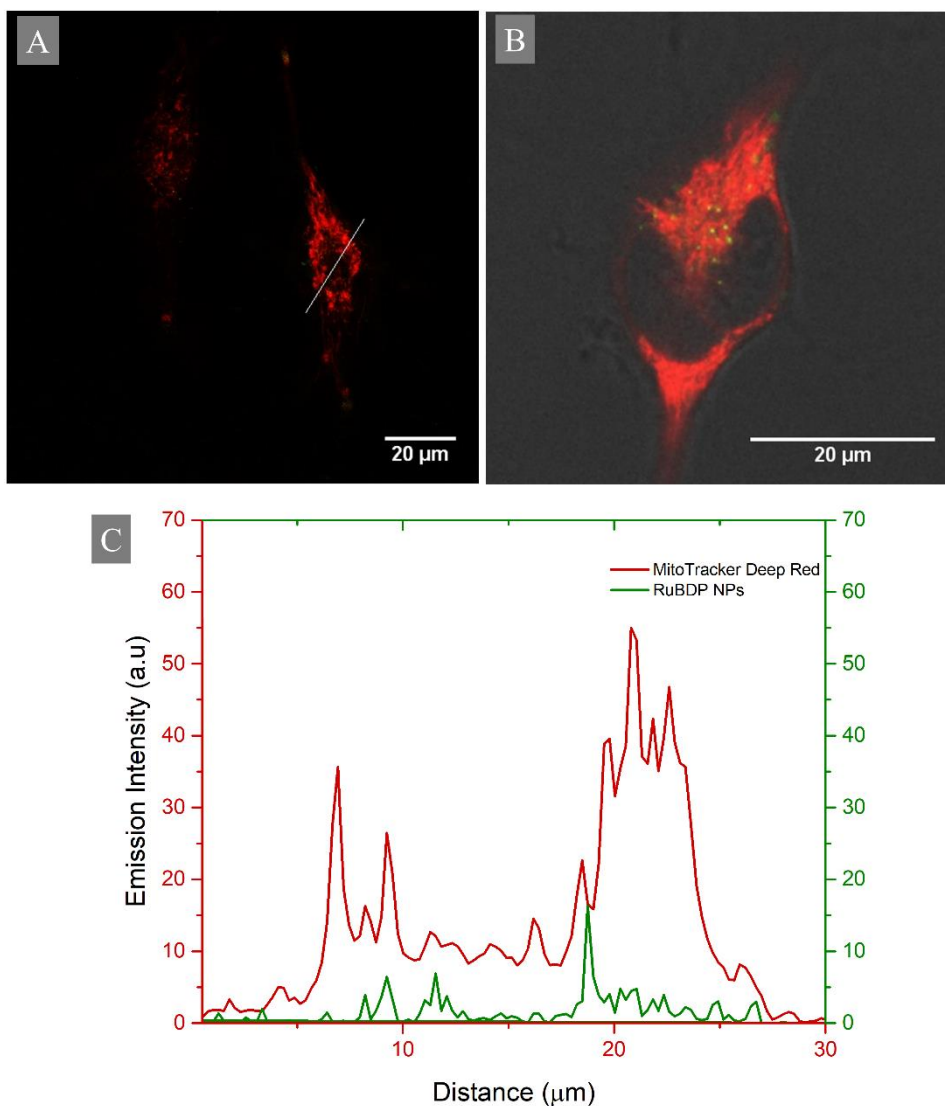




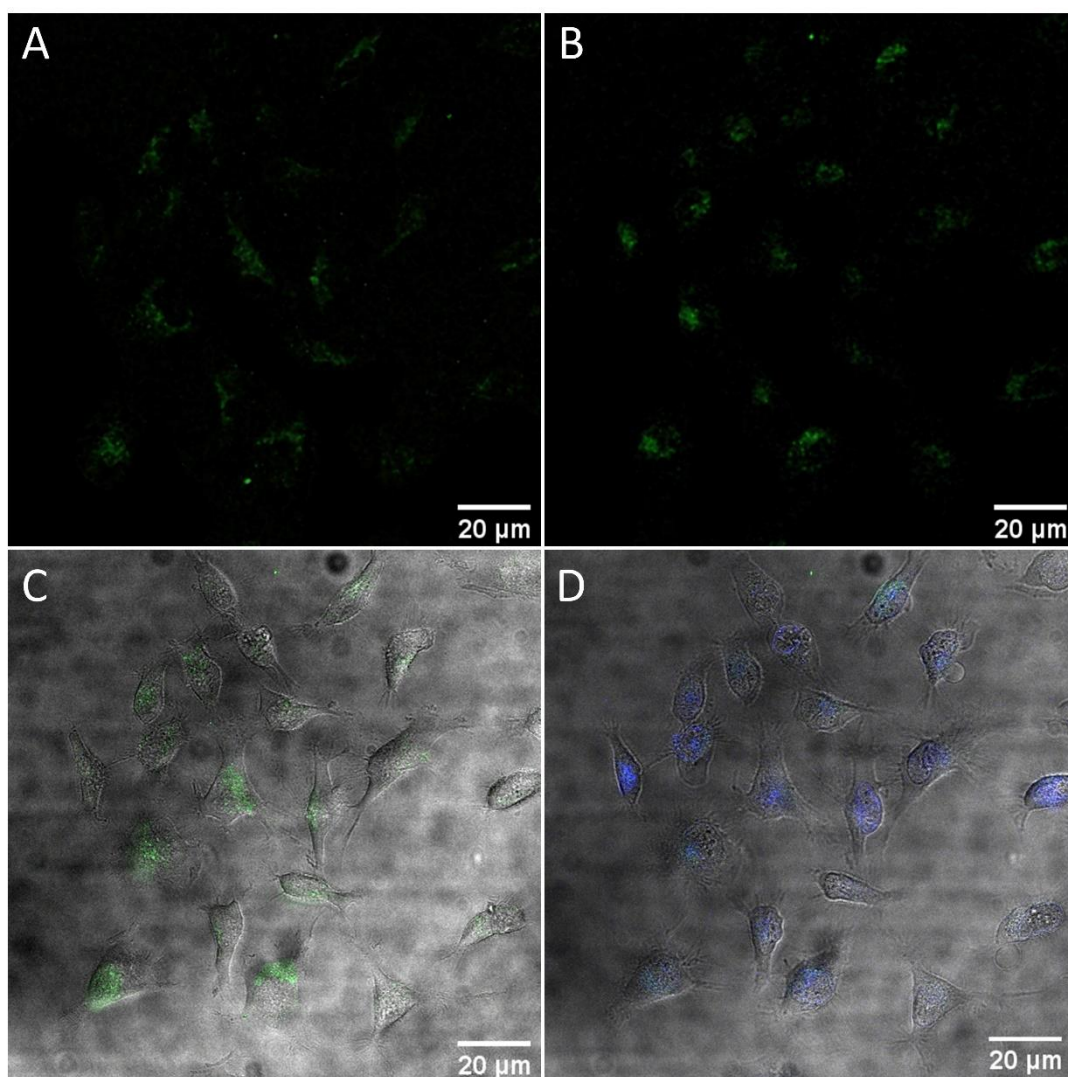
**Figure S5. 22** Co-localization study of RuBDP NPs with Late endosomal staining probe in live A549 cells. (A) Confocal image of Ru(II)- particle component (green) (B) Rab7a-GFP (yellow) and (C) The fluorescence intensity profile of RuBDP NPs and Rab7a-GFP showing strong co-localization between the particles and the late-endosome staining dye. (ImageJ).



**Figure S5. 23** Z-stack derived 3D Confocal Images of co-localization of RuBDP NPs with lysosomal staining probe in live HeLa cells where: (A) RuBDP NPs (green), (B) LysoTracker Deep Red (red;  $\lambda_{exc}$  647 nm,  $\lambda_{em}$  range: 650 – 800 nm)., (C) Merged image, (D) The fluorescence intensity profiles obtained revealing partial co-localization of RuBDP NPs with LysoTracker Deep Red (ImageJ).

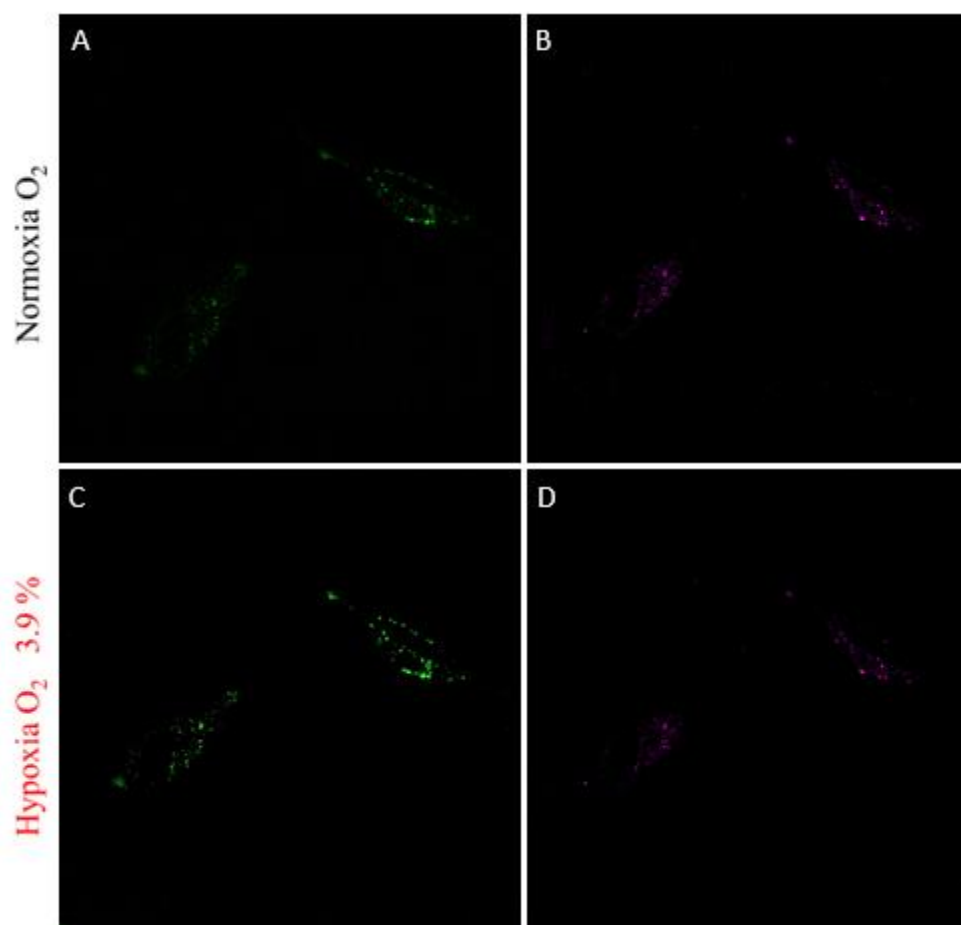


**Figure S5. 24** Co-localization of RuBDP NPs with MitoTracker Deep Red in live HeLa cells. (A-B) RuBDP (green) and MitoTracker Deep Red (red) merged images. (C) The fluorescence intensity profile of RuBDP NPs and MitoTracker Deep red obtained from the line profile across the cell (ImageJ) showed poor co-localization between the particles and the mitochondria-staining dye. MitoTracker Deep Red was excited using the 644 nm white light laser and emission was collected between 650 and 800 nm.



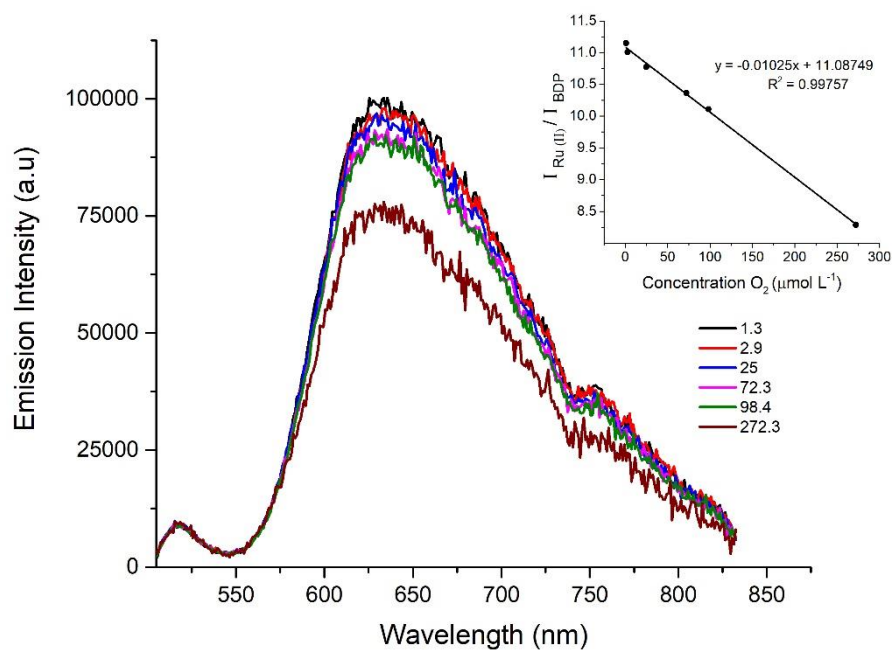
**Figure S5. 25** Phototoxicity of RuBDP NPs in HeLa cells using excitation with 480 nm over time (63 × oil immersion objective lens). (A) Confocal imaging of NPs at  $4.5 \mu\text{g mL}^{-1}$  at the 4 h timepoint, (C) overlay and absence of DRAQ7 confirm cell viability, (B) RuBDP NPs following 2 h of continuous irradiation, (D) overlay with DRAQ7 (blue) internalization confirms damaged cells.

## S5.2.2 Oxygen mapping

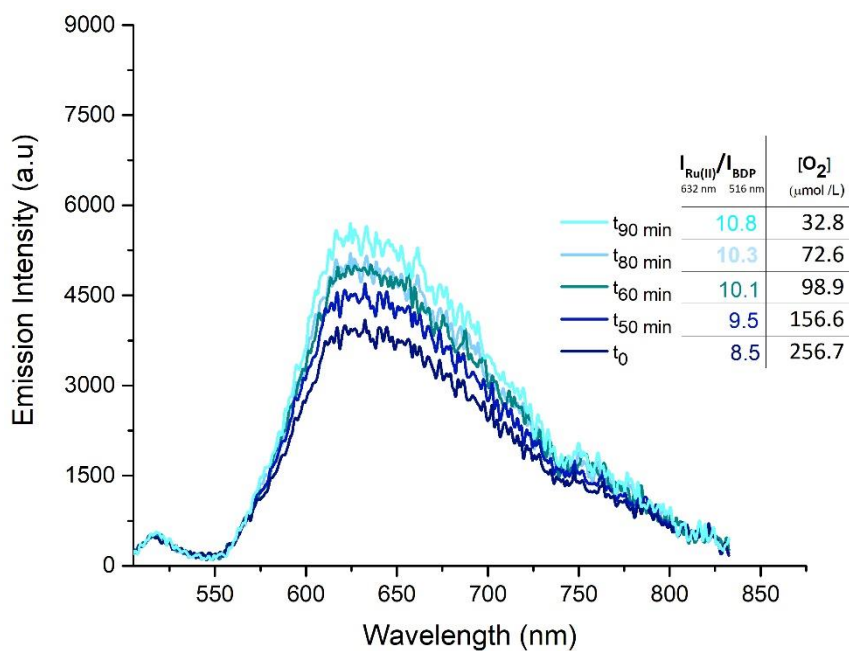


**Figure S5. 26** Confocal imaging of HeLa cells treated with RuBDP NPs at  $4.5 \mu\text{g mL}^{-1}$  for 4 h at  $37^\circ\text{C}$ . Emission was collected corresponding to (A, C) Ru(II) O<sub>2</sub> sensitive component and (B, D) BODIPY reference probe under normoxic and hypoxic conditions.

### S5.2.2 Plate reader-based ratiometric O<sub>2</sub> response assay



**Figure S5. 27** Emission spectra of RuBDP NPs in PBS (pH 7.4) recorded at different concentrations of oxygen on the ClarioStar Plus plate reader. The excitation wavelength was set to 480 nm with a detection range between 505 and 840 nm. Inset: Calibration ratiometric plot of the BODIPY and Ruthenium emission intensities, at 516 nm and 632 nm respectively, as a function of oxygen concentration ( $R^2$  0.99757).



**Figure S5. 28** RuBDP NPs ( $4.5\ \mu\text{g mL}^{-1}$ ) internalized in A549 cells were excited at 480nm and emission spectra between 505 and 840 nm were collected upon treatment with sodium sulfite ( $5\ \text{mg mL}^{-1}$ ). The Stern-Volmer equation obtained from the calibration plot above was used to determine the  $[\text{O}_2]$  in cells following treatment with sodium sulfite using the ratiometric signal of  $I_{\text{Ru(II)}\ 632\ \text{nm}}/I_{\text{BDP}\ 516\ \text{nm}}$ .

### S5.3 References

- 1 C. S. Burke and T. E. Keyes, *RSC Advances*, 2016, **6**, 40869–40877.
- 2 A. Martin, R. D. Moriarty, C. Long, R. J. Forster and T. E. Keyes, *Asian Journal of Organic Chemistry*, 2013, **2**, 763–778.
- 3 A. Byrne, J. Jacobs, C. S. Burke, A. Martin, A. Heise and T. E. Keyes, *Analyst*, 2017, **142**, 3400–3406.